DISS. ETH NO. 22413

# Multi-Physics Computational Modeling of Focused Ultrasound Therapies

A thesis submitted to attain the degree of
DOCTOR OF SCIENCES of ETH ZURICH
(Dr. sc. ETH Zurich)

presented by

**ADAMOS KYRIAKOU**

Diploma in Electrical and Computer Engineering
Democritus University of Thrace

born on 13.01.1987
citizen of Greece

accepted on the recommendation of

Prof. Dr. Gábor Székely, examiner
Prof. Dr. Niels Kuster, co-examiner
Prof. Dr. Theodoros Samaras, co-examiner

2015

To my mama bear…

# Contents

## II  Numerical Modeling of Acoustic Wave Propagation  71

## 4  Mathematical Models of Acoustic Wave Propagation  73

# IV  Epilogue                                                            263

# 11 Summary & Conclusions                                               265

# 12 Next Steps                                                          267

# V  Appendix                                                            269

# A  List of Acronyms                                                    271

# B  List of Symbols                                                     275

# C  List of Publications                                                277

# Abstract

The possibility to apply ultrasonic waves, i.e., high-frequency acoustic waves, for therapeutic purposes was recognized over 60 years ago. Chapter 1 of this dissertation establishes the fundamental physics and mechanisms of ultrasound. However, it was only after the 1990s – when technological breakthroughs, such as magnetic resonance thermometry and magnetic-resonance-compatible piezoelectric materials were made – that focused ultrasound (FUS) emerged as a promising non-invasive alternative to interventional therapies. Chapter 2 details the hardware technology and reviews modern therapeutic systems that utilize FUS.

With FUS, acoustic energy can be precisely and controllably deposited into a focal spot deep within the body to achieve specific therapeutic goals by induction of various physical effects, with no ionizing radiation and without harm to the overlying or surrounding tissues. In addition to mainstream applications in lithotripsy and physiotherapy, successful utilization of FUS has been demonstrated in clinical trials in the fields of neurosurgery for neuropathic pain, essential tremor, and motor disorders, as well as in ablative oncology for cerebral, hepatic, renal, and uterine tumors, to name but a few. Furthermore, the technology has been evaluated for ground-breaking applications such as thrombolysis, targeted and controlled delivery of therapeutic agents — in particular, blood-brain barrier disruption for increased drug permeability — and neuromodulation. However, with the exception of prostatic oncology and the treatment of uterine fibroids, therapeutic FUS has seen limited acceptance by the clinical community. The sheer physical and technical complexity of the modality in conjunction with the need to administer sonication at high power warrants patient-specific treatment planning to minimize risk to the patient as well as to optimize treatment efficiency. A detailed review of available therapeutic applications, the current clinical state-of-the-art, as well as the physical and technological challenges that inhibit widespread application of FUS can be found in Chapter 3. Excerpts from the aforementioned three chapters, most notably the challenges posed by utilization of FUS, were included in a review published in the *International Journal of Hyperthermia* (see Appendix, C).

A software tool to simulate the complex medical scenarios involving propagation of ultrasonic waves is needed to provide better treatment analysis for improved outcomes and offer comprehensive understanding of the underlying processes and mechanisms of FUS.

In addition, such a tool could be used to predict and, therefore, prevent possible negative side effects of these procedures. However, modeling of ultrasonic wave propagation needs to be complemented by numerical modeling of additional physics, most notably regarding the transfer of thermal energy in living organisms. Furthermore, such a tool would need to be embedded within a framework of tools to enable the flexible, yet precise, employment and representation of the geometry and properties of model FUS applicators used in patient-specific anatomical models, as well as flexible visualization and post-processing of the simulation results. Finally, the simulations need to be feasible within reasonable time-frames without the need for cluster-grade computer hardware, the purchase and maintenance of which is too costly to be affordable for most clinical institutions. The development of a novel high-performance computational multi-physics framework to fullfil these requirements constitutes the primary objective of the work in this dissertation.

Dedicated linear and nonlinear acoustic solvers were developed and integrated within a simulation platform to allow full-wave 3D simulation of ultrasonic wave propagation in complicated setups. In the majority of previously available solutions, fundamental models of acoustic wave propagation are used to perform modeling in simplified depictions of human anatomy; Chapter 4 reviews the most commonly used models. In contrast, the framework presented herein allows simulation of detailed inhomogeneous anatomical models generated from medical image data and utilizes accurate propagation models that allow the full complexity of FUS therapy to be taken into account, as described in Chapter 5.

As detailed in Chapter 6, the solvers are complemented by flexible geometric modeling, image segmentation, visualization, and post-processing tools that allow for rapid and precise acoustic and thermal modeling of FUS treatment protocols. Furthermore, utilization of modern but affordable computer hardware, combined with state-of-the-art high-performance computing techniques, enables acoustic and thermal simulation of realistic therapeutic FUS therapies within minutes on a scale that was previously unachievable.

Chapter 7 outlines the analytical solutions, alternative numerical methods, and experimental measurement setups used to perform the validation of the developed acoustic solvers. A paper that describes the development, implementation, parallelization, and validation of the framework, corresponding to Chapters 5-7, is being drafted for submission to *IEEE Transactions on Ultrasonics, Ferroelectrics, and Frequency Control*.

The primary novelty of this work lies in the application of the new platform to realistic FUS treatment scenarios to target the specific challenges that impede the widespread usage and acceptance of FUS technology. Chapter 8 describes the application of transcranial FUS therapies to target neurological conditions, focusing on skull-induced aberration correction techniques and the impact on the resulting pressure and temperature distributions. An extended version of this chapter's preface, which provides a comprehensive overview of over 20 years of research on skull-induced aberration correction techniques, was re-

cently published in the *International Journal of Hyperthermia* and featured on the issue cover (see Appendix C). The numerical study presented in the same chapter constitutes a paper in itself, which has been submitted to *Journal of Therapeutic Ultrasound*.

Chapter 9 pertains primarily to FUS hepatic tumor ablation and the investigation of techniques to compensate for respiration-induced organ motion and intercostal targeting during the FUS treatment of abdominal organs. A manuscript on this work is being prepared for submission to the *Journal of Therapeutic Ultrasound*. Chapter 10 explores approaches aimed at reducing the treatment times involved in ultrasonic ablation of large solid malignancies, where acoustic and thermal simulations are used to investigate the impact of scanning approaches, the presence of vasculature in the vicinity of the tumor, and the effects of standing-wave on therapeutic efficacy. Finally, Chapters 11 and 12 summarize the primary findings and novelty of the overall work and provides an outlook towards possible future extensions and enhancements.

It is believed that this newly developed framework can be used to quickly and accurately model a large variety of therapeutic FUS applications, provide the means for the rapid design, evaluation, and optimization of novel delivery systems, allow the assessment of risk inherent in various therapies, and ultimately permit patient-specific treatment planning and optimization. It is hoped that the increased flexibility and computational speed of this framework, in conjunction with the enhanced accuracy and realism, will be utilized towards improving the safety and efficiency of ultrasound therapies and promote acceptance by the medical community of this promising technology.

# Zusammenfassung

Die Möglichkeit der Verwendung von Ultraschallwellen, d.h., Hochfrequenz-Schallwellen, für therapeutische Zwecke wurde vor über 60 Jahren erkannt. Kapitel 1 präsentiert die Physik und Mechanismen von Ultraschall. Allerdings erwies sich fokussierten Ultraschall (FUS) erst nach den 1990er Jahren — als Technologien wie Magnetresonanz-Thermometrie und magnetresonanzkompatible piezoelektrische Materialien entwickelt wurden — als vielversprechende nicht-invasive Alternative zur interventionellen Therapien. Kapitel 2 behandelt die Hardware-Technologie und modernen Therapiesysteme, die FUS einsetzen.

FUS kann präzise akustische Energie in einem steuerbaren Fokus tief im Körper deponieren, und dadurch spezifische Therapieziele durch verschiedene physikalische Effekte erreichen, ohne ionisierende Strahlung und ohne Schäden in überlagerten oder umliegenden Geweben. Zusätzlich zu seinen Hauptanwendungen, der Lithotripsie und Physiotherapie, haben klinische Studien erfolgreiche Anwendung von FUS in verschiedenen Bereichen nachgewiesen, wie zum Beispiel im Bereich Neurochirurgie zur Behandlung neuropathischer Schmerzen, essentiellen Tremors und Bewegungsstörungen, und im Bereich ablative Onkologie (zerebrale, Leber-, Nieren- und Gebärmuttertumore, um nur einige zu nennen. Außerdem wurde die Nützlichkeit dieser Technik fr bahnbrechende Anwendungen wie Thrombolyse, gezielte und kontrollierte Abgabe von therapeutischen Wirkstoffen – vor allem Blut-Hirnschranken-Öffnung für verbesserte Arzneimittelpermeabilität – und Neuromodulation untersucht. Doch mit Ausnahme von Prostataokologie und der Behandlung von Uterusmyomen hat therapeutischer FUS nur begrenzte Akzeptanz durch die klinische Gemeinschaft erfahren. Die physikalische und technische Komplexitt dieser Modalität in Verbindung mit der Verabreichung hochenergetischer Beschallung machen patientenspezifische Behandlungsplanung erforderlich, um die Risiken für den Patienten zu minimieren sowie die Effizienz der Behandlung zu optimieren. Eine detaillierte Übersicht der verfügbaren therapeutischen Anwendungen und ihres aktuellen klinischen Standes, sowie die physikalischen und technologischen Herausforderungen, welche eine weit verbreitete Anwendung von FUS verhindern, kann in Kapitel 3 gefunden werden. Auszüge aus den oben genannten drei Kapiteln, vor allem im Zusammenhang mit den Herausforderungen der Nutzung von FUS, sind Teil einer veröffentlichten Rezension im *International Journal of Hyperthermie* (siehe Anhang C).

Ein Software Tool für die Simulation komplexer medizinischer Szenarien, welchen die Ausbreitung von Ultraschallwellen zugrundeliegt, könnte verbesserte Behandlungsanalyse und ergebnisse, sowie umfassendes Verständnis der zugrundeliegenden Prozesse und Mechanismen ermöglichen. Zusätzlich könnte solch ein Werkzeug verwendet werden, um negative Nebenwirkungen dieser Verfahren vorherzusagen und somit zu vermeiden. Die Simulation der Ausbreitung von Ultraschallwellen muss hierzu durch die numerische Modellierung zusätzlicher physikalischer Phänomene, insbesondere der Wärmeübertragung in lebenden Organismen, ergänzt werden. Darüber hinaus muss ein solches Simulationswerkzeug in eine Plattform eingebettet werden, welche die flexible, aber dennoch präzise, Modellierung solcher Behandlungsanordnungen, d.h. Applikatormodellierung und Einsatz patientenspezifischer anatomischer Modelle (Gewebegeometrie und eigenschaften), sowie flexible Visualisierung und Prozessierung der Simulationsergebnisse ermöglicht. Schließlich müssen diese Simulationen innert einem akzeptablem Zeitrahmen durchführbar sein, ohne cluster-grade Computer-Hardware zu benötigen, deren Anschaffungs- und Wartungskosten durch klinische Einrichtungen nicht getragen werden knnen. Die Entwicklung einer neuartigen, hochleistungsrechenbefähigten Multi-Physik Simulationsplattform, welche die vorgenannten Anforderungen erfüllt, bildeten das Hauptziel dieser Arbeit.

Optimierte lineare und nichtlineare akustische Löser wurden entwickelt und innerhalb einer Simulationsplattform integriert, sodass full-wave 3D-Simulation von Ultraschallwellenausbreitung in komplizierten Anordnungen möglich wird. In der Mehrzahl der zuvor verfügbaren Simulationswerkzeuge basiert die Modellierung auf stilisierten Darstellungen der menschlichen Anatomie und werden vereinfachte Modelle akustischer Wellenausbreitung verwendet; siehe Kapitel 4 für eine Analyse der prominentesten Modelle. Im Gegensatz zu diesen ermöglicht die vorgestellte Plattform die Simulation von detaillierten, inhomogenen anatomischen Modellen, welche basierend auf medizinischen Bilddaten erzeugt werden können, und nutzt genaue Ausbreitungsmodelle, wodurch die Komplexität von FUS-Therapien vollumfänglich erfasst werden kann, wie in Kapitel 5.

Wie in Kapitel 6 beschrieben, werden diese Löser durch flexible geometrische Modellierung, Bildsegmentierung, Visualisierung, und Post-Processing Tools ergänzt, welche eine schnelle und präzise akustische und thermische Modellierung von FUS Behandlungen ermöglichen. Die Nutzung moderner, aber erschwinglicher, Computer-Hardware, kombiniert mit Hochleistungsrechentechniken, erlaubt realistische akustische und thermische Simulationen von therapeutischen FUS Anwedungen innert Minuten, und das auf einem Niveau, welches bisher unerreichbar war.

Im Anschluss an die Präsentation der Plattform wird im Kapitel 7 die Validierung des entwickelten Akustiklösers dargelegt, welche durch Vergleich mit analytischen Lösungen, alternativen numerischen Methoden und experimentellen Messungen erfolgte. Ein Paper zur Plattform, deren Entwicklung, Anwendung, Parallelisierung, und Validierung, siehe Kapitel 5-7, ist in Vorbereitung und wird bei *IEEE Transactions on Ultrasonics, Ferroelectrics, and Frequency Control* eingereicht werden.

Die primäre Neuheit dieser Arbeit liegt in der Anwendung der neuen Plattform auf realistische FUS Behandlungsszenarien, um bestimmte Herausforderungen, welche die verbreitete Nutzung und Akzeptanz dieser Technologie behindern, zu meistern. Kapitel 8 beschreibt die Anwendung auf transkranielle fokussierte Ultraschalltherapien zur Behandlung neurologischer Erkrankungen, und konzentriert sich auf Techniken zur Korrektur von schädelinduzierten Aberrationen, sowie deren Auswirkungen auf die resultierenden Druck und Temperaturverteilungen. Eine erweiterte Version der Einführung dieses Kapitels, welche einen umfassenden Überblick über mehr als 20 Jahren Forschung zur Kompensation von schädelinduzierten Aberrationen bietet, wurde kürzlich im *International Journal of Hyperthermia* veröffentlicht und auch auf dessen Titelblatt präsentiert (siehe Anhang C). Die numerische Studie im gleichen Kapitel stellt ein eigenständiges Paper dar, welches bei *Ultrasound in Medicine and Biology* eingereicht wurde.

Kapitel 9 betrifft im Wesentlichen FUS Lebertumorablation und erforscht Techniken zur Kompensation atmungsbedingter Organbewegungen während fokussierten Ultraschallbehandlungen von Bauchorganen, sowie die Möglichkeit zwischen den Rippen hindurch zu zielen. Diese Arbeit wird nun in eine Journalpaper umgewandelt und beim *Journal of Therapeutic Ultrasound* eingereicht werden. Kapitel 10 untersucht Ansätze zur Verringerung der Behandlungszeiten in der Ultraschallablation großer, solider Tumore, wobei akustische und thermische Simulationen verwendet werden um die Auswirkungen unterschiedlicher Abtastansätze, sowie den Einfluss von Stehwelleneffekten und der Anwesenheit grosser Blutgefässe in Tumornähe auf die Wirksamkeit der Therapie zu untersuchen. Kapitel 11 und 12 fassen die hauptsächlichen Ergebnisse und Neuheiten dieser Arbeit zusammen und geben einen Ausblick auf mögliche zukünftige Erweiterungen und Verbesserungen.

Es wird angenommen, dass die neuentwickelte Plattform schnelle und präzise Modellierung einer Vielzahl von therapeutischen FUS-Anwendungen erlaubt, die schnelle Entwicklung, Analyse und Optimierung von neuen Applikatorsystemen, wie auch die Risikobewertung von verschiedenen Therapien, ermöglichen wird, und schließlich patientenspezifische Behandlungsplanung und optimierung in greifbare Nähe rückt. Es ist zu hoffen, dass die erhöhte Flexibilität und Rechengeschwindigkeit dieser Plattform, in Verbindung mit deren Genauigkeit und Realismus, zur Erhöhung der Sicherheit und Effizienz von Ultraschall-Therapien und zur verbesserten Akzeptanz dieser vielversprechenden Technologie in der medizinischen Gemeinschaft beitragen knnen.

# Acknowledgements

What a journey this PhD has been! Countless ups and downs, an embarrassing number of backtracks, and a notable amount of circling around. I would like to think that I have grown since July 2009 when I first started. I would certainly like to think I have matured (yes many may go into conniptions here). What I know for a fact though, is that I have learned so very much during my time in Z43, and I gained more than I thought possible, on both a professional and personal level. However, none of it would have been possible without the Z43 family. You taught me so much and it was your friendship and support that turned me from an introverted pariah to the social butterfly I am today. For those and an immeasurable amount of other reasons, I would like to extend my eternal gratitude to all the wonderful people I had the honor of working with over the past 5 years. To all of you, from the bottom of my heart, **"Thank You!"**.

Firstly, I would explicitly like to thank the director of the IT'IS Foundation, **Prof. Niels Kuster**. To this very day I do not have vaguest of ideas as to what he saw in the long-haired country-boy with the uncontrollable perspiration issues he interviewed so long ago. However, by allowing me to study at IT'IS, Prof. Kuster gave me the chance of a lifetime! A true intellectual behemoth, Prof. Kuster has the ability of mentally juggling 1001 topics and at the same time he would without fail hit the proverbial nail on the head and in one fell swoop pinpoint every error and guide me to its solution.

Further, I would like express my gratitude to **Prof. Gábor Székely** for welcoming me into the Computer Vision group and allowing me to work within the amazing environment of the CO-ME project. Special thanks goes to **Prof. Theodoros Samaras**, without whom I would have never gotten the opportunity to work at the IT'IS Foundation, for all his support, and our inspiring talks over the past 5 years.

At this point I need to acknowledge the person without whom this PhD would have never been; my thesis advisor **Dr. Esra Neufeld**. A true genius at work, he has been my friend and mentor in every sense of the word and he was there every step of the way. His insight, dedication, and endless patience with my countless blunders are the reasons why this thesis is more than a glorified portfolio of pretty pictures. Esra, despite the fact that we never saw eye-to-eye regarding the state of your desk and hard-drive, it has been a true pleasure and privilege working with you over these past years. Thank you for all the time you sacrificed and for everything you taught me. I am forever in your debt!

A big thank you to the literary gurus **Jane Fotheringham** and **Patricia Bounds**, and the graphics-design geniuses **Jonathan Gubler**, **Saskia Venema**, and **Anja Burse**, who without fail turned my textual abominations and cave paintings into something I could be proud of.

To the unsung administration, coordination, and support heroes of the foundation, **Martin Daellenbach**, **Eva Jakubcaninova**, **Manuel Rolli**, **Elliot Zarstrow**, **Eric Hainfeld**, **Davnah Payne**, and of course the 'angels' of Z43 as once proclaimed by Niels, **Yvonne Maeder**, and **Jacqueline Pieper**. The devil is indeed in the details and if it wasn't for you cleaning up my mess, and tolerating my mind-numbing incompetence when it came to the world outside research, it would have taken me another 5 years to finish.

I certainly need to thank my family who, despite having no clue as to what it is I was doing, always supported me, believed in me, and showered me with love throughout my entire life. If indirectly, I would like to apologize for how little time I made for them. However, despite my selfishness, they were always there for me, and on the rare occasions when I did visit, they would always make me feel that not a day has gone by since I first left. I would like to thank my father **George** who has always been a role-model for me, my mother **Zoe** for her undying love and support, and my siblings **Giannis**, **Antigoni**, and **Christos** for always cheering me up and simply for being there. I love you all!

Finally, and most importantly, to my incredible wife, **Nancy** who in a utopian world would have been given an honorary PhD just for putting up with me over the past few years. Thank you for not merely tolerating me throughout this process, but for loving me every step of the way. Thank you for making me understand how ephemeral all my problems and worries were. Thank you for sharing in my every moment. Thank you for standing by me. I love you!

# Introduction to this document

This thesis was structured so as to provide a comprehensive overview of this work, clearly separating and defining the theoretical background and the underlying motivation, the mathematical, numerical, and implementation aspects behind the developed framework, and the most prevalent applications that were investigated with it.

Part I discusses the background and motivation behind this work, justifying the need for a comprehensive, high-performance computational multi-physics framework, to be developed.

- Chapter 1: fundamental physics of linear and nonlinear acoustic and ultrasonic wave propagation, physical effects induced by these waves in materials and tissue, and compilations of published acoustic tissue properties.

- Chapter 2: introduction into the theory of piezoelectricity, technology behind ultrasonic transducers and arrays, imaging modalities utilized in the guidance and monitoring of therapeutic ultrasound, and commercial therapeutic ultrasound integrated systems.

- Chapter 3: foremost therapeutic applications of focused ultrasound, their current clinical status, as well as their outlook. Finally, the challenges faced by focused ultrasound therapeutic modalities and the state-of-the-art approaches aimed at their amelioration are presented.

Part II proceeds to discuss the numerical modeling of acoustic wave propagation and presents the development of the numerical framework created for the purposes of this work.

- Chapter 4: review of the different mathematical models of acoustic wave propagation, their mathematical descriptions, shortcomings, and advantages. Lastly, an compendium of existing software capable of modeling acoustic wave propagation is given.

- Chapter 5: numerical implementations developed during this thesis. Thorough mathematical derivations of the implemented models, and a discussion the different numerical concerns, e.g., stability, accuracy, boundary conditions.

- Chapter 6: overview of the software development aspects, parallelization of the framework, coupling to other solvers, and integration into the 'in-house' framework.

- Chapter 7: validation of the developed acoustic solvers. Numerical validation against existing acoustic software, analytical solutions, and in-vitro validation performed through the utilization of a measurement setup designed and manufactured 'in-house'.

Following the detailed presentation of the computational framework developed for the simulation of therapeutic ultrasound applications, Part III delves into three specific applications investigated during this work, each aimed at the amelioration of a particular challenge faced by the clinical community.

- Chapter 8: numerical study of transcranial sonication involving a detailed anatomical head model and a commercial therapy system is presented. Four different approaches, ranging from (semi-)analytical to simulation-based, were employed to calculate aberration corrections for 22 targets in the brain, and their impact on the resulting pressure and temperature distributions was compared.

- Chapter 9: numerical study of hepatic tumor ablation with a transient anatomical model generated through 4D-MRI data. Acoustic and thermal simulations were performed to ascertain the importance of motion-tracking and intercostal targeting.

- Chapter 10: investigation of various potentially complicating factors involved in tumor ablation. Acoustic and thermal simulations performed on a realistic but challenging setup, and used to investigate the impact of scanning approaches, the presence of vasculature in the tumor vicinity, and standing-wave effects on therapy efficacy.

Finally, Chapter 11 provides a summary of the motivation, findings, and foremost points of novelty of this work, and Chapter 12 gives an outlook on possible future work.

# List of Figures

# List of Tables

# Part I

# Background & Motivation

# 1

# Ultrasound Physics

This chapter gives a brief overview of acoustics and introduces terminology and concepts that are used throughout this thesis.

The discussion begins with linear acoustics (Section 1.1), including the nature of acoustic waves (Section 1.1.1), the different acoustic properties of materials and tissue (Section 1.1.2), and the propagation properties and behavior of such waves (Section 1.1.3).

Subsequently, the discussion continues on to nonlinear acoustic wave propagation and its characteristics (Section 1.2), and explains the physical effects of acoustic wave interaction with materials and biological tissue (Section 1.3), such as tissue heating (Section 1.3.1), radiation force (Section 1.3.2.1), acoustic streaming (Section 1.3.2.2), and acoustic cavitation (Section 1.3.2.3). Lastly, different compilations of published acoustic tissue properties are presented (Section 1.4).

It should be mentioned that even though this chapter discusses acoustics in general, all the principles and terminology presented are entirely applicable to ultrasonic waves, which are merely acoustic waves exhibiting frequencies above that of the audible range, as is explained below.

## 1.1  Linear Acoustics

### 1.1.1  Nature of Acoustic Waves

[3, §1.1], [4, §§2.1-2.2], [5, §2.1], [2, §2.2], [6, §1.2], [7, §1.1]

Sound is a mechanical disturbance set up in a medium, such that small parts of the medium, i.e., particles, execute oscillatory movements. This process does not involve any mass transfer, and originates from a local change in the stress or pressure field within the medium. Mechanical energy is 'embedded' in the medium, in the form of elastic strains and vibrations of the molecules which, given the appropriate stimulus, are displaced from

their original equilibrium position by a distance $u$, called *displacement amplitude* and at a rate, or *particle velocity*, of $v$. However, due to the medium's elasticity, when a particle is displaced elastic forces that tend to restore it to its original position are developed. Through this oscillation and the interaction between different particles, acoustic energy can propagate across the medium in the form of a wave. In the case of sound, these waves are called *acoustic waves*. Therefore, sound requires a medium to propagate, be it a gas, liquid, or solid, but cannot propagate in vacuum.

Acoustic waves propagate as a series of compressions and rarefactions of the medium. Such waves with frequencies between $20\,\mathrm{Hz}$ and $20\,\mathrm{kHz}$ are designated as (audible) sound, meaning they can be perceived by a human being, while acoustic waves of higher frequencies are commonly referred to as *ultrasound* or *ultrasonic waves*.

Depending on the direction of the particle motion, acoustic waves can be categorized as *longitudinal* or *transverse* waves. In the case of the former, the particle motion/oscillation occurs along a line parallel to the direction of ultrasound propagation $\vec{p}$ (see Figure 1.1(a)). In transverse waves, also commonly referred to as *shear waves*, the particle motion/oscillation direction is perpendicular to the direction of propagation $\vec{p}$ (see Figure 1.1(b)). It should be mentioned that shear waves are damped out extremely rapidly in liquids and soft tissues, and therefore are not a major mode of wave propagation in most medical ultrasound applications. However, the above does not apply to solids or hard tissues like bones.



*(a)*                                                      *(b)*
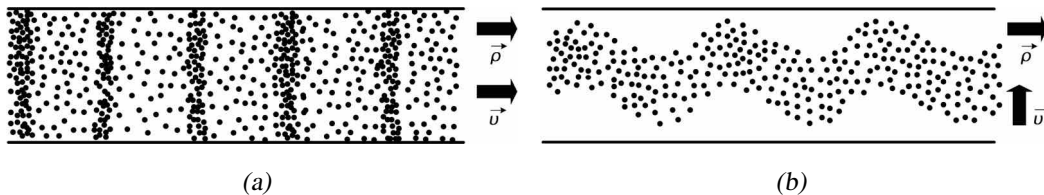
**Figure 1.1**: *One dimensional longitudinal (a) and transverse (b) waves. In longitudinal waves the direction of oscillation $\vec{u}$ is parallel to the direction of propagation $\vec{p}$. The particles oscillate back-and-forth, compressing and expanding the medium. In transverse waves the direction of oscillation $\vec{u}$ is perpendicular to the direction of propagation $\vec{p}$. The particles oscillate up-and-down, altering the shear stress of the medium.*

Acoustic waves can also be classified based on the geometrical shape of their wave-front. Two basic types are the planar and the spherical wave. *Planar waves* feature a wave-front located on a plane that propagates through space, while *spherical waves* propagate symmetrically around a reference point. However, in the case of waves with arbitrarily shaped wave-fronts, one can apply the *Huygen's Principle*, which states that any such wave-front can be considered as an infinite superposition of spherical wave sources (see Figure 1.2).
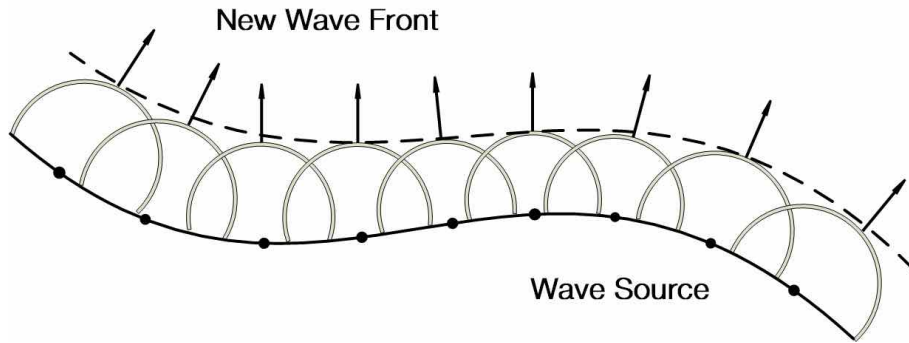
**Figure 1.2**: *Depiction of the Huygen's Principle. Each point on the wave source is assumed to emanate a spherical wave (only a few waves are depicted here for the sake of clarity). The superposition of these minute spherical waves yields the new arbitrarily shaped wave-front.*

## 1.1.2 Acoustic Medium Properties

### 1.1.2.1 Density
[8]

The *density* $\rho$ (in $\text{kg/m}^3$) of a medium is the ratio of the medium's mass per unit volume. Density plays a major role in the behavior of acoustic waves, as it influences a medium's characteristic acoustic impedance $Z$ (see Section 1.1.2.4).

Typical density values are $1.2 \text{ kg/m}^3$ for air, values in the order of $1000 \text{ kg/m}^3$ are observed for most soft tissues (slightly less for fatty tissues and slightly higher for tissues rich in collagen like tendon or skin), and approximately $1900 \text{ kg/m}^3$ for cortical bone.

### 1.1.2.2 Speed of Sound
[3, §3.3], [2, §2.5], [6, §1.2], [9, p.12]

A medium's *speed of sound* $c$ (in $\text{m/s}$), is the speed at which an acoustic wave propagates through that medium. It is related to the wavelength $\lambda$ and frequency $f$, or period $T$, with the below formulas:

$$c = \lambda \cdot f \quad , \quad c = \frac{\lambda}{T} \tag{1.1}$$

It is known from theoretical acoustics, that a medium's $c$ is related to that medium's compressibility $\beta$ (in $\text{m}^2/\text{N}$ or $\text{Pa}^{-1}$) and density $\rho$, and it is depicted in Equation 1.2. *Compressibility* is a measure of the relative volume change of a medium as a response

to a given pressure. Alternatively, $c$ can be calculated through the medium's *elastic bulk modulus* $B$ (measured in Pa), which is the reciprocal of $\beta$, and acts as a measure of the medium's tendency to be deformed elastically, i.e., non-permanently, when a force is applied to it, as shown in Equation 1.3.

$$c = \sqrt{\frac{1}{\beta\rho}} \tag{1.2}$$

$$c = \sqrt{\frac{B}{\rho}} \tag{1.3}$$

Typical $c$ values are $1482$ m/s in water and $343$ m/s in air. In the case of the human body, $c$ lies in the range of $1430 - 1750$ m/s for soft tissues, with fat being in the lower end of the range, skin being in the upper, and tissues like muscle, brain matter and most organs lying in between. The typical $c$ values that have been measured in bone are in the order of $1800 - 3700$ m/s, while values up $6000$ m/s have been measured for tissues like tooth enamel. A more extensive compilation of $c$ values for different biological tissues can be found in Section 1.4.

It should be mentioned that even though the speed of sound in tissues is independent of the acoustic wave frequency, it has been shown to increase gradually as a function of temperature with a slope of $0.04 - 0.08\%$ K$^{-1}$ [9, p.12]. However, given that these variations are minimal, this temperature dependency is commonly ignored.

### 1.1.2.3 Absorption Mechanisms & Coefficient

[10, §§8.1-8.6], [9, pp.12-13], [11, §3.5], [3, §§5.1-5.3], [12, §2.2], [1, §4.1], [2, §2.5], [13, §4.17]

When an acoustic wave is propagating through a medium such as tissue, it experiences a loss of kinetic energy through conversion to thermal energy by a phenomenon called *absorption*.

Absorption is intrinsic to the medium of propagation but it is not attributed to a single mechanism, or type of energy loss. The energy losses of which absorption is comprised can be subdivided into three basic types, for which the physical mechanisms are well known. These types are viscous losses, heat conduction losses and relaxation losses.

*Viscous losses* occur whenever there is relative motion between adjacent portions of the medium, such as in the case of shear deformations or during the neighboring compressions and rarefactions that facilitate the propagation of the acoustic wave. *Viscosity* is a measure of the frictional forces between particles of the medium as they interact with one

another. Therefore, during the acoustic wave propagation, a portion of the acoustic energy is converted to thermal, resulting in energy loss.

*Heat conduction losses* result from the conduction of thermal energy from the higher temperature compression areas of the medium to the lower temperature refraction areas. The increased acoustic pressure in the compression areas implies increased kinetic energy (in comparison to rarefaction areas) which causes these areas to exhibit a higher temperature. This kinetic energy diffuses from these warmer regions to the cooler ones through intermolecular collisions. As this energy dissipates from the warmer region, it is lost to the acoustic process and is converted to random thermal energy of molecular motion.

The third type of absorption losses are *relaxation losses*, also referred to as *molecular losses*, which can be explained as follows: during the compressional phase of the wave cycle, kinetic energy is stored in the medium in a number of different forms such as rotational and vibrational energies, translational energy, potential energy, etc. This stored energy is returned to the wave during the rarefaction phase in an attempt of the medium to return to its equilibrium state. However, this energy transfer takes a certain amount of time, which is referred to as *relaxation time*, an intrinsic characteristic of the medium. The longer this relaxation time is, the more energy has been stored by the molecules. Thus, during the rarefaction cycle, kinetic energy will return 'out of phase' causing destructive interference (see Section 1.1.3.5), manifesting as energy loss.

Based on the mechanisms described above, it is obvious that a medium's absorption of acoustic energy is dependent on the wave frequency. As the wave frequency increases, so do both the viscous, due to increased frictional losses, and relaxation losses. The increase in relaxation losses can be attributed to the fact that while relaxation times remain constant, compressions and rarefactions occur more rapidly, resulting in an increased probability of destructive interference and therefore energy loss.

The *absorption coefficient* $\alpha$ constitutes the sum of all the aforementioned losses and is a frequency dependent medium property, as discussed above. The relation between $\alpha$ and the acoustic wave frequency is approximated as [2, §2.5]:

$$\alpha = \alpha_0 \cdot f^b \tag{1.4}$$

where $\alpha$ is the absorption coefficient, measured in $\mathrm{Np/m}$, for a given frequency $f$, $\alpha_0$ is a medium constant, expressed in $\mathrm{Np/m/Hz}^b$, and $b$ is also a numerical constant dependent on the tissue type.

It should be noted, that $\alpha$ is also often expressed in $\mathrm{dB/m}$ or $\mathrm{dB/cm}$. The relation between $\mathrm{Np}$ and $\mathrm{dB}$ is [2, §2.5]:

$$\alpha_{\mathrm{dB}} = 0.115 \cdot \alpha_{\mathrm{Np}} \tag{1.5}$$

In contrast to the tissue density and speed of sound, the absorption coefficients in tissue are very different to those of water and exhibit large variations between different tissues. A comprehensive list of absorption coefficient values for different tissues is given in Section 1.4.

#### 1.1.2.4 Characteristic Acoustic Impedance
[**3**, §**6.1**], [**2**, §**2.5**], [**5**, §**2.4**], [**9**, **p.13**], [**10**, §**5.10**]

The *characteristic acoustic impedance* $Z$ (measured in Rayls or $\mathrm{kg/m^2/s}$), is an inherent property of a medium and is calculated as the product of the medium's speed of sound and density [**2**, §2.5]:

$$Z = \rho \cdot c \tag{1.6}$$

According to the average $\rho$ and $c$ values, provided in Sections 1.1.2.1 and 1.1.2.2 respectively, air exhibits a $Z$ less than $0.5$ kRayls, that of soft tissue and water is in the order of $1.5$ MRayls, and cortical bone exhibits a $Z$ in the range of $3 - 5$ MRayls. This property is critical with respect to all processes that define acoustic wave behavior, e.g., reflection, scattering, refraction, etc., which are detailed in subsequent sections. A table depicting $Z$ values for different tissue types can be found in Section 1.4.

### 1.1.3 Acoustic Wave Properties

#### 1.1.3.1 Acoustic Intensity
[**3**, §**3.5**], [**12**, §**2.2**], [**2**, §**2.3**], [**4**, §**3.17**], [**10**, §**5.9**], [**14**–**16**]

A definitive parameter associated with an acoustic wave is its intensity. An ultrasound wave carries kinetic energy as it propagates. This energy can be described in terms of an energy density, i.e., the amount of energy per unit volume, or more commonly by intensity, which is defined as the energy propagating through unit area per unit time. However, the quantity that is usually calculated and cited is the time-averaged intensity $I$, which will be simply referred to as *acoustic intensity* from this point forth. Acoustic intensity is measured in $\mathrm{W/m^2}$, and for a sinusoidal acoustic wave it is calculated as [**10**, §5.9]:

$$I = \frac{p^2}{2Z} = \frac{p^2}{2\rho c} \tag{1.7}$$

where $p$ is the absolute acoustic pressure amplitude in $\mathrm{Pa}$ (or $\mathrm{kg/s^2/m}$), $Z$ is the characteristic acoustic impedance of the medium in Rayls (or $\mathrm{kg/m^2/s}$), $\rho$ is the medium's density in $\mathrm{kg/m^3}$, and $c$ is the medium's speed of sound in $\mathrm{m/s}$.

### 1.1.3.2 Reflection & Refraction

[3, §§1.2, 6.3], [6, §1.2], [4, §§3.7-3.8], [5, §2.5], [15]

Consider an acoustic wave propagating within a medium with a characteristic acoustic impedance of $Z_1$ and impinging (incident wave) upon an interface to another medium with a characteristic acoustic impedance of $Z_2$. A portion of that acoustic energy is reflected (reflected wave) at the interface and propagates back towards the first medium, while the remaining energy is transmitted through the second medium (transmitted or refracted wave). This phenomenon is depicted in Figure 1.3.
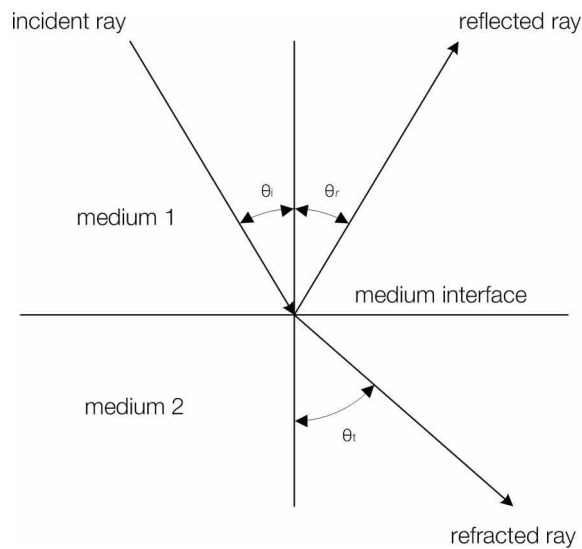


**Figure 1.3**: *An acoustic wave propagating from a medium 1 to a medium 2. Due to the impedance mismatch between the two media, part of the acoustic energy is reflected back to medium 1, while the remaining energy propagates through to medium 2 as a refracted wave.*

The incidence angle $\theta_i$ is equal to the reflection angle $\theta_r$, while the transmission angle $\theta_t$ depends on the speed of sound $c$ of the two media, and can be calculated with *Snell's law* as shown below [3, §6.3]:

$$\frac{\sin \theta_i}{c_1} = \frac{\sin \theta_t}{c_2} \tag{1.8}$$

where $c_1$ and $c_2$ are the speeds of sound in the two media.

The difference in $Z$ between two media is commonly referred to as *impedance mismatch*. The greater the impedance mismatch, the greater the percentage of acoustic energy that will be reflected at the interface between the two media. The ratio of the reflected wave pressure $p_r$ to the incident wave pressure $p_i$ can be calculated through the *reflection coefficient $R$*, while the ratio between the transmitted wave pressure $p_t$ and that of the incident

one can be derived from the *transmission coefficient* $T$ (not to be confused with the period of a wave outlined in Section 1.1.1). These coefficients can be calculated based on the characteristic impedances of the two media, as well as the incidence and transmission angles. The formulas for their calculation can be seen below [3, §6.3]:

$$R = \frac{p_r}{p_i} = \frac{(Z_2 \cos \theta_i - Z_1 \cos \theta_t)}{(Z_2 \cos \theta_i + Z_1 \cos \theta_t)} \tag{1.9}$$

$$T = \frac{p_t}{p_i} = \frac{(2Z_2 \cos \theta_i)}{(Z_2 \cos \theta_i + Z_1 \cos \theta_t)} \tag{1.10}$$

For the unique case when the incident wave impinges perpendicularly to the interface (thus $\theta_i = \theta_t$), the above formulas can be simplified to [3, §6.3]:

$$R = \frac{p_r}{p_i} = \frac{(Z_2 - Z_1)}{(Z_2 + Z_1)} \tag{1.11}$$

$$T = \frac{p_t}{p_i} = \frac{(2Z_2)}{(Z_2 + Z_1)} \tag{1.12}$$

Lastly, it should be mentioned that the ratios of the reflected/incident and transmitted/incident, acoustic energy/intensity can be calculated by the square powers of the above coefficients [3, §6.3]:

$$\frac{I_r}{I_i} = R^2 \quad , \quad \frac{I_t}{I_i} = T^2 \tag{1.13}$$

In the interest of elucidating the significance of the $R$ and $T$ coefficients, the following cases should be noted: If $Z_1 < Z_2$ then $R > 0$, which signifies that the amplitude of the reflected wave is in phase with the incident wave. If $Z_1 > Z_2$ then $R < 0$ which implies that the reflected wave exhibits a $180°$ phase difference, i.e., opposite phase, relative to the incident wave. If $Z_1 \ll Z_2$ then $R \to 1$ which means that the incident wave is almost entirely reflected at the interface between the two media, i.e., the reflected wave has nearly the same amplitude as the incident wave. Lastly, in the case of $Z_1 \gg Z_2$ then $R \to -1$, which implies that the incident wave is once more almost entirely reflected but unlike the previous case, this reflected wave exhibits $180°$ phase difference relative to the incident wave.

### 1.1.3.3 Diffraction
[12, §2.2], [6, §1.2], [4, §3.9], [3, §1.2]

When the incident acoustic wave interacts with a seemingly infinitely extending interface between two different media, only the phenomena of reflection and refraction occur. That interface acts as an *acoustic barrier*, and the space behind it, where the acoustic waves would normally propagate in its absence, is called the *acoustic shadow zone*, as it becomes acoustically obscured due to the barrier's presence. However, when an incident wave impinges upon a barrier with finite length, and therefore edges, the wave tends to spread and/or bend around those edges. A similar phenomenon is observed when that barrier exhibits small openings.

This phenomenon, which is depicted in Figure 1.4, is referred to as *diffraction*, and causes the wave trajectories to bend and propagate in zones that would have been shadowed otherwise. The amount a wave diffracts depends on the size of that barrier or opening, the distance between the sound source and the barrier, as well as the acoustic wavelength $\lambda$ (or frequency $f$). Diffraction is enhanced for lower frequencies, i.e., for wavelengths that are long when compared to the barrier, while if the wavelength is negligible compared to the size of the barrier, diffraction is minimal. In addition, the closer the sound source is located to the barrier, the larger the shadow zone on the other side of the barrier becomes.

### 1.1.3.4 Scattering
[6, §1.2], [12, §2.2], [17, §6.1], [3, §9.3], [1, §8.2]

*Scattering* is a direct consequence of reflection and is the cornerstone of diagnostic ultrasound. Scattering occurs when an acoustic wave travels through an *inhomogeneous medium*, i.e, a medium that contains objects of different characteristic acoustic impedance - also known as *scatterers*, and part of the wave energy is redirected and appears separately to the original incident wave, by being either delayed in time or altered in direction.

As in the case of diffraction, scattering is heavily dependent on the ratio between the acoustic wavelength and the size of the scatterer(s). In addition, it is dependent upon the degree of the impedance mismatch on the interfaces between the propagating medium and the scatterers, as well as the number of scatterers per unit volume.

Depending on the aforementioned wavelength/scatterer-size ratio, three types of scattering can be defined. If the wavelength is much smaller than the size of the scatterer, then the phenomenon is called *specular scattering*. At the other extreme, when the wavelength is large compared to the scattering object the type of scattering is called *diffusive scattering* or *Rayleigh scattering*. This second type finds application in medical imaging, especially in Doppler blood-flow measurements, where each blood cell is essentially a small scatterer, and imaging under ultrasound contrast agents, which are composed of
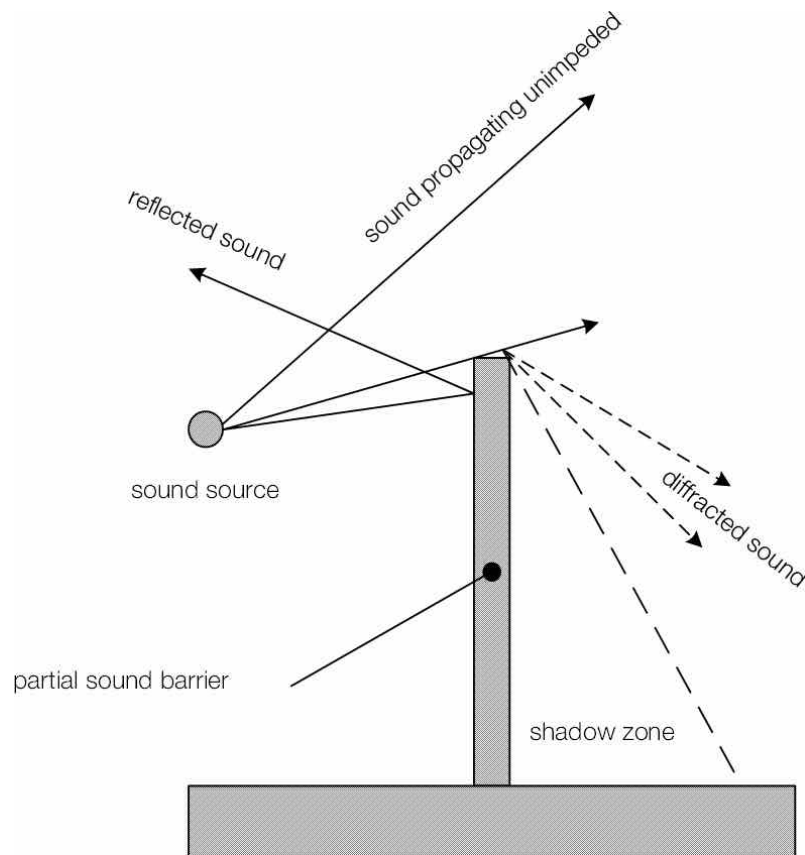
**Figure 1.4**: *Impingement of an acoustic wave on a partial acoustic barrier, resulting in diffraction and the formation of an acoustic shadow zone.*

microscopic air-filled bubbles. The last type of scattering is called *diffractive scattering*, and occurs when the acoustic wavelength and the size of the scatterer are comparable.

### 1.1.3.5   Interference & Standing Waves
[**3**, §**1.2**], [**4**, §**3.4**], [**6**, §**1.2**]

When two acoustic waves 'collide' in space, a phenomenon called *interference* is manifested. This interaction is heavily dependent on the phase of the two waves. If the two waves are 'in-phase' at the location of interaction, then *constructive interference* occurs and the amplitudes of the two waves appear to enhance each other, resulting in a combined wave of higher amplitude (see Figure 1.5(a)). In the event of two waves being 'out of phase', the amplitudes seem to attenuate each other as the waves cancel each other's energy (see Figure 1.5(b)), in what is called *destructive interference*.

A direct consequence of the interference phenomenon are *standing waves*. When a wave propagates through a confined medium, e.g., a medium surrounded by strong reflectors, the wave interferes with its reflection. If the distance between the wave source and the
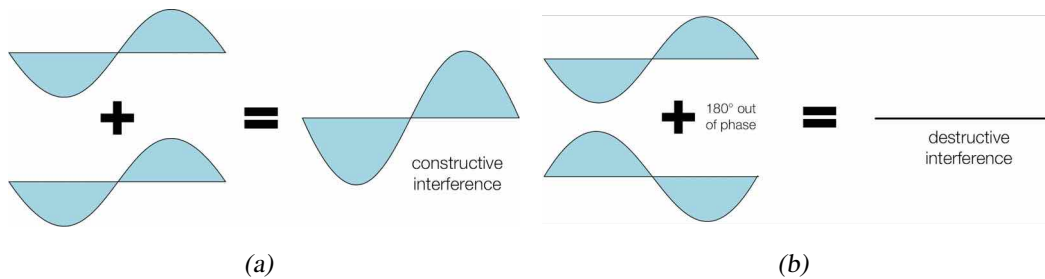
**Figure 1.5**: *Constructive (a) and destructive (b) interference of two waves.*

reflector is a multiple of $\lambda/2$, this interference yields a motion pattern which appears spatially still but with a temporally varying amplitude (see Figure 1.6).
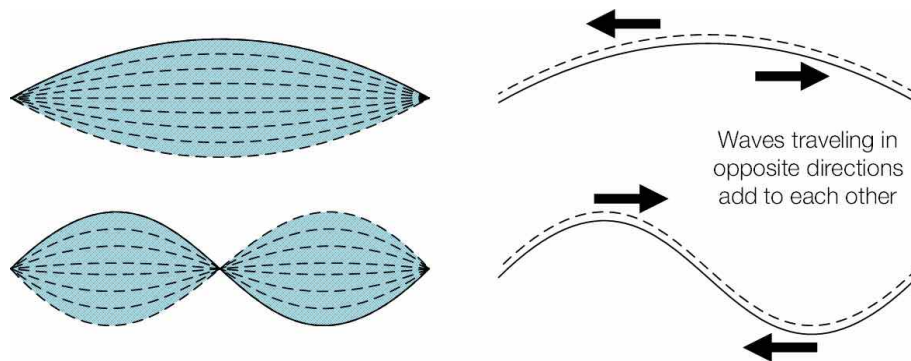


**Figure 1.6**: *Fundamental (up) and second harmonic standing waves (down).*

### 1.1.3.6 Attenuation
[**9**, pp.12-13], [**2**, §2.5], [**11**, §3.7]

When an acoustic wave is propagating through a medium, the amplitude of the acoustic pressure, and all related quantities such as intensity, are reduced exponentially as the wave progresses. This phenomenon is called *attenuation*, and it should be distinguished from absorption which was discussed in Section 1.1.2.3. Absorption relates to the conversion of the acoustic wave's kinetic energy to thermal energy within the medium, whereas attenuation refers to the total propagation losses that result in an abated wave intensity. Attenuation is a result of absorption by the medium, as well as scattering, and determines the extent of penetration of an acoustic wave in a material or tissue.

However, it has been shown experimentally [18], that attenuation is dominated by absorption, and that the amount of scattered energy is typically negligible when compared to the energy losses due to absorption. In addition, scattered energy will inevitably be absorbed by the medium. Therefore, the attenuation coefficient is assumed to be the same as the absorption coefficient $\alpha$ outlined in Section 1.1.2.3.

## 1.2   Nonlinear Acoustics

### 1.2.1   Linearity Assumptions

[2, §§2.1-2.3], [1, §3.1], [17, §1.2], [10, §§5.1-5.2]

In the previous sections, the propagation of acoustic waves was considered to be linear. However, for this simplification to be valid, the acoustic waves need to abide by certain assumptions commonly referred to as *linearity principles*.

The *shape-amplitude proportionality principle* states that the shape and amplitude of the acoustic waves at any location are proportional to the input excitation, i.e., the original acoustic wave.

The *superposition principle*, poses the assumption that the particle displacement generated by two or more acoustic sources is simply the algebraic sum of the displacements generated by each source separately.

Lastly, the *infinitesimal amplitudes principle* states that in order to allow for first-order approximations, i.e., linearization, of the acoustic pressure and particle velocity, it is assumed that the amplitude of the propagating waves is infinitesimally small. Thus, describing waves with large pressure amplitudes, requires higher-order approximations of these quantities.

### 1.2.2   Nonlinear Acoustic Wave Propagation

[1, ch.12], [12, §2.2], [4, §§21.1-21.2], [9, p.14], [2, §2.3], [17, §1.8], [19, §4.5], [3, §5.6], [20, pp.7, 67], [21, §§8.1-8.6], [22, §5.1], [15]

The aforementioned linearity principles are obeyed in certain applications of biomedical ultrasound, especially when low acoustic pressures are employed, such as in imaging systems where linearity is a fundamental prerequisite. However, these assumptions cannot always be applied to the interaction of acoustic waves with tissues, as higher amplitudes are often utilized.

Commonly employed acoustic waves typically exhibit *finite amplitudes* and display nonlinear behavior, even if the inherent nonlinearity of the medium was ignored. As described in Section 1.1.1, acoustic waves propagate within a medium through a series of compressions and rarefactions. Under the linearity regime, an acoustic wave would propagate along the $z$ direction with a speed of:

$$\frac{\mathrm{d}z}{\mathrm{d}t} = c = \sqrt{\frac{1}{\beta\rho}} = \sqrt{\frac{B}{\rho}} \tag{1.14}$$

where $\beta$ is the medium's compressibility, the reciprocal of $\beta$ is the bulk modulus $B$, and $\rho$ is the density (see Equations 1.2 and 1.3 in Section 1.1.2).

However, the above formula only applies for linear acoustics where the infinitesimal amplitudes principle is valid. The speed $c$ and density $\rho$ in the above formula are in fact the *equilibrium sound speed* $c_0$ and *equilibrium density* $\rho_0$, meaning the speed and density of the medium in the absence of an acoustic wave. The infinitesimal amplitudes assumption theorizes that if the amplitudes of the propagating waves are very small, then they should not disturb these equilibrium quantities, and thus the aforementioned formula is assumed to hold. Due to this, the equilibrium speed of sound $c_0$ is often referred to as *small signal sound speed*.

In the case of finite amplitude waves however, this simplification is no longer valid. The propagation speed of an acoustic wave in the nonlinear regime would be:

$$\frac{\mathrm{d}z}{\mathrm{d}t} = c_0 + \beta u \tag{1.15}$$

where $c_0$ is the equilibrium speed of sound mentioned above, $\beta$ is called the *nonlinearity coefficient* (not to be confused with compressibility which uses the same symbol), and $u$ is the particle displacement velocity. The nonlinearity coefficient is defined as $\beta = 1 + 0.5B/A$ with $B/A$ being the *nonlinearity parameter*, an intrinsic property of each material or tissue (not to be confused with the medium's bulk modulus $B$).

During the propagation of an acoustic wave, the compression areas of the medium, i.e., compressed particles due to higher acoustic pressure, exhibit a higher speed while the rarefaction areas exhibit a lower speed. Therefore, the wave propagation speed varies at different points along the wave, and the pressure maxima propagate faster than the pressure minima. Even though the particle velocity $u$ is small in comparison to $c_0$, this effect is cumulative and leads to a gradual *wave distortion*, as shown in Figures 1.7(a) and 1.7(b). This type of nonlinearity is typically referred to as *convective nonlinearity*.

In addition to convective nonlinearity, a second effect called *medium nonlinearity* is observed. Water, as well as most biological tissue, are inherently nonlinear. The *nonlinearity* property of a medium is in direct contradiction to the shape-amplitude proportionality principle, meaning that it cannot be assumed that the shape and amplitude of an acoustic wave within the medium are proportional to those of the original wave. When the medium is compressed, an increase in its bulk modulus $B$, or alternatively a decrease in its compressibility $b$, is observed which causes an increase in the speed of sound, as per Equation 1.2. Therefore, this effect causes waves in compression regions of the medium to propagate faster than rarefaction regions, further amplifying the wave distortion described above.

The foremost consequences of acoustic propagation through a nonlinear medium are the cumulative distortion of the wave, the generation of higher harmonics, and ultimately

saturation. As a harmonic wave, i.e., a wave with a single frequency called the *first harmonic*, propagates, distortion begins and simultaneously creates low levels of secondary harmonics. Consequently, the cumulative distortion creates a sawtooth wave, commonly called a *shock wave*, which exhibits frequencies at harmonic-multiples of the fundamental frequency. As propagation continues, the higher harmonics are attenuated, due to the relation between the absorption coefficient and frequency as outlined in Section 1.1.2. Eventually only an attenuated low-amplitude waveform remains, in a phenomenon called *saturation*. This evolution of the wave is depicted in Figure 1.7.

## 1.3   Physical Effects of Ultrasound

[9, pp.14-15], [2, §§2.3, 4.1], [1, §15.1]

Acoustic waves interact with the medium in which they are propagating through the particle motion and pressure variations. While certain applications of diagnostic or therapeutic ultrasound can be considered to lie in the linear propagation regime, as the utilized acoustic intensities increase, nonlinear phenomena become increasingly prominent.

This interaction yields a number of different physical effects, which can be classified into *thermal effects* and *nonthermal effects*. Thermal effects are mostly related to the medium's temperature increase, due to the conversion of acoustic energy into heat. The nonthermal effects are mechanical in nature and include radiation force, pressure and torque, acoustic streaming and the formation and cavitation of microbubbles. This categorization is depicted in Figure 1.8, while the different effects are discussed below in detail.

### 1.3.1   Thermal Effects

[2, §4.2], [9, p.15-16], [1, §15.3], [23, p.10], [3, §12.1], [24, p.14], [14, 15, 25]

As discussed in Sections 1.1.2.3 and 1.1.3.6, when acoustic waves propagate through a medium they experience a continuous loss of energy as a result of attenuation which is converted to thermal energy and results in that medium's temperature increase. Furthermore, when nonlinear propagation is taken into account, this energy loss becomes even more pronounced due to the faster generation and attenuation of higher harmonics (see Section 1.2.2).

This effect is called the *absorption effect* and is the main source of thermal energy during the propagation of acoustic waves within a material or tissue. The amount of acoustic energy that is irreversibly converted to thermal energy per unit volume is called *acoustic energy density*, it is measured in $\mathrm{W/m^3}$ and is symbolized by $q_v$. Its calculation is shown in the formula below [14, 24–26]:

*(a)*



*(b)*



*(c)*



*(d)*



*(e)*
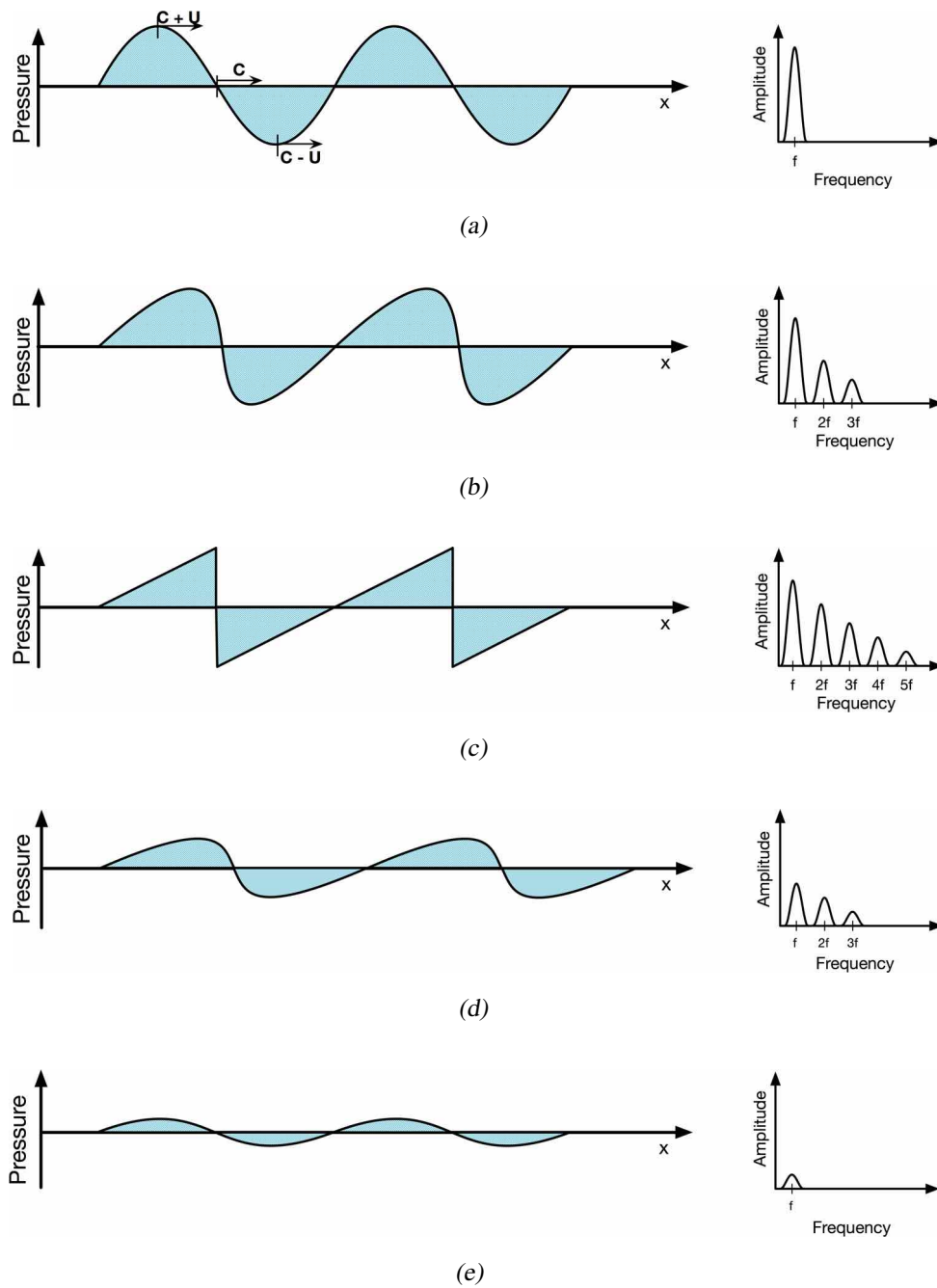
**Figure 1.7**: *Evolution of an acoustic wave propagating in a nonlinear medium. The acoustic wave is shown throughout the different propagation stages, depicted in time on the left of each figure, while its spectral components are shown on the right. The original wave exhibits higher propagation speed in the compressional areas than in the rarefactional (a). Thus, the wave distorts causing the generation of harmonics (b). Eventually a shock wave, rich in harmonics develops (c). As the high harmonics are absorbed at a higher rate by the medium, their energy is absorbed and attenuated (d). Eventually only a low-amplitude, harmonic wave remains (e).*
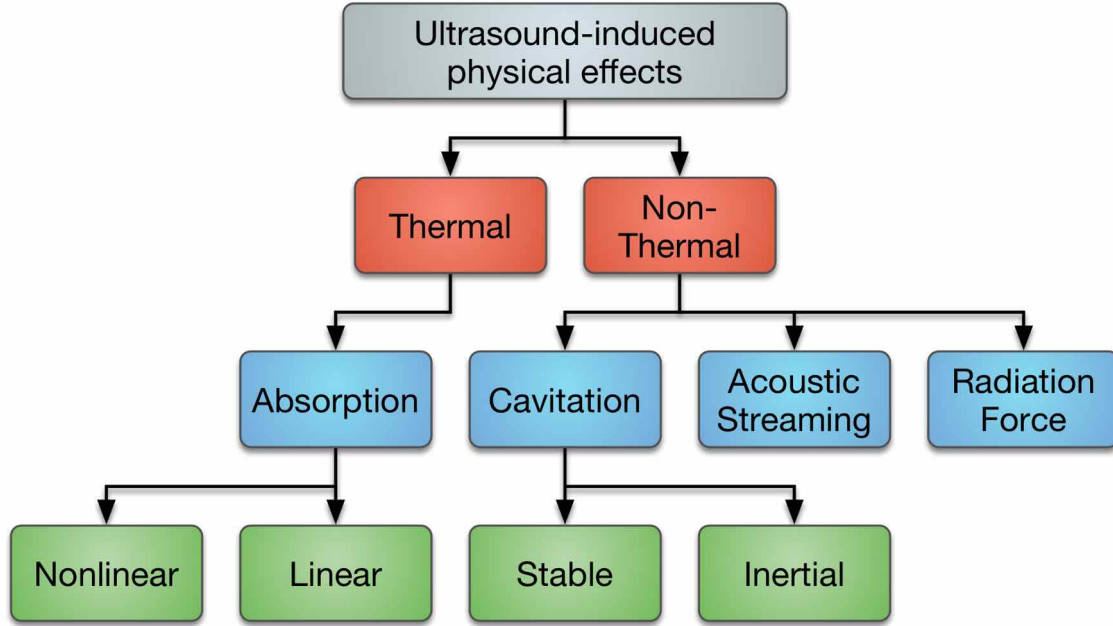
**Figure 1.8**: *Classification of the physical effects induced by ultrasound.*

$$q_v = 2\alpha I = \alpha \frac{p^2}{\rho c} \tag{1.16}$$

where $\alpha$ is the absorption coefficient (see Section 1.1.2.3) in $\mathrm{Np/m}$, and $I$ is the acoustic intensity (see Section 1.1.3.1) at the location in $\mathrm{W/m^2}$. Alternatively, through the use of Equation 1.7, $q_v$ can be expressed as a function of acoustic pressure. $p$ is the absolute acoustic pressure amplitude in $\mathrm{Pa}$ (or $\mathrm{kg/s^2/m}$) [24, p.14], $\rho$ is the medium's density in $\mathrm{kg/m^3}$ and $c$ is the medium's speed of sound in $\mathrm{m/s}$.

Another source of thermal energy present in the therapeutic utilization of acoustic waves, is the *heat conduction effect*, which describes the thermal effect of the transducer, i.e., the source of ultrasonic waves discussed in Section 1.1.3.6, which can itself be a source of heat when in direct contact with the body. This is caused due to impedance mismatches between the transducer surface, its coupling gel, and the surrounding air. The afore-mentioned mismatch causes acoustic energy to be reflected back towards the transducer, increasing its temperature, which in turn heats up the body surface. This effect however, is localized at the patient's skin and typically ignored.

## 1.3.2 Nonthermal Effects

### 1.3.2.1 Radiation Pressure, Force & Torque
[27, §6.4], [1, §12.7], [23, pp.20-23], [2, §§2.3, 4.4], [3, §3.6], [28, §2.5], [17, §§1.8, 12.4], [19, §4.5], [15, 29–31]

When a propagating acoustic wave exhibits low pressure amplitudes, both the acoustic pressure $p$ and the particle velocity $u$ can be assumed to vary sinusoidally with time. Any movement or deformation the wave propagation causes to the particles of the medium during the compression phase of the cycle, can be assumed to reverse during the rarefaction phase. As described in Section 1.2.2 however, at higher amplitudes (finite amplitudes), the effects of nonlinearity cause the compressional and rarefactional cycles of the wave to differ significantly.

Due to this asymmetry between the two cycles, higher positive acoustic pressure is observed during the compression than negative pressure during the rarefaction, resulting in a 'constant' positive average pressure exerted by the acoustic wave to the medium. This average pressure is called *radiation pressure* and is an inherently nonlinear acoustic effect.

When encountering a (partially) reflective surface, i.e., an interface where there is a characteristic acoustic impedance mismatch, this radiation pressure will exert a *radiation force* on that interface, attempting to 'push' it along the direction of propagation. This volumetric force however, acts not only on ordinary objects/bodies within the propagation medium, or interfaces between different media, but even on the medium itself. Radiation force is proportional to acoustic intensity and under a linearized regime this relation can be expressed as follows [31]:

$$F_{rad} = \frac{2\alpha I}{c} \tag{1.17}$$

where $F_{rad}$ is the radiation force in $\mathrm{N/m^3}$ (or $\mathrm{kg/m^2/s^2}$), $\alpha$ is the medium's absorption coefficient in $\mathrm{Np/m}$ (see Section 1.1.2.3), $I$ is the acoustic intensity (see Section 1.1.3.1) at the location in $\mathrm{W/m^2}$, and $c$ is the medium's speed of sound in $\mathrm{m/s}$.

A quantity analogous to radiation force is *radiation torque*. While the former may cause translation displacement of a region in the medium or body, radiation torque is a rotational force and may cause the body to experience an angular displacement. A volume element in a nonlinear acoustic field is subjected both to a translational and rotational force. Radiation torque is greatest at positions in which the velocity gradient is at its maximum, such as at the boundary between two different media.

#### 1.3.2.2  Acoustic Streaming

[23, pp.28-32], [2, §§2.3, 4.4], [17, §12.4], [3, §12.1], [15, 30, 32]

When an acoustic wave is propagating in a fluid, the acoustic radiation force creates a non-oscillatory, fluidic motion which is called *acoustic streaming*. This motion can be steady, known as *jet flow*, and/or circulatory, a behavior commonly referred to as a *vortex*.

The velocity gradients associated with this fluid motion may be quite high, especially in the vicinity of boundaries within the field, and the shear stresses set up may be sufficient to cause changes and/or damage to the medium.

Acoustic streaming can be classified according to its scale. When the scale of the effect is in the order of a few cm, it is simply referred to as *streaming*, while scales in the order of μm classify the effect as *microstreaming*.

#### 1.3.2.3  Acoustic Cavitation

[1, §§14.2-14.4], [28, §10.1], [9, pp.17-18], [17, §12.3], [23, pp.28-32], [3, §12.1], [2, §4.5], [15, 16, 33, 34]

The term *acoustic cavitation* is used to define the interaction between an acoustic field and microscopic bodies of gas in any medium or tissue. In order for cavitation to occur in tissue, the presence of such gaseous bodies, which are often referred to as *cavitation nuclei*, is required. These nuclei, are typically gas-filled bubbles with a size in the order of a few μm, and thus they are typically called *microbubbles*. Microbubbles may either pre-exist within the medium, in the form of dissipated gas/oxygen, or can be introduced in the human body by the injection of an ultrasound *contrast agent* (UCA), a solution which contains a large number of preformed microbubbles.

When such a microbubble is exposed to an oscillating acoustic wave, it starts to expand and contract in a fashion that is inversely related to the acoustic pressure. During the compression cycle, when the pressure amplitude is high, and the bubble is 'pushed' inwards, its gaseous core is compressed by the bubble shell and the whole bubble contracts. During the rarefaction cycle, the low pressure allows the bubble to 'relax' more, its gaseous core decompresses and the bubble expands in size. This type of bubble oscillation is called *stable cavitation* and is depicted in Figure 1.9.

This motion induces microstreaming (see Section 1.3.2.2) of the fluid around the bubble and increases absorption/attenuation of the acoustic wave, as the oscillating bubble may intercept and re-radiate acoustic energy, thereby absorbing much more energy than what would normally be absorbed by the tissue itself. In addition, this oscillation yields highly localized shear stresses on the surrounding medium/tissue which can lead to severe cell damage.
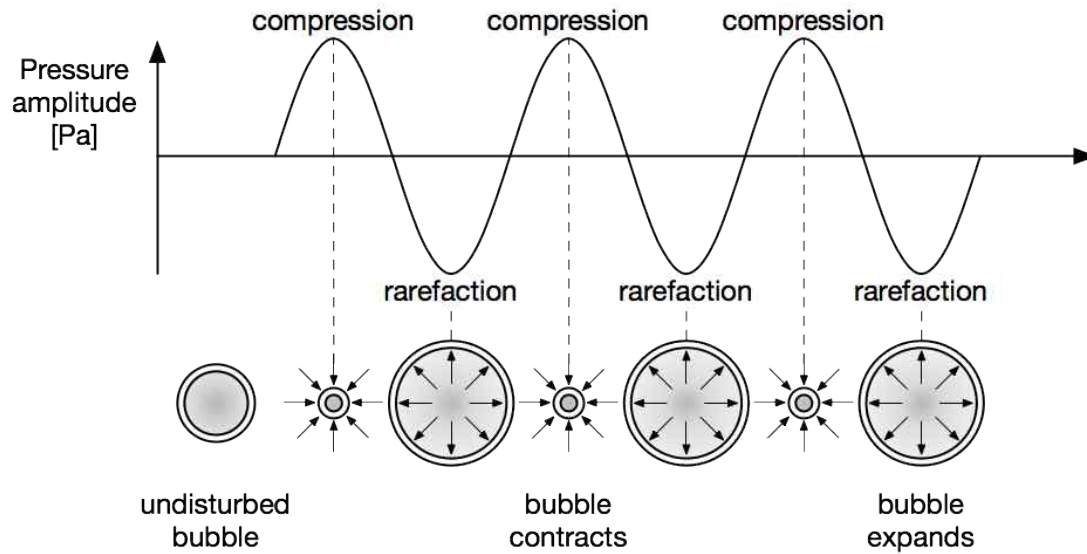
*Figure 1.9*: *Stable cavitation in a microbubble. During compression the pressure amplitude is high and the bubble contracts. During rarefaction the low pressure allows the bubble to expand in size and the whole process is repeated in a sustainable oscillation.*

Stable cavitation, however, applies only for low-intensity acoustic waves and describes a periodic and sustainable bubble oscillation. For high pressure amplitudes, the bubble can expand during the rarefaction cycle but cannot be compressed without limit as the gaseous core of the bubble can only be compressed so far, and this limit is defined by the *minimum bubble radius*. As a result, the pressure response of the bubble becomes highly nonlinear, the bubble expands further in size with every rarefaction cycle by means of *rectified diffusion* [35] until the eventual fragmentation of the bubble shell and bubble collapse. This phenomenon is called *transient* or *intertial cavitation* and a depiction can be seen in Figure 1.10.

In addition to the effects of stable cavitation described above, during inertial cavitation the violent collapse of the bubble can cause a localized acoustic pressure of several thousand atmospheres (the equivalent of several $\mathrm{MPa}$) and temperatures in the order $5000\,^{\circ}\mathrm{C}$. It may also lead to the generation of shock waves, high-velocity liquid jets, and strong shear forces. This bubble collapse can completely disintegrate the surrounding tissue, while the high temperature can yield the generation of free radicals which are chemically active [1, §§14.2-14.4], [28, §10.1], [9, pp.17-18].

The pressure amplitude level at which inertial cavitation may occur is called the *cavitation threshold*, and has been shown experimentally to be proportional to the frequency of the acoustic wave, i.e., inertial cavitation is more likely to occur in lower acoustic frequencies [15, 16, 33, 34]. Moreover, cavitation can be suppressed by degassing the medium/liquid, i.e., removing dissolved gas, or by increasing its viscosity.
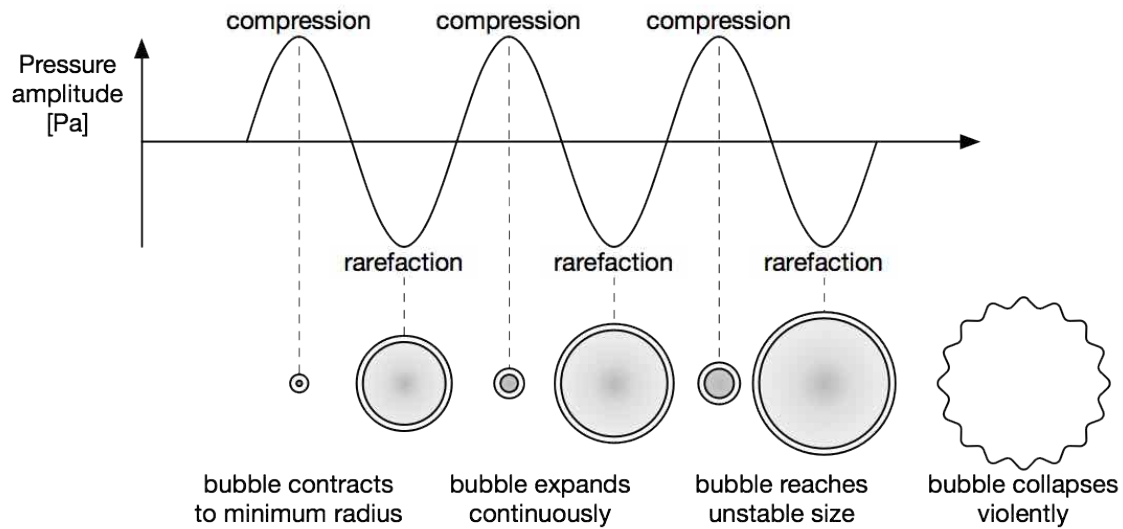
**Figure 1.10**: *Inertial cavitation of a microbubble. The bubble expands with rarefaction each cycle until it reaches its critical size and collapses.*

## 1.4  Acoustic Tissue Properties

Although many artificial materials have been acoustically characterized for use in transducer manufacture or nondestructive testing (NDT), an extensive literature search revealed no comprehensive studies on the acoustic properties of human tissue, apart from the properties of bone which were first investigated by Fry and Barger [36]. While promising projects dealing with the measurement of such properties in porcine and human tissue are underway [37, 38], the only existing literature is generally decades old and comprises empirically measured properties with large discrepancies between different datasets. Such sources can be found in [1–3, 18, 39–45].

In this section, two existing compilations of the acoustic tissue properties discussed in Sections 1.1.2 and 1.2.2 will be provided. The first such compilation, is based on the data compiled by Szabo [1, p.535], derived from existing literature [39–41]. These property values can be seen in Table 1.1. Another such compilation is given in [2], which can be seen in Table 1.2.

One should note the differences in the absorption coefficients (see Section 1.1.2.3) between the two tables. Table 1.1 provides values for $\alpha_0$ and $b$, which can be used to calculate $\alpha$ as shown in Equation 1.4. Table 1.2, however, provides frequency-dependent values of $\alpha$ instead, measured in $\mathrm{Np/m/MHz}$, essentially assuming that $b = 1$.

| Tissue Name (units) | $c$ m/s | $\alpha_0$ dB/m/MHz | $b$ | $\rho$ kg/m$^3$ | $Z$ MRayls | $B/A$ |
|---|---|---|---|---|---|---|
| Blood | 1584 | 14 | 1.21 | 1060 | 1.68 | 6 |
| Bone | 3198 | 354 | 0.9 | 1990 | 6.36 | - |
| Brain | 1562 | 58 | 1.3 | 1035 | 1.62 | 6.55 |
| Breast | 1510 | 75 | 1.5 | 1020 | 1.54 | 9.63 |
| Fat | 1430 | 60 | 1 | 928 | 1.33 | 10.3 |
| Heart | 1554 | 52 | 1 | 1060 | 1.65 | 5.8 |
| Liver | 1578 | 45 | 1.05 | 1050 | 1.66 | 6.75 |
| Muscle | 1580 | 57 | 1 | 1041 | 1.64 | 7.43 |
| Spleen | 1567 | 40 | 1.3 | 1054 | 1.65 | 7.8 |
| Water | 1482.3 | 0.22 | 2 | 1000 | 1.48 | 4.96 |
| Air | 343 | 0.34 | 2 | 1.2 | 0.0004 | - |

**Table 1.1**: *Compilation of acoustic tissue properties published in [1, p.535]. $c$ is the tissue's speed of sound, $\alpha_0$ and $b$ can be used to calculate the tissue's absorption coefficient according to Equation 1.4, $\rho$ is the density, $Z$ is the characteristic acoustic impedance, and $B/A$ is the tissue's nonlinearity parameter.*

| Tissue Name (units) | $c$ m/s | $\alpha$ Np/m/MHz |
|---|---|---|
| Amniotic Fluid | 1510 | 0.17 |
| Blood | 1575 | 1.7 |
| Bone | 3183 | 164 |
| Brain | 1565 | 8.6 |
| Breast (young) | 1450 | 5 |
| Breast (old) | 1430 | 5 |
| Eye (lens) | 1647 | 9 |
| Eye (aqueous) | 1537 | 6 |
| Eye (vitreous) | 1532 | 5 |
| Fat (peritoneal) | 1490 | 24 |
| Fat (subcutaneous) | 1478 | 7 |
| Heart | 1571 | 23 |
| Kidney (cortex) | 1567 | 12 |
| Liver | 1604 | 14 |
| Muscle (perp.) | 1581 | 11 |
| Muscle (par.) | 1581 | 16 |
| Skin | 1720 | 19.7 |
| Spleen | 1601 | 7.8 |
| Tendon (perp.) | 1750 | 43 |
| Tooth (dentine) | 3400 | 51 |
| Tooth (enamel) | 6030 | 77 |
| Uterus | 1629 | 2.7 |

**Table 1.2**: *Compilation of acoustic tissue properties published in [2, §2.5]. $c$ is the tissue's speed of sound, and $\alpha$ is the tissue's absorption coefficient.*

# 2

# Focused Ultrasound Technology

Chapter 1 established the fundamental physics of linear and nonlinear acoustic wave propagation, as well as the physical effects induced by these waves in the propagating medium. This chapter will focus on the technology used to generate and detect ultrasonic waves, with emphasis on the hardware used in therapeutic ultrasound applications, and will no longer be pertaining to audible acoustics.

This chapter begins with an introduction to the theory of *piezoelectricity* (Section 2.1), initially detailing the properties of *piezoelectric ceramics* (Section 2.1.1) and proceeding to explain the *piezoelectric effect* (Section 2.1.2). Subsequently, discussion continues with *ultrasonic transducers*, devices used for the generation and detection of ultrasonic waves (Section 2.2). The key hardware components of such devices are outlined (Section 2.2.1), followed by a presentation of the most commonly employed types of *single-element transducers* (Section 2.2.2) and *transducer arrays* (Section 2.3).

Furthermore, the most prevalent imaging modalities used to guide and monitor therapeutic ultrasound applications, i.e., *diagnostic ultrasonic imaging* and *mangetic resonance imaging*, will be discussed, presenting their strengths and limitations (Section 2.4). Lastly, bringing together all of the above, commercial integrated therapy systems utilizing ultrasound under image guidance, and which are employed in clinical applications, will be discussed (Section 2.5).

## 2.1   Basics of Piezoelectricity

[19, §17.1], [11, §2.1]

Even though several techniques can be employed to generate ultrasonic waves through high-frequency mechanical vibrations, the cornerstone of ultrasound technology is a phenomenon called the *piezoelectric effect*. This phenomenon essentially involves the bidirectional conversion of two forms of energy, namely mechanical and electrical.

### 2.1.1 Piezoelectric Ceramics

[46, §2.3], [13, §5.2], [9, p.6], [19, §17.1], [47, §1.2], [28, §3.1], [48, §7.8], [1, §§5.7-5.8], [49, §1.3]

Materials in which the piezoelectric effect is observed are called *piezoelectric materials*. Some of these materials that occur naturally include quartz and tourmaline, but due to their weak piezoelectric properties they are very rarely employed in medical ultrasonic devices. The typical materials used in this field include barium titanate, lead metaniobate, and perhaps the most commonly used material for the generation/detection of ultrasonic waves, lead zirconate titanate (PZT) . These materials are called *piezoelectric ceramics* and constitute the focus of this section. A noteworthy type of piezoelectric materials which are instrumental to the manufacture of magnetic resonance compatible transducers (see Section 2.4.2), are piezo-composite materials. These are formed by inserting piezo-electric material rods or grains into a polymer matrix to allow for control over the acoustic and electrical properties of the material. However, an in-depth analysis of these materials lies outside the scope of this section.

Piezoelectric ceramics fall under the class of *ferroelectric materials*, and are composed of a multitude of *perovskite crystals*. These crystals are characterized by a nonuniform distribution of positively and negatively charged atoms, that consequently exhibit a *dipole moment*. Within the material, adjoining polarized crystals form regions of local alignment called *Weiss domains*, each of which has a net dipole moment and therefore a net *polarization*. The polarizations of the different domains, however, are entirely random with respect to each other and as a result the material exhibits no overall polarization (see Figure 2.1(a)).

In order for these ceramic materials to become piezoelectric, they undergo a process referred to as *poling*. Poling begins by heating the material above the *Curie temperature* or *Curie point*, a temperature on the order of hundreds of degrees, which allows the dipoles to become mobile, i.e., have the possibility of re-aligning themselves. While the material is heated, a strong direct voltage, known as the *poling voltage*, is applied to the material. This causes the dipoles within the different domains to align themselves to this external field, resulting in non-zero polarization. The direction of this field, and hence the polarization, is called the *polarization axis* or *polarization direction*. While the external field is still in effect, the material is allowed to cool below the Curie point, at which point a permanent polarization remains (see Figure 2.1). After this process, the materials can be classified as poled piezoelectric materials, and exhibit a strong *piezoelectric response*. It should be mentioned that if a piezoelectric material is heated again above the Curie point, the internal dipoles will be free to move and will randomly redistribute themselves, resulting in a zero net polarization and loss of the material's piezoelectric properties.
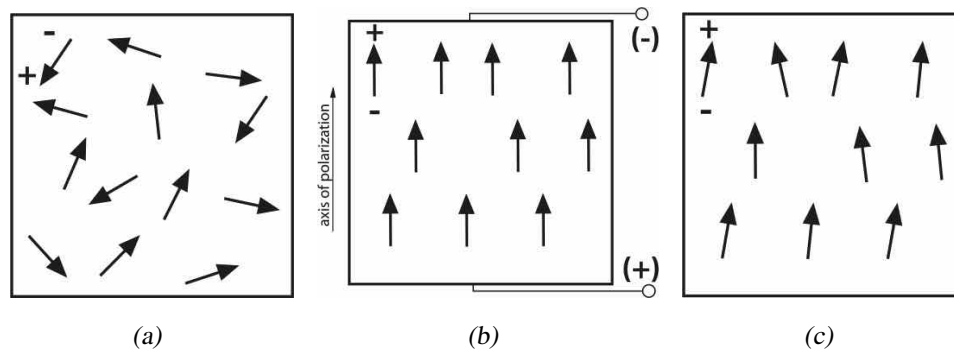
**Figure 2.1**: *Depiction of the poling process employed to create piezoelectric materials. (a) shows the random distribution of the polarized domains which results in a zero net polarization. A strong DC field is used to align the domains (b). After the field is removed the polarization remains (c).*

## 2.1.2 The Piezoelectric Effect

[13, §5.1], [46, §2.3], [27, §11.3], [11, §§2.1-2.2], [19, §17.1], [27, §11.3], [17, §2.2], [49, §1.2]

As mentioned above, the *piezoelectric effect* involves the bi-directional conversion of mechanical and electrical energy. When a mechanical deformation is applied to a poled piezoelectric material – a single unit of which is typically referred to as a *piezoelectric element* – the dipole moment associated with that element changes and a voltage, linearly proportional to that deformation, is generated. This phenomenon is called the *direct piezoelectric effect* and involves the conversion of mechanical energy into electrical. The polarity of the generated voltage depends on the direction and nature of the applied deformation. When a compression along the polarization axis or tension perpendicular to that axis is applied, a voltage with the same polarity as the original poling voltage is generated. On the other hand, a tension along that axis or a compression perpendicular to it produces a voltage with a reverse polarity. This can be seen in Figure 2.2.

The inverse of the above effect involves the conversion of electric energy into mechanical and it is called the *inverse piezoelectric effect*. If a voltage of the same polarity as the poling voltage is applied to a piezoelectric element, the element tends to elongate, i.e., enlarged length with diminished thickness. Alternatively, a voltage with a reverse polarity will cause the element to contract, i.e., enlarged thickness with diminished length. This can be seen in Figure 2.3.

The above two phenomena are also observed when the applied mechanical deformation or electrical voltage are not constant, but alternate in time. An alternating current (AC) will yield a proportional alternating deformation of the piezoelectric element, which produces a mechanical wave. Likewise, an alternating deformation on such an element yields a proportional voltage at its surface. It is this property of piezoelectric materials that allows

(a)                    (b)                    (c)
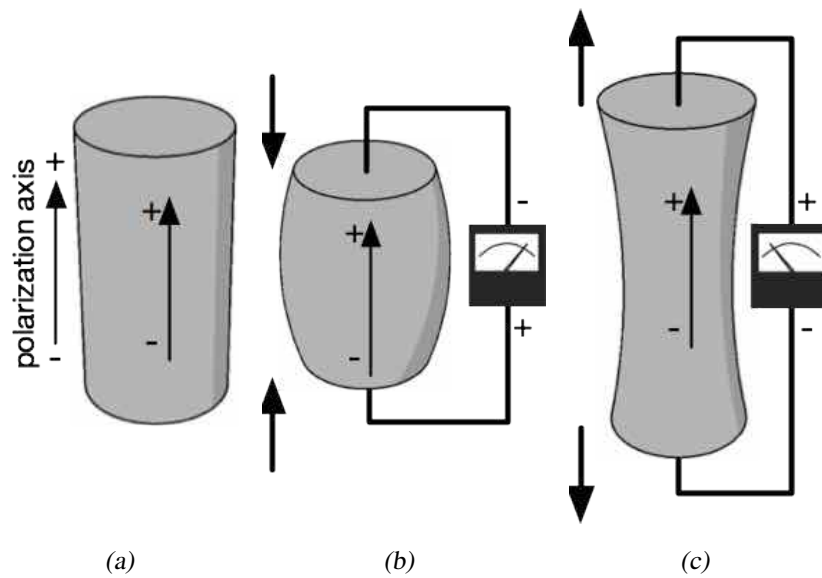
**Figure 2.2**: *Depiction of the direct piezoelectric effect. Undisturbed piezoelectric element with its polarization axis (a). When a compression is applied along that axis, a voltage with the same polarity as the poling voltage is generated (b). When tension is applied along the same axis, the generated voltage has a reverse polarity (c).*



(a)                    (b)                    (c)
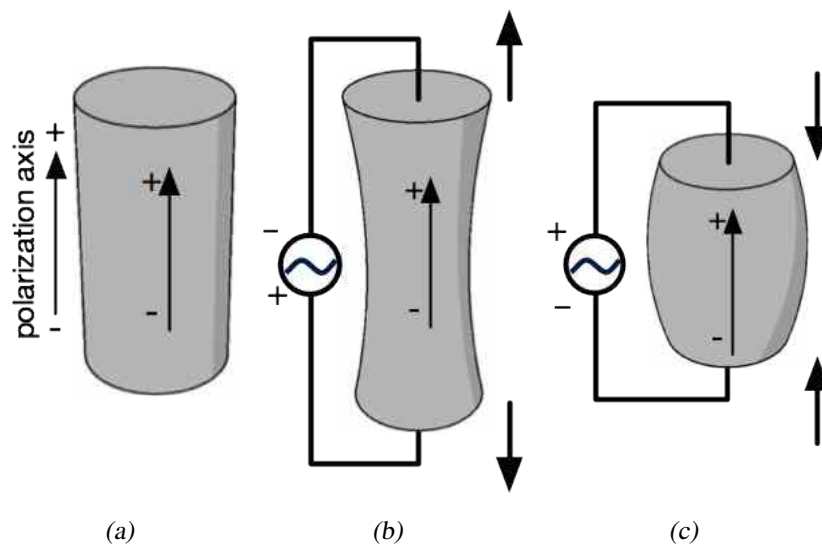
**Figure 2.3**: *Depiction of the inverse piezoelectric effect. Undisturbed piezoelectric element with its polarization axis (a). When a voltage with the same polarity as the poling voltage is applied, the piezoelectric element elongates (b). When the polarity is reversed the element contracts (c).*

them to facilitate both the generation and detection of waves that are mechanical in nature, such as ultrasonic waves (see Figure 2.4).
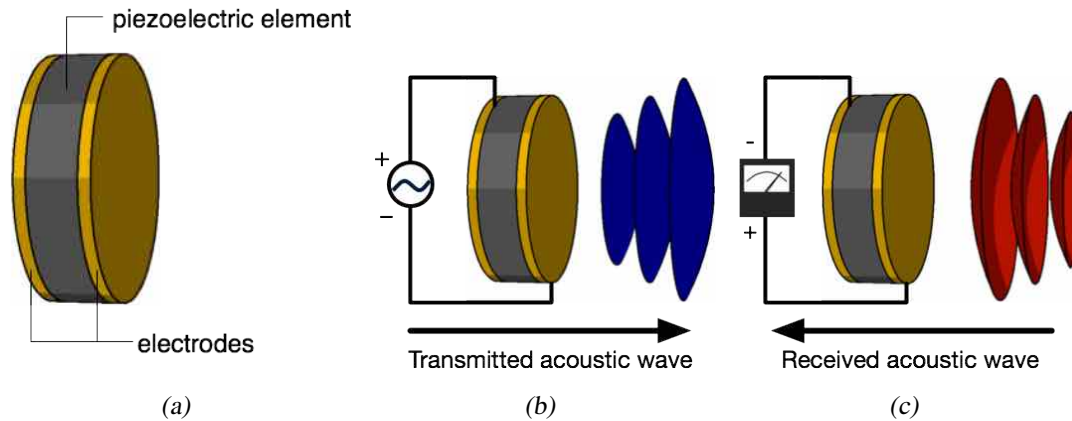


*Figure 2.4: Depiction of the the transmission and reception of acoustic waves. Using the same piezoelectric element with two electrodes bonded to its two opposing faces (a), acoustic waves can be generated by supplying the element with an AC voltage (b). Inversely, an acoustic wave impinging on the transducer will generate a measurable AC voltage proportional to the wave's amplitude (c).*

## 2.2 Single Element Ultrasonic Transducers

[3, §8.1], [2, §3.1]

The term *transducer* is used for devices that can convert one form of energy into another. In this thesis, the term will be reserved for a device that can convert electrical energy to acoustic and vice-versa.

The majority of transducers used in medical ultrasound are made with piezoelectric ceramics (see Section 2.1.1), which can be machined to various shapes and sizes. Fundamental ultrasonic transducers consist of only one such piezoelectric element and are called *single-element transducers*. This section will begin by presenting the basic concepts behind the design of these transducers and will then discuss the function of their different components. Subsequently, the main types of single-element transducers and their characteristics will be outlined.

## 2.2.1   Transducer Components & Assembly

**[3**, §8.1**], [11**, §2.3**], [2**, §3.1**], [50**, §5.3**], [49**, §1.4**]**

Two conductive electrodes are attached to the piezoelectric element to facilitate the transfer of electrical energy. In order to maximize the output of acoustic energy, these two electrodes are bonded to a backing and a matching layer and the entire assembly is placed in a plastic housing. This setup can be seen in Figure 2.5.



*(a)*                                                        *(b)*
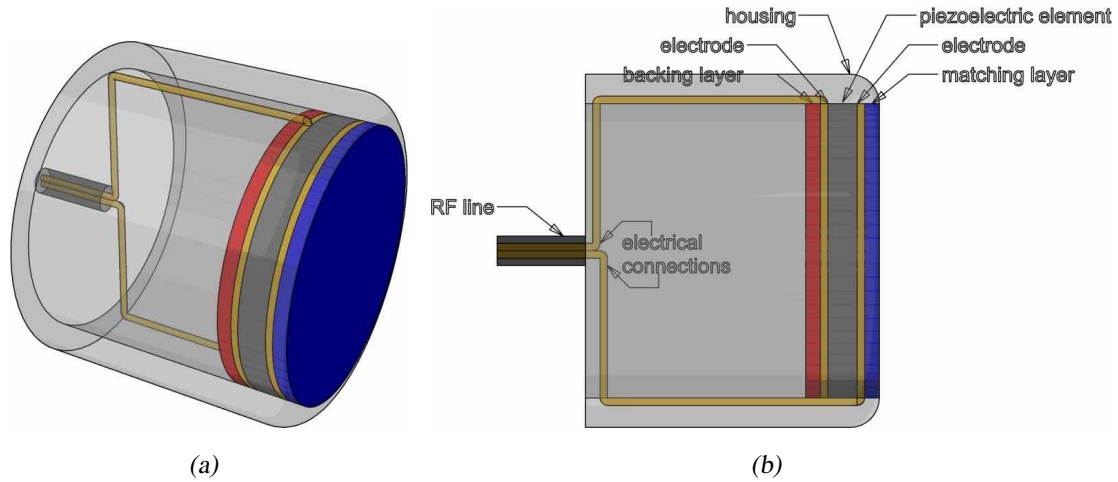
**Figure 2.5**: *Simplified sketch of a single-element transducer assembly.* (a) *is a 3D depiction, while* (b) *shows a cross section of the assembly and marks the individual components.*

### 2.2.1.1   Piezoelectric element
**[11**, §2.3**], [28**, §3.3**], [13**, §5.4**], [49**, §1.4**]**

The core component of any transducer is the piezoelectric element which permits the bi-directional conversion between electrical and acoustic energy. In order to define the frequency at which the element vibrates with maximal efficiency, and therefore the frequency of the generated ultrasonic waves, the dimensions of this element need to be selected appropriately. In the vast majority of transducers used in medical ultrasound, the piezoelectric element exhibits a large lateral extent relative to its thickness, with an aspect ratio greater than $10$. The typically employed resonance type is called *thickness expander* (TE), where the piezoelectric element expands and contracts, i.e., increasing and decreasing its thickness. The resonant frequencies for the TE mode are:

$$f_r = \frac{n c_p}{2 L_p} \tag{2.1}$$

where $f_r$ is the resonant frequency in $\mathrm{Hz}$, $c_p$ is the speed of sound of the piezoelectric material in $\mathrm{m/s}$, and $L_p$ is the thickness of the element in $\mathrm{m}$. The variable $n$ is an odd integer which indicates at which multiple of the *fundamental resonant frequency* ($n = 1$) the element will vibrate. Based on the above formula, it is obvious that the thickness of the element for a given resonant frequency can be calculated as follows:

$$L_p = \frac{nc_p}{2f_r} = \frac{n\lambda_p}{2} \qquad (2.2)$$

where $\lambda_p$ is the acoustic wavelength within the piezoelectric material.

As it can be seen from Equations 2.1 and 2.2, the thickness of the piezoelectric element must be an odd multiple of a half-wavelength, as calculated for the given material, at the required frequency.

An element operating at the fundamental resonant frequency can deliver maximum displacement amplitude, due to constructive interference as will be explained in Section 2.2.1.3, and thus maximum acoustic power, justifying its common use in medical transducers.

### 2.2.1.2   Driving System & Electrical Connections
[11, §2.3], [9, pp.7-8]

As discussed in Section 2.1.2, the reciprocity of the piezoelectric effect allows for piezoelectric material to either generate or detect acoustic waves. When a transducer is used to generate such waves it is said to operate in *transmit mode*, while if it is used to detect acoustic waves, then it is said to be operating in *receive mode*.

In the case of single-element transducers, the piezoelectric element is coated with two thin films of electrically conductive material, typically silver or gold, in order to facilitate the bi-directional transfer of electrical energy. These electrodes are then connected to the radio frequency (RF) line which mediates the transfer of electrical signals. When the element is operating in transmit mode, the RF line transfers the electrical stimulus to the element, thus generating ultrasonic waves. In transmit mode, the RF line transfers the signal generated by the element in the presence of impinging ultrasonic waves. The back electrode is used to transfer the electrical energy while the front electrode is grounded to protect the patient from electrical shocks.

In the case of transmit mode operation, the generation of an RF signal is achieved using a number of hardware components which are external to the transducer, and are referred to as the transducer's *driving system*. An AC current at the operating frequency of the transducer, and with a given amplitude and phase, is generated by a typical RF signal generator. That signal is then amplified by an RF amplifier, and transferred to the transducer through a circuit network matching the electrical impedance of the amplifier to that

of the transducer. Thus, maximum power transfer efficiency is achieved while driving the piezoelectric element.

When the transducer is operating in receive mode, the signal generated by the piezo-electric element is first amplified, and then routed to a measurement device, such as an oscilloscope, which measures and stores the generated signal.

### 2.2.1.3  Backing & Matching Layers
[3, §8.1], [9, p.7], [17, §2.2], [5, §3.1], [47, §§4.1-4.2], [13, §5.4], [28, §3.4]

When the piezoelectric element is electrically stimulated it vibrates, and acoustic waves are produced at both its faces. However, in order to maximize the acoustic energy output from the piezoelectric element towards the front face of the transducer, two additional layers are bonded to it. There are known as the *backing layer* and the *matching layer*, and can be seen in Figure 2.5(b).

The purpose of the backing layer is to force the generated acoustic waves/energy to be radiated through the front face of the element with minimal energy loss. This is achieved by selecting a material with a much smaller characteristic acoustic impedance $Z$ than that of the element (typical piezoelectric ceramics like PZT, exhibit a $Z$ of ca. $30$ MRayls). This results in a high reflection coefficient at the interface (see Section 1.1.3.2) and the produced acoustic energy will be transmitted through the front of the transducer. In order to achieve maximum energy transfer, the piezoelectric element is shaped to a thickness which is an odd multiple of a half-wavelength as described in Section 2.2.1.1. This way the wave that is generated at the back face of the element, and reflected at the backing layer, will experience constructive interference with the wave produced at the front face (see Section 1.1.3.5). As air exhibits a $Z$ lower than $0.5$ kRayls (see Section 1.1.2.4), and fits the above requirements, a common practice in medical ultrasonic transducers, is to omit the backing layer. Such transducers are characterized as being *air-backed*.

As seen in Section 1.1.2, with the exception of bone, the speed of sound $c$ and density $\rho$ of biological tissues, are very similar to those of water, with an average $Z$ of $1.5$ MRayls. Therefore, the reflection coefficient $R$ at an interface between a piezoelectric ceramic and a biological tissue would be larger than $0.9$, meaning that more than $80\%$ of the acoustic energy produced by the piezoelectric element would be reflected back at its interface with tissue. The main function of the matching layer, is to overcome this limitation by pro-viding a more gradual transition in acoustic impedance between the piezoelectric element and tissue. It has been shown [13, p.111], that in an ideal matching layer, the character-istic acoustic impedance would be equal to the geometric average of the impedance of the two media (see Equation 2.3), and would have a thickness of a quarter of the acoustic wavelength in that layer. This is depicted in the formula below:

$$Z_{\text{matching}} = \sqrt{Z_{\text{element}} Z_{\text{water}}} \tag{2.3}$$

## 2.2.2   Transducer Types

### 2.2.2.1   Planar Transducers

[1, §§6.1-6.5], [3, §§8.2-8.5], [51, §3.2], [28, §3.6], [13, §6.1-6.3], [52]

Transducers which feature a 'flat' piezoelectric element, such as the one in Figure 2.5, produce an acoustic wave that (at least in the far-field region) is planar in nature (see Section 1.1.1), and are called *planar transducers* or *unfocused transducers*. The shape or *aperture* of these transducers may be that of a disc, a ring, or even rectangular.

As a consequence of their planar nature, the emitted acoustic fields spread radially around the axis of propagation due to diffraction (see Section 1.1.3.3). Thus, at a certain distance from a transducer, the acoustic intensity of the waves becomes too low to induce the physical effects (see Section 1.3) related with ultrasonic therapy. Planar transducers are therefore outside the scope of this thesis and will only be briefly presented in this section.

In certain applications, focusing of the acoustic energy can be achieved with planar transducers by employing *ultrasonic lenses* or *ultrasonic reflectors*. Ultrasonic lenses are manufactured out of materials with a different characteristic impedance than the propagating medium, which causes the produced planar waves to focus at a given distance through refraction. Ultrasonic reflectors on the other hand, cause the waves to reflect (see Section 1.1.3.2) and can be used to guide them to focus at a single spot. However, due to absorption in the lens material, lenses cause significant attenuation of the acoustic wave energy, while reflectors are costly and difficult to manufacture. Thus, they are generally deemed inappropriate for medical ultrasonic applications and will not be discussed further in this thesis.



*(a)*                                    *(b)*
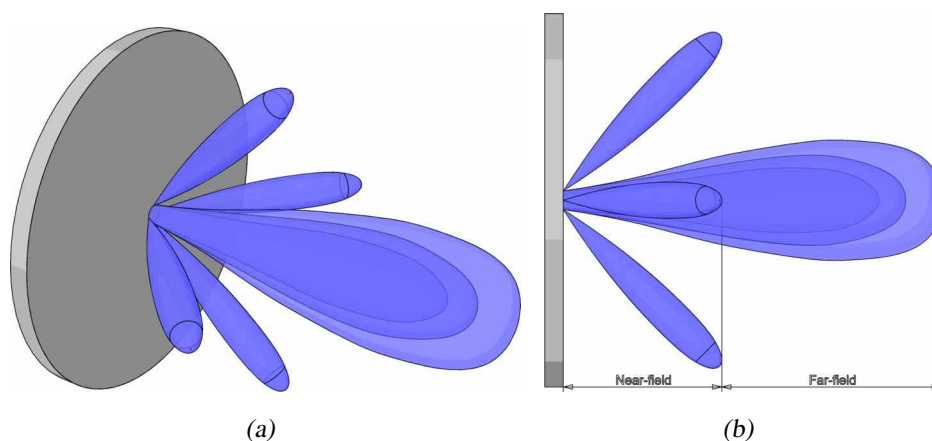
**Figure 2.6**: *Simplified depiction of the acoustic fields produced by a disk-shaped planar transducer. The main and secondary lobes are visible (a). The approximately planar nature of the produced waves can be seen in the far-field region (b).*

### 2.2.2.2 Focused Transducers

[51, §3.3], [1, §6.6], [9, p.9], [28, §3.6], [13, §6.3], [17, §2.5], [52]

Single-element transducers which naturally yield a focused ultrasonic field, employ a piezoeletric element shaped as a hollow segment of either a sphere (see Figure 2.7(a)), or a cylinder (see Figure 2.8(a)), and are commonly referred to as *spherically focused transducers* and *cylindrically focused transducers* respectively.

Spherically focused transducers produce acoustic waves that naturally tend to converge to a single *focal point* and then diverge again as they continue to propagate (see Figure 2.7(b)). This point is commonly referred to as the *geometric focus* of the transducer, and lies at the center of the imaginary sphere the piezoelectric element is a portion of. Naturally, the focal point location in respect to the transducer's face, depends on the *aperture width* of that spherical segment, i.e., *curvature radius* $R$ and the *diameter* $d$ (see Figure 2.7(a)). Because of this geometric dependence, the geometrical focusing of such a transducer is described by the transducer's *F-number*, which is the ratio of $R$ and $d$, i.e., $F = R/d$. Clearly, increasing the curvature radius of such a transducer 'pushes' the focal point further away from the transducer.

The resulting acoustic field at the focal point is technically named the *focal spot* or *focal region*, but may also be referred to as the transducer's *focus* for the sake of simplicity. In the case of spherically focused transducers, the focal spot has the shape of a long, narrow ellipsoid (see Figure 2.7(b)), with dimensions dependent on the transducer's F-number and the acoustic frequency. The size of the focal spot is inversely proportional to the transducer's diameter $d$ and at the same time proportional to the product of the acoustic wavelength $\lambda$ and the transducer's F-number [53]. The above properties also apply to cylindrically focused transducers, with the only difference being that the latter produce a continuous line of such focal spots (see Figure 2.8(b)), and thus are often referred to as *line-focused transducers*.

When employing focused transducers, the convergence of the acoustic waves at the focal point produces an acoustic pressure far higher than the pressure at the face of the transducer, the ratio of which is termed *focal gain*. Due to this, it is possible to produce acoustic waves with intensities that will induce the different thermal and nonthermal physical effects discussed in Section 1.3 at the focal spot, without inducing any effects on the overlaying tissues. This attribute of focused ultrasound is the cornerstone of its applications in therapy.

(a)



(b)
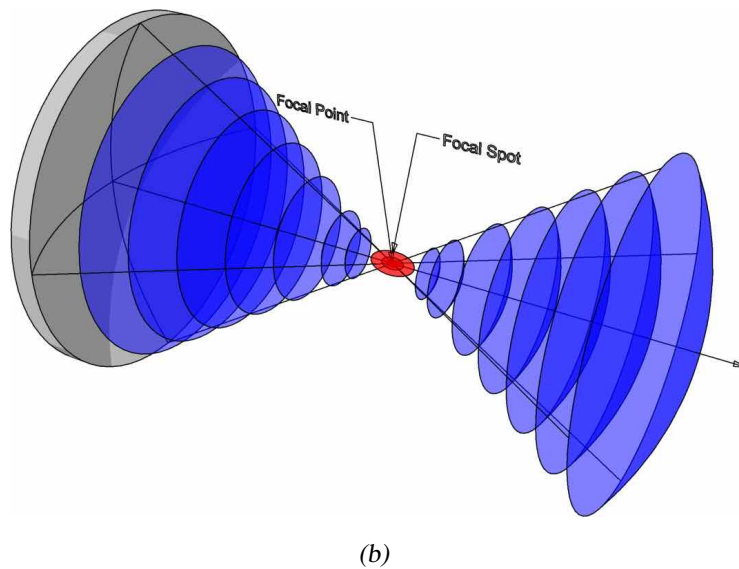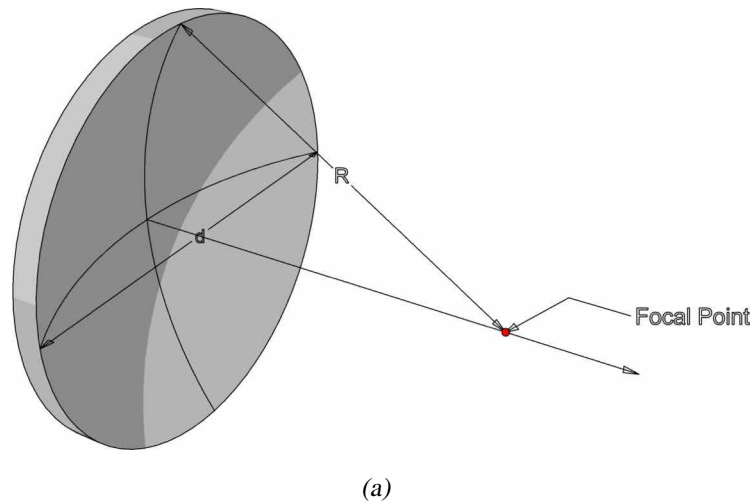
**Figure 2.7**: *Simplified illustration of a spherically focused transducer (a) and its acoustic field (b). The main geometric characteristics, i.e., the curvature radius $R$ and the aperture width $d$, which define the location of the focal spot, can be seen in (a). (b) shows the produced acoustic field where, because of the transducer's geometry, the wave fronts converge forming a focal spot and then diverge as they continue to propagate.*
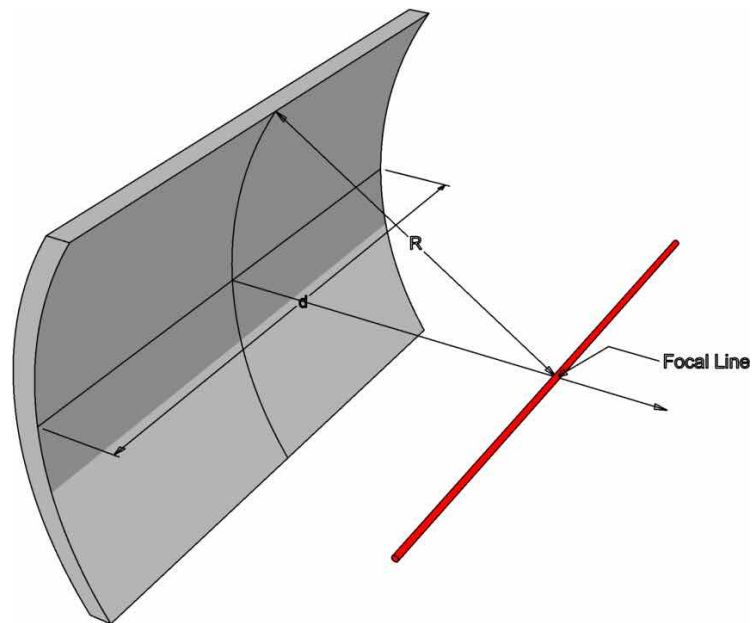
*(a)*
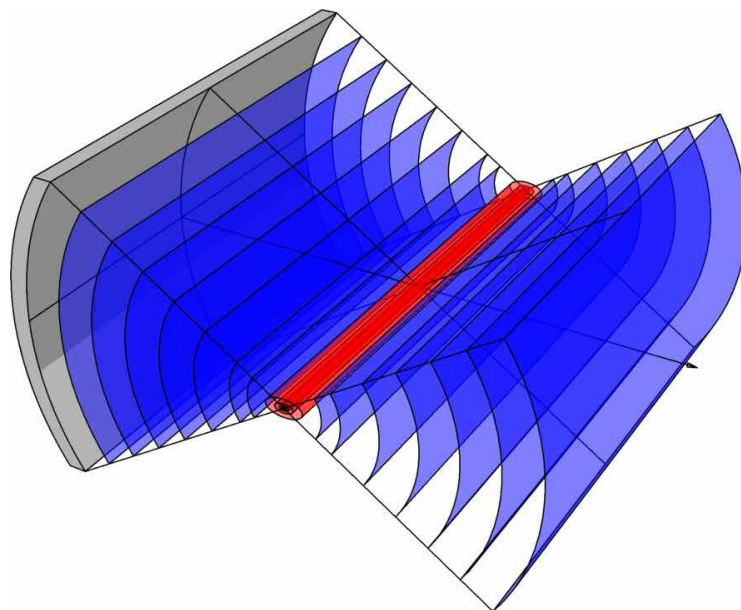


*(b)*

**Figure 2.8**: *Simplified illustration of a cylindrically focused transducer (a) and its acoustic field (b). The main geometric characteristics, i.e., the curvature radius $R$ and the aperture width $d$, which define the location of the focal line, can be seen in (a). (b) shows the produced acoustic field where, because of the transducer's geometry, the wave fronts converge forming a focal line and then diverge as they continue to propagate.*

# 2.3 Ultrasonic Transducer Arrays

[3, §8.6], [1, §7.1], [28, §3.7], [13, §6.4], [17, §2.7], [11, §7.1], [23, p.173]

Single-element focused transducers are still very common in medical ultrasound, as they are easy to manufacture, inexpensive, and only require a simple driving system (see Section 2.2.1.2). However, the main caveat behind these devices is the static nature of their generated acoustic fields, which depends entirely on their geometry and wave characteristics as shown in Section 2.2.2.2. The focal spot size is typically in the order of a few mm, and – assuming propagation in a homogeneous medium – it is always formed at a given location in respect to the transducer. Due to this attribute, single-element transducers are often referred to as *fixed focus transducers*.

However, in medical applications it is often desired to move this focal spot in order to induce physical effects in a larger tissue region. This movement of the focal spot is called *focal steering*. In the case of single-element transducers, this can be achieved by mechanically moving the device, and thus the focal spot, a slow and inflexible approach utilizing 3D translation apparati.

A well established alternative to single element transducers are *transducer arrays*, which essentially are an assembly of multiple smaller piezoelectric elements. Transducer arrays comprise as many as 16 to more than 1000 piezoelectric elements placed next to each other and each connected to its individual driving system. The different driving systems can be controlled in real-time via a computer, allowing for each piezoelectric element to be driven with its individual RF signal, exhibiting a unique amplitude and phase. For this reason such arrays are typically called *phased arrays*.

## 2.3.1 Focal Steering & Field Shaping

[9, pp.10-11], [54, §§1.2-1.4], [55, §1.1], [56]

Having direct control over the driving system of each element in a phased array, allows the operator to introduce a delay in the electrical stimulus of any element. This translates to introducing a phase shift in the ultrasonic wave generated by that element in respect to the wave generated by an element where no delay was introduced.

This property enables the operator to define the relative positions of the different wave fronts and thus the interference patterns between the generated waves (see Section 1.1.3.5) in an infinite number of combinations. Through constructive and/or destructive interference it becomes possible to flexibly shape the overall ultrasonic field within the *field of view* (FOV) of the array.

Through this procedure, transducer arrays exhibit a number of focal steering and field shaping capabilities not possible with single element transducers. These capabilities include steering the focal spot anywhere within the FOV, the simultaneous formation of

multiple focal spots (see Figure 2.9), or even compensation for wave distortion introduced by intervening media (see Figure 2.10).

The only potential disadvantages of transducer arrays, are the higher cost of such devices and the increased complexity of their operation, but the degree of flexibility they permit has established such devices as the instrument of choice in modern medical ultrasound.



(a)                                    (b)                                    (c)
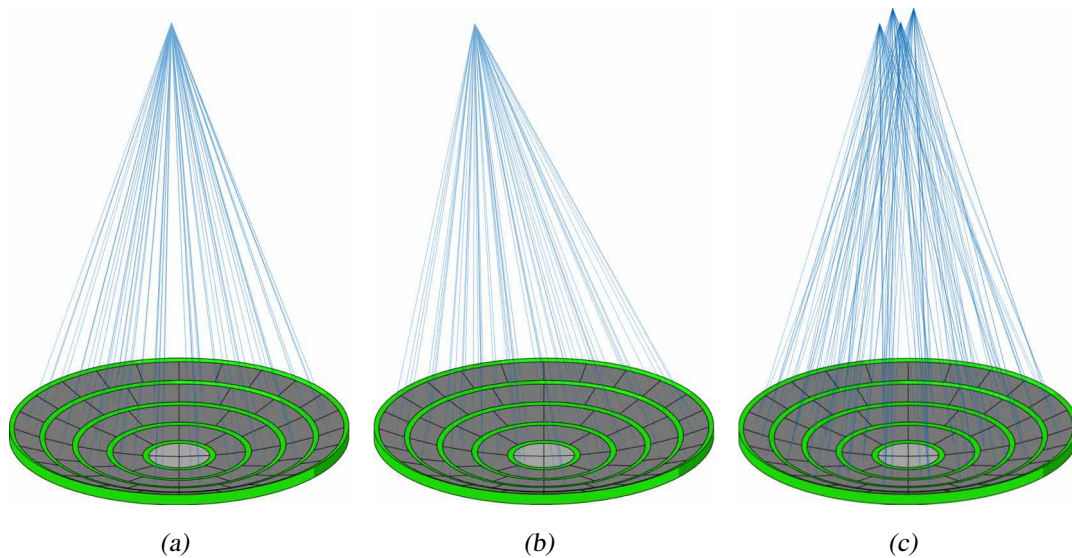
**Figure 2.9**: *Sectored annular transducer array used to create a focal spot (a), steer that spot anywhere in the FOV (b), or even create multiple such spots (c).*

### 2.3.2   Array Types

[28, §3.7], [13, §6.4], [17, §2.7], [11, §7.1], [9, pp.10-11]

Depending on the placement pattern of the different piezoelectric elements in relation to each other, phased arrays are classified into *1D arrays*, *1.5D arrays*, *2D arrays*, and *annular arrays*.

In 1D arrays the typically cuboidal elements are placed along either a straight or a curved line with a given spacing between them. These arrays are called *linear arrays* and *curvilinear arrays* respectively, and are shown in Figures 2.11(a) and 2.11(b). Such arrays exhibit a planar FOV, meaning that steering of the acoustic fields is only possible on the plane parallel to the long axis of the array, also known as the *azimuthal plane*.

The purpose of the original extension to 1D arrays was to add a small number of additional rows of elements in order to expand the FOV, as in the early years of array development the individual driving systems were costly, which limited the total number of elements that could be arrayed. These types of arrays became known as 1.5D arrays, and they
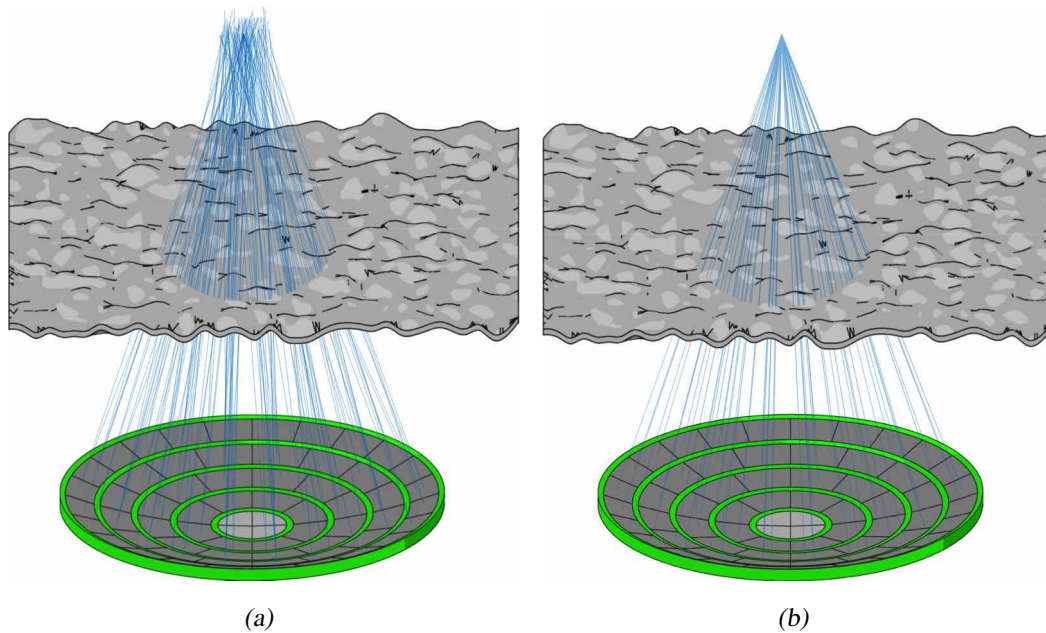
*Figure 2.10: Sectored annular transducer array used to correct for phase aberration in-duced by a surface (a) and achieve refocusing (b).*

allowed for limited steering in the elevation plane (see Figure 2.11(c)). 1D and 1.5D arrays are still very common nowadays, and are typically employed in ultrasonic imaging applications, as they can provide an expanded view of the body and aid diagnosis.

Alternative types of arrays, designed to provide focal steering along the axis of propaga-tion, are annular arrays. These arrays consist of a series of concentric, annular, i.e., ring-shaped, piezoelectric elements forming either a planar or concave surface with a given spacing between them (see Figure 2.12). However, these arrays still required mechanical translation to achieve steering off the propagation axis.

As transducer technology matured, driving systems became cheaper and more efficient. This yielded the natural extension of the 1D and 1.5D arrays, known as 2D arrays. These may consist of hundreds of elements arranged on either a flat or curved surface, thus allowing for a three-dimensional FOV (see Figure 2.11(d)).

A large variety of 2D arrays of piezoelectric elements on concave surfaces, akin to the focused single-element transducers discussed in Section 2.2.2.2, have been developed over the past few years. Examples include *sectored annular arrays* – where the ring-shaped elements are further split into smaller sectors (see Figure 2.12(c)), *randomized arrays* – where small elements are randomly placed on a concave surface (see Figure 2.13(a)), or even *hemispherical arrays* with over 1000 piezoelectric elements (see Figure 2.13(b)). These arrays allow for flexible focal steering, and control over the shape of

*(a)*                                                            *(b)*

*(c)*                                                            *(d)*
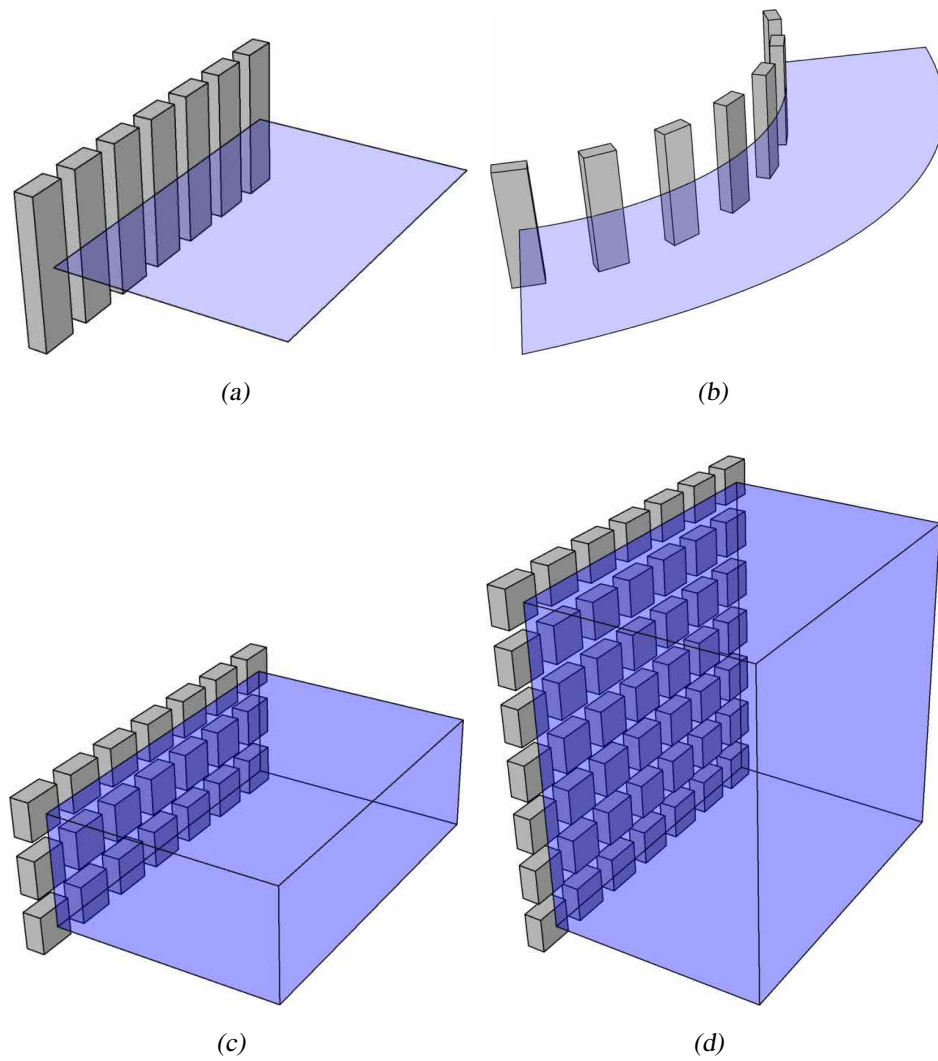
**Figure 2.11**: *Simplified illustrations of linear (a) and curvilinear (b) 1D, 1.5D (c), and 2D (d) arrays. The illustrations show the arrayed piezoelectric elements as well as the FOV, i.e., the area or volume in which it is possible to steer the acoustic focus, for every array.*

*(a)* *(b)* *(c)*
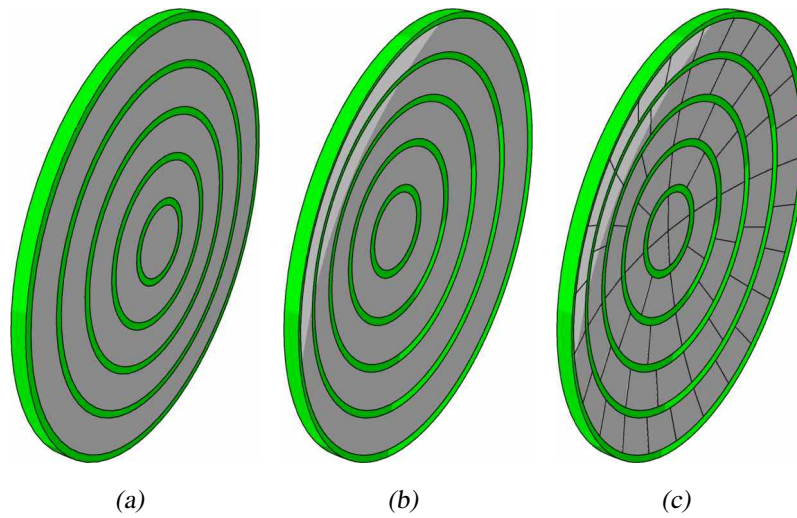
**Figure 2.12**: *Simplified illustrations of annular transducer arrays. The piezoelectric elements can be shaped as concentric rings that form either a planar (a) or a concave (b) surface. While the first two can only steer the focus along the axis of propagation, it is possible to split the annular elements into sectors (c) forming an array with a 3D FOV.*



*(a)* *(b)*
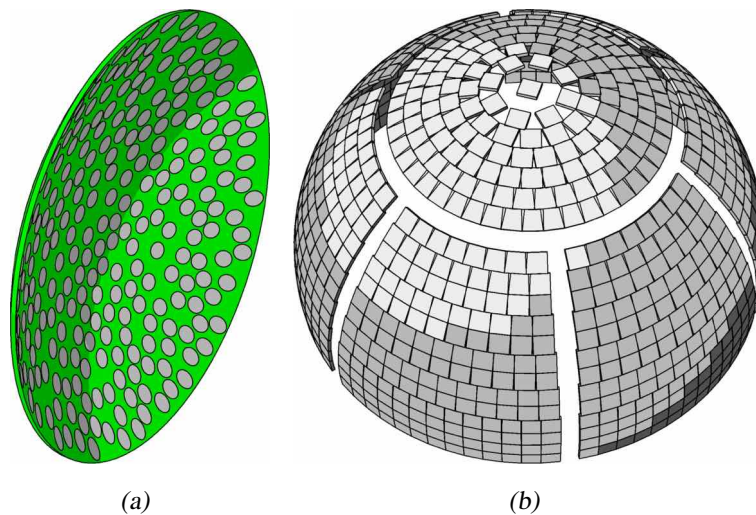
**Figure 2.13**: *Simplified illustrations of clinically used 2D transducer arrays. (a) shows a randomized array, where 256 elements are randomly distributed over a concave surface, which finds use in tissue ablation (e.g., hepatic tumors). (b) shows a large hemispherical array with 1024 piezoelectric elements which finds use in transcranial ultrasonic therapy.*

the produced acoustic fields. Due to this flexibility, these arrays constitute the norm in therapeutic ultrasound applications.

## 2.4   Image Guidance & Monitoring

[9, pp.81-83], [57, §5.5], [23, pp.167-169], [56, 58]

Focused ultrasound (FUS) produced by either single element focused transducers (see Section 2.2.2.2) or transducer arrays (see Section 2.3), finds use in a wide variety of therapeutic applications. The main advantage of employing focused ultrasound, over other interventional modalities in therapy, is its ability to precisely deposit acoustic energy into a controllable focal spot deep within the body, achieving specific therapeutic goals by inducing different physical effects (see Section 1.3), without harming the overlaying or surrounding tissues. An extensive overview of such therapeutic applications can be found in Chapter 3.

Despite the early recognition of the therapeutic potential of FUS, the medical community has been slow in accepting this technology as a viable alternative to conventional methods. The main reason for this was the absence of a method to monitor and control the acoustic energy deposition, or quantify the effects of the tissue's exposure to the ultrasonic waves.

Nowadays, guidance and monitoring by means of an imaging modality is an essential prerequisite of ultrasonic therapies. Ideally the employed modality should permit accurate imaging of the anatomy in order to allow accurate localization of the targeted and surrounding tissue, e.g., tumor surrounded by healthy tissue. Moreover, the ability to define the *acoustic window* for the therapy, i.e., being able to define the entry point for the ultrasonic waves and plan a safe trajectory through the overlaying tissue structures without encountering obstructions such as bones and air viscera, is highly desirable. In addition, it should allow for thermal imaging to verify the location of the focal spot and allow monitoring of the FUS induced tissue temperature increase. Lastly, it should be able to provide post-operative imaging of the treatment's effects for quality assurance purposes.

*Diagnostic ultrasound imaging* and *magnetic resonance imaging* (MRI) are the two foremost modalities employed to provide guidance and monitoring of ultrasonic therapies. Each modality exhibits its own advantages and limitations, which will be briefly outlined in the next sections. The key differences between the two modalities can also be found in [59]. Imaging techniques such as *computed tomography* (CT) and *positron emission tomography* (PET) also find application in FUS therapy, but are mostly used to obtain anatomical information of the patient and evaluate the post-operative effects of the treatment rather than guide the process itself.

### 2.4.1 Diagnostic Ultrasound Imaging

[9, pp. 81-83], [58, 60–63]

Given the low cost and compact size of ultrasonic transducers, diagnostic ultrasound imaging or *sonography* is an obvious option for guidance and monitoring of ultrasonic therapies, yielding *ultrasound guided focused ultrasound* (USgFUS).

The main advantage of USgFUS is that the imaging and therapeutic transducers can be combined into a single, cheap, and portable unit providing real-time monitoring and treatment capabilities. In contrast to the case of MRI (see Section 2.4.2), these transducers do not need to be nonmagnetic and can be manufactured out of conventional piezoelectric materials, and not costly piezo-composites (see Section 2.1.1). Due to the absolute positioning of the imaging and therapeutic units, this combination removes the need for image registration, as is the case in MRI guidance. Another advantage of USgFUS, is that since the imaging modality employs the same form of energy that is used for therapy, it is easy to define the acoustic window (if the target cannot be well visualized with sonography then it is unlikely that FUS therapy will be effective through that window).

The major drawback of sonography is the lack of a clinically viable method for the quantification of temperature increase in the treatment region, and the detection of the subsequently formed lesions. However, a number of research and industrial teams are investigating possible techniques to overcome this limitation [64–68]. Currently, the focal spot is only visible if the ultrasonic waves are strong enough to induce cavitation or tissue boiling (gas exsolution), as the generated bubble cloud is clearly visible with sonography. Furthermore, this modality does not provide adequate contrast between different types of soft tissue, which prevents accurate definition of the targeted tissue and inhibits the utilization of US imaging as a means of guidance.

### 2.4.2 Magnetic Resonance Imaging

[9, pp. 84-85], [58, 60–63, 69]

MRI has been designated as the imaging modality of choice for FUS therapies. Firstly, it exhibits excellent soft tissue contrast, which allows for very accurate targeting and postoperative lesion definition. Moreover, MRI offers the ability to monitor tissue temperature and tissue displacement due to acoustic radiation force (see Section 1.3.2.1).

Thermal monitoring is achieved by means of *magnetic resonance thermometry* (MRT), a technique which utilizes the temperature dependent proton resonance frequency shift and allows for measurement of tissue temperature with an accuracy of $\pm 3\,°C$ at $1.5$ T (with accuracy increasing further at higher fields strengths). Describing the physical mechanisms and operation of MRT is beyond the scope of this work, but extensive overviews on this technique can be found in [70–73].

Tissue displacement can be measured through *magnetic resonance acoustic radiation force imaging* (MR-ARFI) [74]. This recently developed technique utilizes MRI through motion-sensitive encoding MR gradients, similar to those used in MR-elastography [75, 76], to measure the micron-scale static tissue displacement induced by FUS waves as phase shifts in the resulting MR image [77, 78]. This allows for imaging of the focal spot without depending on significant tissue heating.

MRI however is not without limitations. MR scanners are very expensive to purchase and maintain, while image acquisition using this modality is slower and of lower spatial resolution when compared to ultrasonic imaging. The most prominent limitation imposed by MRI however, is the need for the FUS hardware to be nonmagnetic. As discussed in Section 2.1.1, the most common piezoelectric material used to manufacture ultrasonic transducers is PZT. This material however, contains nickel, a magnetic material which is not MR compatible. Thus, specially designed transducers and arrays need to be manufactured from piezo-composite materials, which are more complicated and costly to produce.

Nonetheless, due to the capabilities of MRI, significant effort has been invested over the past two decades in developing integrated therapy systems that combine FUS and MRI technology, which have yielded *magnetic resonance guided focused ultrasound* (MRg-FUS) systems.

## 2.5  Integrated Therapy Systems

A variety of systems utilizing FUS are employed today in the treatment of various diseases, ranging from tumor ablation to thrombolysis and drug delivery. These applications are extensively discussed in Chapter 3. This section will present some of the commonly used systems and their key characteristics, focusing mainly on the ultrasonic transducers they employ. As discussed in Section 2.4, these systems typically employ either ultrasound imaging or MRI for guidance and monitoring of the treatment. As this attribute defines both the capabilities and characteristics of the system's transducer, the presented systems will be categorized as USgFUS and MRgFUS systems. A brief compendium of such devices and their applications is given in some recent reviews [59, 79] which, however, lack details on the systems themselves.

### 2.5.1  USgFUS Systems

#### 2.5.1.1  Ablatherm®
[80, 81]

The Ablatherm® (EDAP-TMS SA, Vaulx en Velin, France) system, is used exclusively for the transrectal treatment of prostate cancer (see Section 3.1.4.1). A probe combining

an ultrasonic imaging transducer operating at 7.5 MHz, and a spherically curved, single-element, focused transducer used for treatment operating at 3.0 MHz, is used to achieve real-time imaging and sonication of prostate tumors. The treatment transducer is focused at a maximum of 45 mm, and can create an adjustable focal spot with dimensions of 1.7 mm in the transverse direction and $19 - 26$ mm along the axis of propagation. As the therapeutic transducer does not allow for steering of the focal spot, this is achieved by means of mechanical translation/rotation facilitated with an articulated robotic arm.

### 2.5.1.2  Sonablate®
[80, 81]

The Sonablate® (Focus Surgery, Indianapolis, Indiana, USA), is a similar system to the Ablatherm®, and is the second most commonly used system in prostate cancer treatment (see Section 3.1.4.1). Instead of employing two transducers, it uses the same single element transducer operating at 4.0 MHz, and either produces low-intensity acoustic waves for imaging purposes or high intensity waves to ablate the targeted tissue. The transducer is focused at 40 mm and produces focal spots with dimensions of $3 \times 3 \times 12$ mm. As in the case of the Ablatherm® system, the Sonablate® employs an articulated probe arm, allowing for mechanical movement of the transducer in order to steer the focal spot.

### 2.5.1.3  Haifu® JC
[81, p.85], [79, 82–84]

The Haifu® JC (Chongqing Haifu (HIFU) TechCo., Ltd., Chongqing, China) is another USgFUS system that has been developed and extensively employed in China. Use of this system has been reported for the treatment of a large variety of tumors, including uterine fibroids, breast, hepatic, renal and pancreatic tumors [59, 79]. Many of these applications are described in detail in Section 3.1.

This system can be operated with different single-element focused transducers, depending on the respective application and location of the tumor, with reported curvature radii varying between 90 and 160 mm. The most commonly reported transducer exhibits a diameter of 120 mm, a curvature radius of 135 mm, and operates at a frequency of 0.8 MHz, producing a fixed focal spot with reported dimensions of $1.1 \times 1.1 \times 3.3$ mm. Imaging transducers are typically placed in the center of the different therapeutic transducers operating at reported frequencies of $1.0 - 8.0$ MHz, in order to provide real-time sonographic monitoring and guidance. The fixed-focus transducer is mounted on a mechanical translation system, allowing for movement in six directions (mechanical focal steering).

### 2.5.1.4   HIFUNIT® 9000
[79, 85, 86]

Another USgFUS system, used predominately in Asia in the field of pancreatic tumor [85, 87] and uterine fibroid [86] ablation, is the HIFUNIT® 9000 (Shanghai Aishen Technology, Shanghai, China). Little information has been published about this system, but it is reported to employ six therapeutic focused transducers arrayed on the periphery of a single system which can be mechanically repositioned to achieve focal steering. The therapeutic transducers operate at $1.0$ MHz, while the system includes an imaging transducer, integrated in the center of the array, operating at a frequency of $4.0$ MHz. No information on the diameter of this transducer array is given, but the curvature radius is reported to be $170$ mm and the dimensions of the generated focal spot are $3 \times 3 \times 8$ mm.

## 2.5.2   MRgFUS Systems

### 2.5.2.1   ExAblate® 2000
[81, pp.84-85], [9, p.56], [59, 88, 89]

The ExAblate® 2000 (InSightec, Haifa, Israel) received a CE mark in 2002, and in 2004 it was approved by the Food and Drug Administration (FDA) for use in the treament of uterine fibroids (see Section 3.1.4.2). However, it has also been used for bone and breast tumors (see Section 3.1.4.4). This system uses an MR-compatible, spherically curved transducer array with a $120$ mm diameter and a $160$ mm curvature radius. Comprising $208$ elements and operating at a frequency of $0.9 - 1.3$ MHz, this array can electronically steer the focal region along the axial direction at a distance between $5 - 20$ cm.

The array is built into a standard MRI table and housed within a water-bath filled with degassed, circulating water, which provides acoustic coupling and cooling for the patient's skin. It should also be mentioned that as this array can only provide axial steering, in order to allow for focal steering off the axis, the array is mounted on a mechanical two-dimensional positioning system that can move it on the plane of the MRI table. In addition, the transducer array can be tilted approximately $20°$ in two directions, thus allowing for flexible focal steering. As the system is integrated into an MRI, it can take advantage of all the relevant imaging technology such as anatomy imaging and MRT.

A new system based on this technology, named ExAblate® 2100, received a CE mark in 2012 and it is currently being developed and evaluated for its use on prostate cancer [90, 91] and pain palliation in bone metastases [92, 93], but no details on the systems transducer have been published to date.

### 2.5.2.2  ExAblate® 3000/4000
[94–99]

The ExAblate® 3000 (InSightec, Haifa, Israel) was the first MRgFUS system targeted entirely at brain treatments by means of transcranial sonication, i.e., treatment without performing a craniotomy. This system employed a hemispherical transducer array (see Section 2.3.2), 30 cm in diameter, with 512 piezoelectric elements individually driven at 220 or 670 kHz. This array was fully integrated into an MRI system allowing for guidance and monitoring, and could steer the focal spot anywhere within its FOV. After a series of animal studies [100], the ExAblate 3000 system was applied to human brain tumor treatments [95], but with limited success.

The ExAblate® 4000 was later developed as an improvement to its precursor. The new transducer array has the same 30 cm diameter but comprises 1024 elements and operates at 230 or 650 kHz. A model of this transducer can be seen in Figure 2.13(b). This system has found many neurosurgical applications – for which it was given the CE mark in 2012 – including neuropathic pain treatment [101, 102], essential tremor [103], and epilepsy [104]. For an overview of these applications see Chapter 3.

It should be mentioned that a system similar to the ExAblate® 4000, using 512 piezo-electric elements, and operating at 1.0 MHz, is currently being developed by SuperSonic Imagine (SSI, Aix en Provence, France) [105], but is still undergoing evaluation [106].

### 2.5.2.3  Sonalleve®
[89, 107–110]

The Sonalleve® (Philips, Netherlands) is a recently developed MRgFUS system, which received a CE mark in 2011 and is currently being clinically evaluated for uterine fibroid ablation [109, 111–114]. Similarly to the ExAblate 2000, it employs a spherically curved transducer with a 130 mm diameter and a 120 mm curvature radius. The array employs 256 randomly distributed (randomized array, see Section 2.3.2) piezoelectric elements to minimize the intensity of the secondary lobes. Operating at 1.2 or 1.45 MHz, this array creates focal regions with dimensions of $1 \times 1 \times 7$ mm which can be steered anywhere in the array's FOV.

A notable attribute of the Sonalleve® is that, unlike the ExAblate® 2000 which performs a *point-by-point ablation*, completely ablating one region of the tumor before proceeding to the next, the Sonalleve system performs *volumetric ablations*. It rapidly and constantly moves the focal spot within the entire targeted region on a spiral trajectory until the tumor is ablated. This approach may allow for ablation of larger tumor volumes and better ablation homogeneity which, if not achieved, is believed to lead to viable tumor cells being spared [107, 115].

#### 2.5.2.4   Haifu® JM 2.5C
[79, 116]

A system called Haifu® JM 2.5C (Chongqing Haifu (HIFU) TechCo., Ltd., Chongqing, China) has also been reported in the treatment of uterine fibroids [116], but no extensive literature exists. This system comprises a single-element focused transducer with a $180\,\mathrm{mm}$ diameter and a $150\,\mathrm{mm}$ curvature radius, operating at $0.7 - 1.2\,\mathrm{MHz}$, and creating $2 \times 2 \times 5\,\mathrm{mm}$ focal spots. In a manner similar to the ExAblate® 2000 and the Sonalleve® systems this transducer is MR compatible and housed in a water-bath. The fixed-focus transducer is mounted on a mechanical translation system, allowing for movement in six directions (mechanical focal steering).

# 3

# Therapeutic Ultrasound Applications

Medical ultrasonic applications fall under two principal classes being sonography, i.e., diagnostic ultrasound imaging, and therapeutic ultrasound, however, the scope of this chapter is limited to the latter. Having discussed the fundamental physics of acoustics in Chapter 1, and the basics of transducers and transducer arrays in Chapter 2, this chapter will present the foremost therapeutic applications of focused ultrasound.

Therapeutic FUS applications utilize the different physical effects induced by the interaction of ultrasonic waves with tissue, be it thermal (Section 1.3.1) or nonthermal (Section 1.3.2), in a wide range of applications. As sonication of tissue, however, may yield a simultaneous combination of different effects, the therapeutic FUS applications will instead be categorized according to the acoustic intensities utilized to achieve those effects.

This categorization yields *high intensity focused ultrasound* (HIFU) and *low intensity focused ultrasound* (LIFU). Unlike sonography, where low acoustic intensities and pressures of $0.1 - 100 \text{ mW/cm}^2$ and $1 - 3 \text{ kPa}$ are typically used, HIFU applies ultrasonic waves with intensities and pressures orders of magnitude higher ($10 - 10000 \text{ W/cm}^2$ and $10 - 30 \text{ MPa}$ respectively). HIFU transducers or arrays typically operate at frequencies of $0.5 - 3.5 \text{ MHz}$, with continuous wave sonication up to multiple seconds, and are commonly used in the ablation of tissue [58, 63, 117], most notably in oncology (Section 3.1).

On the other hand, LIFU utilizes acoustic intensities up to two orders of magnitude lower than those employed in HIFU. The employed frequencies may be anywhere in between $20 \text{ kHz}$ and $8.0 \text{ MHz}$, but the clinically relevant frequencies are typically in the order of $0.2 - 2.0 \text{ MHz}$, with acoustic pressures of a few $\text{MPa}$ [118–121]. Short bursts of ultrasonic pulses with durations of a few milliseconds are used in the LIFU regime, and can be applied to induce cavitation without significant thermal effects. These are commonly employed in applications such as the disruption of the blood brain barrier (Section 3.2.1), sonoporation (Section 3.2.2), thrombolysis (Section 3.2.3) and neuromodulation (Section 3.2.4).

Following the overview of therapeutic FUS applications, the challenges inhibiting this treatment modality, their impact, as well as known approaches that are investigated in order to overcome them are discussed (Section 3.3).

A large number of different applications are also known to utilize therapeutic ultrasound, such as lithotripsy, physiotherapy, tissue and bone repair/healing, or even ultrasonic lipolysis for cosmetic purposes. These applications, however, lie outside the scope of this thesis and will not be discussed, but have been reviewed in a large number of publications [15, 16, 61, 63, 122, 123].

# 3.1　HIFU ablation

## 3.1.1　Therapeutic Principle

[56, 58, 60, 63, 69, 117], [57, §§5.1,5.3]

In HIFU ablation, ultrasonic waves are generated by a transducer and converge into a very small and sharply demarcated focal spot deep inside the body, where they cause significant deposition of acoustic energy while sparing the overlaying or surrounding tissue.

The high acoustic intensities and frequencies result in high tissue absorption coefficients (see Section 1.1.2.3), and as a consequence, a significant percentage of the deposited acoustic energy is converted into thermal (see Section 1.3.1). This causes a rapid tissue temperature increase of over $60 - 80\,°C$ in the focal region in a matter of $1 - 3$ s, inducing coagulation necrosis in the tissue [124]. Simultaneously to the temperature increase, the high acoustic intensities induce inertial cavitation (see Section 1.3.2.3), which leads to extremely high local temperatures and mechanical stresses, severely damaging the targeted tissue through apoptosis [125]. The combination of these two effects leads to immediate cell-death and the formation of a sharply delimited lesion, effectively destroying the targeted tissue region. Even though temperature increase of the targeted tissue is the main goal of this type of therapy, the two effects described above are typically linked and cannot be distinguished in the clinical environment.

## 3.1.2　Therapy Setup

[61, 69, 94]

In HIFU ablation, ultrasonic waves are generated by either a single element focused ultrasonic transducer (see Section 2.2.2.2), or a transducer array (see Section 2.3). Single element transducers can be either extracorporeal, i.e., located outside the body, or transrectal devices, which are used for ablation of the prostate (see Section 3.1.4.1).

As discussed in Section 2.4, guidance and monitoring of this procedure is necessary in order to locate the tissue targeted for ablation, monitor the procedure, as well as to post-operatively ascertain the success of the treatment. Due to the intense thermal effects exhibited in this treatment and the lack of temperature monitoring in diagnostic ultrasound, MRI is typically employed to achieve this.

### 3.1.3 Volume Scanning

[56, 58, 60, 117], [57, §5.3]

An important aspect of HIFU ablation is the size of the generated focal regions, and thus the created lesions, which is predominantly dependent on the transducer geometry and the frequency of the ultrasonic waves. The ultrasonic frequencies typically employed in HIFU are in the order of $0.5 - 3.5\,\mathrm{MHz}$, which result in ellipsoidal focal spots with dimensions in the order of $8 - 15\,\mathrm{mm}$ along the axis of propagation, and $1 - 3\,\mathrm{mm}$ in the transverse direction. Even though this attribute of HIFU allows for very precise tissue ablation, it also means that in order to successfully ablate clinically relevant tissue regions, e.g., tumors, which are multiple $\mathrm{cm}^3$ in size, multiple such lesions must be overlapped to cover the entire targeted volume (see Figure 3.1). This approach is commonly referred to as *volume-scanning*, and is typically achieved by mechanically moving the transducer in the case of single element transducers, or electronically steering the focal spot when using transducer arrays – a technique discussed in Section 2.3.1. As discussed in Section 3.3.1, this aspect of HIFU ablation causes the treatment of large tissue volumes to exceed several hours, as adequate pauses need to be allocated between sonications to allow the overlaying tissue to cool down and avoid collateral tissue damage.

### 3.1.4 Applications

[58, 63, 94]

The applicability and efficacy of HIFU ablation has been assessed for the treatment of a variety of benign and malignant tumors in the body. However, to date only treatment of prostate cancer, uterine fibroids, and to some extent, pain palliation in the case of bone tumors have seen clinical acceptance and application to large patient populations. The foremost therapeutic applications of HIFU ablation are briefly reviewed in the following sections, but the reader is also directed to a large number of relevant reviews published within the past 5 years [58, 59, 63, 79, 81, 94, 96, 98, 123, 126–129], and in particular [123] which offers a comprehensive overview of the currently ongoing clinical trials utilizing HIFU ablation.
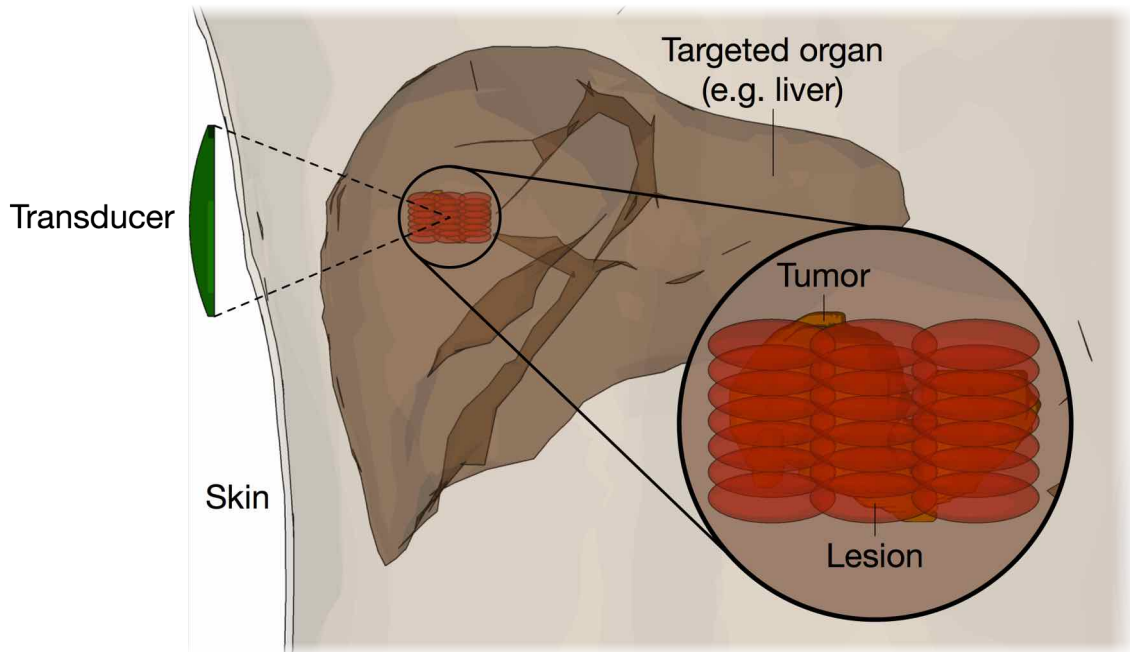
*Figure 3.1*: *Conceptual diagram of volume scanning in HIFU ablation. An example of hepatic tumor ablation is shown here. The entire volume of the tumor is ablated by overlapping multiple lesions either through electronic focal steering or by mechanically moving the transducer.*

### 3.1.4.1 Prostate Cancer

[58, 63, 80, 81, 128]

Second only to lung cancer, localized prostate tumors are the most frequently diagnosed type of cancer in men worldwide [130]. The standard treatment options however, being radical prostatectomy and radiation therapy, have both been associated with significant risks and complications, while a substantial number of patients are deemed unsuitable for these interventions as they cannot tolerate major surgical procedure or radiation. To that end, alternative and minimally invasive procedures have been sought after, among which HIFU ablation is a prevalent one.

This therapy is typically performed under ultrasound guidance (USgFUS, see Section 2.4.1), with a device comprising both an imaging transducer (imaging probe) and a single-element focused transducer which produces the HIFU waves (therapeutic probe). This device is covered with a balloon – wherein degassed, cooled water is circulated – which is then inserted transrectally and positioned close to the prostate. The purpose of this water-filled balloon is to provide acoustic coupling, i.e., to ensure there is no air from the rectum in the probe's FOV and ensure impedance matching (see Section 2.2.1.3), between the device and the rectum wall, as well as to cool the latter and prevent rectal burns.

The prostate tumors are then ablated without harming the healthy tissue, as described in Section 3.1.1, while mechanical rotation or translation of the device, typically by means of an articulated robotic arm, is used to steer the focal spot and overlap multiple lesions.

In the past $15$ years over $30,000$ patients with prostate cancer have been treated with HIFU using the aforementioned clinical systems, mostly in Europe (using the Ablatherm system, see Section 2.5.1.1) and Asia (using the Sonablate system, see Section 2.5.1.2) but also in Canada and the USA. Most of the treatments were performed on patients who were either unsuitable for the conventional treatment modalities or not willing to undergo them. Reported success rates are in the order of $60 - 80\%$ [63, 128], but as these rates depend on a number of treatment specific factors, the reader is directed to several recent, comprehensive review articles on the topic [80, 131–134]. Multiple complications have been reported and include urinary retention, infection of the urinary tract, impotence, chronic pain and incomplete treatment of the disease, but the occurrence rates of these complications are comparable to those reported for the established therapies. However, due to these complications and the lack of longer-term follow-up studies, the overall efficiency of HIFU ablation for the treatment of prostate cancer cannot be fully ascertained. Nevertheless, it is expected that if the available promising results of HIFU treatment in prostate cancer are confirmed in the future, this modality could challenge the current standard therapies.

### 3.1.4.2 Uterine Fibroids
[79, 128, 129, 135], [9, ch. 9], [136, pp.341-348]

Uterine leiomyomas, commonly referred to as uterine fibroids, are the most common benign pelvic tumors observed in premenopausal women. Although many women with uterine fibroids remain asymptomatic, others exhibit adverse symptoms ranging from pelvic pain and menorrhagia, to infertility. Due to the benign nature of these tumors, the definite treatment for this condition is complete hysterectomy, i.e., removal of the uterus and therefore complete tumor excision, which leads, however, to infertility. An alternative invasive treatment is myomectomy, i.e., excision of only the fibroid, which often leads to recurrence and the need for further operations associated with high morbidity rates. The ability of HIFU ablation to noninvasively ablate tissue deep within the body made it an ideal alternative to these surgical procedures.

Due to the nature of the treated anatomical region, these treatments are performed under MRI guidance (MRgFUS, see Section 2.4.2) as its excellent soft-tissue contrast makes the fibroids easy to distinguish and target, while utilization of MRT allows for thermal monitoring of the procedure. The patient's abdomen is fully shaved to remove any hair (which may create air pockets and cause an impedance mismatch) and is then placed on the MRI bed in a prone position. An MR-compatible transducer (single-element or array numbering up to hundreds of elements), is immersed into a degassed water-bath, integrated

into the MRI bed, and coupled to the patient's skin through a gel pack. The ablation procedure starts with low-power sonications under MRT to ensure accurate targeting of the fibroid. Once targeting is assured, sonications with gradually increasing acoustic power are administered until temperatures of over $60\,^{\circ}$C are reached and ablation is achieved. The procedure continues by overlapping multiple lesions, through either mechanical or electronic steering, until the fibroid is completely ablated with the procedure lasting up to ca. $3$ h.

The treatment of uterine fibroids is the only HIFU ablation therapy currently approved by the Food and Drug Administration (FDA). Since the first clinical trials in 2000, more than $8,500$ treatments have been administered with the ExAblate® 2000 system (see Section 2.5.2.1). The reported success rates have been very promising with a significant symptom reduction in more than $75\%$ of the women treated [59]. However, due to the large number of relevant publications over the years, the reader is directed to a number of comprehensive review articles [79, 128, 129, 135] and books [9, ch. 9], [136, pp.341-348]. It is also worth mentioning that multiple successful post-operative pregnancies and births have been reported [137]. Moreover, the reported side-effects of the treatment are minimal, including transient pain, sciatica, and minor skin burns which healed shortly after the treatment. Overall, HIFU ablation of uterine fibroids has be shown to be an excellent alternative to invasive surgery and it is widely employed in medical centers throughout the world.

### 3.1.4.3   Hepatic, Pancreatic and Renal Cancer
[59, 63, 79, 128, 129, 138, 139], [9, pp.87-89]

Hepatic malignancies, referring to both hepatocellular carcinomas and metastases, are a very commonly encountered type of cancer. Invasive surgery for tumor resection or liver transplantation are the current standards in therapy, as radiotherapy and chemotherapy have shown limited success [63, 79]. However, only a small number of patients are eligible for treatment. The main reason for this is the nature of the disease itself, as it usually exhibits multiple tumor nodules scattered throughout the liver, often close to vasculature, making them hard to excise surgically. Multiple (minimally) invasive alternatives to surgery have been explored, including percutaneous radiofrequency, microwave and laser ablation, as well as cryotherapy, and have been shown to successfully treat liver malignancies.

Several investigations into hepatic tumor treatment with FUS have been reported on hundreds of patients with encouraging results, recent reviews of which can be found in [59, 79, 140, 141]. The majority of these treatments were performed in China and the United Kingdom, and either combined FUS with chemotherapy or utilized FUS alone. The most commonly employed treatment system is the Haifu® JC (see Section 2.5.1.3) which employs ultrasonic guidance (USgFUS).

The treatment of hepatic tumors with FUS is hampered by a unique set of challenges which deters the extended use of MRgFUS in this field. Partial obstruction by the ribs limits the treatable volume, introduces the risk of collateral tissue damage, and degrades the overall focus quality. Respiration induced motion of the liver leads to inaccurate MR thermometry and sonication of the targeted tissue region. Lastly, the extensive vasculature network of the organ further complicates treatment, as the high vascular perfusion inhibits the thermal ablation of liver tissue. These issues are further discussed in Sections 3.3.2.3 and 3.3.3.

Multiple clinical trials have also been performed for the treatment of renal and pancreatic tumors, typically employing USgFUS, with encouraging results. However, the aforementioned issues of organ motion and thoracic cage obstruction pose the same limitations as in the case of hepatic tumor treatment. Brief overviews of these clinical trials and their results can be found in review articles [59, 63, 79, 128, 129]. However, additional clinical trials and conclusive results are required before FUS can be recognized as a viable alternative to the well established and clinically accepted percutaneous options mentioned above.

### 3.1.4.4 Bone Cancer
[58, 59, 79, 81], [9, p.89]

FUS has also been used in clinical practice for the treatment of primary bone tumors, as well as to achieve pain palliation in the case of bone metastases. Such metastases develop in $30\%$ of all cancer patients and $50-60\%$ of these cases typically experience severe pain [142, 143].

Both MRgFUS with the ExAblate$^{®}$ 2000 (see Section 2.5.2.1) and USgFUS with the Haifu $^{®}$ JC (see Section 2.5.1.3), have been employed to either ablate primary tumors or reduce pain by means of denervation in the periosteal layer of the bone.

Successful ablations of primary tumors have been reported in recent studies [144, 145] but the suitability of FUS treatments for these conditions remains to be ascertained. Pain palliation, however, shows significant promise, and multiple clinical trials [146–148] have been reported upon with an average of $70-90\%$ pain reduction. Extensive reviews of this type of treatment and the reported results of the different relevant studies is given in [81, 128, 129, 149].

### 3.1.4.5 Brain Surgery
[59, 96, 98, 126, 150]

Traditional neurosurgical interventions are always associated with some degree of collateral tissue damage, as the neurosurgeon needs to resect and remove the targeted deep-

seated brain tissue by cutting or dissecting through healthy tissue. A noninvasive alternative to surgery such as FUS is highly desirable, but the early attempts to employ FUS in the brain for functional neurosurgery or tumor ablation enjoyed limited acceptance by the clinical community. The reason for this was the requirement for a craniotomy to be performed, i.e., removing a part of the skull in order to allow the ultrasonic waves to propagate unimpeded in the brain.

The development of large MR-compatible ultrasonic arrays, such as the ExAblate® 4000 with 1024 piezoelectric elements (see Section 2.5.2.2), combined with the guidance and monitoring capabilities of MRI (see Section 2.4.2), have yielded transcranial FUS (tcFUS) therapies under MR guidance (tcMRgFUS), a noninvasive alternative to conventional surgical approaches.

During tcFUS treatments, the patient's head is fully shaved, fixed to the table with a stereotactic frame, and positioned in the helmet-like cavity of the transducer. The transducer cavity is filled with circulating, degassed water which is held back with a flexible membrane seal and allows for acoustic coupling and scalp cooling (this setup can be seen in Figure 3.2). The treatment typically starts with MR imaging to define the targeted location, followed by low-power sonications which raise the tissue temperature at the focal region by a few degrees, visible under MRT. Once targeting has been verified, multiple high-power sonications are then used to ablate the targeted tissue.
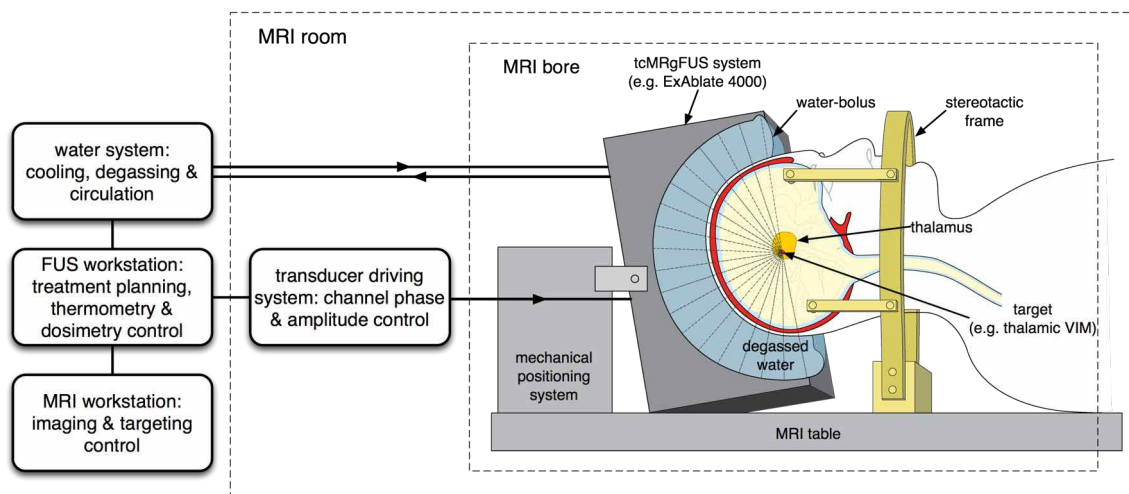


**Figure 3.2**: *Schematic diagram of a tcFUS treatment setup with an integrated therapy system like the ExAblate® 4000.*

Initial clinical trials have indicated successful treatment of patients with brain tumors [95], neuropathic pain [101, 102], and essential tremor [103]. In addition, clinical trials for the treatment of movement disorders, gliomas, obsessive compulsive disorder (OCD), and Parkinson's disease are being set up in medical centers around the world [126]. Apart

from the neurosurgical applications of FUS feasible through noninvasive tissue ablation, this technology has been extensively evaluated for LIFU applications such as thrombolysis [151, 152], blood-brain barrier (BBB) disruption for increased drug delivery [153–155], and even neurostimulation [156, 157], applications which are discussed later in this chapter. Despite the substantial benefits of tcFUS when employed in the clinical setting, complications have been reported in human trials, typically in the form of unforeseen brain hemorrhaging [94, 96, 102]. These issues are typically caused by the presence of the skull which induces phase aberrations and high attenuation, and are discussed in more detail in Section 3.3.2.2.

## 3.2 Non-Ablative Applications

### 3.2.1 Blood-Brain Barrier Disruption

#### 3.2.1.1 The Blood-Brain Barrier: Structure & Function
[158, p. 223], [159, p. 766], [160, p. 14], [150, 161–164]

The exchange of substances between blood and extracellular fluid in the central nervous system (CNS), is regulated by a complex system of barriers which are distinguished into two categories depending on their position. The barrier between the blood and the brain fluid is called the *blood-brain barrier* (BBB), while the barrier between the blood and the *cerebrospinal fluid* (CSF) is called the *blood-cerebrospinal fluid barrier*.

The BBB is the cellular interface between the blood and the CNS. In addition to the physiologic barrier at the level of the basal lamina, the BBB is composed of capillary endothelial cells tightly fused by an elaborate network of intracellular attachments known as *tight junctions* (as well as astrocytic foot processes that abut the endothelium and its basement membrane). A simplified depiction of this structure can be seen in Figure 3.3. The BBB restricts the diffusion of microscopic objects, e.g., bacteria, and large or hydrophilic molecules into the CSF, while allowing the diffusion of small hydrophobic molecules. The factors which limit diffusion through the BBB are lipid solubility, molecular size, charge, and whether they can utilize any carriers of the endothelial cells.

Therefore, these barriers often make it impossible to achieve effective concentrations of therapeutic drugs, such as protein antibodies and nonlipid-soluble drugs, in the cerebrospinal fluid or parenchyma of the brain. Because of this characteristic of the BBB, more than 98% of potential therapeutic drugs [165] tailored to treat many CNS conditions are not usable due to their inability to cross the BBB.

A small subset of drugs which comprise small molecules with high lipid solubility and low molecular mass can cross the BBB, but these drugs only target a few brain diseases like depression, affective disorders, chronic pain and epilepsy. Many other serious disorders
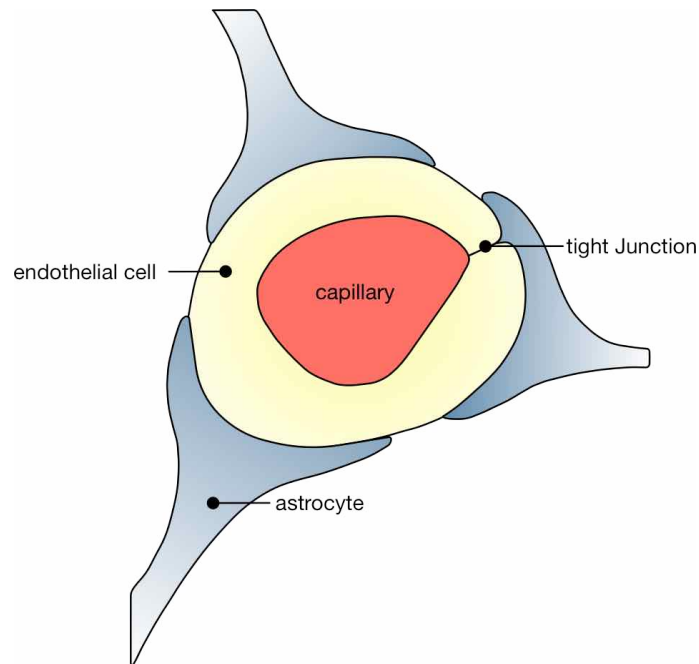
**Figure 3.3**: *Simplified depiction of the BBB structure, showing a cerebral capillary surrounded by the endothelial cell wall and fused by a tight junction.*

such as Alzheimer's disease, stroke, brain cancer, HIV infection of the brain, Parkinson's disease, and multiple sclerosis only respond to large-molecule drugs which cannot cross the BBB.

### 3.2.1.2   Conventional BBB circumvention techniques
[161, 162, 164, 166–172]

Due to the plethora of CNS diseases and the strict limitations imposed by the BBB, various techniques have been examined through the years to overcome these restrictions.

Prominent techniques involve the reformulation of the drug's molecules either to become lipid soluble and cross the BBB through lipid-mediated drug transport, or modifying them so that they can access the endogenous BBB transport systems and enter the brain.

The most common technique of disrupting the BBB in clinical practice is osmotic disruption, which involves the intra-arterial infusion of a hypertonic solution (commonly manittol) into a carotid or vertebral artery through a catheter. This causes the endothelial cells to undergo a transient (lasts for a few hours) and reversible shrinkage, which results in the opening of the tight-junctions. Following this disruption of the BBB, the therapeutic agent is then injected through the same catheter.

Other approaches are intracathecal, intraventricular, and interstitial administration, which involve direct injection of the therapeutic drug into the CSF, ventricles, and brain inter-

stitium respectively. Extensive reviews of existing BBB circumvention techniques can
be found [166–168, 170]. However, all current techniques entail major disadvantages
because they are either invasive – involving penetration of non-targeted tissue and risk
of bleeding and infection, are limited in the amount of drug they can deliver, or are not
targeted, i.e., they deliver the drug everywhere in the brain which may not be desirable.

### 3.2.1.3   FUS Induced BBB Opening
        [59, 150, 162, 173–175]

First evidence that FUS irradiation of the brain can lead to BBB disruption (BBBD) were
published in 1956 by Bakay et al. [176]. However, the earlier attempts to increase vascu-
lar permeability to drugs, employed FUS to induce either tissue temperature increase or
inertial cavitation, and were always associated with some degree of tissue damage. It was
not until 2001 when Hynynen et al. [161] demonstrated that the use of pulsed LIFU waves
in conjunction with intravenously administered microbubbles can yield reproducible and
reversible BBBD without inducing tissue damage. An extensive review of the history of
FUS induced BBBD can be found in [174], while [175] gives a recent overview of this
technology, its principles and its current applications.

Prior to administering FUS, the subject is injected with commercially available US con-
trast agents (UCA), which contain high concentrations of preformed microbubbles. These
microbubbles contain a gas encased in an albumin or lipid shell, with diameters in the
range of $1 - 10$ μm. Once injected, these microbubbles tend to spread throughout the
entire capillary network. Although the mechanisms of FUS induced BBBD are not en-
tirely understood or verified, a working hypothesis is that when these microbubbles are
insonated with short bursts of LIFU waves, they undergo stable cavitation (see Section
1.3.2.3). During this oscillation the developed radiation forces (see Section 1.3.2.1) and
microstreaming (see Section 1.3.2.2) induce large shear stresses on the endothelial cell
walls, creating openings between the cells (see Figure 3.4). These openings allow for per-
meation of large molecules into the brain parenchyma that would normally be impeded
by the BBB. This disruption mechanism of the endothelial layers and the subsequent per-
meation of therapeutic agents is often referred to as *FUS mediated extravasation*.

This approach allows for noninvasive and safe BBBD, as it has been shown that the LIFU
waves do not carry enough energy to induce thermal effects or inertial cavitation. In addi-
tion, as increased permeability is only seen in the vicinity of the focal spot, this technique
allows for targeted drug delivery. Lastly, FUS induced BBBD lasts for approximately $4$ h
and is entirely reversible.

This approach is still being evaluated on animals for the treatment of cancer [177–179],
Alzheimer's disease [153], and the administration of stem cells to the brain [120]. Nonethe-
less, preliminary results appear very promising, and should FUS induced BBBD be proven

*(a)*



*(b)*



*(c)*
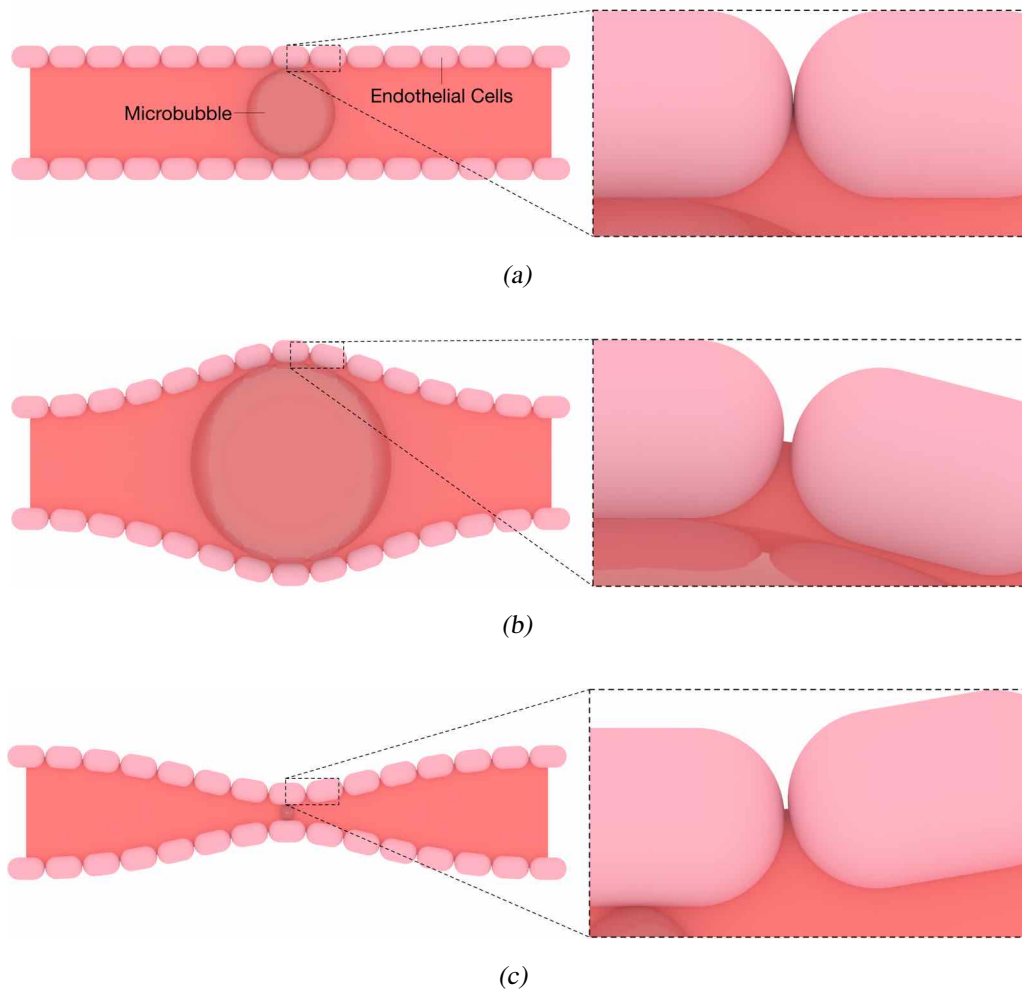
**Figure 3.4**: *Depiction of FUS mediated extravasation, the hypothesized physical mechanism in FUS-induced blood-brain barrier disruption (BBD). (a) shows a blood vessel and its endothelial cell wall containing a single microbubble in the absence of sonication. During sonication stable cavitation occurs and during the rarefactional cycles the bubble expands, applying forces and creating openings in the endothelial walls (b). Similarly, during compressional cycles the bubble contracts and a similar behavior is observed (c).*

successful in patients, it could represent a major advance in neuroscience and be used effectively against the different diseases affecting the CNS. It should be mentioned that FUS mediated extravasation is not limited to BBBD but has also been applied to the heart [180, 181], skeletal muscles [182, 183], as well as a large range of tumors [184–187].

## 3.2.2 Sonoporation & Targeted Drug Delivery

[184, 188–192]

In contrast to FUS mediated extravasation, as discussed in Section 3.2.1.3 and shown in Figure 3.4, where stable cavitation is employed to modify vascular permeability, inertial cavitation can be employed instead to alter the permeability of individual cells. As discussed in Section 1.3.2.3, inertial cavitation may be accompanied by extreme pressures and temperatures, as well as the generation of shock-waves and fluid jets. When this occurs in the vicinity of a cell, it is believed to induce transient pores in the cellular membrane, increasing that cell's permeability and enhancing its uptake of macromolecules. This phenomenon is called *sonoporation*, its effects are reversible (for given tissue types and acoustic intensities), and have been shown to last up to $24\,\mathrm{h}$ after the treatment [193].

Sonoporation has found application in *targeted drug delivery*, as it allows for increased drug uptake localized in the sonicated region. Instead of simply mixing a UCA with a therapeutic agent, the uptake of which is facilitated by the aforementioned transient opening of cell membranes, these microbubbles can also act as drug carriers themselves. They can either be loaded with a particular drug, or in the case of gene therapy, gene load, that will be released upon their collapse and absorbed by the cell. In an alternative approach, they may carry thermo-sensitive liposomes [194–196] which contain the drug and release it when exposed to slightly elevated temperatures, on the order of $39 - 40\,°\mathrm{C}$ [58, 197]. Thus, this combination of sonoporation and targeted drug delivery yields highly localized and controlled release of therapeutic agents, minimizing toxicity to nontargeted tissue, while the increased drug uptake permits for increased efficiency with lower dosages.

This technology is still in an experimental stage, with most applications being performed either in-vitro or in small animals. Significant research remains to be done in order to translate it to the clinical environment, especially due to the use of inertial cavitation which, as discussed previously, may involve significant risks to healthy tissue. Details on the different aspects of this technology can be found in [184, 188–192], whereas an overview of its different applications, most notably in cancer therapy, can be found in [198–200].

### 3.2.3 Thrombolysis

[126, 127, 201, 202]

Extensive investigations have been performed to assess the suitability of FUS for use in cerebro-vascular thrombolysis, i.e., the disintegration of blood clots in the brain vasculature, which, if untreated, may result in a stroke. This treatment modality is often termed as sonothrombolysis, and has been employed in multiple clinical trials with encouraging results [151, 152, 203, 204]. The therapeutic effect is achieved by the administration of ultrasonic waves in (optional) conjunction with thrombolytic agents. Despite the significant number of such studies which verified the thrombolytic effect of US, the underlying mechanisms are not completely understood. The most likely mechanism is acoustic cavitation, either stable or inertial (see Section 1.3.2.3), which leads to clot lysis. In addition, it has been theorized that in the case of the combined use of US and thrombolytic agents, the former induces microstreaming (see Section 1.3.2.2), allowing these drugs to enter the clot itself, and thus augment their therapeutic effects. The delivery of ultrasonic waves has been facilitated by very small transducers that are inserted intravenously into a blood vessel using diagnostic ultrasound to navigate to the clot. Alternatively, this can be achieved extracorporeously with systems such as the ExAblate® 4000, or even with unfocused diagnostic ultrasound. Extensive reviews on sonothrombolysis can be found in [126, 202, 205, 206].

### 3.2.4 Neuromodulation

[98, 157, 207–209]

The ability to stimulate or suppress regional neuronal activity, often termed as *neuromodulation*, allows for a wide range of applications, ranging from functional brain mapping, to the treatment of neurologic diseases, and neuropsychiatric disorders. Both invasive and noninvasive techniques have been devised and are currently employed clinically but exhibit certain limitations. Techniques such as deep brain stimulation (DBS) and vagus nerve stimulation (VNS), have shown great promise [210–212], but are both invasive and involve complicated neurosurgical interventions for the implantation of chronic stimulating devices. Non-invasive alternatives, e.g., transcranial direct current stimulation (tDCS) and transcranial magnetic stimulation (TMS), have also emerged but exhibit limited targeting capabilities and depth of penetration [156, 213, 214].

Apart from its demonstrated use for tumor ablation and functional neurosurgery, as described in Section 3.1.4.5, transcranial FUS can also be employed in the field of neuromodulation. The general potential of US for neuromodulation was first reported 80 years ago by Harvey [215], and a significant number of studies, mostly on animal subjects, have verified this phenomenon since. A brief historical overview of these studies, as well as reviews of recent studies, can be found in [207–209]. Unlike HIFU ablation

applications which are tailored towards the controlled and precise destruction of tissue for therapeutic purposes, FUS-induced neuromodulation effects are explored using LIFU. As such, this technology allows for controllable, and entirely reversible, neuronal stimulation and inhibition. In contrast to existing techniques, and as discussed in Section 3.1.4.5, FUS-induced neuromodulation involves the administration of LIFU pulses, which can be delivered deep inside the brain within a sharply demarcated region, and without any measurable increase in the tissue temperature or observable post-mortem histological findings.

Even though studies have reproducibly confirmed these phenomena, neither the physical mechanisms, nor the optimal sonication parameters of FUS-induced neuromodulation, i.e., frequency, amplitude, and duration, have been well understood or established. Different hypotheses have been formulated in an attempt to explain the observed FUS-induced excitation or suppression of neural activity, many of which are discussed in [157, 207–209]. The same reviews offer extensive discussions on the safety and efficiency of this technique, which has been repeatedly demonstrated on a variety of animals. At this stage, however, it has been established that additional studies, better understanding of the underlying mechanisms and optimal sonication parameters, and human trials are required to further investigate the feasibility of FUS-induced neuromodulation.

## 3.3 Challenges of Therapeutic Ultrasound

As can be seen from the previous sections, therapeutic ultrasound offers tremendous potential in a wide range of applications, promising a noninvasive solution to therapeutic problems that were previously untreatable. There are however, potential limitations and risks associated with both its clinical applications and the actual delivery of the treatment. Even though some of these challenges, in respect to the various areas of application, are discussed briefly in their respective sections, a summary of the FUS limitations, as well as possible ways to overcome them, is given in this section. An extensive overview of the challenges encountered in FUS interventions is given in [123].

### 3.3.1 Treatment Times

[59, 69, 98, 117, 126]

One of the main limitations of FUS treatment, especially in the field of HIFU ablation, is the long treatment time that is involved, which in some applications may extend to over 6 h. The reason for these lengthy treatments lies in the small focal regions created by FUS therapy systems, while MRgFUS involves additional delays due to the need for ongoing MRI during the treatment, either for targeting or thermal monitoring. While these small, sharply demarcated focal regions, and therefore lesions, allow for noninvasive and highly precise ablation, the ablation of large tissue volumes requires *volume-scanning*, i.e., the

overlap of multiple such lesions, as discussed in Section 3.1.3 and shown in Figure 3.1. In order to avoid collateral tissue damage, e.g., skin burns, long pauses are required between sonications in order to allow for cooling of the healthy tissue. This approach is particularly necessary in neurosurgical FUS applications (see Section 3.1.4.5), where pauses on the order of multiple minutes are required to avoid scalp burns.

One method used to decrease treatment times, involves alternative scanning approaches to the volume-scanning ablation discussed above. This includes redefining the spatio-temporal order of sonications in an attempt to minimize the focal region overlap and result in decreased energy absorption in the healthy tissue. Such ablation techniques include *volumetric ablation* [107, 115], employed by the Sonalleve® system (see Section 2.5.2.3), scanning along spiral trajectories [216], or even optimized scanning on a case-by-case basis [217].

Another approach involves *enhanced sonication* by employing microbubbles, which, as discussed in Section 1.3.2.3, enhance the acoustic energy absorption through stable cavitation and may even cause tissue damage by means of inertial cavitation. Therefore, this approach allows for enhanced ablation with lower acoustic power and shorter sonications, but only in the focal region and not the healthy overlaying tissues. However, this approach is difficult to control and potentially dangerous to sensitive healthy tissue [218, 219].

## 3.3.2   Tissue-Air & Tissue-Bone Interfaces

[63, 69, 117, 123, 128]

As has been mentioned repeatedly throughout this thesis, the propagation of ultrasonic waves between different media is dictated by their characteristic acoustic impedance $Z$ (see Section 1.1.2.4). An impedance mismatch (see Section 1.1.3.2) at the interface between two different media leads to reflections which may in turn cause increased energy absorption and damage to the intervening tissues. As discussed in the aforementioned section, air exhibits a $Z$ lower than $0.5$ kRayls, that of soft tissue and water is on the order of $1.5$ MRayls, and cortical bone exhibits a $Z$ in the range of $3 - 5$ MRayls. Therefore, it can be understood that tissue-air and tissue-bone interfaces are a major physical limitation of therapeutic FUS and ultrasonics in general. Based on Equations 1.11 and 1.13 in Section 1.1.3.2, up to $99\%$ of the acoustic energy can be reflected at a tissue-air interface, while this is in the range of $20 - 30\%$ at interfaces between tissue and bone .

Ultrasonic waves cannot propagate through air-filled viscera such as the bladder and the entire gastrointestinal tract, or through porous tissue such as the lung. Due to this, targets such as lung tumors are unlikely to ever be treatable with FUS, while HIFU ablation of targets in close proximity to the bowels introduces the risk of visceral perforation. As this is not a technological limitation, but rather an inherent physical restriction imposed by the nature of acoustic waves themselves, no tangible solutions exist. Workarounds

are, however, employed in some treatments, such as in the case of uterine fibroid ablation (see Section 3.1.4.2), where the bladder is catheterized and emptied of air to minimize perforation risks [9, ch. 9], [136, pp.341-348].

A similar, if not as pronounced phenomenon is evident at interfaces between soft tissue and bones. This issue is of major importance in ablative procedures targeting organs partially obscured by the thoracic cage, such as the case of hepatic tumors, discussed in Section 3.1.4.3, and in transcranial sonications which are hampered by the presence of the skull, as discussed in Section 3.1.4.5. Similar effects are observed in the case of soft tissue calcifications [220–222], which may induce excessive heating, introducing risks and impeding treatment [223].

### 3.3.2.1  Standing Waves
[121, 224–226]

A direct consequence of the tissue-air and tissue-bone interfaces is the formation of standing waves. These result from the combination of multiple reflections, as well as constructive and destructive interference (see Section 1.1.3.5). Standing waves are particularly prominent in transcranial sonications where the presence of the skull causes multiple reflections and favors the creation of such waves. Furthermore, standing waves are much more pronounced during long sonications and at lower acoustic frequencies, on the order of 250 kHz where tissue absorption is decreased (see Section 1.1.2.3).

Standing waves are known to yield several unpredictable and undesirable effects during the administration of FUS treatments. Such secondary effects include thermal hot-spots, which may lead to collateral tissue damage and hemorrhage [152, 227–229], unintentional cavitation [230], or even unexpected BBB disruption [155].

Different techniques have been investigated to achieve suppression of standing wave formation. The employment of large phased arrays over a large aperture (such as the hemispherically shaped array ExAblate® 4000, see Section 2.5.2.2), allows for distribution of the acoustic energy over a large surface array. Not only does the geometric shape of the wavefront reduce the potential for the formation of standing waves, but the acoustic power output of each individual element is low enough that if standing waves do occur, their acoustic pressure, and therefore the induced physical effects, are greatly reduced. In addition, several techniques involve the parameter modification of the RF signals driving the array elements, including frequency sweeping [231, 232] and random phase modulation schemes [224, 229], in order to inhibit standing wave formation.

### 3.3.2.2 Skull-induced aberrations
[1, 59, 96, 98, 105, 126, 150, 233]

The foremost barrier when treating the brain with FUS is the presence of the skull. As discussed above, its acoustic properties are very different to those of soft tissue which causes impedance mismatches and reflections. In addition, the skull exhibits at least an order of magnitude higher absorption than soft tissue, absorbing a large percentage of the acoustic energy, especially at higher frequencies. Combined with the complex heterogeneous nature of the skull, which is multi-layered, liquid-filled, and porous, its presence causes distortion of the acoustic focus, focal shift, and significant decrease of the thermal gain, i.e., the ratio of energy deposition at the focus to the energy deposition on the scalp and skull-bone, thus compromising the treatment (see Figure 3.5).



(a)                                                    (b)
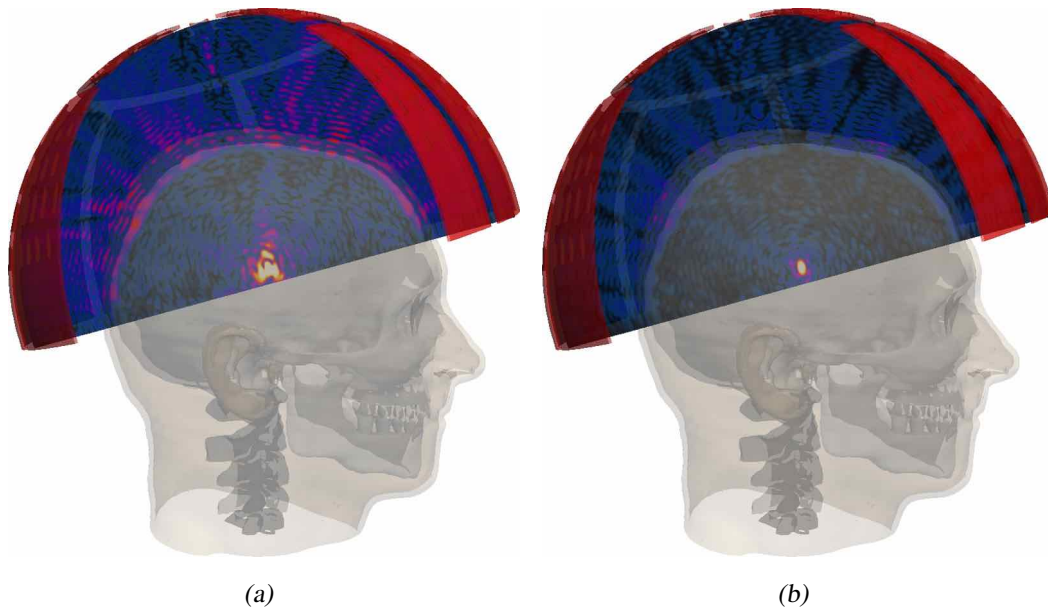
*Figure 3.5*: *Simulated acoustic pressure distributions from an idealized model of the ExAblate® 4000 system applicator in the presence of a human head model segmented from MR data [234] on planes through the location of the geometric focus showing (a) skull-induced aberrations, including shifting and distortion of the focal spot, significant energy deposition on the skull bone and scalp, as well as the potential generation of secondary foci and standing waves; and (b) the pressure distribution after application of a 'Virtual Source' phase-correction approach (see Section 8.1.1.3).*

These effects are commonly termed as *skull-induced aberrations* and have been associated with many of the reported complications in clinical trials, typically in the form of unforeseen brain hemorrhaging [94, 96, 102].

As in the case of standing waves, the solution to the above problem lies in the use of large arrays such as the ExAblate® 4000. The large transducer surface permits the acoustic

energy to be distributed on the skull surface, thus diminishing the local deposition on the scalp and bone. In addition, the ability to drive the transducer elements individually with appropriately corrected phases and amplitudes allows for the compensation of focal distortion effects.

Early approaches to reduce the impact of the aberrations imposed by the skull, involved using of low-frequency ultrasound, on the order of $250\,\mathrm{kHz}$, where the acoustic wavelength in bone (ca. $12\,\mathrm{mm}$) is comparable to the skull thickness. The success of this approach has been demonstrated [235], however, it is known that lowering the ultrasonic frequency exhibits certain drawbacks. The larger acoustic wavelength results in a larger focal size that causes larger lesions. The cavitation threshold, which is proportional to frequency, consequently decreases thus increasing the risk of unwanted cavitation (see Section 1.3.2.3). Finally, as was discussed in Section 1.1.2.3, the absorption in soft tissue is lessened for acoustic waves of lower frequencies. This results in reduced energy deposition, thus requiring increased acoustic intensities in order to ablate the targeted area, which again increases the risk of cavitation.

Because of these issues, the clinical use of tcMRgFUS for thermal ablation is performed at acoustic frequencies on the order of $600 - 1000\,\mathrm{MHz}$. At these frequencies, however, skull-induced aberrations are significant, making precise aberration corrections and focusing mandatory. A large number of different techniques have been investigated to compensate for these skull-induced aberrations, ranging from entirely experimental methods to analytical and simulation-based techniques, an overview of which is presented in Section 8.1.

### 3.3.2.3 Intercostal Targeting
[139, §§4.1-4.2], [236–240]

A major challenge in the FUS treatment of hepatic tumors, as well as other abdominal organs, is the partial obstruction introduced by the thoracic cage, i.e., the ribs. As a first consequence, their presence limits the volume and parts of the liver that can be accessed for treatment due to reflections and the introduction of acoustic shadow zones. Furthermore, it introduces the risk of undesired tissue damage near bony and cartilaginous tissue structures through two mechanisms. The large impedance mismatch at the tissue-rib interfaces causes high energy deposition on the soft tissue and increases their temperature. Simultaneously, the high absorption coefficient exhibited by bone causes the ribs to absorb large amounts of acoustic energy and radiate thermal energy to the surrounding tissue, i.e., not only the tissue interface exposed to the ultrasonic waves [236]. Lastly, the obstruction posed by the ribcage distorts the focal region and decreases its intensity, inhibiting tissue ablation and deteriorating the quality of the treatment [241]. Skin burns of varying degrees, as well as the failure to successfully ablate the targeted tissue have been reported [241–245].

In an attempt to counter the aforementioned effects, partial resection of the obstructing ribs is still used in the clinical environment [242, 246], increasing, however, both the invasiveness of the treatment, the risk of infection, and the recovery time. Other researchers have investigated a *dynamic element activation* approach [238, 247–249], in which transducer arrays are employed for sonication and the elements which contribute to exposure of the ribs, i.e., those whose normal vector crosses the ribs, are turned off to minimize these effects. The ultrasonic waves generated by the remaining active elements are allowed to propagate through the intercostal spaces, i.e., the spaces between the ribs.

Alternative approaches utilize *time-reversal* techniques, which are presented in detail in Section 8.1.1. Such examples are the *Implanted Hydrophone* approach [236, 250], the *Virtual Source* approach [237, 238], while other approaches based on numerical simulations and optimization of the deposited acoustic energy deposition have also been reported [251]. Apart from the invasive option of rib resection, however, the aforementioned techniques have only been investigated in in-vitro and ex-vivo setups, as well as in live animals, but further investigation is required to prove their efficacy for clinical use.

### 3.3.3   Organ Motion Tracking & Compensation

[139, 252–254]

Another major impediment of FUS surgery is respiration-induced organ motion and displacement, an issue of particular importance in the ablation of hepatic and renal tumors as previously mentioned in Section 3.1.4.3. Under free-breathing conditions, these organs exhibit a displacement amplitude on the order of $10 - 30$ mm [255–257]. In addition, the extensive vasculature network of such organs further complicates treatment, as the high perfusion removes thermal energy at a high rate, inhibiting thermal ablation. If unaccounted for, this motion can lead to insufficient energy deposition in the targeted tissue, unsuccessful ablation, or even collateral tissue damage.

To date, such treatments are usually performed either under general anesthesia, permitting the usage of controlled apnea [258], or by employing respiratory gating [259, 260], i.e., administering sonications only during the portion of the respiratory cycle when the organs remain stationary. However, in the case of the latter, these durations are on the order of $1 - 2$ s in an average breathing cycle of $3 - 5$ s [139]. Thus, the time-averaged acoustic energy deposited at the tissue is significantly lessened, and combined with the high vascular perfusion, ablation of the targeted volume is often unsuccessful [261]. For this reason, a method to track and compensate for the organ movement, in order to allow for continuous sonication of the targeted tissue throughout the respiratory cycle, is highly sought after. Given its pivotal role in the successful treatment of abdominal organs, real-time *motion tracking* and *motion compensation* have been extensively investigated. The approaches can be roughly categorized into indirect and direct motion tracking.

In the case of the former, the inherent periodicity of the respiratory-induced motion of the organ is exploited. Prior to the treatment, the motion of the patient's organ is captured, typically through 4D MRI with high spatial and temporal resolution. In addition, an external sensor tracking the movement of the diaphragm or ribcage [253, 262], or a marker implanted in the organ itself [252, 263], is simultaneously monitored throughout the breathing cycle. The 4D MRI data, which are often complemented by statistical models of organ motion, are processed to create a motion model, correlating the temporal location of the tissue volume to be ablated, to the information provided by the aforementioned sensors or implanted markers. During treatment, these sensors or markers continue to be monitored, while the precalculated motion model is used to approximate the location of the targeted tissue volume at any point in time, allowing for focal steering and continuous ablation. Several techniques with the above rationale have been demonstrated in in-vitro, ex-vivo, and even in-vivo animal setups [252, 253, 260, 262, 264, 265]. Indirect motion tracking techniques however, require multiple hours of computationally intensive processing between the initial imaging and the treatment. More importantly, these techniques do not track the motion of the targeted volume directly, but merely rely on the initial imaging results. Thus, such methods are often better suited to sedated or anesthetized patients with mechanically assisted respiration. Otherwise, a change in the rate or nature of respiration, or other forms of movement during treatment, may lead to inappropriate tracking and risk collateral tissue damage.

On the other hand, direct motion tracking uses either MRI [266, 267] or ultrasound imaging [268–270] to track the organ displacement and steer the FUS waves in real-time. While these types of approaches can account for changes in the organ motion pattern and are more suitable for patient treatment under free-breathing conditions, they are also much more technologically challenging. When tracking is performed with 4D MRI, a tradeoff between the imaged tissue volume, the spatial, and the temporal resolution is crucial. With emphasis being placed on high temporal resolution, with acquisition frequencies on the order of $10-20$ Hz so as to accurately track the organ, the allowed imaging is restricted to either highly resolved 2D slices or severely undersampled 3D volumes, resulting in limited imaging accuracy and information. Alternatively, the use of diagnostic ultrasound imaging allows for real-time tracking of the organ motion and has been successfully combined with MR thermometry for thermal monitoring of the process [269].

A detailed overview of both direct and indirect motion tracking and its applications on FUS treatment of the liver and kidney can be found in [139]. None of the aforementioned approaches, however, have been applied in the treatment of actual patients and they warrant further investigation before being adopted in the clinical environment.

# Part II

# Numerical Modeling of Acoustic Wave Propagation

# 4

# Mathematical Models of Acoustic Wave Propagation

Mathematical models describing the propagation of acoustic waves can be roughly categorized into *beam models* (see Section 4.1) and *full-wave models* (see Section 4.2). The former are usually fast, simple, and easy to implement numerically, resulting in their widespread use for simplified problems involving the propagation of acoustic waves. However, modeling the *focused ultrasound* therapeutic applications, which were described in detail in Chapter 3, involves complicated transducers and arrays and large inhomogeneous models of the human body, for which beam models are usually insufficient.

Full-wave models, however, offer a far more realistic depiction of acoustic wave propagation, accounting for the majority of phenomena described in Chapter 1. In contrast to beam models, these models are more complex and result in computationally demanding implementations. Nonetheless, the degree of realism permitted by such models has designated them as the de-facto solution to the modeling of therapeutic FUS applications, especially when involving complex inhomogeneous setups.

## 4.1 Acoustic Beam Models

Acoustic beam models typically provide an approximate mathematical depiction of acoustic wave propagation. These models are easier to understand and implement numerically than the full-wave models presented in Section 4.2, and often result in high computational efficiency. However, beam models are often derived under restricting assumptions, e.g., medium homogeneity, which result in limited modeling capabilities. Nonetheless, their simplicity has resulted in their widespread usage, a large number of proposed extensions and improvements to the original models, and numerous software implementations. Two such models, i.e., the *Rayleigh-Sommerfeld* integral and the *angular spectrum method*, their advantages and limitations, as well as the most prevalent extensions that have been proposed, are presented in this section.

## 4.1.1 Rayleigh-Sommerfeld Integral

The most basic model of acoustic wave propagation is based on the *Rayleigh-Sommerfeld* (RS) integral, first introduced by Lord Rayleigh [271]. Despite its significant limitations, which are discussed in Section 4.1.1.2, the simplicity of this model has established it as the most commonly employed approach in the modeling of ultrasonic wave propagation. As outlined in Section 4.3, multiple numerical implementations and publications have been based on this model, and it is considered to be an important reference and tool.

### 4.1.1.1 Model
[272, p.4], [5, §§2.6-2.8], [273, pp.30-32], [274–280]

The RS model is derived under two fundamental assumptions; that the vibrating surface, i.e., the piezoelectric element, is flat and part of an infinite rigid baffle, and that the generated acoustic waves are propagating within an infinite, homogeneous, linear, and isotropic medium.

The complex velocity potential $\psi$, as a function of distance $r$ between the transducer surface and any point in the medium, can be calculated through the Green's function as such [274]:

$$\psi\left(r\right) = \frac{1}{2\pi} \int_S u_S \frac{e^{ikr}}{r} dS \tag{4.1}$$

where $S$ is the surface area of the transducer, $u_S$ is the particle velocity in the transducer's piezoelectric material, and $k = 2\pi f/c$ is the wavenumber, which depends on the medium's speed of sound $c$ and the frequency $f$ of the acoustic wave. In addition, absorption can be accounted for by replacing the term $e^{ikr}$ with $e^{(ik-\alpha)r}$, where $\alpha$ is the absorption coefficient of the medium. The acoustic pressure $p$, can then be calculated as a function of distance $r$ and time $t$, with the following equation [272]:

$$p\left(r,t\right) = \rho \frac{\partial \psi}{\partial t} = i\omega\rho\psi = ikZ\psi \tag{4.2}$$

where $\rho$ is the medium density, $\omega = 2\pi f$ is the angular frequency, and $Z$ is the medium's characteristic acoustic impedance.

The Rayleigh-Sommerfeld integral, however, does not always permit an analytical solution, and approximate numerical calculations based on the *Huygen's principle* (see Section 1.1.1), are typically employed. Prior to the calculation, the surface of any arbitrarily shaped transducer or array is subdivided into a finite number of *point sources*. In a similar manner, the area or volume of the medium where the acoustic pressure is required is sampled to a number of *observation points*. Subsequently, the contribution, i.e., the

acoustic pressure, generated by each point source of the transducer at each of the observation points, is calculated through Equations 4.1 and 4.2. The total acoustic pressure at each point can then be calculated as the algebraic sum of all contributions. This concept is graphically depicted in Figure 4.1.
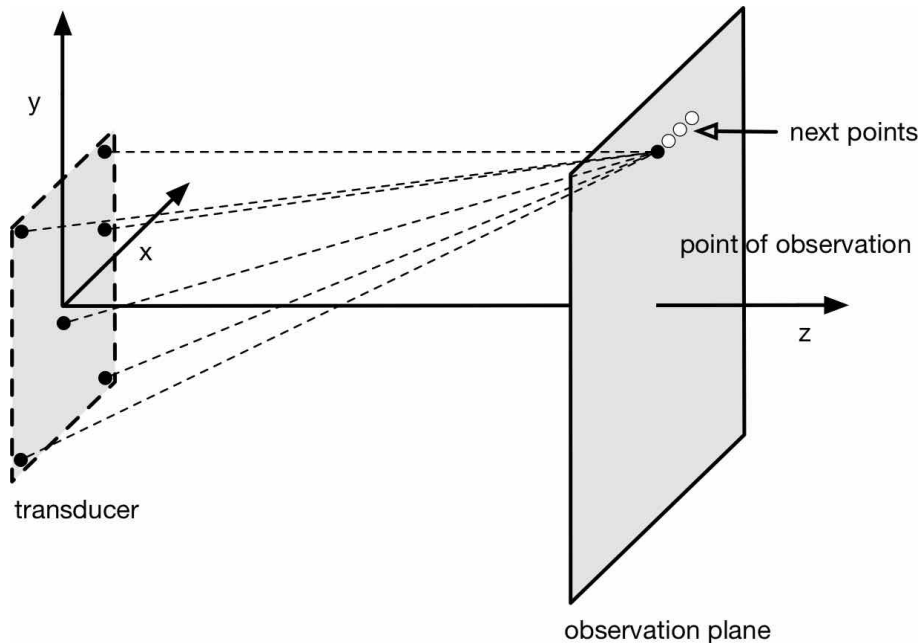


**Figure 4.1**: *Direct numerical calculation of the Rayleigh-Sommerfeld integral, for an arbitrarily shaped ultrasonic transducer.*

### 4.1.1.2   Advantages & Limitations
[273, p.32], [5, p.38], [275, 277, 279, 281–284]

The foremost strength of the RS integral, when calculated numerically as described in Section 4.1.1, lies in its simplicity. This model can be used to easily and quickly evaluate the temporal acoustic pressure from any arbitrarily shaped transducer or array, and at any point in space. The RS integral is simple to implement numerically, while it is amenable to straightforward parallelization of the numerical algorithm, as the pressure value at every observation point can be calculated independently.

This model however, suffers from a number of shortcomings. The most notable limitation stems from the assumption of an infinitely extending homogeneous medium. In addition, the premise of a vibrating surface on an infinite baffle discounts the diffraction effects (see Section 1.1.3.3) at the edges of a real transducer. Moreover, due to the fact that the Green's function is singular at the source, this model is not tailored to numerical calculation of the near-field pressure, especially at high frequencies. Lastly, it should be mentioned that when accurate approximation of the acoustic field is required, both the

transducer and observation volume must be finely discretized, which rapidly increases the required computational time and resources.

A number of extensions or alternative formulations of the Rayleigh-Sommerfeld model, aiming at addressing some of the aforementioned shortcomings, are presented in the following sections.

### 4.1.1.3   Tupholme-Stepanishen Impulse-Response model
#### [281, 285, 286], [5, §2.8]

In order to account for diffraction effects at the edges of the vibrating piezoelectric element, which is not feasible with the original RS model, Tupholme and Stepanishen formulated an alternative expression of the RS integral and derived the *Tupholme-Stepanishen model*, more commonly known as the *impulse-response* model [281, 287–289]. The model entails the application of a boundary condition for the velocity potential on the RS integral, and its calculation through a convolution operation [5, §2.8].

### 4.1.1.4   Layer-based Inhomogeneity
#### [274, 280, 290]

An extension to address the RS model's limitation imposed by the assumption of an infinite, homogeneous medium has been previously proposed in [274]. This extension allows for the modeling of wave propagation through different layers of infinitely extending homogeneous media, by complementing the original RS model with Snell's law, thus permitting for reflection and refraction of the acoustic waves (see Section 1.1.3.2) to be taken into account. Nonetheless, even with this extension, the integral is not tailored to modeling propagation through inhomogeneous anatomies or complex structures.

### 4.1.1.5   Fast Nearfield Method
#### [291–293]

As described in Section 4.1.1.2, the RS model exhibits limited accuracy in the nearfield region [291–293]. In the case of simple transducers, e.g., circular, rectangular, triangular or spherical shells, an alternative formulation of the RS, named the *fast nearfield method* (FNM), has been proposed [291–295]. This method reduces the double integral calculated in the RS model to a rapidly converging single integral, which is then evaluated using Gauss quadrature. Due to the smooth integrand, the FNM achieves exponential convergence within the nearfield region with high accuracy.

## 4.1.2 Angular Spectrum Method

The *angular spectrum method* (ASM), is a numerical technique first introduced in the field of Fourier optics [296], and which was later adopted in the modeling of acoustic wave propagation. Despite the significant caveats of this model's original formulation (see Section 4.1.2.2), the multiple proposed extensions discussed in Section 4.1.2.3, and most notably the recently introduced hybrid ASM (see Section 4.1.2.4), have resulted in a simple but powerful model, employed in a notable number of publications (see Section 4.3).

### 4.1.2.1 Model
[273, p. 32], [296, pp.49-60], [297–300]

The ASM model involves the calculation of an acoustic field's spectral components on an initial plane, called the *source-plane*, and propagation of that plane through space by multiplication of each spectral component with an appropriate *phase propagation factor* (PPF). This numerical procedure is outlined below.

Let us assume a continuous pressure wave field, generated by a set of harmonic sources, and propagating in the $+z$ direction. The complex pressure field $p(x, y, z_0)$, residing on a source-plane located on $z = z_0$, is sampled over a rectangular grid of $N \times N$ points. This field is subsequently decomposed into a two-dimensional *angular spectrum* [296] of component plane waves, each propagating in a different direction. The amplitude and phase of each spatial frequency represent the amplitude and phase of those plane waves. This angular spectrum is denoted by $P(f_x, f_y, z_0)$, and is obtained through a two-dimensional fast Fourier transform (FFT) of the source-plane pressure wave field. This is expressed by the following equation [296, p. 56]:

$$P(f_x, f_y, z_0) = \int\int_{-\infty}^{+\infty} p(x, y, z_0) e^{-i2\pi(f_x x + f_y y)} dx dy \tag{4.3}$$

where $f_x$ and $f_y$ are the spatial frequencies in the $x$ and $y$ directions respectively.

In order to calculate the pressure field at a plane parallel to the source-plane located at $z = z_1$, every $(f_x, f_y)$ component of the source-plane's angular spectrum is multiplied by a PPF. This multiplication is essentially the application of a linear filter on the spectrum. The PPF is expressed as follows [296, p. 60]:

$$G(f_x, f_y, z_0, z_1) = e^{j2\pi \frac{(z_0 - z_1)}{\lambda} \sqrt{1 - (\lambda f_x)^2 - (\lambda f_y)^2}} =$$
$$= e^{j(z_0 - z_1)\sqrt{k^2 - \omega_x^2 - \omega_y^2}} \tag{4.4}$$

where $\lambda$ is the acoustic wavelength within a given medium of propagation and $k = 2\pi f/c$ is the wavenumber, which depends on the medium's speed of sound $c$ and the frequency $f$ of the acoustic wave. Lastly, $\omega_x = 2\pi f_x$ and $\omega_y = 2\pi f_y$ are the angular frequencies in the $x$ and $y$ directions respectively. The PPF shown in Equation 4.4, accounts only for the phase shift the acoustic waves undergo as they propagate through the medium [273, p. 32].

If $P(f_x, f_y, z_1) = P(f_x, f_y, z_0) \cdot G(f_x, f_y, z_0, z_1)$ is the angular spectrum of the target plane, then the pressure field distribution on that plane, denoted by $p(x, y, z_1)$, can be calculated by an inverse FFT as follows [296, p. 56]:

$$p(x, y, z_1) = \int\int\limits_{-\infty}^{+\infty} P(f_x, f_y, z_1) \cdot e^{j2\pi(f_x x + f_y y)} df_x df_y \qquad (4.5)$$

Following a procedure similar to the above, it is possible to calculate the acoustic pressure field distribution on any plane parallel to the source-plane.

### 4.1.2.2 Advantages & Limitations
[273, p. 33], [296, p. 55], [280, 297, 299–302]

The ASM, is usually complemented by the Rayleigh-Sommerfeld model, described in Section 4.1.1, in order to calculate the acoustic wave field from an arbitrary transducer onto a source-plane, which is then propagated through the computational domain as described above.

In terms of modeling, this method is very easy to implement and allows for high computational efficiency, as it permits the calculation of the acoustic pressure on an entire plane through a single inverse FFT operation. As such, numerical simulations where large three-dimensional acoustic fields generated by modern transducers were calculated in a matter of seconds have been reported [280], making it a very attractive alternative to other methods and models. In addition, unlike the full-wave propagation models described in later sections, the ASM restrictions on the required resolution are far less limiting. Lastly, this method permits both forward and backwards propagation, with a direct consequence of the latter being, the ability to reconstruct the source distribution from measurements of a transducer's radiated field.

The 'traditional' formulation of the ASM entails a large number of limitations, most notably the inability to model wave propagation in inhomogeneous media. This method cannot account for important propagation effects such as attenuation, reflection or refraction. Other limitations include the inability to model nonlinear wave propagation and nonharmonic waves, e.g., broadband waves or pulses. Lastly, the simulated source field distributions are restricted to planar distributions. This however, is only a limitation in

transducers or arrays without a principal propagation direction, such as the hemispherical array of the ExAblate® 4000 (see Section 2.5.2.2 and Figure 2.13(b)). Nevertheless, many of the aforementioned limitations have been addressed in alternative formulations and extensions of this method, yielding approximate solutions to these issues, which will be discussed in the following sections.

### 4.1.2.3   Extensions

This section, will present extensions that have been devised in order to counter some of the limitations of the ASM discussed in Section 4.1.2.2.

**Broadband Exictations:**   An approach to simulating nonharmonic excitation, e.g., broadband acoustic waves or pulses with the ASM, involves transforming the broadband excitation signal from the time domain to the frequency domain by means of a one-dimensional FFT and performing a separate ASM simulation, as described in Section 4.1.2.1, for each spectral component. Each of the different acoustic pressure fields can then be calculated by an inverse FFT and their algebraic sum yields the pressure field that would result from that nonharmonic signal [297, 303].

**Layer-based Inhomogeneity:**   As described in Section 4.1.2.2, the ASM precludes modeling medium variations along the plane, e.g., no variations can be modeled in the $x$ and $y$ directions for a plane wave propagating along the $z$ axis. However, it is possible to model inhomogeneities in a layer-based approach along the axis of propagation. As the phase propagation factor (see Equation 4.4), is directly dependent on the wavenumber $k = 2\pi f/c$, it is possible to assign a different speed of sound $c$ for each plane the wave is calculated on [297, 300, 302, 303].

**Absorption/Attenuation:**   The 'traditional' ASM does not account for energy loss during propagation, i.e., absorption and attenuation, as discussed in Sections 1.1.2.3 and 1.1.3.6 respectively. By replacing, however, the real valued wavenumber $k$ in the PPF (see Equation 4.4), with a complex number it is possible to account for these effects. It should be noted that this approach disregards the frequency dependent nature of absorption, and is therefore restricted to harmonic sources. However, by means of multiple harmonic simulations, in a manner identical to modeling broadband excitations as discussed above, this frequency dependency can be considered [280, 297, 303].

**Refraction:**   Refraction, as discussed in Section 1.1.3.2, is the change in propagation direction at interfaces between different media. It was considered in the case of layer-based inhomogeneous media which was mentioned above. Modeling refraction due to

the difference in sound speed between different media, can be achieved by varying the wavenumber $k$ in the PPF from layer to layer [297, 303].

**Phase Aberrations:**   Phase aberration is the loss of phase coherence due to small scale sound speed variations, i.e., weak medium inhomogeneities. It was introduced into the ASM by including a phase error term into the PPF (see Equation 4.4) for each spatial Fourier component $(f_x, f_y)$. This phase error term is essentially a normalized random function that describes the effect of medium inhomogeneities. However, it should be specified that this approach is not equivalent to modeling actual inhomogeneous media which, as discussed above, is not feasible with the 'traditional' ASM.

**Nonlinearity:**   The angular spectrum method can be extended to include nonlinear propagation effects. These were introduced into the model through a frequency domain solution of the *Burger's equation* [20], a simplified one-dimensional version of the WLE model discussed in Section 4.2.3. Burger's equation describes the spectral changes that occur in a finite amplitude acoustic plane wave due to the propagation over an incremental distance. To account for nonlinear effects a field cross-section is forward propagated in a piecewise manner over incremental distances $\Delta z$. Two sub-steps are involved in each incremental propagation step. Firstly, a linear sub-step, is performed to account for diffractive, refractive, dispersive, phase distorting, and absorptive effects as discussed in the previous sections. Subsequently, this is followed by a second, nonlinear sub-step, where the finite amplitude effects are determined based upon the acoustic particle velocity amplitude at each sample point in the cross-sectional grid [298, 304, 305].

### 4.1.2.4   Hybrid Angular Spectrum Method (hASM)
[280, 290]

Viable solutions have been proposed to address the majority of limitations restricting the use of the ASM in realistic simulations. However, the foremost drawback of this method lies in its inability to model wave propagation in a medium exhibiting 3D spatial inhomogeneities. This issue has been recently addressed through the *hybrid angular spectrum method* (hASM) which was proposed in [280, 290].

In this method, the 3D inhomogeneous domain is divided into voxels instead of slices as is the case for the 'traditional' ASM, where each voxel exhibits its own set of acoustic properties, i.e., speed of sound, absorption, and density. The hASM utilizes the Fourier split-step technique [306–308] to alternate between the spatial and spatiospectral domain, allowing for the effect of spatially varying medium properties on the wave to be approximated. The steady-state pressure pattern in the domain is then calculated sequentially, plane-by-plane, through successive transverse planes of voxels progressing in the direction of propagation away from the transducer.

Consequently, the combination of the RS model with the hASM, can simulate the propagation of acoustic waves in entirely inhomogeneous domains with significantly diminished computational resources and time, providing results of comparable accuracy [280, 290] to finite-differences implementations of full-wave models which will be discussed in later sections. However, the combination of these two methods fails to accurately address transducer arrays without a principal propagation direction as outlined in Section 4.1.2.2.

## 4.2 Acoustic Full-Wave Models

As discussed at the beginning of this chapter, *beam models* such as the *Rayleigh - Sommerfeld* integral and the *angular spectrum method*, described in Sections 4.1.1 and 4.1.2 respectively, are derived based on stringent assumptions and approximations, in order to simplify the numerical modeling of wave propagation. Thus, as outlined in Section 4.1, these models suffer from notable limitations, restricting their use to applications with simplified setups.

In contrast to such approaches, *full-wave models* provide far more accurate and realistic depictions of acoustic wave propagation, especially when complex inhomogeneous setups are involved. Their formulations allow them to describe all wave phenomena that were discussed in Section 1.1.3, while some of these models inherently account for nonlinearity effects, or even shear wave propagation. The most prominent full-wave models, which have been employed in a number of software implementations and publications (see Section 4.3), are presented in this section. Even though these models typically stipulate large computational resources and time, their modeling capabilities have designated them as the methods of choice in the modeling of therapeutic FUS applications involving complex inhomogeneous setups.

### 4.2.1 Linear Acoustic Pressure Wave Equation

The most fundamental full-wave model of acoustic wave propagation, in terms of modeled propagation phenomena, is the *linear acoustic pressure wave equation* (LAPWE) which is derived under the linearity principles outlined in Section 1.2.1, and based on three fundamental equations of fluid dynamics outlined in the following section.

#### 4.2.1.1 Model
[273, pp.18-19], [17, pp.3-6], [10, pp.119-120], [21, p.36]

The LAPWE model is derived through the following three fluid dynamics equations. *Euler's equation of motion in fluids* provides a nonlinear relation between acoustic pressure

and particle velocity. Under the assumption of *infinitesimal amplitudes*, linearization of Euler's equation produces:

$$\nabla p = -\rho_0 \frac{\partial \vec{\nu}}{\partial t} \tag{4.6}$$

where $p$ is the acoustic pressure at an arbitrary point in space, $\rho_0$ is the equilibrium density of the medium, and $\vec{\nu}$ is the particle velocity.

The *continuity equation*, which in the field of acoustics is often referred to as the *conservation of mass* equation, states that the net rate of mass flowing into a fixed volume is considered equal to the increase of mass inside the volume. This equation yields a relation between the medium's equilibrium density $\rho_0$ and the particle velocity $\vec{\nu}$, linearization of which results in the following equation:

$$\frac{\partial \rho}{\partial t} = -\rho_0 \nabla \cdot \vec{\nu} \tag{4.7}$$

Lastly, the *consitutive equation* provides a relation between the acoustic pressure $p$ and the medium density $\rho$:

$$\rho = \rho_0 \beta_0 p \tag{4.8}$$

where $\beta_0 = \frac{1}{\rho_0} \left[ \frac{\partial \rho}{\partial p} \right]_{ad}$ is the adiabatic compressibility of the medium.

By combining Equations 4.6, 4.7 and 4.8, it is possible to derive a wave equation for acoustic pressure. Equation 4.8 is used to replace the density $\rho$ in Equation 4.7, as follows:

$$\frac{\partial}{\partial t} (\rho_0 \beta_0 p) = -\rho_0 \nabla \cdot \vec{\nu}$$

Differentiating the above equation with respect to time yields:

$$\frac{\partial^2}{\partial t^2} (\rho_0 \beta_0 p) = -\rho_0 \nabla \cdot \frac{\partial \vec{\nu}}{\partial t} \Rightarrow \rho_0 \beta_0 \frac{\partial p^2}{\partial t^2} = -\rho_0 \nabla \cdot \frac{\partial \vec{\nu}}{\partial t}$$

Substituting the temporal derivative of particle velocity from Equation 4.6 into the above equation, yields the LAPWE *partial differential equation* (PDE):

$$\nabla^2 p - \frac{1}{c^2} \frac{\partial^2 p}{\partial t^2} = 0 \tag{4.9}$$

where $c^2 = (\rho_0 \beta_0)^{-1}$, with $c$ being the speed of sound in the medium, as discussed in Section 1.1.2.2.

### 4.2.1.2  Advantages & Limitations
[309–314]

The LAPWE model is relatively simple to implement with any of the popular methods for solving PDEs, such as the *finite differences time domain* (FDTD) method [315], and the *finite elements method* (FEM) [316]. The fact that the LAPWE is a scalar equation simplifies its implementation even further. Moreover, being a full-wave model, the LAPWE can account for all the wave propagation phenomena discussed in Section 1.1.3, e.g., reflection, refraction, diffraction, scattering, etc.

Due to the simplified nature of this equation, however, the modeling capabilities of the LAPWE are limited. As this model discards high-order terms, nonlinear propagation phenomena cannot be accounted for. This limitation is most prevalent in HIFU applications such as tissue ablation (see Section 3.1), where such phenomena are often prominent. As discussed in Section 1.1.1, acoustic waves may propagate as either longitudinal or transverse/shear waves. Since the LAPWE model is derived from fluid dynamics equations, the resulting PDE can only account for longitudinal waves. While this simplification is of limited impact when modeling the propagation of acoustic waves in fluids or soft tissues, as outlined in the aforementioned section, propagation in solids, e.g., bones, cannot be properly modeled. Another downside to the simplicity of the LAPWE is that it does not account for energy absorption, which was discussed in Section 1.1.2.3. Since energy absorption by the medium is responsible for important phenomena, e.g., temperature increase, this shortcoming diminishes the range of LAPWE's applicability. However, as will be shown in Section 4.2.1.4, such effects can be accounted for by modifying the LAPWE PDE.

### 4.2.1.3  Convected LAPWE
[317, pp.103-104], [273, pp.20-21], [10, pp.140-142], [318, p.196], [319]

As shown in Equation 4.9, the LAPWE model is applicable to regions of space devoid of any sources of acoustic energy. This linearized equation was developed on the basis that the fluid medium was not subject to any external force, did not receive or lose heat or mass, and suffered no intrusion from external agents. In this section, the original LAPWE will be modified to include source terms, resulting in a PDE known as *convected LAPWE*.

*Mass injection* refers to the phenomenon wherein mass is injected into the modeled space at a rate of $G\left(\vec{r}, t\right)$ per unit volume. In such a case, the linearized equation of continuity 4.7 becomes:

$$\frac{\partial \rho}{\partial t} = -\rho_0 \nabla \cdot \vec{\nu} + G\left(\vec{r}, t\right) \tag{4.10}$$

This $G(\vec{r}, t)$ is generated by a closed surface that changes volume, such as the outer surface of an explosion, an imploding glass sphere, or a loudspeaker.

If a *body force* is acting on the fluid, a term $\vec{F}(\vec{r}, t)$ per unit volume must be included in Euler's equation 4.6. The linearised equation of motion then becomes:

$$\nabla p = -\rho_0 \frac{\partial \vec{\nu}}{\partial t} + \vec{F}(\vec{r}, t) \tag{4.11}$$

Examples of this type of force are those produced by a source that moves through the fluid without any change in volume, such as the cone of an unbaffled loudspeaker or a vibrating sphere of constant volume.

*Turbulence sources* were first described by Lighthill [320], and depict the spatial rates of change of momentum flux within the fluid. Lighthill showed that these type of sources are responsible for sound being produced by regions of turbulence, as in the exhaust of a jet engine. These sources can be accounted for by including the following term in the right-hand-side of the LAPWE PDE:

$$
\begin{aligned}
-\rho \frac{\partial^2 (\nu_i \nu_j)}{\partial x_i \partial x_j} = -\rho \Bigg( & \frac{\partial \nu_x \partial \nu_x}{\partial x \partial x} + \frac{\partial \nu_x \partial \nu_y}{\partial x \partial y} + \frac{\partial \nu_x \partial \nu_z}{\partial x \partial z} + \\
& + \frac{\partial \nu_y \partial \nu_x}{\partial y \partial x} + \frac{\partial \nu_y \partial \nu_y}{\partial y \partial y} + \frac{\partial \nu_y \partial \nu_z}{\partial y \partial z} + \\
& + \frac{\partial \nu_z \partial \nu_x}{\partial z \partial x} + \frac{\partial \nu_z \partial \nu_y}{\partial z \partial y} + \frac{\partial \nu_z \partial \nu_z}{\partial z \partial z} \Bigg)
\end{aligned}
\tag{4.12}
$$

wherein the left hand side of the above equation, Einstein's summation convention is used to simplify the expression.

By combining all the above source terms and the LAPWE PDE shown in Equation 4.9, the complete convected LAPWE PDE becomes:

$$\nabla^2 p - \frac{1}{c^2} \frac{\partial^2 p}{\partial t^2} = -\frac{\partial G}{\partial t} + \nabla \cdot \vec{F} - \rho \frac{\partial^2 (\nu_i \nu_j)}{\partial x_i \partial x_j} \tag{4.13}$$

### 4.2.1.4   Lossy LAPWE
[309]

As discussed in Section 4.2.1.2, in its original form, the LAPWE model does not account for the absorption of acoustic energy by the medium. However, it is possible to consider such effects by including an additional term $-\frac{\tilde{a}}{c^2} p$ in the right-hand side of the linear continuity equation, i.e., Equation 4.7. This equation then becomes [309]:

$$\frac{\partial \rho}{\partial t} = -\rho_0 \nabla \cdot \vec{\nu} - \frac{\widetilde{a}}{c^2} p$$

Using the linear constitutive equation (see Equation 4.8), the medium density is related to pressure as follows:

$$\frac{\partial}{\partial t} \left( \rho_0 \beta_0 p \right) = -\rho_0 \nabla \cdot \vec{\nu} - \frac{\widetilde{a}}{c^2} p$$

Differentiating the above equation with respect to time yields:

$$\rho_0 \beta_0 \frac{\partial^2 p}{\partial t^2} = -\rho_0 \nabla \cdot \frac{\partial \vec{\nu}}{\partial t} - \frac{\widetilde{a}}{c^2} \frac{\partial p}{\partial t}$$

Since $c^2 = (\rho_0 \beta_0)^{-1}$ and by using Euler's linear equation of motion (see Equation 4.6), the *Lossy LAPWE* PDE becomes:

$$\nabla^2 p - \frac{1}{c^2} \frac{\partial^2 p}{\partial t^2} - \frac{\widetilde{a}}{c^2} \frac{\partial p}{\partial t} = 0 \tag{4.14}$$

However, the term $\widetilde{a}$ is an abstract quantity and needs to be expressed in known quantities. To that end, the PDE derived above is converted from the time domain to the frequency domain. Given that $\nabla = ik$, and $\frac{\partial}{\partial t} = -i\omega$, Equation 4.14 becomes:

$$(ik)^2 p - \frac{1}{c^2} (-i\omega)^2 p + \frac{\widetilde{a}}{c^2} (i\omega) p = 0 \Leftrightarrow$$

$$\Leftrightarrow -k^2 p + \frac{1}{c^2} \omega^2 p + i \frac{\widetilde{a}}{c^2} \omega p = 0$$

Dividing all terms by $p$, the wavenumber $k$ then becomes:

$$k^2 = \frac{\omega^2}{c^2} + i\omega \frac{\widetilde{a}}{c^2}$$

Let $k = \widetilde{k} + ia$. Squaring $k$ and comparing to the above equation yields:

$$k^2 = \widetilde{k}^2 + 2ia\, \widetilde{k} - a^2 \Rightarrow$$

$$\Rightarrow \left\{ \begin{array}{l} 2a\, \widetilde{k} = \omega \frac{\widetilde{a}}{c^2} \\ \widetilde{k}^2 - a^2 = \frac{\omega^2}{c^2} \end{array} \right\} \Rightarrow \left\{ \begin{array}{l} \widetilde{a} = \frac{2ac^2 \widetilde{k}}{\omega} \\ \widetilde{k} = \sqrt{a^2 + \frac{\omega^2}{c^2}} \end{array} \right\}$$

Solving for $\overset{\sim}{a}$ yields:

$$\overset{\sim}{a} = 2a\sqrt{\frac{a^2c^4}{\omega^2} + c^2} \tag{4.15}$$

where $a$ is the absorption coefficient of the medium in $\mathrm{Np/m}$, as defined in Section 1.1.2.3.

## 4.2.2 Khokhlov-Zabolotskaya-Kuznetsov Equation

The *Khokhlov-Zabolotskaya-Kuznetsov* (KZK) equation describes a one-way parabolic approximation of the non-linear acoustic wave equation. It is derived from the Kuznetsov equation [312, 321] and describes the wave propagation of a finite amplitude beam in a lossy, compressible, and rotation-free fluid medium.

### 4.2.2.1 Model
[322, pp.24-29], [20, p.61],[312, 321, 323–326]

The full derivation of the KZK PDE is outside the scope of this section but can be found in [20]. The PDE in 3D cartesian coordinates for an ultrasonic beam propagating along the z direction is shown below [326], [20, p. 61], [324]:

$$\frac{\partial^2 p}{\partial \tau \partial z} = \frac{c_0}{2}\left(\frac{\partial^2 p}{\partial x^2} + \frac{\partial^2 p}{\partial y^2}\right) + \frac{\delta}{2c_0^3}\frac{\partial^3 p}{\partial \tau^3} + \frac{\beta}{2\rho_0 c_0^3}\frac{\partial^2 p^2}{\partial \tau^2} \tag{4.16}$$

where $p$ is the acoustic pressure, $z$ is the coordinate along the axis of the beam, and $\tau = t - z/c_0$ is the retarded time, with $c_0$ being the equilibrium speed of sound. Finally, $\delta$ is the diffusivity of sound for a thermoviscous fluid, and is calculated as follows:

$$\delta = 2\alpha\frac{c_0^3}{\omega^2} \tag{4.17}$$

where $a$ is the absorption coefficient of the medium in $\mathrm{Np/m}$, and $\omega = 2\pi f$ is the angular frequency of the wave.

$\beta = 1 + 0.5B/A$ is the non-linearity coefficient as defined in Section 1.2.2, and $\rho_0$ is the equilibrium density of the fluid. The Laplacian $\nabla_\perp^2 = \partial^2/\partial x^2 + \partial^2/\partial y^2$ in Equation 4.16 operates in the plane perpendicular to the propagation axis, which in this case is $z$. The first term on the right-hand-side of the KZK PDE represents diffraction, the second accounts for sound absorption as caused by diffusivity, and the third term depicts nonlinearity.

#### 4.2.2.2 Advantages & Limitations
[327, p.6], [312, 321, 323, 326, 328–331]

Sharing some of the advantages of the LAPWE equation, this model is able to account for diffraction effects and the energy absorption in liquid media. However, the foremost advantage of the KZK equation lies in its ability to model nonlinear acoustic wave propagation as described in Section 1.2.2.

Nonetheless, certain assumptions and approximations are employed during the derivation of the KZK equation, yielding a number of drawbacks. In addition to its inability to accurately model solid media, such as is the case of the LAPWE model discussed in Section 4.2.1.2, another limitation of this model is the *paraxial approximation*. During derivation, it is assumed that the pressure field variations transverse to the direction of propagation are slow compared to axial variations. This approximation limits the validity of the equation to approximately $5 - 20°$ off the propagation axis, beyond which errors are introduced. The paraxial approximation also causes errors in the nearfield region since only progressive waves are taken into account, while nonlinear effects near the source are ignored. Moreover, the KZK is a one-way PDE, i.e., it does not allow for the modeling of reflections, scattering, or inhomogeneous media. Overall, the KZK model is inappropriate for focused transducers and arrays, and can only be applied to modeling directive ultrasonic beams in homogeneous media, where the aforementioned assumptions are valid.

### 4.2.3 Westervelt-Lighthill Equation (WLE)

The *Westervelt-Lighthill Equation* (WLE) is a nonlinear full-wave equation mostly used to model acoustic field propagation in nonlinear thermoviscous fluids, a category under which soft tissues fall. It was introduced by Westervelt [332], who derived the second-order wave equation by expanding Lighthill's exact equation of fluid particle motion, retaining all second-order small disturbances, while discarding the Lagrangian density terms, which do not significantly contribute to the scattered field. The full derivation can be found in [20, pp.52-55].

#### 4.2.3.1 Model
[333, p.30],[20, pp.52-55], [326, 330, 331, 334–336]

The WLE model, as seen in Equation 4.18, is considered an appropriate approximation of the full second-order wave equation when cumulative nonlinear effects dominate local nonlinear effects. This is the case when the propagation distance is far greater than a single wavelength $\lambda$. The WLE PDE is shown below:

$$\nabla^2 p - \frac{1}{c_0^2}\frac{\partial^2 p}{\partial t^2} + \frac{\delta}{c_0^4}\frac{\partial^3 p}{\partial t^3} + \frac{\beta}{2\rho_0 c_0^4}\frac{\partial^2 p^2}{\partial t^2} = 0 \qquad (4.18)$$

where $p$ is the acoustic pressure, $c_0$ is the equilibrium speed of sound, $\delta$ is the diffusivity of the medium as defined in Equation 4.17, $\beta$ is the nonlinearity coefficient, and $\rho_0$ is the equilibrium density of the fluid.

The first two terms of Equation 4.18 are essentially the original LAPWE PDE shown in Equation 4.9. The third term accounts for energy losses through medium absorption, due to thermoviscous diffusivity, i.e., viscosity and thermal conductivity of the fluid as discussed in Section 1.1.2.3. The fourth term describes nonlinear distortion of the wave due to finite-amplitude effects, as described in Section 1.2.2. Other formulations of the WLE, may include additional terms to account for variations in the medium density and relaxation mechanisms [331], or simplification of the equation to a linear form by removing the fourth term from Equation 4.18 [326].

### 4.2.3.2   Advantages & Limitations
[330, 331, 336, 337]

The WLE model incorporates the advantages of both the LAPWE and KZK models outlined in Sections 4.2.1.2 and 4.2.2.2 respectively. Therefore, it can account for all wave propagation phenomena, including nonlinearity, without being limited by the paraxial approximation. The only unaddressed caveat of this model lies in its inability to account for the propagation of shear waves, resulting in limited accuracy when modeling solid media.

## 4.2.4   Linear Elastic Wave Equation

The *linear elastic wave equation* (LEWE) model describes wave propagation within three dimensional, linear, isotropic elastic media. It was originally applied to modeling seismic wave propagation [338], and was later adopted into the field of acoustic wave modeling.

### 4.2.4.1   Model
[338–348]

The LEWE model is derived based on the equations of momentum conservation (Equations 4.19-4.21), and the stress-strain relations (Equations 4.22-4.27). The former are formulated as shown below [338]:

$$\rho \frac{\partial^2 \upsilon_x}{\partial t^2} = \frac{\partial \tau_{xx}}{\partial x} + \frac{\partial \tau_{xy}}{\partial y} + \frac{\partial \tau_{xz}}{\partial z} + f_x \tag{4.19}$$

$$\rho \frac{\partial^2 \upsilon_y}{\partial t^2} = \frac{\partial \tau_{xy}}{\partial x} + \frac{\partial \tau_{yy}}{\partial y} + \frac{\partial \tau_{yz}}{\partial z} + f_y \tag{4.20}$$

$$\rho \frac{\partial^2 \upsilon_z}{\partial t^2} = \frac{\partial \tau_{zy}}{\partial x} + \frac{\partial \tau_{zy}}{\partial y} + \frac{\partial \tau_{zz}}{\partial z} + f_z \tag{4.21}$$

where $\rho$ is the medium density, $\upsilon_x, \upsilon_y, \upsilon_z$ are the displacement components along the $x, y$ and $z$ direction respectively, $\tau_{xx}, \tau_{yy}, \tau_{zz}$ and $\tau_{xy}, \tau_{xz}, \tau_{yz}$ are the normal and shear stress components respectively, and $f_x, f_y, f_z$ are the body-force components. The stress-strain relations are [338]:

$$\tau_{xx} = (\lambda + 2\mu) \frac{\partial \upsilon_x}{\partial x} + \lambda \left( \frac{\partial \upsilon_y}{\partial y} + \frac{\partial \upsilon_z}{\partial z} \right) \tag{4.22}$$

$$\tau_{yy} = (\lambda + 2\mu) \frac{\partial \upsilon_y}{\partial y} + \lambda \left( \frac{\partial \upsilon_x}{\partial x} + \frac{\partial \upsilon_z}{\partial z} \right) \tag{4.23}$$

$$\tau_{zz} = (\lambda + 2\mu) \frac{\partial \upsilon_z}{\partial z} + \lambda \left( \frac{\partial \upsilon_x}{\partial x} + \frac{\partial \upsilon_y}{\partial y} \right) \tag{4.24}$$

$$\tau_{xy} = \mu \left( \frac{\partial \upsilon_x}{\partial y} + \frac{\partial \upsilon_y}{\partial x} \right) \tag{4.25}$$

$$\tau_{xz} = \mu \left( \frac{\partial \upsilon_x}{\partial z} + \frac{\partial \upsilon_z}{\partial x} \right) \tag{4.26}$$

$$\tau_{yz} = \mu \left( \frac{\partial \upsilon_y}{\partial z} + \frac{\partial \upsilon_z}{\partial y} \right) \tag{4.27}$$

where $\lambda$ and $\mu$ are the Lamé coefficients [338].

The above equations can be formulated into a set of first-order differential equations by differentiating the stress-strain relations with respect to time and substituting the time-differentiated displacements with velocity components $\nu_x, \nu_y$ and $\nu_z$. The resulting velocity equations are shown in Equations 4.28-4.30, and Equations 4.31-4.36 [338] show the resulting stress relations.

$$\frac{\partial \nu_x}{\partial t} = \frac{1}{\rho} \left( \frac{\partial \tau_{xx}}{\partial x} + \frac{\partial \tau_{xy}}{\partial y} + \frac{\partial \tau_{xz}}{\partial z} + f_x \right) \tag{4.28}$$

$$\frac{\partial \nu_y}{\partial t} = \frac{1}{\rho} \left( \frac{\partial \tau_{xy}}{\partial x} + \frac{\partial \tau_{yy}}{\partial y} + \frac{\partial \tau_{yz}}{\partial z} + f_y \right) \tag{4.29}$$

$$\frac{\partial \nu_z}{\partial t} = \frac{1}{\rho} \left( \frac{\partial \tau_{xz}}{\partial x} + \frac{\partial \tau_{yz}}{\partial y} + \frac{\partial \tau_{zz}}{\partial z} + f_z \right) \tag{4.30}$$

$$\frac{\partial \tau_{xx}}{\partial t} = (\lambda + 2\mu) \frac{\partial \nu_x}{\partial x} + \lambda \left( \frac{\partial \nu_y}{\partial y} + \frac{\partial \nu_z}{\partial z} \right) \tag{4.31}$$

$$\frac{\partial \tau_{yy}}{\partial t} = (\lambda + 2\mu) \frac{\partial \nu_y}{\partial y} + \lambda \left( \frac{\partial \nu_x}{\partial x} + \frac{\partial \nu_z}{\partial z} \right) \tag{4.32}$$

$$\frac{\partial \tau_{zz}}{\partial t} = (\lambda + 2\mu) \frac{\partial \nu_z}{\partial z} + \lambda \left( \frac{\partial \nu_x}{\partial x} + \frac{\partial \nu_y}{\partial y} \right) \tag{4.33}$$

$$\frac{\partial \tau_{xy}}{\partial t} = \mu \left( \frac{\partial \upsilon_x}{\partial y} + \frac{\partial \upsilon_y}{\partial x} \right) \tag{4.34}$$

$$\frac{\partial \tau_{xz}}{\partial t} = \mu \left( \frac{\partial \upsilon_x}{\partial z} + \frac{\partial \upsilon_z}{\partial x} \right) \tag{4.35}$$

$$\frac{\partial \tau_{yz}}{\partial t} = \mu \left( \frac{\partial \upsilon_y}{\partial z} + \frac{\partial \upsilon_z}{\partial y} \right) \tag{4.36}$$

### 4.2.4.2   Advantages & Limitations
[4, p.31], [1, p.48], [17, pp.1-2], [2, p.11], [349, p.1], [339, 348]

Due to the nature of the LEWE sets of equations, this model offers unique modeling capabilities and advantages not available by the other numerical models. Equations 4.28 through 4.36 describe the propagation of a full three-dimensional elastic wave. Therefore, all propagation effects that are taken into account by the LAPWE (see Section 4.2.1), are also accurately modeled with LEWE. The foremost strength of the LEWE model, however, lies in its ability to accurately model the generation and propagation of shear waves in solids, making this model ideal for NDT applications and propagation through bones.

However, there exist practical limitations to the employment of this model for ultrasound simulations. As opposed to the full-wave alternatives, being the LAPWE and WLE models discussed in Sections 4.2.1 and 4.2.3 respectively, where the waves can be described by a single scalar quantity, i.e., acoustic pressure, the LEWE model requires nine such scalar quantities to be discretized and calculated over the entire computational domain. Thus, the required amount of computer memory and calculation time needed to solve the LEWE model are far greater, restraining its applicability to domains of limited sizes. Moreover, in the presented formulation this model cannot account for absorption or non-linearity effects, but formulations that do account for these effects have been proposed [350–354].

## 4.3 Ultrasound Simulation Software

Given the need for numerical simulation of ultrasonic wave propagation, a significant number of different software tools has been developed over the years. While many research teams develop and use their own 'in-house' codes, many such codes have been released either as commercial products or even freely distributed tools. This section will give a brief overview of the most prominent software permitting ultrasonic simulations, their key characteristics, e.g., the numerical model they implement and the technique they employ to do so, as well as publications in which these codes have been used. Many of these codes are listed on the IEEE's Ultrasonics, Ferroelectrics, and Frequency Control Society's website [355].

### 4.3.1 Field II

[286, 356]

Field II® [357], developed by Jensen, J., is possibly the most popular software for the simulation of ultrasonic wave propagation. It implements the Tupholme-Stepanishen model described in Section 4.1.1.3, and can be used to calculate the pressure distribution for any arbitrary transducer or transducer array. It has been developed within MATLAB®, and includes optimized C++ routines to speed up the computationally demanding operations. Its foremost area of application is in the field of diagnostic ultrasound imaging, but it is also actively used for the development of imaging and therapeutic transducer devices.

Field II® is still being developed and maintained by the original author, while its use has been reported in a large number of publications by the author himself [285, 286, 356, 358–367], by other research teams around the world [323, 331, 368–376], as well as by multiple companies listed on the software's website [357].

### 4.3.2 FOCUS

[295, 377–379]

FOCUS® [380] is a freely distributed toolbox allowing for the 2D and 3D simulation of acoustic wave propagation. It was developed by the McGough, R. team, and operates within MATLAB®, along with C++ routines to speed up the computationally demanding operations.

FOCUS® employs a combination of the FNM model (see Section 4.1.1.5) to calculate the pressure distribution from simple single-element transducers or transducer arrays on a plane in a manner similar to the RS model (see Section 4.1.1). Subsequently, it uses a version of ASM (see Section 4.1.2), along with many of the extensions described in Section

4.1.2.3, to propagate that projected field through the domain. It should be noted, however, that FOCUS® does not employ the hASM (see Section 4.1.2.4), and can therefore only model inhomogeneities in the layer-based approach as outlined in Section 4.1.2.3.

Nonetheless, FOCUS® is a valuable tool employed in the modeling, design and optimization of both simplistic transducer and transducer array setups in semi-homogeneous domains. In addition, it provides more accurate depictions of the nearfield pressure distributions, compared to software employing the RS model [379].

The software is actively developed and updated, and has been used in a large number of recent studies [291–295, 377–379, 381–383].

### 4.3.3   SimSonic

[346, 384]

SimSonic® [385] is another freely available MATLAB® toolbox which implements the LEWE model described in Section 4.2.4, with an FDTD implementation of the Virieux scheme [338, 386]. However, in its current form it does not account for energy absorption. This software began with the doctoral studies of Bossy E. in 2003 and today both 2D and 3D mature versions of the code are available for download.

SimSonic® was only recently released and is still actively developed. As it can account for shear waves it has been used predominantly in the simulation of ultrasonic wave propagation in bones and NDT applications, and a large number of studies by the authors of the software and other research teams have been published [346, 347, 384, 387–393].

### 4.3.4   Ultrasim

[277]

Ultrasim® [394] is another toolbox developed in Matlab® implementing the RS model (see Section 4.1.1). It was developed by Holm, S. in order to calculate the pressure field distributions resulting from transducers and arrays. Further information and applications of Ultrasim can be found in [5, 275, 277, 395], but the software's development appears to have ceased in 2007 and no recent publications seem to exist. Nonetheless, the software is still available for download in [394].

### 4.3.5   Abersim

[396, 397]

Abersim® [398] is an open source simulation software developed by the Varslot T. group, implementing the WLE model (see Section 4.2.3) as a combination of MATLAB® and

optimized C routines. This software solves the WLE for forward propagating waves in retarded time coordinates using an operator splitting approach and the ASM (see Section 4.1.2). Optionally, for axisymmetic cases, it uses the parabolic approximation and solves the diffraction using the FDTD method. Thus, this software cannot account for 3D inhomogeneous domains.

Abersim® has been used in a large number of publications [396, 397, 399–404]. However, neither recent publications, nor updates to the software's website have been seen since 2009 and development appears to have ceased.

### 4.3.6 k-Wave

[405–407]

k-Wave® [408] is an open source and freely distributed toolbox, developed for the 1D, 2D and 3D time-domain simulation of acoustic wave propagation. This software was developed by Treeby, B. and Cox, B., and as in the case of Field II and FOCUS, it was developed as a combination of MATLAB® and optimized C++ routines.

The implemented model is based on a generalized version of the WLE (see Section 4.2.3), and allows for both linear and nonlinear wave propagation modeling, inhomogeneous material distributions, and frequency dependent material absorption. The implementation of the WLE is based on a *k-space* pseudospectral (PS) [409, 410]. The main advantage of this implementation is that the PS method requires a much coarser spatial resolution [411], while the k-space method permits the employment temporal discretization beyond the Courant-Friedrichs-Lewy criterion (see Section 5.1.3). Thus, when compared to the FDTD method, the above combination results in reduced memory consumption and computational time, without seriously compromising accuracy.

This software is still being actively developed and has been utilized in many recent publications, [405–407, 412–416].

### 4.3.7 ACEL

[313, 417–419]

ACEL® [420] is an 'in-house' C++ code developed by Tanter, M. within the Laboratoire Ondes et Acoustique laboratory. Even though this code is neither commercially nor freely available, it is mentioned in this section due to the large number of publications reporting its usage. It comprises 2D, axisymmetric 3D, and full 3D FDTD implementations of LAPWE (see Section 4.2.1) and WLE (see Section 4.2.3). In addition, it implements the LEWE model (see Section 4.2.4) allowing for the simulation of ultrasonic shear wave propagation through solid media by means of a longitudinal-shear wave mode conversion module.

The software's website contains some information and examples but has not been recently updated. Some of the numerous publications where this code has been employed are [236, 313, 417–419, 421–431].

### 4.3.8  Wave 2000/2500/3000

[343, 432]

Wave® [433] is a commercial software series by CyberLogic® Inc., implementing the LEWE model described in Section 4.2.4 with the FDTD method. The series comprises multiple numerical solvers, being Wave2000® for 2D simulations, Wave2500® for axisymmetric 3D simulations and Wave3000®, for full 3D simulations.

Due to its ability to accurately model the propagation of shear waves through solids, this software is still being extensively used for non-destructive evaluation of materials and numerical modeling of wave propagation through bone structures by research teams and industrial users [343, 432, 434–451].

### 4.3.9  PZFlex

[452–456]

PZFlex® [457] is perhaps the most widely used commercial software permitting modeling of ultrasonic wave propagation. The software is tailored to the modeling of piezoelectric materials, providing finite element and pseudospectral (see Section 4.3.6) implementations of the LEWE model described in Section 4.2.4. Apart from NDT and some application on therapeutic FUS, this software has also been applied to a variety of industries and applications employing piezoelectrics, such as avionics, oil and gas, etc. As such, a very large number of publications using PZFlex® can be found, many of which are listed on the software's website [457].

### 4.3.10  DREAM

[458–460]

The DREAM® (Discrete Representation Array Modeling) toolbox [461] is another open source code similar to Field II® (see Section 4.3.1) which implements the Tupholme-Stepanishen model described in Section 4.1.1.3, but in the time domain. It was developed by Piwakowski B. in MATLAB® and was first released in 2004. The software is still available and developed, and has been used in a number of recent publications [458, 460, 462–468].

# 5

# Implemented Numerical Models & Methods

Having presented the foremost mathematical models and methods used to model the propagation of ultrasonic waves in Chapter 4, this chapter will outline the numerical implementations that were utilized for the purposes of this thesis. The following sections focus entirely on the work pertaining to this thesis alone and no longer discusses alternative approaches or models.

Discussion begins with a brief overview of the *finite-differences time-domain* (FDTD) method (Section 5.1), which was employed in this work in order to allow for numerical modeling of ultrasonic wave propagation in the human body. Subsequently, detailed stencil derivations of the different variants of the LAPWE and WLE full-wave models, that were presented in Sections 4.2.1 and 4.2.3 respectively and implemented during this work, are given (Section 5.2). This chapter concludes with a detailed analysis of the implemented *absorbing boundary conditions* (ABCs) that were used to effectively truncate the computational domains (Section 5.3).

## 5.1   The Finite-Differences Time-Domain Method

The *finite-differences time-domain* (FDTD) method was first introduced by Yee [469] in electrodynamics, but today it is one of the most prevalent computational methods used to solve PDEs across all disciplines. This section will be limited to the fundamental aspects of this method, being the discretization of simulated geometries (see Section 5.1.1), the numerical approximation of PDEs, i.e., stencil derivation (see Section 5.1.2), as well as the accuracy and stability criteria that ensure the stable operation of this method (see Section 5.1.3). Due to the significant advantages exhibited by FDTD, which are discussed in Section 5.1.4, this was the method of choice for this work, and has been employed throughout this thesis for the numerical modeling of acoustic wave propagation. As an

in-depth review of FDTD is outside the scope of this document, the reader is directed to the definitive textbook on the method by Taflove and Hagness [315].

### 5.1.1   Geometrical Discretization

For the FDTD method to be applied, the *simulation model* – which is typically a set of either 2D or 3D geometries – initially undergoes a process called *discretization*. During this process, the entire setup is initially *gridded*, i.e., virtually divided into *grid cells*, the totality of which forms a rectangular or rectilinear grid, commonly termed as the *computational grid*. These cells can either be rectangular in shape – for 2D problems and geometries – or cuboidal for 3D ones.

Two types of grids are commonly defined in FDTD simulations, namely *uniform* and *nonuniform* computational grids. In the case of the former, all grid-cells exhibit identical widths along each individual cartesian axis. On the other hand, grid-cells on nonuniform grids may each display different dimensions, which allows for more flexible discretization of complex geometries. Two-dimensional depictions of both grid types can be seen in Figure 5.1.



(a)                                              (b)
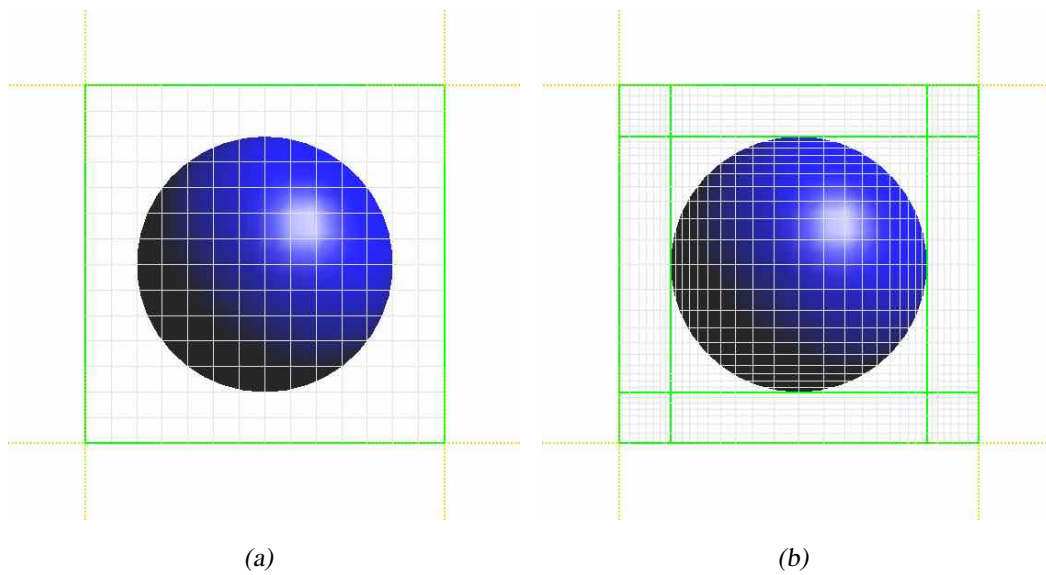
**Figure 5.1**: *Depiction of a uniform (a) and a nonuniform (b) computational grid. In the case of the former, all cells have identical widths along each axis. On a nonuniform grid however, each cell may have a different width.*

Following gridding, a process commonly termed as *voxeling* is performed. During voxeling each grid cell is assigned a single material type, typically based on which geometry of the setup occupies the majority of the grid cell volume. This procedure results in a set

of rectangles or cuboids, commonly referred to as *voxels*. The discretization results of a complex setup, involving a CAD model of the ExAblate® 4000 hemispherical transducer array (see Section 2.5.2.2), and an anatomical head model, can be seen in Figure 5.2.

## 5.1.2 Stencil Derivation

The cornerstone concept of the FDTD method is the approximation of the spatial and temporal derivatives in the modeled PDE, with weighted differences between neighboring points in space and time respectively. The values of the field described by the PDE are assumed to lie on given nodes within the grid cells, which are typically the center of the cell for scalar PDEs, or the edges/faces of the cell for vectorial PDEs (see Figure 5.3).

After the discretization process, as described in Section 5.1.1, calculation of the field quantities is commonly based on *central finite-differences* formulas, which are derived from Taylor series expansions, and can be found in [470–472]. As FDTD is employed throughout this thesis, these formulas will be repeated here.

Let us assume a function $F$, which within the scope of this thesis typically refers to the acoustic pressure $p$, whose values are spatially and temporally dependent. Assuming that the grid cell locations on a uniform grid are defined by a set of $(i, j, k)$ indices as shown in Figure 5.3, the *first-order central finite differences* formulas for spatial derivatives on the X, Y and Z axes respectively are:

$$\frac{\partial F}{\partial x}(i\Delta x, j\Delta y, k\Delta z, n\Delta t) = \frac{F_{i+1,j,k}^n - F_{i-1,j,k}^n}{2\Delta x} \tag{5.1}$$

$$\frac{\partial F}{\partial y}(i\Delta x, j\Delta y, k\Delta z, n\Delta t) = \frac{F_{i,j+1,k}^n - F_{i,j-1,k}^n}{2\Delta y} \tag{5.2}$$

$$\frac{\partial F}{\partial z}(i\Delta x, j\Delta y, k\Delta z, n\Delta t) = \frac{F_{i,j,k+1}^n - F_{i,j,k-1}^n}{2\Delta z} \tag{5.3}$$

Similarly, the *second-order central finite differences* formulas for spatial derivatives are:

$$\frac{\partial^2 F}{\partial x^2}(i\Delta x, j\Delta y, k\Delta z, n\Delta t) = \frac{F_{i+1,j,k}^n - 2F_{i,j,k}^n + F_{i-1,j,k}^n}{\Delta x^2} \tag{5.4}$$

$$\frac{\partial^2 F}{\partial y^2}(i\Delta x, j\Delta y, k\Delta z, n\Delta t) = \frac{F_{i,j+1,k}^n - 2F_{i,j,k}^n + F_{i,j-1,k}^n}{\Delta y^2} \tag{5.5}$$

$$\frac{\partial^2 F}{\partial z^2}(i\Delta x, j\Delta y, k\Delta z, n\Delta t) = \frac{F_{i,j,k+1}^n - 2F_{i,j,k}^n + F_{i,j,k-1}^n}{\Delta z^2} \tag{5.6}$$

*(a)*                                                    *(b)*



*(c)*
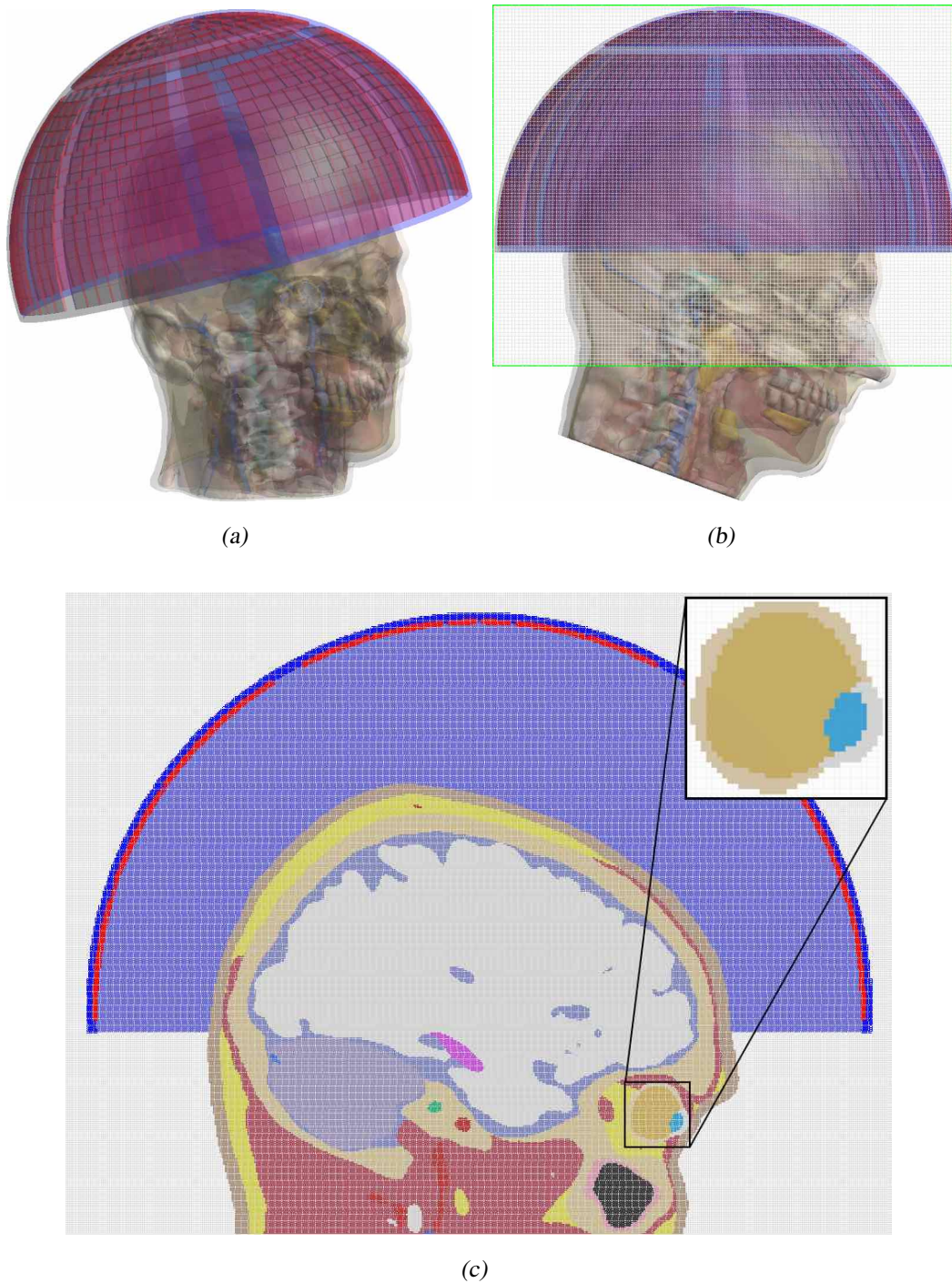
**Figure 5.2**: *Depiction of the gridding and voxeling concepts applied to a complex setup involving a CAD model of the ExAblate® 4000, hemispherical transducer array, and an anatomical head model. The simulation model (a) needs to be gridded with a rectilinear grid (b), and then voxeled so that every single voxels consists of a single material (c).*
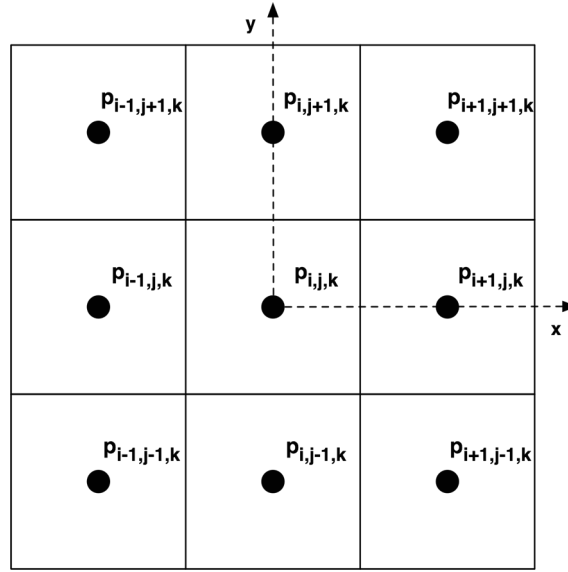
**Figure 5.3**: *Simplified depiction of a finite-differences grid for a scalar pressure wave PDE such as the LAPWE. The variables denoting acoustic pressure $p$ are assumed to lie at the centers of each cell.*

Lastly, assuming that the temporal snapshots of the calculated field are denoted by an index $n$, the first and second order temporal derivatives can be calculated with the following formulas:

$$\frac{\partial F}{\partial t}\left(i\Delta x, j\Delta y, k\Delta z, n\Delta t\right) = \frac{F_{i,j,k}^{n+1} - F_{i,j,k}^{n-1}}{2\Delta t} \tag{5.7}$$

$$\frac{\partial^2 F}{\partial t^2}\left(i\Delta x, j\Delta y, k\Delta z, n\Delta t\right) = \frac{F_{i,j,k}^{n+1} - 2F_{i,j,k}^{n} + F_{i,j,k}^{n-1}}{\Delta t^2} \tag{5.8}$$

Equations 5.1 through 5.8 can be used to decompose full-wave PDEs, such as the ones presented in Section 4.2, to a series of simple arithmetic operations, thus allowing for their straightforward numerical implementation. Such equations are typically called *computational stencils*, the derivations of which are presented in Section 5.2 for the different variants of the LAPWE and WLE PDEs discussed in Section 4.2.1 and 4.2.3 respectively.

### 5.1.3   Accuracy & Stability

[315, §§4.1-4.8]

Relevant parameters in an FDTD implementation of a PDE are the *grid step* and the *time-step*, i.e., the discretization degrees of space and time respectively. As the FDTD method yields an approximate depiction of the propagation of the wave quantity described by the

solved PDE, these parameters are pivotal to the accuracy and stability of the method and, if improperly chosen, can lead to the calculation of entirely erroneous results.

FDTD algorithms of full-wave PDEs are prone to inducing nonphysical *numerical dispersion*, which from this point forward will be simply referred to as *dispersion*. Dispersion is essentially a deviation of the phase velocity of the numerical waves from the physical speed of the wave in the given material, e.g., the speed of sound $c$ in the case of acoustic waves. This deviation is directly dependent on the wavelength, the direction of propagation in the computational grid, and the grid discretization. The unphysical phase velocity induces phase errors and delays in the propagating numerical waves, which tend to accumulate and become more prominent over large propagation distances. An example of dispersion can be seen in Figure 5.4. The effects of dispersion have been extensively investigated and a meticulous analysis can be found in [315, §§4.1-4.7]. To minimize such effects and improve the accuracy of the calculated results, a well-established rule of thumb for FDTD simulations is that the maximum grid-step $\Delta_{max}$ in the entire computational grid must not exceed $1/10$ of the minimum wavelength $\lambda_{min}$, which is expressed in the formula below:

$$\Delta_{max} \leq \frac{\lambda_{min}}{10} \tag{5.9}$$



(a)                      (b)                      (c)                      (d)
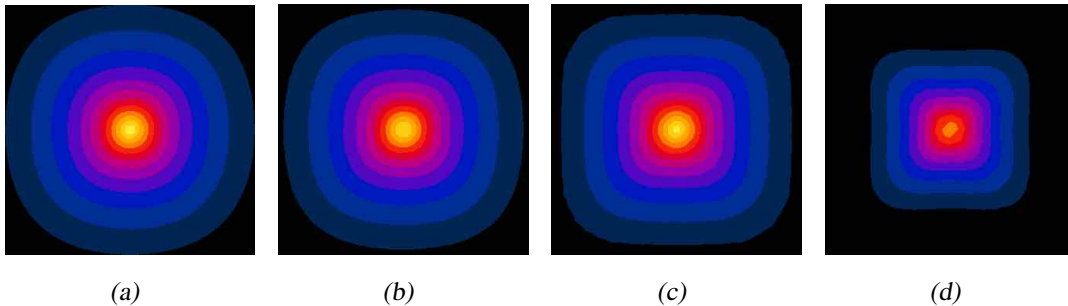
**Figure 5.4**: *Effects of numerical dispersion in an FDTD implementation. The results of simulations of a single point source producing a spherical wave and embedded in an infinitely extending medium are shown. The different computational grids exhibited a maximum grid-step of $\lambda/10$ (a), $\lambda/8$ (b), $\lambda/6$ (c), and $\lambda/5$ (d). As can be seen, larger grid-steps induce higher degrees of dispersion, which manifests itself as an unphysical 'squaring' of the spherical wave.*

In order to ensure numerical stability of the FDTD simulations, the time-step $\Delta t$ must be also be bounded, otherwise numerical errors tend to accumulate throughout the temporal update of the calculated fields, resulting in erroneous results (commonly called *spurious responses*). The de-facto criterion limiting $\Delta t$ in an FDTD implementation is the *Courant-Friedrichs-Lewy condition* (CFL condition) [473], which was derived based on a *von Neumann analysis* of the FDTD scheme. A detailed derivation of the CFL condition

can be found in [315, §§4.7-4.8], while [474] offers a brief history and assessment of the stability criteria of finite-difference schemes.

The CFL condition for uniform FD grids is given below:

$$\Delta t \leq \frac{1}{c_{max}\sqrt{\frac{1}{\Delta x^2} + \frac{1}{\Delta y^2} + \frac{1}{\Delta z^2}}} \tag{5.10}$$

where $c_{max}$ is the maximum speed of sound in the entire computational domain, and $\Delta x$, $\Delta y$, and $\Delta z$ are the uniform grid steps along the entire domain.

However, Equation 5.10 is only valid on uniform grids. The time-step for nonuniform grid schemes must abide the following formula instead:

$$\Delta t \leq \frac{1}{c_{max}\sqrt{\frac{1}{\Delta x_{min}^2} + \frac{1}{\Delta y_{min}^2} + \frac{1}{\Delta z_{min}^2}}} \tag{5.11}$$

where $c_{max}$ is the maximum speed of sound, and $\Delta x_{min}$, $\Delta y_{min}$ and $\Delta z_{min}$ are the minimum cell widths along their respective axes in the entire domain.

### 5.1.4  Advantages & Limitations

[470, 471]

The FDTD method is one of the most prevalent computational methods and it has been employed across all fields of science. It is relatively simple to programmatically implement, highly efficient, and easily adaptable. Its explicit nature is inherently amenable to the implementation of any PDE, and unlike methods like FEM, it does not require a linear system to be solved – requiring far less computational resources and time. This strength of the method becomes more prominent when considering that the computational requirements of FDTD implementations scale linearly with the the computational domain sizes. Furthermore, the simplicity of rectilinear grids required for the discretization of the simulated geometry permits easy implementation and adjustment of the computational domains.

The foremost weakness of the FDTD method lies in its inability to accurately model complex geometries with oblique or curved surfaces. As this method is inherently based on the discretization of the simulated geometry with the use of cartesian grids, such surfaces are typically approximated, resulting in a phenomenon commonly referred to as the *staircase approximation* – evident in Figure 5.2(c). In addition, the CFL condition outlined in Section 5.1.3, which bounds the time-step, is directly dependent on the resolution of the computational grid and the properties of the simulated materials. Thus, simulated setups that require a high spatial discretization in order to accurately depict fine structures,

naturally result in very small time-steps and thus long simulation times. Lastly, a notable limitation is the one imposed by dispersion and the $\Delta_{max} \leq \lambda_{min}/10$ maximum grid-step size, as discussed in Section 5.1.3. Unlike alternatives such as the pseudospectral method [409, 410] mentioned in Section 4.3.6, where bounding the grid step by a Nyquist limit, i.e., $\Delta_{max} \leq \lambda_{min}/2$, is sufficient, this restriction of the FDTD method can easily result in enormous computational domains and small time-steps, especially when simulating the propagation of high-frequency waves.

## 5.2 FDTD Stencil Derivations of Wave Models

The software developed for the purposes of this thesis contains implementations of multiple LAPWE (see Section 4.2.1) and WLE (4.2.3) model variants in order to allow for both linear and nonlinear simulations of ultrasonic wave propagation within the human body. In this section, the FDTD stencil derivations of the different variants of the two models that were numerically implemented for the purposes of this thesis will be presented.

Implementations included lossless and lossy variants of the LAPWE and WLE models, as well as an alternative formulation of the models which takes into account the density variation between the different media. These derivations were performed for both uniform and nonuniform computational grids, so as to allow for flexibility in the discretization.

### 5.2.1 LAPWE Stencil Derivations

#### 5.2.1.1 Lossless LAPWE on a Uniform Grid

In this section, the FDTD stencil derivation of the lossless LAPWE model (see Equation 4.9) discussed in Section 4.2.1 will be presented. The derivation is performed through the central finite-differences equations outlined in Section 5.1.2. Equation 4.9 is repeated below for the sake of convenience:

$$\nabla^2 p - \frac{1}{c^2}\frac{\partial^2 p}{\partial t^2} = 0 \Rightarrow$$
$$\Rightarrow \frac{\partial^2 p}{\partial x^2} + \frac{\partial^2 p}{\partial y^2} + \frac{\partial^2 p}{\partial z^2} - \frac{1}{c^2}\frac{\partial^2 p}{\partial t^2} = 0$$

with $p$ being the acoustic pressure, and $c$ the medium's speed of sound.

Using the second-order spatial and temporal central finite-differences, shown in Equations 5.4, 5.5, 5.6, and 5.8, the above equation is discretized as follows:

$$\frac{p_{i+1,j,k}^{n} - 2p_{i,j,k}^{n} + p_{i-1,j,k}^{n}}{\Delta x^2} +$$

$$+\frac{p_{i,j+1,k}^{n} - 2p_{i,j,k}^{n} + p_{i,j-1,k}^{n}}{\Delta y^2} +$$

$$+\frac{p_{i,j,k+1}^{n} - 2p_{i,j,k}^{n} + p_{i,j,k-1}^{n}}{\Delta z^2} -$$

$$-\frac{1}{c_{i,j,k}^2}\frac{p_{i,j,k}^{n+1} - 2p_{i,j,k}^{n} + p_{i,j,k}^{n-1}}{\Delta t^2} = 0$$

By solving the above equation for $p_{i,j,k}^{n+1}$, the stencil to be implemented is:

$$p_{i,j,k}^{n+1} = 2p_{i,j,k}^{n} - p_{i,j,k}^{n-1} +$$

$$+\frac{c_{i,j,k}^2}{\Delta t^2}\left(\frac{p_{i+1,j,k}^{n} - 2p_{i,j,k}^{n} + p_{i-1,j,k}^{n}}{\Delta x^2} +\right.$$

$$+\frac{p_{i,j+1,k}^{n} - 2p_{i,j,k}^{n} + p_{i,j-1,k}^{n}}{\Delta y^2} +$$

$$\left.+\frac{p_{i,j,k+1}^{n} - 2p_{i,j,k}^{n} + p_{i,j,k-1}^{n}}{\Delta z^2}\right) \tag{5.12}$$

where $c_{i,j,k}$ is the voxels-specific speed of sound in $\mathrm{m/s}$ on a rectangular uniform grid consisting of cells with dimensions of $\Delta x \times \Delta y \times \Delta z$. The time-step $\Delta t$ is derived from the CFL stability condition (see Equation 5.10).

### 5.2.1.2 Lossy LAPWE on a Uniform Grid

In this section, the FDTD stencil derivation of the lossy LAPWE (see Equation 4.14), which was discussed in Section 4.2.1.4, will be presented. Unlike the derivation in Section 5.2.1.1, energy losses due to the medium's absorption are taken into account. Equation 4.14, is discretized with central finite differences and is repeated below for convenience:

$$\nabla^2 p - \frac{1}{c^2}\frac{\partial^2 p}{\partial t^2} - \frac{\tilde{a}}{c^2}\frac{\partial p}{\partial t} = 0 \Rightarrow$$

$$\Rightarrow \frac{\partial^2 p}{\partial x^2} + \frac{\partial^2 p}{\partial y^2} + \frac{\partial^2 p}{\partial z^2} - \frac{1}{c^2}\frac{\partial^2 p}{\partial t^2} - \frac{\tilde{a}}{c^2}\frac{\partial p}{\partial t} = 0$$

where $p$ is the acoustic pressure, $c$ is the medium's speed of sound, and $\tilde{a}$ is related to the medium's absorption, as per Equation 4.15:

$$\widetilde{a} = 2a\sqrt{\frac{a^2 c^4}{\omega^2} + c^2}$$

Using second-order central finite differences, the PDE is discretized as follows:

$$\frac{p_{i+1,j,k}^n - 2p_{i,j,k}^n + p_{i-1,j,k}^n}{\Delta x^2} +$$
$$+ \frac{p_{i,j+1,k}^n - 2p_{i,j,k}^n + p_{i,j-1,k}^n}{\Delta y^2} +$$
$$+ \frac{p_{i,j,k+1}^n - 2p_{i,j,k}^n + p_{i,j,k-1}^n}{\Delta z^2} -$$
$$- \frac{1}{c_{i,j,k}^2} \frac{p_{i,j,k}^{n+1} - 2p_{i,j,k}^n + p_{i,j,k}^{n-1}}{\Delta t^2} -$$
$$- \frac{\widetilde{a}_{i,j,k}}{c_{i,j,k}^2} \frac{p_{i,j,k}^{n+1} - p_{i,j,k}^{n-1}}{2\Delta t} = 0$$

By solving the above equation for $p_{i,j,k}^{n+1}$, the stencil to be implemented is:

$$p_{i,j,k}^{n+1} = \frac{2}{1 + 0.5\,\widetilde{a}_{i,j,k}\,\Delta t} p_{i,j,k}^n - \frac{1 - 0.5\,\widetilde{a}_{i,j,k}\,\Delta t}{1 + 0.5\,\widetilde{a}_{i,j,k}\,\Delta t} p_{i,j,k}^{n-1} +$$
$$+ \frac{\Delta t^2 c_{i,j,k}^2}{1 + 0.5\,\widetilde{a}_{i,j,k}\,\Delta t} \left( \frac{p_{i+1,j,k}^n - 2p_{i,j,k}^n + p_{i-1,j,k}^n}{\Delta x^2} + \right.$$
$$+ \frac{p_{i,j+1,k}^n - 2p_{i,j,k}^n + p_{i,j-1,k}^n}{\Delta y^2} +$$
$$\left. + \frac{p_{i,j,k+1}^n - 2p_{i,j,k}^n + p_{i,j,k-1}^n}{\Delta z^2} \right) \qquad (5.13)$$

where $c_{i,j,k}$ is the voxel-specific speed of sound in $\mathrm{m/s}$ on a uniform computational grid, $f$ is the wave frequency in Hz, and the time-step $\Delta t$ is derived from the CFL stability condition (see Equation 5.10). The term $\widetilde{a}_{i,j,k}$ can be calculated through Equation 4.15 as follows:

$$\widetilde{a}_{i,j,k} = 2a_{i,j,k}\sqrt{\frac{a_{i,j,k}^2 c_{i,j,k}^4}{\omega^2} + c_{i,j,k}^2} \qquad (5.14)$$

where $a_{i,j,k}$ is the absorption coefficient of the medium in $\mathrm{Np/m}$ and $\omega = 2\pi f$ is the angular frequency of the wave.

### 5.2.1.3 Lossy LAPWE on a Nonuniform Grid

The LAPWE stencil derivations in Sections 5.2.1.1 and 5.2.1.2, were based on the assumption that the computational grid is uniform, i.e., the cell width along each axis is the same for every cell (see Figure 5.5(a)). However, as discussed in Section 5.1.1, this is often an inefficient spatial discretization approach, so it is commonly required to perform FDTD simulations on nonuniform grids (see Figure 5.5(b)). The FDTD stencil derivation of the lossy LAPWE (see Equation 4.14), which was presented in Section 5.2.1.2, is repeated in this section for a nonuniform grid.

The spacing in the denominator of the central finite-differences equations (see Section 5.1.2) is equal to the width of the $(i, j, k)$ cell multiplied by the distance between the centers of the two cells. When discretizing over a uniform grid, this term is equal to the square of the $(i, j, k)$ cell width as can be seen in the formula below:

$$\frac{\partial^2 p}{\partial x^2} \Rightarrow \frac{p_{i+1,j,k}^n - 2p_{i,j,k}^n + p_{i-1,j,k}^n}{\Delta x^2}$$

However, this quantity varies for each cell when discretizing over a nonuniform grid where each cell may have a different width along each axis. The amended formulation of the above equation yields:

$$\frac{\partial^2 p}{\partial x^2} \Rightarrow \frac{p_{i+1,j,k}^n - p_{i,j,k}^n}{\Delta x_{i,j,k} \frac{\Delta x_{i+1,j,k} + \Delta x_{i,j,k}}{2}} + + \frac{p_{i-1,j,k}^n - p_{i,j,k}^n}{\Delta x_{i,j,k} \frac{\Delta x_{i-1,j,k} + \Delta x_{i,j,k}}{2}}$$

Apart from this alternative formulation of the central finite-differences equations, the derivation process of the lossy LAPWE, presented in Section 5.2.1.2, is identical for the case of a nonuniform grid. Therefore, by applying the above formula on the central-differences equations (see Section 5.1.2), the stencil derivation for Equation 5.13 becomes:

$$p_{i,j,k}^{n+1} = \frac{2}{1 + 0.5 \, \widetilde{a}_{i,j,k} \, \Delta t} p_{i,j,k}^n - \frac{1 - 0.5 \, \widetilde{a}_{i,j,k} \, \Delta t}{1 + 0.5 \, \widetilde{a}_{i,j,k} \, \Delta t} p_{i,j,k}^{n-1} +$$

$$+ \frac{\Delta t^2 c_{i,j,k}^2}{1 + 0.5 \, \widetilde{a}_{i,j,k} \, \Delta t} \left( \frac{p_{i+1,j,k}^n - p_{i,j,k}^n}{\Delta x_{i,j,k} \frac{\Delta x_{i+1,j,k} + \Delta x_{i,j,k}}{2}} + \frac{p_{i-1,j,k}^n - p_{i,j,k}^n}{\Delta x_{i,j,k} \frac{\Delta x_{i-1,j,k} + \Delta x_{i,j,k}}{2}} + \right.$$

$$+ \frac{p_{i,j+1,k}^n - p_{i,j,k}^n}{\Delta y_{i,j,k} \frac{\Delta y_{i,j+1,k} + \Delta y_{i,j,k}}{2}} + \frac{p_{i,j-1,k}^n - p_{i,j,k}^n}{\Delta y_{i,j,k} \frac{\Delta y_{i,j-1,k} + \Delta y_{i,j,k}}{2}} +$$

$$\left. + \frac{p_{i,j,k+1}^n - p_{i,j,k}^n}{\Delta z_{i,j,k} \frac{\Delta z_{i,j,k+1} + \Delta z_{i,j,k}}{2}} + \frac{p_{i,j,k-1}^n - p_{i,j,k}^n}{\Delta z_{i,j,k} \frac{\Delta z_{i,j,k-1} + \Delta z_{i,j,k}}{2}} \right)$$

$$(5.15)$$

where $\widetilde{a}_{i,j,k}$ is calculated through Equation 5.14, and $\Delta t$ is calculated based on the CFL condition criterion for nonuniform grids (see Equation 5.11).

**Uniform grid**



*(a)*
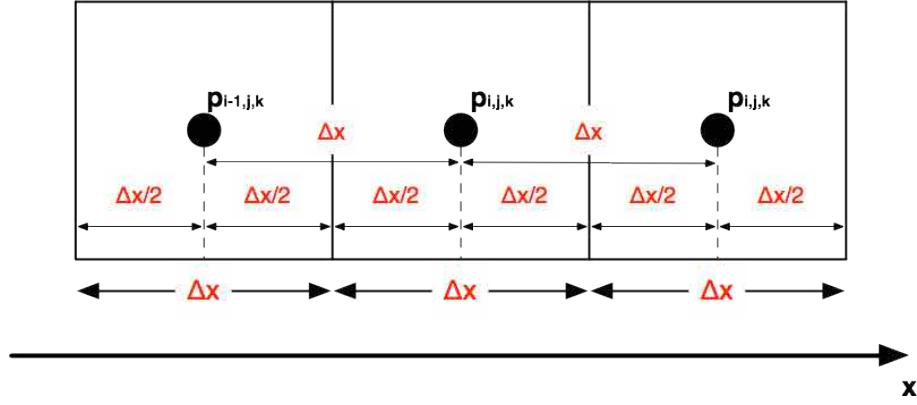
**Non-uniform grid**
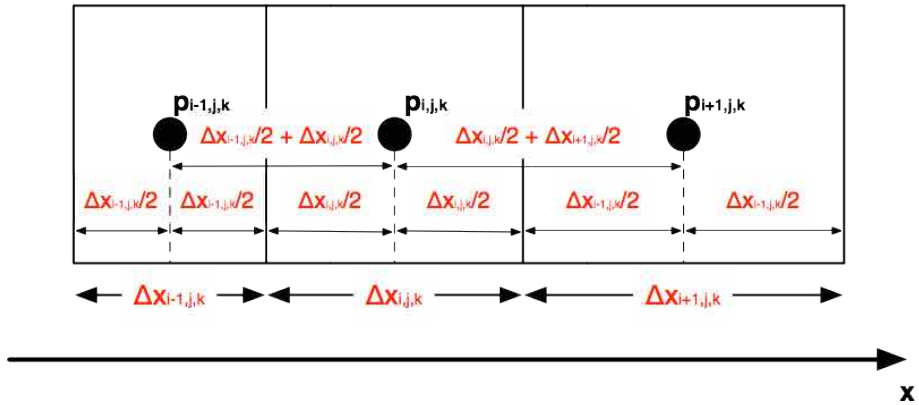


*(b)*

**Figure 5.5**: *Depiction of three cells on a uniform (a) and a nonuniform (b) finite-differences grid. In the case of the former, all cells along each axis have identical widths ($\Delta x$ in this case). In the case of a nonuniform grid, however, each cell may have a different width.*

### 5.2.1.4   Lossy LAPWE with Density-Variations on a Nonuniform Grid

The FDTD stencils presented in the previous sections share one common drawback. While they account for the change in the speed of sound $c$ between the different cells in the computational domain, this does not extend to medium density $\rho$. However, as it has been emphasized throughout this thesis, medium density is a pivotal parameter that influences a given medium's characteristic acoustic impedance $Z$, and therefore dictates

the propagation behavior of the acoustic waves. This section presents an extension to the lossless and lossy LAPWE models discretized in the above sections by including a *density-variation* term in the respective PDEs based on [331, 336].

In order to account for variations in media density, let us first explore a simplified one-dimensional scenario, and assume two cells along the $x$ axis, at locations defined by indices $(i, j, k)$ and $(i + 1, j, k)$, and exhibiting widths of $\Delta x_{i,j,k}$ and $\Delta x_{i+1,j,k}$ respectively. The density of the two cells is $\rho_{i,j,k}$ and $\rho_{i+1,j,k}$, and the pressure values in the centers of these cells are denoted by $p_{i,j,k}$ and $p_{i+1,j,k}$ respectively, as depicted in Figure 5.6. If $p_{int}$ is the pressure value at the interface between the two cells, then based on the mass conservation equation (see Equation 4.7 in Section 4.2.1.1), this quantity can be calculated as a function of the aforementioned quantities as follows:

$$\frac{1}{\rho}\nabla p \Rightarrow \frac{p_{int} - p_{i,j,k}}{\rho_{i,j,k}\Delta x_{i,j,k}} = \frac{p_{i+1,j,k} - p_{int}}{\rho_{i+1,j,k}\Delta x_{i+1,j,k}} \Leftrightarrow$$
$$\Leftrightarrow \rho_{i+1,j,k}\Delta x_{i+1,j,k}\left(p_{int} - p_{i,j,k}\right) = \rho_{i,j,k}\Delta x_{i,j,k}\left(p_{i+1,j,k} - p_{int}\right)$$

Solving the above equation for $p_{int}$ yields:

$$p_{int} = \frac{\rho_{i,j,k}\Delta x_{i,j,k}p_{i+1,j,k} + \rho_{i+1,j,k}\Delta x_{i+1,j,k}p_{i,j,k}}{\rho_{i+1,j,k}\Delta x_{i+1,j,k} + \rho_{i,j,k}\Delta x_{i,j,k}} \tag{5.16}$$

By replacing the term $\nabla^2 p$ in the lossy LAPWE PDE (see Equation 4.14) with $\rho\nabla\frac{1}{\rho}\nabla p$, the new LAPWE PDE, which accounts for media density variation becomes:

$$\rho\nabla\frac{1}{\rho}\nabla p - \frac{1}{c^2}\frac{\partial^2 p}{\partial t^2} - \frac{\widetilde{a}}{c^2}\frac{\partial p}{\partial t} = 0 \tag{5.17}$$

In order to discretize this newly introduced density-variation term, we average over the volume $V$ of the entire cell:

$$\frac{\int_V \rho\nabla\frac{1}{\rho}\nabla p}{V}dV = \frac{\rho}{V}\int_V \nabla\frac{1}{\rho}\nabla p dV$$

Applying Stokes' theorem, the above volume integral can be replaced with an integral over the cell surface $A$ as shown below:

$$\frac{\rho}{V}\int_V \nabla\frac{1}{\rho}\nabla p dV = \frac{\rho}{V}\oint_A \left(\frac{1}{\rho}\nabla p\right)\vec{n}dA$$

This integral can be approximated with a sum over all 6 cell faces ($A_f$ for $f = 1 \div 6$), which it 'shares' with its neighboring cells within the computational grid. The mass

continuity expressed in Equation 5.16 and Figure 5.6 is assumed for each one of those faces. Therefore, the above integral becomes:

$$\frac{\rho}{V} \oint_A \left(\frac{1}{\rho}\nabla p\right) \vec{n} dA \approx \sum_{f=1}^{N=6} \frac{A_f \rho}{V}\frac{1}{\rho}\partial n_f p$$

Since $A_f/V$ is equal to the cell width (let this width be $\Delta$ on the axis perpendicular to that face, i.e., parallel to the respective $\vec{n}$ vector), and assuming a linear relation between the pressure value $p$ at the center of each cell with the $p_{int}$ value at the cell interfaces, then for a cell $(i, j, k)$ the sum shown above becomes:

$$\sum_{f=1}^{N=6} \frac{A_f \rho}{V}\frac{1}{\rho}\partial n_f p = \sum_{f=1}^{N=6} \frac{1}{\Delta_{i,j,k}}\frac{p_{int,f} - p_{i,j,k}}{\Delta_{i,j,k}/2}$$

where $\Delta_{i,j,k}$ is the width of the $(i, j, k)$ cell along the axis perpendicular to the particular cell face in the sum, $p_{int}$ is the pressure on the interface between the two neighboring cells on that face, and $p_{i,j,k}$ is the pressure in the center of the $(i, j, k)$ cell. Therefore, for the case of two cells along the X axis (see Figure 5.6), replacing $p_{int}$ in Equation 5.16, the term within the above sum becomes:

$$\frac{1}{\Delta_{i,j,k}}\frac{p_{int,f} - p_{i,j,k}}{\Delta_{i,j,k}/2} \Rightarrow \frac{p_{int} - p_{i,j,k}}{\Delta x_{i,j,k}^2/2} \qquad =$$

$$= \frac{\frac{\rho_{i,j,k}p_{i+1,j,k}\Delta x_{i,j,k}+\rho_{i+1,j,k}p_{i,j,k}\Delta x_{i+1,j,k}}{\rho_{i+1,j,k}\Delta x_{i+1,j,k}+\rho_{i,j,k}\Delta x_{i,j,k}} - p_{i,j,k}}{\Delta x_{i,j,k}^2/2} \qquad =$$

$$= \frac{2\rho_{i,j,k}\Delta x_{i,j,k}\left(p_{i+1,j,k} - p_{i,j,k}\right)}{\Delta x_{i,j,k}^2\left(\rho_{i+1,j,k}\Delta x_{i+1,j,k} + \rho_{i,j,k}\Delta x_{i,j,k}\right)} \qquad \overset{\times\frac{1}{\rho_{i,j,k}\Delta x_{i,j,k}}}{=}$$

$$\overset{\times\frac{1}{\rho_{i,j,k}\Delta x_{i,j,k}}}{=} \frac{2}{\Delta x_{i,j,k}^2 + \frac{\rho_{i+1,j,k}\Delta x_{i+1,j,k}\Delta x_{i,j,k}}{\rho_{i,j,k}}}\left(p_{i+1,j,k} - p_{i,j,k}\right) \qquad (5.18)$$

In order to apply the above discretization approach on the FDTD stencil shown in Equation 5.15, the terms within the parentheses that describe the spatial differences need to be replaced with the density-variation equivalents shown above (essentially, this includes repeating the above discretization for every face of the $(i, j, k)$ cell and replacing the respective term). The rest of the derivation remains exactly the same. Thus, the stencil for the lossy LAPWE, accounting for density-variations, and derived on a nonuniform grid is:

$$p_{i,j,k}^{n+1} = \frac{2}{1 + 0.5\, \widetilde{a}_{i,j,k}\, \Delta t} p_{i,j,k}^{n} - \frac{1 - 0.5\, \widetilde{a}_{i,j,k}\, \Delta t}{1 + 0.5\, \widetilde{a}_{i,j,k}\, \Delta t} p_{i,j,k}^{n-1} +$$

$$+ \frac{\Delta t^2 c_{i,j,k}^2}{1 + 0.5\, \widetilde{a}_{i,j,k}\, \Delta t} \left( \frac{2\,(p_{i+1,j,k} - p_{i,j,k})}{\Delta x_{i,j,k}^2 + \frac{\rho_{i+1,j,k}\Delta x_{i+1,j,k}\Delta x_{i,j,k}}{\rho_{i,j,k}}} + \right.$$

$$+ \frac{2\,(p_{i-1,j,k} - p_{i,j,k})}{\Delta x_{i,j,k}^2 + \frac{\rho_{i-1,j,k}\Delta x_{i-1,j,k}\Delta x_{i,j,k}}{\rho_{i,j,k}}} +$$

$$+ \frac{2\,(p_{i,j+1,k} - p_{i,j,k})}{\Delta y_{i,j,k}^2 + \frac{\rho_{i,j+1,k}\Delta y_{i,j+1,k}\Delta y_{i,j,k}}{\rho_{i,j,k}}} +$$

$$+ \frac{2\,(p_{i,j-1,k} - p_{i,j,k})}{\Delta y_{i,j,k}^2 + \frac{\rho_{i,j-1,k}\Delta y_{i,j-1,k}\Delta y_{i,j,k}}{\rho_{i,j,k}}} +$$

$$+ \frac{2\,(p_{i,j,k+1} - p_{i,j,k})}{\Delta z_{i,j,k}^2 + \frac{\rho_{i,j,k+1}\Delta z_{i,j,k+1}\Delta z_{i,j,k}}{\rho_{i,j,k}}} +$$

$$\left. + \frac{2\,(p_{i,j,k-1} - p_{i,j,k})}{\Delta z_{i,j,k}^2 + \frac{\rho_{i,j,k-1}\Delta z_{i,j,k-1}\Delta z_{i,j,k}}{\rho_{i,j,k}}} \right) \tag{5.19}$$

where $\widetilde{a}_{i,j,k}$ is calculated through Equation 5.14, and $\Delta t$ is calculated based on the CFL condition criterion for nonuniform grids (see Equation 5.11).



**Figure 5.6**: *Concept of density variations between two cells on a FD grid.*

## 5.2.2   WLE Stencil Derivations

### 5.2.2.1   WLE on a Uniform Grid

The FDTD stencil for the WLE PDE (see Equation 4.18), which was presented in Section 4.2.3.1, is derived on a uniform computational grid in a manner similar to the derivation shown in Section 5.2.1.1. Equation 4.18 is repeated here for convenience:

$$\nabla^2 p - \frac{1}{c_0^2}\frac{\partial^2 p}{\partial t^2} + \frac{\delta}{c_0^4}\frac{\partial^3 p}{\partial t^3} + \frac{\beta}{2\rho_0 c_0^4}\frac{\partial^2 p^2}{\partial t^2} = 0$$

The first two terms of the above equation are identical to the lossless LAPWE PDE and can be discretized as was shown in Section 5.2.1.1. However, this PDE additionally includes both a third-order temporal derivative and a nonlinearity term which, using central finite-differences, are discretized as shown below [331, 336]:

$$\frac{\partial^3 p}{\partial t^3} = \frac{6p_{i,j,k}^n - 23p_{i,j,k}^{n-1} + 34p_{i,j,k}^{n-2} - 24p_{i,j,k}^{n-3} + 8p_{i,j,k}^{n-4} - p_{i,j,k}^{n-5}}{8\Delta t^3} \tag{5.20}$$

The nonlinearity term can be approximated as follows with second-order finite differences:

$$\frac{\partial^2 p^2}{\partial t^2} = 2\left(\left(\frac{\partial p}{\partial t}\right)^2 + p\frac{\partial^2 p}{\partial t^2}\right) \approx$$

$$\approx 2\left(\left(\frac{p_{i,j,k}^n - p_{i,j,k}^{n-1}}{\Delta t}\right)^2 + p_{i,j,k}^n \frac{p_{i,j,k}^{n+1} - 2p_{i,j,k}^n + p_{i,j,k}^{n-1}}{\Delta t^2}\right) \tag{5.21}$$

which can be simplified further as follows:

$$2\left(\left(\frac{p_{i,j,k}^n - p_{i,j,k}^{n-1}}{\Delta t}\right)^2 + p_{i,j,k}^n \frac{p_{i,j,k}^{n+1} - 2p_{i,j,k}^n + p_{i,j,k}^{n-1}}{\Delta t^2}\right) =$$

$$= 2\left(\frac{p_{i,j,k}^n p_{i,j,k}^n - 2p_{i,j,k}^n p_{i,j,k}^{n-1} + p_{i,j,k}^{n-1} p_{i,j,k}^{n-1}}{\Delta t^2} + \right.$$

$$\left. + \frac{p_{i,j,k}^n p_{i,j,k}^{n+1} - 2p_{i,j,k}^n p_{i,j,k}^n + p_{i,j,k}^n p_{i,j,k}^{n-1}}{\Delta t^2}\right) =$$

$$= \frac{2}{\Delta t^2}\left(p_{i,j,k}^n p_{i,j,k}^n - 2p_{i,j,k}^n p_{i,j,k}^{n-1} + p_{i,j,k}^{n-1} p_{i,j,k}^{n-1} + \right.$$

$$\left. + p_{i,j,k}^n p_{i,j,k}^{n+1} - 2p_{i,j,k}^n p_{i,j,k}^n + p_{i,j,k}^n p_{i,j,k}^{n-1}\right) =$$

$$= \frac{2}{\Delta t^2}\left(p_{i,j,k}^n p_{i,j,k}^{n+1} - p_{i,j,k}^n p_{i,j,k}^n - p_{i,j,k}^n p_{i,j,k}^{n-1} + p_{i,j,k}^{n-1} p_{i,j,k}^{n-1}\right) \tag{5.22}$$

Replacing the respective partial derivatives with these discretized terms, the FDTD stencil derivation for the WLE PDE becomes:

$$\nabla^2 p - \frac{1}{c^2}\frac{\partial^2 p}{\partial t^2} + \frac{\delta}{c^4}\frac{\partial^3 p}{\partial t^3} + \frac{\beta}{\rho_0 c^4}\frac{\partial^2 p^2}{\partial t^2} = 0 \Leftrightarrow$$

$$\Leftrightarrow \frac{\partial^2 p}{\partial x^2} + \frac{\partial^2 p}{\partial y^2} + \frac{\partial^2 p}{\partial z^2} - \frac{1}{c^2}\frac{\partial^2 p}{\partial t^2} + \frac{\delta}{c^4}\frac{\partial^3 p}{\partial t^3} + \frac{\beta}{\rho_0 c^4}\frac{\partial^2 p^2}{\partial t^2} = 0 \Leftrightarrow$$

$$\Leftrightarrow \frac{p_{i+1,j,k}^n - 2p_{i,j,k}^n + p_{i-1,j,k}^n}{\Delta x^2} +$$

$$+ \frac{p_{i,j+1,k}^n - 2p_{i,j,k}^n + p_{i,j-1,k}^n}{\Delta y^2} +$$

$$+ \frac{p_{i,j,k+1}^n - 2p_{i,j,k}^n + p_{i,j,k-1}^n}{\Delta z^2} -$$

$$- \frac{1}{c_{i,j,k}^2}\frac{1}{\Delta t^2}\left(p_{i,j,k}^{n+1} - 2p_{i,j,k}^n + p_{i,j,k}^{n-1}\right) +$$

$$+ \frac{\delta_{i,j,k}}{c_{i,j,k}^4}\frac{1}{8\Delta t^3}\left(6p_{i,j,k}^n - 23p_{i,j,k}^{n-1} + 34p_{i,j,k}^{n-2} - 24p_{i,j,k}^{n-3} + 8p_{i,j,k}^{n-4} - p_{i,j,k}^{n-5}\right) +$$

$$+ \frac{2\beta_{i,j,k}}{\rho_{0i,j,k}c_{i,j,k}^4 \Delta t^2}\left(p_{i,j,k}^n p_{i,j,k}^{n+1} - p_{i,j,k}^n p_{i,j,k}^n - p_{i,j,k}^n p_{i,j,k}^{n-1} + p_{i,j,k}^{n-1} p_{i,j,k}^{n-1}\right) = 0$$

Isolating the the $p_{i,j,k}^{n+1}$ terms yields:

$$\frac{p^n_{i+1,j,k} - 2p^n_{i,j,k} + p^n_{i-1,j,k}}{\Delta x^2} +$$

$$+\frac{p^n_{i,j+1,k} - 2p^n_{i,j,k} + p^n_{i,j-1,k}}{\Delta y^2} +$$

$$+\frac{p^n_{i,j,k+1} - 2p^n_{i,j,k} + p^n_{i,j,k-1}}{\Delta z^2} -$$

$$-\frac{1}{c^2_{i,j,k}}\frac{1}{\Delta t^2}p^{n+1}_{i,j,k} + \frac{1}{c^2_{i,j,k}}\frac{1}{\Delta t^2}\left(2p^n_{i,j,k} - p^{n-1}_{i,j,k}\right) +$$

$$+\frac{\delta_{i,j,k}}{c^4_{i,j,k}}\frac{1}{8\Delta t^3}\left(6p^n_{i,j,k} - 23p^{n-1}_{i,j,k} + 34p^{n-2}_{i,j,k} - 24p^{n-3}_{i,j,k} + 8p^{n-4}_{i,j,k} - p^{n-5}_{i,j,k}\right) +$$

$$+\frac{2\beta_{i,j,k}}{\rho_{0\,i,j,k}c^4_{i,j,k}\Delta t^2}p^n_{i,j,k}p^{n+1}_{i,j,k} -$$

$$-\frac{2\beta_{i,j,k}}{\rho_{0\,i,j,k}c^4_{i,j,k}\Delta t^2}\left(p^n_{i,j,k}p^n_{i,j,k} + p^n_{i,j,k}p^{n-1}_{i,j,k} - p^{n-1}_{i,j,k}p^{n-1}_{i,j,k}\right) = 0$$

Finally, solving for $p^{n+1}_{i,j,k}$ yields the WLE FDTD stencil on a uniform grid is as follows:

$$p^{n+1}_{i,j,k} = \frac{1}{\frac{1}{c^2_{i,j,k}}\frac{1}{\Delta t^2} - \frac{2\beta_{i,j,k}}{\rho_{0\,i,j,k}c^4_{i,j,k}}\frac{1}{\Delta t^2}p^n_{i,j,k}}$$

$$\left[\frac{p^n_{i+1,j,k} - 2p^n_{i,j,k} + p^n_{i-1,j,k}}{\Delta x^2} +\right.$$

$$+\frac{p^n_{i,j+1,k} - 2p^n_{i,j,k} + p^n_{i,j-1,k}}{\Delta y^2} +$$

$$+\frac{p^n_{i,j,k+1} - 2p^n_{i,j,k} + p^n_{i,j,k-1}}{\Delta z^2} +$$

$$+\frac{1}{c^2_{i,j,k}}\frac{1}{\Delta t^2}\left(2p^n_{i,j,k} - p^{n-1}_{i,j,k}\right) +$$

$$+\frac{\delta_{i,j,k}}{c^4_{i,j,k}}\frac{1}{8\Delta t^3}\left(6p^n_{i,j,k} - 23p^{n-1}_{i,j,k} + 34p^{n-2}_{i,j,k} - 24p^{n-3}_{i,j,k} + 8p^{n-4}_{i,j,k} - p^{n-5}_{i,j,k}\right) -$$

$$-\frac{2\beta_{i,j,k}}{\rho_{0\,i,j,k}c^4_{i,j,k}\Delta t^2}\left(p^n_{i,j,k}p^n_{i,j,k} + p^n_{i,j,k}p^{n-1}_{i,j,k} - p^{n-1}_{i,j,k}p^{n-1}_{i,j,k}\right)\left.\right]$$

$$(5.23)$$

where, as shown in Section 4.2.2.1, the parameters $\beta_{i,j,k}$ and $\delta_{i,j,k}$ can be calculated as follows:

$$\beta_{i,j,k} = 1 + \frac{1}{2}\left(\frac{B}{A}\right)_{i,j,k} \tag{5.24}$$

$$\delta_{i,j,k} = \frac{2\alpha_{i,j,k}c_{i,j,k}^3}{\omega^2} \tag{5.25}$$

### 5.2.2.2 WLE on a Nonuniform Grid

Based on the process shown in Section 5.2.1.3, the WLE stencil shown in Equation 5.2.2.1, can easily be extended to a nonuniform grid stencil simply by replacing the terms describing the spatial differences. Thus the WLE FDTD stencil on a nonuniform grid becomes:

$$p_{i,j,k}^{n+1} = \frac{1}{\frac{1}{c_{i,j,k}^2}\frac{1}{\Delta t^2} - \frac{2\beta_{i,j,k}}{\rho_{0\,i,j,k}c_{i,j,k}^4}\frac{1}{\Delta t^2}p_{i,j,k}^n}$$

$$\left[\frac{p_{i+1,j,k}^n - p_{i,j,k}^n}{\Delta x_{i,j,k}\frac{\Delta x_{i+1,j,k}+\Delta x_{i,j,k}}{2}} + \frac{p_{i-1,j,k}^n - p_{i,j,k}^n}{\Delta x_{i,j,k}\frac{\Delta x_{i-1,j,k}+\Delta x_{i,j,k}}{2}} + \right.$$

$$+ \frac{p_{i,j+1,k}^n - p_{i,j,k}^n}{\Delta y_{i,j,k}\frac{\Delta y_{i,j+1,k}+\Delta y_{i,j,k}}{2}} + \frac{p_{i,j-1,k}^n - p_{i,j,k}^n}{\Delta y_{i,j,k}\frac{\Delta y_{i,j-1,k}+\Delta y_{i,j,k}}{2}} +$$

$$+ \frac{p_{i,j,k+1}^n - p_{i,j,k}^n}{\Delta z_{i,j,k}\frac{\Delta z_{i,j,k+1}+\Delta z_{i,j,k}}{2}} + \frac{p_{i,j,k-1}^n - p_{i,j,k}^n}{\Delta z_{i,j,k}\frac{\Delta z_{i,j,k-1}+\Delta z_{i,j,k}}{2}} +$$

$$+ \frac{1}{c_{i,j,k}^2}\frac{1}{\Delta t^2}\left(2p_{i,j,k}^n - p_{i,j,k}^{n-1}\right) +$$

$$+ \frac{\delta_{i,j,k}}{c_{i,j,k}^4}\frac{1}{8\Delta t^3}\left(6p_{i,j,k}^n - 23p_{i,j,k}^{n-1} + 34p_{i,j,k}^{n-2} - 24p_{i,j,k}^{n-3} + 8p_{i,j,k}^{n-4} - p_{i,j,k}^{n-5}\right) -$$

$$\left. - \frac{2\beta_{i,j,k}}{\rho_{0i,j,k}c_{i,j,k}^4\Delta t^2}\left(p_{i,j,k}^n p_{i,j,k}^n + p_{i,j,k}^n p_{i,j,k}^{n-1} - p_{i,j,k}^{n-1} p_{i,j,k}^{n-1}\right)\right] \tag{5.26}$$

where $\beta_{i,j,k}$ and $\delta_{i,j,k}$ can be calculated through Equations 5.24 and 5.25 respectively.

### 5.2.2.3 WLE with Density-Variations on a Nonuniform Grid

In order to derive the WLE stencil with density-variations, and on a nonuniform grid, the same concepts and derivations presented in Section 5.2.1.4, are applied to the stencil shown in Equation 5.26. By including the density-variation term the WLE PDE becomes:

$$\rho\nabla\frac{1}{\rho}\nabla p - \frac{1}{c_0^2}\frac{\partial^2 p}{\partial t^2} + \frac{\delta}{c_0^4}\frac{\partial^3 p}{\partial t^3} + \frac{\beta}{2\rho_0 c_0^4}\frac{\partial^2 p^2}{\partial t^2} = 0$$

Replacing the terms describing the spatial differences in the stencil shown in Equation 5.26 yields the WLE stencil with density-variations and discretized on a nonuniform grid becomes:

$$p_{i,j,k}^{n+1} = \frac{1}{\frac{1}{c_{i,j,k}^2}\frac{1}{\Delta t^2} - \frac{2\beta_{i,j,k}}{\rho_{0\,i,j,k}c_{i,j,k}^4}\frac{1}{\Delta t^2}p_{i,j,k}^n}$$

$$\left[\frac{2\left(p_{i+1,j,k}-p_{i,j,k}\right)}{\Delta x_{i,j,k}^2 + \frac{\rho_{i+1,j,k}\Delta x_{i+1,j,k}\Delta x_{i,j,k}}{\rho_{i,j,k}}} + \right.$$

$$+ \frac{2\left(p_{i-1,j,k}-p_{i,j,k}\right)}{\Delta x_{i,j,k}^2 + \frac{\rho_{i-1,j,k}\Delta x_{i-1,j,k}\Delta x_{i,j,k}}{\rho_{i,j,k}}} +$$

$$+ \frac{2\left(p_{i,j+1,k}-p_{i,j,k}\right)}{\Delta y_{i,j,k}^2 + \frac{\rho_{i,j+1,k}\Delta y_{i,j+1,k}\Delta y_{i,j,k}}{\rho_{i,j,k}}} +$$

$$+ \frac{2\left(p_{i,j-1,k}-p_{i,j,k}\right)}{\Delta y_{i,j,k}^2 + \frac{\rho_{i,j-1,k}\Delta y_{i,j-1,k}\Delta y_{i,j,k}}{\rho_{i,j,k}}} +$$

$$+ \frac{2\left(p_{i,j,k+1}-p_{i,j,k}\right)}{\Delta z_{i,j,k}^2 + \frac{\rho_{i,j,k+1}\Delta z_{i,j,k+1}\Delta z_{i,j,k}}{\rho_{i,j,k}}} +$$

$$+ \frac{2\left(p_{i,j,k-1}-p_{i,j,k}\right)}{\Delta z_{i,j,k}^2 + \frac{\rho_{i,j,k-1}\Delta z_{i,j,k-1}\Delta z_{i,j,k}}{\rho_{i,j,k}}} +$$

$$+ \frac{1}{c_{i,j,k}^2}\frac{1}{\Delta t^2}\left(2p_{i,j,k}^n - p_{i,j,k}^{n-1}\right) +$$

$$+ \frac{\delta_{i,j,k}}{c_{i,j,k}^4}\frac{1}{8\Delta t^3}\left(6p_{i,j,k}^n - 23p_{i,j,k}^{n-1} + 34p_{i,j,k}^{n-2} - 24p_{i,j,k}^{n-3} + 8p_{i,j,k}^{n-4} - p_{i,j,k}^{n-5}\right) -$$

$$\left. - \frac{2\beta_{i,j,k}}{\rho_{0\,i,j,k}c_{i,j,k}^4\Delta t^2}\left(p_{i,j,k}^n p_{i,j,k}^n + p_{i,j,k}^n p_{i,j,k}^{n-1} - p_{i,j,k}^{n-1}p_{i,j,k}^{n-1}\right)\right]$$

$$(5.27)$$

where $\beta_{i,j,k}$ and $\delta_{i,j,k}$ can be calculated through Equations 5.24 and 5.25 respectively.

## 5.3 Absorbing Boundary Conditions

Typical domains simulated with the FDTD method can be roughly classified into *closed domains*, *open domains*, or a combination of the two. A closed computational domain,

commonly termed as *bounded domain*, is one where all its boundaries have been mathematically defined, e.g., by enforcing a fixed value with the use of *boundary conditions*. In contrast to such cases, open domains, which are often referred to *unbounded domains*, i.e., domains where the boundaries would normally be expected to stretch infinitely, cannot be mathematically prescribed. However, as it is not computationally feasible to model infinitely extending spaces, it becomes necessary to apply a form of *domain truncation*. This is commonly achieved by enforcing an *absorbing boundary condition* (ABC) on each of the domain boundaries. ABCs allow for the numerical absorption of propagating waves in order to create the 'illusion' of an infinitely extending boundary.

The two most prominent types of ABCs that have been utilized in FDTD simulations are *analytical ABCs* and the *perfectly matched layer* (PML), which are detailed in [315, Ch. 6] and [315, Ch. 7] respectively. While analytical ABCs are typically easy to implement and require limited computational resources, they do not provide highly accurate solutions, resulting in reflections at the domain boundaries, and thus erroneous results. PML on the other hand are highly effective ABCs, and even though their computational requirements far outweigh those of analytical ABCs, the increase in computational power over the past 20 years has designated them as the norm in artificial truncation of computational domains. The most commonly employed analytical ABCs are the *Mur ABCs* which are presented in Section 5.3.1, while other prevalent formulations, e.g., the Bayliss-Turkel radiation operators, the Higdon operators, and the Liao ABCs are discussed in [315, Ch. 6]. The formulation of the PML ABCs that was implemented for the purposes of this work is presented in detail in Section 5.3.2, while [315, Ch. 7], [475] offer an extensive review on alternative formulations.

## 5.3.1   Mur Absorbing Boundary Conditions

[315, §**6.3**], [476]

The *Mur absorbing boundary conditions* (Mur ABCs), were first introduced in 1981 by Mur [476]. Mur used the *Enqguist-Majda one-way wave equation* [477], a PDE that permits wave propagation only in certain directions in order to derive a finite-difference numerical scheme which, when applied on the boundary of a computational domain numerically absorbs outgoing waves. Depending on whether one or two Taylor terms are used to derive a numerical approximation of the Enqguist-Majda PDE, the resulting finite-difference ABCs are characterized as *first-order* and *second-order* Mur ABCs respectively.

### 5.3.1.1   Model

[315, §6.3], [476]

An implementation of the first-order Mur ABCs was implemented during this work but was quickly replaced by the PML formulation discussed in Section 5.3.2 to improve the quality of domain truncation. Therefore, the derivation of the Mur PDEs and their respective stencils, which have been well established and can be found in [315, §6.3], will not be repeated here for the sake of brevity. However, the final stencils that were implemented during the course of this work, and which can be used in conjunction with any of the stencils presented in Section 5.2, are repeated below for the six boundaries of a FDTD domain:

$$\text{boundary } x = 0 \quad : \quad p_{0,j,k}^{n+1} = p_{1,j,k}^{n} + \frac{c_{0,j,k}\Delta t - \Delta x}{c_{0,j,k}\Delta t + \Delta x}\left(p_{1,j,k}^{n+1} - p_{0,j,k}^{n}\right)$$

$$\text{boundary } x = h \quad : \quad p_{h,j,k}^{n+1} = p_{h-1,j,k}^{n} + \frac{c_{h,j,k}\Delta t - \Delta x}{c_{h,j,k}\Delta t + \Delta x}\left(p_{h-1,j,k}^{n+1} - p_{h,j,k}^{n}\right)$$

$$\text{boundary } y = 0 \quad : \quad p_{i,0,k}^{n+1} = p_{i,1,k}^{n} + \frac{c_{i,0,k}\Delta t - \Delta y}{c_{i,0,k}\Delta t + \Delta y}\left(p_{i,1,k}^{n+1} - p_{i,0,k}^{n}\right)$$

$$\text{boundary } y = w \quad : \quad p_{i,v,k}^{n+1} = p_{i,v-1,k}^{n} + \frac{c_{i,v,k}\Delta t - \Delta y}{c_{i,v,k}\Delta t + \Delta y}\left(p_{i,v-1,k}^{n+1} - p_{i,v,k}^{n}\right)$$

$$\text{boundary } z = 0 \quad : \quad p_{i,j,0}^{n+1} = p_{i,j,1}^{n} + \frac{c_{i,j,0}\Delta t - \Delta z}{c_{i,j,0}\Delta t + \Delta z}\left(p_{i,j,1}^{n+1} - p_{i,j,0}^{n}\right)$$

$$\text{boundary } z = v \quad : \quad p_{i,j,w}^{n+1} = p_{i,j,w-1}^{n} + \frac{c_{i,j,w}\Delta t - \Delta z}{c_{i,j,w}\Delta t + \Delta z}\left(p_{i,j,w-1}^{n+1} - p_{i,j,w}^{n}\right)$$

where the domain is assumed to lie within $x = 0 \div h$, $y = 0 \div w$ and $z = 0 \div v$ (see Section 6.1.2) and $c$ is the speed of sound at the different boundary voxels.

## 5.3.2   Perfectly Matched Layer

[475, 478, 479]

The most salient approach to truncating computational domains, applied but not limited to FDTD implementations, is currently the *perfectly matched layer* (PML), first introduced into electrodynamics by Berenger [480]. Unlike analytical ABCs, such as the case of Mur ABCs presented in Section 5.3.1, Berenger suggested that multiple layers of an artificial absorbing material be placed adjacent to the boundaries of the computational grid. The entire computational domain is then surrounded by a perfectly reflecting boundary (a 3D depiction of this setup is shown in Section 6.1.2). This artificial material is 'matched' to the material with which it was in contact to avoid reflections at their interfaces (see Section 1.1.3.2). Thus, the outgoing waves would enter this material where they would

attenuate and decay exponentially, and even though they would eventually reflect off the boundary, the returning wave would be negligibly small. Detailed analysis of the PML concept and implementation can be found in [315, Ch.7], [475].

Even though PML was originally formulated for electrodynamics, this approach can easily be tailored to the case of acoustics. The derivation of the appropriate equations in the case of the LAPWE PDE, which can be found in [478], [481, p. 68], is repeated in the following section.

### 5.3.2.1 Model
[315, Ch.7], [481, pp.67-70], [475, 478, 479]

The PML approach implemented for the purposes of this work was applied on the original LAPWE PDE (see Equation 4.9) and was based on the stretched-coordinate approach proposed by Chew and Weedon [482]. The LAPWE PDE is repeated below for the sake of convenience:

$$\nabla^2 p - \frac{1}{c^2} \frac{\partial^2 p}{\partial t^2} = 0$$

where $c$ is the speed of sound of the material the absorbing layers are matched against. By using the stretched coordinate approach, the time-harmonic Equation 5.3.2.1 in the complex-coordinate stretched space is expressed as:

$$\widetilde{\nabla}_s^2 \widetilde{p} - \frac{1}{c^2} \left(j\omega\right)^2 \widetilde{p} = 0 \tag{5.28}$$

with

$$\widetilde{\nabla}_s = \frac{1}{s_x} \frac{\partial}{\partial x} + \frac{1}{s_y} \frac{\partial}{\partial y} + \frac{1}{s_z} \frac{\partial}{\partial z} \tag{5.29}$$

where $s_x$, $s_y$, and $s_z$ are the stretched coordinates in the x, y, and z directions respectively. Using Equation 5.29, the term $\widetilde{\nabla}_s$ in Equation 5.28 can be substituted, resulting in the following equation:

$$\frac{1}{s_x} \frac{\partial}{\partial x} \left( \frac{1}{s_x} \frac{\partial}{\partial x} \widetilde{p} \right) + \frac{1}{s_y} \frac{\partial}{\partial y} \left( \frac{1}{s_y} \frac{\partial}{\partial y} \widetilde{p} \right) + \frac{1}{s_z} \frac{\partial}{\partial z} \left( \frac{1}{s_z} \frac{\partial}{\partial z} \widetilde{p} \right) - \frac{1}{c^2} \left(j\omega\right)^2 \widetilde{p} = 0 \tag{5.30}$$

Equation 5.30 can then be rewritten with the aid of two auxiliary variables, $D_1'$ and $D_2'$, introduced on each of the three axes as such:

$$j\omega \, \widetilde{D}'_{x_1} \;\; = \;\; \frac{1}{s_x}\frac{\partial}{\partial x}\,\widetilde{p} \tag{5.31}$$

$$j\omega \, \widetilde{D}'_{x_2} \;\; = \;\; \frac{1}{s_x}\frac{\partial}{\partial x}\left(j\omega\,\widetilde{D}'_{x_1}\right) = \frac{1}{s_x}\frac{\partial}{\partial x}\left(\frac{1}{s_x}\frac{\partial}{\partial x}\,\widetilde{p}\right) \tag{5.32}$$

$$j\omega \, \widetilde{D}'_{y_1} \;\; = \;\; \frac{1}{s_y}\frac{\partial}{\partial y}\,\widetilde{p} \tag{5.33}$$

$$j\omega \, \widetilde{D}'_{y_2} \;\; = \;\; \frac{1}{s_y}\frac{\partial}{\partial y}\left(j\omega\,\widetilde{D}'_{y_1}\right) = \frac{1}{s_y}\frac{\partial}{\partial y}\left(\frac{1}{s_y}\frac{\partial}{\partial y}\,\widetilde{p}\right) \tag{5.34}$$

$$j\omega \, \widetilde{D}'_{z_1} \;\; = \;\; \frac{1}{s_z}\frac{\partial}{\partial z}\,\widetilde{p} \tag{5.35}$$

$$j\omega \, \widetilde{D}'_{z_2} \;\; = \;\; \frac{1}{s_z}\frac{\partial}{\partial z}\left(j\omega\,\widetilde{D}'_{z_1}\right) = \frac{1}{s_z}\frac{\partial}{\partial z}\left(\frac{1}{s_z}\frac{\partial}{\partial z}\,\widetilde{p}\right) \tag{5.36}$$

Replacing the partial derivatives in Equation 5.30 with Equations 5.31–5.36, results in:

$$j\omega \, \widetilde{D}'_{x_2} + j\omega \, \widetilde{D}'_{y_2} + j\omega \, \widetilde{D}'_{z_2} - \frac{1}{c^2}\left(j\omega\right)^2\widetilde{p} = 0 \tag{5.37}$$

Depending on the direction of wave propagation, the stretched-coordinates are designated a value of either $1$, denoting absence of propagation in that direction, or $1+\sigma/j\omega$, denoting propagation, with $\sigma$ being the value of the conductivity profile in the PML region. Thus, in a rectangularly shaped computational domain, the above rationale yields 26 distinct PML sub-domains (6 faces, 12 edges and 8 corners) with 7 different equations (3 equations for the X, Y and Z PML faces, 3 equations for the XY, XZ and YZ PML edges and 1 equation for all PML corners). This is depicted in Figure 5.7.

Equation 5.37 must be solved for each one of the PML domains, but in the interest of notational simplicity the derivation will be restricted to the case of the 'Z Face', where $s_x = 1$, $s_y = 1$ and $s_z = 1 + \sigma_z/j\omega$. Thereby, converting back to the time domain, Equation 5.37 becomes:
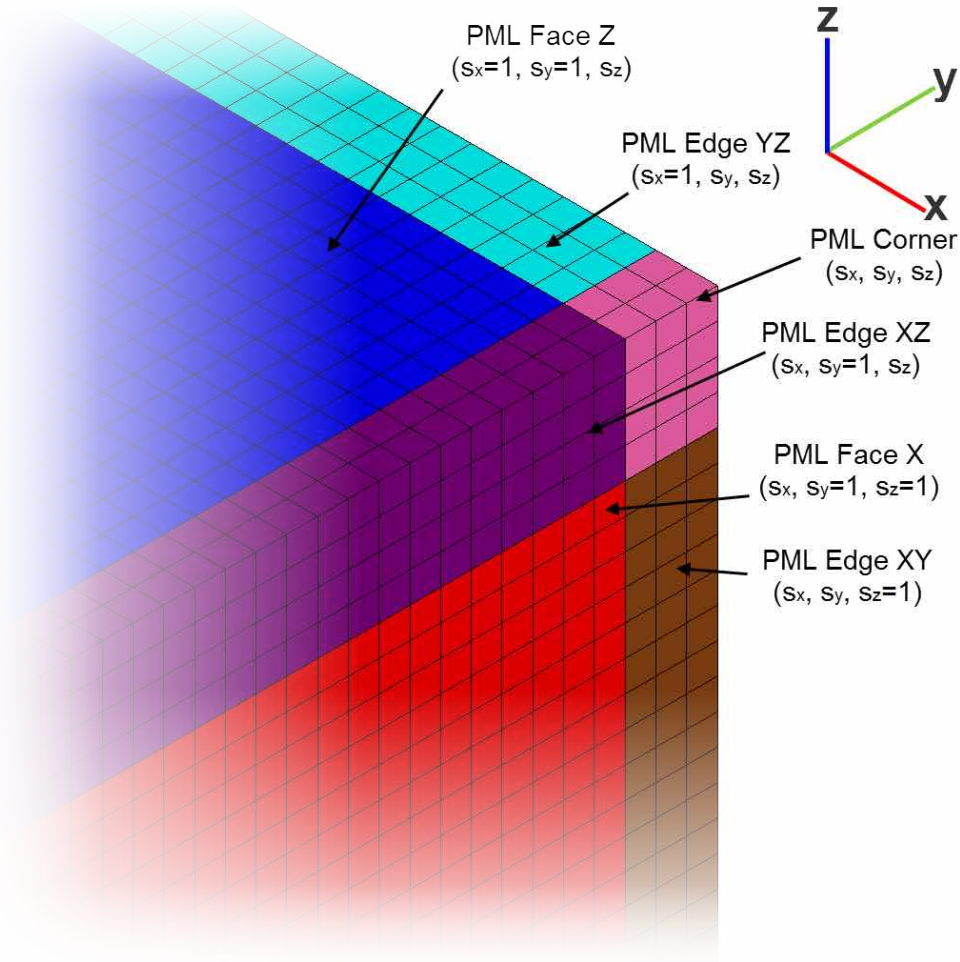
**Figure 5.7**: *Depiction of a subset of the PML regions surrounding the computational domain and the respective values of the stretched-coordinates for the different PML domains.*

$$\frac{\partial^2 p}{\partial x^2} + \frac{\partial^2 p}{\partial y^2} + \frac{\partial^2 D'_{z_2}}{\partial t} - \frac{1}{c^2}\frac{\partial^2 p}{\partial t^2} = 0 \tag{5.38}$$

while the auxiliary variables in Equations 5.35 and 5.36 yield:

$$\begin{aligned}
\frac{\partial D'_{z_1}}{\partial t} + \sigma_z D'_{z_1} &= \frac{\partial p}{\partial t} \\
\frac{\partial D'_{z_2}}{\partial t} + \sigma_z D'_{z_2} &= \frac{\partial^2 D'_{z_1}}{\partial z \partial t}
\end{aligned}$$

Before discretizing the above equations with central finite-differences, in a manner akin to the discretization of the LAPWE and WLE PDEs as shown in Section 5.2, the place-

ment of the auxiliary variables on the computational grid in relation to the pressure field warrants elucidation. Both $D'_1$ and $D'_2$ are regarded as two field components without any physical meaning and are only manifested within the PML sub-domains surrounding the main domain. $D'_2$ is located at the same location in the grid as the pressure variable $p$, i.e., the center of each cell in the computational domain, as was shown in Figure 5.3. The auxiliary variable $D'_1$, however, is located half a grid cell away, on the edges of each grid cell along the direction of propagation (in this case the $z$ direction). The above is depicted in Figure 5.8.
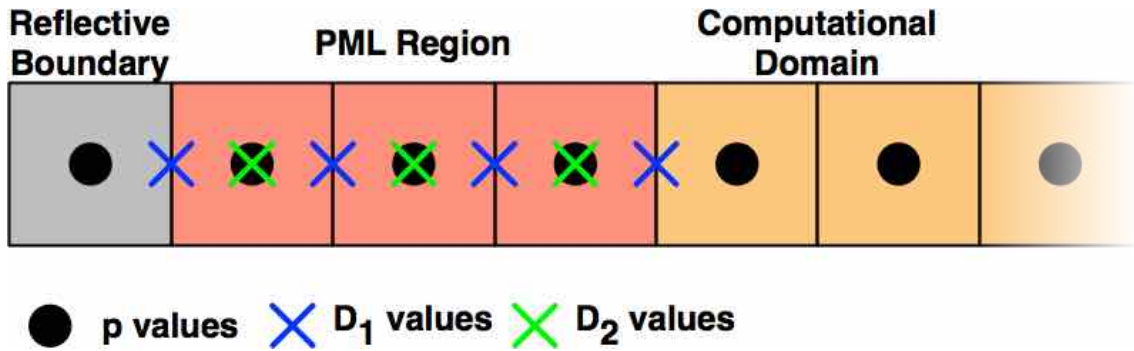


**Figure 5.8**: *Depiction of the computational grid within the PML sub-domains for propagation along the $z$ axis. The auxiliary variables $D'_1$ and $D'_2$ are only manifested within the PML sub-domains, with $D'_1$ being placed on the edges of the grid cells half a grid cell away from the pressure $p$ values. The auxiliary variable $D'_2$, however, is located at the same locations as the $p$ values, i.e., the centers of each grid cell.*

Following the derivation presented in [478], the auxiliary variables are normalized as follows:

$$D'_{z_1} = \frac{\Delta t}{\Delta z} D_{z_1} \quad , \quad D'_{z_2} = \frac{\Delta t}{\Delta z^2} D_{z_2} \tag{5.39}$$

Thus, employing central finite-differences, the discretization of the normalized auxiliary variables $D_{z_1}$ is shown below:

$$\frac{\partial D'_{z_1}}{\partial t} + \sigma_z D'_{z_1} = \frac{\partial p}{\partial t} \Rightarrow \frac{\partial}{\partial t}\left(\frac{\Delta t}{\Delta z}D_{z_1}\right) + \sigma_z \frac{\Delta t}{\Delta t}D_{z_1} = \frac{\partial p}{\partial z} \Rightarrow$$

$$\Rightarrow \frac{\Delta t}{\Delta z}\frac{\partial}{\partial t}D_{z_1} + \frac{\Delta t}{\Delta z}\sigma_z D_{z_1} = \frac{\partial p}{\partial z} \Rightarrow$$

$$\Rightarrow \frac{\Delta t}{\Delta z}\frac{D_{z_1}|_{i,j,k+1/2}^{n+1/2} - D_{z_1}|_{i,j,k+1/2}^{n-1/2}}{\Delta t} +$$

$$+\sigma_z\frac{\Delta t}{\Delta z}\frac{D_{z_1}|_{i,j,k+1/2}^{n+1/2} + D_{z_1}|_{i,j,k+1/2}^{n-1/2}}{\Delta t} = \frac{p_{i,j,k+1}^n - p_{i,j,k}^n}{\Delta z} \cdot \frac{\Delta z}{\Delta t} \Rightarrow$$

$$\Rightarrow \frac{D_{z_1}|_{i,j,k+1/2}^{n+1/2} - D_{z_1}|_{i,j,k+1/2}^{n-1/2}}{\Delta t} +$$

$$+\sigma_z\frac{D_{z_1}|_{i,j,k+1/2}^{n+1/2} + D_{z_1}|_{i,j,k+1/2}^{n-1/2}}{2} = \frac{p_{i,j,k+1}^n - p_{i,j,k}^n}{\Delta t} \Rightarrow$$

$$\Rightarrow D_{z_1}|_{i,j,k+1/2}^{n+1/2}\left(1 + \sigma_z\Delta t/2\right) - D_{z_1}|_{i,j,k+1/2}^{n-1/2}\left(1 - \sigma_z\Delta t/2\right) =$$

$$= p_{i,j,k+1}^n - p_{i,j,k}^n$$

which yields the discretized equation:

$$D_{z_1}|_{i,j,k+1/2}^{n+1/2} =$$

$$= \frac{1 - \sigma_z\Delta t/2}{1 + \sigma_z\Delta t/2}\, D_{z_1}|_{i,j,k+1/2}^{n-1/2} + \frac{1}{1 + \sigma_z\Delta t/2}\left(p_{i,j,k+1}^n - p_{i,j,k}^n\right) \qquad (5.40)$$

Similarly to the case of $D_{z_1}$, the discretization of $D_{z_2}$ is shown below:

$$\frac{\partial D'_{z_2}}{\partial t} + \sigma_z D'_{z_2} = \frac{\partial^2 D'_{z_1}}{\partial z \partial t} \Rightarrow$$

$$\Rightarrow \frac{\Delta t}{\Delta z^2}\frac{\partial D_{z_2}}{\partial t} + \sigma_z\frac{\Delta t}{\Delta z^2}D_{z_2} = \frac{\Delta t}{\Delta z}\frac{\partial^2 D_{z_1}}{\partial z \partial t} \Rightarrow$$

$$\Rightarrow \frac{\Delta t}{\Delta z^2}\frac{\partial D_{z_2}}{\partial t} + \sigma_z\frac{\Delta t}{\Delta z^2}D_{z_2} = \frac{\Delta t}{\Delta z}\frac{\partial}{\partial z}\left(\frac{\partial D_{z_1}}{\partial t}\right)$$

The term $\frac{\partial}{\partial z}\left(\frac{\partial D_{z_1}}{\partial t}\right)$ in the above equation is discretized separately here to simplify the notation:

$$\frac{\partial}{\partial z}\left(\frac{\partial D_{z_1}}{\partial t}\right) = \frac{\partial}{\partial z}\left(\frac{D_{z_1}\big|_{i,j,k+1/2}^{n+1/2} - D_{z_1}\big|_{i,j,k+1/2}^{n-1/2}}{\Delta t}\right) =$$

$$= \frac{\frac{D_{z_1}\big|_{i,j,k+1/2}^{n+1/2} - D_{z_1}\big|_{i,j,k+1/2}^{n-1/2}}{\Delta t} - \frac{D_{z_1}\big|_{i,j,k-1/2}^{n+1/2} - D_{z_1}\big|_{i,j,k-1/2}^{n-1/2}}{\Delta t}}{\Delta z} =$$

$$= \frac{D_{z_1}\big|_{i,j,k+1/2}^{n+1/2} - D_{z_1}\big|_{i,j,k+1/2}^{n-1/2} - D_{z_1}\big|_{i,j,k-1/2}^{n+1/2} + D_{z_1}\big|_{i,j,k-1/2}^{n-1/2}}{\Delta z \Delta t}$$

which when replaced in the previous equation yields:

$$\frac{\Delta t}{\Delta z^2}\frac{D_{z_2}\big|_{i,j,k}^{n+1/2} - D_{z_2}\big|_{i,j,k}^{n-1/2}}{\Delta t} + \sigma_z\frac{\Delta t}{\Delta z^2}\frac{D_{z_2}\big|_{i,j,k}^{n+1/2} + D_{z_2}\big|_{i,j,k}^{n-1/2}}{2} =$$

$$= \frac{\Delta t}{\Delta z}\frac{D_{z_1}\big|_{i,j,k+1/2}^{n+1/2} - D_{z_1}\big|_{i,j,k+1/2}^{n-1/2} - D_{z_1}\big|_{i,j,k-1/2}^{n+1/2} + D_{z_1}\big|_{i,j,k-1/2}^{n-1/2}}{\Delta z \Delta t} \cdot \frac{\Delta z^2}{\frac{\Delta t}{}}\overset{\Rightarrow}{}$$

$$\Rightarrow \frac{D_{z_2}\big|_{i,j,k}^{n+1/2} - D_{z_2}\big|_{i,j,k}^{n-1/2}}{\Delta t} + \sigma_z\frac{D_{z_2}\big|_{i,j,k}^{n+1/2} + D_{z_2}\big|_{i,j,k}^{n-1/2}}{2} =$$

$$= \frac{D_{z_1}\big|_{i,j,k+1/2}^{n+1/2} - D_{z_1}\big|_{i,j,k+1/2}^{n-1/2} - D_{z_1}\big|_{i,j,k-1/2}^{n+1/2} + D_{z_1}\big|_{i,j,k-1/2}^{n-1/2}}{\Delta t}$$

and results in the following discretized equation:

$$D_{z_2}\big|_{i,j,k}^{n+1/2} = \frac{1 - \sigma_z\Delta t/2}{1 + \sigma_z\Delta t/2}\,D_{z_2}\big|_{i,j,k}^{n-1/2} +$$

$$+ \frac{1}{1 + \sigma_z\Delta t/2}\left(D_{z_1}\big|_{i,j,k+1/2}^{n+1/2} - D_{z_1}\big|_{i,j,k+1/2}^{n-1/2} -\right.$$

$$\left. - D_{z_1}\big|_{i,j,k-1/2}^{n+1/2} + D_{z_1}\big|_{i,j,k-1/2}^{n-1/2}\right)$$

$$(5.41)$$

Lastly, based on Equation 5.38 the discretization of the wave equation is as follows:

$$\frac{\partial^2 p}{\partial x^2} + \frac{\partial^2 p}{\partial y^2} + \frac{\partial^2 D'_{z_2}}{\partial t} - \frac{1}{c^2}\frac{\partial^2 p}{\partial t^2} = 0 \Rightarrow$$

$$\Rightarrow \frac{\partial^2 p}{\partial x^2} + \frac{\partial^2 p}{\partial y^2} + \frac{\Delta t}{\Delta z^2}\frac{\partial^2 D_{z_2}}{\partial t} - \frac{1}{c^2}\frac{\partial^2 p}{\partial t^2} = 0 \Rightarrow$$

$$\Rightarrow \frac{p^n_{i+1,j,k} - 2p^n_{i,j,k} + p^n_{i-1,j,k}}{\Delta x^2} + \frac{p^n_{i,j+1,k} - 2p^n_{i,j,k} + p^n_{i,j-1,k}}{\Delta y^2} +$$

$$+\frac{\Delta t}{\Delta z^2}\frac{D_{z_2}|^{n+1/2}_{i,j,k} - D_{z_2}|^{n-1/2}_{i,j,k}}{\Delta t} - \frac{1}{c^2}\frac{p^{n+1}_{i,j,k} - 2p^n_{i,j,k} + p^{n-1}_{i,j,k}}{\Delta t^2} = 0 \Rightarrow$$

$$\Rightarrow p^{n+1}_{i,j,k} - 2p^n_{i,j,k} + p^{n-1}_{i,j,k} =$$

$$= \frac{c^2\Delta t^2}{\Delta x^2}\left(p^n_{i+1,j,k} - 2p^n_{i,j,k} + p^n_{i-1,j,k}\right) +$$

$$+\frac{c^2\Delta t^2}{\Delta y^2}\left(p^n_{i,j+1,k} - 2p^n_{i,j,k} + p^n_{i,j-1,k}\right) +$$

$$+\frac{c^2\Delta t^2}{\Delta z^2}\left(D_{z_2}|^{n+1/2}_{i,j,k} - D_{z_2}|^{n-1/2}_{i,j,k}\right)$$

which finally yields the discretized equation:

$$
\begin{aligned}
p^n_{i+1,j,k} &= \\
&= 2p^n_{i,j,k} + p^{n-1}_{i,j,k} + \\
&+ \frac{c^2\Delta t^2}{\Delta x^2}\left(p^n_{i+1,j,k} - 2p^n_{i,j,k} + p^n_{i-1,j,k}\right) + \\
&+ \frac{c^2\Delta t^2}{\Delta y^2}\left(p^n_{i,j+1,k} - 2p^n_{i,j,k} + p^n_{i,j-1,k}\right) + \\
&+ \frac{c^2\Delta t^2}{\Delta z^2}\left(D_{z_2}|^{n+1/2}_{i,j,k} - D_{z_2}|^{n-1/2}_{i,j,k}\right)
\end{aligned}
\tag{5.42}
$$

Therefore, applying the PML boundary conditions on the Z face of the PML regions requires implementation of Equations 5.40, 5.41, and 5.42. The equations for the remaining PML subdomains can easily be derived by following the procedure shown above.

Lastly, the values of $\sigma_z$, i.e., the conductivity profile, can be calculated with the following equation [481, p. 70], [478]:

$$\sigma_z(z) = -\left(\frac{z}{d}\right)^m \frac{c\,(m+1)\,ln(R_0)}{2d} \tag{5.43}$$

where $d$ is the thickness of the PML, $m$ is the order of the PML, and $R_0$ is the reflection from the PML at normal incidence. Based on the parameter optimization study presented

in [478], these last two parameters were set to $m = 4$ and $R_0 = 10^{-2}$. Parameter $z$ is the distance of the currently calculated auxiliary variable (on the grid) from the edge of the PML. This parameter takes different values for $D_1$ and $D_2$ due to their placement on the computational grid (see Figure 5.8).

It should be mentioned that the PML formulation presented above can be applied to the FDTD implementation of any scalar pressure wave PDE, including any of the LAPWE and WLE discretized equations presented in Section 5.2.

# 6

# Implementation

The implementation details of the acoustic solvers that were developed for the purposes of this work are detailed in this chapter. Prototypes of the acoustic solvers were initially developed in Matlab in order to perform some conceptual simulations and ascertain their efficacy. However, the final solvers, which have been utilized for the various applications presented in this thesis, were developed in C++ in the Microsoft Visual Studio 2008 and the VC9 compiler, and were later on migrated to Visual Studio 2010 and VC10 compiler respectively. The GPU-accelerated solvers were initially developed on NVIDIA CUDA v3.2 but have been now ported to CUDA v5.0.

The core concepts and philosophy behind the implementation of these solvers are presented (Section 6.1) and are followed by the parallelization concepts and techniques used to speed up execution, including benchmarking results (Section 6.2). Lastly, the integration of these solvers into the 'in-house' simulation framework, their coupling to other solvers, and critical aspects of the framework that allowed for simulations of therapeutic FUS applications are discussed (Section 6.3).

## 6.1 Core Development Concepts

### 6.1.1 Development Philosophy

During the process of this work, the entire development was guided by two often conflicting objectives, being *maximum execution speed* and *minimum memory requirements*. The former objective aimed at providing the fastest possible execution of extremely large computational domains, often comprising $10^7 - 10^9$ grid cells. The second objective was to utilize the minimum amount of *random access memory* (RAM), in order to allow for such simulations to be performed on commonly available hardware.

Since the ultimate purpose of the developed acoustic solvers was their eventual integration and use in a clinical environment, both of the above objectives were well-justified. The

ability to perform realistic simulations in viable time-frames is a necessity for the clinical environment. At the same time it should be possible to do so without the need for large cluster-level hardware, which is not available outside large research institutes or multinational organizations, and requires vast resources to purchase, setup, and maintain.

However, these two objectives often conflict with each other. In many cases a compromise between speed and memory requirements had to be reached, e.g., in the case of per-voxel constants, which could either be pre-calculated and stored in memory to reduce the simulation time but increase the memory requirements, or vice-versa. Therefore, it was often required to prioritize and opt for one of the two objectives. The solvers developed for the purposes of this thesis, give higher priority to the 'minimum memory requirements' objective, in order to extend the range of hardware on which these simulations would be feasible. Nonetheless, the code was hand-optimized and the usage of modern programming frameworks and libraries was limited to the non-computationally-intensive modules during development in order to achieve the maximum feasible execution speed. In addition, as will be shown in Section 6.2, significant effort was placed into efficiently parallelizing the developed solvers to further increase the computational speed.

## 6.1.2   Computational Domain

During the development of the ultrasonic solvers presented in this thesis, the computational domain was assumed to consist of a *main domain*, the surrounding *PML sub-domains*, and the *reflective acoustic boundary* (RAB) layer which in turn surrounds the PML sub-domains. A depiction of the entire computational domain, wherein each domain is incrementally added to demonstrate its position, can be seen in Figure 6.2. In addition, Figure 6.3 shows three cross-sections through the center of the computational domain, perpendicularly to each of the three cartesian axes.

As described in Section 5.1.1, when employing the FDTD method each 3D model to be simulated needs to initially undergo geometrical discretization, through gridding and voxeling. This process, which is graphically depicted in Figure 5.2, results in a set of voxels, each of which consists of a single material. This voxeled model comprises the main domain of the computational domain.

For the purposes of this work, the artificial truncation of the computational domain was achieved through an implementation of the PML scheme, which was detailed in Section 5.3.2. As discussed in the aforementioned section, the PML consists of 26 individual sub-domains, including 6 PML faces, 12 PML edges, and 8 PML corners, which entirely surround the main domain. Each PML domain may exhibit a different thickness along each direction. Lastly, the PML domains need to be terminated with a RAB layer, which has a thickness of a single voxel and surrounds all PML sub-domains.

Given the large number of PML sub-domains, the following notation was used to define which sub-domain is discussed at any time. The entire computational domain lies parallel

to the X, Y and Z axes of the cartesian system. One corner of the rectangular computational domain coincides with the cartesian origin with indices $(0, 0, 0)$, while the opposite corner lies on a point with indices $(h, w, v)$, this can be seen in Figure 6.1. Thus, the name of each PML sub-domain was defined according to which of the aforementioned points it was adjacent to, as well as its type, i.e., face, edge or corner, and its location, e.g., 'PML Edge X0Yw' or 'PML Corner XhY0Zv'.
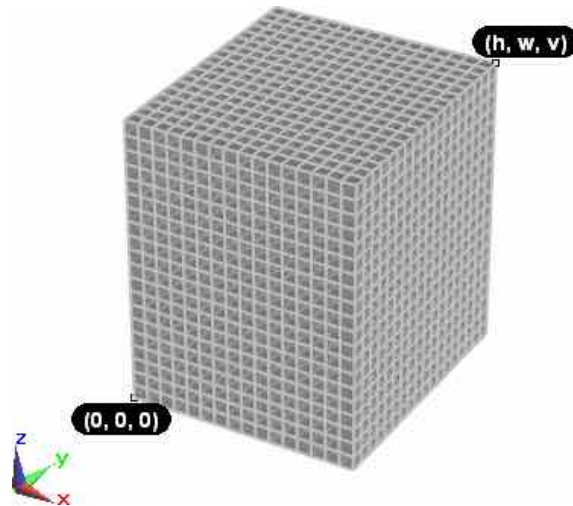


**Figure 6.1**: *Positioning of the computational domain on the cartesian coordinates system.*

## 6.1.3  Material handling

As discussed in Section 5.1.1, the FDTD method requires each voxel of the computational domain to consist of a single material with its own set of acoustic properties, e.g., speed of sound $c$, density $\rho$, etc. However, in accordance with the 'minimum memory requirements' philosophy mentioned in Section 6.1.1, and given the nature of the simulated setups these solvers were developed for, a different approach was chosen during development.

Following the voxeling of a given simulation setup, every voxel of the computational domain was linked to a material through an index. Each material contains all acoustic properties necessary to perform simulations using the LAPWE and WLE stencils presented in Section 5.2. As the total number of materials within such a simulation is relatively small when compared to the number of voxels (e.g., a setup involving a full-body anatomical model and a transducer array will comprise only a few hundred materials, while its computational domain will consist of hundreds of millions of voxels), this approach minimizes the computer memory required for the simulation.

As can be seen from the derived stencils shown in Section 5.2, the actual computation rarely involves the independent acoustic properties of the different materials, but rather
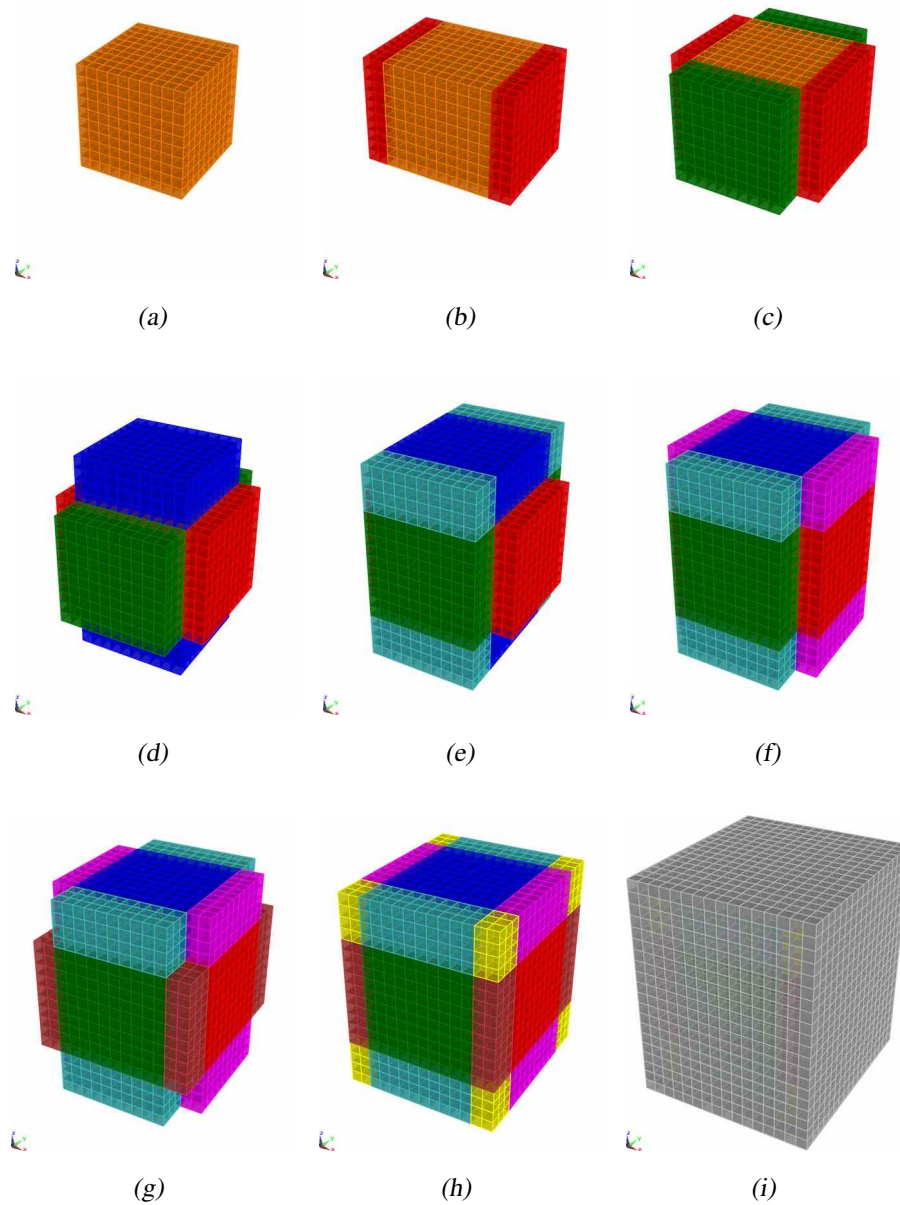
*Figure 6.2*: Depiction of the computational domain concept. *(a)* shows the main domain, i.e., the voxeled simulation model. Each subsequent figure shows an additional PML sub-domain to demonstrate their position in relation to the main domain and other PML sub-domains. *(b)* PML Faces X, *(c)* PML Faces Y, *(d)* PML Faces Z, *(e)* PML Edges YZ, *(f)* PML Edges XZ, *(g)* PML Edges XY, *(h)* PML Corners. *(i)* adds the RAB around all PML sub-domains and shows the complete computational domain.
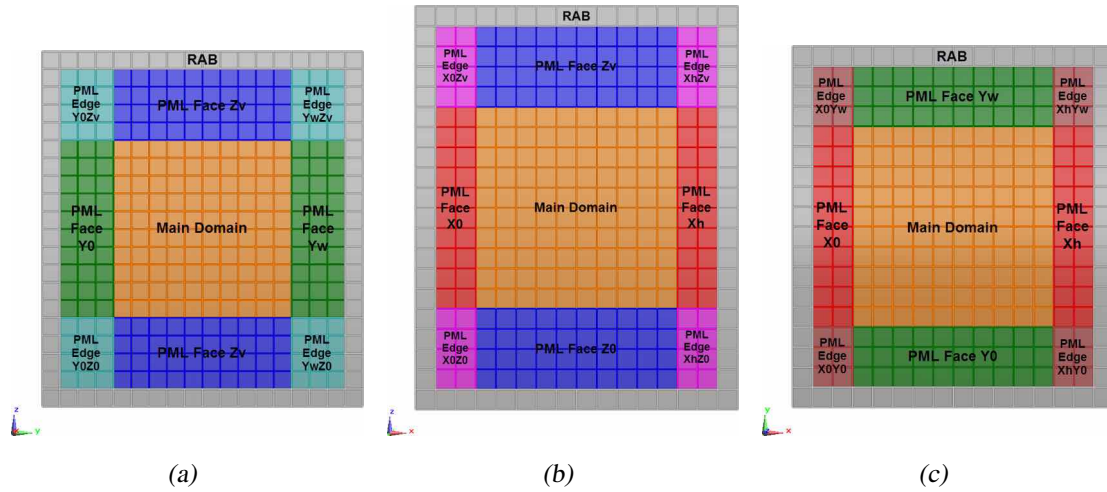
**Figure 6.3**: *Cross-sections through the center of the computational domain, perpendicular to each of the three cartesian axes.* (a) *shows an X cross-section (perpendicular to the X axis), while* (b) *and* (c) *show a Y and Z slice respectively.*

requires composite terms that remain constant for each material. Thus, in the interest of 'maximum execution speed' these parameters were precalculated for the different stencils and stored on a per-material basis, thus achieving both minimal computational overhead and memory requirements.

## 6.1.4   Source Modeling

As discussed in Section 4.2.1, the LAPWE and WLE PDEs do not account for the presence of acoustic energy sources within the computational domain. While it is possible to modify these equations and include the so-called 'source-terms' (see Section 4.2.1.3), such modifications result in additional variables that need to be discretized over the computational domain, resulting in larger computational requirements.

Within the scope of this work, the numerical modeling of ultrasonic sources, i.e., transducers and arrays, was based on the Huygen's principle outlined in Section 1.1.1. As with any geometries simulated with the FDTD method, the ultrasonic source undergoes gridding and voxeling, as was described in Section 5.1.1. Consequently, each piezoelectric element of the source is decomposed into a large number of *source-voxels*, which can be considered as the point-source equivalent of the FDTD method. During simulation, each of these voxel-sources generates a spherical acoustic wave with a given pressure amplitude, frequency, and phase. When these voxel-sources are driven with identical properties, their totality yields a wave equivalent to that of a nondiscretized piezoelectric element.

This discretization is shown in Figure 6.4 for the case of a single-element transducer, but this approach is entirely applicable to transducer arrays, audible acoustic sources,

e.g., speakers, and any vibrating object which causes the generation of such mechanical waves. In addition, this concept allows for advanced source-modeling capabilities, e.g., modeling sources with a nonuniform pressure distribution.



*(a)*            *(b)*
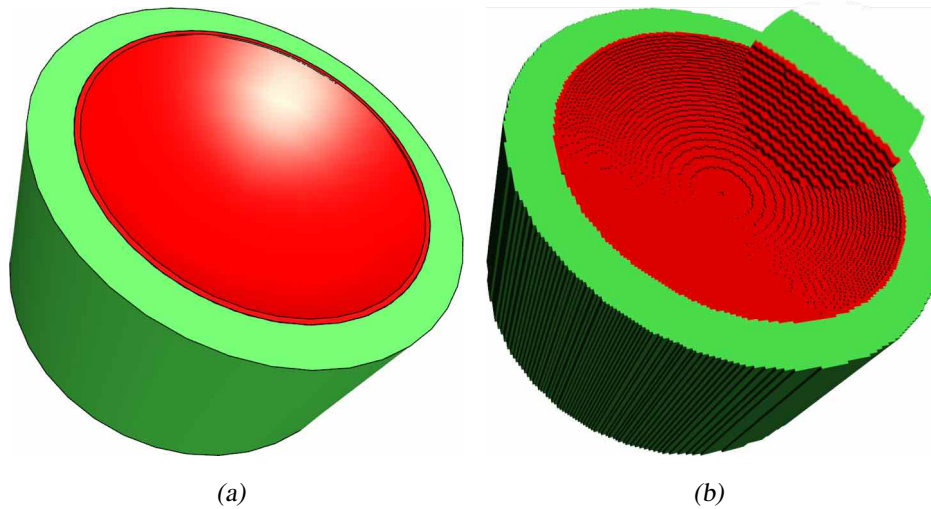
**Figure 6.4**: *A simulated single-element transducer shown both as a CAD model (a) and a discretized collection of voxels with a zoomed view of the voxels (b). The backing and housing of the transducer is shown in green while the piezoelectric element is shown in red.*

## 6.2 Parallelization

The numerical simulation of acoustic wave propagation with the FDTD method is a very computationally intense problem and requires vast computational resources, especially in the case of ultrasonic frequencies, e.g., in medical & industrial applications. Such setups typically utilize frequencies on the order of $100 - 7000$ kHz, and based on the accuracy and stability conditions of the FDTD method described in Section 5.1.3, this results in very high spatial and temporal discretization, thus requiring large amounts of computer memory and resulting in very long simulation times.

Such an example would be the case of a simulation involving the ExAblate® 4000 applicator (see Section 2.5.2.2) and an anatomical head model, as shown in Figure 5.2. As described in the aforementioned section, the applicator comprises a transducer array of $30$ cm in diameter and with $1024$ piezoelectric elements operating at a frequency of $650$ kHz. For an average speed of sound in soft-tissue (see Section 1.4) of $1500$ m/s, the resulting acoustic wavelength $\lambda$ is approximately $2.3$ mm. Thus, as per the accuracy and stability limits defined in Section 5.1.3, such a computational domain with a volume of approximately $30 \times 30 \times 30$ cm would require at least $2.2$ billion cells, resulting in over

30 gigabytes of memory (assuming 3 pressure arrays – for the temporal update – and one voxel array amounting to 14 bytes/voxel for a single-precision simulation).

Therefore, efficient parallelization of the implemented solvers was mandatory to permit for simulations of therapeutic ultrasound setups to be performed within viable timeframes. Fortunately, the FDTD method is inherently amenable to parallelization as the variables within every cell of the computational domain can be calculated concurrently. The ultrasound solvers implemented during the course of this work were parallelized on both multi-core CPU systems using OpenMP (see Section 6.2.1), and GPU systems using CUDA (see Section 6.2.2), in order to harness the computational power offered by modern hardware without requiring large, expensive clusters. A conceptual presentation of the parallelization approaches followed in this work, as well as benchmarking results of the different solvers will be presented in the following sections.

## 6.2.1  Multi-Core Parallelization

[483–485]

For over 30 years the foremost approach to improving the performance of computing devices was to increase the CPU clock speed. However, in recent years, manufacturers have encountered fundamental limitations to this approach due to power and heating restrictions, as well as a rapidly approaching physical limit to silicon transistor sizes. Due to these restrictions, performance gain is now achieved with the usage of multiple processors which operate in tandem and share the computational load. Nowadays, all modern computers and workstations employ multiple processors/cores. Typical numbers of cores are $2 - 4$ cores in small devices and laptops, while large computers and workstations employ $12 - 16$ cores.

### 6.2.1.1  OpenMP Parallelization Concept

In order to harness the power of multi-core systems, the implemented solvers were parallelized using the OpenMP library. OpenMP is a parallel programming model for shared memory multi-processor systems and has been established as the norm in CPU parallelization. Detailed information on OpenMP can be found in [484, 485].

In order to maximize the performance gain, and thus solver speed, the computational domains are decomposed into as many sub-domains as the available number of CPU cores, which can either be all available cores in the system, or limited to a subset as defined by the user. The pressure variables in each sub-domain are then calculated based on the respective FDTD stencil by an individual core. Due to the shared-memory architecture of multi-core systems, every core can access all data in the computer memory. Thus,

OpenMP parallelization does not require data exchange between cores (unlike MPI), barring the need for data/computation overlap and offering high performance gains. The concept of multi-core parallelization adopted for this work can be seen in Figure 6.5.
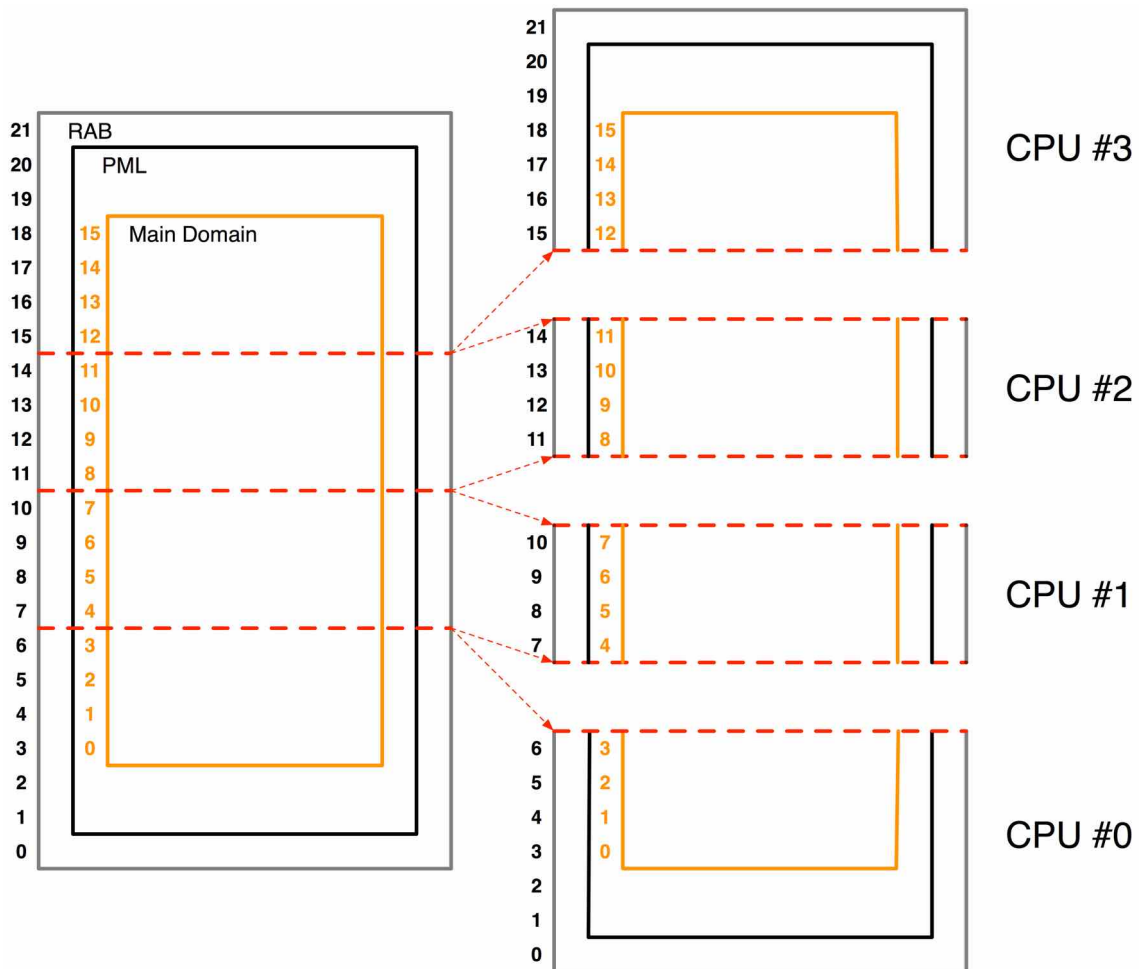


**Figure 6.5**: *Simplified depiction of domain decomposition in the case of multi-core parallelization. The entire computational domain is split into as many sub-domains as the available number of cores. Each core is then responsible for the calculation of their respective subdomain. Due to the shared-memory architecture of multi-core systems no data needs to be exchanged between the cores.*

## 6.2.2   Parallelization using GPUs

[483]

As will be shown in Section 6.2.3, when employing multi-core parallelization as described in Section 6.2.1, the performance gain remains insufficient for the simulation of very large

computational domains. In order to further improve the performance of the implemented solvers, thus allowing for a further decrease in simulation times, they were parallelized utilizing Graphics Processing Units (GPUs).

GPUs are tailored to data-massive and compute-intensive applications, namely graphics processing, and are classified as 'many-core' devices, employing multiple hundreds of small (compared to the CPU) cores. In recent years, GPUs have evolved into very fast parallel co-processors capable of executing general purpose computations with extreme efficiency, making them ideal for computationally intensive numerical applications.

GPU programming, however, was previously feasible exclusively through the usage of low-level libraries like OpenGL and DirectX, requiring programmers to entirely redesign their code and invest a large amount of time into learning graphics programing and utilizing these devices. The introduction of the Compute Unified Device Architecture (CUDA) by NVIDIA in 2006, leverages the computational power of GPUs and allows their programming for parallel computation without any prior knowledge of graphics programing.

In order to explain the rationale behind the GPU parallelization of the presented solvers, a minimal overview of GPU architecture and the CUDA programming model will be given.

### 6.2.2.1   GPU and CUDA Architecture
[483, 486, 487]

A high-level representation of GPU architecture can be seen in Figure 6.6. A GPU can be considered as a set of *multi-processors* (MPs), each with its own set of individual *stream-processors* (SPs), and a small amount of *shared-memory* (SMEM) accessible only to the SPs. The GPU also contains a large amount of *global-memory*, which is accessible by all MPs and their respective SPs. It should be mentioned that access of the global-memory for read/write operations is at least two orders of magnitude slower than shared-memory access. In total, a typical GPU contains multiple hundreds of SPs, which are capable of concurrently executing arithmetic operations through computing *threads*, allowing for massive parallelization of applications. Thus, employing GPUs for inherently parallel problems (as in the case of the FDTD method) can provide far greater performance gains than CPU systems.

CUDA arranges threads into *thread-blocks*, which are further arranged onto a *thread-grid*. Each thread-block is assigned to a single MP, which divides the threads in *warps*, i.e., groups of 32 threads, and each thread then executes the same operations as per the *single-instruction multiple thread* (SIMT) model. In addition, CUDA provides barrier functionality to ensure synchronization between the different thread-blocks.

A detailed overview of the architecture and programing of GPUs with CUDA is outside the scope of this thesis but these topics have been extensively discussed and further information can be found in books on CUDA such as [483, 488, 489]. In addition, multiple

studies have employed CUDA in order to boost simulation performance in the fields of electromagnetics, flow-dynamics, atmospherics, seismic modeling, etc. [486, 487, 490–495].
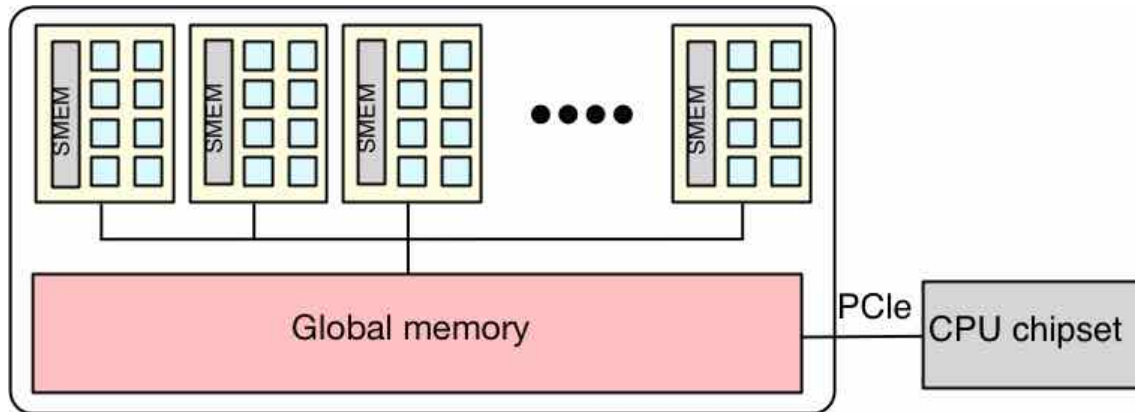


***Figure 6.6****: A high-level view of GPU architecture.*

#### 6.2.2.2   CUDA Parallelization Concept

The GPU parallelization approach employed in this work was based on the technique proposed by Micikevicius [486]. The approach utilizes thousands of threads on a 2D thread-grid with a size equal to a 2D X-Y slice of the simulated computational domain. The different threads update the cells on the initial plane and then propagate along the Z axis of the domain until the entire domain is fully updated. Within every thread-block the required data are first transferred from the global memory to the shared memory of the given MP in order to minimize the memory-access related latency, as the same data are read multiple times by different threads. In addition, texture and constant memories were used to store constant data, e.g., material constants, axes coordinates etc. to maximize performance.

### 6.2.3   Performance Benchmarking

In order to evaluate the performance gains offered by the parallelized versions of the developed solvers, multiple benchmarking simulations were performed on three different systems. All systems were equipped with different models of multi-core CPUs and CUDA-enabled GPUs. Nine computational domains of increasing size were simulated with identical parameters. The results of the benchmarks can be seen in Figure 6.7.

The GPU implementation of the developed solvers offers speedup factors of up to 45 for large computational domains, when compared to the single-core implementation. Furthermore, while the speeds of both CPU implementations, i.e., single-core and multi-core, are

relatively independent of the computational domain size, the GPU implementation exhibits an almost linear domain size – speed behavior. That can be attributed to the fact that larger computational domains allow for increased parallelism and permit GPU implementations to take full advantage of the available resources.

Overall, it is obvious that the GPU implementation is highly efficient and allows for the execution of large simulations in a fraction of the time required by CPU implementations. However, GPUs suffer from the significant drawback of limited memory. which can be seen in Figure 6.7, as very large computational domains cannot cannot be accommodated by the memory of typical GPUs.

# 6.3   Integration

For the purposes of acoustic and thermal modeling of therapeutic FUS applications such as the ones described in Chapter 3, the developed acoustic solvers were integrated into the 'in-house' simulation platform SEMCAD-X (SPEAG, Zürich, Switzerland) and coupled to the existing thermal solver.

## 6.3.1   SEMCAD-X Simulation Platform

SEMCAD-X was originally developed for electrodynamic and thermal modeling of a wide variety of applications, ranging from mobile phone and MRI safety evaluation to biomedical applications employing detailed anatomical models (see Section 6.3.3). It allows for flexible 3D modeling of the simulation setup and, as the software was tailored to simulations with the FDTD method, powerful gridding and voxeling capabilities. The entire framework is supported by a versatile Python scripting interface, which allows for the entire modeling, simulation, and post-processing procedure to be automated, with powerful Visualization Toolkit (VTK) based post-processing built into the platform to permit flexible visualization and evaluation of the results.

The framework was modified to allow for modeling of acoustic simulations, i.e., assignment of the acoustic properties of materials/tissues and acoustic source modeling. In addition, the framework's post-processing capabilities were extended to acoustic pressure fields and the calculation of relevant quantities, e.g., acoustic intensity and deposited energy. Furthermore, the framework's scripting interface allowed for quick prototyping of tools and scripts tailored to particular therapeutic FUS applications, e.g., calculation of phase-aberration compensation factors and focal steering.
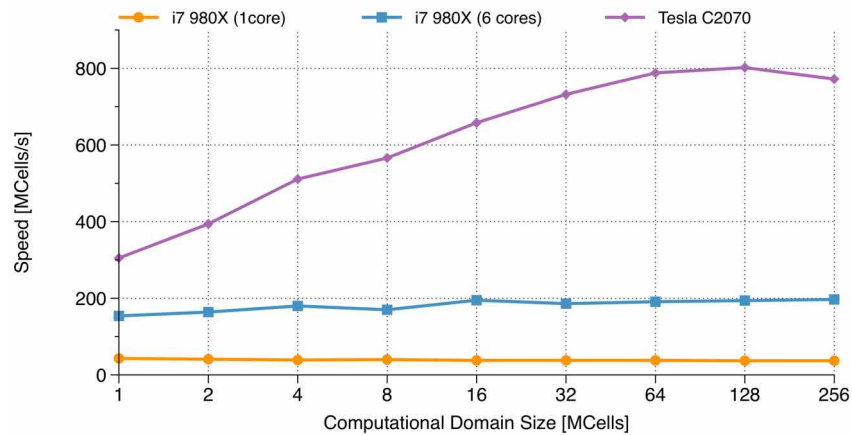
*(a)*
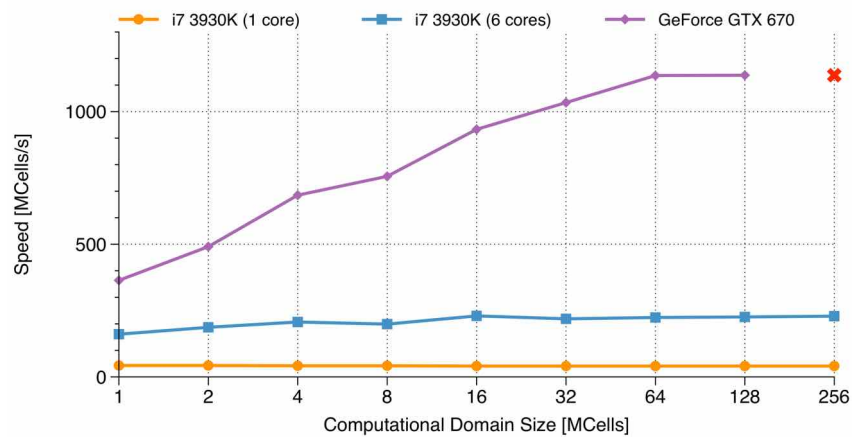


*(b)*
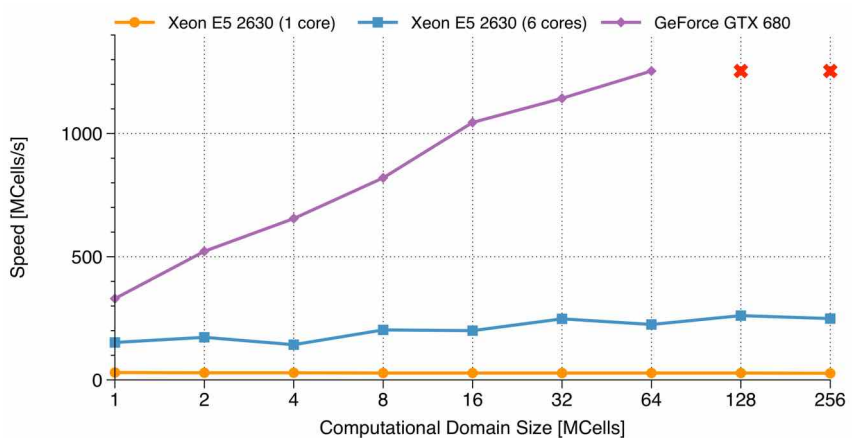


*(c)*

**Figure 6.7**: *Performance results of the solvers' benchmarking for the three different systems. The performance of the single-core, multi-core (OpenMP), and GPU (CUDA) solvers are presented. Points marked with 'x' on the GPU results signify that the utilized GPUs did not have adequate memory to support the size of the simulated computational domain.*

## 6.3.2 SEMCAD-X Thermal Solver

A thermal solver tailored to biomedical applications has been previously developed, validated, and integrated into SEMCAD-X. The solver is based on a finite-differences implementation with conformal corrections of the Pennes' bioheat equation (BHE) [496]:

$$\rho C \frac{\partial T}{\partial t} = \nabla \cdot (k \nabla T) + \rho Q + \rho S - \rho_b C_b \rho \omega \left( T - T_b \right) \tag{6.1}$$

where $\rho$ is the medium density, $C$ is the specific heat capacity, $T$ is the tissue temperature, $k$ is the thermal conductivity, $Q$ is the metabolic heat generation rate, $\omega$ is the perfusion rate, and $\rho_b$, $C_b$ and $T_b$ are the density, specific heat capacity, and temperature of the blood respectively. The symbol $S$ denotes the time-averaged rate of heat generation by relaxation absorption in a tissue of a continuous sound field. The equation for this term, which was given in Section 1.3.1, is repeated here [14]:

$$S = \alpha \frac{p^2}{\rho c} \tag{6.2}$$

where $\alpha$ is the medium's absorption coefficient, $p$ is the absolute acoustic pressure, $\rho$ is the medium density, and $c$ is the medium's speed of sound.

By introducing this term into Equation 6.1, it is possible to couple the two solvers and calculate the temperature induced in the tissue due to exposure to acoustic fields.

The thermal solver has the ability to account for thermoregulation and vascular shutdown, and has been augmented with a wide range of perfusion models, including the discrete vasculature (DIVA) [497] and Weinbaum-Jiji (WJ) [498] models, support for MRI perfusion maps, as well as Arrhenius tissue damage and thermal dose models [499], thus permitting realistic modeling and assessment of thermal effects in the body.

In addition, the thermal solver allows boundary conditions to be applied to selected interfaces between different tissues or regions. Three types of boundary conditions can be employed: *Dirichlet* boundary conditions, where a fixed temperature can be enforced at the interface, i.e., $T = T_{boundary}$. *Neumann* boundary conditions, where a fixed thermal energy flux can be enforced at the interface, i.e., $k \frac{dT}{dn} = F_{boundary}$. Lastly, the thermal solver also offers *mixed/convenctive* boundary conditions, which allows the user to set an energy flux that depends on the local surface temperature and equilibrates it to the specified environment temperature $T_{outside}$ based on a heat transfer coefficient $h$ in $\mathrm{W/m/^2K}$, while in addition a fixed heat flux can also be $F_{boundary}$ added $k \frac{dT}{dn} + h \left( T - T_{outside} \right) = F_{boundary}$. Further details on the thermal solver can be found in [500, 501].

### 6.3.3   The Virtual Population Anatomical Models

In addition to SEMCAD-X, an integrated medical image segmentation platform iSEG (ZMT, Zürich, Switzerland), allowed for the generation of patient-specific anatomical surface-models from MRI and CT image data. This tool, further information on which can be found in [500], was used by Christ et al. [234] to develop 'Virtual Population', a collection of surface-based anatomical models segmented from MRI data of healthy volunteers and animals. The Virtual Population currently comprises 10 human anatomical models of different gender, age, weight and body type, with over 200 distinguished tissues (see Figure 6.8). In addition, it contains multiple animal models, e.g., mice, rats and pigs.



*(a)*



*(b)*                                        *(c)*
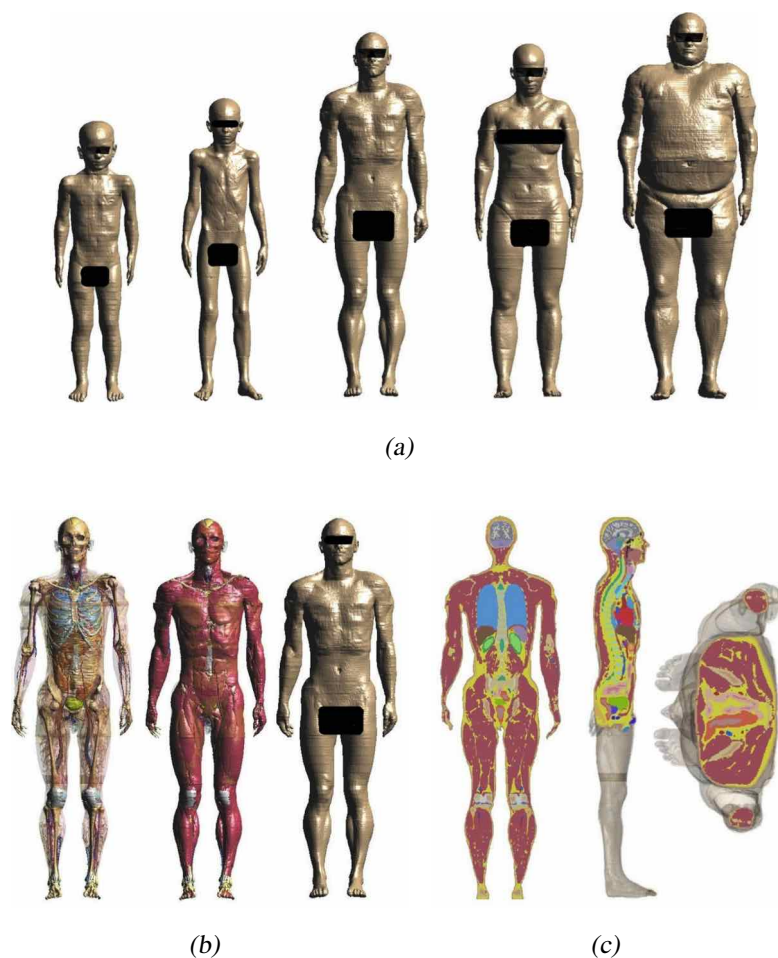
**Figure 6.8**: *Examples of Virtual Population anatomical models segmented with iSEG (ZMT, Zürich, Switzerland) from MR image data of healthy volunteers. Five models of varying sex, age and weight are shown in (a). The 'Duke' model, depicting a 34yr old male volunteer, which has been used extensively during the course of this thesis, is shown in (b) and (c).*

# 7

# Validation

In order to ensure the sound operation of the acoustic solvers developed during this work, analytical, numerical (Section 7.1), and experimental (Section 7.2) validation was performed.

Simulations of simplified setups were compared against FOCUS, which was detailed in Section 4.3.2, yielding excellent agreement (on the order of $98\%$). Analytical validation based on the calculation of reflection $R$ and transmission $T$ coefficients, at the interface between media with varying impedances $Z$, was also performed yielding perfect agreement (Section 7.1.2).

Experimental validation was performed against acoustic fields measured in an in-vitro setup which was designed and manufactured 'in-house'. The setup consisted of a water-tank with a single-element focused transducer and a hydrophone mounted to an articulated robotic arm allowing for 3D pressure scans to be acquired. Measurements in both homogeneous setups, and setups involving focus distorting samples were performed and compared against acoustic simulations, using the gamma dose distribution comparison method.

## 7.1 Numerical & Analytical Validation

### 7.1.1 Numerical Validation against FOCUS

Numerical validation of the lossless and the lossy LAPWE solvers (PDEs in Sections 4.2.1 and 4.2.1.4 respectively, stencil derivations in Sections 5.2.1.1 and 5.2.1.2), was performed against the freely available FOCUS software presented in Section 4.3.2. The FOCUS software has been extensively validated by its authors against analytical solutions [291, 379, 383].

Simplified transducers were initially simulated with the fast nearfield method (FNM) module available in FOCUS and which was presented in Section 4.1.1.5. Subsequently,

simulations of the same transducers were performed with the presented framework using the LAPWE model FDTD implementation. Comparison of the resulting pressure distributions yielded excellent agreement.

### 7.1.1.1 Particle Velocity Sources

As discussed in Section 6.1.4, the LAPWE and WLE stencils implemented in this work only discretize acoustic pressure $p$ and thus, acoustic transducers and acoustic sources in general need to be prescribed through this quantity alone. However, models such as the FNM, which are based on the Rayleigh-Sommerfeld integral (see Section 4.1.1), depend on the prescription of (a typically uniform) particle velocity on the transducer surface, through which pressure is subsequently calculated. The pressure distributions resulting from a uniform particle velocity prescription on a circular, and a rectangular transducer aperture can be seen in Figures 7.1(a) and 7.1(b) respectively.



*(a)*                                                        *(b)*
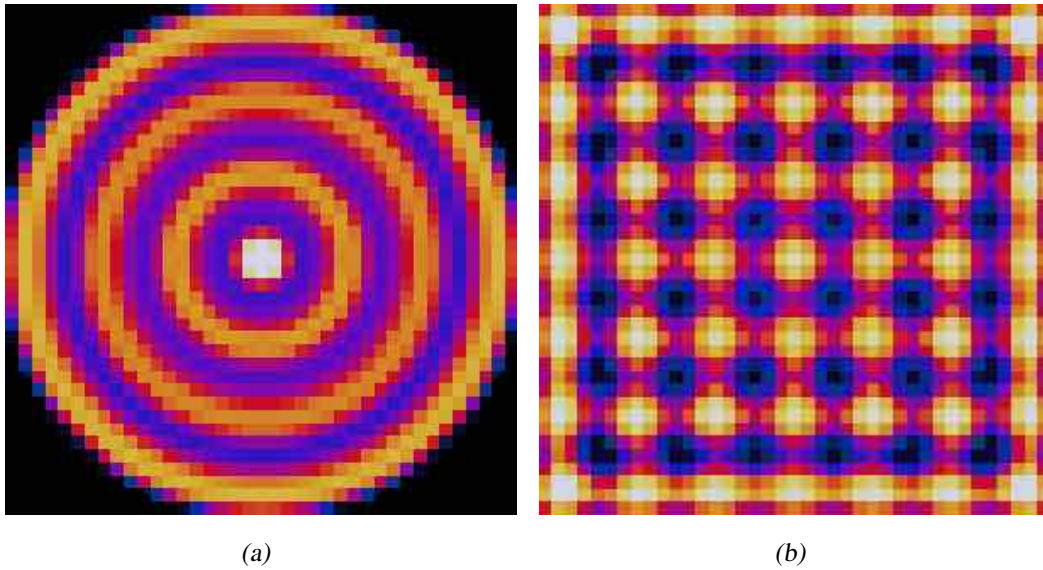
**Figure 7.1**: *Absolute pressure distribution on the surface of a circular (a) and a rectangular (b) transducer as a result of a uniform particle velocity prescription.*

Therefore, it is not possible to directly compare the results calculated by these two different types of models. In order to overcome this limitation the acoustic pressure distribution was initially calculated on the surface of the corresponding transducer with the FNM module provided by FOCUS. Subsequently, this pressure distribution was mapped on the surface of the transducer simulated with the acoustic solvers presented in this work. This mapping ensured that the two acoustic sources are identical, and allowed for the propagated fields, as calculated by the FNM and LAPWE models, to be directly compared.

### 7.1.1.2   Simplified Transducers in a Homogeneous Medium

Three distinct transducers sonicating at $500$ kHz were simulated both in FOCUS and the presented LAPWE acoustic solvers. These were, a circular transducer with a radius of $10$ mm, a rectangular transducer with dimensions of $20 \times 20$ mm, and a planar ring transducer with inner and outer radii of $7.5$ and $10.0$ mm respectively. The transducers were embedded in an infinite homogeneous medium with acoustic properties akin to those of water, i.e., speed of sound $c$ of $1500$ m/s and density $\rho$ of $1000$ kg/m$^3$.

In order to separately validate the lossless and the lossy LAPWE solvers, two series of validations were performed. In the first series, a lossless medium was assumed, while in the second, an attenuation coefficient $\alpha$ of $1$ dB/cm/MHz, which is equivalent to $11.512$ Np/m/MHz (see Equation 1.5), was considered instead.

The transducers were assumed parallel to the X-Y plane, and centered around the origin of the cartesian coordinate system. Thus, the generated acoustic waves were assumed to propagate in the +Z direction. The truncated computational domains had dimensions of $40 \times 40 \times 90$ mm and were discretized with a $0.25$ mm grid-step, which amounts to $\lambda/12$, where $\lambda$ is the acoustic wavelength for the given frequency and medium. In the case of the LAPWE solver, these domains were truncated with 16 layers of PML in order to inhibit the manifestation of spurious reflections at the domain boundaries.

While the FNM model directly calculates the steady-state pressure distribution, the acoustic solvers presented in this work are explicit, time-domain solvers using the FDTD method. Thus, to assess the necessary number of simulated periods required to achieve steady-state, multiple simulations over $50-90$ periods were performed. It was ascertained that $60$ periods were sufficient to achieve steady-state, as longer durations resulted in less than $0.1\%$ difference in terms of absolute pressure.

In the case of the circular transducer in the lossless medium, the absolute pressure distributions, as calculated by both FOCUS and the LAPWE solver, and plotted on an X-Z plane through the center of the transducer, can be seen in Figure 7.2. Excellent visual agreement between the two models can be seen. However, as the resulting absolute pressure distributions calculated by FOCUS and the LAPWE solver exhibit no discernible visual differences, only those calculated by the latter are shown here for the cases of the rectangular (see Figure 7.3(a)), and planar ring (see Figure 7.3(b)) transducers.

To allow for accurate comparisons, the absolute pressure was plotted along the axis of propagation for both FOCUS and LAPWE. The pressure plots for the circular transducer can be seen in Figure 7.4(a), while the plots for the rectangular and planar ring transducers can be seen in Figures 7.4(b) and 7.4(c) respectively. Very good agreement was achieved between FOCUS and the LAPWE solver for all six comparison cases with only minor differences in the far-field regions, which are attributed to the cumulative phase dispersion errors inherent to the FDTD method (see Section 5.1.3). In order to further quantify the agreement between the two pressure plots, the normalized standard deviation was
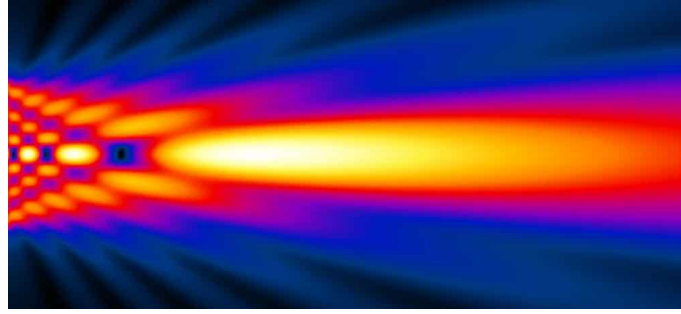
*(a)*
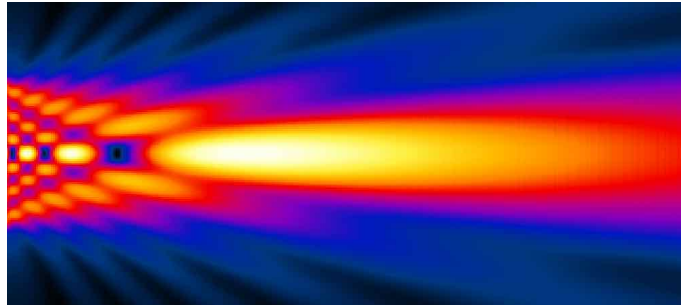


*(b)*

**Figure 7.2**: *Absolute pressure distributions on a X-Z plane through the center of the transducer as calculated by FOCUS (a) and the lossless LAPWE acoustic solver presented in this framework (b). Excellent visual agreement can be seen between the two distributions.*

calculated as the ratio of the $\ell^2$ norm of the pressure difference between the two lines and the $\ell^2$ norm of the FOCUS results:

$$\text{Normalized Standard Deviation } \% = 100 \frac{\ell^2(p^{LAPWE} - p^{FOCUS})}{\ell^2(p^{FOCUS})} \tag{7.1}$$

with $\ell^2$ norm being the square root of the sum of squares of all absolute pressure values for the respective line. These results can be seen in Table 7.1.

## 7.1.2 Analytical Validation of the Density-Variation LAPWE

In order to validate the density-variation LAPWE solver, which was presented in Section 5.2.1.4, simulations were performed where a $2\,\mathrm{MHz}$ acoustic plane wave, was propagated through different media with varying densities but an identical speed of sound of $1500\,\mathrm{m/s}$. The reflection $R$ and transmission $T$ coefficients were calculated both analytically, through Equations 1.11 and 1.12 respectively, and through the pressure amplitudes of the incident, reflected and transmitted waves at the interfaces of the different media.
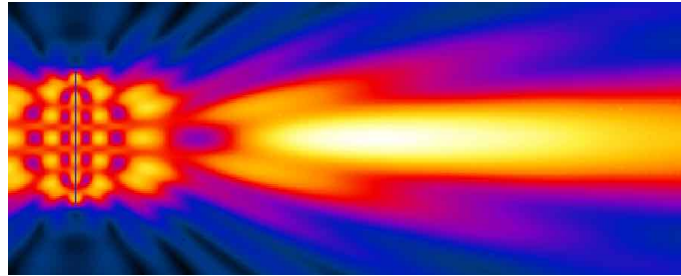
*(a)*
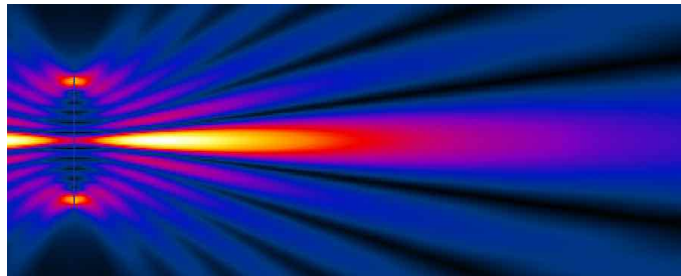


*(b)*

**Figure 7.3**: *Absolute pressure distributions on a X-Z plane through the center of the transducer as calculated by the lossless LAPWE solver. The distribution of both a rectangular (a) and a planar ring transducer (b) can be seen.*

| Transducer | Normalized Standard Deviation % | |
|---|---|---|
| | Lossless Medium | Lossy Medium |
| Circular | 3.1% | 3.5% |
| Rectangular | 1.9% | 3.4% |
| Ring | 2.7% | 3.1% |

**Table 7.1**: *The normalized standard deviation values between the FOCUS and the LAPWE solver presented in this work. Excellent agreement between the two solvers can be seen for all transducer types and media examined.*
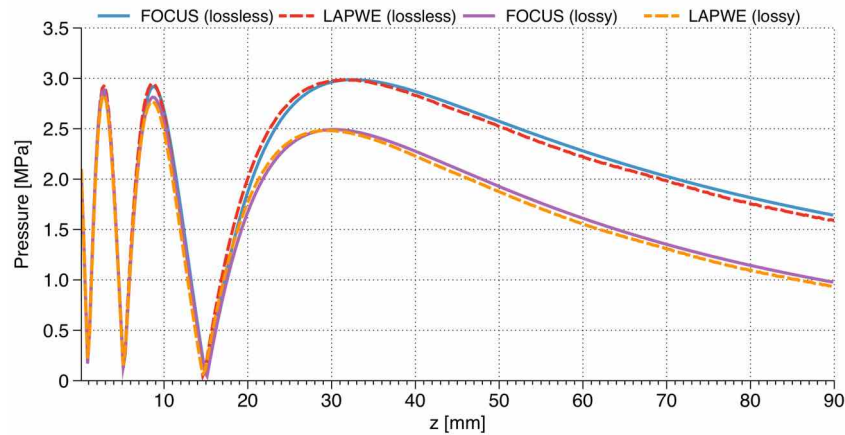
*(a)*
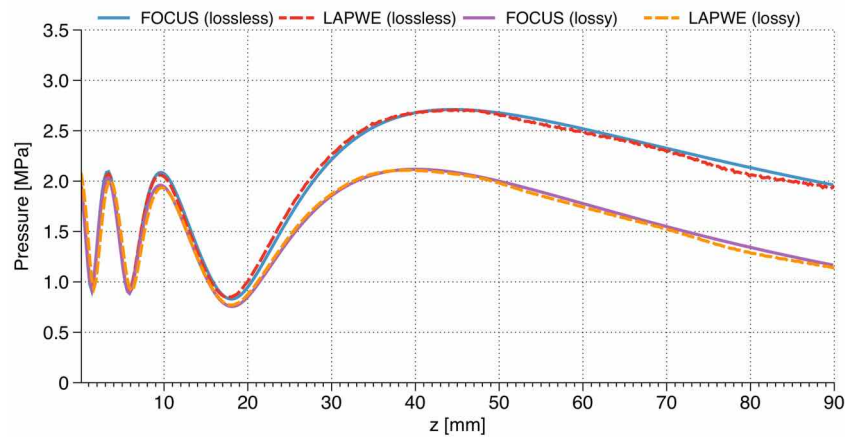


*(b)*
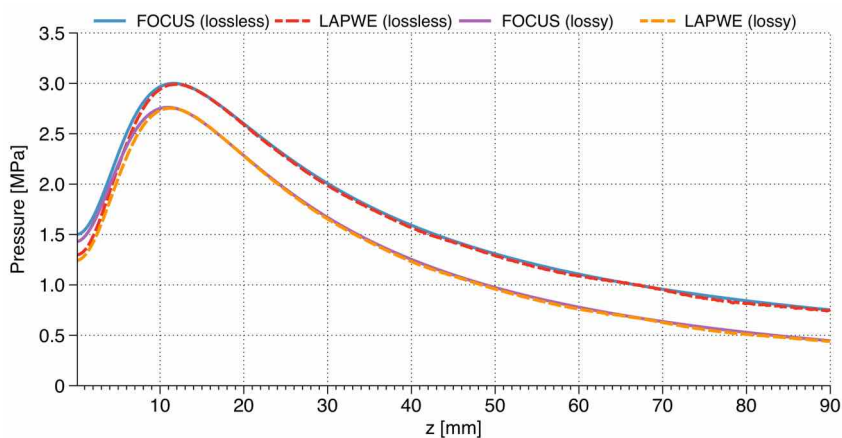


*(c)*

**Figure 7.4**: *Absolute pressure line-plots along the axis of propagation as calculated by both FOCUS and the LAPWE solver. The pressure comparisons within a lossless and a lossy medium can be seen for the cases of a circular (a), a rectangular (b), and a planar ring (c) transducers. Excellent agreement can be seen for all cases.*

In a first simulation, the plane wave propagated from a medium with a density $\rho$ of $1000 \text{ kg/m}^3$ to a medium with a density of $1900 \text{ kg/m}^3$, thus $Z_2 > Z_1$. In the case of the second simulation, the plane wave propagated from a medium with a density of $1000 \text{ kg/m}^3$ to a medium with a density of $600 \text{ kg/m}^3$, thus $Z_2 < Z_1$.

The resulting absolute pressure plotted along the axis of propagation, as well as the incident, reflected, and transmitted amplitudes, are shown in Figure 7.5(a) for the $Z_2 > Z_1$ case and Figure 7.5(b) for the $Z_2 < Z_1$ case. The calculation of the reflection and transmission coefficients is based on Equations 1.11 and 1.12 respectively, which are repeated below:

$$R = \frac{p_r}{p_i} = \frac{(Z_2 - Z_1)}{(Z_2 + Z_1)} \qquad T = \frac{p_t}{p_i} = \frac{(2Z_2)}{(Z_2 + Z_1)} \tag{7.2}$$

where $p_i$, $p_r$, and $p_t$ are the pressure amplitudes of the incident, reflected, and transmitted waves respectively. Both the analytical (reference) and the numerical calculations of these coefficients can be seen in Table 7.2. It should be noted that a negative coefficient implies that the reflected wave exhibits a $180°$ phase-shift relative to the incident wave (see Section 1.1.3.2). Perfect agreement can be seen between the two calculations which verifies the sound operation of the density-variation LAPWE solver.

| Case | Analytical | | | | Numerical | | | | |
| | Z [MRayls] | | Coefficient | | Amplitude [MPa] | | | Coefficient | |
| | $Z_1$ | $Z_2$ | R | T | $p_i$ | $p_r$ | $p_t$ | R | T |
| --- | --- | --- | --- | --- | --- | --- | --- | --- | --- |
| $Z_2 > Z_1$ | 1.50 | 2.85 | 0.31 | 1.31 | 0.98 | 0.31 | 1.29 | 0.31 | 1.31 |
| $Z_2 < Z_1$ | 1.50 | 0.90 | -0.25 | 0.75 | 1.08 | -0.27 | 0.81 | -0.25 | 0.75 |

**Table 7.2**: *Analytical and numerical calculations of the reflection $R$ and transmission $T$ coefficients for the $Z_2 > Z_1$ and $Z_2 < Z_1$ cases. In the analytical case, the coefficients are calculated based on the acoustic impedance of the two media according to Equations 1.11 and 1.12 respectively. The numerical calculations are based on the ratios between the pressure amplitudes of the reflected and transmitted waves to the amplitude of the incident wave.*

## 7.2   Experimental Validation

In addition to the analytical and numerical validation, which validated separate aspects of the presented solvers in simplified setups, in-vitro validation was performed against a custom-made measurement setup in order thus assessing the accuracy of the solvers in a realistic setup. This setup consisted of a water-tank lined with absorbing material (see
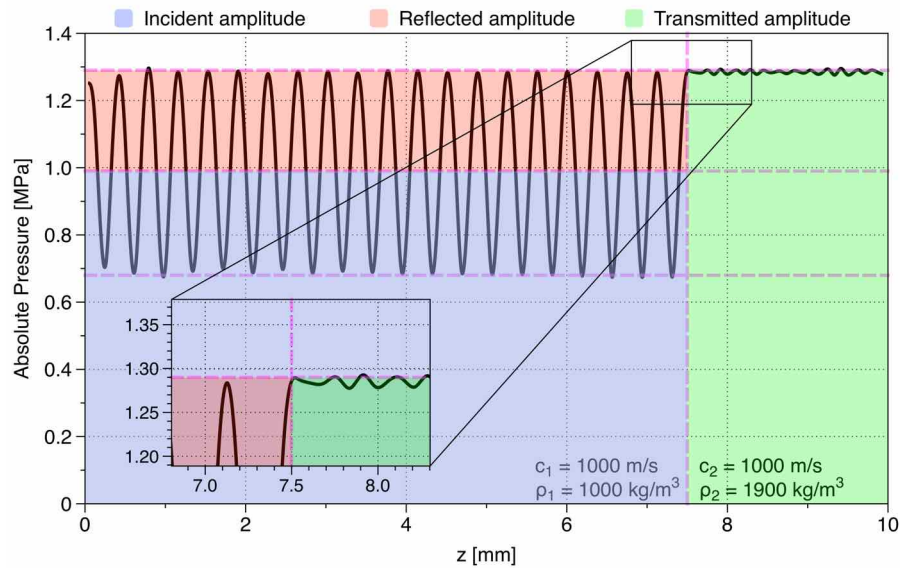
*(a)*
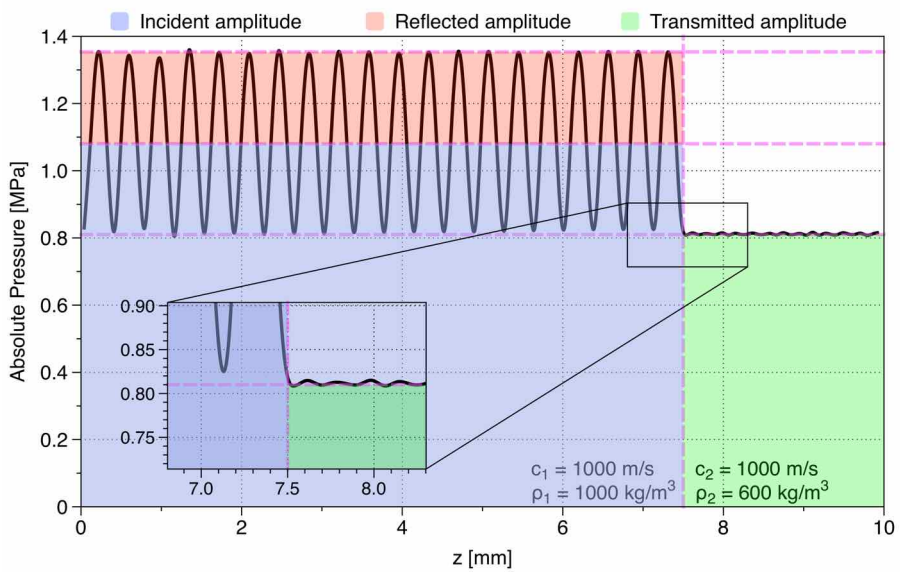


*(b)*

**Figure 7.5**: *Absolute pressure plots used in the validation of the density variation LAPWE. Pressure is plotted along the axis of propagation and the incident, reflected, and transmitted amplitudes are shown for the $Z_2 > Z_1$ (a) and $Z_2 < Z_1$ (b) cases.*

Section 7.2.1.1), and utilized a single-element focused transducer sonicating at 550 kHz. Measurements were performed using a hydrophone mounted on an articulated robotic arm, which allowed for 3D pressure scans to be acquired (see Section 7.2.1.2). Different setups, both homogeneous and in the presence of acoustically characterized materials in the beam path (see Section 7.2.1.3), were measured and compared against identical simulations.

## 7.2.1  Measurement Setup

### 7.2.1.1  Water-tank & Sample Holder

A rectangularly-shaped water-tank (see Figure 7.6(a)), exhibiting internal dimensions of $353 \times 353 \times 600$ mm, was designed and constructed in-house from polymethylmethacrylate (PMMA). The four side-walls of the water-tank were lined with AptFlex F48 (Precision Acoustics, England), a polyurethane rubber acoustic absorber, tailored to reducing reflections in the sub-MHz frequency range with a thickness of 26.5 mm. The absorbing material was permanently glued to the side-walls of the water-tank with the AptFlex F41 Acoustic Putty (Precision Acoustics, England). However, the bottom of the water-tank was not lined itself since the removable sample holder base, which is described below, was lined around the transducer instead.

A removable acetal copolymer (POM-C) sample holder, consisting of a base and four vertical columns was also constructed (see Figure 7.6(b)). Its primary function was to suspend an acoustically characterized sample between the transducer and its geometric focus, so that the effect of the different samples on the 3D pressure field distribution can be measured and compared to simulations. The transducer was placed on the holder base and securely fastened to minimize positional uncertainties, while the holder base was also lined with AptFlex F48 to minimize acoustic reflections. The four vertical columns had 5 mm diameter holes every 5 mm, i.e., the center-to-center distance between the holes is 10 mm. These holes served to place the two plexiglass rods, which were also 5 mm in diameter, and which run through holes in the different samples, in order to hold the sample at a given distance between the transducer surface and its geometrical focus (see Figure 7.6(c)). The combined setup of the water-tank and the sample holder, with the transducer fastened to its base, can be seen in Figure 7.6(d).

### 7.2.1.2  Transducer, Hydrophone & Measurement Hardware

This setup utilized a single-element, high-power transducer (R7835A101, Imasonic, France) with a working frequency of 550 kHz, and an acoustic wavelength $\lambda$ in water of ca. 2.7 mm. The aperture of the transducer exhibited an active diameter of 80 mm, and a

(a)                                              (b)

(c)                                              (d)
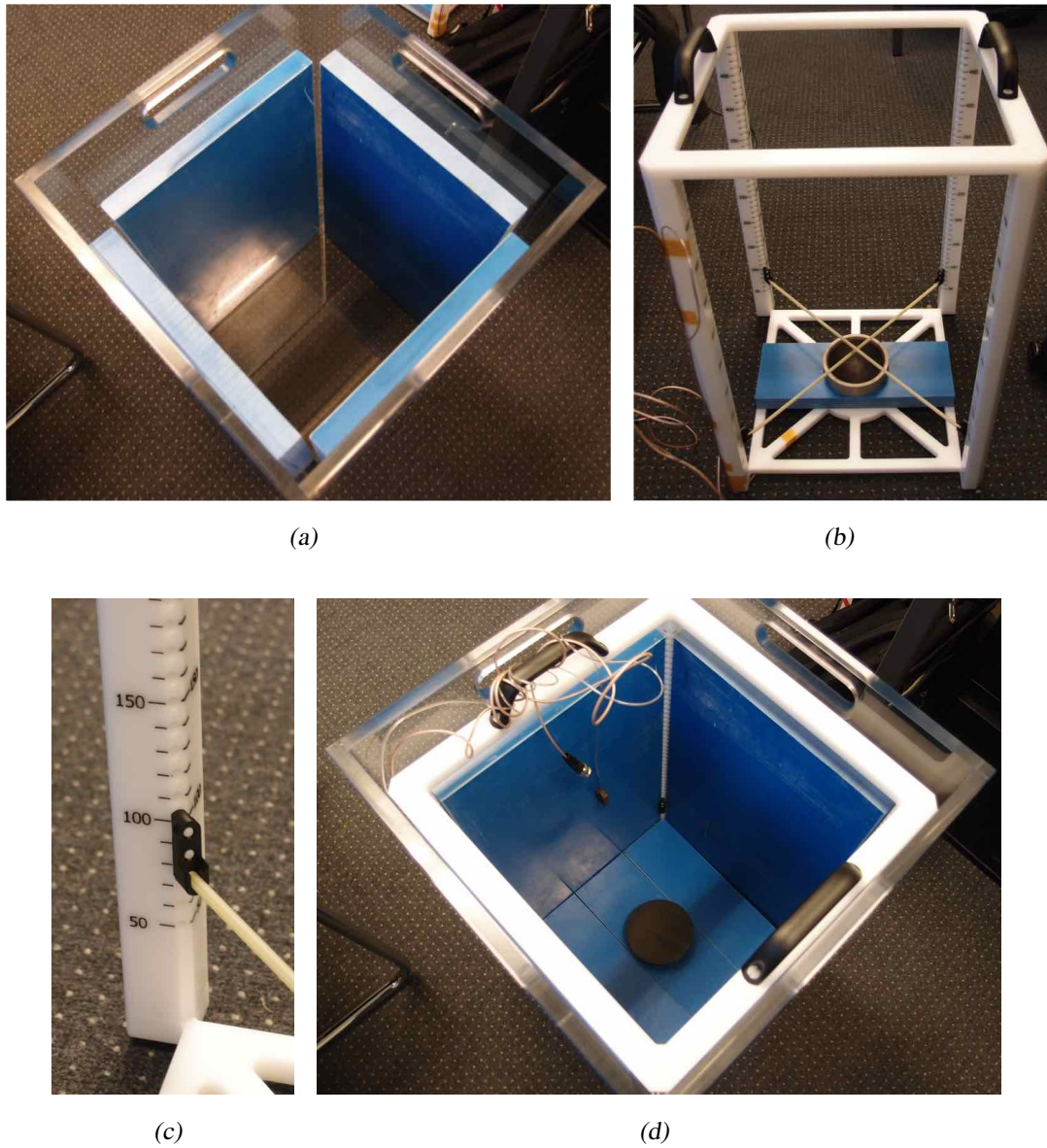
**Figure 7.6**: *Photos of the water-tank and sample holder that were constructed for the purposes of the in-vitro ultrasonic measurements. The side-walls of the water-tank were lined with an acoustic absorber to minimize reflections (a). The sample holder (b) served to accurately position the transducer and provide support for the different samples placed between the transducer and its geometric focus (c). The entire setup (without the rods or a sample) can be seen in (d).*

64 mm radius of curvature, resulting in an F-number of 0.8. The transducer was connected to an Agilent 33250A signal generator (Agilent, Santa Clara, CA, USA), which served as the device's driving system.

A HNR-0500 (Onda Corporation, CA, USA) needle-type hydrophone with a 0.5 mm active element diameter was attached to a 450 mm carbon fiber extension. This extension was mounted onto a DASY52 NEO (SPEAG, Zurich, Switzerland) with a TX90 articulated robotic arm (Staubli Robotics, Faverges, France), which facilitated fast and accurate measurements on a 3D grid around the geometric focus of the transducer. The hydrophone was connected through a BNC cable to an AH-1100 (Onda Corporation, CA, USA) pre-amplifier, which was subsequently connected to a TDS 460A (Tektronix, Oregon, USA) oscilloscope. Both the signal generator and oscilloscope were connected to a computer through an Agilent 82357B GPIB/USB interface cable which allowed for automatic setup and control of both devices through Python and PyVISA along with the Agilent IO drivers. A photo of the entire measurement setup can be seen in Figure 7.7.

### 7.2.1.3 Focus Distorting Samples

As described in Section 7.2.1.1, the sample holder of the water-tank setup was used to position a material sample between the transducer and its geometric focus in order to validate the focal distortion effects induced by the presence of an inhomogeneity. Samples of varying shapes, dimensions, and materials were manufactured and acoustically characterized (CIRS Inc., Norfolk, VA, USA). A block, a sphere and two cylindrical samples were each manufactured out of Delrin, Polyurethane, and RTV Silicone rubber, amounting to a total of twelve different samples. The dimensions of the different samples can be seen in Table 7.3, while a photograph can be seen in Figure 7.8. Dimensional measurements were perfromed with calibrated Vernier calipers with an accuracy of 0.01 mm, while the manufacturing precision was estimated at $\pm 0.1$ mm by performing multiple measurements of each dimension.

The samples were acoustically characterized to precisely define their acoustic properties. This characterization involved measurement of the speed of sound $c$, the absorption coefficient $\alpha$, and the density $\rho$ for all three materials. The measured acoustic properties of the different materials can be seen in Table 7.4. Speed of sound and absorption measurements were performed via a broadband substitution technique [40, 502, 503], with an estimated accuracy of $\pm 5\%$. Density measurements were performed on a precision scale via water displacement measurements with an estimated accuracy of $\pm 1\%$.

**Figure 7.7**: *Photo of the entire measurement setup including the water-tank and the DASY52 NEO (SPEAG, Zurich, Switzerland) robot arm. The hydrophone was attached to a carbon fiber extension, which was in turn mounted to the articulated robotic arm. This setup facilitated fast and accurate measurements on a 3D grid around the geometric focus of the transducer.*

|                   | Delrin                          | Polyurethane                    | RTV Silicone                    |
|-------------------|---------------------------------|---------------------------------|---------------------------------|
| Block             | $33.2 \times 32.3 \times 38.1$  | $32.1 \times 37.1 \times 36.7$  | $31.5 \times 31.5 \times 31.5$  |
| Sphere            | D= 38.1                         | D=38.2                          | D=32.4                          |
| Cylinder (Short)  | D=31.8, H=30.2                  | D=31.8, H=30.2                  | D= 31.5, H= 31.2               |
| Cylinder (Long)   | D=31.8, H=79.8                  | D=31.8, H=79.9                  | D= 31.4, H= 80.7               |

**Table 7.3**: *Physical dimensions of the twelve manufactured samples. All values are in* mm. *The abbreviations 'D' and 'H' stand for 'diameter' and 'height' respectively. The manufacturing precision was estimated at* $\pm 0.1$ mm.

**Figure 7.8**: *Photo of the different acoustically characterized material samples used to validate focal distortion effects induced by the presence of an inhomogeneity.*

| | Delrin | Polyurethane | RTV Silicone |
|---|---|---|---|
| Speed of Sound [m/s] | 2430 | 1700 | 1000 |
| Absorption [dB/cm/MHz] | 3 | 6 | 2 |
| Density [kg/m$^3$] | 1430 | 1130 | 1080 |

**Table 7.4**: *Acoustic properties of the three materials used in the manufacture of the samples. The estimated accuracy was $\pm 5\%$ for the speed of sound and absorption measurements, and $\pm 1\%$ for the density measurements.*

## 7.2.2  Measurement Procedure

### 7.2.2.1  Setup Preparation

Prior to each measurement with the in-vitro setup described in Section 7.2.1, water was removed from the water-tank with a submersible electric pump and the entire setup was disassembled, thoroughly cleaned, and allowed to dry for a period of no less than $12$ h before the next measurement. In order to minimize the amount of impurities in the water-tank, the setup was cleaned again before any subsequent measurements.

For each measurement, approximately $50$ L of deionized water was degassed with a vacuum-tank degasser until the levels of dissipated oxygen in the water were below ca. $3 - 4$ ppm. Furthermore, in order to prevent the gradual contamination of the water, Preventol-D7 was introduced into the water with a concentration of $0.05\%$. At these levels, it was determined that Preventol-D7 does not pose any risk to the equipment or alter the properties of the water [504].

The temperature of the room was continuously monitored and kept to a constant $22\,^{\circ}\mathrm{C}$ through an air-conditioning and filtration system which minimized the amount of impurities in the air.

### 7.2.2.2  Setup Registration & Focal Tracking

Upon filling the water-tank with deionized and degassed water, its position was manually registered to the DASY NEO robotic arm through three fiducial points embedded on the measurement setup. This was pivotal to minimizing positioning uncertainties, and defining an initial approximate location of the transducer's geometrical focal point. Subsequently, the hydrophone, which was mounted to the extension attached the robotic arm, was scanned with a LED light beam switch mounted to the robotic arm in order to correct its orientation. This ensured that the hydrophone would be perpendicularly oriented to the transducer in order to minimize directivity uncertainties.

Prior to introducing a focus distorting sample to the setup, automatized focus-tracking pressure scans were performed. During these scans, the pressure was measured around the geometric focal point defined through the registration of the measurement setup to the DASY NEO system. Gradually decreasing volumes were scanned around the initially defined focal point, with proportionally increasing spatial resolution to define the focal point location. Upon completion of these scans, the cartesian coordinate origin was set at that point and the respective focus distorting sample was then suspended between the transducer and its geometric focal point.

#### 7.2.2.3   Acoustic Measurements

Simulations of the setup with each focus distorting sample (see Table 7.3 and Figure 7.8), were initially performed to define the extents of the scanned volume for every individual case. Scanning volumes were centered around the tracked focal point, and exhibited dimensions on the order of $85 \times 85$ mm on the plane parallel to the transducer, and $20$ mm along the propagation axis. The spatial resolutions of the measurement grid were typically $0.5$ mm on the parallel plane and $1 - 2$ mm along the propagation axis. The measurement grid was then defined in the DASY NEO software, while the entire measurement process was automatically controlled through a Python script as described in Section 7.2.1.2.

After the hydrophone was moved to the location of each measurement point, the signal generator driving the transducer was triggered, and ultrasonic waves were generated for a duration of $40$ periods before seizing sonication. The oscilloscope connected to the hydrophone was automatically triggered along with the signal generator and recorded $5000$ pressure measurements at each given grid point over these $40$ periods. This approach ensured that the acoustic waves reflected off the hydrophone mounting, and subsequently off the transducer surface, would not be recorded. Furthermore, this allowed for sonication breaks between points, which prevented the transducer's piezoelectric element from overheating. The captured waveforms were then stored for every measurement point and processed to yield the steady-state absolute pressure amplitude at that point.

### 7.2.3   Acoustic Simulations

Identical acoustic simulations were performed for each measured setup. The simulation domains exhibited dimensions of approximately $155 \times 155$ mm on the plane parallel to the transducer, and $130$ mm along the propagation axis. These domains were discretized with a $0.25$ mm grid-step, and terminated with $16$ layers of PML on all domain boundaries, in order to inhibit the manifestation of spurious reflections. Such a simulation setup can be seen in Figure 7.9. All acoustic simulations were performed for $40$ periods in accordance to the measurements described in Section 7.2.2.3.

The acoustic properties of water were set as follows: speed of sound $c$ of $1500$ m/s, attenuation coefficient $\alpha$ of $0.0076$ Np/m for a frequency of $550$ kHz, and a density $\rho$ of $1000$ kg/m$^3$. The properties of the respective focus distorting sample were set according to Table 7.4, where $\alpha$ was converted to Np/m through Equation 1.5 for the transducer frequency. The plexiglass material, from which the suspension rods of the sample holder were constructed, was not acoustically characterized and no literature defining its properties was available. Therefore, the acoustic properties for this material were set to those of PMMA as defined in [505], i.e., $c = 2750$ m/s, $\alpha = 6.875$ Np/m, and $\rho = 1192$ kg/m$^3$.
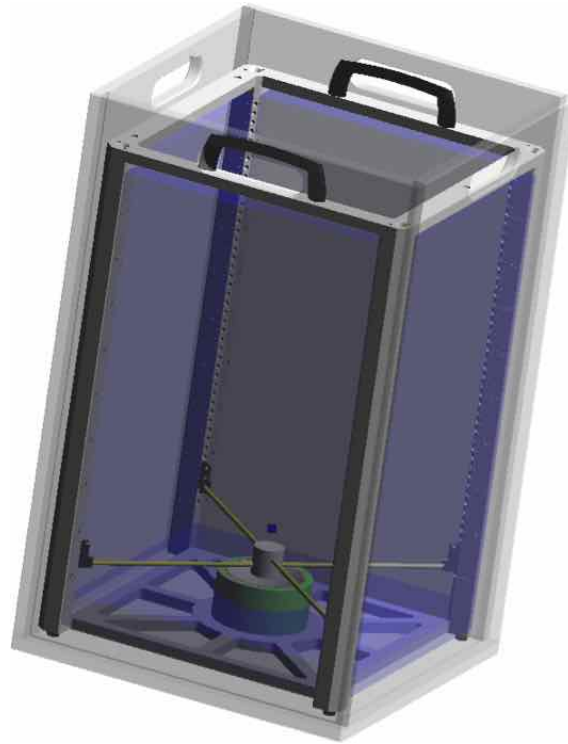
**Figure 7.9**: *Simulated CAD model of the measured setup used in the case of the 'Delrin Cylinder (Short)' focus distorting sample (see Table 7.3 and Figure 7.8). The model of the transducer employed in this study is seen embedded in the acoustic absorbers, while the geometric focus of the transducer is marked with a point.*

## 7.2.4   Uncertainty Analysis & Tolerance Definition

A detailed uncertainty analysis, akin to the process presented by Neufeld et al. [501], was performed for every measurement setup compared against simulations. Considering the simulation setup described in Section 7.2.3 to be the *reference-simulation*, subsequent simulations, termed *evaluation-simulations*, were performed where in each one only a single parameter would be varied in relation to the reference simulation (from a value denoted by 'Ref.' to a value denoted by 'Eval.' in the uncertainty tables). This allowed for the impact of each individual parameter on the simulation results to be ascertained.

In order to ascertain the impact of every single parameter variation an automatized connected-component analysis was performed on all absolute pressure distributions resulting from each reference-evaluation simulation pair. Firstly, the distributions were cropped to the measurable volume. In the case of simulations involving focus distorting samples, this volume was limited to the region above the samples. Subsequently, the peak absolute pressure within that volume was identified, the distributions were thresholded at 50% of that value, and the different connected-components were analyzed. This yielded the full-width half-maximum (FWHM) size of the focal region along the X, Y and Z axes, the

distance between that region and the intended focal point (focal shift), as well as the volume of the region, calculated as the sum of the voxel volumes belonging to the particular component. These focal region characteristics were the investigated variables that were compared in each reference-evaluation simulation pair in order to quantify the impact of the varied parameters.

Assuming linear dependence of the varied parameter on the investigated variables, a sensitivity factor $f$ was determined for each variable. Multiplying the sensitivity factor with the parameter variation $\Delta$ yielded the uncertainty contribution $U$ of this parameter.

Three categories of parameters were varied and their impact was investigated through simulations: the various geometrical aspects of the simulated geometries (dimensions, position, rotation), the numerical aspects pertaining to the simulation (resolution, number of PML layers, simulated periods, grid rotation), and the acoustic properties (speed of sound, attenuation coefficient, density) of the different materials involved in each setup.

Upon calculating the individual uncertainty contributions $U$ for each varied parameter and investigated variable, the combined and expanded ($k = 2$) uncertainty contribution for each parameter category was calculated. The combined uncertainty contribution was calculated as the square-root of the sum-of-squares of the individual contributions. The expanded uncertainty was calculated as the square-root of the sum-of-squares of the same contributions multiplied either by 2 if their corresponding parameters following a normal $N$ distribution or 1.65 if they follow a rectangular $R$ distribution [506, 507].

A detailed overview of the examined simulation parameters is provided in Sections 7.2.4.2-7.2.4.4.

### 7.2.4.1   Uncertainties in the Measurement Setup

In order to calculate the uncertainty contributions pertaining to the measurement setup itself, the following uncertainties were ascertained:

- **Inter-Point Variation of Hydrophone Positioning**: As discussed in Section 7.2.1.2, the hydrophone was mounted on a $450$ mm extension, which was in turn mounted to the TX90 articulated robotic arm of the DASY52 NEO system. In addition to the positional uncertainty of the robotic arm itself, which per the manufacturer's specifications is $\pm 0.035$ mm, an additional positional uncertainty pertains to shifts of the extension and hydrophone relative to the robot. The latter type of shift may manifest itself while the extension and hydrophone move through the water as a result of the medium's inertia. This uncertainty was estimated at $\pm 1$ mm or $\pm 0.37\,\lambda$ where $\lambda$ is the acoustic wavelength in water with a value of ca. $2.73$ mm.

- **Hydrophone Spatial Averaging**: As discussed in Section 7.2.1.2, the hydrophone used in these measurements exhibits an active element diameter of $0.5$ mm. Thus, a

spatial averaging of the measured datafields occurs over the area of the hydrophone's aperture and given its size it introduces a positional uncertainty of $\pm 0.25$ mm or $\pm 0.092\ \lambda$.

- **Hydrophone Orientation**: As outlined in Section 7.2.2.2, prior to each measurement the hydrophone orientation would be corrected through a light beam unit attached to the robotic arm. Due to the inherent directivity of the hydrophone this ensured that the embedded piezoelectric element would be perpendicular to the propagation axis. However, as was discussed above, the inertia of the water may result in local shifts of the hydrophone as it moved through the medium (on the order of $\pm 1$ mm). Given the length of the extension and the magnitude of these shifts the worst-case orientation uncertainty of the hydrophone was calculated at $0.14°$, which according to the device's specifications yields less than $0.5\%$ uncertainty in the measured pressure. Thus this factor was not taken into account during the uncertainty analysis.

- **Measurement Sensitivity/Noise Level**: In order to assess the level of measurement 'noise', the 'low signal' regions of the measurement volume, i.e., regions in the measurement volume where the pressure was below $5\%$ of the pressure peak, were analyzed. By averaging this 'noise signal', the hydrophone's noise level was estimated to be ca. $3.0\%$ of the peak pressure amplitude measured in these volumes or $0.26$ dB.

- **Measurement Nonlinearity**: Based on the reported specifications of the hydrophone and amplifier combination used, the impact of their nonlinearity on pressure was estimated to be less than $0.1$ dB.

- **Transducer Drift**: Per the transducer specifications, its stability over time, i.e., the pressure drift, was evaluated to be less than $0.1$ dB.

- **Registration**: As detailed in Section 7.2.2.2, the water-tank is manually registered to the robotic arm through fiducial points embedded in the measurement setup. Subsequently, focal tracking is performed to locate the location of the geometric focus in each setup and minimize the positional uncertainties stemming from the aforementioned registration. Nevertheless, upon completion of the measurements, shifts of the geometric focus from its expected location were observed. To account for this, the measured and simulated fields were shifted so that the peak pressure locations between them match. This registration was performed as follows:

    - The shift between the peak pressure location and the cartesian origin was manually defined in the measured fields.

    - The reference-simulation results were then subset to an extended volume equal to that of the measured fields plus twice the approximate measurement shift

calculated previously. This was performed to avoid registration of a false peak in the vicinity of the transducer which lies outside the measured volume.

    – The measured and simulated fields were then shifted so that the peak pressure locations coincide with the cartesian origin.

As these focal region shifts are automatically accounted for in the comparison process they were not included in the uncertainty analysis.

The measurement uncertainties that were included and accounted for in this study are summarized in Table 7.5. It should be noted that the positional uncertainty $U_D$ and focal region distortion $U_\Delta$ were considered identical in value for the different measurement parameters.

| Parameter | N/R | $U_P$ [dB] | $U_D$ [$\lambda$] | $U_\Delta$ [$\lambda$] |
|---|---|---|---|---|
| Hydrophone Positioning | N | 0.00 | 0.37 | 0.37 |
| Hydrophone Spatial Averaging | R | 0.00 | 0.053 | 0.053 |
| Measurement Noise Level | N | 0.26 | 0.00 | 0.00 |
| Measurement Nonlinearity | N | 0.10 | 0.00 | 0.00 |
| Transducer Drift | N | 0.10 | 0.00 | 0.00 |
| Comb. Meas. Setup Uncert. | | 0.29 | 0.37 | 0.37 |
| Exp. Meas. Setup Uncert. (k=2) | | 0.59 | 0.75 | 0.75 |

**Table 7.5**: *Uncertainties inherent to the measurement setup that were included in the uncertainty analysis. $U_P$ denotes the uncertainty a given aspect of the measurement setup contributes to the pressure measurements in* dB, *while $U_D$ and $U_\Delta$ signify the positional uncertainty and focal region distortion as a fraction of the wavelength $\lambda$. The combined and expanded uncertainties of the measurement setup can also be seen.*

#### 7.2.4.2 Acoustic Properties

As an inherent uncertainty is related to the measurement of a material's acoustic properties, the speed of sound $c$, attenuation coefficient $\alpha$, and the density $\rho$ of each material involved were varied and their impact was investigated. This pertains to the following materials:

- **Water**: Even though the acoustic properties of water are well defined in literature, it was considered important to not exclude it from this analysis as water constitutes the primary medium of propagation and a $\pm 1\%$ variation was considered for all its properties.

- **Plexiglass**: As discussed in Section 7.2.3, the acoustic properties of plexiglass were set to those of PMMA [505]. Due to this uncertainty and in order to concretely assess the impact of its properties, a $\pm 10\%$ variation was considered for its $c$ and $\alpha$ properties, while $\rho$ was varied by $\pm 20\%$.

- **Focus distorting sample materials**: Per Section 7.2.1.3, the different materials of the focus distorting samples were acoustically characterized by their manufacturer (CIRS Inc., Norfolk, VA, USA). The different acoustic properties can be seen in Table 7.4. However, the manufacturer reported an estimated accuracy of $\pm 5\%$ for the $c$ and $\alpha$ measurements, and $\pm 1\%$ for the $\rho$ measurements. Therefore, these reported variations were applied to the different materials and their impact on the simulation results was ascertained.

The acoustic properties varied for the different materials, their variation percentages, as well as the reference and evaluation values of these properties are summarized in Table 7.6.

### 7.2.4.3 Numerical Aspects

Per Section 5.1.3, the accuracy and stability of the FDTD method is dependent on various numerical parameters related to the computational grid characteristics, the simulation duration, and the absorbing boundary conditions. Thus the following parameters were examined:

- **Simulation resolution**: The impact of the spatial discretization, i.e., the grid-step, which in the reference-simulation (see Section 7.2.3) defaults to $0.25 \, \text{mm}$ or ca. $\lambda/11$, was investigated. This was performed by performing several simulations with increased or decreased grid-step and ascertaining the impact of this variation. The simulated modifications of the grid-step, relative to the default grid-step of $0.25 \, \text{mm}$ were: $-30\%, -25\%, \pm 20\%, \pm 15\%, \pm 10\%$. Note that while a decrease of the default grid-step by $25\%$ and $30\%$ was simulated and included in the analysis, no matching increase in the grid-step was considered. The reason for this is that such an increase in grid-step, and therefore decrease in resolution, would result in an overly under-discretized simulation, which would yield very large cumulative numerical errors, and invalidate the results of the simulation.

- **Number of simulated periods**: The measurement setup was configured so as to only generate acoustic wave for $40$ periods, which was reproduced in the reference-simulation setup (see Sections 7.2.2.3 and 7.2.3). However, it was deemed necessary to vary the number of simulated periods and assess the influence of this parameter. Variations of $\pm 10\%, \pm 15\%$, and $\pm 20\%$ were considered.

| Material | Parameter | Unit | Variation (%) | Ref. | Eval. |
|---|---|---|---|---|---|
| Water | $c \uparrow$ | m/s | +1 | 1500 | 1515 |
| | $c \downarrow$ | m/s | -1 | 1500 | 1485 |
| | $\alpha \uparrow$ | Np/m | +1 | 0.0076 | 0.007676 |
| | $\alpha \downarrow$ | Np/m | -1 | 0.0076 | 0.007524 |
| | $\rho \uparrow$ | kg/m$^3$ | +1 | 1000 | 1010 |
| | $\rho \downarrow$ | kg/m$^3$ | -1 | 1000 | 990 |
| Plexiglass | $c \uparrow$ | m/s | +10 | 2750 | 3025 |
| | $c \downarrow$ | m/s | -10 | 2750 | 2475 |
| | $\alpha \uparrow$ | Np/m | +10 | 6.875 | 7.5625 |
| | $\alpha \downarrow$ | Np/m | -10 | 6.875 | 6.1875 |
| | $\rho \uparrow$ | kg/m$^3$ | +20 | 1192 | 1430.3 |
| | $\rho \downarrow$ | kg/m$^3$ | -20 | 1192 | 953.6 |
| Delrin | $c \uparrow$ | m/s | +5 | 2430 | 2551.5 |
| | $c \downarrow$ | m/s | -5 | 2430 | 2308.5 |
| | $\alpha \uparrow$ | Np/m | +5 | 18.975 | 19.92375 |
| | $\alpha \downarrow$ | Np/m | -5 | 18.975 | 18.02625 |
| | $\rho \uparrow$ | kg/m$^3$ | +1 | 1430 | 1444.3 |
| | $\rho \downarrow$ | kg/m$^3$ | -1 | 1430 | 1415.7 |
| Polyurethane | $c \uparrow$ | m/s | +5 | 1700 | 1785 |
| | $c \downarrow$ | m/s | -5 | 1700 | 1615 |
| | $\alpha \uparrow$ | Np/m | +5 | 37.95 | 39.8475 |
| | $\alpha \downarrow$ | Np/m | -5 | 37.95 | 36.0525 |
| | $\rho \uparrow$ | kg/m$^3$ | +1 | 1130 | 1141.3 |
| | $\rho \downarrow$ | kg/m$^3$ | -1 | 1130 | 1118.7 |
| RTV Silicone | $c \uparrow$ | m/s | +5 | 1000 | 1050 |
| | $c \downarrow$ | m/s | -5 | 1000 | 950 |
| | $\alpha \uparrow$ | Np/m | +5 | 12.65 | 13.2825 |
| | $\alpha \downarrow$ | Np/m | -5 | 12.65 | 12.0175 |
| | $\rho \uparrow$ | kg/m$^3$ | +1 | 1080 | 1090.8 |
| | $\rho \downarrow$ | kg/m$^3$ | -1 | 1080 | 1069.2 |

**Table 7.6**: *Acoustic properties investigated during the uncertainty assessment for the materials involved in the different measurement setups.*

- **Number of PML layers**: As detailed in Section 7.2.3, the behavior of the acoustic absorbers lining the water-tank (see Section 7.2.1.1), was numerically modeled through 16 PML layers, a model extensively discussed in Section 5.3.2, at the computational domain boundaries. This number of layers was varied by $\pm 25\%$ to determine the influence of this approximation on the simulation results.

- **Grid Rotation**: In order to ascertain the impact of numerical dispersion, a phenomenon inherent to the FDTD method which was discussed in Section 5.1.3, the entire setup was rotated by $45°$. Thusly, the impact of wave propagation along oblique directions, relative to the cartesian axes, could be ascertained.

The numerical aspects described above, their variation percentages, as well as the reference and evaluation values of these parameters are summarized in Table 7.7.

| Parameter | Unit | Variation (%) | Ref. | Eval. |
|---|---|---|---|---|
| No. PML Layers ↑ | - | +25 | 16 | 20 |
| No. PML Layers ↓ | - | -25 | 16 | 12 |
| Grid Step ↑ | mm | +20 | 0.25 | 0.30 |
| Grid Step ↑ | mm | +15 | 0.25 | 0.2875 |
| Grid Step ↑ | mm | +10 | 0.25 | 0.275 |
| Grid Step ↓ | mm | -10 | 0.25 | 0.225 |
| Grid Step ↓ | mm | -15 | 0.25 | 0.2125 |
| Grid Step ↓ | mm | -20 | 0.25 | 0.20 |
| Grid Step ↓ | mm | -25 | 0.25 | 0.1875 |
| Grid Step ↓ | mm | -30 | 0.25 | 0.175 |
| No. Periods ↑ | - | +20 | 40 | 48 |
| No. Periods ↑ | - | +15 | 40 | 46 |
| No. Periods ↑ | - | +10 | 40 | 44 |
| No. Periods ↓ | - | -10 | 40 | 36 |
| No. Periods ↓ | - | -15 | 40 | 34 |
| No. Periods ↓ | - | -20 | 40 | 32 |
| Grid Rotation | ° | - | 0 | 45 |

**Table 7.7**: *Numerical aspects that were investigated during the uncertainty assessment.*

### 7.2.4.4  Geometric Parameters

It can be expected that variations in the geometric characteristics of the entire simulated geometry would greatly affect the simulation results. Therefore, the following parameters were examined:

- **Sample translation and rotation along the suspension rods**: Even though the utmost care was taken and high precision drills were employed while forming the holes in the focus distortion samples, that would house the suspension rods, this process was very challenging, particularly for the cylindrical and spherical samples. Should these holes not be perfectly centered and perpendicular to each other, the sample would be suspended at a shifted position and angle relative to the transducer and the geometric focus. This would result in the sample not being symmetrically positioned around the propagation axis and yielding a different interference pattern to the expected one. Therefore, evaluation simulations were performed where the sample was translated/rotated along/around each of the two suspension rods. Furthermore, additional evaluation simulation were performed where the sample was translated along the propagation axis.

- **Sample dimensions**: As discussed in Section 7.2.1.3 and shown in Table 7.3, the sample dimensions were measured with a $\pm 0.1$ mm accuracy. However, this variation cannot be taken into account as the minimum grid-step in the computational grid was set to $0.25$ mm (see Section 7.2.3). Nevertheless, for an acoustic wavelength of ca. $2.73$ mm, potential inaccuracies of this order are smaller than $\lambda/27$ and can be safely dismissed. Thus, this uncertainty was not included into the analysis.

- **Transducer curvature radius and aperture width**: Per the specifications of the transducer's manufacturer (Imasonic, France), the transducer's curvature radius and aperture width cannot be defined with absolute precision and an uncertainty is given for these dimensions. However, as discussed in Section 2.2.2.2, these characteristics define the focal depth of the transducer (and therefore the location of the geometric focus) and the size of the focal region. As these quantities are pivotal to the characteristics of the acoustic pressure distribution, they were varied within the uncertainty limits defined by the manufacturer.

The geometrical aspects described above and the reference and evaluation values of these parameters are summarized in Table 7.8.

## 7.2.5 Comparison in Homogeneous Setup

Initial comparisons were performed with a homogeneous setup, i.e., in the absence of a focus distorting sample and the plexiglass suspension rods detailed in Section 7.2.1.1. Two studies in setups involving the focus distorting samples discussed in Section 7.2.1.3, namely the smaller Delrin cylinder and Polyurethane block, are presented in Sections 7.2.6 and 7.2.7 respectively.

| | Parameter | Unit | Ref. | Eval. |
|---|---|---|---|---|
| | Curvature Radius ↑ | mm | 64 | 66 |
| | Curvature Radius ↓ | mm | 64 | 62 |
| Transducer | Aperture Width ↑ | mm | 80 | 80.2 |
| | Aperture Width ↓ | mm | 80 | 79.8 |
| | Along Lower Rod ↑ | mm | 0 | 2.5 |
| | Along Lower Rod ↓ | mm | 0 | -2.5 |
| | Along Propagation Axis ↑ | mm | 0 | 2.5 |
| Sample Translation | Along Propagation Axis ↓ | mm | 0 | -2.5 |
| | Along Upper Rod ↑ | mm | 0 | 2.5 |
| | Along Upper Rod ↓ | mm | 0 | -2.5 |
| | Around Lower Rod ↑ | ° | 0 | 2.5 |
| | Around Lower Rod ↓ | ° | 0 | -2.5 |
| Sample Rotation | Around Upper Rod ↑ | ° | 0 | 2.5 |
| | Around Upper Rod ↓ | ° | 0 | -2.5 |

**Table 7.8**: *Geometrical parameters that were investigated during the uncertainty assessment for the geometries involved in the measurement setups.*

A full uncertainty analysis, as described in Section 7.2.4, was performed for this case and is presented in Section 7.2.5.1. The comparison between the measured and simulated pressure distributions was performed with the gamma method, which is presented in Section 7.2.5.2. Finally, the comparison results for this case are outlined in Section 7.2.5.3.

### 7.2.5.1   Uncertainty Analysis

In addition to the connected-component analysis described in Section 7.2.4, an automatized local-maxima analysis was performed for the case of the homogeneous setup in order to ascertain the local distortion of the focal region as a result of the varying parameters in each reference-evaluation simulation pair.

In this secondary analysis, the peak absolute pressure was identified and the distributions were thresholded between 25% and 50% of that peak pressure thus removing the primary focal region that was analyzed in the connected-component analysis (see Section 7.2.4). Subsequently, all local maxima were extracted within this thresholded distribution, and, based on their intensity and relative location, 5 maxima denoting secondary focal regions were automatically identified. These maxima, named $SS$, $SW$, $SE$, $NW$, and $NE$ can be seen in Figure 7.10.

*(a)* *(b)*
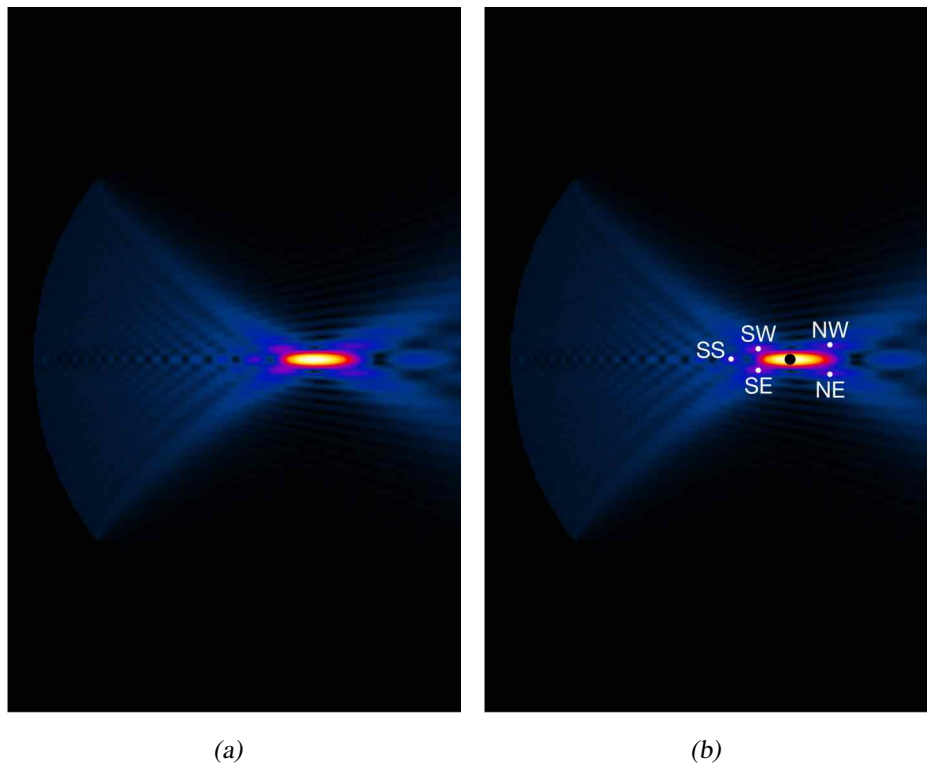
**Figure 7.10**: *Cross-section of absolute pressure amplitude through the location of the peak for the reference simulation of the homogeneous setup case (a). The local maxima named $SS$, $SW$, $SE$, $NW$, and $NE$, extracted in order to ascertain the local distortion effects of the focal region, are marked as white points (b), while the center of the focal region as extracted in the connected-component analysis (see Section 7.2.4), is marked as a black point.*

The coordinates of these local maxima were identified for each reference-evaluation simulation pair. The shift of the primary focal region's connected component center (see Section 7.2.4) was used to 'correct' the absolute shifts of these local maxima in order to obtain the local shifts and ascertain the focal region distortion. These corrected shifts were calculated for each reference-evaluation simulation pair and were included in the uncertainty analysis for the homogeneous setup case.

The results of the uncertainty analysis for the different material, numerical, and geometrical parameters detailed in Section 7.2.4, were grouped and summarized in Tables 7.9, 7.10, and 7.11 respectively.

As can be seen in Table 7.9, the only material parameter with a notable influence on the simulation results was the sound speed $c$ of water, while the attenuation coefficient $\alpha$ and density $\rho$ had little to no effect. This behavior can be attributed to the fact that the acoustic wavelength in a medium is directly dependent on the acoustic frequency and the medium's

| Material | Param. | Unit | Ref. | Eval. | Δ | $\Delta_P$ [dB] | $\Delta_{SS}$ [λ] | $\Delta_{SW}$ [λ] | $\Delta_{SE}$ [λ] | $\Delta_{NW}$ [λ] | $\Delta_{NE}$ [λ] | $\Delta_V$ [dB] | $\Delta_D$ [λ] | $f_P$ [dB/%] | $f_{SS}$ [λ/%] | $f_{SW}$ [λ/%] | $f_{SE}$ [λ/%] | $f_{NW}$ [λ/%] | $f_{NE}$ [λ/%] | $f_V$ [dB/%] | $f_D$ [λ/%] |
|---|---|---|---|---|---|---|---|---|---|---|---|---|---|---|---|---|---|---|---|---|---|
|  | $c\uparrow$ | m/s | 1500 | 1515 | 1% | -0.09 | 0.00 | 0.00 | 0.00 | 0.20 | 0.20 | 0.00 | -0.09 | 0.00 | 0.00 | 0.00 | 0.00 | 0.20 | 0.20 | 0.21 | 0.00 |
|  | $c\downarrow$ | m/s | 1500 | 1485 | -1% | 0.09 | 0.09 | 0.18 | 0.18 | 0.09 | 0.09 | -0.27 | 0.09 | -0.09 | 0.09 | 0.18 | 0.18 | 0.09 | 0.09 | 0.26 | 0.09 |
| Water | $\alpha\uparrow$ | Np/m | 0.0076 | 0.007676 | 1% | 0.00 | 0.00 | 0.00 | 0.00 | 0.00 | 0.00 | 0.00 | 0.00 | 0.00 | 0.00 | 0.00 | 0.00 | 0.00 | 0.00 | 0.00 | 0.00 |
|  | $\alpha\downarrow$ | Np/m | 0.0076 | 0.007524 | -1% | 0.00 | 0.00 | 0.00 | 0.00 | 0.00 | 0.00 | 0.00 | 0.00 | 0.00 | 0.00 | 0.00 | 0.00 | 0.00 | 0.00 | 0.00 | 0.00 |
|  | $\rho\uparrow$ | kg/m³ | 1000 | 1010 | 1% | 0.00 | 0.00 | 0.00 | 0.00 | 0.00 | 0.00 | 0.00 | 0.00 | 0.00 | 0.00 | 0.00 | 0.00 | 0.00 | 0.00 | 0.00 | 0.00 |
|  | $\rho\downarrow$ | kg/m³ | 1000 | 990 | -1% | 0.00 | 0.00 | 0.00 | 0.00 | 0.00 | 0.00 | 0.00 | 0.00 | 0.00 | 0.00 | 0.00 | 0.00 | 0.00 | 0.00 | 0.00 | 0.00 |

**Table 7.9:** *Results of the uncertainty analysis for the material parameters (see Table 7.6) investigated in the homogeneous setup. The value of each parameter for both the reference (Ref.) and evaluation (Eval.) simulations as well as the variation between the two (Δ) can be seen. The impact of this parameter variation on the focal region's peak absolute pressure ($\Delta_P$), focal region distortion ($\Delta_{SS}$, $\Delta_{SW}$, $\Delta_{SE}$, $\Delta_{NW}$, $\Delta_{NE}$), volume ($\Delta_V$), and absolute focal shift ($\Delta_D$) can also be seen. Lastly, the sensitivity factors ($f_P$, $f_{SS}$, $f_{SW}$, $f_{SE}$, $f_{NW}$, $f_{NE}$, $f_V$, $f_D$) resulting from the uncertainty analysis can be seen for all investigated variables.*

| Param. | Unit | Ref | Eval | $\Delta_P$ [dB] | $\Delta_{SS}$ [$\lambda$] | $\Delta_{SW}$ [$\lambda$] | $\Delta_{SE}$ [$\lambda$] | $\Delta_{NW}$ [$\lambda$] | $\Delta_{NE}$ [$\lambda$] | $\Delta_V$ [dB] | $\Delta_D$ [$\lambda$] |
|---|---|---|---|---|---|---|---|---|---|---|---|
| No. PML Layers ↑ | - | 16 | 20 | 0.00 | 0.00 | 0.00 | 0.00 | 0.00 | 0.00 | 0.00 | 0.00 |
| No. PML Layers ↓ | - | 16 | 12 | 0.00 | 0.00 | 0.00 | 0.00 | 0.00 | 0.00 | 0.00 | 0.00 |
| Grid Step ↑ | mm | 0.25 | 0.3 | -0.24 | 0.14 | 0.25 | 0.26 | 0.05 | 0.10 | -0.74 | 0.44 |
| Grid Step ↑ | mm | 0.25 | 0.2875 | -0.24 | 0.13 | 0.19 | 0.19 | 0.07 | 0.05 | -0.18 | 0.32 |
| Grid Step ↑ | mm | 0.25 | 0.275 | -0.19 | 0.03 | 0.06 | 0.07 | 0.15 | 0.14 | -0.08 | 0.18 |
| Grid Step ↓ | mm | 0.25 | 0.225 | -0.08 | 0.11 | 0.09 | 0.05 | 0.12 | 0.13 | 0.15 | 0.13 |
| Grid Step ↓ | mm | 0.25 | 0.2125 | -0.17 | 0.15 | 0.16 | 0.16 | 0.19 | 0.19 | 0.32 | 0.23 |
| Grid Step ↓ | mm | 0.25 | 0.2 | -0.13 | 0.22 | 0.08 | 0.10 | 0.27 | 0.29 | 0.33 | 0.28 |
| Grid Step ↓ | mm | 0.25 | 0.1875 | -0.09 | 0.19 | 0.13 | 0.13 | 0.35 | 0.36 | 0.14 | 0.32 |
| Grid Step ↓ | mm | 0.25 | 0.175 | -0.10 | 0.18 | 0.12 | 0.12 | 0.32 | 0.32 | 0.21 | 0.39 |
| No. Periods ↑ | - | 40 | 48 | 0.00 | 0.00 | 0.00 | 0.00 | 0.13 | 0.13 | 0.00 | 0.00 |
| No. Periods ↑ | - | 40 | 46 | 0.00 | 0.00 | 0.00 | 0.00 | 0.13 | 0.13 | 0.00 | 0.00 |
| No. Periods ↑ | - | 40 | 44 | 0.00 | 0.00 | 0.00 | 0.00 | 0.13 | 0.13 | -0.01 | 0.00 |
| No. Periods ↓ | - | 40 | 36 | 0.00 | 0.09 | 0.18 | 0.18 | 0.18 | 0.18 | 0.00 | 0.09 |
| No. Periods ↓ | - | 40 | 34 | 0.00 | 0.09 | 0.09 | 0.09 | 0.29 | 0.29 | 0.00 | 0.09 |
| No. Periods ↓ | - | 40 | 32 | 0.00 | 0.09 | 0.09 | 0.09 | 0.29 | 0.29 | 0.00 | 0.09 |
| Grid Rotation | ° | 0 | 45 | -0.79 | 0.40 | 0.27 | 0.27 | 1.60 | 1.60 | 1.58 | 0.91 |

**Table 7.10**: *Results of the uncertainty analysis for the numerical parameters (see Table 7.7) investigated in the homogeneous setup. The value of each parameter for both the reference (Ref.) and evaluation (Eval.) simulations can be seen. The impact of this parameter variation on the focal region's peak absolute pressure ($\Delta_P$), focal region distortion ($\Delta_{SS}$, $\Delta_{SW}$, $\Delta_{SE}$, $\Delta_{NW}$, $\Delta_{NE}$), volume ($\Delta_V$), and absolute focal shift ($\Delta_D$) can also be seen. It should be noted that given the nature of these parameters, the calculation of sensitivity factors and uncertainty was not applicable and was therefore omitted.*

speed of sound (see Equation 1.1). Such changes in the the acoustic wavelength may alter the interference patterns between the different wavefronts, a phenomenon detailed in Section 1.1.3.5, and result in significantly different acoustic pressure distributions.

In terms of the uncertainties pertaining to the numerical aspects of the homogeneous setup simulations (see Table 7.10), it can be seen that the uncertainty analysis was dominated by the case of the grid-rotation were the entire setup was rotated by $45°$ (see Section 7.2.4.3). These large uncertainties can be attributed to numerical dispersion effects, described in Section 5.1.3, which become prominent when the setup is positioned at oblique angles to the cartesian axes. Amelioration of such effects would require higher grid resolutions, i.e., discretization, of the simulated setup.

Similarly, a noticeable impact was observed when varying the grid-step, and thus the resolution of the computational domain. It should, however, be noted that decreasing the grid-step, thus increasing resolution, yielded a more modest impact on the simulation results than was observed with a decrease in resolution. In particular, the observed deviations (see Table 7.10), appear to converge with increasing resolution to values similar

| Param. | Unit | Ref. | Eval. | Δ | $\Delta_P$ [dB] | $\Delta_{SS}$ [λ] | $\Delta_{SW}$ [λ] | $\Delta_{SE}$ [λ] | $\Delta_{NW}$ [λ] | $\Delta_{NE}$ [λ] | $\Delta_V$ [dB] | $\Delta_D$ [λ] | $f_P$ [dB/mm] | $f_{SS}$ [λ/mm] | $f_{SW}$ [λ/mm] | $f_{SE}$ [λ/mm] | $f_{NW}$ [λ/mm] | $f_{NE}$ [λ/mm] | $f_V$ [dB/mm] | $f_D$ [λ/mm] |
|---|---|---|---|---|---|---|---|---|---|---|---|---|---|---|---|---|---|---|---|---|
| Curvature Radius ↑ | mm | 64 | 66 | 2mm | -0.30 | 0.27 | 0.18 | 0.18 | 0.29 | 0.29 | 1.09 | 0.64 | -0.15 | 0.14 | 0.09 | 0.09 | 0.14 | 0.14 | 0.55 | 0.32 |
| Curvature Radius ↓ | mm | 64 | 62 | -2mm | 0.22 | 0.20 | 0.20 | 0.20 | 0.18 | 0.18 | -1.02 | 0.64 | -0.11 | 0.10 | 0.10 | 0.10 | 0.09 | 0.09 | 0.51 | 0.32 |
| Aperture Width ↑ | mm | 80 | 80.2 | 0.2mm | 0.00 | 0.00 | 0.00 | 0.00 | 0.00 | 0.00 | 0.00 | 0.00 | 0.00 | 0.00 | 0.00 | 0.00 | 0.00 | 0.00 | 0.01 | 0.00 |
| Aperture Width ↓ | mm | 80 | 79.8 | -0.2mm | -0.16 | 0.09 | 0.00 | 0.00 | 0.13 | 0.13 | 0.22 | 0.00 | 0.78 | 0.46 | 0.00 | 0.00 | 0.65 | 0.65 | -1.11 | 0.00 |

**Table 7.11**: *Results of the uncertainty analysis for the geometrical parameters (see Table 7.8) investigated in the homogeneous setup. The value of each parameter for both the reference (Ref.) and evaluation (Eval.) simulations as well as the variation between the two (Δ) can be seen. The impact of this parameter variation had on the focal region's peak absolute pressure ($\Delta_P$), focal region distortion ($\Delta_{SS}$, $\Delta_{SW}$, $\Delta_{SE}$, $\Delta_{NW}$, $\Delta_{NE}$), volume ($\Delta_V$), and absolute focal shift ($\Delta_D$) can also be seen. Lastly, the sensitivity factors ($f_P$, $f_{SS}$, $f_{SW}$, $f_{SE}$, $f_{NW}$, $f_{NE}$, $f_V$, $f_D$) resulting from the uncertainty analysis can be seen for all investigated variables.*

to those observed for the reference simulation. Thus in order to calculate the uncertainty contribution for this particular case a nonlinear fit was performed on the observed deviations and given that this uncertainty was an offset rather than a symmetrical errors, the calculated value was multiplied by 2 to account for either an increase or decrease in the investigated variables.

Lastly, in regards to the investigated geometrical parameters, it can be seen that variations in the geometrical characteristics of the transducer can yield a significant uncertainty in the simulation results. Of course, that can be attributed to the fact that the curvature radius and aperture width of a spherically-focused single element transducer directly affect the characteristics of the focal region as was detailed in Sections 2.2.2.2 and 2.3. The fact that these large deviations were observed when varying these parameters within the transducer's manufacturing uncertainty, as was discussed in Section 7.2.4.4, suggests that precise characterization of the measurement setup is pivotal to the accuracy of the results.

Uncertainty budgets were compiled from the findings in Tables 7.9, 7.10, and 7.11 in order to calculate the final uncertainty contribution of each parameter in the homogeneous setup. The uncertainty budgets for the investigated material, numerical, and geometrical parameters can be seen in Tables 7.12, 7.13, and 7.14 respectively.

It should be noted that for the majority of examined parameters these tables were compiled by selecting the absolute maximum uncertainty contribution for each of the the investigated variables, i.e., focal region peak pressure, local maxima shifts, volume, and focal shift that resulted from the decrease or increase of each investigated parameter. In the case of the focal distortion uncertainty, the maximum uncertainty contribution of the local-maxima shift evaluations was considered. Lastly, in the case of parameters like the number of simulated periods and grid-step (see Section 7.2.4.3), as the values of the examined variables appear to converge with increasing number of periods and resolution respectively, the deviation between the case with the greatest number of periods/resolution and the reference simulation was selected instead.

The combined and expanded (k=2) uncertainties for the simulation and measurement setup are presented in Tables 7.15 and 7.16, while Table 7.17 shows the total combined uncertainty resulting from the uncertainties in both the simulated and measurement setups.

Given the precise nature of the simulated setup in regards to geometrical and material parameters, the uncertainty contribution of those parameters was considered to be part of the measurement uncertainty budget. The reason for this was that while the precise material properties and geometrical attributes of the water medium, the plexiglass rods, and the material samples could be precisely defined in the simulated setups, this precision would not be feasible in the measurement setups. Thus, the simulation uncertainty budget presented in Table 7.15 contained only the uncertainty contributions of the numerical parameters presented in Table 7.10. However, the uncertainty budget of the measurement

setup presented in Table 7.16 comprised the uncertainty contributions of the measurement components (Table 7.5), the material parameters (Table 7.9), as well as geometrical parameters (Table 7.11).

It should also be noted that the total simulation uncertainty only included the focal region peak pressure uncertainty, the maximum absolute positional uncertainty, and the maximum uncertainty of the local maxima shifts which was considered as the focal distortion uncertainty.

### 7.2.5.2 Gamma Method

In order to compare the 3D absolute pressure distributions between measurements and the corresponding simulations, the gamma dose distribution comparison method [508, 509], from here on referred to simply as the 'gamma method', was employed. Since its introduction by Low et al. [508], this method has been extensively employed in the explicit verification of radiotherapy plans [510–513].

This method performs a comparison between 3D distributions for each point in the reference distribution, which in this case is the measured absolute pressure distribution, against an evaluated distribution, i.e., the simulation results. Comparison is performed in both the 'dose' and spatial domain by combining a distance-to-agreement (DTA), and a dose-difference (DD) criterium calculating a $\gamma$ index for each reference point. A $\gamma$ index below 1.0 signifies agreement between the two distributions at a particular reference point for the given DTA and DD criteria, while larger values indicate disagreement. A detailed description of this method can be found in [508, 509, 514].

The gamma method is akin to the classic uncertainty analysis [515], which determines whether a certain simulation point agrees with the corresponding measurement point within the (expanded) combined uncertainty. The two differences are:

- Instead of always comparing the simulation and measurement points at the same location while considering the position uncertainty as a value uncertainty based on the local gradient, the gamma method gives more freedom in finding corresponding points and penalizes the distance disagreement based on the positioning uncertainty. These two uncertainties are finally combined in a root-sum-square manner making the local gamma agreement value very comparable to a normalized combined uncertainty based agreement analysis.

- The gamma method provides a natural way of visualizing the spatial variation of the measurement-simulation agreement, while a simple absolute or relative difference has a tendency of automatically highlighting regions with high gradients.

| Material | Param. | $\Delta$ | $\sigma$ | N/R | $f_P$ [dB/%] | $f_{SS}$ [λ/%] | $f_{SW}$ [λ/%] | $f_{SE}$ [λ/%] | $f_{NW}$ [λ/%] | $f_{NE}$ [λ/%] | $f_V$ [dB/%] | $f_D$ [λ/%] | $U_P$ [dB] | $U_{SS}$ [λ] | $U_{SW}$ [λ] | $U_{SE}$ [λ] | $U_{NW}$ [λ] | $U_{NE}$ [λ] | $U_V$ [dB] | $U_D$ [λ] |
|---|---|---|---|---|---|---|---|---|---|---|---|---|---|---|---|---|---|---|---|---|
| Water | $c$ | 1% | 15 | N | -0.09 | 0.09 | 0.18 | 0.18 | 0.20 | 0.20 | 0.27 | 0.09 | | | | | | | | |
| | $\alpha$ | 1% | 7.6e-5 | N | 0.00 | 0.00 | 0.00 | 0.00 | 0.00 | 0.00 | 0.00 | 0.00 | | | | | | | | |
| | $\rho$ | 1% | 10 | N | 0.00 | 0.00 | 0.00 | 0.00 | 0.00 | 0.00 | 0.00 | 0.00 | | | | | | | | |
| Combined Uncertainty | | | | | | | | | | | | | 0.09 | 0.09 | 0.18 | 0.18 | 0.20 | 0.20 | 0.27 | 0.09 |
| Expanded Uncertainty (k=2) | | | | | | | | | | | | | 0.18 | 0.18 | 0.37 | 0.37 | 0.41 | 0.41 | 0.54 | 0.18 |

**Table 7.12**: *Uncertainty budget for the material parameters (see Table 7.6) investigated in the homogeneous setup. The variation ($\Delta$), standard deviation ($\sigma$), and distribution shape (Normal/Rectangular - N/R) of each parameter can be seen. In addition, the sensitivity factors ($f_P$, $f_{SS}$, $f_{SW}$, $f_{SE}$, $f_{NW}$, $f_{NE}$, $f_V$, $f_D$), and the calculated uncertainties ($U_P$, $U_{SS}$, $U_{SW}$, $\Delta_{SE}$, $\Delta_{NW}$, $\Delta_{NE}$, $\Delta_V$, $\Delta_D$) can be seen for all investigated variables.*

| Param. | N/R | $U_P$ [dB] | $U_{SS}$ [$\lambda$] | $U_{SW}$ [$\lambda$] | $U_{SE}$ [$\lambda$] | $U_{NW}$ [$\lambda$] | $U_{NE}$ [$\lambda$] | $U_V$ [dB] | $U_D$ [$\lambda$] |
|---|---|---|---|---|---|---|---|---|---|
| No. PML Layers | N | 0.00 | 0.00 | 0.00 | 0.00 | 0.00 | 0.00 | 0.00 | 0.00 |
| Grid Step | R | 0.11 | 0.21 | 0.14 | 0.14 | 0.37 | 0.37 | 0.24 | 0.64 |
| No. Periods | N | 0.00 | 0.00 | 0.00 | 0.00 | 0.07 | 0.07 | 0.00 | 0.00 |
| Grid Rotation | R | 0.46 | 0.23 | 0.16 | 0.16 | 0.92 | 0.92 | 0.91 | 0.53 |
| Combined Uncertainty | | 0.47 | 0.31 | 0.21 | 0.21 | 1.00 | 1.00 | 0.94 | 0.83 |
| Expanded Uncertainty (k=2) | | 0.78 | 0.51 | 0.35 | 0.35 | 1.65 | 1.65 | 1.55 | 1.36 |

*Table 7.13*: *Uncertainty budget for the numerical parameters (see Table 7.7) investigated in the homogeneous setup. The calculated uncertainties ($U_P$, $U_{SS}$, $U_{SW}$, $U_{SE}$, $U_{NW}$, $U_{NE}$, $U_V$, $U_D$) can be seen for all investigated variables. It should be noted that given the nature of these parameters, the calculation of sensitivity factors was not applicable and was therefore omitted.*

### 7.2.5.3  Results

In the interest of defining the DD and DTA tolerances for use in the gamma method comparison described above, the expanded (k=2) total uncertainty in focal region peak pressure $U_P$ and focal distortion $U_\Delta$ were used. As can be seen in Table 7.17, a $k = 2$ uncertainty would result in a DD tolerance of $1.04$ dB or $12.72\%$, while the DTA tolerance was calculated at $1.88\lambda$ with $\lambda$ being the acoustic wavelength in water for the given setup.

Prior to comparing the measured and simulated pressure distributions, the latter was normalized in order to account for the lack of absolute pressure measurements. Following registration of the two datafields, as described in Section 7.2.4.1, the deposited acoustic energy was calculated within the measurement volume based on Equation 1.16. Subsequently, the same quantity was calculated in a matching volume in the simulated datafield. Normalization was then performed by multiplying the simulated pressure field by a factor $f$ calculated as shown below:

$$f = \frac{P_{measurement}}{P_{simulation}} \tag{7.3}$$

where $P_{measurement}$ is the integrated deposited acoustic energy within the measured volume and $P_{simulation}$ is the same quantity calculated in a matching volume on the simulated distribution.

The gamma method comparison results can be seen in Figure 7.11. Perfect agreement can be seen for these tolerances as all $\gamma$ indices lie below a value of 1.0. The minor disagreements, within the uncertainty, observed between the two pressure distributions can

| Param. | $\Delta$ | $\sigma$ | N/R | $f_P$ [dB/mm] | $f_{SS}$ [$\lambda$/mm] | $f_{SW}$ [$\lambda$/mm] | $f_{SE}$ [$\lambda$/mm] | $f_{NW}$ [$\lambda$/mm] | $f_{NE}$ [$\lambda$/mm] | $f_V$ [dB/mm] | $f_D$ [$\lambda$/mm] | $U_P$ [dB] | $U_{SS}$ [$\lambda$] | $U_{SW}$ [$\lambda$] | $U_{SE}$ [$\lambda$] | $U_{NW}$ [$\lambda$] | $U_{NE}$ [$\lambda$] | $U_V$ [dB] | $U_D$ [$\lambda$] |
|---|---|---|---|---|---|---|---|---|---|---|---|---|---|---|---|---|---|---|---|
| Curvature Radius | 2mm | 2 | R | -0.15 | 0.14 | 0.10 | 0.10 | 0.14 | 0.14 | 0.55 | 0.32 | 0.18 | 0.16 | 0.12 | 0.12 | 0.17 | 0.17 | 0.63 | 0.37 |
| Aperture Width | 0.2mm | 0.2 | R | 0.78 | 0.46 | 0.00 | 0.00 | 0.65 | 0.65 | -1.11 | 0.00 | 0.09 | 0.05 | 0.00 | 0.00 | 0.07 | 0.07 | 0.13 | 0.00 |
| Combined Uncertainty | | | | | | | | | | | | 0.20 | 0.17 | 0.12 | 0.12 | 0.18 | 0.18 | 0.64 | 0.37 |
| Expanded Uncertainty (k=2) | | | | | | | | | | | | 0.33 | 0.28 | 0.20 | 0.20 | 0.30 | 0.30 | 1.07 | 0.61 |

**Table 7.14**: *Uncertainty budget for the geometrical parameters (see Table 7.8) investigated in the homogeneous setup. The variation ($\Delta$), standard deviation ($\sigma$), and distribution shape (Normal/Rectangular - N/R) of each parameter can be seen. In addition, the sensitivity factors ($f_P$, $f_{SS}$, $f_{SW}$, $f_{SE}$, $f_{NW}$, $f_{NE}$, $f_V$, $f_D$), and the calculated uncertainties ($U_P$, $U_{SS}$, $U_{SW}$, $U_{SW}$, $\Delta_{SE}$, $\Delta_{NW}$, $\Delta_{NE}$, $\Delta_V$, $\Delta_D$) can be seen for all investigated variables.*

|  | $U_P$ [dB] | $U_{SS}$ [λ] | $U_{SW}$ [λ] | $U_{SE}$ [λ] | $U_{NW}$ [λ] | $U_{NE}$ [λ] | $U_V$ [dB] | $U_D$ [λ] |
|---|---|---|---|---|---|---|---|---|
| Comb. Num. Uncert. (Table 7.13) | 0.47 | 0.31 | 0.21 | 0.21 | 1.00 | 1.00 | 0.94 | 0.83 |
| Comb. Sim. Uncert. | 0.47 | 0.31 | 0.21 | 0.21 | 1.00 | 1.00 | 0.94 | 0.83 |
| Exp. Sim. Uncert. (k=2) | 0.78 | 0.51 | 0.35 | 0.35 | 1.65 | 1.65 | 1.55 | 1.36 |

**Table 7.15**: *Combined and expanded (k=2) simulation uncertainty budget for the homogeneous setup.*

|  | $U_P$ [dB] | $U_{shift}^{max}$ [λ] | $U_\Delta$ [λ] |
|---|---|---|---|
| Comb. Mat. Uncert. (Table 7.12) | 0.09 | 0.09 | 0.20 |
| Comb. Geom. Uncert. (Table 7.14) | 0.20 | 0.37 | 0.18 |
| Comb. Meas. Setup Uncert. (Table 7.5) | 0.29 | 0.37 | 0.37 |
| Comb. Meas. Uncert. | 0.36 | 0.53 | 0.46 |
| Exp. Meas. Uncert. (k=2) | 0.69 | 0.98 | 0.90 |

**Table 7.16**: *Combined and expanded (k=2) measurement uncertainty budget for the homogeneous setup.*

|  | $U_P$ [dB] | $U_{shift}^{max}$ [λ] | $U_\Delta$ [λ] |
|---|---|---|---|
| Comb. Sim. Uncert. | 0.47 | 0.83 | 1.00 |
| Comb. Meas. Uncert. | 0.36 | 0.53 | 0.46 |
| Comb. Total Uncert. | 0.60 | 0.98 | 1.10 |
| Exp. Total Uncert. (k=2) | 1.04 | 1.68 | 1.88 |

**Table 7.17**: *Combined and expanded (k=2) total uncertainty budget for the homogeneous setup.*

be attributed to the coarse resolution employed in the measurements as well as manufacturing deviations in the measurement equipment.


### 7.2.5.4 Conclusions

The detailed validation between measurements in a homogeneous experimental setup and matching simulations using the solver detailed in this work was presented in this section. An extensive uncertainty analysis was performed where the sensitivity and impact of each parameter pertaining to the measurement setup were quantified. The results of the uncertainty analysis were then used to perform a comparison between the measured and simulated pressure fields using the Gamma method where perfect agreement, within the defined tolerances, was accrued.

*(a)*



*(b)*



*(c)*
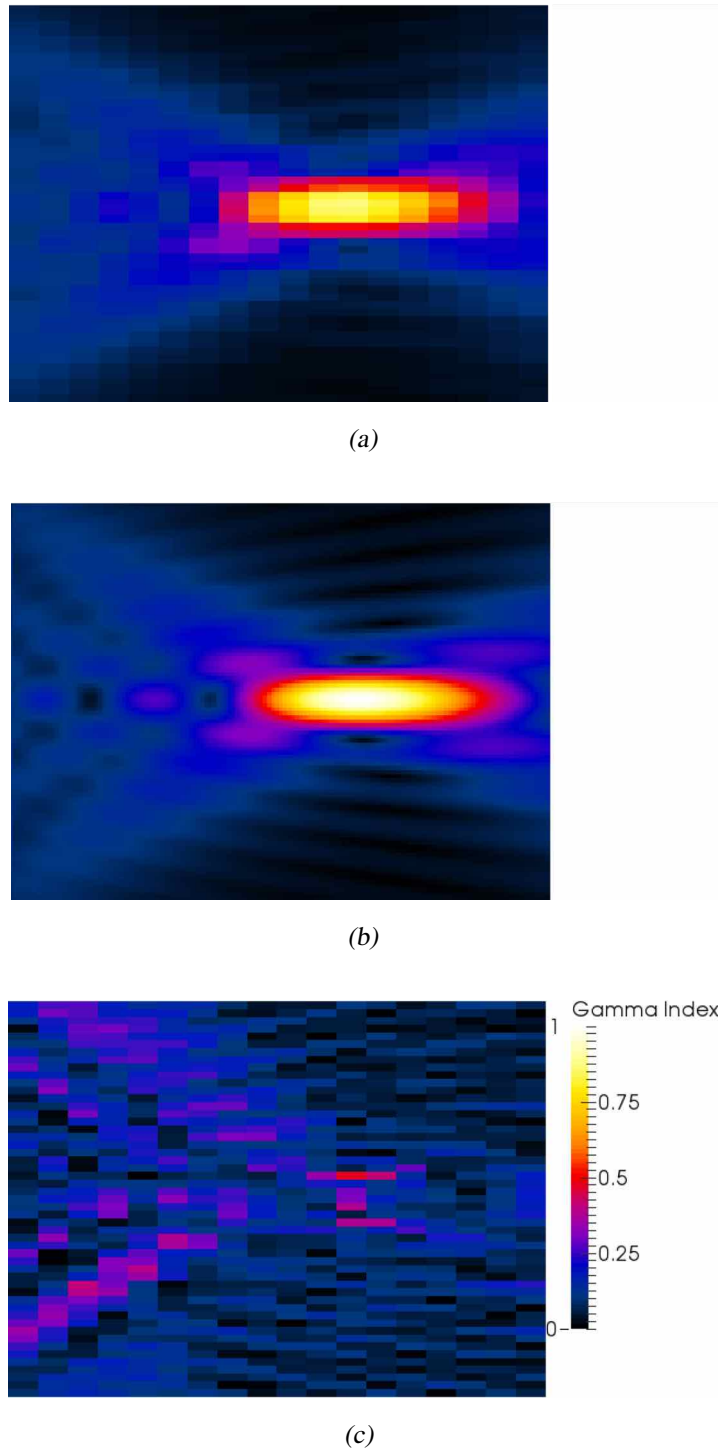
**Figure 7.11**: *Gamma method comparison results for the homogeneous measurement setup, a DTA tolerance of $1.88\lambda$, and a DD tolerance of $1.04$ dB or $12.72\%$ (as calculated during the uncertainty analysis, see Table 7.17). The normalized pressure resulting from the measurements (a) and the simulation (b) can be seen plotted on a plane through the maximum, while (c) shows the corresponding $\gamma$ indices. Perfect agreement can be seen for these tolerances as all $\gamma$ indices lie below a value of $1.0$*

## 7.2.6 Comparison in Delrin Setup

In the cases involving focus distorting samples, a qualitative comparison between measurements and simulations was performed. The reason for this was the large topological changes in the pressure distributions, induced by small variations in the relevant parameters, which precluded the usage of the gamma method.

The impact of the investigated parameters on the pressure distributions will be detailed in the next section.

Figure 7.12 shows the measured and simulated normalized pressure distributions on a plane through the location of the maximum measured pressure and the matching simulated cross-section. As can be seen, the major features of the interference pattern are well reproduced between measurements and simulations. These include the peak pressure in the focal region, the concentric rings around it, as well as the influence of the suspension rods on the distribution which appear as 'breaks' in the outer concentric rings.

The blur in the measured pressure fields can be attributed to the relatively coarse measurement resolution of $\lambda/5$ as opposed to a simulation grid-step of $\lambda/11$. Other differences between measurements and simulations, such as slightly different focal shifts, deviation in the concentric ring locations, and changes in the secondary lobe widths, can be elucidated when considering the results of the uncertainty analysis which is presented in the next section.

### 7.2.6.1 Uncertainty Analysis

The aforementioned large topological changes in the pressure distributions precluded the secondary uncertainty analysis involving local-maxima that was performed for the case of the homogeneous setup (see Section 7.2.5.1). Therefore, the uncertainty analysis was limited to the connected-component approach described in Section 7.2.4.

The results of the uncertainty analysis for the material, numerical, and geometrical parameters (see Section 7.2.4), were appropriately grouped and summarized in Tables 7.18, 7.19, and 7.20 respectively.

Similarly to the case of the homogeneous setup discussed in Section 7.2.5.3, the material parameter uncertainties presented in Table 7.18 are dominated by changes in the sound speed $c$ of the different media, most notably that of water and delrin. As was outlined in the aforementioned section, such variations can be attributed to the alteration of the interference pattern due to changes in the acoustic wavelength. This effect can be seen in Figure 7.13, where the absolute pressure distribution is compared between the reference simulation of the delrin setup and the evaluation simulation where the sound speed of the delrin sample was decreased by $5\%$. As can be seen, very significant distortion of the focal region can be seen which justifies the resulting uncertainties.

*(a)*



*(b)*
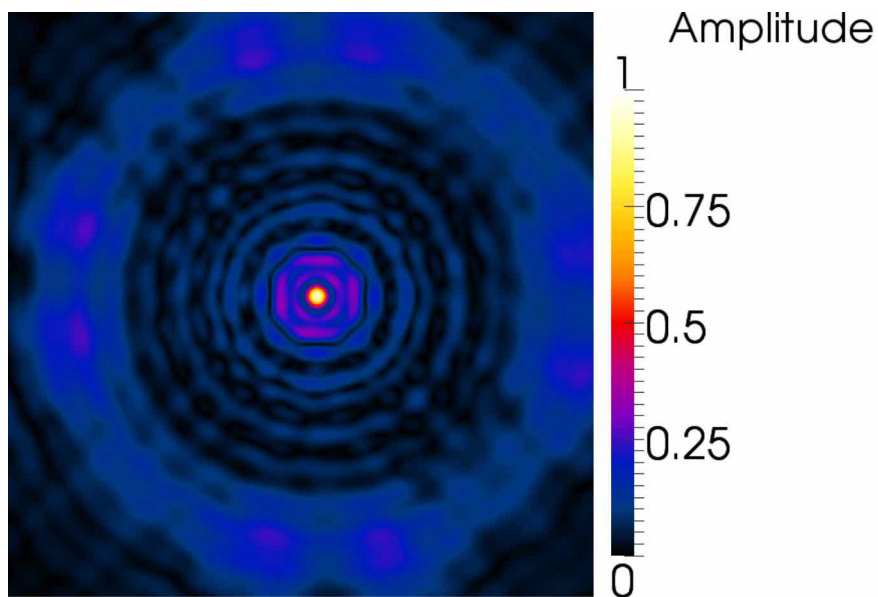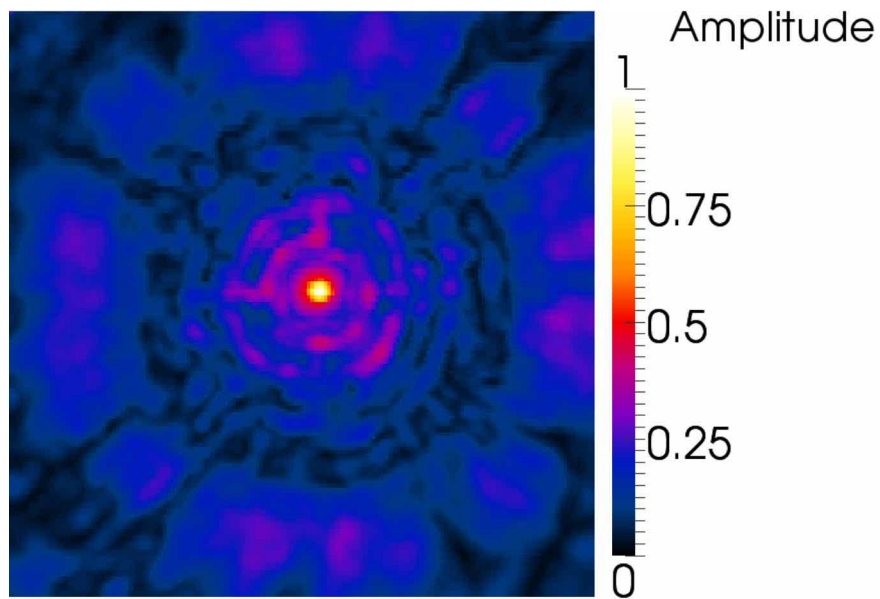
**Figure 7.12**: *Qualitative comparison of the measured* (a) *and simulated* (b) *normalized pressure distributions in the setup with the smaller Delrin cylinder. The distributions are shown plotted on a plane through the location of the maximum measured pressure and the matching simulated cross-section. Good agreement in the the major features of the interference pattern can be seen.*
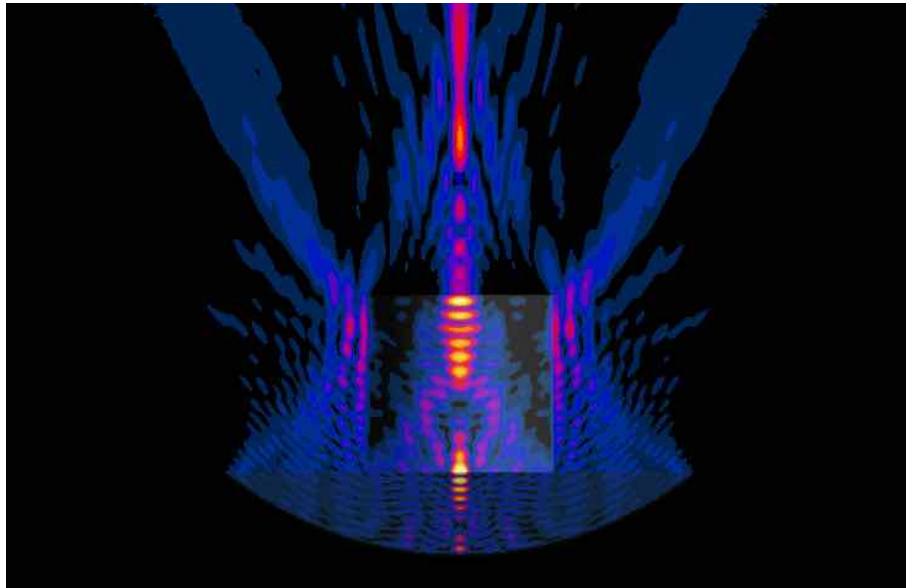
*(a)*
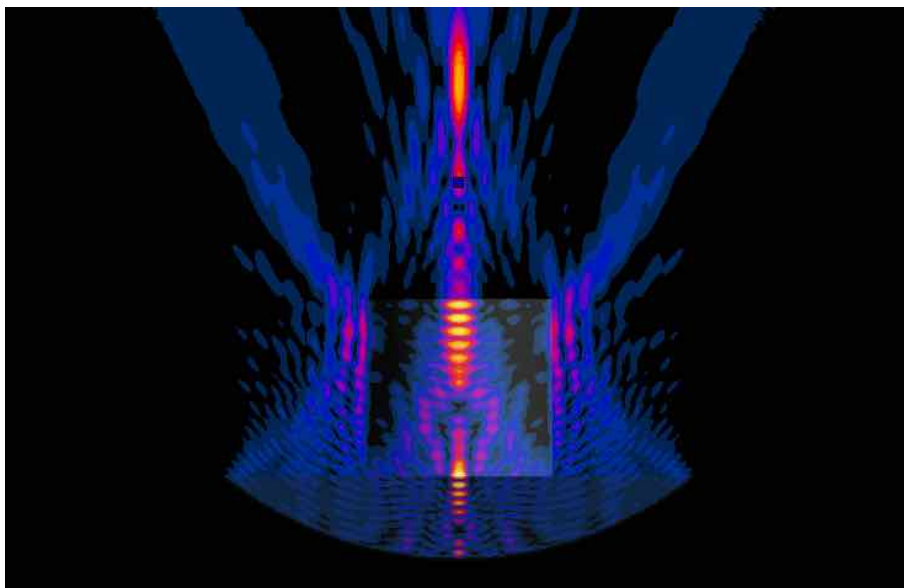


*(b)*

**Figure 7.13**: *Visual comparison of the absolute pressure distributions between the Delrin setup reference simulation (a) and the evaluation simulation where the sound-speed $c$ of the Delrin sample was increased by $5\%$ (b). The notable distortion of the pressure field can be attributed to the fact that the acoustic wavelength in a medium is directly dependent on the acoustic frequency and the medium's speed of sound (see Equation 1.1). Such changes in the the acoustic wavelength may alter the interference patterns between the different wavefronts and result in significantly different distributions of acoustic pressure (see Section 1.1.3.5).*

| Material | Param. | Unit | Ref. | Eval. | $\Delta$ | $\Delta_P$ [dB] | $\Delta_D$ [$\lambda$] | $\Delta_V$ [dB] | $f_P$ [dB/%] | $f_D$ [$\lambda$/%] | $f_V$ [dB/%] |
|---|---|---|---|---|---|---|---|---|---|---|---|
| Water | $c\uparrow$ | m/s | 1500 | 1515 | 1% | -0.28 | -0.27 | 1.71 | -0.28 | -0.27 | 1.71 |
|  | $c\downarrow$ | m/s | 1500 | 1485 | -1% | 0.30 | 0.27 | -2.05 | -0.31 | -0.27 | 1.66 |
|  | $\alpha\uparrow$ | Np/m | 0.0076 | 0.007676 | 1% | 0.00 | 0.00 | 0.00 | 0.00 | 0.00 | 0.00 |
|  | $\alpha\downarrow$ | Np/m | 0.0076 | 0.007524 | -1% | 0.00 | 0.00 | 0.00 | 0.00 | 0.00 | 0.00 |
|  | $\rho\uparrow$ | kg/m$^3$ | 1000 | 1010 | 1% | 0.01 | 0.00 | 0.01 | 0.01 | 0.00 | 0.01 |
|  | $\rho\downarrow$ | kg/m$^3$ | 1000 | 990 | -1% | -0.01 | 0.00 | 0.00 | 0.01 | 0.00 | 0.00 |
| Plexiglass | $c\uparrow$ | m/s | 2750 | 3025 | 10% | -0.02 | 0.00 | 0.00 | 0.00 | 0.00 | 0.00 |
|  | $c\downarrow$ | m/s | 2750 | 2475 | -10% | 0.05 | 0.00 | -0.08 | 0.00 | 0.00 | 0.01 |
|  | $\alpha\uparrow$ | Np/m | 6.875 | 7.5625 | 10% | 0.00 | 0.00 | 0.00 | 0.00 | 0.00 | 0.00 |
|  | $\alpha\downarrow$ | Np/m | 6.875 | 6.1875 | -10% | 0.00 | 0.00 | 0.00 | 0.00 | 0.00 | 0.00 |
|  | $\rho\uparrow$ | kg/m$^3$ | 1192 | 1430.3 | 20% | 0.02 | 0.00 | 0.02 | 0.00 | 0.00 | 0.00 |
|  | $\rho\downarrow$ | kg/m$^3$ | 1192 | 953.6 | -20% | -0.03 | 0.00 | -0.03 | 0.00 | 0.00 | 0.00 |
| Delrin | $c\uparrow$ | m/s | 2430 | 2551.5 | 5% | 0.98 | -0.27 | -3.99 | 0.21 | -0.05 | -0.66 |
|  | $c\downarrow$ | m/s | 2430 | 2308.5 | -5% | 0.99 | -0.96 | -0.23 | -0.21 | 0.19 | 0.05 |
|  | $\alpha\uparrow$ | Np/m | 18.975 | 19.92375 | 5% | -0.05 | 0.00 | 0.07 | -0.01 | 0.00 | 0.01 |
|  | $\alpha\downarrow$ | Np/m | 18.975 | 18.02625 | -5% | 0.05 | 0.00 | -0.05 | -0.01 | 0.00 | 0.01 |
|  | $\rho\uparrow$ | kg/m$^3$ | 1430 | 1444.3 | 1% | -0.01 | 0.00 | 0.00 | -0.01 | 0.00 | 0.00 |
|  | $\rho\downarrow$ | kg/m$^3$ | 1430 | 1415.7 | -1% | 0.01 | 0.00 | 0.01 | -0.01 | 0.00 | -0.01 |

**Table 7.18**: *Results of the uncertainty analysis for the material parameters (see Table 7.6) investigated in the Delrin setup. The value of each parameter for both the reference (Ref.) and evaluation (Eval.) simulations as well as the variation between the two ($\Delta$) can be seen. The impact of this parameter variation had on the focal region's peak absolute pressure ($\Delta_P$), focal shift ($\Delta_D$), volume ($\Delta_V$) can also be seen. Lastly, the sensitivity factors ($f_P$, $f_D$, and $f_V$) resulting from the uncertainty analysis can be seen for all three investigated variables.*

As can be seen in Table 7.19, the primary numerical uncertainties were observed due to the decrease of the computational domain's resolution and the grid-rotation which is in accordance to the findings in the homogeneous setup (see Section 7.2.5). A visual comparison of the pressure distributions between the reference simulation and the evaluation simulation where the grid-step was increased by 10% can be seen in Figure 7.14 where a narrowing of the focal region and a decrease in its peak pressure can be seen.

In terms of the geometrical uncertainties shown in Table 7.20, it can be seen that the majority of the investigated parameters have a severe impact on the resulting pressure distribution. It can be seen that geometric changes in the piezoelectric element of the transducer can adversely affect the location, size, and intensity of the focal region as can be expected. As discussed prior, amelioration of these effects would require more precise characterization of the transducer by the manufacturer.

Translation of the focus distorting sample along the rods around was also shown to significantly impact the distributions. However, the uncertainty is dominated by translation

| Param. | Unit | Ref | Eval | $\Delta_P$ [dB] | $\Delta_D$ [$\lambda$] | $\Delta_V$ [dB] |
|---|---|---|---|---|---|---|
| No. PML Layers ↑ | - | 16 | 20 | 0.00 | 0.00 | 0.01 |
| No. PML Layers ↓ | - | 16 | 12 | 0.00 | 0.00 | -0.01 |
| Grid Step ↑ | mm | 0.25 | 0.275 | -1.02 | 0.08 | 1.48 |
| Grid Step ↓ | mm | 0.25 | 0.225 | 0.21 | 0.03 | -0.72 |
| No. Periods ↑ | - | 40 | 44 | 0.00 | 0.00 | 0.00 |
| No. Periods ↓ | - | 40 | 36 | 0.01 | 0.00 | 0.27 |
| Grid Rotation | ° | 0 | 45 | 0.61 | 0.48 | -0.45 |

**Table 7.19**: *Results of the uncertainty analysis for the numerical parameters (see Table 7.7) investigated in the Delrin setup. The value of each parameter for both the reference (Ref.) and evaluation (Eval.) simulations as well as the variation between the two ($\Delta$) can be seen. The impact of this parameter variation had on the focal region's peak absolute pressure ($\Delta_P$), focal shift ($\Delta_D$), volume ($\Delta_V$) can also be seen. It should be noted that given the nature of these parameters, the calculation of sensitivity factors and uncertainty was not applicable and was therefore omitted.*

| | Param. | Unit | Ref. | Eval. | $\Delta$ | $\Delta_P$ [dB] | $\Delta_D$ [$\lambda$] | $\Delta_V$ [dB] | $f_P$ [dB/mm] | $f_D$ [$\lambda$/mm] | $f_V$ [dB/mm] |
|---|---|---|---|---|---|---|---|---|---|---|---|
| Transducer | Curvature Radius ↑ | mm | 64 | 66 | 2 | 1.09 | 0.27 | -2.12 | 0.54 | 0.14 | -1.06 |
| | Curvature Radius ↓ | mm | 64 | 62 | -2 | -0.89 | -0.32 | 1.87 | 0.45 | 0.16 | -0.93 |
| | Aperture Width ↑ | mm | 80 | 80.2 | 0.2 | 0.00 | 0.00 | 0.00 | -0.01 | 0.00 | 0.00 |
| | Aperture Width ↓ | mm | 80 | 79.8 | -0.2 | -0.58 | 0.00 | 0.56 | 2.89 | 0.00 | -2.81 |
| Sample Translation | Along Upper Rod ↑ | mm | 0 | 2.5 | 2.5 | 0.91 | -0.59 | -1.08 | 0.36 | -0.24 | -0.43 |
| | Along Upper Rod ↓ | mm | 0 | -2.5 | -2.5 | 0.91 | -0.59 | -1.11 | -0.36 | 0.24 | 0.45 |
| | Along Propagation Axis ↑ | mm | 0 | 2.5 | 2.5 | -1.53 | -3.02 | -9.26 | -0.61 | -1.21 | -3.70 |
| | Along Propagation Axis ↓ | mm | 0 | -2.5 | -2.5 | 3.04 | -0.60 | -4.36 | -1.21 | 0.24 | 1.74 |
| | Along Lower Rod ↑ | mm | 0 | 2.5 | 2.5 | 0.91 | -0.63 | -0.83 | 0.36 | -0.25 | -0.33 |
| | Along Lower Rod ↓ | mm | 0 | -2.5 | -2.5 | 0.90 | -0.63 | -0.85 | -0.36 | 0.25 | 0.34 |
| Sample Rotation | Around Upper Rod ↑ | ° | 0 | 2.5 | 2.5 | 0.58 | 0.00 | -1.04 | 0.23 | 0.00 | -0.41 |
| | Around Upper Rod ↓ | ° | 0 | -2.5 | -2.5 | 0.58 | 0.00 | -1.04 | -0.23 | 0.00 | 0.41 |
| | Around Lower Rod ↑ | ° | 0 | 2.5 | 2.5 | 0.55 | 0.00 | -0.90 | 0.22 | 0.00 | -0.36 |
| | Around Lower Rod ↓ | ° | 0 | -2.5 | -2.5 | 0.56 | 0.00 | -0.92 | -0.22 | 0.00 | 0.37 |

**Table 7.20**: *Results of the uncertainty analysis for the geometrical parameters (see Table 7.8) investigated in the Delrin setup. The value of each parameter for both the reference (Ref.) and evaluation (Eval.) simulations as well as the variation between the two ($\Delta$) can be seen. The impact of this parameter variation had on the focal region's peak absolute pressure ($\Delta_P$), focal shift ($\Delta_D$), volume ($\Delta_V$) can also be seen. Lastly, the sensitivity factors ($f_P$, $f_D$, and $f_V$) resulting from the uncertainty analysis can be seen for all three investigated variables.*
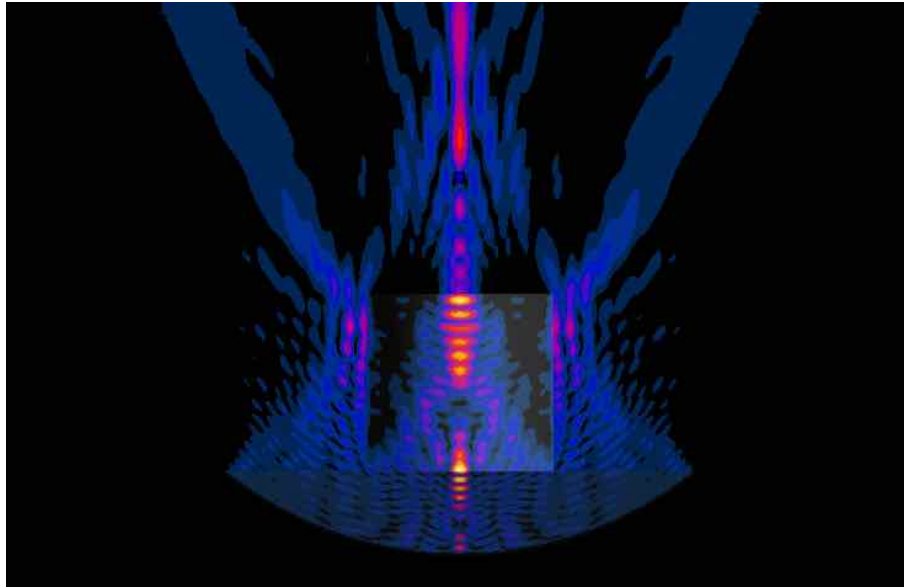
*(a)*
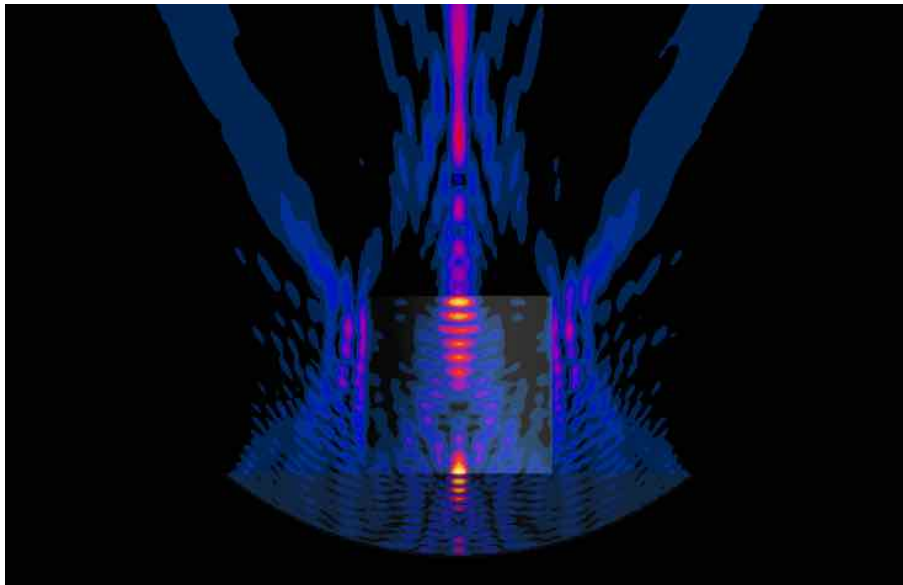


*(b)*

**Figure 7.14**: *Visual comparison of the absolute pressure distributions between the Delrin setup reference simulation (a) and the evaluation simulation where the grid-step was increased by 10% (b). Due to numerical dispersion effects (see Section 5.1.3), a narrowing can be observed in the proximal end of the focal region, accompanied by decreased pressure values.*

along the propagation axis. This effect can be seen in Figures 7.15 and 7.16, where the absolute pressure distribution is compared between the reference simulation of the delrin setup and the evaluation simulation where the sample was translated along the propagation axis by $-2.5$ mm. A prominent enhancement of the focal region can be seen, accompanied by prevalent changes in the entire interference pattern. Figure 7.16 shows the case of sample translation along the lower suspension rod by $2.5$ mm, where obvious asymmetries can be observed in the interference pattern.

Uncertainty budgets were compiled from the findings in Tables 7.18, 7.19, and 7.20. The uncertainty budgets for the investigated material, numerical, and geometrical parameters can be seen in Tables 7.21, 7.22, and 7.23 respectively. It should be noted that these tables were compiled by selecting the absolute maximum uncertainty for each of the the three investigated variables, i.e., focal region peak pressure, focal shift, and volume, that resulted from the decrease or increase of each investigated parameter. The combined and expanded (k=2) uncertainties for the simulation and measurement setup are presented in Tables 7.24 and 7.25, while Table 7.26 shows the total combined uncertainty resulting from the uncertainties in both the simulated and measurement setups.

As can be seen, very large uncertainties are inherent to the measurement setup when a focus distorting sample is involved. Disagreements between the measurements and simulations can be attributed to small deviations in the measurement setup, such as the geometrical characteristics of the transducer and the absolute location of the focus distorting sample. However, these parameters could not be characterized with absolute precision in the presented measurement setup and taking into account the large related uncertainties, the agreement between measurements and simulations was deemed satisfactory.

### 7.2.7 Comparison in Polyurethane Setup

Due to the same type of topological changes observed in the Delrin cylinder case (see Section 7.2.6), the comparison in the case involving the polyurethane block sample was performed qualitatively.

Figure 7.17 shows the measured and simulated normalized pressure distributions on a plane through the location of the maximum measured pressure and the matching simulated cross-section. As can be seen, the major features of the interference pattern are well reproduced between measurements and simulations. These include the location and peak pressure in the four prominent side-lobes as well as the influence of the suspension rods on the distribution which appears as tertiary lobes with higher pressure values for the upper suspension rod than the lower.

The blur in the measured pressure fields and the failure to replicate the complex interference pattern can once more be attributed to the relatively coarse measurement resolution while other differences between measurements and simulations, such as the intensity of
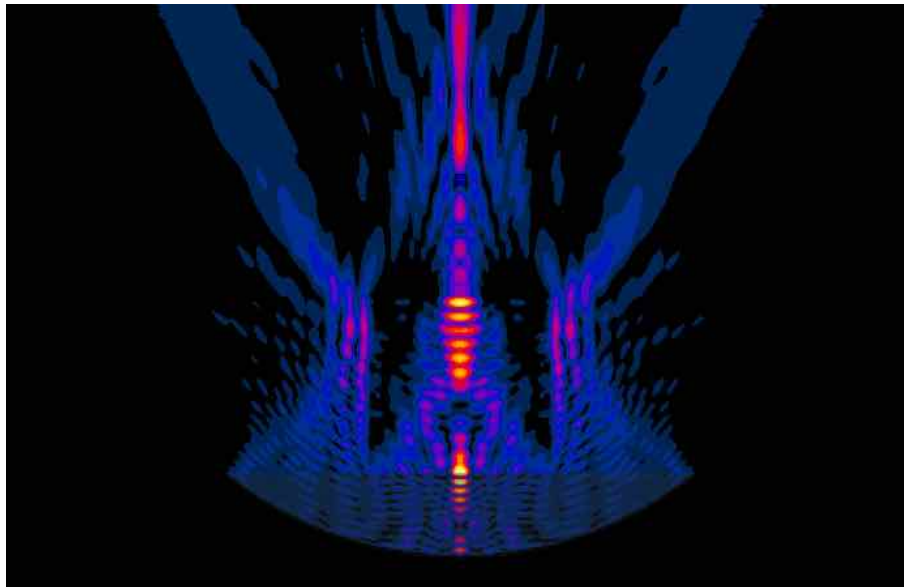
*(a)*
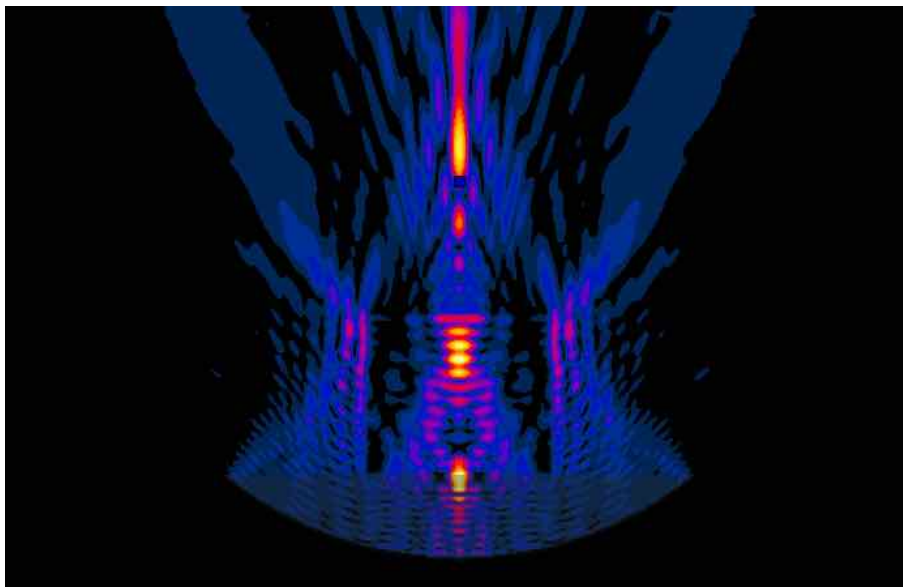


*(b)*

**Figure 7.15**: *Visual comparison of the absolute pressure distributions between the Delrin setup reference simulation (a) and the evaluation simulation where the Delrin sample was translated along the propagation axis by* $-2.5$ mm *(b). Significant pressure increase can be observed in the proximal end of the focal region along with prevalent changes in the entire interference pattern.*

*(a)*



*(b)*

**Figure 7.16**: *Visual comparison of the absolute pressure distributions between the Delrin setup reference simulation (a) and the evaluation simulation where the Delrin sample was translated along the lower suspension rod by* 2.5 mm *(b). Obvious asymmetries can be observed in the interference pattern.*

| Material | Param. | $\Delta$ | $\sigma$ | N/R | $f_P$ [dB/%] | $f_D$ [$\lambda$/%] | $f_V$ [dB/%] | $U_P$ [dB] | $U_D$ [$\lambda$] | $U_V$ [dB] |
|---|---|---|---|---|---|---|---|---|---|---|
| | $c$ | 1% | 15 | N | -0.30 | -0.27 | 2.05 | 0.30 | 0.27 | 2.05 |
| Water | $\alpha$ | 1% | 0.000076 | N | 0.00 | 0.00 | 0.00 | 0.00 | 0.00 | 0.00 |
| | $\rho$ | 1% | 10 | N | 0.01 | 0.00 | 0.01 | 0.01 | 0.00 | 0.01 |
| | $c$ | 10% | 275 | N | 0.00 | 0.00 | 0.01 | 0.05 | 0.00 | 0.08 |
| Plexiglass | $\alpha$ | 10% | 0.6875 | N | 0.00 | 0.00 | 0.00 | 0.00 | 0.00 | 0.00 |
| | $\rho$ | 20% | 238.4 | N | 0.00 | 0.00 | 0.00 | 0.03 | 0.00 | 0.03 |
| | $c$ | 5% | 121.5 | N | -0.20 | 0.19 | -0.80 | 0.99 | 0.96 | 3.99 |
| Delrin | $\alpha$ | 5% | 0.94875 | N | -0.01 | 0.00 | 0.01 | 0.05 | 0.00 | 0.07 |
| | $\rho$ | 1% | 14.3 | N | -0.01 | 0.00 | -0.01 | 0.01 | 0.00 | 0.01 |
| Combined Uncertainty | | | | | | | | 1.03 | 1.00 | 4.49 |
| Expanded Uncertainty (k=2) | | | | | | | | 2.07 | 2.00 | 8.97 |

***Table 7.21****: Uncertainty budget for the material parameters (see Table 7.6) investigated in the Delrin setup. The variation ($\Delta$), standard deviation ($\sigma$), and distribution shape (Normal/Rectangular - N/R) of each parameter can be seen. In addition, the sensitivity factors ($f_P$, $f_D$, and $f_V$), and the calculated uncertainties ($U_P$, $U_D$, and $U_V$) can be seen for all three investigated variables.*

| Param. | N/R | $U_P$ [dB] | $U_D$ [$\lambda$] | $U_V$ [dB] |
|---|---|---|---|---|
| No. PML Layers | N | 0.00 | 0.00 | 0.01 |
| Grid Step | R | 0.59 | 0.05 | 0.85 |
| No. Periods | N | 0.01 | 0.00 | 0.27 |
| Grid Rotation | R | 0.35 | 0.28 | 0.26 |
| Combined Uncertainty | | 0.68 | 0.28 | 0.93 |
| Expanded Uncertainty (k=2) | | 1.13 | 0.46 | 1.57 |

***Table 7.22****: Uncertainty budget for the numerical parameters (see Table 7.7) investigated in the Delrin setup. The calculated uncertainties ($U_P$, $U_D$, and $U_V$) can be seen for all three investigated variables. It should be noted that given the nature of these parameters, the calculation of sensitivity factors and uncertainty was not applicable and was therefore omitted. Instead, uncertainty was considered to be the variation in the investigated variables.*

| | Param. | $\Delta$ | $\sigma$ | N/R | $f_P$ [dB/%] | $f_D$ [$\lambda$/%] | $f_V$ [dB/%] | $U_P$ [dB] | $U_D$ [$\lambda$] | $U_V$ [dB] |
|---|---|---|---|---|---|---|---|---|---|---|
| Transducer | Curvature Radius | 2mm | 2 | R | 0.54 | 0.16 | -1.06 | 0.63 | 0.18 | 1.22 |
| | Aperture Width | 0.2mm | 0.2 | R | 2.89 | 0.00 | -2.81 | 0.33 | 0.00 | 0.32 |
| Sample Translation | Along Upper Rod | 2.5mm | 2.5 | R | 0.36 | -0.24 | 0.45 | 0.53 | 0.34 | 0.64 |
| | Along Propagation Axis | 2.5mm | 2.5 | R | -1.21 | -1.21 | -3.70 | 1.75 | 1.74 | 5.35 |
| | Along Lower Rod | 2.5mm | 2.5 | R | 0.36 | -0.25 | 0.34 | 0.52 | 0.37 | 0.49 |
| Sample Rotation | Around Upper Rod | 2.5° | 2.5 | R | -0.23 | 0.00 | 0.41 | 0.34 | 0.00 | 0.60 |
| | Around Lower Rod | 2.5° | 2.5 | R | -0.22 | 0.00 | 0.37 | 0.32 | 0.00 | 0.53 |
| Combined Uncertainty | | | | | | | | 2.08 | 1.82 | 5.61 |
| Expanded Uncertainty (k=2) | | | | | | | | 3.45 | 3.01 | 9.27 |

**Table 7.23**: *Uncertainty budget for the geometrical parameters (see Table 7.8) investigated in the Delrin setup. The variation ($\Delta$), standard deviation ($\sigma$), and distribution shape (Normal/Rectangular - N/R) of each parameter can be seen. In addition, the sensitivity factors ($f_P$, $f_D$, and $f_V$), and the calculated uncertainties ($U_P$, $U_D$, and $U_V$) can be seen for all three investigated variables.*

| | $U_P$ [dB] | $U_D$ [$\lambda$] | $U_V$ [dB] |
|---|---|---|---|
| Combined Uncertainty (Numerical, Table 7.22) | 0.68 | 0.28 | 0.93 |
| Combined Simulation Uncertainty | 0.68 | 0.28 | 0.93 |
| Expanded Simulation Uncertainty (k=2) | 1.13 | 0.46 | 1.57 |

**Table 7.24**: *Combined and expanded (k=2) simulation uncertainty budget for the Delrin setup.*

| | $U_P$ [dB] | $U_D$ [$\lambda$] |
|---|---|---|
| Comb. Mat. Uncert. (Table 7.21) | 1.03 | 1.00 |
| Comb. Geom. Uncert. (Table 7.23) | 2.08 | 1.82 |
| Comb. Meas. Setup Uncert. (Table 7.5) | 0.29 | 0.37 |
| Comb. Meas. Uncert. | 2.35 | 2.11 |
| Exp. Meas. Uncert. (k=2) | 4.06 | 3.69 |

**Table 7.25**: *Combined and expanded (k=2) measurement uncertainty budget for the Delrin setup.*

|                                       | $U_P$ [dB] | $U_D$ [$\lambda$] |
|---------------------------------------|------------|-------------------|
| Combined Simulation Uncertainty       | 0.68       | 0.28              |
| Combined Measurement Uncertainty      | 2.35       | 2.11              |
| Combined Total Uncertainty            | 2.44       | 2.13              |
| Expanded Total Uncertainty (k=2)      | 4.22       | 3.72              |

**Table 7.26**: *Combined and expanded (k=2) total uncertainty budget for the Delrin setup.*

the tertiary lobes can be elucidated when considering the results of the uncertainty analysis which is presented in the next section.

### 7.2.7.1    Uncertainty Analysis

The results of the uncertainty analysis for the material, numerical, and geometrical parameters (see Section 7.2.4), were appropriately grouped and summarized in Tables 7.27, 7.28, and 7.29 respectively.

Similarly to the previous cases, the material parameter uncertainties presented in Table 7.27 are dominated by changes in the sound speed $c$ of the focus distorting sample. This effect can be seen in Figure 7.18, where the absolute pressure distribution is compared between the reference simulation of the polyurethane setup and the evaluation simulation where the sound speed of the polyurethane sample was decreased by 5%. As can be seen, a severe distortion and enhancement of the focal region can be seen which justifies the resulting uncertainties.

In regards to the geometrical uncertainties shown in Table 7.29, prominent deviations can be observed for the majority of the investigated parameters. The most prevalent such case occurs during the translation of the focus distorting sample along the lower suspension rod. This case is shown in Figure 7.19, where obvious asymmetries and strong secondary focal regions can be observed in the interference pattern.

Uncertainty budgets were compiled from the findings in Tables 7.27, 7.28, and 7.29. The uncertainty budgets for the investigated material, numerical, and geometrical parameters can be seen in Tables 7.30, 7.31, and 7.32 respectively. It should be noted that these tables were compiled by selecting the absolute maximum uncertainty for each of the the three investigated variables, i.e., focal region peak pressure, focal shift, and volume, that resulted from the decrease or increase of each investigated parameter. The combined and expanded (k=2) uncertainties for the simulation and measurement setup are presented in Tables 7.33 and 7.34, while Table 7.35 shows the total combined uncertainty resulting from the uncertainties in both the simulated and measurement setups.

*(a)*



*(b)*
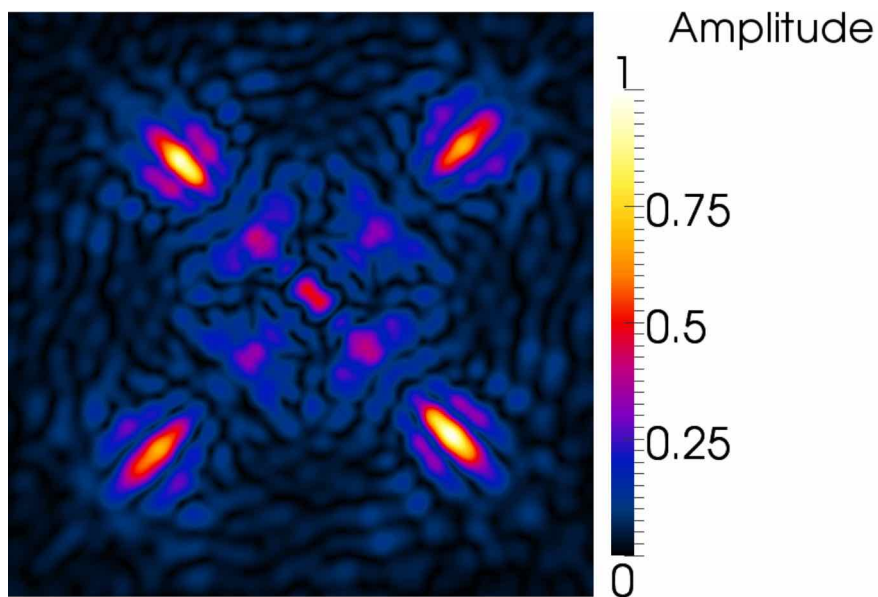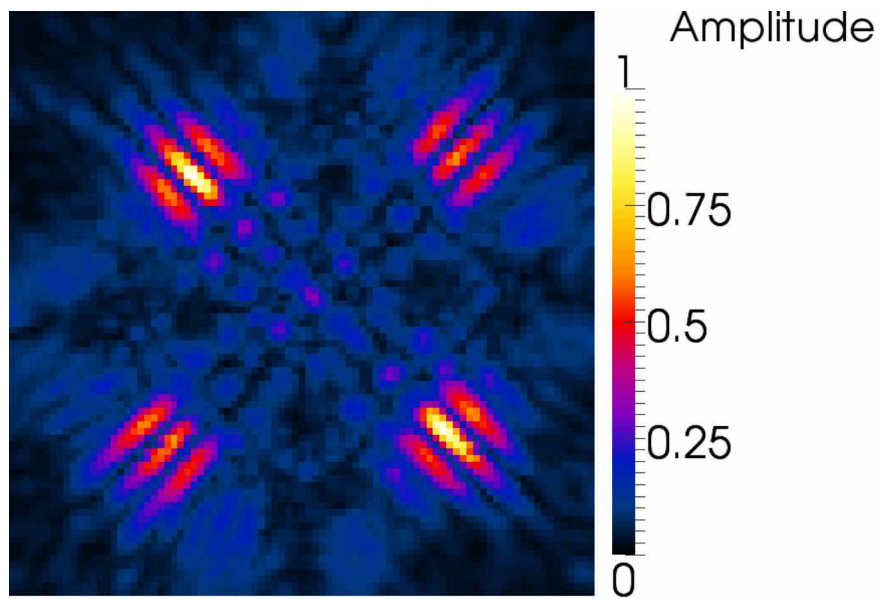
**Figure 7.17**: *Qualitative comparison of the measured (a) and simulated (b) normalized pressure distributions in the setup with the Polyurethane block. The distributions are shown plotted on a plane through the location of the maximum measured pressure and the matching simulated cross-section. Good agreement in the the major features of the interference pattern can be seen.*
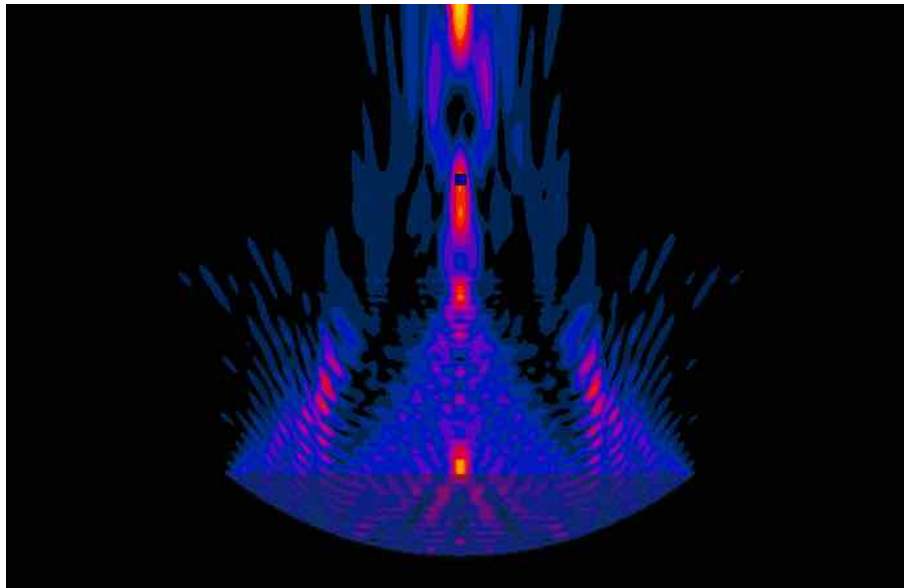
*(a)*
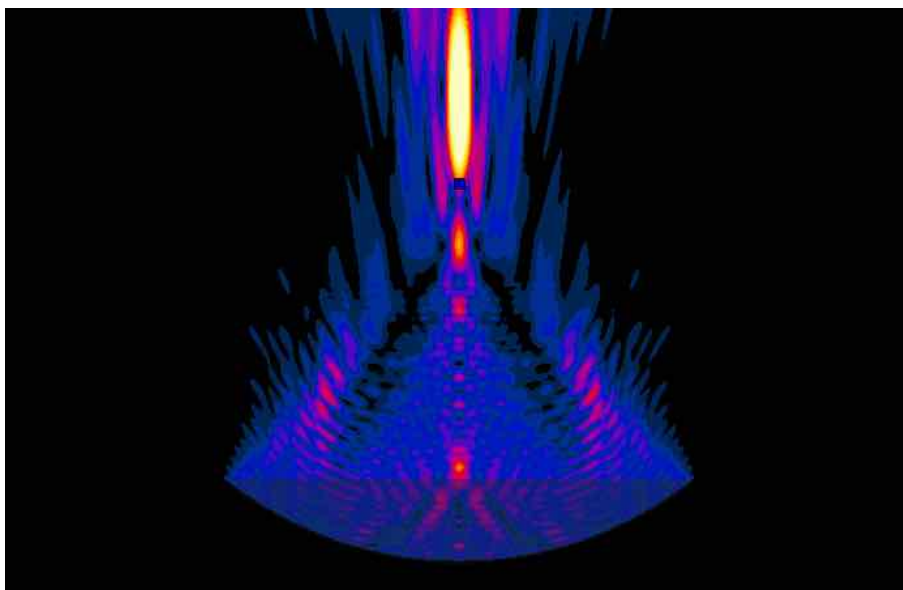


*(b)*

**Figure 7.18**: *Visual comparison of the absolute pressure distributions between the Polyurethane setup reference simulation (a) and the evaluation simulation where the sound-speed $c$ of the Polyurethane sample was increased by $5\%$ (b). The severe distortion of the pressure field can be attributed to the fact that the acoustic wavelength in a medium is directly dependent on the acoustic frequency and the medium's speed of sound (see Equation 1.1). Such changes in the the acoustic wavelength may alter the interference patterns between the different wavefronts and result in significantly different distributions of acoustic pressure (see Section 1.1.3.5).*
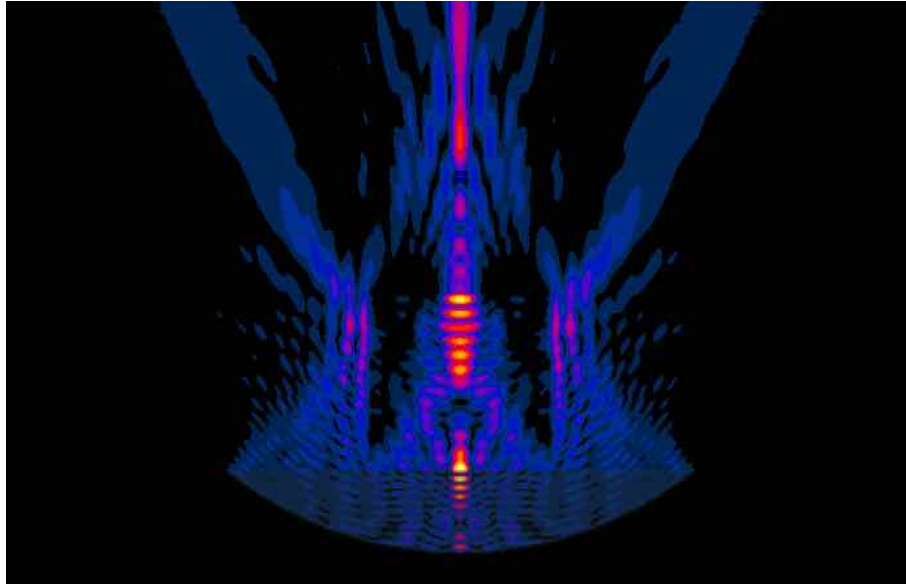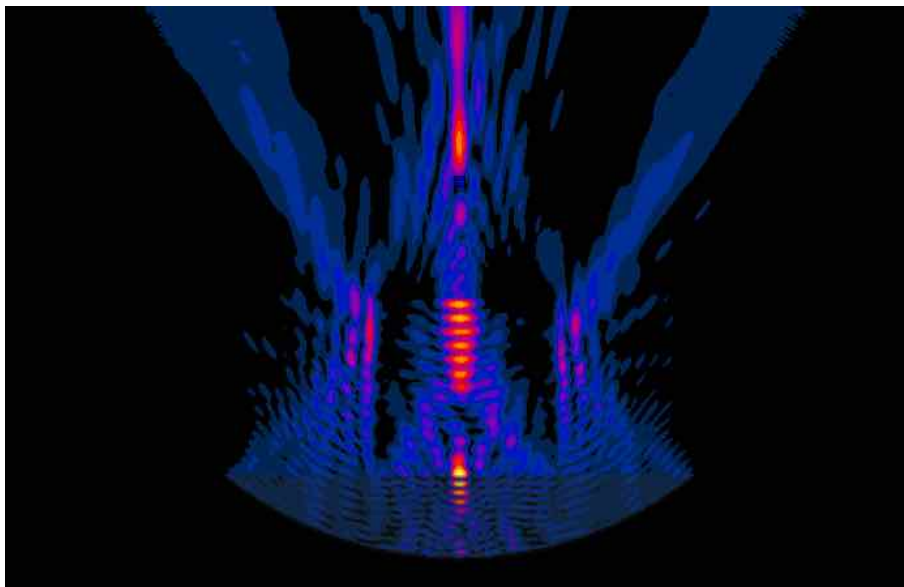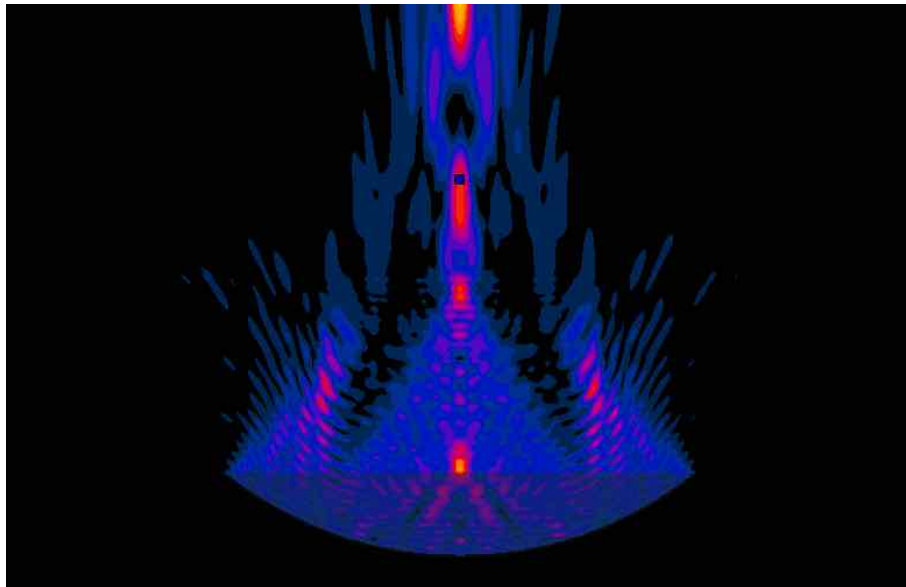
*(a)*
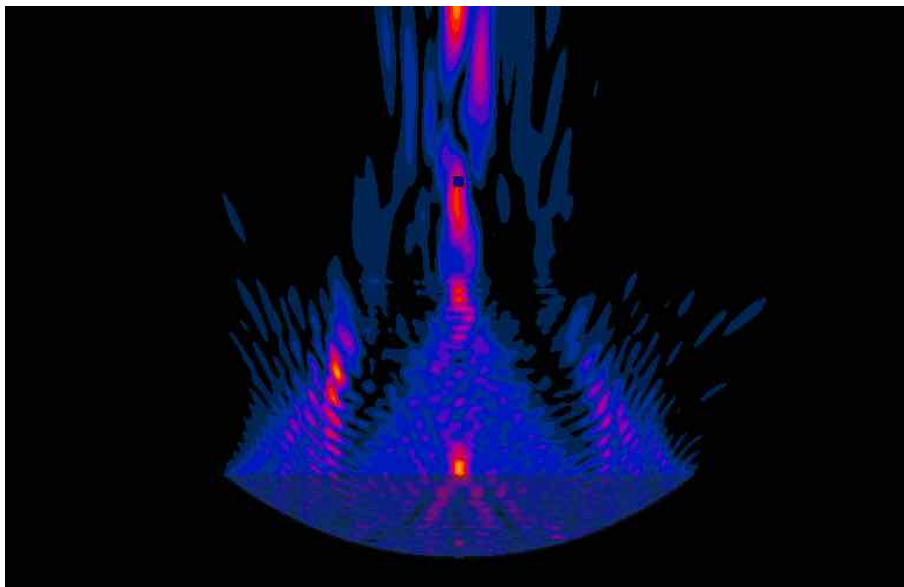


*(b)*

**Figure 7.19**: *Visual comparison of the absolute pressure distributions between the Polyurethane setup reference simulation (a) and the evaluation simulation where the Polyurethane sample was translated along the propagation axis by* −2.5 mm *(b). Obvious asymmetries and strong secondary focal regions can be observed in the interference pattern.*

| Material | Param. | Unit | Ref. | Eval. | Δ | $\Delta_P$ [dB] | $\Delta_D$ [$\lambda$] | $\Delta_V$ [dB] | $f_P$ [dB/%] | $f_D$ [$\lambda$/%] | $f_V$ [dB/%] |
|---|---|---|---|---|---|---|---|---|---|---|---|
| | $c\uparrow$ | m/s | 1500 | 1515 | 1% | 0.54 | -3.54 | -11.61 | 0.54 | -3.54 | -11.61 |
| | $c\downarrow$ | m/s | 1500 | 1485 | -1% | 0.64 | -0.06 | -0.36 | -0.69 | 0.06 | 0.35 |
| Water | $\alpha\uparrow$ | Np/m | 0.0076 | 0.007676 | 1% | 0.00 | 0.00 | 0.00 | 0.00 | 0.00 | 0.00 |
| | $\alpha\downarrow$ | Np/m | 0.0076 | 0.007524 | -1% | 0.00 | 0.00 | 0.00 | 0.00 | 0.00 | 0.00 |
| | $\rho\uparrow$ | kg/m³ | 1000 | 1010 | 1% | -0.03 | 0.00 | 0.01 | -0.03 | 0.00 | 0.01 |
| | $\rho\downarrow$ | kg/m³ | 1000 | 990 | -1% | 0.03 | 0.06 | -0.01 | -0.03 | -0.06 | 0.01 |
| | $c\uparrow$ | m/s | 2750 | 3025 | 10% | -0.01 | 0.03 | -0.03 | 0.00 | 0.00 | 0.00 |
| | $c\downarrow$ | m/s | 2750 | 2475 | -10% | 0.03 | 0.00 | -0.01 | 0.00 | 0.00 | 0.00 |
| Plexiglass | $\alpha\uparrow$ | Np/m | 6.875 | 7.5625 | 10% | 0.00 | 0.00 | 0.00 | 0.00 | 0.00 | 0.00 |
| | $\alpha\downarrow$ | Np/m | 6.875 | 6.1875 | -10% | 0.00 | 0.00 | 0.00 | 0.00 | 0.00 | 0.00 |
| | $\rho\uparrow$ | kg/m³ | 1192 | 1430.3 | 20% | 0.04 | 0.00 | 0.04 | 0.00 | 0.00 | 0.00 |
| | $\rho\downarrow$ | kg/m³ | 1192 | 953.6 | -20% | -0.06 | 0.06 | -0.06 | 0.00 | 0.00 | 0.00 |
| | $c\uparrow$ | m/s | 1700 | 1758 | 5% | 1.55 | 0.33 | -0.17 | 0.48 | 0.10 | -0.05 |
| | $c\downarrow$ | m/s | 1700 | 1615 | -5% | 4.45 | -5.69 | -10.84 | -1.25 | 1.14 | 1.16 |
| Polyurethane | $\alpha\uparrow$ | Np/m | 37.95 | 39.8475 | 5% | -0.07 | 0.06 | -0.01 | -0.01 | 0.01 | 0.00 |
| | $\alpha\downarrow$ | Np/m | 37.95 | 36.0525 | -5% | 0.07 | 0.00 | 0.01 | -0.01 | 0.00 | 0.00 |
| | $\rho\uparrow$ | kg/m³ | 1130 | 1141.3 | 1% | 0.03 | 0.06 | -0.01 | 0.03 | 0.06 | -0.01 |
| | $\rho\downarrow$ | kg/m³ | 1130 | 1118.7 | -1% | -0.03 | 0.00 | 0.01 | 0.03 | 0.00 | -0.01 |

**Table 7.27**: *Results of the uncertainty analysis for the material parameters (see Table 7.6) investigated in the Polyurethane setup. The value of each parameter for both the reference (Ref.) and evaluation (Eval.) simulations as well as the variation between the two ($\Delta$) can be seen. The impact of this parameter variation had on the focal region's peak absolute pressure ($\Delta_P$), focal shift ($\Delta_D$), volume ($\Delta_V$) can also be seen. Lastly, the sensitivity factors ($f_P$, $f_D$, and $f_V$) resulting from the uncertainty analysis can be seen for all three investigated variables.*

Similarly to the case of the Delrin focus distorting sample, the very large uncertainties inherent to these setups can the small deviations seen in the comparison results. Lacking, however, a very precise characterization of each measurement setup, the current degree of agreement between measurements and simulations was considered to be satisfactory.

## 7.2.8   Conclusions

The analytical, numerical, and experimental validations performed to ensure the sound operation of the acoustic solvers developed during this work, were presented in this chapter. Excellent agreement agreement was achieved in both analytical and numerical validation, while the detailed validation between measurements in experimental setups and matching simulations yielded satisfactory agreement within the uncertainty tolerances which resulted from a comprehensive uncertainty analysis.

| Param. | Unit | Ref | Eval | $\Delta_P$ [dB] | $\Delta_D$ [$\lambda$] | $\Delta_V$ [dB] |
|---|---|---|---|---|---|---|
| No. PML Layers $\uparrow$ | - | 16 | 20 | 0.00 | 0.00 | 0.00 |
| No. PML Layers $\downarrow$ | - | 16 | 12 | 0.00 | 0.00 | 0.00 |
| Grid Step $\uparrow$ | mm | 0.25 | 0.275 | -0.15 | 0.14 | 0.28 |
| Grid Step $\downarrow$ | mm | 0.25 | 0.225 | -0.12 | -0.10 | 0.46 |
| No. Periods $\uparrow$ | - | 40 | 44 | 0.01 | 0.00 | -0.05 |
| No. Periods $\downarrow$ | - | 40 | 36 | -0.02 | -0.07 | 0.04 |
| Grid Rotation | $\circ$ | 0 | 45 | 1.22 | 0.68 | -15.74 |

**Table 7.28**: *Results of the uncertainty analysis for the numerical parameters (see Table 7.7) investigated in the Polyurethane setup. The value of each parameter for both the reference (Ref.) and evaluation (Eval.) simulations as well as the variation between the two ($\Delta$) can be seen. The impact of this parameter variation had on the focal region's peak absolute pressure ($\Delta_P$), focal shift ($\Delta_D$), volume ($\Delta_V$) can also be seen. It should be noted that given the nature of these parameters, the calculation of sensitivity factors and uncertainty was not applicable and was therefore omitted.*

| | Param. | Unit | Ref. | Eval. | $\Delta$ | $\Delta_P$ [dB] | $\Delta_D$ [$\lambda$] | $\Delta_V$ [dB] | $f_P$ [dB/mm] | $f_D$ [$\lambda$/mm] | $f_V$ [dB/mm] |
|---|---|---|---|---|---|---|---|---|---|---|---|
| | Curvature Radius $\uparrow$ | mm | 64 | 66 | 2 | -0.10 | -0.95 | 2.28 | -0.05 | -0.48 | 1.14 |
| Transducer | Curvature Radius $\downarrow$ | mm | 64 | 62 | -2 | -0.07 | 0.00 | -1.00 | 0.04 | 0.00 | 0.50 |
| | Aperture Width $\uparrow$ | mm | 80 | 80.2 | 0.2 | 0.00 | 0.00 | 0.00 | 0.00 | -0.01 | -0.01 |
| | Aperture Width $\downarrow$ | mm | 80 | 79.8 | -0.2 | -0.19 | 0.06 | 0.46 | 0.96 | -0.32 | -2.30 |
| | Along Upper Rod $\uparrow$ | mm | 0 | 2.5 | 2.5 | -0.04 | -0.51 | 0.74 | -0.02 | -0.20 | 0.30 |
| | Along Upper Rod $\downarrow$ | mm | 0 | -2.5 | -2.5 | -0.04 | -0.51 | 0.74 | 0.02 | 0.20 | -0.30 |
| Sample Translation | Along Propagation Axis $\uparrow$ | mm | 0 | 2.5 | 2.5 | -0.36 | 0.00 | 0.21 | -0.15 | 0.00 | 0.09 |
| | Along Propagation Axis $\downarrow$ | mm | 0 | -2.5 | -2.5 | 0.19 | 0.13 | -0.14 | -0.08 | -0.05 | 0.05 |
| | Along Lower Rod $\uparrow$ | mm | 0 | 2.5 | 2.5 | 0.74 | -2.01 | 0.79 | 0.30 | -0.80 | 0.32 |
| | Along Lower Rod $\downarrow$ | mm | 0 | -2.5 | -2.5 | 0.74 | -2.01 | 0.79 | -0.30 | 0.80 | -0.32 |
| | Around Upper Rod $\uparrow$ | $\circ$ | 0 | 2.5 | 2.5 | 0.32 | -1.80 | 0.86 | 0.13 | -0.72 | 0.35 |
| Sample Rotation | Around Upper Rod $\downarrow$ | $\circ$ | 0 | -2.5 | -2.5 | 0.33 | -1.80 | 0.86 | -0.13 | 0.72 | -0.34 |
| | Around Lower Rod $\uparrow$ | $\circ$ | 0 | 2.5 | 2.5 | 0.04 | -0.50 | 0.17 | 0.01 | -0.20 | 0.07 |
| | Around Lower Rod $\downarrow$ | $\circ$ | 0 | -2.5 | -2.5 | 0.04 | -0.50 | 0.17 | -0.01 | 0.20 | -0.07 |

**Table 7.29**: *Results of the uncertainty analysis for the geometrical parameters (see Table 7.8) investigated in the Polyurethane setup. The value of each parameter for both the reference (Ref.) and evaluation (Eval.) simulations as well as the variation between the two ($\Delta$) can be seen. The impact of this parameter variation had on the focal region's peak absolute pressure ($\Delta_P$), focal shift ($\Delta_D$), volume ($\Delta_V$) can also be seen. Lastly, the sensitivity factors ($f_P$, $f_D$, and $f_V$) resulting from the uncertainty analysis can be seen for all three investigated variables.*

| Material | Param. | $\Delta$ | $\sigma$ | N/R | $f_P$ [dB/%] | $f_D$ [$\lambda$/%] | $f_V$ [dB/%] | $U_P$ [dB] | $U_D$ [$\lambda$] | $U_V$ [dB] |
|---|---|---|---|---|---|---|---|---|---|---|
| | $c$ | 1% | 15 | N | -0.64 | -3.54 | -11.61 | 0.64 | 3.54 | 11.61 |
| Water | $\alpha$ | 1% | 0.000076 | N | 0.00 | 0.00 | 0.00 | 0.00 | 0.00 | 0.00 |
| | $\rho$ | 1% | 10 | N | -0.03 | -0.06 | 0.01 | 0.03 | 0.06 | 0.01 |
| | $c$ | 10% | 275 | N | 0.00 | 0.00 | 0.00 | 0.03 | 0.03 | 0.03 |
| Plexiglass | $\alpha$ | 10% | 0.6875 | N | 0.00 | 0.00 | 0.00 | 0.00 | 0.00 | 0.00 |
| | $\rho$ | 20% | 238.4 | N | 0.00 | 0.00 | 0.00 | 0.06 | 0.06 | 0.06 |
| | $c$ | 5% | 121.5 | N | -0.89 | 1.14 | 2.17 | 4.45 | 5.69 | 10.84 |
| Polyurethane | $\alpha$ | 5% | 0.94875 | N | -0.01 | 0.01 | 0.00 | 0.07 | 0.06 | 0.01 |
| | $\rho$ | 1% | 14.3 | N | 0.03 | 0.06 | -0.01 | 0.03 | 0.06 | 0.01 |
| Combined Uncertainty | | | | | | | | 4.50 | 6.71 | 15.88 |
| Expanded Uncertainty (k=2) | | | | | | | | 9.00 | 13.41 | 31.76 |

**Table 7.30**: *Uncertainty budget for the material parameters (see Table 7.6) investigated in the Polyurethane setup. The variation ($\Delta$), standard deviation ($\sigma$), and distribution shape (Normal/Rectangular - N/R) of each parameter can be seen. In addition, the sensitivity factors ($f_P$, $f_D$, and $f_V$), and the calculated uncertainties ($U_P$, $U_D$, and $U_V$) can be seen for all three investigated variables.*

| Param. | N/R | $U_P$ [dB] | $U_D$ [$\lambda$] | $U_V$ [dB] |
|---|---|---|---|---|
| No. PML Layers | N | 0.00 | 0.00 | 0.00 |
| Grid Step | R | 0.09 | 0.08 | 0.26 |
| No. Periods | N | 0.02 | 0.07 | 0.05 |
| Grid Rotation | R | 0.71 | 0.39 | 9.09 |
| Combined Uncertainty | | 0.71 | 0.40 | 9.09 |
| Expanded Uncertainty (k=2) | | 1.18 | 0.67 | 15.03 |

**Table 7.31**: *Uncertainty budget for the numerical parameters (see Table 7.7) investigated in the Polyurethane setup. The calculated uncertainties ($U_P$, $U_D$, and $U_V$) can be seen for all three investigated variables. It should be noted that given the nature of these parameters, the calculation of sensitivity factors and uncertainty was not applicable and was therefore omitted. Instead, uncertainty was considered to be the variation in the investigated variables.*

|  | Param. | $\Delta$ | $\sigma$ | N/R | $f_P$ [dB/%] | $f_D$ [$\lambda$/%] | $f_V$ [dB/%] | $U_P$ [dB] | $U_D$ [$\lambda$] | $U_V$ [dB] |
|---|---|---|---|---|---|---|---|---|---|---|
| Transducer | Curvature Radius | 2mm | 2 | R | -0.05 | -0.48 | 1.14 | 0.06 | 0.55 | 1.32 |
|  | Aperture Width | 0.2mm | 0.2 | R | 0.96 | -0.32 | -2.30 | 0.11 | 0.04 | 0.27 |
| Sample Translation | Along Upper Rod | 2.5mm | 2.5 | R | 0.02 | 0.20 | 0.30 | 0.03 | 0.29 | 0.43 |
|  | Along Propagation Axis | 2.5mm | 2.5 | R | -0.15 | -0.05 | 0.09 | 0.21 | 0.07 | 0.12 |
|  | Along Lower Rod | 2.5mm | 2.5 | R | 0.30 | -0.80 | 0.32 | 0.43 | 1.16 | 0.46 |
| Sample Rotation | Around Upper Rod | 2.5° | 2.5 | R | -0.13 | -0.72 | 0.35 | 0.19 | 1.04 | 0.50 |
|  | Around Lower Rod | 2.5° | 2.5 | R | -0.01 | 0.20 | -0.07 | 0.02 | 0.29 | 0.10 |
| Combined Uncertainty |  |  |  |  |  |  |  | 0.53 | 1.71 | 1.57 |
| Expanded Uncertainty (k=2) |  |  |  |  |  |  |  | 0.88 | 2.82 | 2.60 |

**Table 7.32**: *Uncertainty budget for the geometrical parameters (see Table 7.8) investigated in the Polyurethane setup. The variation ($\Delta$), standard deviation ($\sigma$), and distribution shape (Normal/Rectangular - N/R) of each parameter can be seen. In addition, the sensitivity factors ($f_P$, $f_D$, and $f_V$), and the calculated uncertainties ($U_P$, $U_D$, and $U_V$) can be seen for all three investigated variables.*

|  | $U_P$ [dB] | $U_D$ [$\lambda$] | $U_V$ [dB] |
|---|---|---|---|
| Combined Uncertainty (Numerical, Table 7.31) | 0.71 | 0.40 | 9.09 |
| Combined Simulation Uncertainty | 0.71 | 0.40 | 9.09 |
| Expanded Simulation Uncertainty (k=2) | 1.18 | 0.67 | 15.03 |

**Table 7.33**: *Combined and expanded (k=2) simulation uncertainty budget for the Polyurethane setup.*

|  | $U_P$ [dB] | $U_D$ [$\lambda$] |
|---|---|---|
| Comb. Mat. Uncert. (Table 7.30) | 4.50 | 6.71 |
| Comb. Geom. Uncert. (Table 7.32) | 0.53 | 1.71 |
| Comb. Meas. Setup Uncert. (Table 7.5) | 0.29 | 0.37 |
| Comb. Meas. Uncert. | 4.54 | 6.93 |
| Exp. Meas. Uncert. (k=2) | 9.06 | 13.73 |

**Table 7.34**: *Combined and expanded (k=2) measurement uncertainty budget for the Polyurethane setup.*

|                                        | $U_P$ [dB] | $U_D$ [$\lambda$] |
|----------------------------------------|------------|-------------------|
| Combined Simulation Uncertainty        | 0.71       | 0.40              |
| Combined Measurement Uncertainty       | 4.54       | 6.93              |
| Combined Total Uncertainty             | 4.60       | 6.94              |
| Expanded Total Uncertainty (k=2)       | 9.14       | 13.74             |

**Table 7.35**: *Combined and expanded (k=2) total uncertainty budget for the Polyurethane setup.*

# Part III

# Applications

# 8

# Modeling of Transcranial Focused Ultrasound in Neurosurgical Applications

As discussed in Section 3.3.2.2, the foremost challenge encountered when employing transcranial FUS (tcFUS) for neurosurgical applications and cerebral tumor treatment, is the presence of the skull and the phase-aberrations it induces. These aberrations induce significant distortion of the acoustic energy deposition, shifting of the focus, and thermal gain decrease. Phased-array transducers featuring hundreds of elements allow for the partial compensation of skull-induced aberrations by calculation and application of appropriate phase and amplitude corrections. Precise focusing however, remains a necessity, especially at high acoustic frequencies.

This chapter will begin by providing an extensive review of the large number of different techniques that have been investigated to compensate for these skull-induced aberrations, which range from entirely experimental methods to analytical and simulation-based techniques (Section 8.1).

The remainder of this chapter is dedicated to the presentation of a numerical study on the transcranial sonication of a detailed anatomical head model by a CAD model of the InSightec ExAblate® 4000. Four different approaches, ranging from (semi-)analytical to simulation-based, were employed to calculate aberration corrections for 22 targets in the brain, and their impact on the resulting pressure and temperature distributions was ascertained.

## 8.1 Preface: tcFUS Aberration Correction Techniques

This section will provide a comprehensive overview of over 20 years of in-vitro, ex-vivo, in-vivo, and in-silico approaches to the calculation of skull-induced aberration correc-

tions. These approaches can be roughly categorized into *time-reversal* techniques (Section 8.1.1), experimental and numerical techniques based on computed tomography (CT) image data (Section 8.1.2), and novel approaches utilizing magnetic resonance acoustic radiation force imaging (MR-ARFI) presented in Section 8.1.3. Finally, a critical assessment of the different techniques, their strengths and shortcomings, as well as the necessary provisions required for the individual techniques to be applied in the clinical environment is given in Sections 8.1.4 and 8.1.5 respectively.

## 8.1.1    Time-reversal techniques

The phase conjugate mirror (PCM) approach for phase aberration correction, which involves insonation of an acoustically reflective target and the use of the transducer elements as receivers to measure relative time delays in the different elements, was first proposed for transcranial ultrasonic imaging by Phillips et al. [516]. After inversion, the appropriate phase-shifts are computed to achieve in-phase superposition [517]. The time-reversal approach was initially presented as a wave mirroring method by Fink [518]. Instead of merely detecting and inverting the phases of reflected waves, the entire temporal pressure waveform is stored, reversed, and re-emitted to focus on a reflective target (convergent waves) that behaves as a source when insonated (divergent waves), providing both phase and amplitude corrections. The main advantage of the time-reversal over the PCM approach is that it can be applied to broadband acoustic signals and is not limited to harmonic waves. This method was first applied to lithotripsy, where such reflective sources, e.g., kidney stones, occur naturally in the body [518]. Later, for application of this approach to brain therapy involving transcranial sonication, it was proposed that the lack of such a reflector in the brain could be compensated for by implanting an artificial source or sensor in the targeted area, e.g., a monoelement transducer or a hydrophone in a tumor [519, 520]. This method saw further improvement, e.g., amplitude compensation [521], in the following years, although a detailed historical overview is outside the scope of this article. Fink et al. [520] published a review of time-reversal techniques and their applications in acoustics in general, ranging from imaging to lithotripsy and brain therapy. Another brief review of the time-reversal approaches can be found in [522]. Three types of approaches employing time-reversal, are presented below.

### 8.1.1.1    Implanted hydrophone

Hynynen and Jolesz [523] presented an 'implanted' hydrophone approach, where in ex-vivo skull studies, a hydrophone was placed at the location of the desired focus. After placement, every element of the transducer array was powered separately, and this procedure was followed sequentially for all involved elements. With the hydrophone, the phase shifts induced by the presence of the skull were measured, inverted, and applied to

all elements in the array thus correcting for the phase shifts and making the waves converge at the focal spot in phase, resulting in maximum deposited acoustic energy through constructive interference. A schematic diagram of this approach is shown in Figure 8.1.

While this approach is believed to provide the best possible aberration correction – and therefore, maximum energy deposition compared to any other focusing approach – it exhibits two substantial limitations. First, the approach is invasive, requiring the insertion of a receiver hydrophone in the brain when applied in-vivo. Second, to produce a new focal point in another location, e.g., when overlapping multiple smaller lesions for the treatment of a large tumor volume, the receiver would need to be moved and the procedure repeated, which would increase both the treatment time and the risk of complications.

In a later study, Clement and Hynynen [524] from the same group, expanded upon this method to overcome the latter of the two restrictions by introducing a beam-steering approach. The method still depends on the use of a small catheter-inserted hydrophone at the location of the intended focus and measurement of the phase shifts for all array elements, as described above. However, when the initial pressure measurements are performed at locations remote from the focus, in the absence of the ex-vivo skull, it was possible to analytically calculate new phase corrections for those remote locations and reconstruct the focus after the skull was re-introduced. Thus, this study demonstrated the ability to steer the focus without repositioning the implanted hydrophone within the skull. This approach produced clinically viable acoustic intensity values and temperature increases within a $25\ \mathrm{mm}$ radius of the catheter location as determined by a ca. $50\%$ drop in acoustic intensity.

It should be mentioned that the 'refocusing' strategy in [524] was previously introduced by Seip et al. [525], where similar dynamic refocusing approaches and resulting ranges were reported, but only in soft tissue. Clement and Hynynen [524] verified this approach in the presence of an ex-vivo skull and in-vivo in [526]. This hydrophone approach is still considered the 'gold standard' in experimental studies. It has also been used in recent ex-vivo studies [226]. The study by Pernot et al. [527] demonstrated in-vivo the ability to produce thermal lesions deep inside the brains of 10 sheep with implanted hydrophones by means of time-reversal techniques.

### 8.1.1.2 'Acoustic Stars'

In an attempt to compensate for the absence of passive or active sources in the brain with a non-invasive technique, Pernot et al. [528] suggested the use of two ultrasonic arrays: first, a high-power array to generate a short, intense ultrasonic pulse focused in one area of the brain to create a cavitation bubble, the collapse of which generates a shock wave that is detected by a second ultrasonic imaging array. With this application of a time-reversal approach, the authors reported successful refocusing in an in-vitro study involving an artificial rubber aberrator placed in front of a tissue phantom, and claim that,
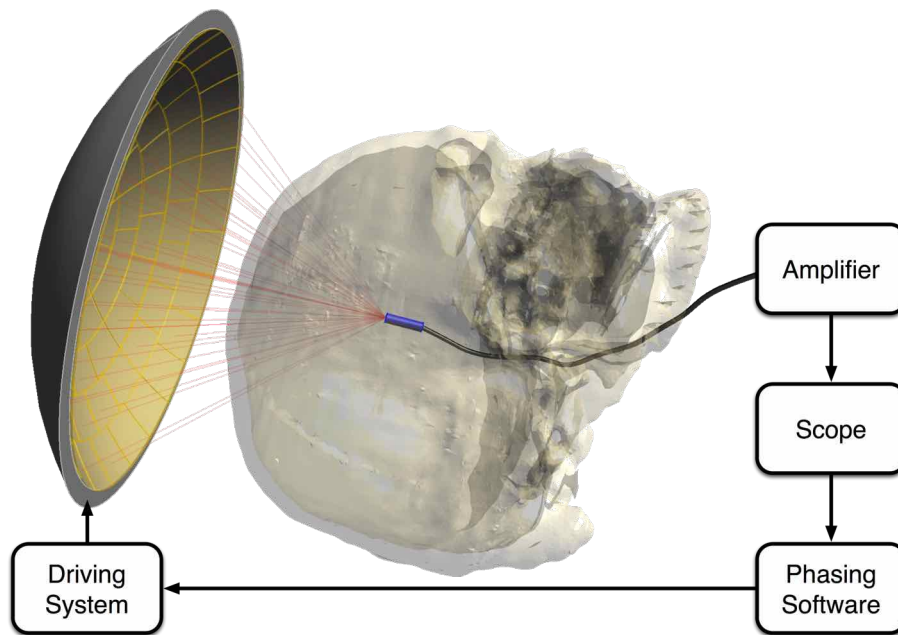
**Figure 8.1**: *Schematic diagram of the 'Implanted hydrophone' correction technique, which is considered the 'gold standard' in experimental studies. A hydrophone implanted at the intended target location records the complex pressure for each element of a phased-array transducer activated in a sequential manner. The recorded phases are processed and inverted before being applied back to the transducer elements to correct for the skull aberrations and refocus at the target location.*

as this approach generates only a single cavitation bubble, it should be possible to prevent the occurrence of any tissue damage.

This method was improved and applied to focusing in a tissue-mimicking phantom contained in an ex-vivo half skull in a later study [529]. Instead of two transducer arrays, a single cylindrical array was employed to induce cavitation, record the generated shock wave, and focus on the target through time-reversal. The presence of the skull, however, caused strong wave aberrations and did not initially allow the pressure amplitudes to rise high enough and induce cavitation at the target. To compensate, initial aberration corrections were computed through a 3D finite-difference time-domain (FDTD) simulation based on CT image data (first presented in [313]) with a 'virtual' point source at the location of the desired focus as described below. This initial focusing allowed for the induction of cavitation and application of the focusing approach presented in the first study, whereby 97% of the implanted hydrophone-based reference pressure amplitude was restored at the focal location.

To avoid the high pressures required to induce cavitation, a technique was developed by Haworth et al. [530] that involves injection of liquid droplets into the target volume that are consequently vaporized with a high-frequency, high-power ultrasonic array to

create cavitation bubbles before time-reversal based aberration correction is performed as described in [528].

### 8.1.1.3 'Virtual Source'

The recent increase in computational power has allowed for efficient simulations of acoustic wave propagation, which has yielded a 'virtual' version of the time-reversal approach, first applied to transcranial sonication by Marquet et al. [422]. In this study, CT image data from an ex-vivo primate and human skulls were segmented and used as input in a 3D FDTD code to solve a linear acoustic wave equation. In a simulation of this setup with a 'virtual' point source placed at the desired focus location, the temporal pressure waveforms at the level of the transducer elements were recorded and transmitted experimentally with a 300-element spherical array transducer system after time-reversal: precise focusing, with a positioning error of $0.7$ mm at $90\%$ of the peak pressure amplitude recorded with an implanted hydrophone, was reported.

A similar approach was recently reported in [226], involving the sonication of an ex-vivo skull with the ExAblate® 4000 system operating at $230$ kHz. In this study, linear acoustic equations for propagation in soft tissues and elastic wave equations for propagation within the bone were used in an attempt to investigate standing wave effects during transcranial sonication; a point source was used at each of four desired focal locations to record the waves at the transducer element level, with only the phase of the impinging waves inverted and without amplitude correction.

Many recent studies have employed this approach to correct for skull aberrations, e.g., the numerical studies on tcFUS by Pinton et al. [531], in which a 3D FDTD linear acoustic solver was used to explore cavitation effects, and Pinton et al. [532], where a non-linear 3D FDTD solver was utilized to investigate the impact of acoustic non-linearity. Alternative numerical approaches have recently been investigated, and demonstrated a significant reduction in computational time. These include the work by Pinton et al. [533], which demonstrated the use of a hybrid finite-different and phase-projection algorithm, and the study by Jing et al. [534], where a k-space numerical propagation model was used instead. In another recent article by Leduc et al. [535], the authors employed the 'Virtual Source' approach with a 3D FDTD linear acoustic solver, not only to achieve refocusing at the intended target location, but also to eliminate secondary foci by iteratively placing additional point sources at those locations, and inducing destructive interference in subsequent simulations. A schematic diagram of the 'Virtual Source' approach is shown in Figure 8.2.
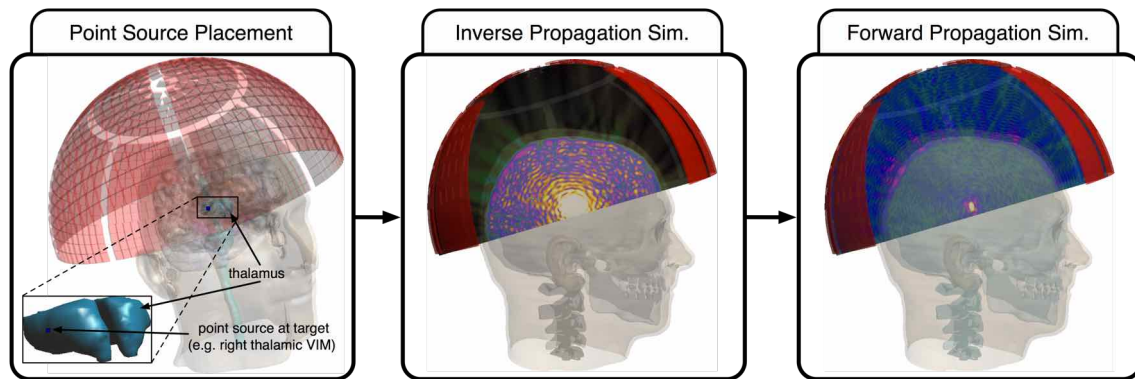
*Figure 8.2*: *Schematic diagram showing the concept of the 'Virtual Source' correction technique. A point source is placed at the intended target location, here, in the right thalamic ventral intermediate nucleus (VIM). The elements of the phased array transducer are used as receivers, and an 'inverse propagation' simulation allows the elements to record the pressure waves as either the entire waveform or the complex pressure phasors. These recorded pressure waves are inverted – either reversed in time for waveforms or conjugated for complex pressure phasors – and a forward propagation simulation or experiment yields refocusing at the intended target.*

## 8.1.2   CT-based techniques

### 8.1.2.1   Analytical techniques

Clement and Hynynen [536] employed computed tomography (CT) scans of ex-vivo human skulls segmented to either a single bone layer or three distinct outer cortical, central trabecular, and inner cortical layers. The segmented models were assumed to exhibit either homogeneous speed of sound across a layer or an averaged 'effective' speed of sound based on CT-derived density variation information. Phase corrections – analytically calculated based on the thickness of the different skull layers, the wave frequency, and the speed of sound, either homogeneous or effective, in bone – were applied to each of the four skull segmentation types in 10 ex-vivo skulls, and hydrophone-based measurements at the focal location yielded $63\%$ and $76\%$ (with and without density variation corrections) of the focal peak of the non-aberrated case in the absence of the skull.

A slightly modified version of this approach is commonly employed today by modern tcFUS systems. CT scans and hydrophone measurements of multiple ex-vivo skulls were used to derive a statistical model, which establishes a linear relation between an 'effective' speed of sound in bone and the Hounsfield units (HU). For every patient, a new CT scan is performed and the image data is used as input for the tcFUS system's planning software. The skull is segmented as a single bone layer, and the software performs ray-tracing analysis on the ray cast from the element center towards the intended target for each of

the array elements to calculate the average HU along each ray's path. The data is entered into the statistical model, from which an effective speed of sound is obtained and used to analytically calculate the phase correction for each element. This procedure is graphically depicted in Figure 8.3.

### 8.1.2.2 Simulation techniques

Clement and Hynynen [537] used CT images of the skull to derive thickness, density, and geometry information, which was entered into a planar propagation numerical model. The model involves splitting the transducer into groups of elements, the acoustic fields of which are projected onto a plane directly above the skull, and an approach similar to the FFT-based angular spectrum method (ASM) employed in the FOCUS software [381] is used to propagate those fields through the focus. The quality of this focusing approach was evaluated by comparing the acoustic focus created by the simulation-based corrections against an ideal case of hydrophone-based corrections, where the phase-shift of each transducer segment is measured at the intended focal location and applied to achieve focusing. The algorithm was applied to 10 ex-vivo skulls to yield an average peak value of $45\%$ compared to the ideal case. In a later study [538], the same authors used the above approach with deliberately induced shear waves at the skull to enhance their propagation algorithm with longitudinal-shear wave conversion at the skull, to evaluate whether the transmission of focused ultrasound beams purely as shear waves is possible and advantageous. Results showed that the peak amplitude due to shear-wave propagation was $35 - 55\%$ smaller than the peak achieved with longitudinal waves. However, they reported that, due to the similar shear wave speed in water, soft tissues, and bone, these waves suffer less distortion. Thus, this shear wave transmission method could be used as an additional delivery strategy, especially for focusing at high incident angles, e.g., when focusing close to the skull surface where shear waves are prominent. The approach presented in [537], when applied to sonication of rabbit thigh muscle and brain tissue with an ex-vivo human skull between the tissue and a 500-element hemispherical transducer, yielded consistent results [526].

### 8.1.3 MR-ARFI techniques

MR acoustic radiation force imaging (MR-ARFI) [74] is a recently developed technique that utilizes MRI through motion-sensitive encoding MR gradients, similar to those used in MR-elastography [75, 76], to measure the micron-scale static tissue displacement induced by FUS waves as phase shifts in the resulting MR image [77, 78]. Since this tissue displacement is proportional to the local acoustic intensity, i.e., the square of the acoustic pressure, MR-ARFI allows non-invasive pressure measurements anywhere in the insonated anatomy.
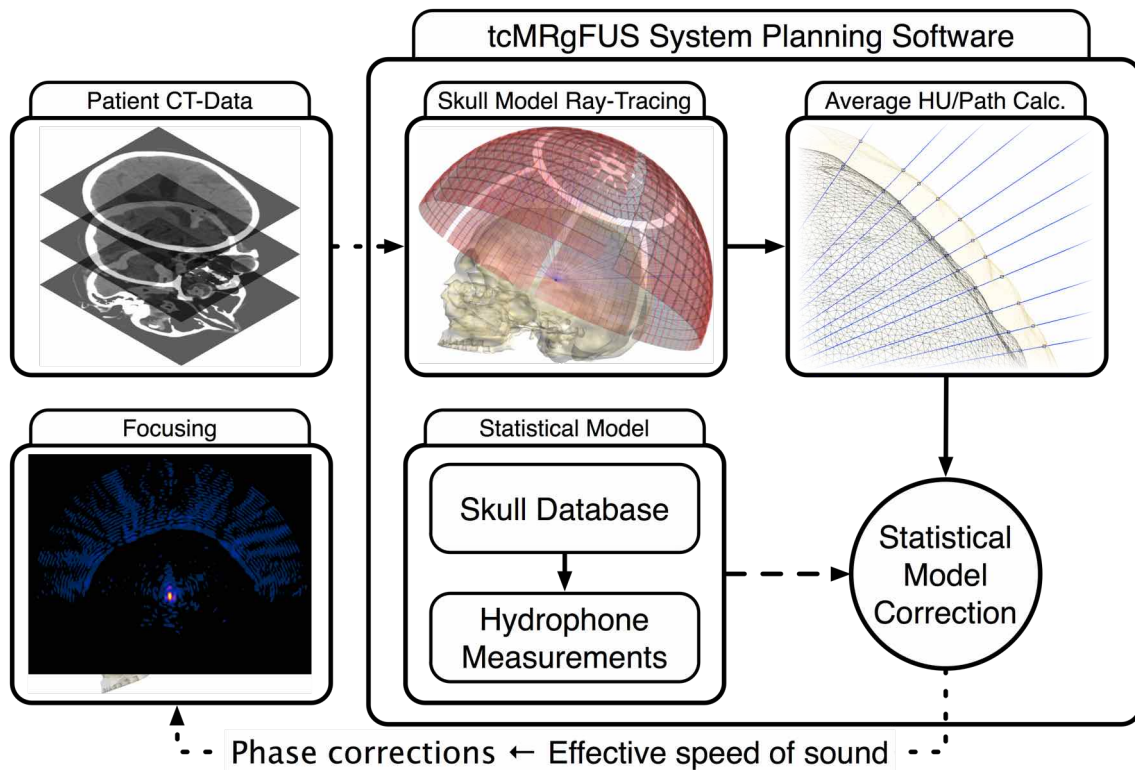
**Figure 8.3**: *Schematic diagram of a CT-based phase correction approach concept commonly employed in modern tcFUS systems. The patient's CT scan is entered into the system's planning software, which segments the skull as a single layer of bone and performs a ray-tracing analysis to calculate the average Hounsfield units (HU) values along the path of the ray for each array element. These HU values are entered into an existing statistical model, based on measurements of ex-vivo skulls, to yield an effective speed of sound, which can be used to calculate phase corrections and achieve re-focusing.*

Larrat et al. [31] proposed a method called 'energy-based adaptive focusing' in which MR-ARFI measurements are used to estimate the local tissue displacement induced by the acoustic radiation force of the beams at the location of the desired focus. With one of the transducer elements as a reference, four such acquisitions are performed for each of the other elements of the transducer to estimate the phase shift between that element and the chosen focal spot. Those calculated phase shifts are then inverted and applied to the transducer elements to achieve a strong focus. This approach was successfully applied on a simple phantom setup in [31], in which a fivefold increase in intensity was reported. In a previous study [78], the same research group applied this theoretical model to speckle-tracking obtained from pulse-echo ultrasound sequences to define tissue displacement in simplified phantoms containing reflective targets/scatterers. However, despite the success of this technique in a proof-of-concept experiment, the authors reported in [31] that ultrasound imaging cannot be accurately used in the presence of a medium which causes

strong aberrations, e.g., the skull, which prompted the use of MR-ARFI. The same group recently published a study [539] where this MR-ARFI approach, applied to a 512-element transcranial sonication system with human cadaver heads, resulted in a factor of $2.2$ higher intensity at the focal spot compared to the non-phase-corrected sonication, and a factor of $1.5$ compared to the focusing pattern achieved through CT-based aberration corrections. However, this case required over $10,000$ sonications and MR-ARFI acquisitions, which amount to ca. 2 hours of measurements, to define the phase corrections for a single focal spot. This implies that the method, although promising, may not yet be appropriate for the clinical environment, especially for treatment of large volumes with multiple overlapping focal spots.

In an attempt to decrease the number of MR-ARFI acquisitions, Hertzberg et al. [540] employed a similar approach – instead of calculating the phase correction for each element in reference to another, they grouped the transducer array elements and assigned a total of $26$ random phases to each group. Subsequently, they performed MR-ARFI acquisitions for sonications with different phase shifts for each group to identify the optimal phases, i.e., the phases that produce the maximal displacement at the focal location. This approach was applied in-vivo with the ExAblate$^{\circledR}$ 4000 system to sonicate a porcine brain exposed by craniotomy, with a human skull between the animal tissue and the transducer to mimic human treatments. The maximum tissue displacements induced at the intended focus by the employed method were compared to those found with CT-based and hydrophone correction approaches and against the displacement in the absence of aberrations. The presented MR-ARFI approach yielded a $27\%$ maximum displacement compared to the non-aberrated case, better than the $8-12\%$ obtained with CT-image based corrections, and was deemed comparable to the hydrophone approach, which yielded a $40\%$ displacement.

Grissom et al. [541] and Vyas et al. [542] proposed the use of MR-ARFI measurements to improve the numerically calculated phase corrections obtained through unfocused simulations, i.e., random phases that disregard actual patient anatomy, using the Field II [286] and the hybrid angular spectrum methods [280], respectively. The proposed method allowed for successful refocusing when applied to a simple phantom setup with a significantly smaller number of MR-ARFI acquisitions (4 and 1 respectively) when compared to the 'energy-based adaptive focusing' approach presented above.

The study by Kaye et al. [77] is built on the method presented in [31], which requires four MR-ARFI acquisitions for each transducer element to measure the acoustic intensity at given locations in the brain. However, an alternative ultrasonic wave encoding, based on Zernike polynomials instead of Hadamard matrices, allowed to achieve $90\%$ of the non-aberrated focal intensity with less than $20\%$ of the MR-ARFI acquisitions. The same study proposed the utilization of a phase correction 'database' based on CT datasets of other patients, similar to the approach presented in [536], to extract an initial approximate phase correction set, which is then improved based on the MR-ARFI measurements.

### 8.1.4   Critical Assessment

The techniques presented above range from purely analytical or numerical calculations of the required aberration corrections, to entirely experimental approaches with a varying degree of invasiveness, usability, and success. A qualitative comparison of the presented approaches can be seen in Table 8.1.

Highly effective time-reversal techniques, like the 'Implanted Hydrophone' (see Section 8.1.1.1) and the 'Acoustic Stars' (see Section 8.1.1.2), undoubtedly provide the highest re-focusing quality achievable. In the case of the former, the only viable solution that would allow the clinical use of this technique would involve a catheter-inserted microscopic hydrophone, that can be introduced in the vicinity of the intended focal region through the cerebral vascular network. However, this approach would be invasive and could even result in undesirable tissue damage, i.e., brain hemorrhage. Moreover, even when complemented with semi-analytical steering capabilities, as proposed in [524], the resulting steering range is limited to a couple centimeters around the implanted hydrophone, after which the focusing quality deteriorates with distance. The 'Acoustic Stars' technique is a non-invasive alternative, and could theoretically be employed to achieve refocusing anywhere in the insonated soft tissue of the anatomy. However, as it depends on the administration of sonications exhibiting HIFU level pressure amplitudes, and acoustically induced micro-bubble cavitation, this approach may entail safety risks. It has been theorized that by focusing acoustic energy only in the intended target location, and with sonications gradually increasing in power, the technique should avoid uncontrolled cavitation outside that region. However, there exists no indication as to whether it may induce any of the tissue damage or disruption effects that have been associated with acoustic cavitation [15, 16]. The aforementioned concerns and the absence of literature on the in-vivo application of these techniques, suggest that these approaches are unlikely to be utilized in the clinical environment. Nonetheless, they remain an invaluable tool for in-vitro and ex-vivo experiments, feasibility studies, and the development of tcFUS systems.

Approaches based entirely on analytical calculations or simulations to derive phase and, optionally, amplitude corrections (see Section 8.1.1.3 and 8.1.2) are entirely non-invasive, do not require the presence of the patient, and are already being employed on modern tcFUS systems. However, despite their speed and ease-of-use, the purely analytical methods are inherently limited as they do not account for the entire range of wave propagation phenomena, unlike full-wave simulation-based techniques. Thus, these methods are not entirely effective for estimating the corrections required, resulting in a limited treatment envelope and focusing quality. Moreover, the existing statistical models utilized for these analytical approaches, are based on measurements of a limited number of adult ex-vivo skulls, which limits the applicability of the models, e.g., excluding pedriatic patients.

Simulation-based techniques have shown great promise and will undoubtedly replace their analytical counterparts, since they allow modeling of the complex patient anatomy, most notably the skull, in far higher detail than analytical approaches, potentially even in a

patient-specific manner. Full-wave simulations can also account for most of the physical phenomena, e.g., reflections, refractions, and attenuation, that occur during wave-propagation, while some models can even account for non-linear wave propagation, cavitation and shear waves. Simulation-based techniques are inherently amenable to permitting treatment planning and optimization, e.g., through multiple simulations or even genetic optimization techniques. They offer the possibility to predict and avoid secondary effects of the treatment, e.g., skull heating, the formation of secondary foci and unwanted cavitation. The complexity of acoustic wave-propagation, however, in highly complex, heterogeneous anatomical structures, is a computationally intensive problem that requires huge amounts of computational resources to allow such simulations to run in viable time frames. The required resources and computational time increase even further at higher acoustic frequencies (e.g., $1$ MHz), or when accounting for effects such as non-linearity and shear waves. The choice of the simulation technique typically involves a trade-off between physical accuracy, simulation time and computational resources, and requires validation of the chosen method. But the employment of high-end hardware and state-of-the-art parallelization techniques is a promising track, and such simulations are now becoming feasible; multiple optimization simulations that can be run overnight will soon be achievable with affordable hardware.

The MR-ARFI techniques (see Section 8.1.3) also show promise and could prove invaluable for estimating required corrections. These techniques are entirely non-invasive and have demonstrated the ability to produce high quality focusing. In addition, they exhibit the unique characteristic of directly monitoring the quantity of interest, i.e., acoustic pressure, and offer the possibility of closed-loop control of transcranial sonication. Nonetheless, MR-ARFI techniques are still in an experimental stage and, in their current form, require hours of measurements in the presence of the patient and the careful management of the transducer element grouping and activation. Despite this, the promise of MR-ARFI aberration correction approaches captures the interest of many researchers, and may well prove to be a valuable clinical solution if technical advances are made that help overcome the aforementioned challenges.

## 8.1.5 Conclusions and outlook

Despite the inherent limitations of therapeutic ultrasound, and, in the case of tcFUS, the major problems caused by skull-induced aberrations, this modality has shown great promise in a number of neurosurgical interventions, including cancer treatment, motor disorders such as essential tremor and Parkinson's disease, and improved drug delivery for treatment of conditions such as Alzheimer's disease and multiple sclerosis. Consequently, medical centers throughout the world are establishing clinical trials to explore the capabilities of this technology.

| Approach | Refocusing quality | Speed | Invasive or potentially harmful | Increase in table time |
|---|---|---|---|---|
| *Time-reversal techniques* | | | | |
| Implanted hydrophone | ++++ | + | Yes | Yes |
| 'Acoustic Stars' | ++++ | ++ | Yes | Yes |
| 'Virtual Source' | +++ | + | No | No |
| *CT-based techniques* | | | | |
| Analytical | + | ++++ | No | No |
| Numerical simulations | ++ | + | No | No |
| *MR-ARFI techniques* | | | | |
| Focused adaptive | ++ | + | No | Yes |
| Unfocused adaptive | ++ | ++ | No | Yes |

**Table 8.1**: *A qualitative comparison of the presented approaches.*

Many different approaches to compensate for skull-induced aberrations have been reported over the years. Each has its own set of advantages and limitations which are discussed in this section. As the aberrations constitute the main obstacle to the efficacious employment of this technology, significant progress has been noted towards resolving this issue over the past decade, but further research is clearly required to establish an effective, efficient, and non-invasive procedure for tcFUS to be accepted by the clinical community.

In view of their non-invasive nature, flexibility, and the wealth of information offered by 3D simulations, their use will likely become increasingly common and they will be available for online treatment delivery adaptation and correction, e.g., by leveraging precomputed solutions.

## 8.2 Acoustic and Thermal Modeling of tcFUS Neurosurgical Applications

The purpose of this study was to investigate the impact of skull-induced aberrations, compare different phase and amplitude correction approaches used to compensate for these aberrations and achieve refocusing, extend the treatment envelope of tcFUS therapy, as well as to explore acoustic and thermal secondary effects of the treatment.

The simulated setup consists of an idealized model of the commercial tcMRgFUS system, ExAblate® 4000 (InSightec, Haifa, Israel) and the detailed anatomical head model of a 34-year old, healthy male; 22 targets, in various locations in the brain of the head model, were defined and examined. Phase and amplitude corrections for each of these targets

were calculated according to 4 different approaches, and the impacts on the acoustic focus and the induced temperature increase were investigated. In addition, the impact of acoustic nonlinearity on the pressure distribution and temperature increase and the effect of temperature-dependent perfusion on the temperature distribution were also explored.

## 8.3 Materials & Methods

### 8.3.1 Simulation Setup

#### 8.3.1.1 Applicator Model

The applicator model used in these simulations was based on the ExAblate® 4000 (InSightec, Haifa, Israel), which was described in Section 2.5.2.2. As was outlined in the aforementioned section, the ExAblate® 4000 consists of a $30\ \mathrm{cm}$ diameter hemispherical phased-array transducer with $1024$ elements operating at either $230\ \mathrm{kHz}$ or $650\ \mathrm{kHz}$. This device is coupled with a 1024-channel amplifier, which allows phase and amplitude control of each individual transducer element in the phased array.

A model applicator, shown in Figure 8.4, was generated to mimic the actual applicator, with the same number of transducer elements in similar groupings. All elements were modeled identically, with a surface area of $1\ \mathrm{cm}^2$.

#### 8.3.1.2 Head Model

The head model used in these simulations is an improved version of the 'Duke' model described in Section 6.3.3. This improved version of the model, shown in Figures 8.4 and 8.5, was developed as part of the Virtual Population project [543], where the original MRI dataset was re-sampled with a resolution of $0.5 \times 0.5 \times 0.5\ \mathrm{mm}$ and re-segmented, yielding over 50 individual tissues and anatomical structures in the region of the head.

#### 8.3.1.3 Patient Positioning and Target Definition

To replicate clinically relevant setups, the head model was placed so that the right thalamic ventral intermediate (VIM) nucleus was located at the geometric center of the transducer, i.e., where the acoustic waves of all the elements, driven in phase with no source of phase aberrations – e.g., the presence of the skull – would converge according to the arrangement of the elements in the array, as shown in Figure 8.4.

To evaluate the different refocusing approaches that are described in the next section, and the ability of each to focus the acoustic waves at a given location further away from the

transducer's geometric focus than is currently considered feasible, two types of targets, 'structure targets' and 'cortex targets', were defined in the anatomical model. Structure targets, regions of the human brain that have been associated with different neuropathic conditions, are very desirable targets for tcFUS neurosurgery; 14 such targets were defined and are shown in Figure 8.5(b). In addition, 8 cortex targets in different cortices of the brain were defined, as shown in Figure 8.5(a), which, because of close proximity to the skull, are thought by the FUS community to be untreatable. A summary of all targets and their distance from the transducer's geometric focus can be seen in Table 8.2.
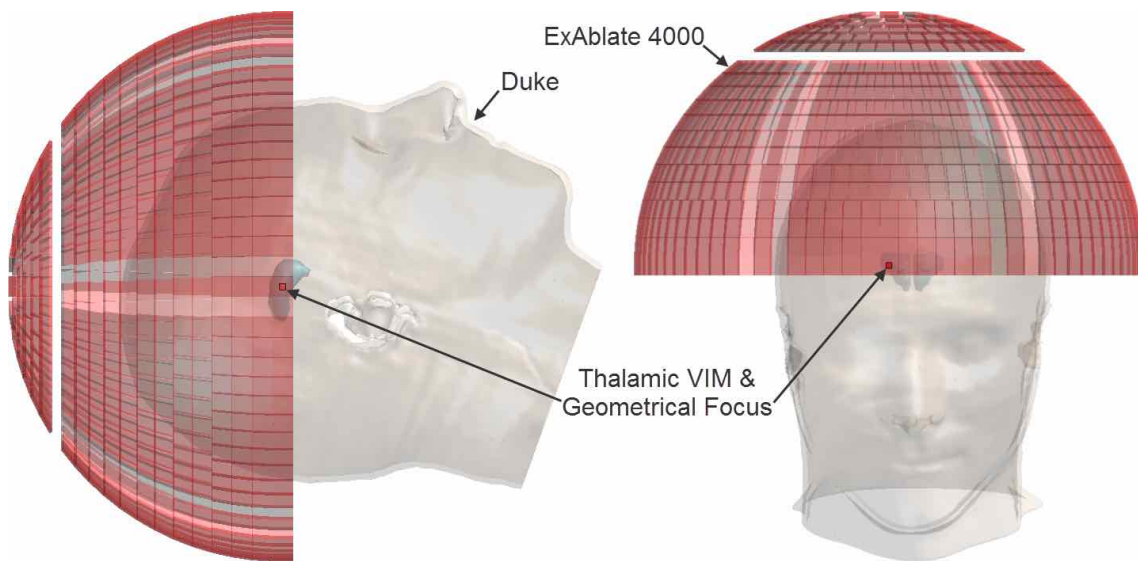


**Figure 8.4**: *The 'Duke' anatomical head model and the ExAblate® 4000 transducer array used in this study. The positioning of the head model within the transducer as well as the location of the geometric focus in the right thalamic ventral intermediate (VIM) nucleus can be seen.*

### 8.3.2   Acoustic Simulations

Linear acoustic simulations were performed at $230\,\mathrm{kHz}$, with the LAPWE solver described in Section 5.2.1.4. The simulation domain was discretized with a $0.65\,\mathrm{mm}$ grid-step, truncated to approximately $308 \times 308 \times 240\,\mathrm{mm}$, and terminated with 16 layers of PML on all domain boundaries to inhibit the manifestation of spurious reflections. All acoustic simulations were performed for $1000\,\mathrm{W}$ of acoustic power (see Section 8.3.2.3) and their duration was set to 230 periods which correspond to a propagation distance of approximately $1.5\,\mathrm{m}$. The acoustic properties of the different tissues were set according to the values presented in Table 1.2, while the material density $\rho$ values were based on the IT'IS Foundation Tissue Properties Database [8]. Given that the anatomical model

*(a)*



*(b)*
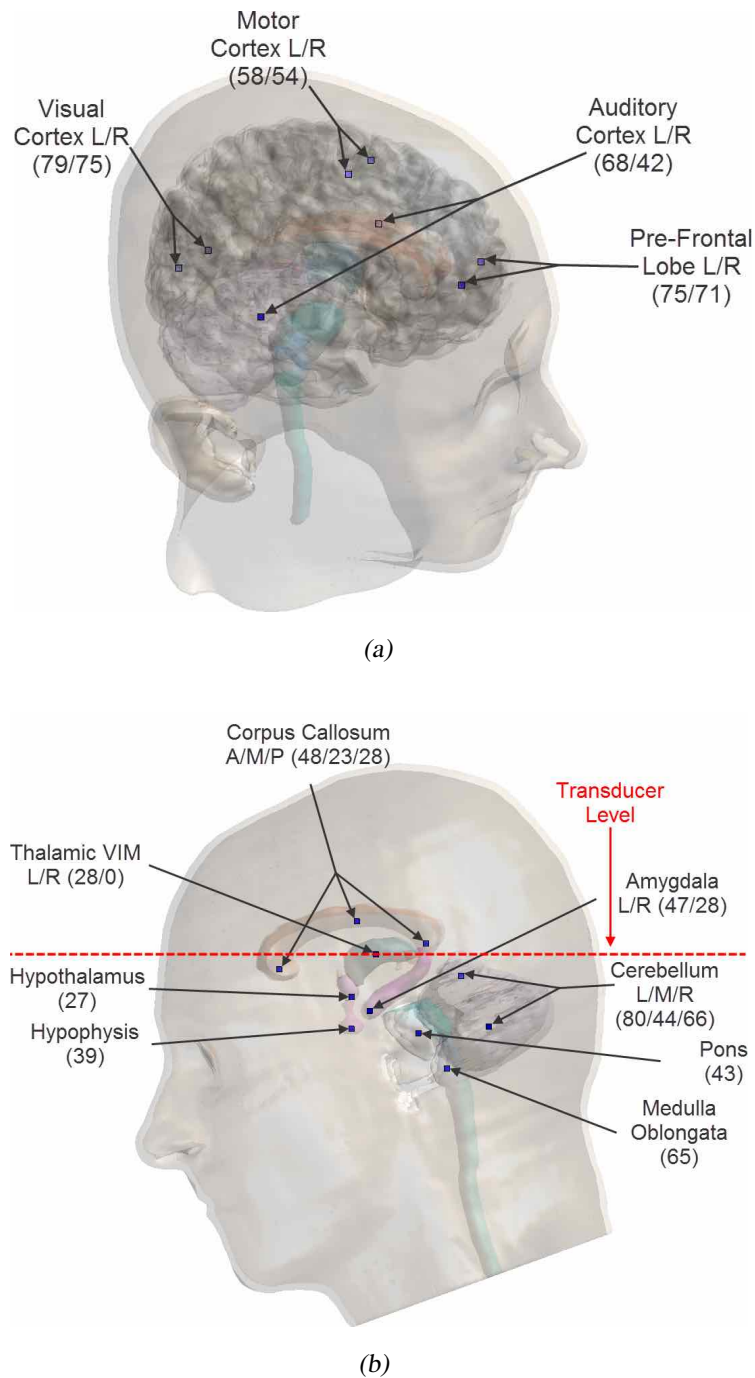
**Figure 8.5**: *The targets defined in the head model:* (a) *'cortex targets', which all lie above the transducer level, and* (b) *'structure targets', where the red dashed line shows the transducer level in relation to the targets, which heavily influences the achievable focusing. The initials L, R, A, M, and P stand for left, right, anterior, medial, and posterior, respectively, and the numbers in parentheses are the target distances in* mm *from the geometric focus of the transducer.*

| Target Name | Distance [mm] |
|---|---|
| *Structure Targets* | |
| Amygdala (Left/Right) | 47.2 / 28.1 |
| Cerebellum (Left/Medial/Right) | 79.5 / 43.7 / 65.6 |
| Corpus Callosum (Anterior/Medial/Posterior) | 48.4 / 23.4 / 28.3 |
| Hypophysis | 39.2 |
| Hypothalamus | 26.7 |
| Medulla Oblongata | 64.6 |
| Pons | 44.3 |
| Thalamic VIM (Left/Right) | 28.0 / 0.0 |
| *Cortex Targets* | |
| Auditory Cortex (Left/Right) | 68.0 / 42.0 |
| Motor Cortex (Left/Right) | 58.8 / 54.3 |
| Prefrontal Lobe (Left/Right) | 75.1 / 71.0 |
| Visual Cortex (Left/Right) | 79.5 / 75.2 |

**Table 8.2**: *The different targets that were defined in the head model and evaluated with the different aberration-correction approaches, as well as their distance in* mm *from the geometric focus of the transducer.*

used was based on MRI data, it wasn't possible to acquire voxel-specific bone properties through Hounsfield units, thus, constant acoustic properties were assigned per tissue.

### 8.3.2.1   Target Focusing and Aberration Correction

To correct both amplitudes and phases for every element of the array, the LAPWE-based linear acoustic solver (see Equation 4.9) was applied to each of the defined targets according to the following procedure: Initially, a point source, driven with an arbitrary amplitude, was placed at the intended target location. Afterwards, an inverse-propagation acoustic simulation of the entire head and applicator in which the waves from the point source were allowed to propagate for $1.0$ ms, i.e., 230 periods at 230 kHz resulting in a propagation distance of ca. $1.5$ m, was performed. During the simulation, the transducer elements were used as receivers to record the complex pressure values, i.e., amplitude and phase, at the surface center of every element. Subsequently four distinct focusing strategies were applied and evaluated.

*Distance-based Phase Corrections (DPC)*: Analytical phase corrections for every element were calculated based on the distance between each element's surface center and the desired target, assuming that the transducer is in a homogeneous water medium, thus without wave distortion taken into account. The calculated distance-based phase correc-

tions are applied to each element, the amplitudes of which are fixed to the appropriate pressure level for a given acoustic input power (see Section 8.3.2.3).

*Ray-Tracing-based Phase Corrections (RTPC)*: As an extension of the DPC approach, a ray-tracing algorithm that takes the skull properties into account and allows calculation of improved effective distance-based phase corrections was devised. The algorithm calculates the skull entry/exit, i.e., intersection, points of the rays between each element's surface center and the desired target and uses that information to calculate the thickness of the skull through which the waves from a given element propagate on the way to the target. Similarly to the DPC approach, the improved phase-corrections and fixed pressure amplitudes are applied to each element.

*Simulation-based Phase Corrections (SPC)*: The phases of the pressure phasors recorded during the inverse-propagation simulation are conjugated and the amplitudes are fixed to the appropriate constant pressure level for a given acoustic input power.

*Simulation-based Phase and Amplitude Corrections (SPAC)*: The phases of the pressure phasors recorded during the inverse-propagation simulation are conjugated and the recorded amplitudes, normalized to a given acoustic input power, are used (see Section 8.3.2.4).

Finally, for each of the 4 focusing strategies, the calculated phase – and in the case of the SPAC approach, amplitude – corrections were applied to their respective elements and a forward-propagation acoustic simulation was performed to investigate the acoustic and thermal impact of those corrections.

### 8.3.2.2   Non-Linear Acoustic Simulations

To investigate the effects of non-linear acoustic propagation on the pressure distribution and resulting temperature increase, the WLE (see Section 5.2.2.3) was used. To facilitate these simulations, the computational domain described prior was re-gridded with a $0.3 \, \mathrm{mm}$ grid-step. The phase corrections of the SPC approach were used to repeat the forward-propagation simulations (see Section 8.3.2.1) for the 'Thalamic VIM (Left)' and 'Thalamic VIM (Right)' targets (see Figure 8.5) to account for the generation of the first ($230 \, \mathrm{kHz}$), i.e., fundamental, and second harmonic ($460 \, \mathrm{kHz}$) frequencies. Consequently, these results were compared to those of the linear simulations, both acoustically and thermally.

### 8.3.2.3   Pressure Levels

The definition of the actual pressure amplitude level(s) for the array elements for a given acoustic input power is crucial for obtaining realistic pressure values at the focus location, for accurate modeling of non-linearity effects, and to calculate the induced temperature

increase. The following formula was used to calculate the average element surface pressure for a given acoustic input power:

$$p_{element} = \sqrt{\frac{P_{total} \cdot Z_{water}}{N_{elements} \cdot A_{element}}} \qquad (8.1)$$

where $p_{element}$ is the pressure at the surface of an array element in $\mathrm{Pa}$, $P_{total}$ is the total acoustic input power in $\mathrm{W}$, $Z_{water}$ is the characteristic impedance of water in $\mathrm{kg/m^2/s}$, $N_{elements}$ is the number of active elements in the array, and $A_{element}$ is the area of the element surface in $\mathrm{m^2}$.

Assuming that water has a sound propagation speed of $1482.3\,\mathrm{m/s}$ (see Table 1.1) and a density of $1000\,\mathrm{kg/m^3}$, the resulting characteristic impedance $Z_{water}$ is $1.4823 \cdot 10^6\,\mathrm{kg/m^2/s}$. Therefore, when all 1024 elements are active, sonicating at the same pressure and have a surface area $A_{element}$ of $1.0\,\mathrm{cm^2}$, the pressure $p_{element,1000\,W}$ at the surface of every element for $1000\,\mathrm{W}$ of acoustic input power is ca. $120.31\,\mathrm{kPa}$.

#### 8.3.2.4   Amplitude Normalization

In the inverse-propagation approach, a point source with an arbitrary amplitude is used to capture the complex pressure waves, the pressure amplitudes of which must be normalized to realistic pressure values as discussed above. The factor $f$ used for normalization of the captured complex pressure values is defined as:

$$f = \sqrt{\frac{N_{elements} \cdot p_{element}^2}{\sum_{i=1}^{N_{elements}} p_{captured_i}^2}} \qquad (8.2)$$

where $N_{elements}$ is the number of active elements in the array, $p_{element}$ is the pressure amplitude calculated above and $p_{captured_i}$ is the pressure recorded at the $i^{th}$ element of the array in the inverse-propagation simulation.

### 8.3.3   Thermal Simulations

Following the acoustic simulations, the deposited acoustic energy was calculated for every voxel of the computational domain, and used as input in the thermal solver (see Section 6.3.2).

To realistically model the entire treatment setup, convective thermal boundary conditions (see Section 6.3.2) were applied at the interfaces between tissues and the water-bolus surrounding the head as well as at tissue-air interfaces, both for the internal air in head cavities and the air surrounding the head. The water temperature was fixed to $16\,^{\circ}\mathrm{C}$

[101, 102] and a heat-transfer coefficient $h$ of $70 \ \mathrm{W/m^2/K}$ was applied [500, p. 77]. Similarly, both internal and external air were fixed to $25 \ \mathrm{^\circ C}$ with an $h$ of $6 \ \mathrm{W/m^2/K}$.

To properly account for the cooling effect of the water-bolus on the scalp, thermal simulations were performed for $30 \ \mathrm{min}$ in the absence of sonication to allow the different tissues to reach thermal equilibrium, generally achieved after ca. $10 \ \mathrm{min}$. This was then followed by $20 \ \mathrm{s}$ of sonication to calculate the temperature increase induced by the deposited acoustic energy during treatment. During these simulations, the effects of perfusion were taken into account, and the thermal properties for all tissues were based on the IT'IS Foundation Tissue Properties Database [8].

These thermal simulations were repeated for every target in the head in order to calculate the induced temperature increase.

### 8.3.3.1   Vascular Shutdown and Temperature-Dependent Tissue Perfusion

The above thermal simulations were performed with the assumption that thermal tissue properties are not temperature dependent. However, it is known that during thermal ablation, the high temperatures induce vascular shutdown, thus eliminating perfusion in those locations and causing the temperature to increase more rapidly [544, 545]. To assess the importance of this effect, additional thermal simulations were performed for a few select targets where perfusion was assumed to start decreasing linearly when the tissue temperature exceeded $50 \ \mathrm{^\circ C}$ and cease entirely above $51 \ \mathrm{^\circ C}$. Vascular dilation, which would cause an exponential increase in blood perfusion as a function of temperature, is not taken into account, as this effect manifests itself only after several minutes of exposure to increased local temperature [546–548].

## 8.4   Results

The four aberration correction approaches described under Section 8.3.2.1 were applied to all targets shown in Figure 8.5. The resulting pressure distributions were used to calculate the temperature increase as described under Section 8.3.3.

Due to the target location diversity, the targets were loosely categorized as cortex targets, structure targets at or above the transducer level, and structure targets below the transducer level.

To analyze the acoustic and thermal performance of the different approaches for each target in a consistent manner, an automatized local maxima and connected-component analysis was performed on all calculated 3D pressure and temperature distributions. Firstly, the distributions were filtered to detect all local maxima which were subsequently analyzed to detect the highest local maximum nearest to the intended target. Once that maximum and

the peak absolute pressure or temperature increase were identified, the original fields were thresholded at $50\%$ of the peak pressure or temperature level, and the different connected components were analyzed. This yielded the full-width half-maximum (FWHM) size of the focal region or thermal lesion along the X, Y and Z axes, the distance between that region and the intended target, as well as the volume of the region, calculated as the sum of the voxel volumes belonging to the particular component. The results of the analyses are summarized in Table 8.3 for the acoustic pressure distributions and in Table 8.4 for the temperature increase distributions.

A plot of the peak absolute pressure in these detected foci for all targets and approaches is shown in Figure 8.6. The absolute pressure distribution obtained with the four approaches, in the case of the 'Thalamic VIM (Right)' target – which coincides with the geometric focus of the transducer — can be seen in Figure 8.7. In addition, the absolute pressure distributions resulting from the use of the SPC approach in the case of four selected targets can be seen in Figure 8.8.

A plot of the peak FUS-induced temperature increase achieved in each of the defined targets for all focusing approaches after 20 seconds of sonication is shown in Figure 8.9.
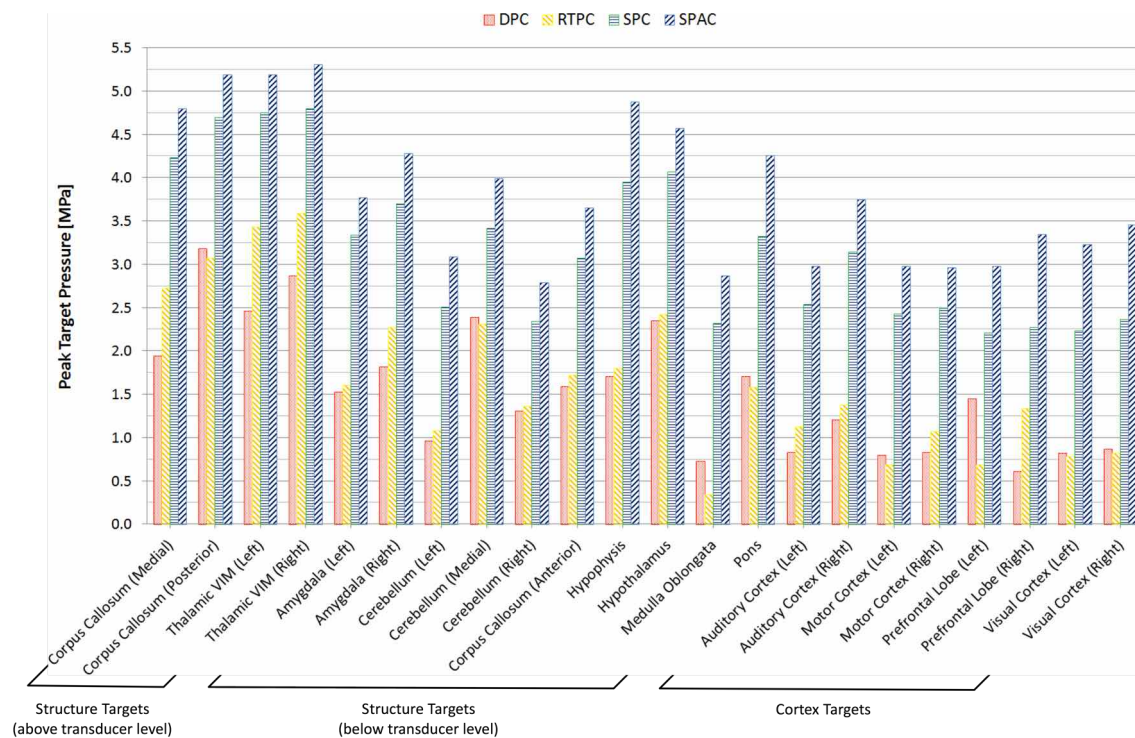


**Figure 8.6**: *The peak absolute pressure (in* MPa*) achieved near each of the defined targets for all focusing approaches. It can be clearly seen that the SPC and SPAC approaches yield far stronger foci than the DPC and RTPC approaches.*

*(a)*

*(b)*

*(c)*

*(d)*
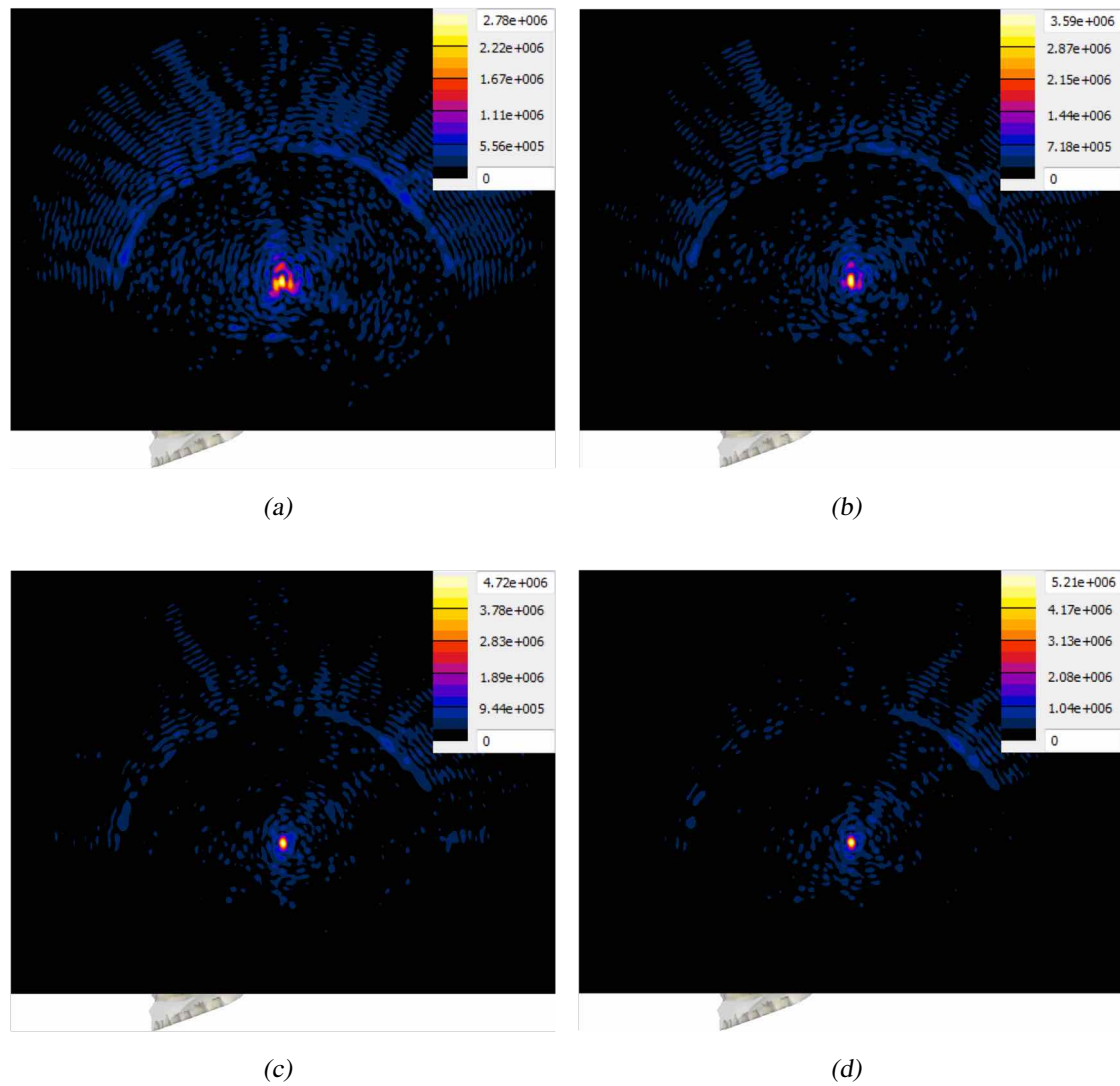
**Figure 8.7**: *Absolute pressure distribution in* MPa *resulting from the use of the four approaches with the 'Thalamic VIM (Right)' target. Each distribution is plotted on the sagittal plane through the target, accompanied by the respective color map and scaled to the respective maximum absolute pressure. The distribution resulting from the DPC approach (a) shows a heavily distorted focal region and relatively low pressure amplitude at the target. Delineation of the focal region and amplitude improve slightly with the RTPC approach (b), while a significant improvement is seen in the case of the SPC (c) and SPAC (d) approaches.*

(a)



(b)



(c)



(d)
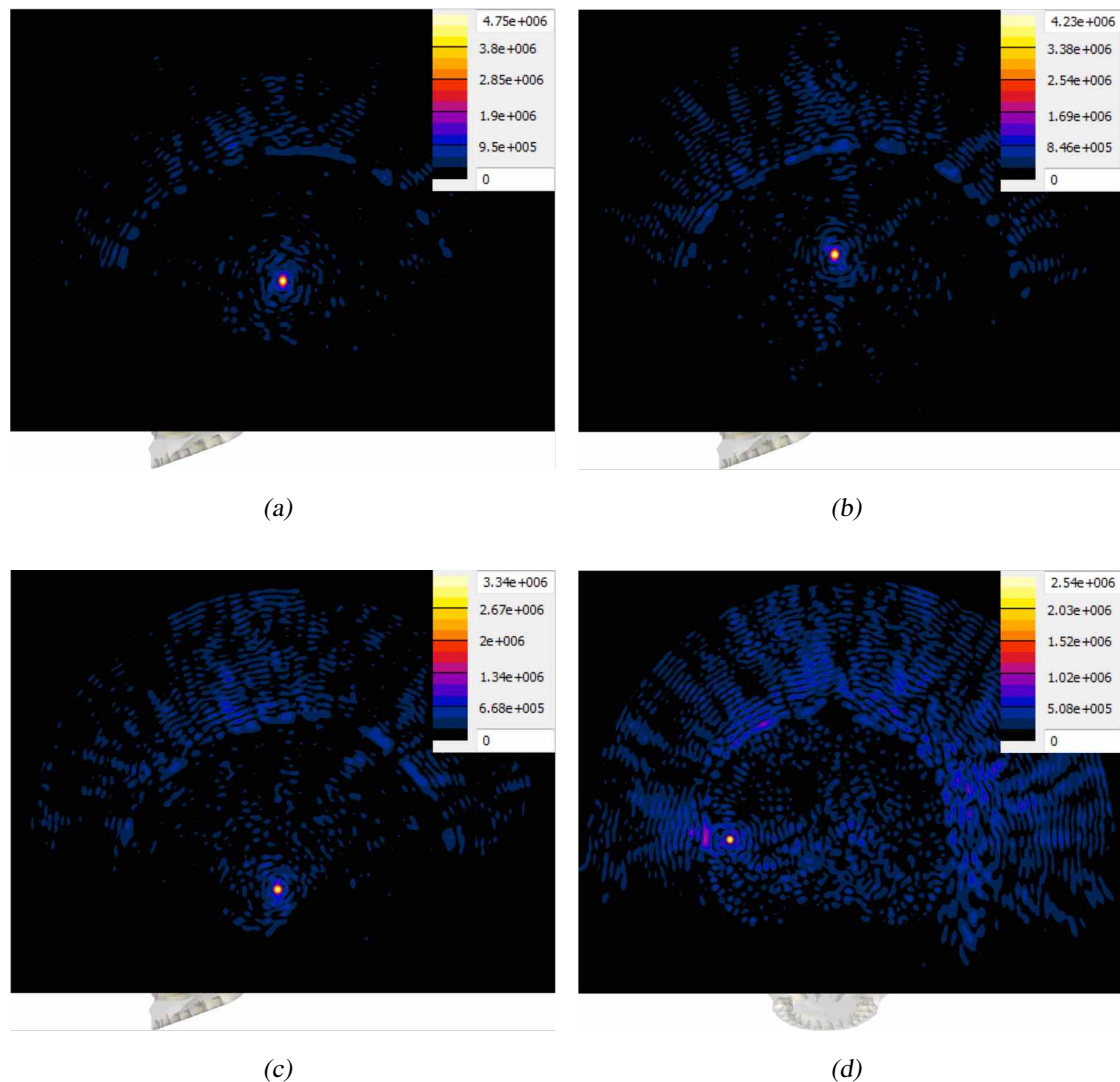
**Figure 8.8**: *Absolute pressure distribution in* MPa *resulting from the use of the SPC approach with four selected targets. Each distribution is plotted on a plane through the target, accompanied by the respective color map and scaled to the respective maximum absolute pressure. Distributions (a) – (c) are plotted on the sagittal plane, while distribution (d) is plotted on the coronal plane. The two structure targets above the transducer level, 'Thalamic VIM (Left)' (a) and 'Corpus Callosum (Medial)' (b), show sharply delineated focal regions with very high pressure amplitudes. The resulting distribution for 'Amygdala (Left)' (c), a structure target below the transducer level shows successful refocusing but significantly lower pressure amplitude. In the case of the cortex target 'Auditory Cortex (Left)' (d), a focus is visible at the target location but significant energy deposition in the patient's scalp and skull is observed.*

| Quantity | Approach | ST above TL | ST below TL | CT | All Targets |
|---|---|---|---|---|---|
| $D[\text{mm}]$ | DPC | 2.2 (0.6) | 2.5 (1.0) | 5.9 (6.4) | 3.7 (4.3) |
| | RTPC | 0.8 (0.1) | 2.6 (1.7) | 6.5 (8.3) | 3.7 (5.6) |
| | SPC | 0.5 (0.1) | 0.7 (0.2) | 0.7 (0.2) | 0.6 (0.2) |
| | SPAC | 0.6 (0.0) | 0.6 (0.2) | 0.6 (0.2) | 0.6 (0.2) |
| $p[\text{MPa}]$ | DPC | 2.6 (0.5) | 1.6 (0.5) | 0.9 (0.3) | 1.5 (0.7) |
| | RTPC | 3.2 (0.3) | 1.6 (0.6) | 1.0 (0.3) | 1.7 (0.9) |
| | SPC | 4.6 (0.2) | 3.2 (0.6) | 2.5 (0.3) | 3.2 (0.9) |
| | SPAC | 5.1 (0.2) | 3.8 (0.7) | 3.2 (0.3) | 3.8 (0.8) |
| $F_{shape}$ | DPC | 1.8 (0.6) | 1.7 (0.5) | 4.2 (2.9) | 2.6 (2.2) |
| | RTPC | 2.1 (0.2) | 1.9 (0.6) | 1.0 (0.3) | 1.7 (0.9) |
| | SPC | 1.6 (0.2) | 1.4 (0.3) | 1.3 (0.1) | 1.4 (0.2) |
| | SPAC | 1.5 (0.1) | 1.5 (0.4) | 1.4 (0.1) | 1.5 (0.3) |
| $V[\text{mm}^3]$ | DPC | 185.7 (52.4) | 303.4 (386.4) | 225.1 (256.6) | 253.5 (310.3) |
| | RTPC | 78.5 (2.8) | 250.3 (543.8) | 196.3 (238.1) | 244.9 (407.4) |
| | SPC | 51.6 (3.5) | 50.3 (11.8) | 38.3 (1.3) | 46.2 (10.1) |
| | SPAC | 50.8 (3.5) | 51.2 (19.8) | 48.1 (7.7) | 50.0 (14.3) |

**Table 8.3**: *The results, mean (standard deviation), of the connected-component analysis on the absolute acoustic pressure distributions for the four focusing approaches for the different target categories. $D$ is the distance between the intended target and the nearest focal region, $p$ is the peak absolute pressure in that region, $F_{shape}$ is the shape-factor, i.e., the ratio of the maximum to minimum dimensions of the focal region, and $V$ is the volume of that region. Abbreviations used: structure targets (ST), cortex targets (CT), and transducer level (TL).*

## 8.5   Discussion

### 8.5.1   Acoustic Distributions

As can be seen from Table 8.3, the acoustic pressure achieved in the focal regions nearest to the targets is lowest for the DPC approach — which neglects the impact of the skull — slightly higher for the RTPC approach ($+10\%$ in average), and much higher for the SPC and SPAC approaches ($+107\%$ and $+148\%$ respectively). In terms of target location, structure targets above the transducer level exhibited higher pressures than those below, while the achievable pressure in the cortex targets was the lowest.

The pressure level dependence on the focusing strategy can be mostly understood when the volume $V$ of the different focal regions is considered. The phase corrections calculated
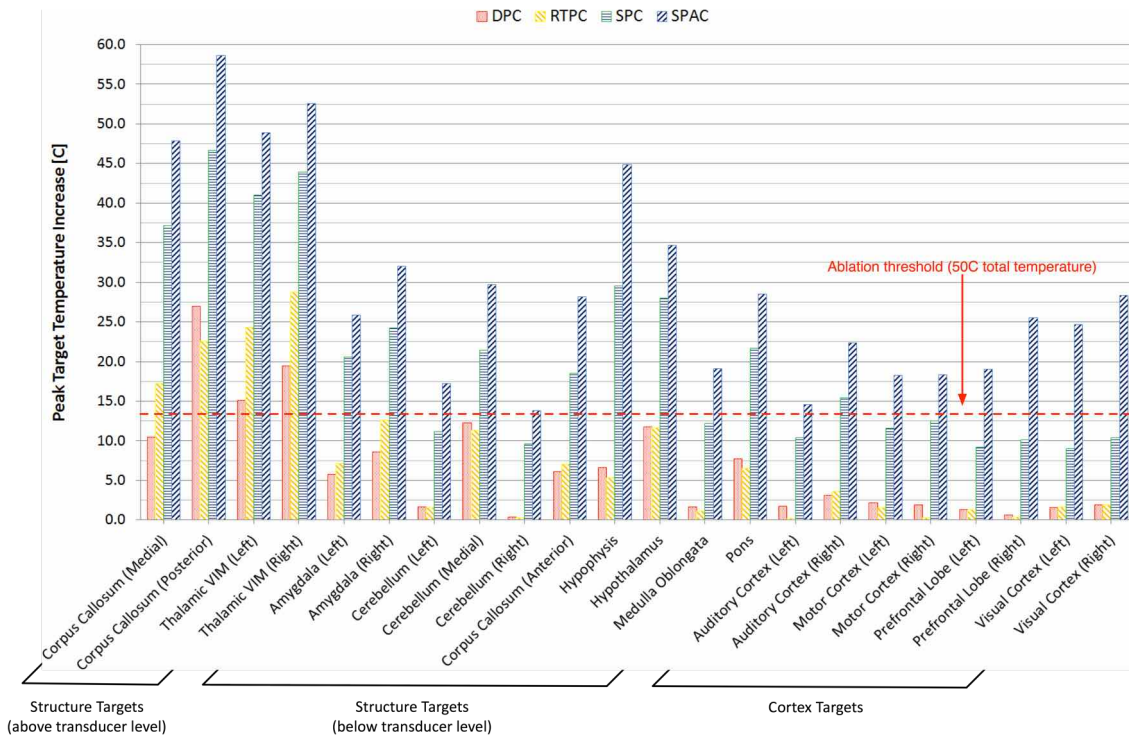
***Figure 8.9***: *The peak FUS-induced temperature increase, not absolute temperature, achieved with each of the defined targets for all focusing approaches after* 20 *seconds of sonication. The red dashed line shows the* 50 °C *threshold, assumed to be the ablation threshold for a base tissue temperature of* 37 °C.

through the DPC and RTPC approaches resulted in focal regions much larger, by a factor of 5.2 on average, than those obtained with simulation-based methods (see Figure 8.7).

While the SPC and SPAC approaches yielded a nearly constant region size and shape for the different targets, focusing sharpness drastically decreased in the case of the DPC and RTPC approaches for structure targets below the transducer level and even further for cortex targets, where dramatic size variations were observed. In general terms and regardless of the correction approach, focusing quality decreases as the distance between the intended target and the geometric focus of the array increases (see Figure 8.8). As described by $F_{shape}$ in Table 8.3, the focal regions were more spherical for the simulation-based approaches than for the DPC and RTPC approaches, which yielded more elongated regions with substantial shape variations.

In terms of focal shift, precisions on the order of the discretization resolution were typically achieved with simulation-based approaches, as can be seen from $D$ in Table 8.3, while the DPC and RTPC approaches showed an average shift of 3.7 mm, which was even more pronounced for cortex targets.

| Quantity | Approach | ST above TL | ST below TL | CT | All Targets |
|---|---|---|---|---|---|
| $D$[mm] | DPC | 0.9 (0.3) | 2.3 (2.3) | 11.0 (10.6) | 5.2 (7.9) |
| | RTPC | 0.6 (0.2) | 3.0 (2.7) | 8.7 (9.5) | 4.7 (6.8) |
| | SPC | 0.3 (0.1) | 0.8 (1.1) | 0.5 (0.2) | 0.6 (0.8) |
| | SPAC | 0.3 (0.1) | 0.5 (0.1) | 0.5 (0.1) | 0.5 (0.1) |
| $T$[°C] | DPC | 17.9 (6.1) | 6.2 (3.9) | 1.7 (0.7) | 6.7 (6.8) |
| | RTPC | 23.2 (4.1) | 6.5 (4.2) | 1.7 (0.5) | 7.8 (8.3) |
| | SPC | 42.2 (3.5) | 19.7 (6.5) | 11.0 (2.0) | 20.6 (11.9) |
| | SPAC | 51.9 (4.2) | 27.4 (8.6) | 21.3 (4.3) | 29.6 (12.7) |
| $V$[mm³] | DPC | 134.0 (47.4) | 434.0 (594.9) | 450.4 (544.2) | 385.4 (532.1) |
| | RTPC | 71.0 (4.7) | 305.6 (386.2) | 214.5 (176.6) | 229.8 (294.0) |
| | SPC | 51.5 (3.6) | 62.6 (43.8) | 38.5 (3.9) | 51.8 (31.6) |
| | SPAC | 51.3 (4.8) | 52.0 (11.0) | 66.9 (35.7) | 57.3 (24.0) |

**Table 8.4**: *The results, mean (standard deviation), of the connected-component analysis on the temperature increase distributions for the four focusing approaches for the different target categories. $D$ is the distance between the intended target and the nearest lesion, $T$ is the peak temperature increase, and $V$ is the volume of the region. Abbreviations used: structure targets (ST), cortex targets (CT), and transducer level (TL).*

### 8.5.2 Thermal Distributions

When considering the temperature increase results after 20 s of sonication (see Figure 8.9 and Table 8.4), the DPC and RTPC approaches achieved ablative temperatures only in the case of structure targets above the transducer level. As observed with the acoustic results, temperature rise was highest for structure targets above the transducer level.

The SPAC was clearly superior to the other approaches, and achieved ablative temperatures in all investigated targets. Utilization of the SPC approach attained ablation in all structures targets above the transducer level, and the majority of targets below. In the case of cortical targets, even though focusing was achievable with these this approach, the limited number of elements that could contribute to the focusing (due to the absence of a line-of-sight between many of the elements and the intended target) resulted in high energy deposition on the skull and scalp, while the temperature rise at the targets showed inverse proportionality to the distance between them and the transducer's geometric focus. Effective thermal treatment of those targets would require the patient to be repositioned so that the desired targets would lie above the transducer level.

The thermal lesion and acoustic focus volumes exhibited similar behaviors, with the simulation-based approaches being clearly superior to the DPC and RTPC, especially for the cortex and structure targets below the transducer line where these approaches were unable to produce sharply demarcated lesions.

### 8.5.3   Skull Heating

With the SPC approach, high acoustic energy deposition and subsequent thermal hotspots were observed near the skull surface for the majority of targets, which would result in significant heating of the patient's scalp and skull. This phenomenon was partly alleviated for targets near the geometric focus with the use of RTPC, where improvements in thermal and focal gain were seen. This would suggest that, even though the RTPC approach did not achieve ablative temperatures within $20\,\mathrm{s}$ of sonication in any but the structure targets above the transducer level, it could be employed with longer sonication durations, or, for non-thermal therapy modalities such as targeted drug delivery.

In the case of the simulation-based approaches, these adverse effects were mostly observed for cortex targets and structure targets below the transducer level, where only a small number of elements could contribute to the focus, thus resulting in significant energy deposition on the scalp and skull bone (see Figure 8.8). This trend was visible for both approaches, which leads us to conclude that these targets would benefit from further optimization of the steering parameters, e.g., de-activation of the nearby elements.

### 8.5.4   Impact of Acoustic Non-Linearity and Vascular Shutdown

Non-linear acoustic simulations were performed for the 'Thalamic VIM (Left)' and 'Thalamic VIM (Right)' targets, with the phase corrections of the SPC approach and with the generation of the second harmonics taken into account. The impact of the second harmonic was negligible both acoustically and thermally. In terms of absolute pressure amplitude, the second harmonic was approximately $30\,\mathrm{dB}$ lower than the first. Consequently, the thermal impact was similarly insignificant, on the order of $0.01 - 0.02\ ^{\circ}\mathrm{C}$ additional temperature increase. This can be explained by the low base frequency ($230\,\mathrm{kHz}$) and the resulting low attenuation coefficient (see Table 1.2). The impact of non-linearity is expected to be much more pronounced at higher acoustic frequencies, e.g., in the case of the $650\,\mathrm{kHz}$ system, since the tissue absorption coefficients are proportionally higher.

Furthermore, as discussed under 8.3.3.1, additional thermal simulations were performed where the impact of vascular shutdown was considered. As in the case of the non-linear acoustic simulations, the phase corrections of the SPC approach were used in vascular shutdown simulations for the 'Thalamic VIM (Left)' and 'Thalamic VIM (Right)' targets. The impact of vascular shutdown was visible but minimal. Thermal simulations, where the perfusion was assumed to decrease linearly after the tissue temperature exceeded $50\ ^{\circ}\mathrm{C}$ and cease entirely after $51\ ^{\circ}\mathrm{C}$, showed a steeper temperature increase, but, after $20\,\mathrm{s}$ of sonication, only $1\ ^{\circ}\mathrm{C}$ of total additional temperature increase was observed in tissues where vascular shutdown occurred.

# 8.6 Conclusions

A well known limitation of tcFUS therapy are the skull-induced aberrations, which can induce focal shift and distortion as well as significant energy deposition on the patient's skull and scalp, resulting in a significant decrease in the treatment's focal and thermal gain. A numerical study was performed here to investigate the efficacy of four compensation techniques, ranging from (semi-)analytical to simulation-based, that aim to provide phase – and optionally amplitude – corrections to achieve refocusing, counter the aforementioned effects, and increase the treatment envelope of tcFUS therapy. To that end, acoustic and thermal simulations of a detailed anatomical head model sonicated with a model of the ExAblate® 4000 applicator, were performed. The acoustic and thermal results of these correction approaches were ascertained for 22 distinct targets in various locations of the brain, while the impacts of acoustic nonlinearity and vascular shutdown were also evaluated.

Evaluation of the acoustic pressure, location, and size of the focal regions as well as the FUS-induced temperature increase and lesion volume/size suggest that simulation-based approaches provide far superior corrections than the analytical and semi-analytical ones. While the latter could be employed in thermal therapies for targets in the vicinity of the transducer's geometric focus, their efficiency decreased dramatically when targeting more remote brain regions. Simulation-based approaches, on the other hand, could be employed clinically to extend the treatment envelope of tcFUS treatments as well as predict, and therefore, avoid, possible secondary effects of these procedures, such as standing waves and skull heating. Utilization of modern but affordable computer hardware, combined with state-of-the-art high-performance computing techniques, enable realistic acoustic and thermal simulations in complicated setups to be performed within minutes. Thus, due to their increased refocusing efficiency and their ability to predict the acoustic and thermal effects of FUS therapies, simulation-based correction approaches may soon replace their analytical counterparts.

In a next step it will be investigated, how many of the large number of tissues distinguished in the head model are actually required. The impact of inhomogeneity, particularly skull inhomogeneity which can be estimated from CT data, needs to be considered, and the analysis should be repeated for higher frequencies.

# 9

# HIFU Hepatic Tumor Ablation: Modeling of Focusing and Motion Tracking Approaches

## 9.1 Introduction

As outlined in Sections 3.1.4.3, 3.3.2.3, and 3.3.3, despite the encouraging results reported in clinical trials [59, 79, 140, 141], FUS treatments of hepatocellular carcinomas are hampered by two significant impediments. These are the partial obstruction introduced by the thoracic cage, i.e., the ribs, and the respiration-induced organ motion and displacement. The former limits the treatable volume, introduces the risk of collateral tissue damage, and degrades the overall focus quality. Respiratory motion leads to inaccurate MR thermometry and compromises the targeting accuracy. This may result in insufficient energy deposition in the targeted tissue, unsuccessful ablation, or even damage to the surrounding healthy tissue.

Significant amounts of research have been dedicated to countering the aforementioned effects. As was discussed in Section 3.3.2.3, obstruction by the thoracic cage is clinically circumvented through partial resection of the obstructing ribs [242, 246], which however, increases both the invasiveness and risk of the treatment. Alternative approaches involve dynamic element activation [238, 247–249], and treatment planning through time-reversal techniques [236–238, 250, 251]. Respiratory-induced organ motion necessitates the employment of techniques based on controlled apnea [258], or respiratory gating [259, 260], which nevertheless often prove unsuccessful [139, 261]. These findings suggest that continuous ablation, in combination with motion tracking and compensation may be necessary. Several indirect [252, 253, 260, 262–265] and direct [266–270] motion tracking and compensation techniques have been investigated (see Section 3.3.3). However, the majority of the aforementioned studies are ordinarily carried out on in-vitro and ex-vivo setups, involving only a thoracic cage, usually extracted from animals, which is embedded in a water-tank. Furthermore, numerical studies are typically performed on strongly

simplified depictions of the human anatomy, in most cases lacking a realistic model of respiratory motion. Therefore, further investigations applied on representative setups are warranted, and the feasibility of these approaches needs to be ascertained before they can be adopted into the clinical environment.

In this study, a transient anatomical model with 14 temporal snapshots, was generated by deforming a static model, based on the 4D-MRI images of a volunteer's respiratory cycle. The model of a randomized phased array transducer with 256 circular elements was then employed to perform acoustic and thermal simulations of hepatic tumor ablation, and ascertain the importance of motion-tracking, as well as intercostal targeting approaches. Acoustic simulations were performed for each step of the respiratory cycle with both analytical and simulation-based (time-reversal) steering and compensation. The deposited acoustic energy was calculated, and transient thermal simulations of gated and continuous ablation procedures, with and without motion compensation, were performed.

## 9.2    Materials & Methods

### 9.2.1    Simulation Setup

#### 9.2.1.1    Transducer Model

The model of a randomized phased array transducer (RPAT) was designed based on the prototype presented by Hand et al. [549]. Such arrays have been shown to reduce grating lobes and secondary maxima [550], and their use in transcostal hepatic tumor treatment with HIFU has been ascertained by several research teams [236, 238, 549].

The RPAT model used in this study (see Figure 9.1), featured 256 circular elements operating at 0.5 MHz, which were randomly distributed on a spherical surface with a curvature radius of 130 mm, and a diameter of 170 mm. The model was automatically designed by a Python script where the boundary conditions were set such that each element was 7 mm in diameter, while the minimum inter-element (center-to-center) distance was set to 7.5 mm. According to Hand et al. [549], this array could deliver a maximum acoustic power of 2.3 W per element, amounting to a total of 588.8 W, at which all acoustic and thermal simulations were performed.

#### 9.2.1.2    Transient Anatomical Model

The static anatomical model utilized in this study was an improved version of the 'Duke' model described in Section 6.3.3. This improved version of the model was developed as part of the Virtual Population project [543], where the original MR image dataset was re-sampled with a resolution of $0.5 \times 0.5 \times 0.5$ mm, and then re-segmented, yielding over

*(a)*                                    *(b)*
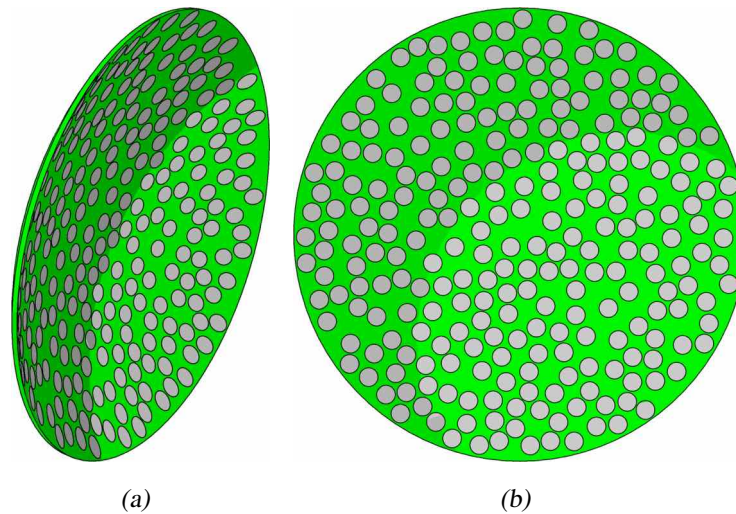
**Figure 9.1**: *Randomized phased array transducer (RPAT) designed for the purposes of this study. The array features* $256$ *circular elements operating at* $0.5$ MHz.

96 tissues and anatomical structures in the region of the torso. The model of a tumor was artificially implanted in the right posterior hepatic lobe. The dimensions of the tumor were approximately $32 \times 28 \times 22$ mm, and the tumor was placed behind the 10th rib, at an approximate distance of $70$ mm from the dorsal end of the model's skin. This static version of the model, which represents the full exhalation stage in the respiratory cycle, can be seen in Figure 9.2.

This model was registered to the 4D-MRI images of a volunteer's respiratory cycle, and warped to generate a transient model comprising 14 steps, i.e., temporal snapshots throughout the cycle. The 4D-MRI images were acquired at intervals of $390$ ms, resulting in a respiratory cycle with a total duration of $5.46$ s. A reference exhalation image was registered to each 3D MR image in order to obtain the displacement vector field of the abdomen at each time step. Because of discontinuities between abdominal organs and the chest wall, this was initially performed on a masked region containing only abdominal organs, and subsequently on the inverted mask containing the chest wall. The resulting displacement fields were combined using a Gaussian kernel at the mask interfaces. The full inhalation and full exhalation 4D-MRI images and the corresponding steps of this transient model can be seen in Figure 9.3.

### 9.2.1.3   Transducer Positioning and Target Definition

The RPAT (see Section 9.2.1.1) was positioned behind the model's back, so that the geometric focus of the array would coincide with the center of the implanted tumor in the static version of the model. This configuration allowed for the replication of clinically

*(a)*      *(b)*
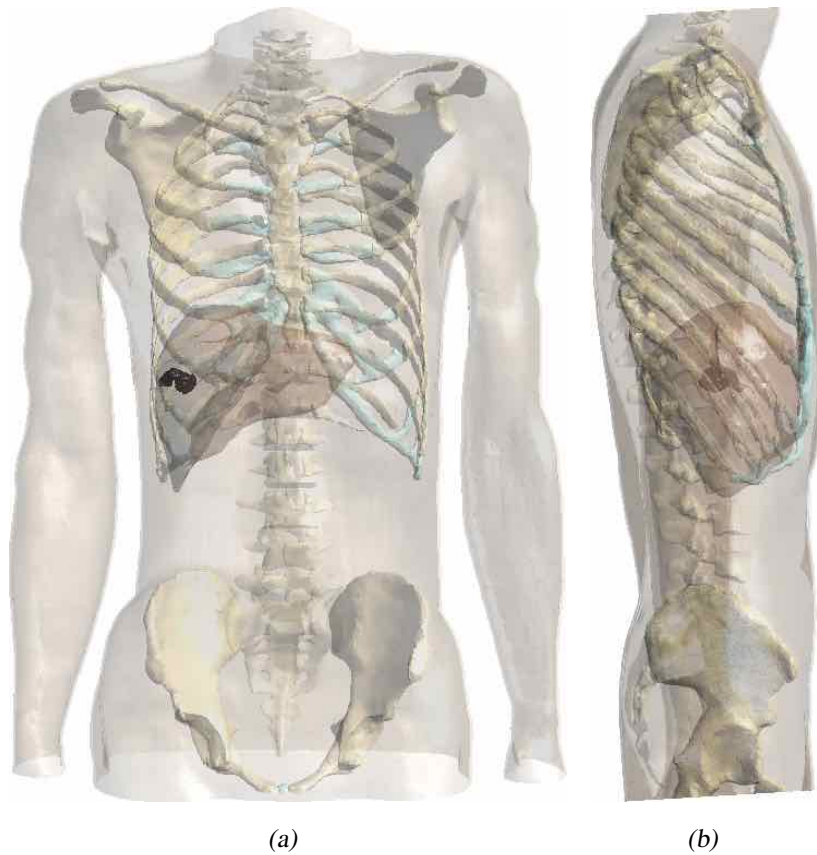
**Figure 9.2**: *Front (a) and side (b) view of the static version of the improved 'Duke' model. The tumor model, marked in black, was implanted in the right posterior hepatic lobe behind the 10th rib.*

relevant setups, as well as to ascertain the impact of the thoracic cage and organ motion on the targeting accuracy, focusing quality, and target tracking capabilities of the array. The 3D simulation setup and a sagittal voxel slice through the center of the tumor, can be seen in Figure 9.4.

## 9.2.2   Acoustic Simulations

Linear acoustic simulations were performed at $0.5$ MHz with the LAPWE solver described in Section 5.2.1.4. The simulation domain was discretized with a $0.3$ mm gridstep, truncated to approximately $207 \times 230 \times 210$ mm – resulting in ca. $370$ million cells, and terminated with 16 layers of PML on all domain boundaries to inhibit the manifestation of spurious reflections. All acoustic simulations were performed for $588$ W of acoustic power and their duration was set to $300$ periods, which corresponds to a propagation distance of ca. $900$ mm. The acoustic properties of the different tissues were set

(a)    (b)    (c)
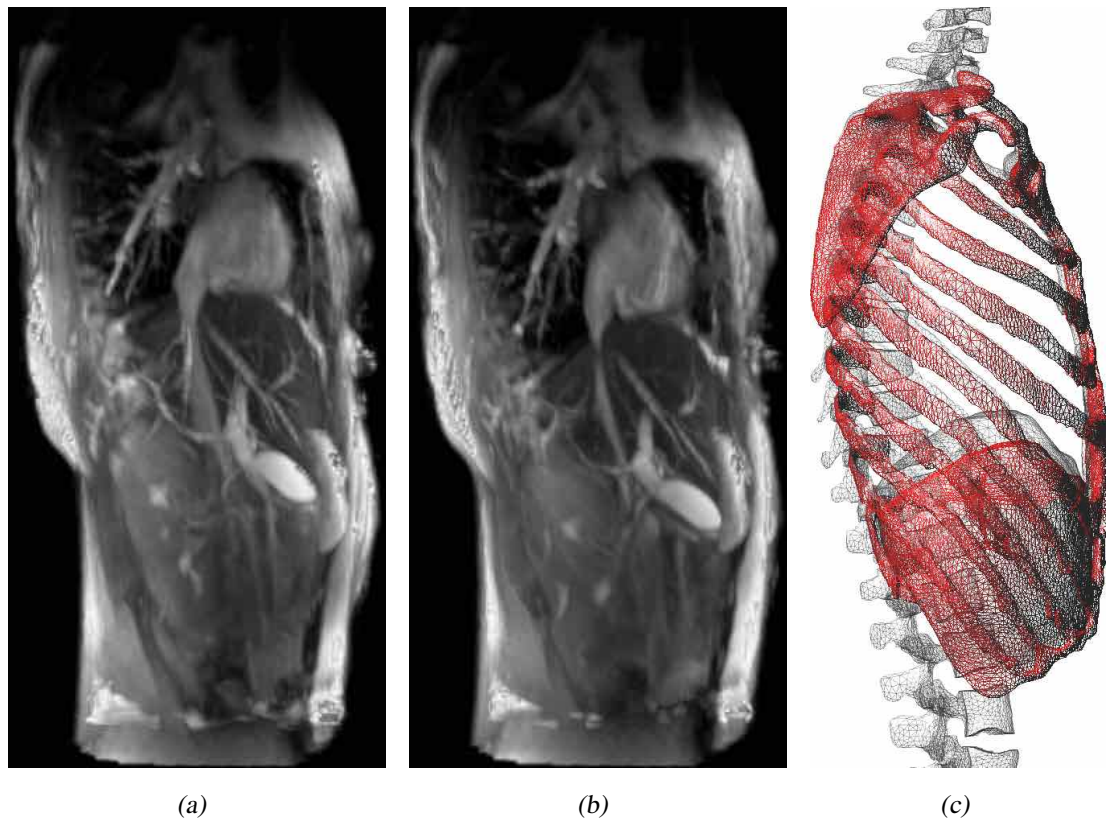
**Figure 9.3**: *4D-MRI data of the volunteer's respiratory cycle during the full exhalation (a) and full inahlation (b) stages. The equivalent stages of the transient anatomical model warped to the 4D-MRI images are depicted in (c). The surface mesh of the liver, vertebral column, and thoracic cage at the full inhalation and full exhalation steps can be seen.*

according to the values presented in Table 1.2, the properties of the tumor were set to those of liver, while the properties of lung were set to the average values between muscle and air.

### 9.2.2.1 Static Model Simulations

Initial acoustic simulations were performed with the static anatomical model in the setup described in the previous section, i.e., with the geometric focus of the RPAT coinciding with the tumor center. This setup permitted the investigation of the impact of intercostal targeting and compensation within a single sonication, and these acoustic simulations served as a baseline for the corresponding transient model simulations.

Three approaches were employed to steer the acoustic beams and compensate for the presence of aberration sources, most notably the skin, thoracic cage, and lungs. These were the distance-based phase correction (DPC), the simulation-based phase correction
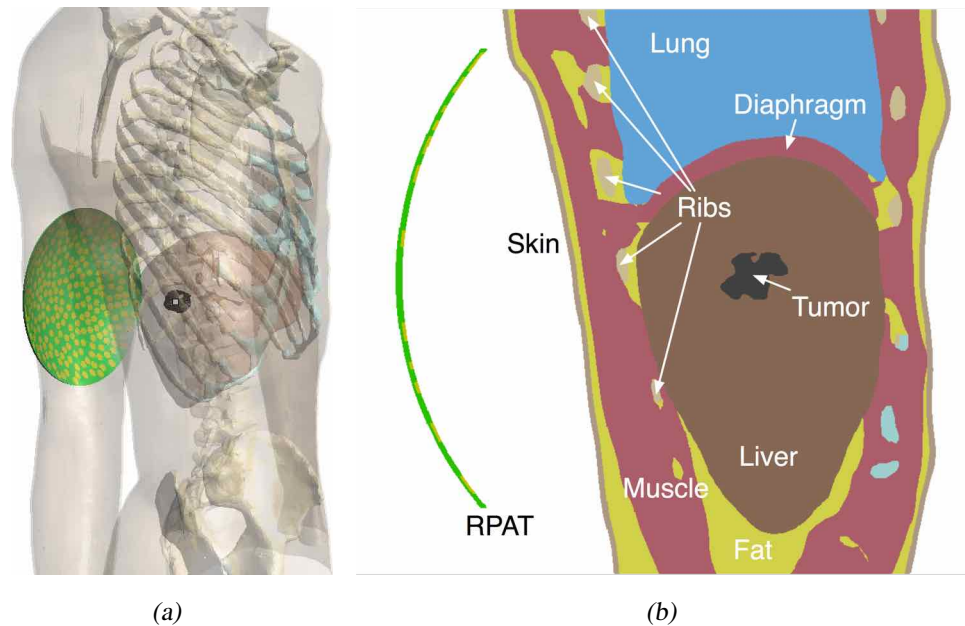
*Figure 9.4*: *3D view of the simulation setup showing the location of the RPAT relative to the anatomical model (a), and a sagittal voxel slice through the center of the tumor marking the most prominent tissues (b).*

(SPC), and the simulation-based phase and amplitude correction (SPAC), which were detailed in Section 8.3.2.1.

As outlined in the aforementioned section, the DPC approach does not account for the presence of inhomogeneities, i.e., the anatomy, and merely calculates the appropriate phases that would steer the focal region to a particular location if the transducer was embedded in a homogeneous medium. Unlike the DPC, the SPC and SPAC approaches employ time-reversal techniques to calculate phase and, in the case of the SPAC, amplitude corrections, thus attempting to both steer the focal region and compensate for aberration effects. Therefore, utilizing these approaches required the placement of a point source at the intended location of the focal region, i.e., the tumor center, and an inverse propagation simulation which provided the required phase and amplitude corrections (see Section 8.3.2.1).

### 9.2.2.2  Transient Model Simulations

The acoustic simulations described above were repeated for every step of the transient model described in Section 9.2.1.2, using the DPC, SPC, and SPAC approaches. This facilitated the assessment of respiratory motion effects, and the evaluation of the aforementioned steering/compensation techniques. In addition, these simulations permitted

for the importance of motion tracking, and the transient effects associated with respiratory movement to be ascertained. The sonication target for each step was relocated based on the same deformation field used to warp the anatomical model, and used to steer the acoustic beams using the three aforementioned approaches. These targets can be seen in Figure 9.5.
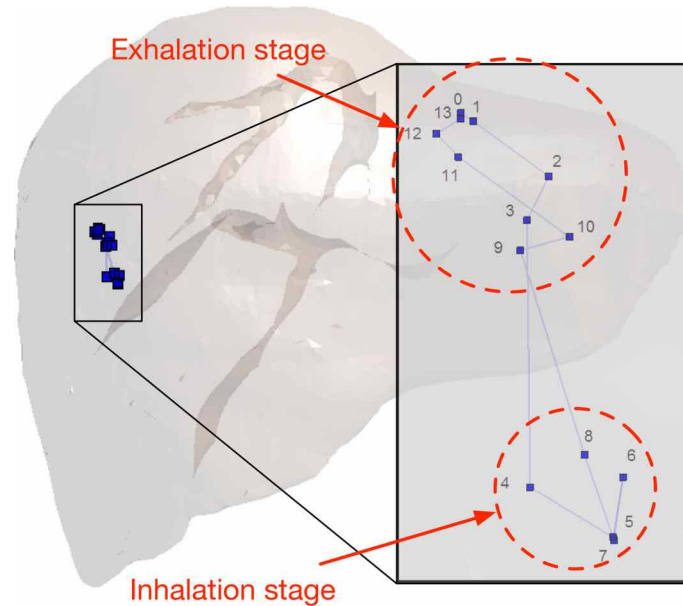


**Figure 9.5**: *Sonication target points (tumor center) for the different steps of the transient model. These points are displayed over the static liver but in relation to the body, as organs deform and translate throughout the respiratory cycle. The target marked with '0' depicts the tumor center of the transient model during the first step.*

These targets and their distance from the initial target, i.e., the tumor center in the static model, were used to define the displacement profile throughout the respiratory cycle. This profile, which can be seen in Figure 9.6, was used to define the duration of the full inhalation stage and thus the respiratory gating window which amounted to $1.95$ s, a value in accordance to the published literature [139, 259].

Lastly, in order to quantify the importance of motion tracking, the corrections calculated through the three steering/compensation approaches when applied to the static model (see Section 9.2.2.1) were used without further modifications across all acoustic simulations of transient model's different steps. This resulted in simulations where only initial targeting and compensation were employed, i.e., only for the non-displaced target in the tumor center of the static model, while no motion tracking was applied, i.e., the phase/amplitude corrections were not updated for the subsequent targets.
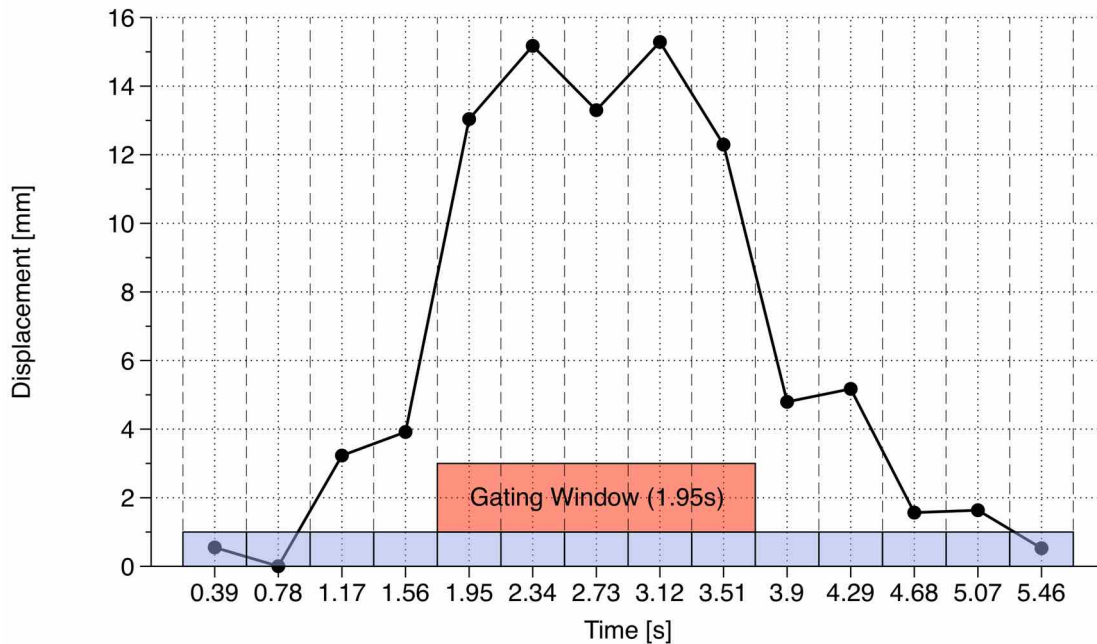
**Figure 9.6**: *Respiratory displacement profile. The duration of each step (shown as blue rectangles) in the acquired 4D-MRI data was* 390 ms, *amounting to a respiratory cycle with a total duration of* 5.46 s. *The duration of the full-inhalation stage, and thus the gating window (shown as a red rectangle), was thus defined to be equal to* 1.95 s.

### 9.2.3   Thermal Simulations

The deposited acoustic energy was calculated for each of the aforementioned acoustic simulations, and used to perform thermal simulations of the ablation procedure as described in Section 6.3.2. The patient's skin was assumed to be in contact with circulating water at a temperature of 16 °C [101]. This thermal behavior was modeled through application of a convective boundary condition (see Section 6.3.2), with a heat transfer coefficient $h$ of 200 W/m$^2$/K [551–553]. Prior to the administration of sonications, all thermal simulations were performed for 30 min, in order to allow for the different tissues to reach thermal equilibrium. During these simulations, the effects of perfusion were taken into account, but vascular shutdown and tissue evaporation were not considered. Thermal properties for all tissues were based on the IT'IS Foundation Tissue Properties Database [8], while the properties of the tumor were set to those of liver. The cumulative equivalent minutes at 43 °C (CEM43) [499], was calculated for all tissues during these simulations to evaluate the administered thermal dose, and ascertain whether a given tissue has been ablated as a result of the sonications. A CEM43 threshold value of 240 min was assumed to signify ablation [554, 555].

Two ablation scenarios were investigated and evaluated using the deposited energy distributions resulting from the acoustic simulations performed with the DPC, SPC, and SPAC approaches described in Section 9.2.2. These were continuous and gated ablation, and were performed on both the static and transient model acoustic simulations outlined in Sections 9.2.2.1 and 9.2.2.2 respectively. The different cases simulated within these scenarios are further discussed below and summarized in Table 9.1.

### 9.2.3.1    Static Model Simulations

The static model ablation simulations, mimic an idealized scenario where motion is absent, and served as a frame of reference to evaluate the performance of the transient model ablation approaches (see Section 9.2.3.2). The acoustic simulations performed on this model with the different steering/compensation techniques (see Section 9.2.2.1), were used to perform thermal simulations where continuous sonication aimed at the center of the tumor was administered for a total of $11$ respiratory cycles, amounting to a treatment duration of ca. $60.06$ s. Depending on the steering/compensation approach employed, these ablation cases will from now on be referred to as $DPC_{static}^{cont.}$, $SPC_{static}^{cont.}$, and $SPAC_{static}^{cont.}$ respectively.

The gated ablation simulations were identical to the ones described above, with the exception that respiratory gating was considered in order to reproduce a clinically relevant scenario with a suboptimal technique. The sonications resulting from the acoustic simulations on the static model (see Section 9.2.2.1), were administered only during the gating window, i.e., the full-inhalation stage, as defined in Section 9.2.2.2, which amounts to ca. $35.7\%$ ($1.95$ s) of the full respiratory cycle ($5.46$ s). Similarly to the previous scenario, the total treatment time was set to $11$ respiratory cycles and $60.06$ s. Depending on the steering/compensation approach employed, these ablation cases will from now on be referred to as $DPC_{static}^{gated}$, $SPC_{static}^{gated}$, and $SPAC_{static}^{gated}$ respectively.

### 9.2.3.2    Transient Model Simulations

In the context of continuous ablation under respiratory motion, the acoustic simulations performed with the DPC, SPC, and SPAC steering/compensation approaches on the transient model (see Section 9.2.2.2) were used. The deposited acoustic energy distributions resulting from the simulations of each step of the transient model, were inversely warped and projected back to the static model in order to perform transient thermal simulations of the entire ablation procedure, while accounting for respiratory motion. The overall duration of the treatment was identical to that of the previous scenarios ($11$ respiratory cycles, $60.06$ s). Depending on the steering/compensation approach employed, these ablation cases will from now on be referred to as $DPC_{transient}^{tracked}$, $SPC_{transient}^{tracked}$, and $SPAC_{transient}^{tracked}$ respectively.

Furthermore, in order to investigate a realistic gated ablation scenario, the inversely warped distributions corresponding to the steps within the gating window (see Section 9.2.2.2 and Figure 9.6), resulting from all three approaches mentioned above, were applied during only this window. This yielded three cases referred to as $\text{DPC}_{\text{transient}}^{\text{gated}}$, $\text{SPC}_{\text{transient}}^{\text{gated}}$, and $\text{SPAC}_{\text{transient}}^{\text{gated}}$ respectively.

Lastly, as described in Section 9.2.2.2, in order to quantify the importance of motion tracking, three additional cases were simulated where only initial steering/compensation was applied (for the target marked with '0' in Figure 9.5) using the different approaches, but without tracking the subsequent targets throughout the respiratory cycle. These cases will be referred to as $\text{DPC}_{\text{transient}}^{\text{untracked}}$, $\text{SPC}_{\text{transient}}^{\text{untracked}}$, and $\text{SPAC}_{\text{transient}}^{\text{untracked}}$ respectively.

| Name | Anatomical Model | Scenario | Compensation | Tracking |
|---|---|---|---|---|
| $\text{DPC}_{\text{static}}^{\text{cont.}}$ | Static | Continuous | No | - |
| $\text{SPC}_{\text{static}}^{\text{cont.}}$ | Static | Continuous | Yes | - |
| $\text{SPAC}_{\text{static}}^{\text{cont.}}$ | Static | Continuous | Yes | - |
| $\text{DPC}_{\text{static}}^{\text{gated}}$ | Static | Gated | No | - |
| $\text{SPC}_{\text{static}}^{\text{gated}}$ | Static | Gated | Yes | - |
| $\text{SPAC}_{\text{static}}^{\text{gated}}$ | Static | Gated | Yes | - |
| $\text{DPC}_{\text{transient}}^{\text{untracked}}$ | Transient | Continuous | No | No |
| $\text{SPC}_{\text{transient}}^{\text{untracked}}$ | Transient | Continuous | Yes | No |
| $\text{SPAC}_{\text{transient}}^{\text{untracked}}$ | Transient | Continuous | Yes | No |
| $\text{DPC}_{\text{transient}}^{\text{tracked}}$ | Transient | Continuous | No | Yes |
| $\text{SPC}_{\text{transient}}^{\text{tracked}}$ | Transient | Continuous | Yes | Yes |
| $\text{SPAC}_{\text{transient}}^{\text{tracked}}$ | Transient | Continuous | Yes | Yes |
| $\text{DPC}_{\text{transient}}^{\text{gated}}$ | Transient | Gated | No | Yes |
| $\text{SPC}_{\text{transient}}^{\text{gated}}$ | Transient | Gated | Yes | Yes |
| $\text{SPAC}_{\text{transient}}^{\text{gated}}$ | Transient | Gated | Yes | Yes |

**Table 9.1**: *Summary of the ablation cases examined in this study. For each case the type of the anatomical model, the ablation scenario, as well as whether the approach employs targeting compensation and tracking can be seen.*


## 9.3 Results

The absolute pressure distributions resulting from the acoustic simulations of the static model with the DPC and SPC approaches, i.e., with and without the application of phase aberration correction as described in Section 9.2.2.1, can be seen in Figure 9.7. Pressure is plotted on sagittal planes through the geometric focus, which coincides with the center of the tumor, and shows the impact of phase aberrations introduced by inhomogeneities, most notably the skin, the thoracic cage, and the lungs.

The temperature increase resulting from continuous administration of these sonications for a total of 11 respiratory cycles, i.e., ablation cases $DPC_{static}^{cont.}$ and $SPC_{static}^{cont.}$ (see Section 9.2.3.1 and Table 9.1), are plotted on the same planes in Figure 9.8. Moreover, Figure 9.9 shows the temperature increase resulting from ablation cases $SPAC_{transient}^{tracked}$ and $SPAC_{transient}^{untracked}$ (see Section 9.2.3.2 and Table 9.1), where the importance of motion tracking becomes evident. Lastly, Figure 9.10 shows selected CEM43 isosurfaces, thresholded at 240 min signifying the ablated tissue volumes. These isosurfaces are shown for the $DPC_{transient}^{tracked}$, $SPC_{transient}^{untracked}$, and $SPC_{transient}^{tracked}$ ablation cases, highlighting the importance of intercostal targeting with aberration corrections and continuous motion tracking.



*(a)*                                          *(b)*
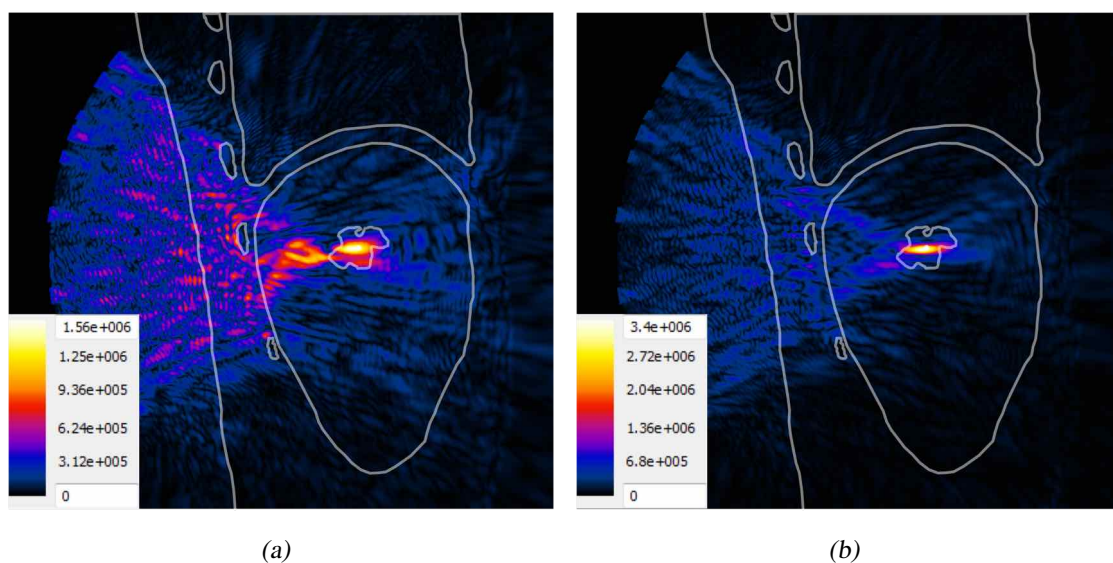
**Figure 9.7**: *Absolute pressure distributions resulting from the simulations of the static model with the DPC (a) and SPC (b) approaches. Each pressure distribution is plotted, with its distinct colormap, on the sagittal plane through the geometric focus which coincides with the center of the tumor. The voxeled outlines of the skin, ribs, lung, liver, and tumor as shown in Figure 9.4(b), can be seen.*

In order to separate the focal shift from focal distortion effects, an automated local maxima and connected-component analyses were performed on each temporal snapshot of the temperature increase distributions. Firstly, the distributions were filtered to detect all local maxima, which were subsequently analyzed to detect the highest local maximum nearest to the intended target (through evaluation of a value to distance ratio). Once that maximum and the peak temperature increase were identified, the original fields were thresholded at 50% of that value, and the different connected-components were analyzed. This yielded the full-width half-maximum (FWHM) size of the thermal hotspot along the X, Y and Z axes, the distance between that hotspot and the intended target, as well as the volume of the hotspot, calculated as the sum of the voxel volumes belonging to the particular component.
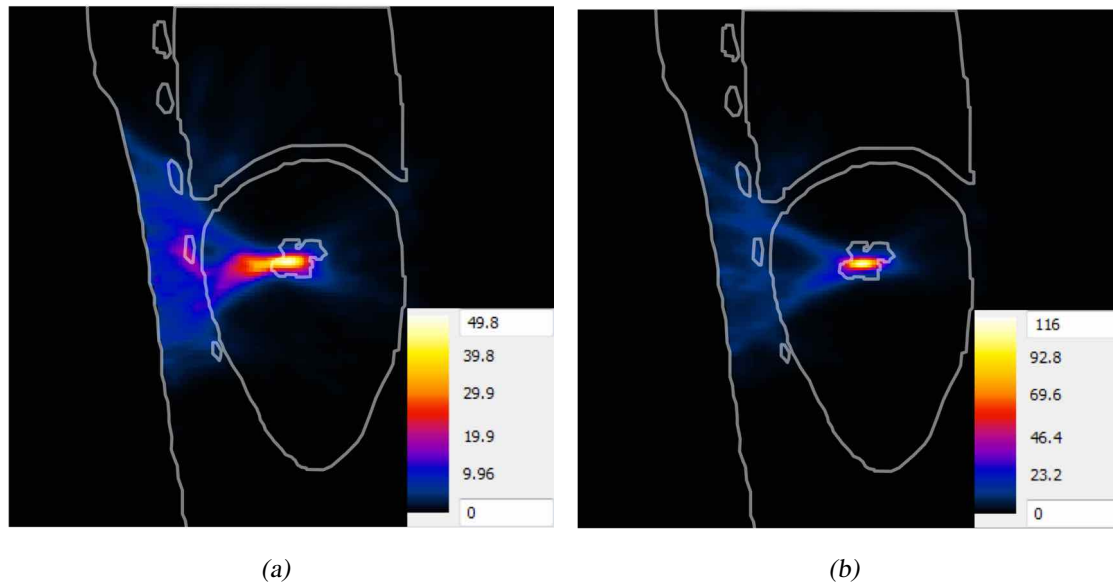
*Figure 9.8*: *Temperature increase distributions after continuous sonication of the static model for* $60.06$ s *with the DPC (a) and SPC (b) approaches, i.e., ablation cases* $DPC_{static}^{cont.}$ *and* $SPC_{static}^{cont.}$ *(see Section 9.2.3.1 and Table 9.1). Each temperature increase is plotted, with its distinct colormap, on the sagittal plane through the geometric focus which coincides with the center of the tumor. The voxeled outlines of the skin, ribs, lung, liver, and tumor as shown in Figure 9.4(b), can be seen.*

These calculated focal shifts, the component volumes, as well as the average temperatures within each component, are plotted over time for the last three simulated respiratory cycles in Figures 9.11, 9.12, and 9.13 respectively. In addition, the average and standard-deviation values of the results plotted in the aforementioned figures are summarized in Table 9.2.

Lastly, in order to quantify the overall targeting performance and focusing quality yielded by each of the ablation cases listed in Table 9.1, a spatiotemporal analysis of their respective temperature increase distributions was performed. Firstly, each time-dependent temperature increase distribution, resulting from the respective ablation case, was temporally averaged over the final respiratory cycle. Subsequently, these temporally averaged distributions were spatially averaged within cubical volumes centered around the intended target, i.e., the tumor center as defined in the static model. These averaging cubes exhibited edge lengths ranging from $0$, i.e., non-averaged temperature, to $50$ mm. These spatiotemporal temperature increase averages were divided by the the corresponding values resulting from thermal simulations in the static model with continuous sonication, i.e., the reference ablation cases $DPC_{static}^{cont.}$, $SPC_{static}^{cont.}$, and $SPAC_{static}^{cont.}$ (see Section 9.2.3.1).

*(a)*                 *(b)*
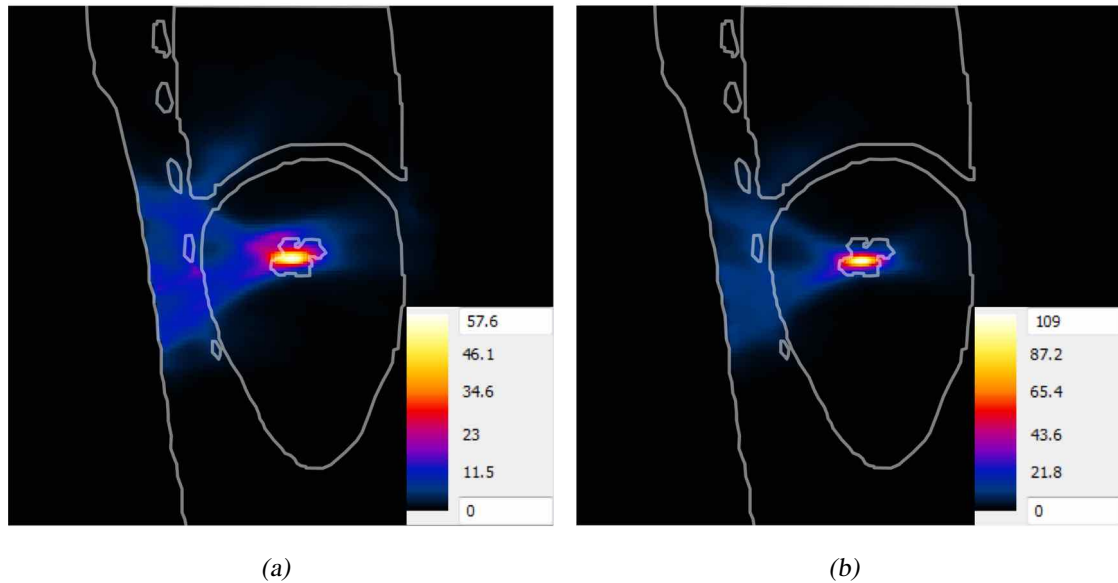
**Figure 9.9**: *Temperature increase distributions after continuous sonication of the transient model for* $60.06$ s, *with the SPAC approach and with (b) and without (a) target tracking , i.e., ablation cases* SPAC$_{transient}^{tracked}$ *and* SPAC$_{transient}^{untracked}$ *(see Section 9.2.3.2 and Table 9.1). Each temperature increase is plotted, with its distinct colormap, on the sagittal plane through the geometric focus which coincides with the center of the tumor. The voxeled outlines of the skin, ribs, lung, liver, and tumor as shown in Figure 9.4(b), can be seen.*



*(a)*            *(b)*            *(c)*
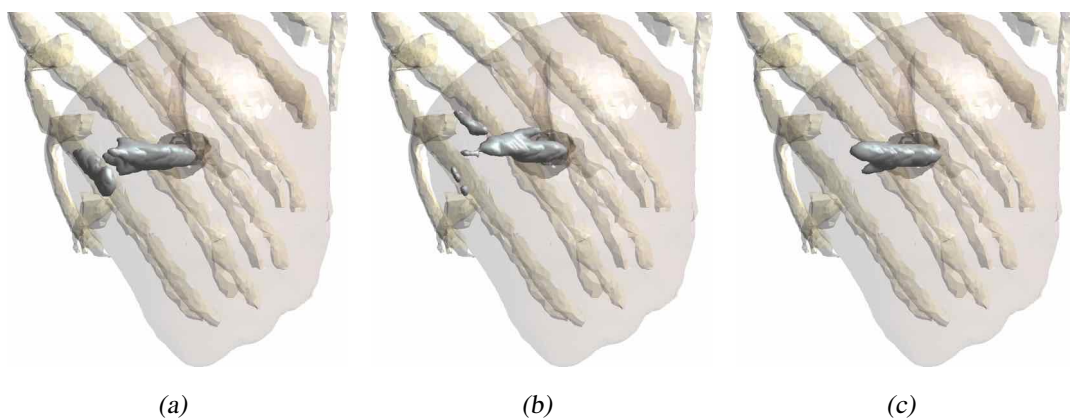
**Figure 9.10**: *CEM43 isosurfaces thresholded at* $240$ min *for the the the* DPC$_{transient}^{tracked}$, SPAC$_{transient}^{untracked}$, *and* SPAC$_{transient}^{tracked}$ *ablation cases (see Table 9.1). The importance of accurate steering and compensation, as well as continuous motion tracking are evident.*
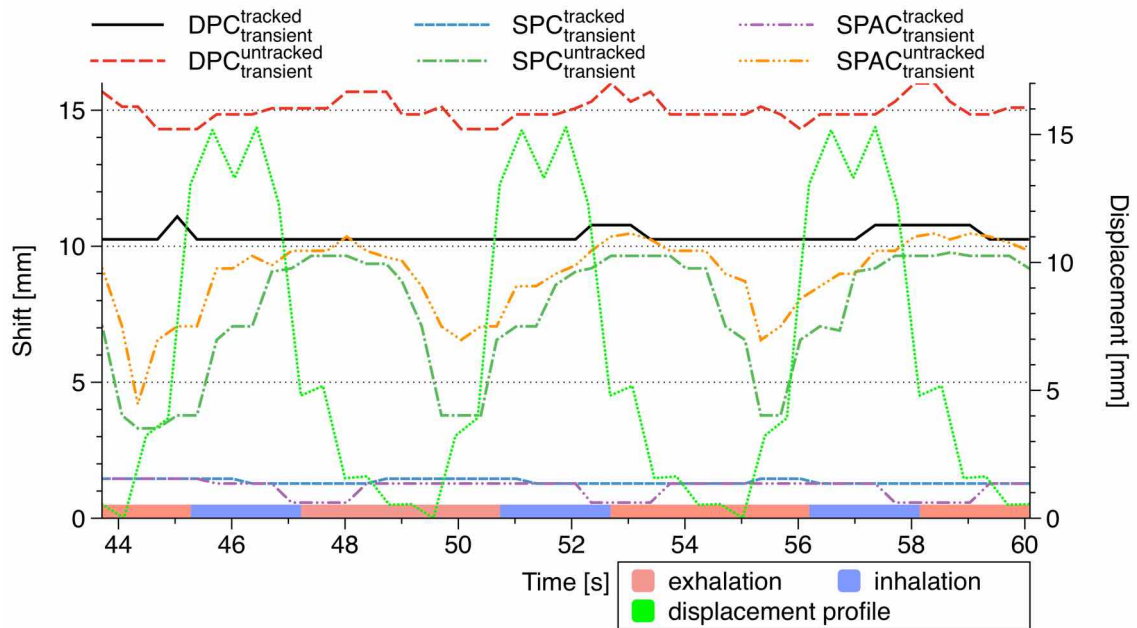
**Figure 9.11**: *Thermal hotspot focal shifts (in* mm*) over time, as calculated by the connected-component analyses of each temporal snapshot of the thermal simulations. The focal shifts are calculated as the distance between the intended target and the center of each detected connected-component, and are plotted here over the last three simulated respiratory cycles, for the different continuous ablation cases in the transient model.*

| Ablation Case | $D$[mm] | $V$[mm$^3$] | $T_{avg}$[$^\circ$C] |
|---|---|---|---|
| DPC$_{transient}^{untracked}$ | 15.0 (0.4) | 1138 (116) | 30.4 (1.2) |
| SPC$_{transient}^{untracked}$ | 7.6 (2.2) | 626 (153) | 27.0 (1.8) |
| SPAC$_{transient}^{untracked}$ | 8.9 (1.4) | 770 (180) | 35.4 (2.2) |
| DPC$_{transient}^{tracked}$ | 10.4 (0.2) | 477 (34) | 45.3 (1.3) |
| SPC$_{transient}^{tracked}$ | 1.3 (0.1) | 235 (29) | 52.1 (1.8) |
| SPAC$_{transient}^{tracked}$ | 1.1 (0.3) | 254 (29) | 68.4 (2.2) |

**Table 9.2**: *The results, mean (standard deviation), of the connected-component analysis on the temperature increase distributions for the 'untracked' and 'tracked' ablation cases simulated on the transient model, with the three steering/compensation approaches (see Table 9.1). $D$ is the calculated focal shift, $V$ is the full-width half-maximum (FWHM) volume of the component, and $T_{avg}$ is its average temperature increase.*
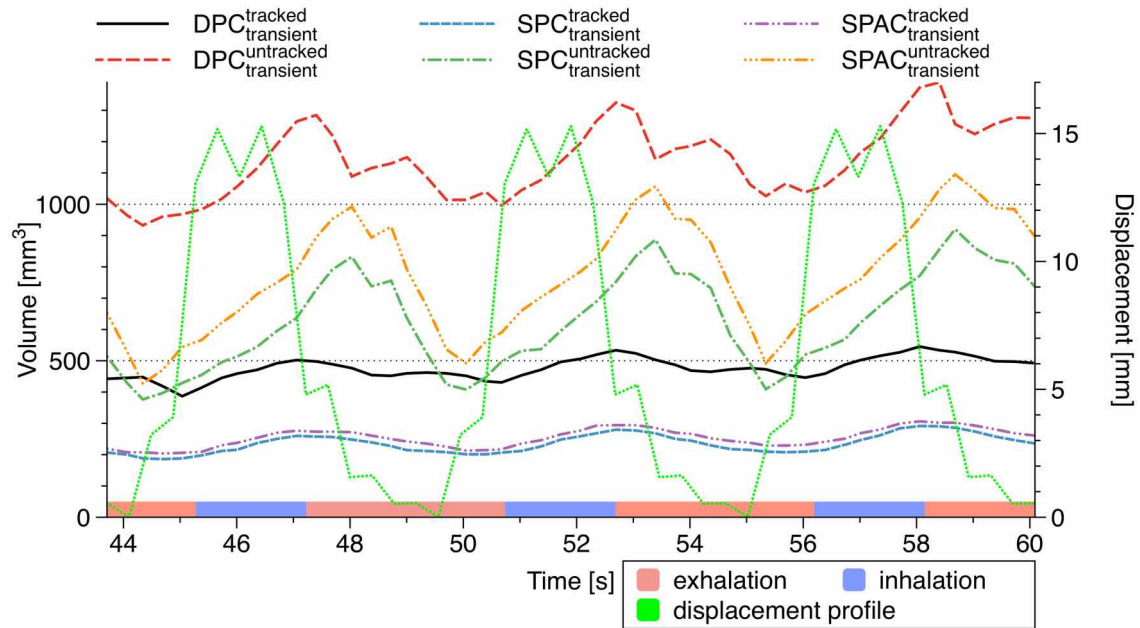
**Figure 9.12**: *Full-width half-maximum (FWHM) volumes (in* $\mathrm{mm}^3$*) of the thermal hotspots over time, as calculated by the connected-component analyses of each temporal snapshot of the thermal simulations. The hotspot volumes are calculated as the sum of the voxel volumes belonging to the particular component, and are plotted here over the last three simulated respiratory cycles, for the different continuous ablation cases in the transient model.*

Figure 9.14, shows the spatiotemporal average temperature increase ratios for every ablation case listed in Table 9.1, over the respective continuous static case, e.g., all cases based on the SPC approach were divided by the average values resulting from the $\mathrm{SPC}_{\mathrm{static}}^{\mathrm{cont.}}$ etc. Figures 9.15 and 9.16, show the ratios of all ablation cases over the $\mathrm{DPC}_{\mathrm{static}}^{\mathrm{cont.}}$ which is considered to be the least favorable reference ablation case (as defined in Section 9.2.3.1), and $\mathrm{SPAC}_{\mathrm{static}}^{\mathrm{cont.}}$ which is considered to be the best reference ablation case respectively.

## 9.4 Discussion

### 9.4.1 Intercostal Targeting and Aberration Corrections

As is suggested by Figures 9.7-9.10, accurate aberration corrections and precise intercostal targeting are both pivotal to effective hepatic tumor ablation. Simulations performed on the static anatomical model, show that the application of analytical steering methods, i.e., the DPC approach, yields prominent focal shifts and distortions, resulting
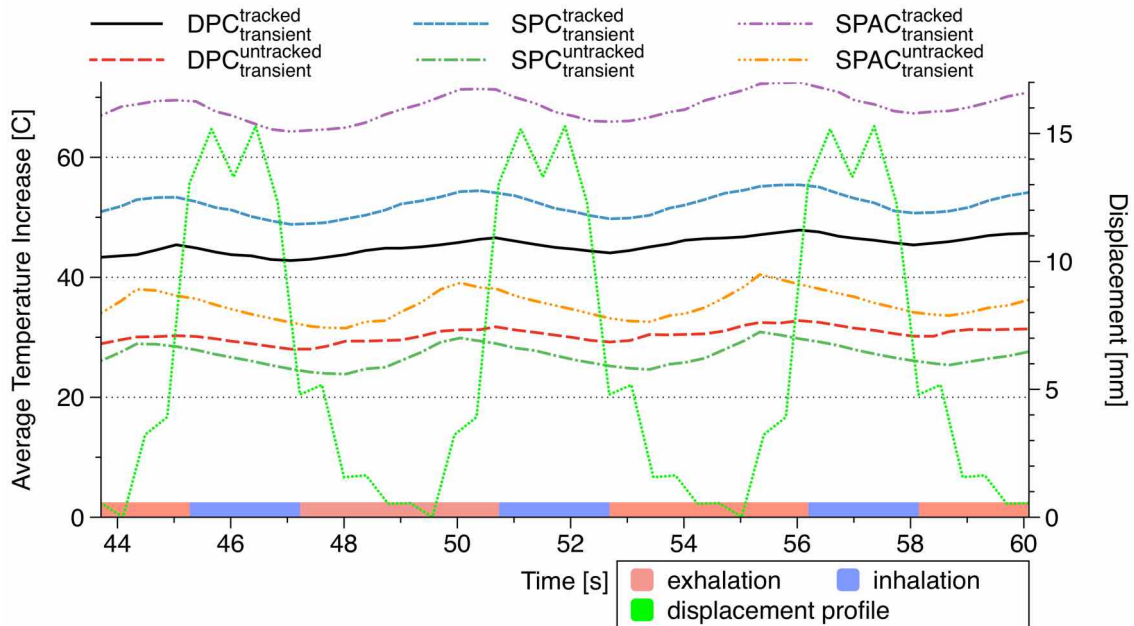
**Figure 9.13**: *Average temperatures of the full-width half-maximum (FWHM) connected-components. These averages are calculated over all voxels belonging to the respective components, and are plotted here over the last three simulated respiratory cycles, for the different continuous ablation cases in the transient model.*

in significant exposure of the pericostal tissue in the form of secondary hotspots (see Figures 9.7(a), 9.8(a), and 9.10(a)). Furthermore, as shown in the aforementioned figures, high energy deposition in the form of streaks, is observed in large areas of healthy tissue between the RPAT and the tumor, inducing collateral tissue damage in the intercostal regions.

Utilization of time-reversal simulation techniques, as is the case in SPC/SPAC-based approaches, results in a significant improvement in targeting accuracy. As can be seen in Figures 9.7(b) and 9.8(b), these techniques result in highly concentrated energy deposited entirely within the tumor, and sharply demarcated focal regions and thermal lesions. Furthermore, an obvious improvement of the treatment's focal and thermal gains can be observed, since there is a significant increase of the targeted tissue exposure, accompanied by a simultaneous decrease of the healthy tissue exposure.

These findings are equally applicable to the transient model simulations, where the exposure of healthy tissue exhibits the same dependency on the chosen steering/compensation approach.
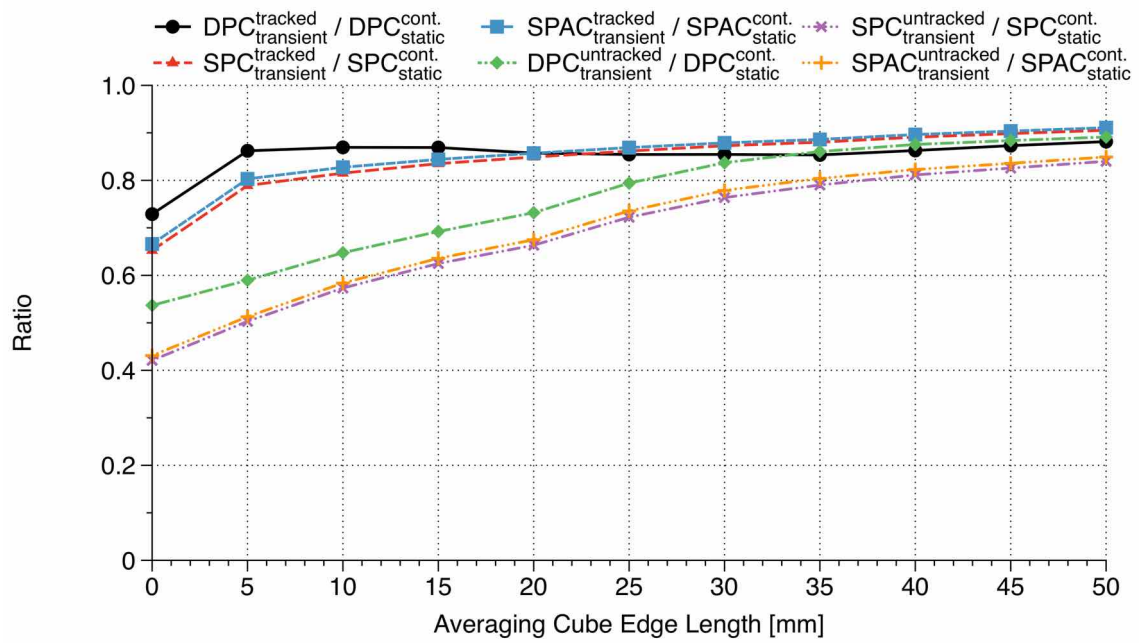
*(a)*
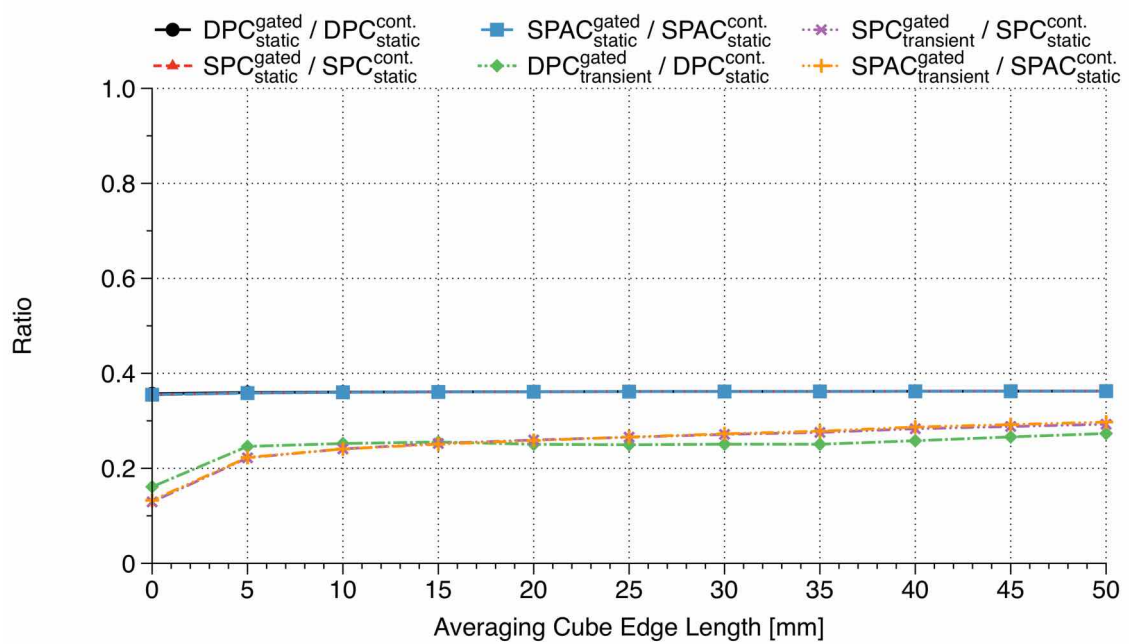


*(b)*

**Figure 9.14**: *Spatiotemporal average temperature increase ratios over the corresponding continuous static ablation case. The ratios of each continuous (a) and gated (b) ablation case listed in Table 9.1, are plotted in respect to the length of the averaging cube edge.*
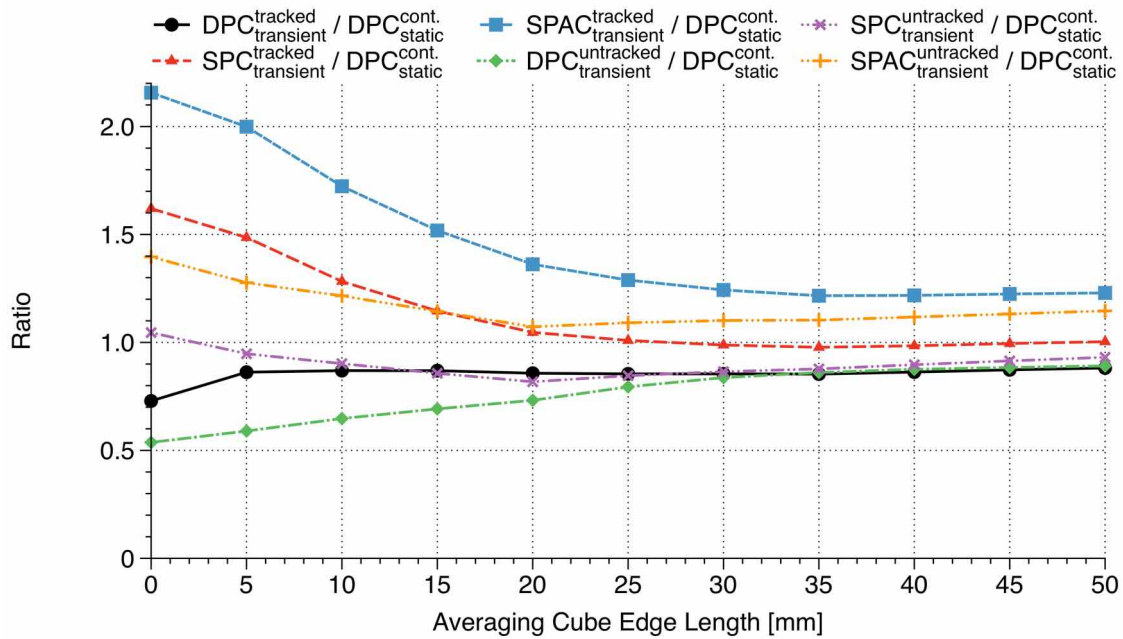
*(a)*
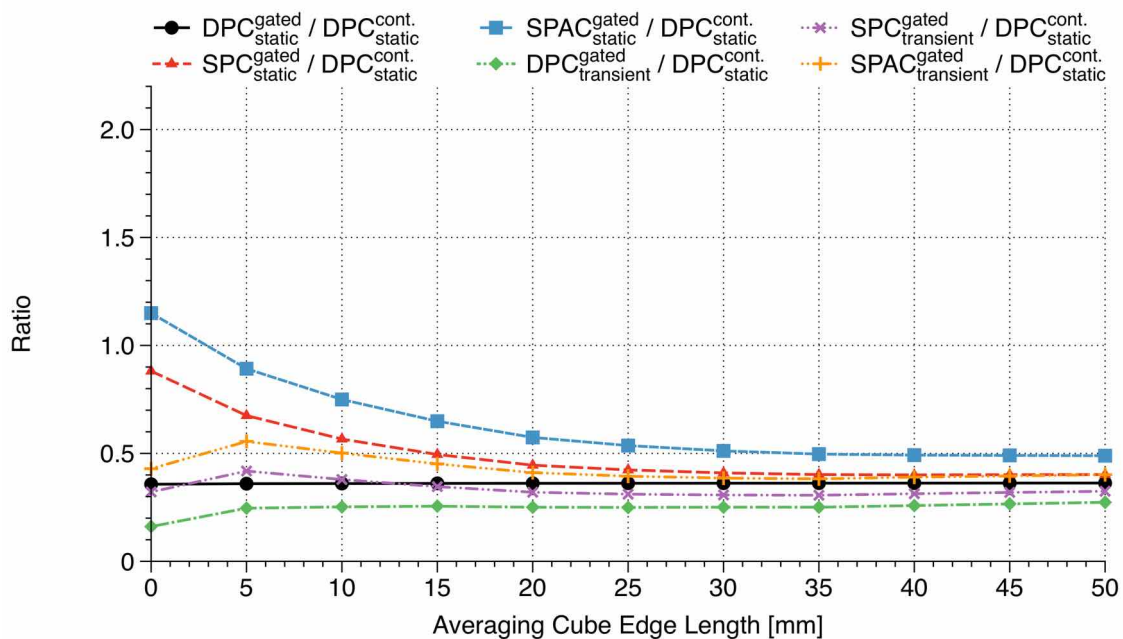


*(b)*

**Figure 9.15**: *Spatiotemporal average temperature increase ratios over the $DPC_{static}^{cont.}$, which is considered to be the least favorable reference ablation case (as defined in Section 9.2.3.1). The ratios of each continuous (a) and gated (b) ablation case listed in Table 9.1, are plotted in respect to the length of the averaging cube edge.*
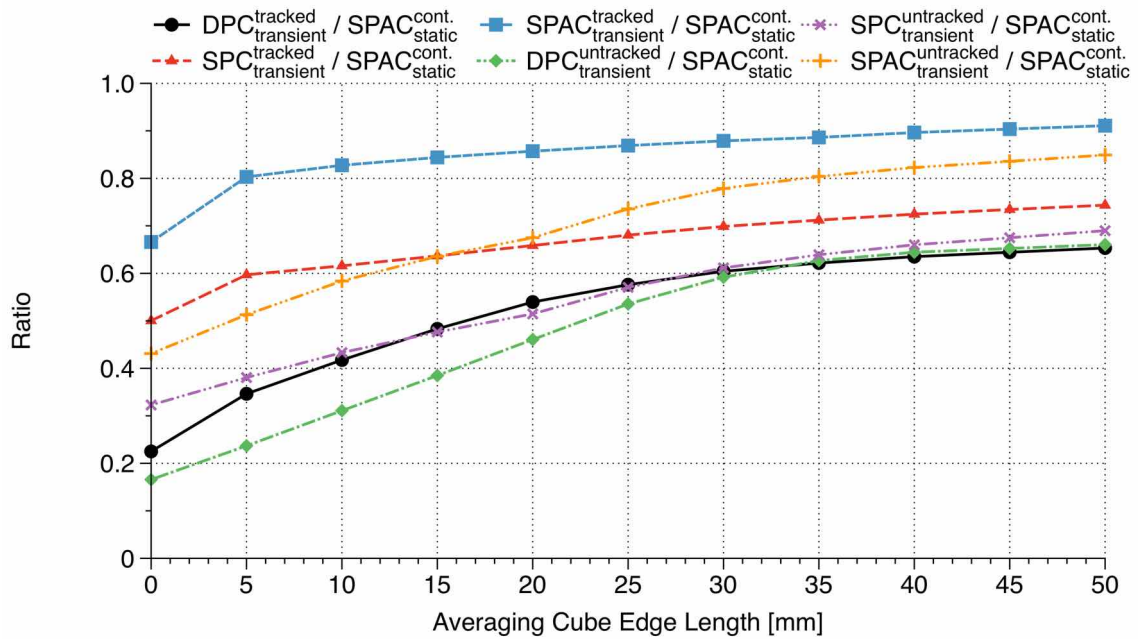
*(a)*
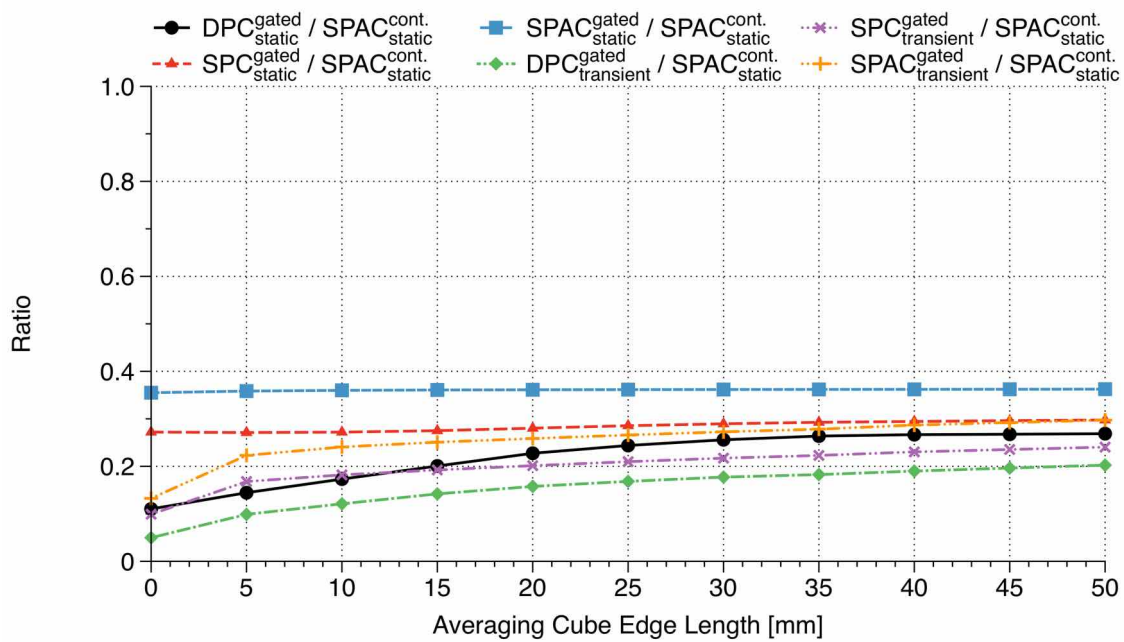


*(b)*

**Figure 9.16**: *Spatiotemporal average temperature increase ratios over the SPAC$_{static}^{cont.}$, which is considered to be the best reference ablation case (as defined in Section 9.2.3.1). The ratios of each continuous (a) and gated (b) ablation case listed in Table 9.1, are plotted in respect to the length of the averaging cube edge.*

## 9.4.2　Motion Tracking

As was discussed in Section 9.2.2.2, the target points for every step of the transient model throughout the respiratory cycle were defined as the center of the tumor which was accordingly warped along with the rest of the static model. These different targets tend to form two clusters temporally and spatially arranged in the full-exhalation and full-inhalation stages of the respiratory cycle (see Figure 9.5). As can be derived from Figure 9.6, the exhalation stage targets are located in the vicinity of the initial sonication target (marked with a '0') and exhibit a displacement, i.e., distance from the initial target, of ca. $2.4 \pm 1.8$ mm. The inhalation stage targets, however, show a much larger displacement of ca. $13.8 \pm 1.2$ mm.

Therefore, it becomes obvious that application of only initial steering/compensation, i.e., steering the focal beams to target '0' throughout the entire respiratory cycle without employment of motion tracking, as was the case for the $\text{DPC}^{\text{untracked}}_{\text{transient}}$, $\text{SPC}^{\text{untracked}}_{\text{transient}}$, and $\text{SPAC}^{\text{untracked}}_{\text{transient}}$ simulations, will result in large focal shifts and distorted distributions. In order to elucidate the phenomena stemming from the spatiotemporal distribution of the sonication targets, a magnified version of Figure 9.9(a), can be seen in Figure 9.17.
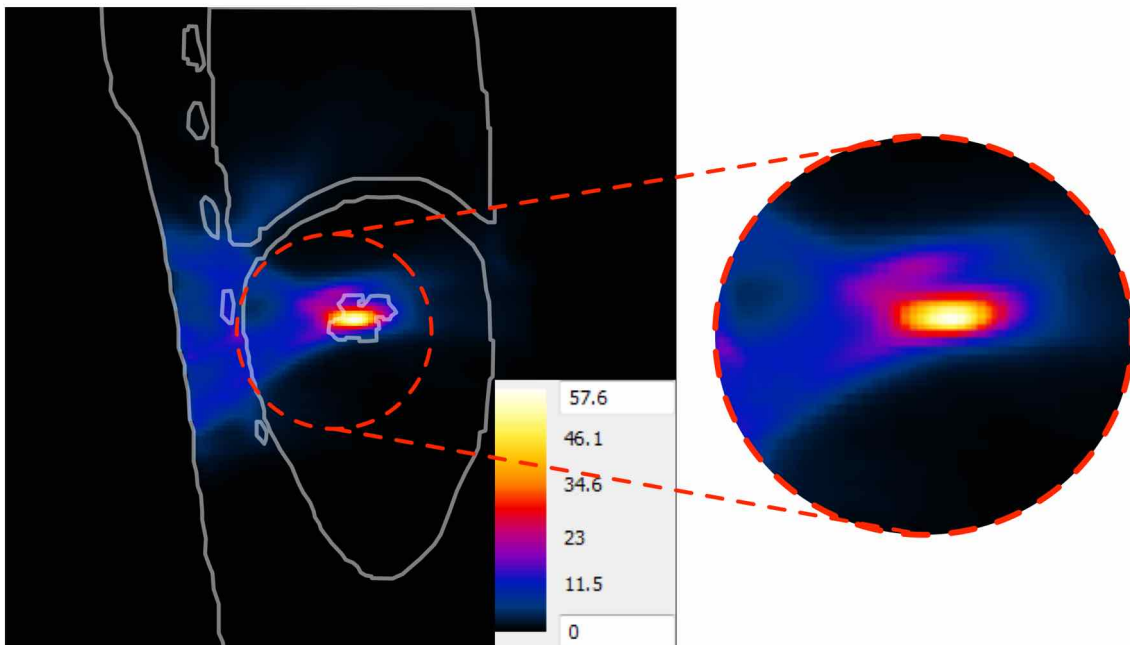


**Figure 9.17**: *Formation of secondary focal region, and therefore thermal hotspot, in the absence of motion tracking. This figure is a magnified version of Figure 9.9(a).*

The focal regions observed in the static model simulations with the SPC/SPAC approaches were approximately $5.2$ mm in diameter and $14.5$ mm in length. The corresponding dimensions in the case of DPC-based approaches were $8.2$ mm and $20.9$ mm respectively,

due to focal distortion effects. Therefore, during the exhalation stage the displacement observed at the sonication targets is smaller than the focal region diameter. Thus, in the absence of motion tracking the focal regions generated during this stage tend to overlap and yield a larger, distorted region. However, during the inhalation stage the target displacement is much larger, and as a result a second distorted region manifests (see Figure 9.17). This phenomenon is exhibited as a pulsating oscillation of the deposited acoustic energy between the two aforementioned foci.

Temperature in this secondary region increases rapidly throughout inhalation, but during exhalation it decreases as a result of perfusion, and drops below the FWHM threshold of the primary region. Consequently, during the connected-component analysis outlined in Section 9.3, within a given temporal window in the respiratory cycle the two regions are treated as one. This affects the values of the focal shift, the lesion volume, and the average temperatures which are plotted in Figures 9.11-9.13.

### 9.4.2.1  Focal Shifts

As can be seen in Table 9.2 and Figure 9.11, DPC-based ablation cases exhibited a large focal shift of $10.4 \pm 0.2$ mm when motion tracking is employed ($\text{DPC}_{\text{transient}}^{\text{tracked}}$), and $15 \pm 0.4$ mm when respiratory motion is not taken into account ($\text{DPC}_{\text{transient}}^{\text{untracked}}$).

Amelioration of these effects can be achieved with the employment of the SPC and SPAC approaches. Shifts in the order of $1.3 \pm 0.1$ mm and $1.1 \pm 0.3$ mm are observed for cases $\text{SPC}_{\text{transient}}^{\text{tracked}}$ and $\text{SPAC}_{\text{transient}}^{\text{tracked}}$ respectively, where motion tracking was employed. The 'untracked' counterparts of the aforementioned cases however, show significantly higher shifts of $7.6 \pm 2.2$ mm and $8.9 \pm 1.4$ mm for SPC and SPAC respectively.

### 9.4.2.2  Lesion Volumes

As previously discussed, simulation-based aberration correction techniques like the SPC and SPAC yield small, sharply delimited regions. This becomes evident when considering the thermal hotspot volumes, plotted over time in Figure 9.12, for the different ablation cases in the transient model.

The application of motion tracking in conjunction with time-reversal compensation techniques ($\text{SPC}_{\text{transient}}^{\text{tracked}}$ and $\text{SPAC}_{\text{transient}}^{\text{tracked}}$), ensures that the acoustic energy is concentrated at the intended target, resulting in sharp thermal hotspots approximately $50\%$ in size when compared to those observed in the $\text{DPC}_{\text{transient}}^{\text{tracked}}$ case.

### 9.4.2.3  Amplitude Normalization

The highly precise steering/compensation capabilities achievable with time-reversal simulation techniques ensure significant acoustic and thermal gain increases when compared

to the analytical alternative per the discussion in the previous sections. However, complimenting these techniques with amplitude corrections yields further improvement of the focusing quality. According to the findings presented in Table 9.2, an average enhancement of ca. $30\%$ can be seen in the target temperature increases observed with the SPAC-based approaches (see Figure 9.13).

Given the fact that amplitude normalization mostly 're-routes' the total sonicated acoustic power through the transducer elements with an unimpeded line-of-sight to the target, the aforementioned enhancement suggests that the SPAC approach could also be employed to diminish the exposure of healthy tissue. In addition, this method may permit a decrease in the total treatment time as ablative temperatures can be reached in the targeted tissue within shorter sonication durations.

### 9.4.3  Overall Performance

In accordance to the discussion in Section 9.2.3.1, the continuous ablation thermal simulations performed on the static model, i.e., $\text{DPC}_{\text{static}}^{\text{cont.}}$, $\text{SPC}_{\text{static}}^{\text{cont.}}$, and $\text{SPAC}_{\text{static}}^{\text{cont.}}$ (see Table 9.1), were idealized ablation cases where the maximum performance achievable with each steering/compensation was observed. These cases were mostly meant as a frame of reference to evaluate the performance of the subsequent ablation cases performed on the transient model.

Figure 9.14, shows the ratios of each ablation case over its continuous static counterpart, thus offering a relative quality metric for each case, independent of the corresponding steering/compensation approach employed. This figure however, does not provide an unbiased comparison between these different approaches. Such a comparison can be seen in Figures 9.15 and 9.16, where all examined ablation cases are compared to a single continuous static reference ($\text{DPC}_{\text{static}}^{\text{cont.}}$ and $\text{SPAC}_{\text{static}}^{\text{cont.}}$ respectively).

#### 9.4.3.1  Continuous Ablation Cases

Considering Figure 9.14(a), it can be seen that 'untracked' continuous ablation cases, i.e., $\text{DPC}_{\text{transient}}^{\text{untracked}}$, $\text{SPC}_{\text{transient}}^{\text{untracked}}$, and $\text{SPAC}_{\text{transient}}^{\text{untracked}}$, show a considerable quality drop compared to their corresponding continuous static counterpart. Ratios for these cases, however, increase with the averaging cube volume, which can be attributed to the focal shift/distortion effects and secondary region formation described in Section 9.4.2. This fact can be verified when considering that for averaging cube lengths larger than $15\,\text{mm}$, which lies in the upper range of the average focal shifts observed in untracked cases (see Table 9.2), the trends exhibited by the tracked and untracked counterparts become similar.

On the other hand, the comparable trend observed (see Figure 9.14(a)) for the 'tracked' equivalents of the aforementioned cases stems from a different effect. As can be seen,

the ratios for these cases improve rapidly with the increasing averaging volume and quickly reach a plateau. This behavior suggests that even with the application of steering/compensation, and continuous motion tracking, small focal shifts and distortions (which can also be seen in Figures 9.11 and 9.12), are still present in the presence of respiratory motion. Nevertheless, utilization of sophisticated steering, compensation, and tracking with the SPC/SPAC approaches was shown to achieve to $80 - 90\%$ of the performance observed in the static simulation where respiratory motion was not taken into account.

### 9.4.3.2   Gated Ablation Cases

The gated ablation cases performed on the static model, i.e., cases $DPC_{static}^{gated}$, $SPC_{static}^{gated}$, and $SPAC_{static}^{gated}$, exhibit a nearly constant ratio of ca. $0.36$ (see Figure 9.14(b)). This is in agreement to the ratio of the gating window duration to that of the entire respiratory cycle (ca. $35.7\%$, see Section 9.2.3.1).

Decreased performance, however, was observed for the gated transient simulations ($DPC_{transient}^{gated}$, $SPC_{transient}^{gated}$, and $SPAC_{transient}^{gated}$). This behavior stems from imperfect focusing as outlined in the above section. It can be seen that the calculated ratios for these cases are approximately equal to the product of the ratios observed for the continuous, tracked cases in the transient model, and the ratios observed for the static gated simulations.

## 9.5   Conclusions

Despite the encouraging results reported by many clinical trials, partial obstruction by the thoracic cage and respiration-induced organ motion hinders the extended use of FUS in the field of hepatic tumor ablation, and deters its recognition as a viable alternative to the well established and clinically accepted (minimally) invasive options, e.g., percutaneous radio-frequency, microwave and laser ablation, as well as cryotherapy which have been shown to successfully treat liver malignancies.

A numerical study was performed, where a transient anatomical model, deformed throughout a respiratory cycle based on 4D-MRI images, and the model of a randomized phased array transducer were used to perform acoustic and thermal simulations of hepatic ablation. The impact of motion tracking, as well as intercostal targeting and compensation, were investigated with three analytical and simulation-based approaches. Connected-component and spatiotemporal averaging analyses revealed that employment of simulation-based time-reversal techniques offered significant diminution of the pericostal tissue exposure, and acoustic shadowing effects induced by the thoracic cage, when compared to their analytical counterparts. Furthermore, such approaches yielded a visible increase of

the deposited acoustic energy in the targeted volume, improved targeting accuracy, augmented demarcation of the generated lesions, and higher temperature increases.

Application of such modeling techniques on a patient-specific basis may be utilized to understand and optimize HIFU energy deposition for hepatic tumor ablation, allowing for secondary effects of these procedures to be predicted and possibly avoided. Further benefits may include decrease of the total treatment time, and elimination of the need for invasive procedures, such as partial rib resection or utilization of controlled apnea.

In a next step, a population-based parametric liver motion and drift model that has been developed [263, 264], will be used to assess deformation in real-time based on sparse MRI measurements, and allow to overcome motion as well as focus distortion issues.

# 10

# Numerical Investigation of Scanning Approaches, Vasculature Impact and Standing-Wave Effects in HIFU Tumor Ablation with a Novel Transducer 'SonoKnife'

## 10.1   Introduction

As was extensively discussed in Section 3.3.1, therapeutic FUS modalities, most notably HIFU ablation, exhibit long treatment times, often in excess of several hours. This stems from the small focal regions, and therefore thermal lesions, produced by typical therapeutic FUS systems, with volumes on the order of $\mathrm{mm}^3$, and the relatively large target volumes to be treated, e.g. tumors, which are in the order of several $\mathrm{cm}^3$. In an attempt to alleviate this restriction, approaches such as volumetric ablation and microbubble-enhanced sonication, which were also discussed in the aforementioned section, are being actively developed and evaluated. The former, however, is in an experimental stage, while enhanced sonication is difficult to control and potentially harmful to healthy tissue.

An alternative technique to ameliorate this issue lies in the use of cylindrically-shaped transducers (see Section 2.2.2.2), which produce a continuous line of focal regions instead of a single ellipsoidal one, thus yielding larger lesions and potentially decreasing the treatment time. Such a line-focused transducer, which produces a 'blade'-like focal region, was introduced by Chen et al. [556] under the name 'SonoKnife'.

The SonoKnife was tailored to the HIFU ablation of superficial tumors, and in particular head and neck squamous cell carcinomas (HNSCCs), since patients suffering from such tumors are a challenging group and face a poor prognosis [557, 558]. The SonoKnife aims at the ablation of tumors which are not located deeper than $5\ \mathrm{cm}$ from the skin, and

are not larger than $3\,\mathrm{cm}$ in diameter [556]. The transducer prototypes operate at either 1 or $3.5\,\mathrm{MHz}$, exhibit a radius of curvature (R) of $60\,\mathrm{mm}$, a width (r) of $60\,\mathrm{mm}$, and a length (L) of $30\,\mathrm{mm}$. A conceptual sketch of the SonoKnife depicting the aforementioned parameters can be seen in Figure 10.1(b), while Figure 10.1(a) shows a photo of a prototype.

These prototypes have been evaluated both numerically and experimentally in in-vitro, ex-vivo, and in-vivo setups involving live piglets, wherein highly precise ablation was successfully demonstrated [556, 559–561]. In the recent study by Chen et al. [561] where the aforementioned prototypes were evaluated, the authors concluded that operating at $3.5\,\mathrm{MHz}$ leads to unavoidable skin-burns due to the high absorption of the skin, despite the utilization of continuous and efficient skin cooling. Thus, even though the utilization of lower acoustic frequencies imposes limitations on the ablation targeting precision, the authors recommended the use of the $1\,\mathrm{MHz}$ transducer with continuous application of skin cooling.

However, optimal treatment parameters, e.g., sonication duration, acoustic input power, the choice of an acoustic window, and volume-scanning approaches (i.e., the number and order of overlapping sonications needed to fully ablate a tumor), were not extensively investigated. The purpose of this study was to numerically evaluate the effect of these parameters by performing relevant acoustic and transient thermal simulations of the ablation of an HNSCC implanted into an anatomical model. Different phase-steering and aberration compensation techniques were applied to perform scans of the entire tumor volume, and their effect on the treatment outcome was ascertained by means of thermal dose evaluation. A challenging setup was defined, where the tumor was located in the immediate vicinity of large vessels and bone structures. This allowed for the impact of vasculature cooling and standing-wave effects on the efficacy of the treatment to be investigated.

## 10.2   Materials & Methods

### 10.2.1   Simulation Setup

#### 10.2.1.1   SonoKnife Model

While the original SonoKnife prototypes comprised a single piezoelectric element for evaluation and manufacturing purposes, per the authors recommendation the transducer was modeled as an array of $2 \times 2\,\mathrm{mm}$ rectangular piezoelectric elements [556, 561]. Given the dimensions of the transducer defined in the previous section, the modeled array consisted of $15 \times 30$ such elements, as shown in Figure 10.1(c), amounting to a total of $450$ elements. This design allowed for phase-steering and aberration correction techniques to be applied without requiring the transducer to be repositioned.

According to Chen et al. [561], the SonoKnife exhibits an electro-acoustic efficiency of $65\%$ and has been tested with up to $120$ W of electric input power, in continuous soni-cation mode for $60$ s. This yields a maximum acoustic input power of $78$ W, at which all acoustic simulations were performed. The acoustic pressure amplitude at the surface of each piezoelectric element was thus calculated using Equation 8.1, and resulted in $253.4$ kPa.



*(a)*                                      *(b)*                                      *(c)*
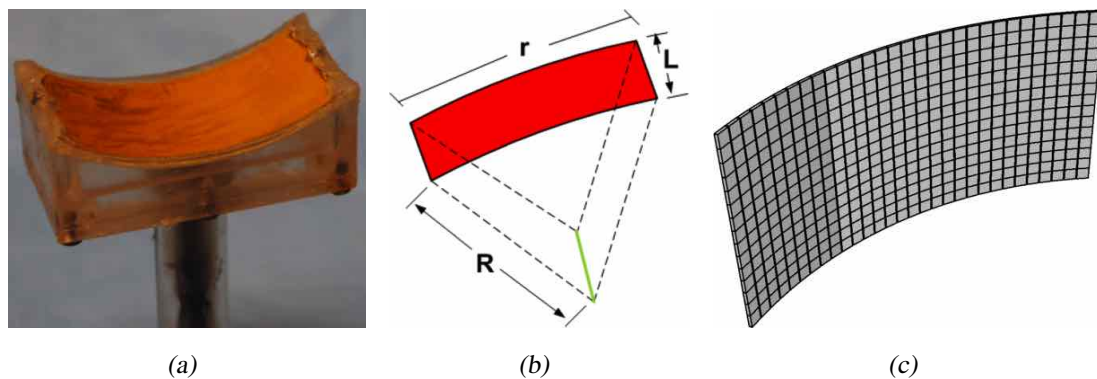
**Figure 10.1**: *A photo (a), a sketch (b), and the simulated model (c) of the SonoKnife cylindrically-focused transducer. While (a) and (b) depict the SonoKnife as a single-element transducer, the simulated model was that of a phased array comprising $15 \times 30$ rectangular piezoelectric elements with dimensions of $2 \times 2$ mm.*

### 10.2.1.2   Anatomical Model

A model of an HNSCC segmented from CT data, was provided by our collaborators Chen et al. [560], and artificially implanted into the 'Duke' anatomical model, depicting a 34yr old male, from the 'Virtual Population' anatomical model collection (see Section 6.3.3). The tumor was placed approximately $8$ mm from the skin surface, and its dimensions were approximately $22.6 \times 20.6 \times 30$ mm. The tumor was located in the immediate vicinity of the vertebral column and the mandible, in order to investigate the impact of reflections caused by the presence of bone structures in the acoustic beam path. Further-more, the tumor was assumed to surround the jugular vein and lie in close proximity to the carotid artery, allowing for the investigation of the impact of the large vessel cooling effect on thermal ablation. The SonoKnife transducer was placed such that its geometric focus coincided with the center of the tumor. The simulated anatomical model and voxel slices through the center of the tumor can be seen in Figure 10.2.
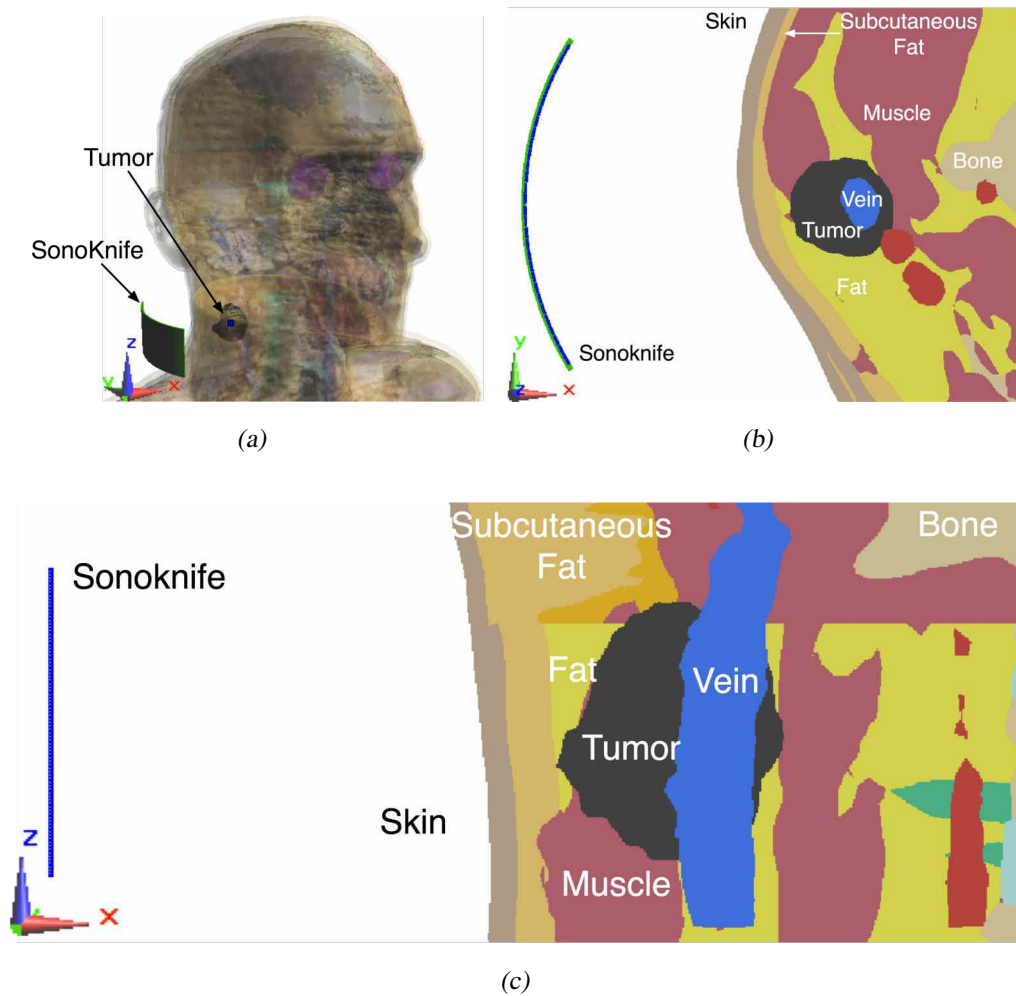
*Figure 10.2*: *3D view of the 'Duke' anatomical model with an implanted HNSCC tumor (a). A transverse (b) and coronal (c) voxel slice through the center of the tumor, marking the location of the SonoKnife and the most prominent tissue types.*

## 10.2.2 Acoustic Simulations

Linear acoustic simulations of the SonoKnife were performed at $1$ MHz, with the LAPWE solver described in Section 5.2.1.4. The simulation domain was discretized with a $0.14$ mm grid-step, truncated to approximately $100 \times 80 \times 40$ mm, and terminated with $16$ layers of PML on all domain boundaries to inhibit the manifestation of spurious reflection. This simulation was performed for $78$ W of acoustic power, and its duration was set to $150$ periods which correspond to a propagation distance of approximately $225$ mm. Each of these simulations was performed in approximately $15$ min with the GPU-accelerated variant of the LAPWE solver (see Section 6.2.2).

#### 10.2.2.1   Single-Sonication Simulations

Simulations were initially performed in a homogeneous and infinitely extending water medium in order to validate the model, compare the size of the generated focal region against the reported dimensions [556], and investigate its steering capabilities. The acoustic properties of water were set according to the values presented in Table 1.1. The simulation was performed without the application of any phase steering or compensation, i.e., the ultrasonic waves converged at the geometric focus of the array, at a 60 mm distance from the transducer surface.

The simulation described above was repeated in the presence of the anatomical model described in Section 10.2.1.2, where the geometric focus of the SonoKnife coincided with the center of the tumor. The acoustic properties of the different tissues were set according to the values presented in Table 1.2, while the properties of the HNSCC tumor were set to those of muscle.

In order to ascertain the impact of focal shift and distortion induced by the intervening tissues, most notably skin and subcutaneous fat, and investigate the possibility of compensating for these aberrations, two simulations in the presence of the anatomical model were performed. In a first simulation, the elements of the array were driven in phase without applying any aberration correction. In a second simulation, the simulation-based phase correction (SPC) time-reversal approach described in Section 8.3.2.1, was used instead to calculate phase corrections for each element, attempt to compensate for the presence of the intervening tissues, and minimize focal shift and distortion. As the SonoKnife generates a continuous line of focal regions, the virtual source used in the SPC simulation was modeled as a 28 mm line of such point sources instead of a single point, thus allowing for the recreation of the intended blade-like focal region.

#### 10.2.2.2   Tumor Ablation Simulations

Subsequently, acoustic and thermal simulations of HIFU ablation of the HNSCC tumor implanted in the anatomical model were performed. A total of 63 acoustic simulations with the settings outlined in Section 10.2.2.1 were performed, where in each simulation the steering settings of the transducer array's elements were set so as to steer the focus to a different region of the tumor. These steering settings were calculated both analytically through the distance-based phase correction (DPC) approach presented in Section 8.3.2.1, and through the SPC time-reversal approach mentioned above, in order to compare the two steering/correction techniques and their effect on the treatment outcome. Based on the focal region dimensions as calculated during the simulation of the SonoKnife in water (see below), a 50% overlap of the focal region size in a homogeneous medium was considered between the different focal regions. The target point for each of these sonications, their relative overlap, as well as an idealized depiction of the resulting focal regions can be seen in Figure 10.3.
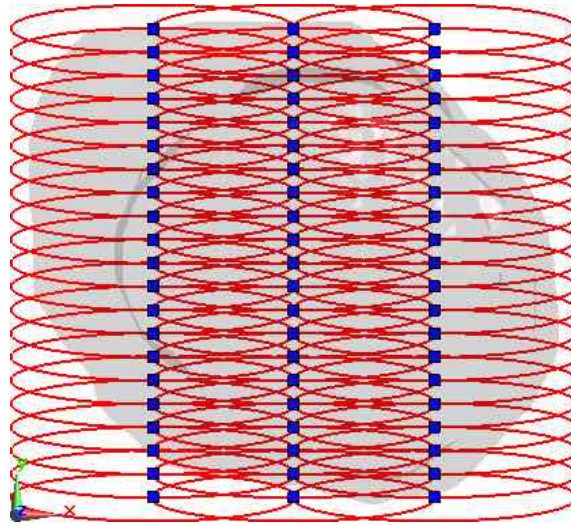
**Figure 10.3**: *Simplified depiction of the overlapping sonications simulated to investigate the ablation of the HNSCC tumor with SonoKnife. The target point for each of these sonications, their relative overlap, as well as an idealized depiction of the resulting focal regions can be seen.*

## 10.2.3   Thermal Simulations

The deposited acoustic energy was calculated for each of the aforementioned acoustic simulations, and used to perform thermal simulations of the ablation procedure as described in Section 6.3.2. In accordance to the treatment scenario proposed by Chen et al. [561], the patient's skin was assumed to be in contact with circulating water at a temperature of $8\,°C$. This was modeled through application of a convective boundary condition (see Section 6.3.2), with a heat transfer coefficient $h$ of $200\ W/m^2/K$ [551–553]. Prior to the administration of sonications, all thermal simulations were performed for $30\ min$ to allow for the different tissues to reach thermal equilibrium. During these simulations, the effects of perfusion were taken into account, and the thermal properties for all tissues were based on the IT'IS Foundation Tissue Properties Database [8], while the properties of the HNSCC tumor were set to those of muscle. The cumulative equivalent minutes at $43\,°C$ (CEM43) [499] was calculated for all tissues during these simulations to evaluate the administered thermal dose and ascertain whether a given tissue has been ablated as a result of the sonications. A CEM43 threshold value of $240\ min$ was assumed to signify ablation [554, 555].

Two distinct ablation strategies were simulated, namely point-to-point (sequential) volume-scanning (Section 3.1.3) and volumetric ablation (Section 3.3.1). In the case of the former, each sonication was administered for 30 or $60$ s, and followed by $30\ sec$ in the absence of sonication in order to allow for the intervening tissues, e.g., skin, to cool. Two orders of sonication administration, starting from the region of the tumor closest to the SonoKnife to the region furthest away, and vice-versa, were simulated. This volume-scanning ab-

lation resulted in a total number of $63$ sonications. A summary of these point-to-point volume-scanning ablation cases, as well as the total treatment time for each case can be seen in Table 10.1. In the context of volumetric ablation, instantaneous steering of the focal region was assumed. Therefore, the deposited energy distributions, resulting from all $63$ acoustic simulations, were averaged and applied for $30$ or $60$ s, and followed by either $0$ or $30$ sec in the absence of sonication. A summary of these volumetric ablation cases, as well as the total treatment time for each case can be seen in Table 10.2.

| Case | Order | $T_{sonication}[\text{s}]$ | $T_{pause}[\text{s}]$ | $T_{treatment}[\text{min}]$ |
|---|---|---|---|---|
| P2P-30-30-F | Forward | 30 | 30 | 63 |
| P2P-30-30-R | Reverse | 30 | 30 | 63 |
| P2P-60-30-F | Forward | 60 | 30 | 94.5 |
| P2P-60-30-R | Reverse | 60 | 30 | 94.5 |

**Table 10.1**: *Summary of the point-to-point volume-scanning ablation cases examined in this study. The order of sonication (forward or reverse), the duration of each sonication $T_{sonication}$, the pause duration between sonications $T_{pause}$, and the total treatment time $T_{treatment}$ for each case can be seen.*

| Case | $T_{sonication}[\text{s}]$ | $T_{pause}[\text{s}]$ | $T_{treatment}[\text{min}]$ |
|---|---|---|---|
| VOL-30-30 | 30 | 30 | 63 |
| VOL-30-0 | 30 | 0 | 31.5 |
| VOL-60-30 | 60 | 30 | 94.5 |
| VOL-60-0 | 60 | 0 | 63 |

**Table 10.2**: *Summary of the volumetric ablation cases examined in this study. The duration of each sonication $T_{sonication}$, the pause duration between sonications $T_{pause}$, and the total treatment time $T_{treatment}$ for each case can be seen.*

## 10.3 Results

The absolute pressure distributions resulting from the simulation of the SonoKnife in water are plotted on planes through the geometric focus in Figure 10.4. The dimensions of the $-3$ dB focal region, i.e., the region extending up to a $50\%$ absolute pressure drop relative to the peak, were measured and compared to the dimensions reported by Chen et al. [556] who performed simulations using FOCUS (see Section 4.3.2) and validated them against in-vitro measurements. The focal region dimensions observed in this simulation were approximately $12 \times 2 \times 28$ mm along the X, Y and Z axes respectively. These are in agreement to the reported dimensions for a sonication frequency of $1$ MHz (exact measurements were not given in the cited publication but were presented in a graph).
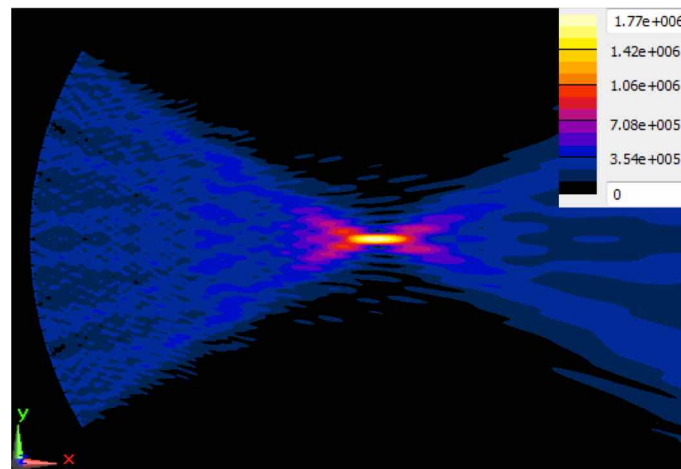
*(a)*
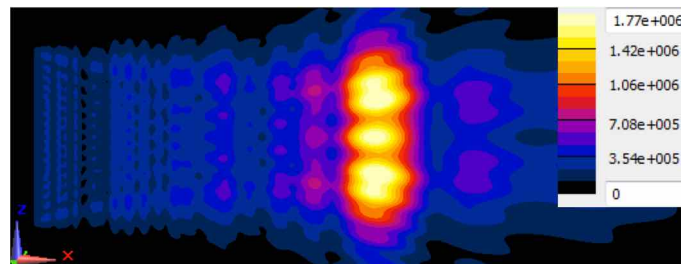


*(b)*

**Figure 10.4**: *Absolute pressure distributions resulting from the simulation of the SonoKnife in water on a Z (a) and Y (b) plane through the geometric focus.*

The pressure distributions resulting from the simulations in the presence of the anatomical model, with and without the application of phase aberration correction, are plotted on a coronal plane through the geometric focus which coincides with the center of the tumor, in Figure 10.5.

CEM43 isosurfaces thresholded at 240 min can be seen in Figures 10.6 and 10.7 for selected ablation cases with the SPC and DPC steering/correction approaches. In addition, the percentage of tissue volume within the region of interest (i.e., the computational domain), with a calculated CEM43 value exceeding 240 min, are summarized in Table 10.3 for all ablation cases described in the previous section.

## 10.4  Discussion

As can be seen in Figure 10.5(a), the presence of the anatomical model induces distortion and shift of the focal region in relation to the intended target, while the impact of
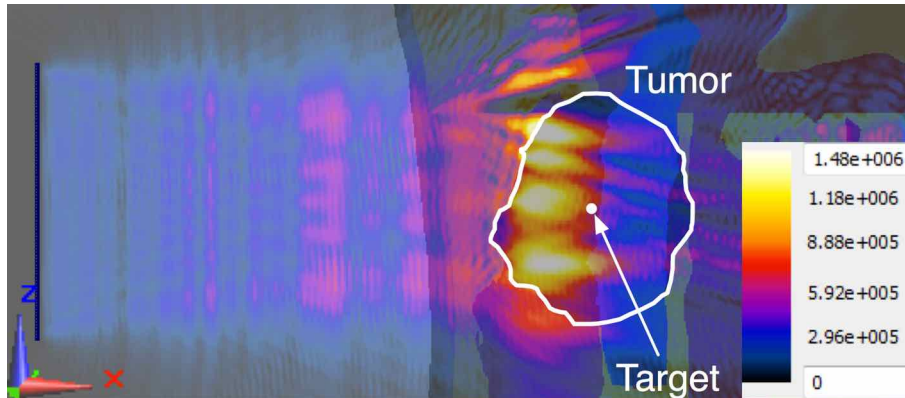
*(a)*
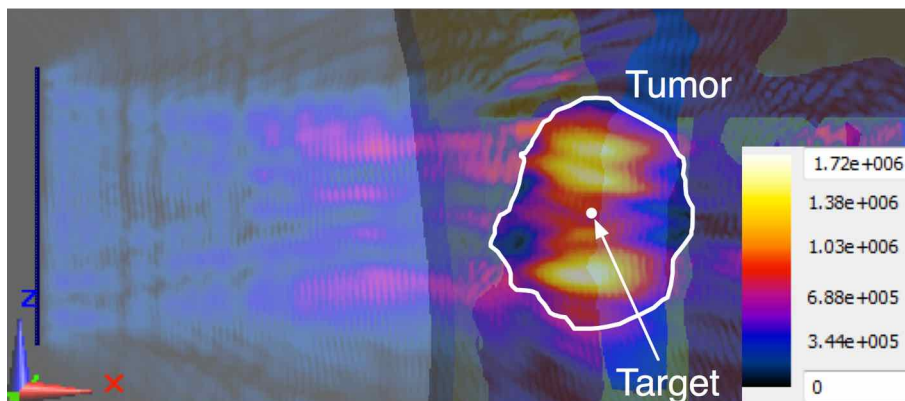


*(b)*

**Figure 10.5**: *Absolute pressure distributions resulting from the simulation of the SonoKnife in the presence of the anatomical model with* (b) *and without* (a) *the application of aberration correction. The pressure is plotted on the coronal plane through the geometric focus which coincides with the center of the tumor. The presence of the anatomical model induces distortion and shift of the focal region, while the effects of the intervening and surrounding tissues, most notably the tissue-bone interfaces, are evident. Application of aberration correction through the SPC approach, however, visibly diminishes these effects.*

(a)



(b)
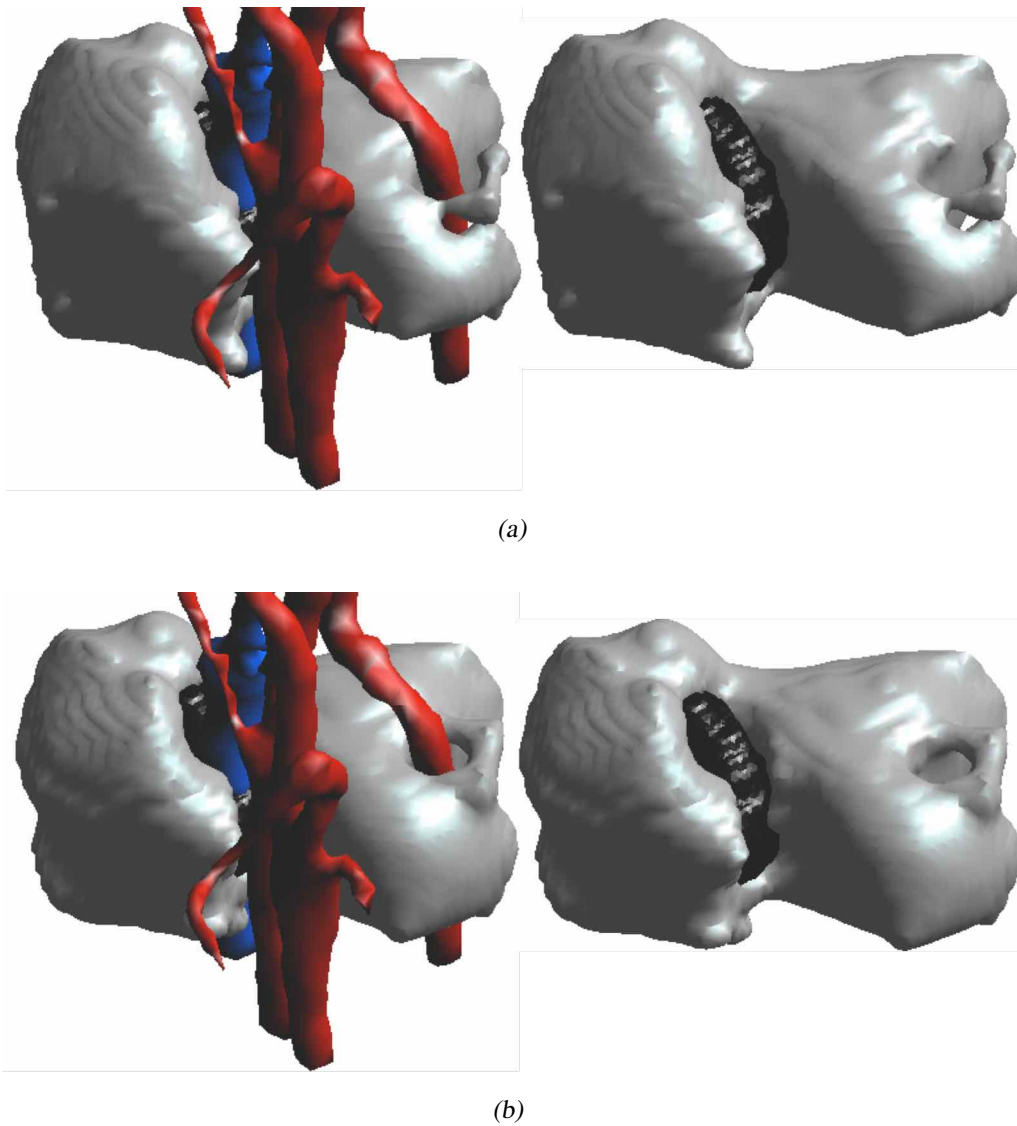
**Figure 10.6**: *CEM43 isosurfaces thresholded at* 240 min *for the P2P-30-30-F ablation case, with the DPC* (a) *and the SPC* (b) *approaches (see Table* 10.1*). The figures on the left show the jugular vein and carotid artery which lie in close proximity to the tumor, while the figures on the left only show the tumor and the CEM43 isosurface. The regions of the tumor that failed to receive ablative thermal doses due to the presence of the vasculature are clearly visible.*

(a)



(b)
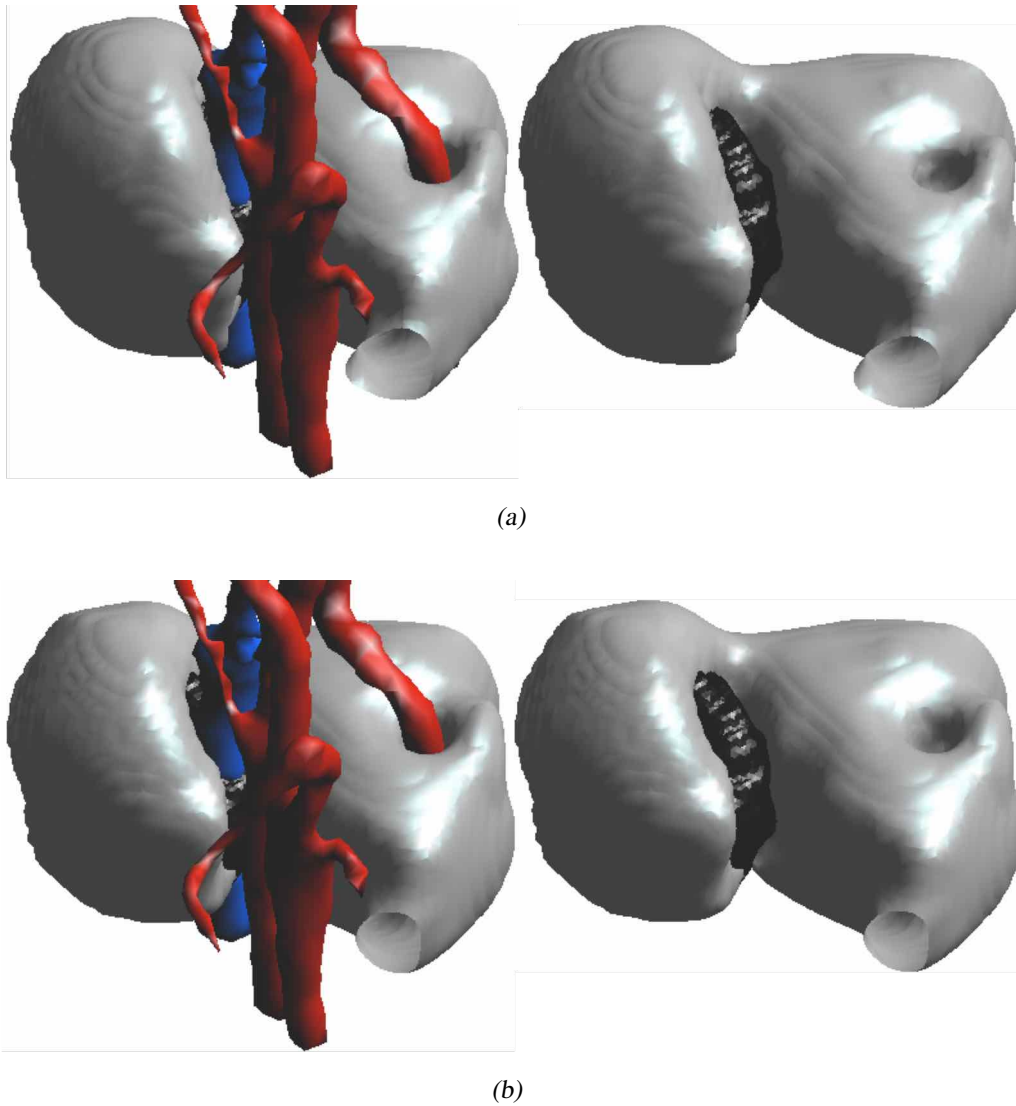
**Figure 10.7**: *CEM43 isosurfaces thresholded at* 240 min *for the VOL-30-0 ablation case, with the DPC* (a) *and the SPC* (b) *approaches (see Table* 10.2*). The figures on the left show the jugular vein and carotid artery which lie in close proximity to the tumor, while the figures on the left only show the tumor and the CEM43 isosurface. The regions of the tumor that failed to receive ablative thermal doses due to the presence of the vasculature are clearly visible.*

| Case | Tissue volume % exceeding CEM43 of 240min | | | | | | | | | |
|---|---|---|---|---|---|---|---|---|---|---|
| | Tumor | | Skin | | Muscle | | Fat | | SAT | |
| | DPC | SPC | DPC | SPC | DPC | SPC | DPC | SPC | DPC | SPC |
| P2P-30-30-F | 85 | 87 | 10 | 3 | 20 | 22 | 40 | 41 | 32 | 25 |
| P2P-30-30-R | 84 | 87 | 12 | 5 | 18 | 21 | 41 | 43 | 36 | 30 |
| P2P-60-30-F | 93 | 95 | 22 | 15 | 37 | 38 | 59 | 59 | 43 | 38 |
| P2P-60-30-R | 93 | 96 | 23 | 16 | 35 | 37 | 60 | 61 | 46 | 42 |
| VOL-30-30 | 66 | 64 | 0 | 0 | 10 | 11 | 23 | 23 | 17 | 11 |
| VOL-30-0 | 88 | 88 | 11 | 10 | 33 | 33 | 50 | 49 | 40 | 33 |
| VOL-60-30 | 82 | 82 | 4 | 3 | 25 | 26 | 41 | 41 | 30 | 23 |
| VOL-60-0 | 91 | 91 | 13 | 11 | 41 | 41 | 57 | 55 | 42 | 36 |

**Table 10.3**: *The percentages of the different tissue volumes within the region of interest that are considered to be ablated, i.e., exhibiting a calculated CEM43 value exceeding* 240 min. *The values for all ablation cases examined in this study with both the DPC and SPC approaches can be seen. 'SAT' stands for 'subcutaneous adipose tissue'.*

the surrounding tissues, such as the skin and bone structures, is clearly visible. The presence of these tissues results in the formation of prominent standing waves and therefore significant energy deposition in the healthy tissue, most notably fat, SAT, and muscle. This result signifies that analytically calculated focal steering without additional phase aberration correction yields suboptimal distributions. This becomes evident when considering Figure 10.5(b), where the SPC approach was employed to calculate aberration corrections. Focal shift and distortion effects are visibly improved and accompanied by a significant increase of 16% in peak pressure. However, standing-wave effects induced by tissues behind the target cannot be compensated for even with the application of the SPC approach and alternative acoustic windows would need to be defined in cases where the targeted volume lies in the vicinity of bone structures.

As can be seen from Table 10.3, as well as Figures 10.6 and 10.7, treatment of the HNSCC with the SonoKnife can result in ablation of nearly the entire tumor within treatment times of approximately 30 − 90 min. Thus, this novel transducer may significantly decrease patient table-time in comparison to treatments employing spherically focused transducers (see Section 3.3.1). However, in this particular case significant regions of the tumor fail to receive an adequate thermal dose to achieve ablation, resulting in viable tumor cells surviving the procedure. This stems from the presence of the jugular vein through the tumor and the carotid artery in its vicinity (see Figure 10.2(b)), which act as very effective heat-sinks and cool the surrounding tissue.

Moreover, significant heating, and thus ablation of the healthy tissue behind the tumor can be seen, which can be attributed to the prominent standing waves induced by the presence of bone structures in the acoustic beam path. In terms of treatment quality, the

order of sonication administration in point-to-point volume scanning, i.e., forward and reverse, appears to have negligible effects and does not improve tumor coverage. Furthermore, the point-to-point volume scanning approaches appear to yield superior tumor coverage in comparison to volumetric approaches for the same switching settings, i.e., the same sonication and pause durations, due to the nonlinearity of CEM43. However, it can be seen that continuous volumetric ablation approaches, i.e., cases where no pause was considered between sonications, can achieve therapeutic effects of comparable quality to volume-scanning approaches in half of the total treatment time. In addition, volumetric techniques offer a more homogenized energy distribution which can be deduced by the smoothness of the CEM43 isosurfaces shown in Figure 10.7.

Lastly, in the context of the steering/compensation approach, there was no significant improvement of the tumor coverage between the DPC and SPC methods (see Table 10.3). Nevertheless, a notable consequence of employing the SPC approach to steer the focal region and compensate for the intervening tissues, instead of its analytical counterpart, is the significant exposure reduction of the skin and subcutaneous fat which lie between the SonoKnife and the tumor. While no decrease in the exposure of other tissues, e.g., muscle and fat, is observed, these results suggest that utilizing sophisticated time-reversal approaches may allow for adequate tumor coverage with decreased acoustic intensities, thus allowing for successful treatment and minimal collateral tissue damage.

## 10.5 Conclusions and Outlook

The small size of the generated focal regions in relation to the extents of the targeted tissue region, and the necessity for long pauses between sonications, result in HIFU ablation of tumors to exhibit long treatment times, often extending up to $6$ h. Furthermore, while novel transducers and alternative volume scanning techniques have been introduced in an attempt to counter this issue, their efficacy has not been tested on realistic setups, while the published literature on the optimal treatment parameters is sparse.

A numerical study was presented where a line-focused transducer array was used to investigate various potentially complicating factors involved in the ablation process, particularly when targeting larger tumors. Acoustic and transient thermal simulations were performed to investigate a realistic but challenging setup, involving a head and neck squamous cell carcinoma implanted into an anatomical model. Beam steering was applied to the array, with both analytical and simulated time-reversal approaches, to overlap multiple focal regions and ensure coverage of the entire tumor. Multiple ablation approaches, namely sequential volume-scanning and volumetric ablation were investigated. In addition, the treatment parameters, i.e., sonication duration and intensity, pause duration between sonications, scanning scheme etc., were varied and their impact on the treatment outcome was quantified by calculating CEM43 and applying thresholds to delimit damaged/ablated regions.

This study showed that high-resolution acoustic and thermal simulations allow for entire HIFU ablation procedures to be modeled in detail. Parameters pivotal to the treatment can be easily evaluated and optimized, while full-wave modeling permits for secondary effects to be predicted and possibly compensated for.

The reported findings suggest that in challenging ablation scenarios where the targeted volume lies in the vicinity of strongly reflecting structures and large vessels, such as the one presented here, a simplified lesion overlap approach is not sufficient. Furthermore, in order to maximize tumor exposure while sparing healthy tissue, optimization of the input power, sonication duration, scanning scheme, and potentially frequency may be necessary on a individual sonication basis. Therefore, the formulation of a more sophisticated treatment plan would be warranted. Actively cooled regions of the target would require increased input power, sonication duration, or denser region overlap. On the contrary, the boundaries of the target should be less exposed to minimize collateral tissue damage.

Lastly, sophisticated steering and correction techniques, such as the SPC approach presented here, can compensate for the presence of intervening tissues, significantly reducing focal shift and distortion effects. However, such approaches fail to ameliorate strong reflections and standing wave effects from bone structures, diminution of which would require alternative acoustic windows to be defined prior to the treatment.

# Part IV

# Epilogue

# 11

# Summary & Conclusions

As was shown in Chapter 3 of this thesis, focused ultrasound (FUS) technology offers a highly effective and non-invasive therapeutic modality that has already been successfully employed in neurosurgical operations and ablative oncology. Furthermore, utilization of FUS for alternative therapies of pathological conditions that were previously thought to be untreatable, is being fervently investigated by research institutions and medical centers throughout the world.

Despite its promise, however, FUS has not been widely accepted by the clinical community as a viable alternative to the mainstream interventional therapies. These inhibitions exhibited by medical and clinical professionals, are predominantly stemming from the sheer complexity of this modality, as well as the different inherent and technical challenges faced during its employment, which were detailed in Section 3.3.

This thesis presented a newly developed computational multi-physics framework, capable of realistically modeling the complex medical scenarios involving therapeutic FUS procedures. The framework comprised dedicated full 3D wave acoustic solvers, which were experimentally validated and augmented with state-of-the-art high-performance computing techniques in order to allow for complex setups involving detailed anatomical models to be accurately simulated within minutes. Complemented by powerful image segmentation, visualization, and post-processing tools, this framework can be used to perform patient-specific treatment planing and optimization of such therapies and their outcomes, permit prediction and avoidance of adverse secondary effects, as well as provide in-depth understanding of the underlying mechanisms that define them.

This framework was applied to several modern therapeutic FUS treatment scenarios particularly transcranial FUS treatments for neurosurgical applications, hepatic tumor ablation under respiratory organ motion, and the evaluation of a novel ultrasonic transducer tailored to the treatment of superficial tumors. The presented framework did not only permit for these complex treatment scenarios to be accurately modeled and simulated within viable time-frames, but further allowed for the specific challenges afflicting these therapies to be investigated and compensated for, by assessing different ameliorative approaches.

The presented framework exhibits the following competitive advantages when compared to other available solutions:

- **Extended Modeling Scale**: The efficiently developed acoustic solvers, in conjunction with high-end parallelization techniques, allowed for therapeutic FUS treatment scenarios to be simulated on a scale previously unachievable. Setups comprising large anatomical models and realistic transducer arrays were possible to simulate within minutes, significantly extending the range of investigable applications.

- **Accuracy & Realism**: The majority of available solutions, and therefore studies, on therapeutic FUS, is typically performed on simplified depictions of the human anatomy and employs fundamental models of acoustic wave propagation, resulting in limited realism and applicability. Contrary to this, the presented framework allows for the simulation of detailed inhomogeneous anatomical models, generated from medical image data, and utilizes accurate propagation models, thus accounting for the full complexity of FUS therapy.

- **Multi-Physics Modeling**: A significant advantage of the presented framework lies in the possibility to extend its computational modeling capabilities to include multiple physics and processes. By coupling the developed acoustic solvers to Bioheat equation solvers, it was possible to model the thermal effects of each respective therapy, accurately ascertain its efficacy, as well as to predict the manifestation of adverse secondary effects.

- **Flexibility & Ease-of-Use**: Being complemented by powerful geometrical modeling, image segmentation, visualization, and post-processing tools allows for the automatic design and evaluation of any therapeutic transducer or array as was demonstrated during this work. In addition, the versatile Python scripting interface permits for the quick prototyping of novel evaluation tools for the analysis of the simulation results, e.g., hotspot detection and analysis, treatment optimization, etc., as shown in the featured applications.

# 12

# Next Steps

The following points should be addressed next:

- **Multi-GPU Parallelization**: Despite the high performance gains offered by the variants of the developed acoustic solvers parallelized on graphics processing units (GPUs), the foremost caveat of this technology lies in the limited amounts of memory available on such devices. Applicable to even the highest-end devices of this type, modern GPUs cannot accommodate extremely large computational domains, thus limiting their usability to the simulation of smaller setups, or to those involving lower acoustic frequencies. In order to enable the modeling of larger setups, the developed solvers would need to be extended with support for the concurrent utilization of multiple GPUs, thus permitting for any therapeutic FUS scenario to be simulated within viable time-frames.

- **Additional Experimental Validation**: While the different solvers developed and employed in the context of this thesis were meticulously validated, both analytically and experimentally, further validation is clearly required. Replication of clinical ex-vivo and in-vivo setups would in addition validate the representation of the utilized transducer arrays and the steering/compensation techniques utilized to optimize the treatment outcomes.

- **Optimization**: The steering/compensation simulation techniques that were extensively employed throughout this thesis, were predominantly based on time-reversal approaches. While such methods were shown to be significantly superior to the semi-analytical techniques employed currently, these approaches require a-priori knowledge of the intended target region and would not be amenable to real-time optimization of the treatment. Additional interference matrix-based optimization approaches, akin to the techniques utilized in hyperthermic oncology, would need to be devised. Such techniques would utilize precomputed solutions and fast genetic-optimization algorithms, in order to permit the real-time re-evaluation of the transducer arrays steering parameters, and allow the operator to consider patient-feedback or monitoring information during the treatment.

- **Multi-modal Anatomical Models**: The anatomical models utilized in this study resulted from the segmentation of MR image data, thus requiring the assignment of a single set of acoustic tissue properties per tissue type. However, the inhomogeneous nature of bone structures has been shown to affect the treatment planning significantly. By combining MR and CT image datasets of the same patients, multi-modal anatomical models should be created, leveraging the superior soft-tissue contrast offered by MRI, and the density-variation information available in CT data.

- **Alternative Model Implementations**: While full-wave models offer the most accurate depiction of acoustic wave propagation, their computational and time resource requirements far outweigh those of the more fundamental beam models. Furthermore, as simpler setups, e.g., transducer evaluation in homogeneous setups, do not require such degrees of accuracy, additional acoustic solvers combining the fast nearfield method (FNM) and the hybrid angular spectrum method (hASM) are being developed.

# Part V

# Appendix

# A

# List of Acronyms

| | |
|---|---|
| 1D | One-dimensional |
| 2D | Two-dimensional |
| 3D | Three-dimensional |
| 4D | Four-Dimensional |
| ABC | Absorbing Boundary Conditions |
| AC | Alternating Current |
| ASM | Angular Spectrum Method |
| BBB | Blood-Brain Barrier |
| BBBD | Blood-Brain Barrier Disruption |
| BNC | Bayonet Neill-Concelman |
| CAD | Computer Aided Design |
| CEM43 | Cumulative Equivalent Minutes at $43\,°C$ |
| CFL | Courant-Friedrichs-Lewy |
| CNS | Central Nervous System |
| CO-ME | Computer-Aided and Image-Guided Medical Interventions |
| CPU | Central Processing Unit |
| CSF | Cerebrospinal Fluid |
| CT | Computed Tomography |
| CUDA | Compute Unified Device Architecture |
| DASY | Dosimetric Assessment System |
| DBS | Deep Brain Stimulation |
| DC | Direct Current |
| DD | Dose Difference |
| DFT | Discrete Fourier Transform |
| DIVA | Discrete Vasculature |
| DPC | Distance-based Phase Correction |
| DREAM | Discrete Representation Array Modeling |
| DTA | Distance to Agreement |
| EM | Electro-Magnetic |
| ESHO | European Society for Hyperthermic Oncology |

| | |
|---|---|
| ETH | Eidgenössische Technische Hochschule |
| FD | Finite Difference(s) |
| FDA | Food and Drug Administration |
| FDTD | Finite-Difference Time-Domain |
| FEM | Finite-Element Method |
| FFT | Fast Fourier Transform |
| FNM | Fast Nearfield Method |
| FOCUS | Fast Object-Oriented C++ Ultrasound Simulator |
| FOV | Field of View |
| FUS | Focused Ultrasound |
| FWHM | Full-Width Half-Maximum |
| GPU | Graphics Processing Unit |
| hASM | Hybrid Angular Spectrum Method |
| HIFU | High Intensity Focused Ultrasound |
| HIV | Human Immunodeficiency Virus |
| HNSCC | Head and Neck Squamous Cell Carcinoma |
| HU | Hounsfield Units |
| IEEE | Institute of Electrical and Electronics Engineers |
| IT'IS | Foundation for Research on Information Technologies in Society |
| KTI/CTI | Kommission für Technologie und Innovation |
| KZK | Khokhlov-Zabolotskaya-Kuznetsov |
| LAPWE | Linear Acoustic Pressure Wave Equation |
| LEWE | Linear Elastic Wave Equation |
| LIFU | Low Intensity Focused Ultrasound |
| MATLAB | Matrix Laboratory |
| MP | Multi Processor |
| MR-ARFI | Magnetic Resonance Acoustic Radiation Force Imaging |
| MRgFUS | Magnetic Resonance guided Focused Ultrasound |
| MRgHIFU | Magnetic Resonance guided High Intensity Focused Ultrasound |
| MRI | Magnetic Resonance Imaging |
| MRT | Magnetic Resonance Thermometry |
| MW | Microwave |
| NDE | Non-Destructive Evaluation |
| NDT | Non-Destructive Testing |
| OCD | Obsessive Compulsive Disorder |
| PBE | Pennes Bioheat Equation |
| PCM | Phase Conjugate Mirror |
| PDE | Partial Differential Equation |
| PET | Positron Emission Tomography |
| PML | Perfectly Matched Layers |
| PMMA | Polymethylmethacrylate |
| POM-C | Acetal Polymer |

| | |
|---|---|
| PPF | Phase Propagation Factor |
| PS | Pseudo-Spectral |
| PyVISA | Python Virtual Instrument Software Architecture |
| PZT | Lead Zirconate Titanate |
| RAB | Reflective Acoustic Boundary |
| RAM | Random Access Memory |
| RF | Radio-Frequency |
| RMS | Root Mean Square |
| RPAT | Randomized Phased Array Transducer |
| RS | Rayleigh-Sommerfeld |
| RTPC | Ray Tracing-based Phase Correction |
| RTV | Room Temperature Vulcanizing |
| SAR | Specific Absorption Rate |
| SAT | Subcutaneous Adipose Tissue |
| SEMCAD | Simulation Platform for Electromagnetic Compatibility, Antenna Design, and Dosimetry |
| SIMT | Single Instruction Multiple Data |
| SMEM | Shared Memory |
| SP | Stream Processor |
| SPAC | Simulation-based Phase and Amplitude Correction |
| SPC | Simulation-based Phase Correction |
| SPEAG | Schmid and Partner Engineering AG |
| tcFUS | Transcranial Focused Ultrasound |
| tcMRgFUS | Transcranial Magnetic Resonance guided Focused Ultrasound |
| tDCS | Transcranial Direct Current Stimulation |
| TMS | Transcranial Magnetic Stimulation |
| UCA | Ultrasound Contrast Agent |
| US | Ultrasound |
| USgFUS | Ultrasound guided Focused Ultrasound |
| VIM | Ventral Intermediate Nucleus |
| ViP | Virtual Population |
| VISA | Virtual Instrument Software Architecture |
| VNS | Vagus Nerve Stimulation |
| VTK | Visualization Toolkit |
| WJ | Weinbaum-Jiji |
| WLE | Westervelt-Lighthill Equation |
| ZMT | Zurich MedTech |

# B

## List of Symbols

| Symbol | Quantity | Unit |
|---|---|---|
| $\alpha$ | Absorption Coefficient | Np/m or dB/m |
| $\beta$ | Compressibility | $\text{Pa}^{-1}$ |
| | Nonlinearity Coefficient | – |
| $\beta_0$ | Adiabatic Compressibility | $\text{Pa}^{-1}$ |
| $B$ | Elastic Bulk Modulus | Pa |
| $B/A$ | Nonlinearity Parameter | – |
| $c$ | Speed of Sound | m/s |
| $C$ | Specific Heat Capacity | J/kg/K |
| $c_0$ | Equilibrium Speed of Sound | m/s |
| $d$ | Aperture Diameter | m |
| $\delta$ | Diffusivity | – |
| $\Delta x$ | Voxel/Grid Size along X axis | m |
| $\Delta y$ | Voxel/Grid Size along Y axis | m |
| $\Delta z$ | Voxel/Grid Size along Z axis | m |
| $\Delta t$ | Time Step | s |
| $f$ | Wave Frequency | Hz |
| $F$ | F-number | – |
| $F_{rad}$ | Acoustic Radiation Force | $\text{N/m}^3$ |
| $h$ | Heat Transfer Coefficient | $\text{W/m}^2\text{/K}$ |
| $I$ | Acoustic Intensity | $\text{W/m}^2$ |
| $\kappa$ | Acoustic Wavenumber | – |
| | Thermal Conductivity | W/m/K |
| $\lambda$ | Acoustic Wavelength | m |
| $\omega$ | Angular Frequency | radians |
| | Perfusion | mL/min/kg |
| $p$ | Acoustic Pressure | Pa |
| $\psi$ | Acoustic Velocity Potential | – |
| $q_v$ | Acoustic Energy Density | $\text{W/m}^3$ |
| $\rho$ | Density | $\text{kg/m}^3$ |

| | | |
|---|---|---|
| $\rho_0$ | Equilibrium Density | $\mathrm{kg/m^3}$ |
| $R$ | Reflection Coefficient | − |
| $R$ | Aperture Radius | m |
| $T$ | Wave Period | s |
| | Transmission Coefficient | − |
| | Temperature | °C or K |
| $t$ | Time | s |
| $u$ | Displacement Amplitude | m |
| $v$ | Particle Velocity | m/s |
| $Z$ | Characteristic Acoustic Impedance | Rayl or $\mathrm{kg/m^2/s}$ |

# C

# List of Publications

## C.1  Journal Publications Included in this Thesis

The following publications relating to the thesis content have been written, or co-written, by the author:

1. Kyriakou A., Neufeld E., Werner B., Paulides MM., Szekely G. & Kuster N., "A review of numerical and experimental compensation techniques for skull-induced phase aberrations in transcranial focused ultrasound", *International Journal of Hyperthermia*, 2014, 30(1): 36-46.

2. Paulides MM., Stauffer PR., Neufeld E., Maccarini PF., Kyriakou A., Canters RA., Diederich CJ., Bakker JF. & van Rhoon GC., "Simulation techniques in hyperthermia treatment planning", *International Journal of Hyperthermia*, 2012, 29(4):1-12.

3. Kyriakou A., Neufeld E., Werner B., Szekely G. & Kuster N., "Full-Wave Acoustic and Thermal Modeling of Transcranial Ultrasound Propagation and Induced Lesioning in Focused Ultrasound Neurosurgery Applications", *Journal of Therapeutic Ultrasound*, submitted December 2014.

## C.2  Other Journal Publications

In addition, the author of this thesis has (co-)authored the following journal publications:

1. Kyriakou A., Neufeld E., Szczerba D., Kainz W., Luechinger R., Kozerke S., McGregor R. & Kuster N., "Patient-specific simulations and measurements of the magneto-hemodynamic effect in human primary vessels", *Physiological measurement*, (2012), 33(2):117.

2. Kyriakou A., Christ A., Neufeld E. & Kuster N., "Local tissue temperature increase of a generic implant compared to the basic restrictions defined in safety guidelines", *Bioelectromagnetics*, 2011, 33(5):366-374.

3. Kyriakou A., Aitides E. & Chryssomallis M., "Development of a FDTD Simulator for the Calculation of Temperature Rise in Human Heads", *Mobile Phones Operation. Wireless Mobile Communication and Healthcare*, 2011, 403-407.

## C.3   Other Publications

Furthermore, the author has (co-)authored the following conference contributions and technical reports:

1. Kyriakou A., Neufeld E., Werner B., Szekely G. & Kuster N. (2014). Focusing and Aberration Correction for Transcranial Focused Ultrasound. Poster presentation at the Society for Thermal Medicine (STM) 2014 Conference, Minneapolis, USA.

2. Kyriakou A., Neufeld E., Preiswerk F., Lloyd B., Cattin P., Szekely G. & Kuster N. (2014). HIFU Hepatic Tumor Ablation: Modeling of Focusing and Motion Tracking Approaches. Poster presentation at the Society for Thermal Medicine (STM) 2014 Conference, Minneapolis, USA.

3. Kyriakou A., Neufeld E., Shafirstein G., Moros E., Szekely G. & Kuster N. (2014). Numerical Investigation of HIFU Tumor Ablation: Focus Scanning Approaches, Vasculature, and Standing-Waves. Oral presentation at the Society for Thermal Medicine (STM) 2014 Conference, Minneapolis, USA.

4. Neufeld E., Kyriakou A. & Kuster N. (2014). Tools and Models for In Silico Investigation of EM- and US-Based Thermal Therapies in Complex Anatomies. Oral presentation at the Society for Thermal Medicine (STM) 2014 Conference, Minneapolis, USA.

5. Kyriakou A., Neufeld E., Werner B., Szekely G. & Kuster N. (2014). Calculation and Simulation-Based Steering Approaches for Transcranial Focused Ultrasound. Oral presentation at the International Society for Focused Ultrasound (ISTU) 2014 Conference, Las Vegas, USA.

6. Kyriakou A., Neufeld E., Preiswerk F., Lloyd B., Cattin P., Szekely G. & Kuster N. (2014). Modeling of Motion Tracking and Focusing Strategies in HIFU Ablation of Hepatic Tumors. Oral presentation at the International Society for Focused Ultrasound (ISTU) 2014 Conference, Las Vegas, USA.

7. Kyriakou A., Neufeld E., Shafirstein G., Moros E., Szekely G. & Kuster N. (2014). Numerical Investigation of Scanning Approaches, Vasculature Impact and Standing-Wave Effects in HIFU Based Tumor Ablation. Oral presentation at the International Society for Focused Ultrasound (ISTU) 2014 Conference, Las Vegas, USA.

8. Neufeld E., Kyriakou A., Werner B. & Kuster N. (2013). Multiphysics Framework for Modeling of FUS/HIFU and Induced Effects. Oral presentation at the American Association of Physicists in Medicine (AAPM) 2013 Conference, Indianapolis, USA.

9. Neufeld E., Kyriakou A., Szczerba D., Kainz W. & Kuster N. (2013). Taking Image Based Anatomical Models Beyond Geometry: A Study of the MHD Effect. Oral presentation at the 2013 International Workshop on Computational Phantoms for Radiation Protection, Imaging and Radiotherapy (CP), Zurich, Switzerland.

10. Kyriakou A., Neufeld E., Werner B. & Kuster N. (2013). Full Wave Acoustic and Thermal Modeling of Transcranial Focused Ultrasound Surgery in a Detailed Anatomical Head Model. Oral presentation at the International Society for Focused Ultrasound (ISTU) 2013 Conference, Shanghai, China.

11. Kyriakou A., Neufeld E., Fuetterer M., Rijnen Z., Numan W., Paulides M., van Rhoon G. & Kuster N. (2010). Multi-Objective Optimization with Automatic Risk Region Detection for Interactive Hyperthermia Treatment Planning and Adjustment. Poster presentation at the Society for Thermal Medicine (STM) 2013 Conference, Aruba.

12. Kyriakou A., Neufeld E., Chen D., Moros E.G., Kuster N. & Shafirstein G. (2012). Numerical and experimental evaluation of a novel ultrasonic transducer for superficial tumor ablation. Poster presentation at the Focused Ultrasound 2012 Conference, Washington DC, USA.

13. Kyriakou A., Neufeld E., Petrusca L., Salomir R. & Kuster N. (2012). Acoustic and thermal modeling of in-vivo tumor ablation with MRgHIFU. Poster presentation at the Focused Ultrasound 2012 Conference, Washington DC, USA.

14. Kyriakou A., Neufeld E. & Kuster N. (2012). Numerical modeling of HIFU ablation of solid malignancies. Poster presentation at the ICHO-JCTM 2012 Conference, Kyoto, Japan.

15. Kyriakou A., Neufeld E., Wiedemair W., Kurtcuoglu V. & Kuster N. (2012). High performance computational framework for full wave FUS/HIFU modeling in anatomical models. Oral presentation at the International Society for Focused Ultrasound (ISTU) 2012 Conference, Heidelberg, Germany.

16. Kyriakou A., Neufeld E., Szczerba D., Kainz W., Luechinger R., Kozerke S., Mc-Gregor R. & Kuster N. (2012). Magneto-Hemo Dynamic (MHD) Response for application as a biomarker of vascular blood flow. Poster presentation at the 2012 ECI Conference on Computational Fluid Dynamics (CFD) in Medicine and Biology, Dead Sea, Israel.

17. Kyriakou A., Neufeld E., Wiedemair W., Kurtcuoglu V. & Kuster N. (2011). Modeling Tools for HIFU and Induced In-Vivo Effects. Oral presentation at the Society for Thermal Medicine (STM) 2011 Conference, New Orleans, USA.

18. Kyriakou A., Neufeld E., Wiedemair W., Kurtcuoglu V. & Kuster N. (2011). Modeling Tools for HIFU and Induced In-Vivo Effects. Oral presentation at the European Society for Hyperthermic Oncology (ESHO) 2011 Conference, Aarhus, Denmark.

19. Kyriakou A., Christ A., Neufeld E., Cabot E., Kuhn S., Douglas M. & Kuster N. (2010). Maximum Local Tissue Temperature Increase of Implanted Medical Devices at ICNIRP Exposure Limits. Poster presentation at the Bioelectromagnetics (BEMS) 2010 Conference, Seoul, Korea.

20. Neufeld E., Kyriakou A., Paulides M., Bakker J., van Rhoon G. & Kuster N. (2010). Enabling Operator Interaction in Hyperthermia Treatment Planning Using Pareto Optimization. Oral presentation at the Society for Thermal Medicine (STM) 2010 Conference, New Orleans, USA.

21. Neufeld E., Kyriakou A., Paulides M., Bakker J., van Rhoon G. & Kuster N. (2010). Enabling Operator Interaction in Hyperthermia Treatment Planning Using Pareto Optimization. Oral presentation at the European Society for Hyperthermic Oncology (ESHO) 2010 Conference, Rotterdam, Netherlands.

## C.4   Awards

1. The article "A review of numerical and experimental compensation techniques for skull-induced phase aberrations in transcranial focused ultrasound" in the *International Journal of Hyperthermia*, was featured on the January 2014 issue cover.

2. Travel Award, *International Society for Therapeutic Ultrasound (ISTU)*, May 2013

3. Excellent Performance Award, *Technical Chamber of Greece*, 2012

4. State award for excellent performance during the pre-graduate studies in DUTH between 2004 and 2009

5. Young Investigator Award, *ICHO & JCTM*, August 2012

6. Student Award, *European Society for Hyperthermic Oncology (ESHO)*, May 2010

7. Undergraduate/Pre-Graduate Scholarship Award, *IEEE Microwave Theory and Techniques Society (MTT-S)*, 2009

8. Scholarship and award for graduating 1st in his class, *Greek State Scholarships Foundation*, 2009

9. Scholarship and Award for 4th ranking in university entries, *Greek State Scholarships Foundation*, 2004

10. Excellent performance Award for all high school classes, *Ministry of National Education and Religious Affairs*, 2003

# Bibliography

[1]     Thomas Szabo. *Diagnostic Ultrasound Imaging: Inside Out*. Academic Pr, 2004. (document), 1.1.2.3, 1.1.3.4, 1.2.1, 1.2.2, 1.3, 1.3.1, 1.3.2.1, 1.3.2.3, 1.3.2.3, 1.4, 1.1, 2.1.1, 2.2.2.1, 2.2.2.2, 2.3, 3.3.2.2, 4.2.4.2

[2]     National Council of Radiation Protection (NCRP). National council of radiation protection & measurements report no.74: Biological effects of ultrasound: Mechanisms and clinical implications (report no. 74). Technical report, NCRP, 1983. (document), 1.1.1, 1.1.2.2, 1.1.2.3, 1.1.2.3, 1.1.2.4, 1.1.3.1, 1.1.3.6, 1.2.1, 1.2.2, 1.3, 1.3.1, 1.3.2.1, 1.3.2.2, 1.3.2.3, 1.4, 1.2, 2.2, 2.2.1, 4.2.4.2

[3]     H. Azhari. *Basics of Biomedical Ultrasound for Engineers*. Wiley, 2010. ISBN 9780470561461. 1.1.1, 1.1.2.2, 1.1.2.3, 1.1.2.4, 1.1.3.1, 1.1.3.2, 1.1.3.2, 1.1.3.2, 1.1.3.2, 1.1.3.2, 1.1.3.3, 1.1.3.4, 1.1.3.5, 1.2.2, 1.3.1, 1.3.2.1, 1.3.2.2, 1.3.2.3, 1.4, 2.2, 2.2.1, 2.2.1.3, 2.2.2.1, 2.3

[4]     Daniel R. Raichel. *The Science and Applications of Acoustics*. Springer, 2nd edition, January 2006. 1.1.1, 1.1.3.1, 1.1.3.2, 1.1.3.3, 1.1.3.5, 1.2.2, 4.2.4.2

[5]     K. Epasinghe. *Simulation and visualization of ultrasound fields*. PhD thesis, Master's thesis, University of Oslo, Department of Informatics, 1997. 1.1.1, 1.1.2.4, 1.1.3.2, 2.2.1.3, 4.1.1.1, 4.1.1.2, 4.1.1.3, 4.3.4

[6]     A. Karamalis. GPU ultrasound simulation and volume reconstruction. Master's thesis, Fakultat fur Informatik Der Technischen Universitat München, 2009. 1.1.1, 1.1.2.2, 1.1.3.2, 1.1.3.3, 1.1.3.4, 1.1.3.5

[7]     Harald T Lutz and Hassen A Gharbi. *Manual of diagnostic ultrasound in infectious tropical diseases*, volume 218. Springer, 2006. 1.1.1

[8]     PA Hasgall, E Neufeld, MC Gosselin, A Klingenböck, and N Kuster. IT'IS database for thermal and electromagnetic parameters of biological tissues. *September 26th*, 2011. 1.1.2.1, 8.3.2, 8.3.3, 9.2.3, 10.2.3

[9]     Ferenc A Jolesz and Kullervo H Hynynen. *MRI-guided focused ultrasound surgery*. CRC Press, 2007. 1.1.2.2, 1.1.2.2, 1.1.2.3, 1.1.2.4, 1.1.3.6, 1.2.2, 1.3, 1.3.1, 1.3.2.3,

1.3.2.3, 2.1.1, 2.2.1.2, 2.2.1.3, 2.2.2.2, 2.3.1, 2.3.2, 2.4, 2.4.1, 2.4.2, 2.5.2.1, 3.1.4.2, 3.1.4.3, 3.1.4.4, 3.3.2

[10]  Lawrence E. Kinsler, Austin R. Frey, Alan B. Coppens, and James V. Sanders. *Fundamentals of Acoustics*. Wiley, 4th edition, 1999. 1.1.2.3, 1.1.2.4, 1.1.3.1, 1.2.1, 4.2.1.1, 4.2.1.3

[11]  Nimrod M Tole. *Basic Physics of Ultrasonographic Imaging*. World Health Organization, 2005. 1.1.2.3, 1.1.3.6, 2.1, 2.1.2, 2.2.1, 2.2.1.1, 2.2.1.2, 2.3, 2.3.2

[12]  Lise Retat. *Characterisation of the acoustic, thermal and histological properties of tissue required for high intensity focused ultrasound (HIFU) treatment planning*. PhD thesis, Institute of Cancer Research (University Of London), 2011. 1.1.2.3, 1.1.3.1, 1.1.3.3, 1.1.3.4, 1.2.2

[13]  Michiel Postema. *Fundamentals of medical ultrasonics*. Taylor & Francis, 2011. 1.1.2.3, 2.1.1, 2.1.2, 2.2.1.1, 2.2.1.3, 2.2.2.1, 2.2.2.2, 2.3, 2.3.2

[14]  Wesley L Nyborg. Heat generation by ultrasound in a relaxing medium. *The Journal of the Acoustical Society of America*, 70:310, 1981. 1.1.3.1, 1.3.1, 6.3.2

[15]  Victor F Humphrey. Ultrasound and matter-physical interactions. *Progress in biophysics and molecular biology*, 93(1-3):195–211, 2007. ISSN 0079-6107. doi: 10.1016/j.pbiomolbio.2006.07.024. URL http://www.ncbi.nlm.nih.gov/pubmed/17079004. 1.1.3.2, 1.2.2, 1.3.1, 1.3.2.1, 1.3.2.2, 1.3.2.3, 1.3.2.3, 3, 8.1.4

[16]  Timothy G Leighton. What is ultrasound? *Progress in biophysics and molecular biology*, 93(1-3):3–83, 2007. 1.1.3.1, 1.3.2.3, 1.3.2.3, 3, 8.1.4

[17]  C. R. Hill, J. C. Bamber, and G. R. ter Haar. *Physical Principles of Medical Ultrasonics*. Wiley, 2002. 1.1.3.4, 1.2.1, 1.2.2, 1.3.2.1, 1.3.2.2, 1.3.2.3, 2.1.2, 2.2.1.3, 2.2.2.2, 2.3, 2.3.2, 4.2.1.1, 4.2.4.2

[18]  SA Goss, LA Frizzell, and F Dunn. Ultrasonic absorption and attenuation in mammalian tissues. *Ultrasound in medicine & biology*, 5(2):181–186, 1979. 1.1.3.6, 1.4

[19]  Heinrich Kuttruff. *Acoustics: an introduction*. Taylor & Francis, 2007. 1.2.2, 1.3.2.1, 2.1, 2.1.1, 2.1.2

[20]  M.F. Hamilton and D.T. Blackstock. *Nonlinear acoustics*. Academic Pr, 1998. 1.2.2, 4.1.2.3, 4.2.2.1, 4.2.3, 4.2.3.1

[21]  T.D. Rossing. *Springer handbook of acoustics*. Springer Verlag, 2007. 1.2.2, 4.2.1.1

[22] Herman Medwin and Clarence S Clay. *Fundamentals of acoustical oceanography*. Access Online via Elsevier, 1997. 1.2.2

[23] Junru Wu and Wesley Le Mars Nyborg. *Emerging therapeutic ultrasound*. World Scientific, 2006. 1.3.1, 1.3.2.1, 1.3.2.2, 1.3.2.3, 2.3, 2.4

[24] Aki Pulkkinen. *Simulation Methods in Transcranial Ultrasound Therapy*. PhD thesis, University of Eastern Finland, 2014. 1.3.1, 1.3.1

[25] Mathieu Burtnyk, William Apoutou N'Djin, Ilya Kobelevskiy, Michael Bronskill, and Rajiv Chopra. 3d conformal mri-controlled transurethral ultrasound prostate therapy: validation of numerical simulations and demonstration in tissue-mimicking gel phantoms. *Physics in medicine and biology*, 55(22):6817, 2010. 1.3.1

[26] TJ Cavicchi and WD O'Brien Jr. Heat generated by ultrasound in an absorbing medium. *The Journal of the Acoustical Society of America*, 76:1244, 1984. 1.3.1

[27] JDN Cheeke. *Fundamentals and applications of ultrasonic waves*. CRC Press, New York, 2002. 1.3.2.1, 2.1.2

[28] K Kirk Shung. *Diagnostic ultrasound: Imaging and blood flow measurements*. CRC press, 2005. 1.3.2.1, 1.3.2.3, 1.3.2.3, 2.1.1, 2.2.1.1, 2.2.1.3, 2.2.2.1, 2.2.2.2, 2.3, 2.3.2

[29] HC Starritt, FA Duck, and VF Humphrey. Forces acting in the direction of propagation in pulsed ultrasound fields. *Physics in Medicine and Biology*, 36(11):1465, 1991. 1.3.2.1

[30] Hideto Mitome. The mechanism of generation of acoustic streaming. *Electronics and Communications in Japan (Part III: Fundamental Electronic Science)*, 81(10): 1–8, 1998. 1.3.2.2

[31] Benoît Larrat, Mathieu Pernot, Gabriel Montaldo, Mathias Fink, and Mickaël Tanter. MR-guided adaptive focusing of ultrasound. *Ultrasonics, Ferroelectrics and Frequency Control, IEEE Transactions on*, 57(8):1734–1747, 2010. 1.3.2.1, 8.1.3

[32] N. Riley. Acoustic Streaming. *Theoretical and Computational Fluid Dynamics*, 10 (1-4):349–356, 1998. 1.3.2.2

[33] John R Blake, Giles S Keen, Robert P Tong, and Miles Wilson. Acoustic cavitation: the fluid dynamics of non–spherical bubbles. *Philosophical Transactions of the Royal Society of London. Series A: Mathematical, Physical and Engineering Sciences*, 357(1751):251–267, 1999. 1.3.2.3, 1.3.2.3

[34] EA Brujan, T Ikeda, and Y Matsumoto. Jet formation and shock wave emission during collapse of ultrasound-induced cavitation bubbles and their role in the therapeutic applications of high-intensity focused ultrasound. *Physics in medicine and biology*, 50(20):4797, 2005. 1.3.2.3, 1.3.2.3

[35] Milton S Plesset and Andrea Prosperetti. Bubble dynamics and cavitation. *Annual Review of Fluid Mechanics*, 9(1):145–185, 1977. 1.3.2.3

[36] FJ Fry and JE Barger. Acoustical properties of the human skull. *The Journal of the Acoustical Society of America*, 63:1576, 1978. 1.4

[37] MA El-Brawany, DK Nassiri, G Terhaar, A Shaw, I Rivens, and K Lozhken. Measurement of thermal and ultrasonic properties of some biological tissues. *Journal of Medical Engineering & Technology*, 33(3):249–256, 2009. 1.4

[38] Urvi Vyas, Allison Payne, Nick Todd, Dennis L Parker, Robert B Roemer, and Douglas A Christensen. Non-invasive patient-specific acoustic property estimation for mr-guided focused ultrasound surgery. In *AIP Conference Proceedings*, volume 1481, page 419, 2012. 1.4

[39] JC Bamber and CR Hill. Ultrasonic attenuation and propagation speed in mammalian tissues as a function of temperature. *Ultrasound in medicine & biology*, 5 (2):149–157, 1979. 1.4

[40] Alan R Selfridge. Approximate material properties in isotropic materials. *IEEE transactions on sonics and ultrasonics*, 32(3):381–394, 1985. 7.2.1.3

[41] Francis A Duck. *Physical Properties of Tissue: A Comprehensive Reference Book*. Academic Press, London, 1990. 1.4

[42] Jeffrey C Bamber. Ultrasonic properties of tissues. *Ultrasound in medicine*, pages 57–88, 1998.

[43] SA Goss, RL Johnston, and Fry Dunn. Comprehensive compilation of empirical ultrasonic properties of mammalian tissues. *The Journal of the Acoustical Society of America*, 64:423, 1978.

[44] Sun Yongchen, Dong Yanwu, Tong Jie, and Tang Zhensheng. Ultrasonic propagation parameters in human tissues. In *IEEE 1986 Ultrasonics Symposium*, pages 905–908. IEEE, 1986.

[45] Avi Schroeder, Joseph Kost, and Yechezkel Barenholz. Ultrasound, liposomes, and drug delivery: principles for using ultrasound to control the release of drugs from liposomes. *Chemistry and physics of lipids*, 162(1):1–16, 2009. 1.4

[46] SO Moheimani, Andrew John Fleming, et al. Piezoelectric transducers for vibration control and damping— nova. the university of newcastle's digital repository. 2006. 2.1.1, 2.1.2

[47] Antonio Arnau Vives and Antonio Arnau. *Piezoelectric transducers and applications*. Springer, 2008. 2.1.1, 2.2.1.3

[48] J Tichy, J Erhart, E Kittinger, and J Privratska. Fundamentals of piezoelectric sensorics, 2010. 2.1.1

[49] K. Nakamura. *Ultrasonic Transducers: Materials and Design for Sensors, Actuators and Medical Applications*. Woodhead Publishing Series in Electronic and Optical Materials. Woodhead Publishing Limited, 2012. ISBN 9781845699895. 2.1.1, 2.1.2, 2.2.1, 2.2.1.1

[50] Dale Ensminger and Leonard J Bond. *Ultrasonics: Fundamentals, Technologies, and Applications*. CRC Press, 2008. 2.2.1

[51] Gordon S Kino. *Acoustic waves: devices, imaging, and analog signal processing*, volume 107. Prentice-Hall Englewood Cliffs, NJ, 1987. 2.2.2.1, 2.2.2.2

[52] NDT Olympus. Ultrasonic transducers technical notes. *Technical brochure: Olympus NDT, Waltham, MA*, 2006. 2.2.2.1, 2.2.2.2

[53] Bjørn AJ Angelsen, Hans Torp, Sverre Holm, Kjell Kristoffersen, and TA Whittingham. Which transducer array is best? *European journal of ultrasound*, 2(2): 151–164, 1995. 2.2.2.2

[54] NDT Olympus. Phased array testing: Basic theory for industrial applications. *Olympus NDT*, 2010. 2.3.1

[55] NDT Olympus. Introduction to phased array ultrasonic technology applications: R/d tech guideline. *Olympus NDT, MA, USA.[Links]*, 2007. 2.3.1

[56] Ferenc A Jolesz. MRI-guided focused ultrasound surgery. *Medicine*, 60(1):417, 2009. 2.3.1, 2.4, 3.1.1, 3.1.3

[57] J.G. Webster. *Tissue Ablation: Devices And Procedures*. John Wiley & Sons Australia, Limited, 2005. 2.4, 3.1.1, 3.1.3

[58] Jürgen W Jenne, Tobias Preusser, and Matthias Günther. High-intensity focused ultrasound: principles, therapy guidance, simulations and applications. *Zeitschrift für Medizinische Physik*, 2012. 2.4, 2.4.1, 2.4.2, 3, 3.1.1, 3.1.3, 3.1.4, 3.1.4.1, 3.1.4.4, 3.2.2

[59] Clare MC Tempany, Nathan J McDannold, Kullervo Hynynen, and Ferenc A Jolesz. Focused ultrasound surgery in oncology: overview and principles. *Radiology*, 259(1):39–56, 2011. 2.4, 2.5, 2.5.1.3, 2.5.2.1, 3.1.4, 3.1.4.2, 3.1.4.3, 3.1.4.4, 3.1.4.5, 3.2.1.3, 3.3.1, 3.3.2.2, 9.1

[60] GT Clement. Perspectives in clinical uses of high-intensity focused ultrasound. *Ultrasonics*, 42(10):1087–1093, 2004. 2.4.1, 2.4.2, 3.1.1, 3.1.3

[61] Gail ter Haar. Therapeutic applications of ultrasound. *Progress in biophysics and molecular biology*, 93(1):111–129, 2007. 3, 3.1.2

[62] ¿ Gail ter Haar and Constantin Coussios. High intensity focused ultrasound: physical principles and devices. *International Journal of Hyperthermia*, 23(2):89–104, 2007.

[63] Theodore J Dubinsky, Carlos Cuevas, Manjiri K Dighe, Orpheus Kolokythas, and Joo Ha Hwang. High-intensity focused ultrasound: current potential and oncologic applications. *American journal of roentgenology*, 190(1):191–199, 2008. 2.4.1, 2.4.2, 3, 3.1.1, 3.1.4, 3.1.4.1, 3.1.4.3, 3.3.2

[64] Rémi Souchon, Olivier Rouvière, Albert Gelet, Valérie Detti, Seshadri Srinivasan, Jonathan Ophir, and Jean-Yves Chapelon. Visualisation of hifu lesions using elastography of the human prostate¡ i¿ in vivo¡/i¿: preliminary results. *Ultrasound in medicine & biology*, 29(7):1007–1015, 2003. 2.4.1

[65] Elisa Konofagou, Jonathan Thierman, and Kullervo Hynynen. The use of ultrasound-stimulated acoustic emission in the monitoring of modulus changes with temperature. *Ultrasonics*, 41(5):337–345, 2003.

[66] Ajay Anand and Peter J Kaczkowski. Monitoring formation of high intensity focused ultrasound (hifu) induced lesions using backscattered ultrasound. *Acoustics Research Letters Online*, 5:88, 2004.

[67] Zu Wen Qian, Liulin Xiong, Jinshen Yu, Daoyuan Shao, Houqing Zhu, and Xiaodong Wu. Noninvasive thermometer for hifu and its scaling. *Ultrasonics*, 44: e31–e35, 2006.

[68] Naomi R Miller, Konstantin M Bograchev, and Jeffrey C Bamber. Ultrasonic temperature imaging for guiding focused ultrasound surgery: effect of angle between imaging beam and therapy beam. *Ultrasound in medicine & biology*, 31(3):401–413, 2005. 2.4.1

[69] JE Kennedy, GR Ter Haar, and D Cranston. High intensity focused ultrasound: surgery of the future? *British Journal of Radiology*, 76(909):590–599, 2003. 2.4.2, 3.1.1, 3.1.2, 3.3.1, 3.3.2

[70] Viola Rieke and Kim Butts Pauly. Mr thermometry. *Journal of Magnetic Resonance Imaging*, 27(2):376–390, 2008. 2.4.2

[71] N McDannold. Quantitative mri-based temperature mapping based on the proton resonant frequency shift: review of validation studies. *International journal of hyperthermia*, 21(6):533–546, 2005.

[72] B Denis de Senneville, Bruno Quesson, and Chrit TW Moonen. Magnetic resonance temperature imaging. *International journal of hyperthermia*, 21(6):515–531, 2005.

[73] Bruno Quesson, Jacco A de Zwart, and Chrit TW Moonen. Magnetic resonance temperature imaging for guidance of thermotherapy. *Journal of Magnetic Resonance Imaging*, 12(4):525–533, 2000. 2.4.2

[74] Nathan McDannold and Stephan E Maier. Magnetic resonance acoustic radiation force imaging. *Medical physics*, 35:3748, 2008. 2.4.2, 8.1.3

[75] Rémi Souchon, Rares Salomir, Olivier Beuf, Laurent Milot, Denis Grenier, Denis Lyonnet, Jean-Yves Chapelon, and Olivier Rouvière. Transient mr elastography (t-mre) using ultrasound radiation force: Theory, safety, and initial experiments in vitro. *Magnetic Resonance in Medicine*, 60(4):871–881, 2008. 2.4.2, 8.1.3

[76] DB Plewes, I Betty, SN Urchuk, and I Soutar. Visualizing tissue compliance with mr imaging. *Journal of Magnetic Resonance Imaging*, 5(6):733–738, 1995. 2.4.2, 8.1.3

[77] Elena A Kaye, Yoni Hertzberg, Michael Marx, Beat Werner, Gil Navon, Marc Levoy, and Kim Butts Pauly. Application of Zernike polynomials towards accelerated adaptive focusing of transcranial high intensity focused ultrasound. *Medical physics*, 39:6254, 2012. 2.4.2, 8.1.3

[78] Eric Herbert, Mathieu Pernot, Gabriel Montaldo, Mathias Fink, and Mickael Tanter. Energy-based adaptive focusing of waves: application to noninvasive aberration correction of ultrasonic wavefields. *Ultrasonics, Ferroelectrics and Frequency Control, IEEE Transactions on*, 56(11):2388–2399, 2009. 2.4.2, 8.1.3

[79] Osama Al-Bataineh, Jürgen Jenne, and Peter Huber. Clinical and future applications of high intensity focused ultrasound in cancer. *Cancer treatment reviews*, 38 (5):346–353, 2012. 2.5, 2.5.1.3, 2.5.1.4, 2.5.2.4, 3.1.4, 3.1.4.2, 3.1.4.3, 3.1.4.4, 9.1

[80] Ernesto R Cordeiro, Xavier Cathelineau, Stefan Thüroff, Michael Marberger, Sebastien Crouzet, and Jean JMCH de la Rosette. High-intensity focused ultrasound (HIFU) for definitive treatment of prostate cancer. *BJU international*, 110(9): 1228–1242, 2012. 2.5.1.1, 2.5.1.2, 3.1.4.1

[81]  M Raphael Pfeffer, Tatiana Rabin, Yael Inbar, Arik Hananel, and Raphael Catane. Image-guided high-intensity focused ultrasound in the treatment of cancer. 2013. 2.5.1.1, 2.5.1.2, 2.5.1.3, 2.5.2.1, 3.1.4, 3.1.4.1, 3.1.4.4

[82]  Dong Jin Chung, Se Hyun Cho, Jae Mun Lee, and Seong-Tae Hahn. Effect of microbubble contrast agent during high intensity focused ultrasound ablation on rabbit liver in vivo. *European Journal of Radiology*, 81(4):e519–e523, 2012. 2.5.1.3

[83]  Song Peng, Yu Xiong, Kequan Li, Min He, Yongbin Deng, Li Chen, Min Zou, Wenzhi Chen, Zhibiao Wang, Jia He, et al. Clinical utility of a microbubble-enhancing contrast ("sonovue") in treatment of uterine fibroids with high intensity focused ultrasound: A retrospective study. *European Journal of Radiology*, 81(12): 3832–3838, 2012.

[84]  Islam Ahmed Shehata. Treatment with high intensity focused ultrasound: secrets revealed. *European journal of radiology*, 81(3):534–541, 2012. 2.5.1.3

[85]  Bo Xie, Jiajun Ling, Weiming Zhang, Xueqin Huang, Jihua Zhen, and Yanzhe Huang. The efficacy of high-intensity focused ultrasound (HIFU) in advanced pancreatic cancer. *Chinese Journal of Clinical Oncology*, 5(3):183–186, 2008. ISSN 1672-7118. doi: 10.1007/s11805-008-0183-3. URL http://dx.doi.org/10.1007/s11805-008-0183-3. 2.5.1.4

[86]  Xin Meng, Guangbin He, Jun Zhang, Zenghui Han, Ming Yu, Miaomiao Zhang, Yu Tang, Ling Fang, and Xiaodong Zhou. A comparative study of fibroid ablation rates using radio frequency or high-intensity focused ultrasound. *Cardiovascular and interventional radiology*, 33(4):794–799, 2010. 2.5.1.4

[87]  Hong Zhao, Guowang Yang, Daoyuan Wang, Xiangrong Yu, Yu Zhang, Junqiu Zhu, Yongle Ji, Baoliang Zhong, Wenshuo Zhao, Zhong Yang, et al. Concurrent gemcitabine and high-intensity focused ultrasound therapy in patients with locally advanced pancreatic cancer. *Anti-cancer drugs*, 21(4):447–452, 2010. 2.5.1.4

[88]  EA Dick and WMW Gedroyc. Exablate magnetic resonance-guided focused ultrasound system in multiple body applications. *Expert review of medical devices*, 7 (5):589–597, 2010. 2.5.2.1

[89]  Anne Roberts. The role of magnetic resonance guided focused ultrasound for uterine fibroids. 2013. 2.5.2.1, 2.5.2.3

[90]  Chiara Zini, Elisabeth Hipp, Stephen Thomas, Alessandro Napoli, Carlo Catalano, and Aytekin Oto. Ultrasound-and mr-guided focused ultrasound surgery for prostate cancer. *World journal of radiology*, 4(6):247, 2012. 2.5.2.1

[91] Uri Lindner, Sangeet Ghai, Paula Spensieri, Eugen Hlasny, Theodorus H Van der Kwast, Stuart A McCluskey, Masoom A Haider, Walter Kucharczyk, and John Trachtenberg. Focal magnetic resonance guided focused ultrasound for prostate cancer: Initial north american experience. *Canadian Urological Association Journal*, 6(6):E283, 2012. 2.5.2.1

[92] Giovanni Borasi, Giorgio Russo, Filippo Alongi, Alan Nahum, Giuliana Carmela Candiano, Alessandro Stefano, Maria Carla Gilardi, and Cristina Messa. High-intensity focused ultrasound plus concomitant radiotherapy: a new weapon in oncology? *Journal of Therapeutic Ultrasound*, 1(1):6, 2013. 2.5.2.1

[93] Alessandro Napoli, Michele Anzidei, Beatrice Cavallo Marincola, Giulia Brachetti, Federica Ciolina, Gaia Cartocci, Claudia Marsecano, Fulvio Zaccagna, Luca Marchetti, Enrico Cortesi, et al. Primary pain palliation and local tumor control in bone metastases treated with magnetic resonance-guided focused ultrasound. *Investigative radiology*, 48(6):351–358, 2013. 2.5.2.1

[94] Kullervo Hynynen. MRI-guided focused ultrasound treatments. *Ultrasonics*, 50 (2):221–229, 2010. 2.5.2.2, 3.1.2, 3.1.4, 3.1.4.5, 3.3.2.2

[95] Nathan McDannold, Greg Clement, Peter Black, Ferenc Jolesz, and Kullervo Hynynen. Transcranial mri-guided focused ultrasound surgery of brain tumors: Initial findings in three patients. *Neurosurgery*, 66(2):323, 2010. 2.5.2.2, 3.1.4.5

[96] Ernst Martin and Ferenc A Jolesz. Noninvasive treatment for brain tumors: Magnetic resonance-guided focused ultrasound surgery. In *Tumors of the Central Nervous system, Volume 3*, pages 227–236. Springer, 2011. 3.1.4, 3.1.4.5, 3.1.4.5, 3.3.2.2, 3.3.2.2

[97] Thilo Hölscher, Golnaz Ahadi, Daniel Lotz, Cheryl Schendel, David Fisher, and Arne Voie. Transcranial high-intensity focused ultrasound for sonothrombolysis in stroke. In *Translational Stroke Research*, pages 753–776. Springer, 2012.

[98] Ernst Martin and Beat Werner. Focused ultrasound surgery of the brain. *Current Radiology Reports*, pages 1–10, 2013. 3.1.4, 3.1.4.5, 3.2.4, 3.3.1, 3.3.2.2

[99] Fabrice Marquet, Anne-Laure Boch, Mathieu Pernot, Gabriel Montaldo, Danielle Seilhean, Mathias Fink, Mickael Tanter, and Jean-Francois Aubry. Non-invasive ultrasonic surgery of the brain in non-human primates. *The Journal of the Acoustical Society of America*, 134:1632, 2013. 2.5.2.2

[100] Kullervo Hynynen, Nathan McDannold, Greg Clement, Ferenc A Jolesz, Eyal Zadicario, Ron Killiany, Tara Moore, and Douglas Rosen. Pre-clinical testing of a phased array ultrasound system for MRI-guided noninvasive surgery of the brain—a primate study. *European journal of radiology*, 59(2):149–156, 2006. 2.5.2.2

[101] Ernst Martin, Daniel Jeanmonod, Anne Morel, Eyal Zadicario, and Beat Werner. High-intensity focused ultrasound for noninvasive functional neurosurgery. *Annals of neurology*, 66(6):858–861, 2009. 2.5.2.2, 3.1.4.5, 8.3.3, 9.2.3

[102] Daniel Jeanmonod, Beat Werner, Anne Morel, Lars Michels, Eyal Zadicario, Gilat Schiff, and Ernst Martin. Transcranial magnetic resonance imaging–guided focused ultrasound: noninvasive central lateral thalamotomy for chronic neuropathic pain. *Neurosurgical Focus*, 32(1):E1, 2012. 2.5.2.2, 3.1.4.5, 3.3.2.2, 8.3.3

[103] W. Jeffrey Elias, Diane Huss, Tiffini Voss, Johanna Loomba, Mohamad Khaled, Eyal Zadicario, Robert C. Frysinger, Scott A. Sperling, Scott Wylie, Stephen J. Monteith, Jason Druzgal, Binit B. Shah, Madaline Harrison, and Max Wintermark. A pilot study of focused ultrasound thalamotomy for essential tremor. *New England Journal of Medicine*, 369(7):640–648, 2013. 2.5.2.2, 3.1.4.5

[104] Byoung-Kyong Min, Alexander Bystritsky, Kwang-Ik Jung, Krisztina Fischer, Yongzhi Zhang, Lee-So Maeng, Sang In Park, Yong-An Chung, Ferenc A Jolesz, and Seung-Schik Yoo. Focused ultrasound-mediated suppression of chemically-induced acute epileptic eeg activity. *BMC neuroscience*, 12(1):23, 2011. 2.5.2.2

[105] JF Aubry, L Marsac, M Pernot, M Tanter, B Robert, Y Martin, C Cohen-Bacrie, J Souquet, and M Fink. MR-guided ultrasonic brain therapy: High frequency approach. In *Ultrasonics Symposium (IUS), 2009 IEEE International*, pages 321–324. IEEE, 2009. 2.5.2.2, 3.3.2.2

[106] Dorian Chauvet, Laurent Marsac, Mathieu Pernot, Anne-Laure Boch, Rémy Guillevin, Najat Salameh, Line Souris, Luc Darrasse, Mathias Fink, Mickaël Tanter, et al. Targeting accuracy of transcranial magnetic resonance–guided high-intensity focused ultrasound brain therapy: a fresh cadaver model: Laboratory investigation. *Journal of neurosurgery*, 118(5):1046–1052, 2013. 2.5.2.2

[107] Max O Köhler, Charles Mougenot, Bruno Quesson, Julia Enholm, Brigitte Le Bail, Christophe Laurent, Chrit TW Moonen, and Gösta J Ehnholm. Volumetric HIFU ablation under 3D guidance of rapid MRI thermometry. *Medical physics*, 36:3521, 2009. 2.5.2.3, 3.3.1

[108] M Köhler, J Enholm, C Mougenot, and T Andreae. Sonalleve MR-HIFU: Philips MR-guided high intensity focused ultrasound. 2011.

[109] Marlijne E Ikink, Marianne J Voogt, Helena M Verkooijen, Paul NM Lohle, Karlijn J Schweitzer, Arie Franx, P Th M Willem, Lambertus W Bartels, and Maurice AAJ van den Bosch. Mid-term clinical efficacy of a volumetric magnetic resonance-guided high-intensity focused ultrasound technique for treatment of symptomatic uterine fibroids. *European Radiology*, pages 1–8, 2013. 2.5.2.3

[110] Nelly Tan and Steven S Raman. Magnetic resonance-guided high-intensity focused ultrasound: Gynecological applications. 2013. 2.5.2.3

[111] MJ Voogt, H Trillaud, YS Kim, WP Th M Mali, J Barkhausen, LW Bartels, R Deckers, N Frulio, H Rhim, HK Lim, et al. Volumetric feedback ablation of uterine fibroids using magnetic resonance-guided high intensity focused ultrasound therapy. *European radiology*, 22(2):411–417, 2012. 2.5.2.3

[112] Eric J Dorenberg, Frédéric Courivaud, Eva Ring, Kirsten Hald, Jarl Å Jakobsen, Erik Fosse, and Per Kristian Hol. Volumetric ablation of uterine fibroids using sonalleve high-intensity focused ultrasound in a 3 Tesla scanner-first clinical assessment. *Minimally Invasive Therapy & Allied Technologies*, 22(2):73–79, 2012.

[113] Min Jung Park, Young-sun Kim, Bilgin Keserci, Hyunchul Rhim, and Hyo Keun Lim. Volumetric mr-guided high-intensity focused ultrasound ablation of uterine fibroids: treatment speed and factors influencing speed. *European radiology*, pages 1–8, 2013.

[114] Aradhana M Venkatesan, Ari Partanen, Tajana Klepac Pulanic, Matthew R Dreher, John Fischer, Robert K Zurawin, Raja Muthupillai, Sham Sokka, Heikki J Nieminen, Ninet Sinaii, et al. Magnetic resonance imaging–guided volumetric ablation of symptomatic leiomyomata: Correlation of imaging with histology. *Journal of Vascular and Interventional Radiology*, 23(6):786–794, 2012. 2.5.2.3

[115] Magalie Viallon, Lorena Petrusca, Vincent Auboiroux, Thomas Goget, Loredana Baboi, Christoph D Becker, and Rares Salomir. Experimental methods for improved spatial control of thermal lesions in magnetic resonance-guided focused ultrasound ablation. *Ultrasound in medicine & biology*, 2013. 2.5.2.3, 3.3.1

[116] Lian Zhang, Wen-Zhi Chen, Yin-Jiang Liu, Xiao Hu, Kun Zhou, Li Chen, Song Peng, Hui Zhu, Hui-Ling Zou, Jin Bai, et al. Feasibility of magnetic resonance imaging-guided high intensity focused ultrasound therapy for ablating uterine fibroids in patients with bowel lies anterior to uterus. *European journal of radiology*, 73(2):396–403, 2010. 2.5.2.4

[117] James E Kennedy. High-intensity focused ultrasound in the treatment of solid tumours. *Nature reviews cancer*, 5(4):321–327, 2005. 3, 3.1.1, 3.1.3, 3.3.1, 3.3.2

[118] Diane Dalecki. Mechanical bioeffects of ultrasound. *Annu. Rev. Biomed. Eng.*, 6: 229–248, 2004. 3

[119] MR Bailey, VA Khokhlova, OA Sapozhnikov, SG Kargl, and LA Crum. Physical mechanisms of the therapeutic effect of ultrasound (a review). *Acoustical Physics*, 49(4):369–388, 2003.

[120] Alison Burgess, Carlos A Ayala-Grosso, Milan Ganguly, Jessica F Jordão, Isabelle Aubert, and Kullervo Hynynen. Targeted delivery of neural stem cells to the brain using mri-guided focused ultrasound to disrupt the blood-brain barrier. *PLoS One*, 6(11):e27877, 2011. 3.2.1.3

[121] Meaghan A O'Reilly, Yuexi Huang, and Kullervo Hynynen. The impact of standing wave effects on transcranial focused ultrasound disruption of the blood–brain barrier in a rat model. *Physics in medicine and biology*, 55(18):5251, 2010. 3, 3.3.2.1

[122] Kerry G Baker, Valma J Robertson, and Francis A Duck. A review of therapeutic ultrasound: biophysical effects. *Physical Therapy*, 81(7):1351–1358, 2001. 3

[123] David Schlesinger, Stanley Benedict, Chris Diederich, Wladyslaw Gedroyc, Alexander Klibanov, and James Larner. Mr-guided focused ultrasound surgery, present and future. *Medical physics*, 40:080901, 2013. 3, 3.1.4, 3.3, 3.3.2

[124] Feng Wu, Wen-Zhi Chen, Jin Bai, Jian-Zhong Zou, Zhi-Long Wang, Hui Zhu, and Zhi-Biao Wang. Pathological changes in human malignant carcinoma treated with high-intensity focused ultrasound. *Ultrasound in medicine & biology*, 27(8): 1099–1106, 2001. 3.1.1

[125] Natalia Vykhodtseva, Nathan Mcdannold, Heather Martin, Roderick T Bronson, and Kullervo Hynynen. Apoptosis in ultrasound-produced threshold lesions in the rabbit brain. *Ultrasound in medicine & biology*, 27(1):111–117, 2001. 3.1.1

[126] Stephen Monteith, Jason Sheehan, Ricky Medel, Max Wintermark, Matthew Eames, John Snell, Neal F Kassell, and W Jeff Elias. Potential intracranial applications of magnetic resonance–guided focused ultrasound surgery: A review. *Journal of neurosurgery*, 118(2):215–221, 2013. 3.1.4, 3.1.4.5, 3.1.4.5, 3.2.3, 3.3.1, 3.3.2.2

[127] Timothy J Mason. Therapeutic ultrasound an overview. *Ultrasonics sonochemistry*, 18(4):847–852, 2011. 3.2.3

[128] Yu-Feng Zhou. High intensity focused ultrasound in clinical tumor ablation. *World journal of clinical oncology*, 2(1):8, 2011. 3.1.4.1, 3.1.4.2, 3.1.4.3, 3.1.4.4, 3.3.2

[129] Lian Zhang and Zhi-Biao Wang. High-intensity focused ultrasound tumor ablation: Review of ten years of clinical experience. *Frontiers of medicine in China*, 4(3): 294–302, 2010. 3.1.4, 3.1.4.2, 3.1.4.3, 3.1.4.4

[130] Ahmedin Jemal, Freddie Bray, Melissa M Center, Jacques Ferlay, Elizabeth Ward, and David Forman. Global cancer statistics. *CA: a cancer journal for clinicians*, 61(2):69–90, 2011. 3.1.4.1

[131] Sebastien Crouzet, Francois J Murat, Gilles Pasticier, Philippe Cassier, Jean Y Chapelon, and Albert Gelet. High intensity focused ultrasound (HIFU) for prostate cancer: Current clinical status, outcomes and future perspectives. *International Journal of Hyperthermia*, 26(8):796–803, 2010. 3.1.4.1

[132] Marisa Warmuth, Tim Johansson, and Philipp Mad. Systematic review of the efficacy and safety of high-intensity focussed ultrasound for the primary and salvage treatment of prostate cancer. *European urology*, 58(6):803–815, 2010.

[133] H Lukka, T Waldron, J Chin, L Mayhew, P Warde, E Winquist, G Rodrigues, and B Shayegan. High-intensity focused ultrasound for prostate cancer: a systematic review. *Clinical Oncology*, 23(2):117–127, 2011.

[134] Christian Chaussy, Derya Tilki, and Stefan Thüroff. Transrectal high-intensity focused ultrasound for the treatment of localized prostate cancer: Current role. *Journal of Cancer Therapy*, 4:59–73, 2013. 3.1.4.1

[135] Fiona M Fennessy and Clare M Tempany. An update on magnetic resonance guided focused ultrasound surgery (MRgFUS) of uterine fibroids. *Current Radiology Reports*, pages 1–11, 2013. 3.1.4.2

[136] Thomas Kahn and Harald Busse. *Interventional Magnetic Resonance Imaging*. Springer, 2012. 3.1.4.2, 3.3.2

[137] Jaron Rabinovici, Matthias David, Hidenobu Fukunishi, Yutaka Morita, Bobbie S Gostout, Elizabeth A Stewart, et al. Pregnancy outcome after magnetic resonance-guided focused ultrasound surgery for conservative treatment of uterine fibroids. *Obstetrical & Gynecological Survey*, 65(5):316–318, 2010. 3.1.4.2

[138] Gail ter Haar, Sadaf Zahur, and Chaturika Jayadewa. High-intensity focused ultrasound (hifu) treatment of liver cancer. *Interventional Radiological Treatment of Liver Tumors*, page 92, 2009. 3.1.4.3

[139] Baudouin Denis de Senneville, Mario Ries, Lambertus W Bartels, and Chrit TW Moonen. MRI-guided high-intensity focused ultrasound sonication of liver and kidney. In *Interventional Magnetic Resonance Imaging*, pages 349–366. Springer, 2012. 3.1.4.3, 3.3.2.3, 3.3.3, 9.1, 9.2.2.2

[140] Krisztina Fischer, Wladyslaw Gedroyc, and Ferenc A Jolesz. Focused ultrasound as a local therapy for liver cancer. *The Cancer Journal*, 16(2):118–124, 2010. 3.1.4.3, 9.1

[141] Jean-Francois Aubry, Kim Butts Pauly, Chrit Moonen, Gail ter Haar, Mario Ries, Rares Salomir, Sham Sokka, Kevin Michael Sekins, Yerucham Shapira, Fangwei Ye, et al. The road to clinical use of high-intensity focused ultrasound for liver

cancer: technical and clinical consensus. *Journal of Therapeutic Ultrasound*, 1(1): 13, 2013. 3.1.4.3, 9.1

[142] Ursula Falkmer, Johannes Järhult, Peter Wersäll, and Eva Cavallin-ståhl. A systematic overview of radiation therapy effects in skeletal metastases. *Acta Oncologica*, 42(5-6):620–633, 2003. 3.1.4.4

[143] E Chow, P Hoskin, Y van der Linden, A Bottomley, and G Velikova. Quality of life and symptom end points in palliative bone metastases trials. *Clinical Oncology*, 18 (1):67–69, 2006. 3.1.4.4

[144] Wenzhi Chen, Hui Zhu, Lian Zhang, Kequan Li, Haibing Su, Chengbin Jin, Kun Zhou, Jin Bai, Feng Wu, and Zhibiao Wang. Primary bone malignancy: Effective treatment with high-intensity focused ultrasound ablation. *Radiology*, 255(3):967–978, 2010. 3.1.4.4

[145] Chuanxing Li, Weidong Zhang, Weijun Fan, Jinhua Huang, Fujun Zhang, and Peihong Wu. Noninvasive treatment of malignant bone tumors using high-intensity focused ultrasound. *Cancer*, 116(16):3934–3942, 2010. 3.1.4.4

[146] R Catane, A Beck, Y Inbar, T Rabin, N Shabshin, S Hengst, RM Pfeffer, A Hanannel, O Dogadkin, B Liberman, et al. MR-guided focused ultrasound surgery (MRg-FUS) for the palliation of pain in patients with bone metastases—preliminary clinical experience. *Annals of Oncology*, 18(1):163–167, 2007. 3.1.4.4

[147] David Gianfelice, Chander Gupta, Walter Kucharczyk, Patrice Bret, Deborah Havill, and Mark Clemons. Palliative treatment of painful bone metastases with MR imaging–guided focused ultrasound. *Radiology*, 249(1):355–363, 2008.

[148] Boaz Liberman, David Gianfelice, Yael Inbar, Alexander Beck, Tatiana Rabin, Noga Shabshin, Gupta Chander, Suzanne Hengst, Raphael Pfeffer, Aharon Chechick, et al. Pain palliation in patients with bone metastases using mr-guided focused ultrasound surgery: a multicenter study. *Annals of surgical oncology*, 16 (1):140–146, 2009. 3.1.4.4

[149] Ronit Machtinger, Fiona M Fennessy, and Mark D Hurwitz. High-intensity focused ultrasound treatment for bone metastases. 2013. 3.1.4.4

[150] Rivka R Colen and Ferenc A Jolesz. MR-guided focused ultrasound of the brain. In *Interventional Magnetic Resonance Imaging*, pages 367–380. Springer, 2012. 3.1.4.5, 3.2.1.1, 3.2.1.3, 3.3.2.2

[151] Andrei V Alexandrov, Carlos A Molina, James C Grotta, Zsolt Garami, Shiela R Ford, Jose Alvarez-Sabin, Joan Montaner, Maher Saqqur, Andrew M Demchuk, Lemuel A Moyé, et al. Ultrasound-enhanced systemic thrombolysis for acute

ischemic stroke. *New England Journal of Medicine*, 351(21):2170–2178, 2004. 3.1.4.5, 3.2.3

[152] Michael Daffertshofer, Achim Gass, Peter Ringleb, Matthias Sitzer, Ulrich Sliwka, Thomas Els, Oliver Sedlaczek, Walter J Koroshetz, and Michael G Hennerici. Transcranial low-frequency ultrasound-mediated thrombolysis in brain ischemia increased risk of hemorrhage with combined ultrasound and tissue plasminogen activator: Results of a phase II clinical trial. *Stroke*, 36(7):1441–1446, 2005. 3.1.4.5, 3.2.3, 3.3.2.1

[153] Jessica F Jordão, Carlos A Ayala-Grosso, Kelly Markham, Yuexi Huang, Rajiv Chopra, JoAnne McLaurin, Kullervo Hynynen, and Isabelle Aubert. Antibodies targeted to the brain with image-guided focused ultrasound reduces amyloid-$\beta$ plaque load in the TgCRND8 mouse model of alzheimer's disease. *PLoS One*, 5(5):e10549, 2010. 3.1.4.5, 3.2.1.3

[154] Kullervo Hynynen, Nathan McDannold, Natalia Vykhodtseva, Scott Raymond, Ralph Weissleder, Ferenc A Jolesz, and Nickolai Sheikov. Focal disruption of the blood-brain barrier due to 260-kHz ultrasound bursts: a method for molecular imaging and targeted drug delivery. *Journal of neurosurgery*, 105(3):445–454, 2006.

[155] Matthias Reinhard, Andreas Hetzel, Sebastian Krüger, Stefan Kretzer, Jochen Talazko, Sargon Ziyeh, Johannes Weber, and Thomas Els. Blood-brain barrier disruption by low-frequency ultrasound. *Stroke*, 37(6):1546–1548, 2006. 3.1.4.5, 3.3.2.1

[156] Timothy Wagner, Antoni Valero-Cabre, and Alvaro Pascual-Leone. Noninvasive human brain stimulation. *Annu. Rev. Biomed. Eng.*, 9:527–565, 2007. 3.1.4.5, 3.2.4

[157] Seung-Schik Yoo, Alexander Bystritsky, Jong-Hwan Lee, Yongzhi Zhang, Krisztina Fischer, Byoung-Kyong Min, Nathan J McDannold, Alvaro Pascual-Leone, and Ferenc A Jolesz. Focused ultrasound modulates region-specific brain activity. *Neuroimage*, 56(3):1267–1275, 2011. 3.1.4.5, 3.2.4

[158] E.P. Widmaier, H. Raff, and K.T. Strang. *Vander's human physiology*. McGraw Hill, 2006. ISBN 007111677X. 3.2.1.1

[159] A.C. Guyton and J.E. Hall. Textbook of medical physiology. *London: W. B. Saunders Co*, 1981. 3.2.1.1

[160] Bruce M. Koeppen John T. Hansen. *Netter's Atlas of Human Physiology*. Netter Basic Science. Saunders, 1st edition, 2002. 3.2.1.1

[161] K. Hynynen, N. McDannold, N. Vykhodtseva, and F.A. Jolesz. Noninvasive MR imaging–guided focal opening of the blood-brain barrier in rabbits. *Radiology*, 220 (3):640, 2001. 3.2.1.1, 3.2.1.2, 3.2.1.3

[162] K. Hynynen. Ultrasound for drug and gene delivery to the brain. *Advanced drug delivery reviews*, 60(10):1209–1217, 2008. 3.2.1.2, 3.2.1.3

[163] W.M. Pardridge. Drug and gene targeting to the brain with molecular trojan horses. *Nature Reviews Drug Discovery*, 1(2):131–139, 2002.

[164] Yan Chen and Lihong Liu. Modern methods for delivery of drugs across the blood–brain barrier. *Advanced drug delivery reviews*, 64(7):640–665, 2012. 3.2.1.1, 3.2.1.2

[165] William M Pardridge. The blood-brain barrier: bottleneck in brain drug development. *NeuroRx*, 2(1):3–14, 2005. 3.2.1.1

[166] R. Langer. New methods of drug delivery. *Science*, 249(4976):1527, 1990. 3.2.1.2

[167] N.J. Abbott and I.A. Romero. Transporting therapeutics across the blood-brain barrier. *Molecular Medicine Today*, 2(3):106–113, 1996.

[168] D.R. Groothuis. The blood-brain and blood-tumor barriers: a review of strategies for increasing drug delivery. *Neuro-oncology*, 2(1):45, 2000. 3.2.1.2

[169] W.M. Pardridge. Blood-brain barrier drug targeting: the future of brain drug development. *Molecular interventions*, 3(2):90, 2003.

[170] A. Misra, S. Ganesh, A. Shahiwala, and S.P. Shah. Drug delivery to the central nervous system: a review. *J Pharm Pharm Sci*, 6(2):252–273, 2003. 3.2.1.2

[171] Group Health Cooperative. Blood brain barrier (BBB) osmotic disruption for treating brain tumors.

[172] Feng-Yi Yang, Yu-Shi Lin, Kai-Hsiang Kang, and Tai-Kuang Chao. Reversible blood–brain barrier disruption by repeated transcranial focused ultrasound allows enhanced extravasation. *Journal of Controlled Release*, 150(1):111–116, 2011. 3.2.1.2

[173] J.J. Choi, M. Pernot, S.A. Small, and E.E. Konofagou. Noninvasive, transcranial and localized opening of the blood-brain barrier using focused ultrasound in mice. *Ultrasound in medicine & biology*, 33(1):95–104, 2007. 3.2.1.3

[174] N. Vykhodtseva, N. McDannold, and K. Hynynen. Progress and problems in the application of focused ultrasound for blood-brain barrier disruption. *Ultrasonics*, 48(4):279–296, 2008. 3.2.1.3

[175] Alison Burgess and Kullervo Hynynen. Noninvasive and targeted drug delivery to the brain using focused ultrasound. *ACS chemical neuroscience*, 4(4):519–526, 2013. 3.2.1.3

[176] L. Bakay, TF Hueter, HT Ballantine Jr, and D. Sosa. Ultrasonically produced changes in the blood-brain barrier. *Archives of Neurology and Psychiatry*, 76(5): 457, 1956. 3.2.1.3

[177] Nathan McDannold, Costas D Arvanitis, Natalia Vykhodtseva, and Margaret S Livingstone. Temporary disruption of the blood–brain barrier by use of ultrasound and microbubbles: safety and efficacy evaluation in rhesus macaques. *Cancer research*, 72(14):3652–3663, 2012. 3.2.1.3

[178] Eun-Joo Park, Yong-Zhi Zhang, Natalia Vykhodtseva, and Nathan McDannold. Ultrasound-mediated blood–brain/blood-tumor barrier disruption improves outcomes with trastuzumab in a breast cancer brain metastasis model. *Journal of Controlled Release*, 2012.

[179] Ryan Alkins, Alison Burgess, Milan Ganguly, Giulio Francia, Robert Kerbel, Winfried S Wels, and Kullervo Hynynen. Focused ultrasound delivers targeted immune cells to metastatic brain tumors. *Cancer research*, 73(6):1892–1899, 2013. 3.2.1.3

[180] Nicolas A Geis, Christian R Mayer, Richard D Kroll, Stefan E Hardt, Hugo A Katus, and Raffi Bekeredjian. Spatial distribution of ultrasound targeted microbubble destruction increases cardiac transgene expression but not capillary permeability. *Ultrasound in medicine & biology*, 35(7):1119–1126, 2009. 3.2.1.3

[181] Ralf Seip, Chien Ting Chin, Christopher S Hall, Balasundar I Raju, Alexander Ghanem, and Klaus Tiemann. Targeted ultrasound-mediated delivery of nanoparticles: on the development of a new hifu-based therapy and imaging device. *Biomedical Engineering, IEEE Transactions on*, 57(1):61–70, 2010. 3.2.1.3

[182] Ji Song, John C Chappell, Ming Qi, Eric J VanGieson, Sanjiv Kaul, and Richard J Price. Influence of injection site, microvascular pressureand ultrasound variables on microbubble-mediated delivery of microspheres to muscle. *Journal of the American College of Cardiology*, 39(4):726–731, 2002. 3.2.1.3

[183] Richard J Price, Danny M Skyba, Sanjiv Kaul, and Thomas C Skalak. Delivery of colloidal particles and red blood cells to tissue through microvessel ruptures created by targeted microbubble destruction with ultrasound. *Circulation*, 98(13): 1264–1267, 1998. 3.2.1.3

[184] Victor Frenkel. Ultrasound mediated delivery of drugs and genes to solid tumors. *Advanced drug delivery reviews*, 60(10):1193–1208, 2008. 3.2.1.3, 3.2.2

[185] Raffi Bekeredjian, Richard D Kroll, Evelyn Fein, Steliyan Tinkov, Conrad Coester, Gerhard Winter, Hugo A Katus, and Hasan Kulaksiz. Ultrasound targeted microbubble destruction increases capillary permeability in hepatomas. *Ultrasound in medicine & biology*, 33(10):1592–1598, 2007.

[186] Peter Hauff, Stefanie Seemann, Regina Reszka, Marcus Schultze-Mosgau, Michael Reinhardt, Tivadar Buzasi, Thomas Plath, Stefan Rosewicz, and Michael Schirner. Evaluation of gas-filled microparticles and sonoporation as gene delivery system: Feasibility study in rodent tumor models. *Radiology*, 236(2):572–578, 2005.

[187] Douglas L Miller and Jianming Song. Tumor growth reduction and dna transfer by cavitation-enhanced high-intensity focused ultrasound¡ i¿ in vivo¡/i¿. *Ultrasound in medicine & biology*, 29(6):887–893, 2003. 3.2.1.3

[188] Sophie Hernot and Alexander L Klibanov. Microbubbles in ultrasound-triggered drug and gene delivery. *Advanced drug delivery reviews*, 60(10):1153–1166, 2008. 3.2.2

[189] Roel Deckers and Chrit TW Moonen. Ultrasound triggered, image guided, local drug delivery. *Journal of Controlled Release*, 148(1):25–33, 2010.

[190] Bart Geers, Ine Lentacker, Niek N Sanders, Joseph Demeester, Stephen Meairs, and Stefaan C De Smedt. Self-assembled liposome-loaded microbubbles: The missing link for safe and efficient ultrasound triggered drug-delivery. *Journal of Controlled Release*, 152(2):249–256, 2011.

[191] Michiel Postema and Odd Helge Gilja. Contrast-enhanced and targeted ultrasound. *World journal of gastroenterology: WJG*, 17(1):28, 2011.

[192] Bart Geers, Heleen Dewitte, Stefaan C De Smedt, and Ine Lentacker. Crucial factors and emerging concepts in ultrasound-triggered drug delivery. *Journal of Controlled Release*, 2012. 3.2.2

[193] Anna Yudina, Matthieu Lepetit-Coiffé, and Chrit TW Moonen. Evaluation of the temporal window for drug delivery following ultrasound-mediated membrane permeability enhancement. *Molecular Imaging and Biology*, 13(2):239–249, 2011. 3.2.2

[194] Daryl C Drummond, Charles O Noble, Mark E Hayes, John W Park, and Dmitri B Kirpotin. Pharmacokinetics and in vivo drug release rates in liposomal nanocarrier development. *Journal of pharmaceutical sciences*, 97(11):4696–4740, 2008. 3.2.2

[195] Gerben A Koning, Alexander MM Eggermont, Lars H Lindner, and Timo LM ten Hagen. Hyperthermia and thermosensitive liposomes for improved delivery of chemotherapeutic drugs to solid tumors. *Pharmaceutical research*, 27(8):1750–1754, 2010.

[196] Ana M Ponce, Zeljko Vujaskovic, Fan Yuan, David Needham, and Mark W De-whirst. Hyperthermia mediated liposomal drug delivery. *International Journal of Hyperthermia*, 22(3):205–213, 2006. 3.2.2

[197] Ari Partanen, Pavel S Yarmolenko, Antti Viitala, Sunil Appanaboyina, Dieter Haemmerich, Ashish Ranjan, Genevieve Jacobs, David Woods, Julia Enholm, Bradford J Wood, et al. Mild hyperthermia with magnetic resonance-guided high-intensity focused ultrasound for applications in drug delivery. *International Journal of Hyperthermia*, 28(4):320–336, 2012. 3.2.2

[198] Evan C Unger, Thomas Porter, William Culp, Rachel Labell, Terry Matsunaga, and Reena Zutshi. Therapeutic applications of lipid-coated microbubbles. *Advanced drug delivery reviews*, 56(9):1291–1314, 2004. 3.2.2

[199] Yiyao Liu, Hirokazu Miyoshi, and Michihiro Nakamura. Encapsulated ultrasound microbubbles: therapeutic application in drug/gene delivery. *Journal of controlled release*, 114(1):89–99, 2006.

[200] Alexander L Klibanov. Microbubble contrast agents: targeted ultrasound imaging and ultrasound-assisted drug-delivery applications. *Investigative radiology*, 41(3): 354–362, 2006. 3.2.2

[201] Gianmarco F Pinton, J-F Aubry, Mathias Fink, and Mickael Tanter. Numerical prediction of frequency dependent 3d maps of mechanical index thresholds in ul-trasonic brain therapy. In *Ultrasonics Symposium (IUS), 2010 IEEE*, pages 2258–2261. IEEE, 2010. 3.2.3

[202] Stephen Meairs, Angelika Alonso, and Michael G Hennerici. Progress in sonothrombolysis for the treatment of stroke. *Stroke*, 43(6):1706–1710, 2012. 3.2.3

[203] Carlos A Molina, Marc Ribo, Marta Rubiera, Joan Montaner, Esteban Santamarina, Raquel Delgado-Mederos, Juan F Arenillas, Rafael Huertas, Francisco Purroy, Pi-lar Delgado, et al. Microbubble administration accelerates clot lysis during contin-uous 2-mhz ultrasound monitoring in stroke patients treated with intravenous tissue plasminogen activator. *Stroke*, 37(2):425–429, 2006. 3.2.3

[204] Fabienne Perren, Jaouad Loulidi, Davide Poglia, Theodor Landis, and Roman Sz-tajzel. Microbubble potentiated transcranial duplex ultrasound enhances iv throm-bolysis in acute stroke. *Journal of thrombosis and thrombolysis*, 25(2):219–223, 2008. 3.2.3

[205] Robert J Siegel and Huai Luo. Ultrasound thrombolysis. *Ultrasonics*, 48(4):312–320, 2008. 3.2.3

[206] Georgios Tsivgoulis, William C Culp, and Andrei V Alexandrov. Ultrasound enhanced thrombolysis in acute arterial ischemia. *Ultrasonics*, 48(4):303–311, 2008. 3.2.3

[207] Yusuf Tufail, Alexei Matyushov, Nathan Baldwin, Monica L Tauchmann, Joseph Georges, Anna Yoshihiro, Stephen I Helms Tillery, and William J Tyler. Transcranial pulsed ultrasound stimulates intact brain circuits. *Neuron*, 66(5):681–694, 2010. 3.2.4

[208] William J Tyler. Noninvasive neuromodulation with ultrasound? a continuum mechanics hypothesis. *The Neuroscientist*, 17(1):25–36, 2011.

[209] Alexander Bystritsky, Alex S Korb, Pamela K Douglas, Mark S Cohen, William P Melega, Amit P Mulgaonkar, Antonio DeSalles, Byoung-Kyong Min, and Seung-Schik Yoo. A review of low-intensity focused ultrasound pulsation. *Brain stimulation*, 4(3):125–136, 2011. 3.2.4

[210] Mark S George and Gary Aston-Jones. Noninvasive techniques for probing neurocircuitry and treating illness: vagus nerve stimulation (VNS), transcranial magnetic stimulation (TMS) and transcranial direct current stimulation (tDCS). *Neuropsychopharmacology*, 35(1):301–316, 2009. 3.2.4

[211] Kate E Hoy and Paul B Fitzgerald. Brain stimulation in psychiatry and its effects on cognition. *Nature Reviews Neurology*, 6(5):267–275, 2010.

[212] Thomas E Schlaepfer, Michael X Cohen, Caroline Frick, Markus Kosel, Daniela Brodesser, Nikolai Axmacher, Alexius Young Joe, Martina Kreft, Doris Lenartz, and Volker Sturm. Deep brain stimulation to reward circuitry alleviates anhedonia in refractory major depression. *Neuropsychopharmacology*, 33(2):368–377, 2007. 3.2.4

[213] Felipe Fregni and Alvaro Pascual-Leone. Technology insight: noninvasive brain stimulation in neurology—perspectives on the therapeutic potential of rTMS and tDCS. *Nature Clinical Practice Neurology*, 3(7):383–393, 2007. 3.2.4

[214] Friedhelm C Hummel and Leonardo G Cohen. Non-invasive brain stimulation: a new strategy to improve neurorehabilitation after stroke? *The Lancet Neurology*, 5 (8):708–712, 2006. 3.2.4

[215] E Newton Harvey. The effect of high frequency sound waves on heart muscle and other irritable tissues. *American Journal of Physiology–Legacy Content*, 91(1): 284–290, 1929. 3.2.4

[216] Charles Mougenot, Rares Salomir, Jean Palussiere, Nicolas Grenier, and Chrit TW Moonen. Automatic spatial and temporal temperature control for mr-guided focused ultrasound using fast 3d mr thermometry and multispiral trajectory of the focal point. *Magnetic resonance in medicine*, 52(5):1005–1015, 2004. 3.3.1

[217] Dhiraj Arora, Mark A Minor, Mikhail Skliar, and Robert B Roemer. Control of thermal therapies with moving power deposition field. *Physics in medicine and biology*, 51(5):1201, 2006. 3.3.1

[218] Doron Kopelman, Yael Inbar, Arik Hanannel, David Freundlich, Shuki Vitek, Rita Schmidt, Amit Sokolov, Ossama A Hatoum, and Jaron Rabinovici. Magnetic resonance-guided focused ultrasound surgery using an enhanced sonication technique in a pig muscle model. *European journal of radiology*, 59(2):190–197, 2006. 3.3.1

[219] Nathan J McDannold, Natalia I Vykhodtseva, and Kullervo Hynynen. Microbubble contrast agent with focused ultrasound to create brain lesions at low power levels: Mr imaging and histologic study in rabbits. *Radiology*, 241(1):95–106, 2006. 3.3.1

[220] Susumu Okada, Yoshiharu Ohaki, Kohei Inoue, Takashi Kawamura, Toshihiko Hayashi, Tomoyasu Kato, and Tatsuo Kumazaki. Calcifications in mucinous and serous cystic ovarian tumors. *Journal of Nippon Medical School*, 72(1):29–33, 2005. 3.3.2

[221] Sergio Marrone Ribeiro, Sergio Aron Ajzen, and José Carlos Souza Trindade. Comparison of imaging methods for diagnosis of renal tumors and their calcifications. *Revista da Associação Médica Brasileira*, 50(4):403–412, 2004.

[222] Mark LC Khoo, Sylvia L Asa, Ian J Witterick, and Jeremy L Freeman. Thyroid calcification and its association with thyroid carcinoma. *Head & neck*, 24(7):651–655, 2002. 3.3.2

[223] Beat Werner, Anne Morel, Eyal Zadicario, Daniel Jeanmonod, and Ernst Martin. Transcranial mr-guided high intensity focused ultrasound for non-invasive functional neurosurgery. In *AIP Conference Proceedings*, volume 1215, page 101, 2010. 3.3.2

[224] Sai Chun Tang and Gregory T Clement. Standing-wave suppression for transcranial ultrasound by random modulation. *Biomedical Engineering, IEEE Transactions on*, 57(1):203–205, 2010. 3.3.2.1

[225] Vincent Auboiroux, Erik Dumont, Lorena Petrusca, Magalie Viallon, and Rares Salomir. An MR-compliant phased-array HIFU transducer with augmented steering range, dedicated to abdominal thermotherapy. *Physics in Medicine and Biology*, 56(12):3563, 2011.

[226] Junho Song, Aki Pulkkinen, Yuexi Huang, and Kullervo Hynynen. Investigation of standing-wave formation in a human skull for a clinical prototype of a large-aperture, transcranial mr-guided focused ultrasound (mrgfus) phased array: an experimental and simulation study. *Biomedical Engineering, IEEE Transactions on*, 59(2):435–444, 2012. 3.3.2.1, 8.1.1.1, 8.1.1.3

[227] Christopher W Connor and Kullervo Hynynen. Patterns of thermal deposition in the skull during transcranial focused ultrasound surgery. *Biomedical Engineering, IEEE Transactions on*, 51(10):1693–1706, 2004. 3.3.2.1

[228] Cecile Baron, Jean-François Aubry, Mickael Tanter, Stephen Meairs, and Mathias Fink. Simulation of intracranial acoustic fields in clinical trials of sonothrombolysis. *Ultrasound in medicine & biology*, 35(7):1148–1158, 2009.

[229] Sai Chun Tang and Gregory T Clement. Acoustic standing wave suppression using randomized phase-shift-keying excitations. *The Journal of the Acoustical Society of America*, 126:1667, 2009. 3.3.2.1

[230] Takashi Azuma, Ken-ichi Kawabata, Shin-ichiro Umemura, Makoto Ogihara, Jun Kubota, Akira Sasaki, and Hiroshi Furuhata. Bubble generation by standing wave in water surrounded by cranium with transcranial ultrasonic beam. *Japanese journal of applied physics*, 44:4625, 2005. 3.3.2.1

[231] Farid G Mitri, James F Greenleaf, and Mostafa Fatemi. Chirp imaging vibro-acoustography for removing the ultrasound standing wave artifact. *Medical Imaging, IEEE Transactions on*, 24(10):1249–1255, 2005. 3.3.2.1

[232] Todd N Erpelding, Kyle W Hollman, and Matthew O'Donnell. Bubble-based acoustic radiation force using chirp insonation to reduce standing wave effects. *Ultrasound in medicine & biology*, 33(2):263–269, 2007. 3.3.2.1

[233] Samuel Pichardo, Vivian W Sin, and Kullervo Hynynen. Multi-frequency characterization of the speed of sound and attenuation coefficient for longitudinal transmission of freshly excised human skulls. *Physics in medicine and biology*, 56(1): 219, 2011. 3.3.2.2

[234] Andreas Christ, Wolfgang Kainz, Eckhart G Hahn, Katharina Honegger, Marcel Zefferer, Esra Neufeld, Wolfgang Rascher, Rolf Janka, Werner Bautz, Ji Chen, et al. The virtual family—development of surface-based anatomical models of two adults and two children for dosimetric simulations. *Physics in medicine and biology*, 55(2):N23, 2010. 3.5, 6.3.3

[235] Xiangtao Yin and Kullervo Hynynen. A numerical study of transcranial focused ultrasound beam propagation at low frequency. *Physics in medicine and biology*, 50(8):1821, 2005. 3.3.2.2

[236] Jean-François Aubry, Mathieu Pernot, Fabrice Marquet, Mickaël Tanter, and Mathias Fink. Transcostal high-intensity-focused ultrasound: ex vivo adaptive focusing feasibility study. *Physics in medicine and biology*, 53(11):2937, 2008. 3.3.2.3, 4.3.7, 9.1, 9.2.1.1

[237] Etienne Cochard, C Prada, Jean-François Aubry, and Mathias Fink. Ultrasonic focusing through the ribs using the DORT method. *Medical physics*, 36:3495, 2009. 3.3.2.3

[238] Svetlana Bobkova, Leonid Gavrilov, Vera Khokhlova, Adam Shaw, and Jeffrey Hand. Focusing of high-intensity ultrasound through the rib cage using a therapeutic random phased array. *Ultrasound in medicine & biology*, 36(6):888–906, 2010. 3.3.2.3, 9.1, 9.2.1.1

[239] SA Ilyin, SM Bobkova, VA Khokhlova, and LR Gavrilov. Simulation of thermal lesions in biological tissues irradiated by high-intensity focused ultrasound through the rib cage. *Physics of Wave Phenomena*, 19(1):62–67, 2011.

[240] F Marquet, JF Aubry, M Pernot, M Fink, and M Tanter. Optimal transcostal high-intensity focused ultrasound with combined real-time 3d movement tracking and correction. *Physics in Medicine and Biology*, 56(22):7061, 2011. 3.3.2.3

[241] Faqi Li, Xiaobo Gong, Kai Hu, Chongyan Li, and Zhibiao Wang. Effect of ribs in HIFU beam path on formation of coagulative necrosis in goat liver. In *AIP Conference Proceedings*, volume 829, page 477, 2006. 3.3.2.3

[242] Wen-Zhi Chen, Hui Zhu, Jin Bai, Jian-Zhong Zou, Ke-Quan Li, Cheng-Bing Jin, Fang-Lin Xie, and Hai-Bing Su. Extracorporeal high intensity focused ultrasound ablation in the treatment of patients with large hepatocellular carcinoma. *Annals of surgical oncology*, 11(12):1061–1069, 2004. 3.3.2.3, 9.1

[243] Feng Wu, Zhi-Biao Wang, Wen-Zhi Chen, Wei Wang, Yongzhong Gui, Ming Zhang, Guoqiang Zheng, Yongjian Zhou, Guoliang Xu, Ming Li, et al. Extracorporeal high intensity focused ultrasound ablation in the treatment of 1038 patients with solid carcinomas in china: an overview. *Ultrasonics sonochemistry*, 11(3): 149–154, 2004.

[244] JE Kennedy, F Wu, GR Ter Haar, FV Gleeson, RR Phillips, MR Middleton, and D Cranston. High-intensity focused ultrasound for the treatment of liver tumours. *Ultrasonics*, 42(1):931–935, 2004.

[245] Jian-Jun Li, Guo-Liang Xu, Mo-Fa Gu, Guang-Yu Luo, Zhang Rong, Pei-Hong Wu, and Jian-Chuan Xia. Complications of high intensity focused ultrasound in patients with recurrent and metastatic abdominal tumors. *World Journal of Gastroenterology*, 13(19):2747, 2007. 3.3.2.3

[246] Hui Zhu, Kun Zhou, Lian Zhang, Chengbin Jin, Song Peng, Wei Yang, Kequan Li, Haibing Su, Wenzhi Chen, Jin Bai, et al. High intensity focused ultrasound (hifu) therapy for local treatment of hepatocellular carcinoma: Role of partial rib resection. *European journal of radiology*, 72(1):160–166, 2009. 3.3.2.3, 9.1

[247] John Civale, Robert Clarke, Ian Rivens, and Gail Ter Haar. The use of a segmented transducer for rib sparing in HIFU treatments. *Ultrasound in medicine & biology*, 32(11):1753–1761, 2006. 3.3.2.3, 9.1

[248] Hao-Li Liu, Hsu Chang, Wen-Shiang Chen, Tzu-Ching Shih, Jong-Kai Hsiao, and Win-Li Lin. Feasibility of transrib focused ultrasound thermal ablation for liver tumors using a spherically curved 2d array: A numerical study. *Medical physics*, 34:3436, 2007.

[249] Bruno Quesson, Mathilde Merle, Max O Köhler, Charles Mougenot, Sebastien Roujol, Baudouin Denis de Senneville, and Chrit T Moonen. A method for mri guidance of intercostal high intensity focused ultrasound ablation in the liver. *Medical physics*, 37:2533, 2010. 3.3.2.3, 9.1

[250] Mickaël Tanter, Mathieu Pernot, J-F Aubry, Gabriel Montaldo, Fabrice Marquet, and Mathias Fink. Compensating for bone interfaces and respiratory motion in high-intensity focused ultrasound. *International Journal of Hyperthermia*, 23(2): 141–151, 2007. 3.3.2.3, 9.1

[251] Hao-Li Liu, Chia-Lung Hsu, Sheng-Min Huang, and Yi-Wen Hsi. Focal beam distortion and treatment planning for transrib focused ultrasound thermal therapy: A feasibility study using a two-dimensional ultrasound phased array. *Medical physics*, 37:848, 2010. 3.3.2.3, 9.1

[252] Patrik Arnold, Frank Preiswerk, Beat Fasel, Rares Salomir, Klaus Scheffler, and Philippe Cattin. Model-based respiratory motion compensation in MRgHIFU. In *Information Processing in Computer-Assisted Interventions*, pages 54–63. Springer, 2012. 3.3.3, 9.1

[253] RH Abhilash and Sunita Chauhan. Empirical modeling of renal motion for improved targeting during focused ultrasound surgery. *Computers in biology and medicine*, 2013. 3.3.3, 9.1

[254] Andrew B Holbrook, Pejman Ghanouni, Juan M Santos, Charles Dumoulin, Yoav Medan, and Kim Butts Pauly. Respiration based steering for high intensity focused ultrasound liver ablation. *Magnetic Resonance in Medicine*, 2013. 3.3.3

[255] Huanmei Wu, Gregory C Sharp, Qingya Zhao, Hiroki Shirato, and Steve B Jiang. Statistical analysis and correlation discovery of tumor respiratory motion. *Physics in Medicine and Biology*, 52(16):4761, 2007. 3.3.3

[256] SC Davies, AL Hill, RB Holmes, M Halliwell, and PC Jackson. Ultrasound quantitation of respiratory organ motion in the upper abdomen. *British Journal of Radiology*, 67(803):1096–1102, 1994.

[257] NR Ahmad, MS Huq, and BW Corn. Respiration-induced motion of the kidneys in whole abdominal radiotherapy: implications for treatment planning and late toxicity. *Radiotherapy and oncology*, 42(1):87–90, 1997. 3.3.3

[258] Wladyslaw Michal Gedroyc. New clinical applications of magnetic resonance-guided focused ultrasound. *Topics in Magnetic Resonance Imaging*, 17(3):189–194, 2006. 3.3.3, 9.1

[259] Atsuya Okada, Takamichi Murakami, Koji Mikami, Hiromitsu Onishi, Noboru Tanigawa, Taro Marukawa, and Hironobu Nakamura. A case of hepatocellular carcinoma treated by mr-guided focused ultrasound ablation with respiratory gating. *Magnetic Resonance in Medical Sciences*, 5(3):167–171, 2006. 3.3.3, 9.1, 9.2.2.2

[260] Erik-Jan Rijkhorst, Ian Rivens, Gail ter Haar, David Hawkes, and Dean Barratt. Effects of respiratory liver motion on heating for gated and model-based motion-compensated high-intensity focused ultrasound ablation. In *Medical Image Computing and Computer-Assisted Intervention–MICCAI 2011*, pages 605–612. Springer, 2011. 3.3.3, 9.1

[261] M Allen, I Rivens, A Visioli, and G Ter Haar. Focused ultrasound surgery (FUS): a non-invasive technique for the thermal ablation of liver metastases. In *Proceedings of the 2nd International Symposium on Therapeutic Ultrasound*, 2002. 3.3.3, 9.1

[262] Benjamin M Schwartz and Nathan J McDannold. Ultrasound echoes as biometric navigators. *Magnetic Resonance in Medicine*, 2012. 3.3.3, 9.1

[263] Frank Preiswerka, Valeria De Lucab, Patrik Arnolda, Zarko Celicaninc, Lorena Petruscad, Christine Tannerb, Rares Salomird, and Philippe C Cattina. Model-guided respiratory organ motion prediction of the liver from 2d ultrasound. *Medical Image Analysis*, 2013. 3.3.3, 9.5

[264] Frank Preiswerk, Patrik Arnold, Beat Fasel, and Philippe C Cattin. A bayesian framework for estimating respiratory liver motion from sparse measurements. In *Abdominal Imaging. Computational and Clinical Applications*, pages 207–214. Springer, 2012. 3.3.3, 9.5

[265] Kuo-Tai Teng, Kai-Hsiang Chang, Yung-Yaw Chen, and Tsu-Chin Tsao. Respiration induced liver motion tracking control for high intensity focused ultrasound treatment. In *Advanced Intelligent Mechatronics (AIM), 2012 IEEE/ASME International Conference on*, pages 57–62. IEEE, 2012. 3.3.3, 9.1

[266] Daisuke Kokuryo, Toshiva Kaihara, Etsuko Kumamoto, Susumu Fujii, and Kagayaki Kuroda. Method for target tracking in focused ultrasound surgery of liver using magnetic resonance filtered venography. In *Engineering in Medicine and*

*Biology Society, 2007. EMBS 2007. 29th Annual International Conference of the IEEE*, pages 2614–2617. IEEE, 2007. 3.3.3, 9.1

[267] M Ries, B Denis De Senneville, S Roujol, S Hey, G Maclair, MO Köhler, B Quesson, and CTW Moonen. Three dimensional motion compensation for real-time mri guided focused ultrasound treatment of abdominal organs. In *AIP Conference Proceedings*, volume 1215, page 239, 2010. 3.3.3

[268] WA N'Djin, NR Miller, JC Bamber, JY Chapelon, and D Melodelima. Effects of respiratory motion on in-vivo HIFU treatments: a comparative study in the liver. In *AIP Conference Proceedings*, volume 1215, page 203, 2010. 3.3.3

[269] Philippe Lourenço de Oliveira, Baudouin Denis de Senneville, Iulius Dragonu, and Chrit TW Moonen. Rapid motion correction in MR-guided high-intensity focused ultrasound heating using real-time ultrasound echo information. *NMR in Biomedicine*, 23(9):1103–1108, 2010. 3.3.3

[270] Emma J Harris, Naomi R Miller, Jeffrey C Bamber, J Richard N Symonds-Tayler, and Philip M Evans. Speckle tracking in a phantom and feature-based tracking in liver in the presence of respiratory motion using 4d ultrasound. *Physics in medicine and biology*, 55(12):3363, 2010. 3.3.3, 9.1

[271] J.W.S. Rayleigh. *The theory of sound: in two volumes*. Macmillan, 1896. 4.1.1

[272] J. Blauert and N. Xiang. *Acoustics for Engineers: Troy Lectures*. Springer Verlag, 2009. 4.1.1.1, 4.1.1.1

[273] Jan Ove Erstad. *Design of sparse and non-equally spaced arrays for medical ultrasound*. PhD thesis, University of Oslo, November 1994. 4.1.1.1, 4.1.1.2, 4.1.2.1, 4.1.2.1, 4.1.2.2, 4.2.1.1, 4.2.1.3

[274] Xiaobing Fan and Kullervo Hynynen. The effect of wave reflection and refraction at soft tissue interfaces during ultrasound hyperthermia treatments. *The Journal of the Acoustical Society of America*, 91:1727, 1992. 4.1.1.1, 4.1.1.4

[275] S. Holm. Simulation of acoustic fields from medical ultrasound transducers of arbitrary shape. In *Proc. Nordic Symp. in Physical Acoustics, Ustaoset*. Citeseer, 1995. 4.1.1.2, 4.3.4

[276] DW Herrin, TW Wu, and AF Seybert. Case study evaluation of the Rayleigh integral method. *The Journal of the Acoustical Society of America*, 108:2451, 2000.

[277] S. Holm. Ultrasim-a toolbox for ultrasound field simulation. In *Nordic Matlab Conference, Oslo, Norway*. Citeseer, 2001. 4.1.1.2, 4.3.4

[278] Tomoo Kamakura, Tsuneo Ishiwata, and Kazuhisa Matsuda. Model equation for strongly focused finite-amplitude sound beams. *The Journal of the Acoustical Society of America*, 107:3035, 2000.

[279] Victor Nascov and Petre Cătălin Logofătu. Fast computation algorithm for the rayleigh-sommerfeld diffraction formula using a type of scaled convolution. *Applied optics*, 48(22):4310–4319, 2009. 4.1.1.2

[280] Urvi Vyas and Douglas Christensen. Ultrasound beam simulations in inhomogeneous tissue geometries using the hybrid angular spectrum method. *Ultrasonics, Ferroelectrics and Frequency Control, IEEE Transactions on*, 59(6):1093–1100, 2012. 4.1.1.1, 4.1.1.4, 4.1.2.2, 4.1.2.3, 4.1.2.4, 8.1.3

[281] Peter R Stepanishen. Pulsed transmit/receive response of ultrasonic piezoelectric transducers. *The Journal of the Acoustical Society of America*, 69:1815, 1981. 4.1.1.2, 4.1.1.3

[282] VA Khokhlova, R Souchon, J Tavakkoli, OA Sapozhnikov, and D Cathignol. Numerical modeling of finite-amplitude sound beams: Shock formation in the near field of a CW plane piston source. *The Journal of the Acoustical Society of America*, 110:95, 2001.

[283] Tim Mellow. On the sound field of a resilient disk in free space. *The Journal of the Acoustical Society of America*, 123:1880, 2008.

[284] Sohrab Behnia, Amin Jafari, Farzan Ghalichi, and Ashkan Bonabi. Finite-element simulation of ultrasound brain surgery: effects of frequency, focal pressure, and scanning path in bone-heating reduction. *Central European Journal of Physics*, 6 (2):211–222, 2008. 4.1.1.2

[285] Jørgen Arendt Jensen. A model for the propagation and scattering of ultrasound in tissue. *The Journal of the Acoustical Society of America*, 89:182, 1991. 4.1.1.3, 4.3.1

[286] Jørgen Arendt Jensen and Niels Bruun Svendsen. Calculation of pressure fields from arbitrarily shaped, apodized, and excited ultrasound transducers. *Ultrasonics, Ferroelectrics and Frequency Control, IEEE Transactions on*, 39(2):262–267, 1992. 4.1.1.3, 4.3.1, 8.1.3

[287] GE Tupholme. Generation of acoustic pulses by baffled plane pistons. *Mathematika*, 16(209-224):149, 1969. 4.1.1.3

[288] Peter R Stepanishen. Transient radiation from pistons in an infinite planar baffle. *The Journal of the Acoustical Society of America*, 49:1629, 1971.

[289] PR Stepanishen. The time-dependent force and radiation impedance on a piston in a rigid infinite planar baffle. *The Journal of the Acoustical Society of America*, 49: 841, 1971. 4.1.1.3

[290] Urvi Vyas and Douglas Christensen. Ultrasound beam propagation using the hybrid angular spectrum method. In *Engineering in Medicine and Biology Society, 2008. EMBS 2008. 30th Annual International Conference of the IEEE*, pages 2526–2529. IEEE, 2008. 4.1.1.4, 4.1.2.4

[291] Robert J McGough. Rapid calculations of time-harmonic nearfield pressures produced by rectangular pistons. *The Journal of the Acoustical Society of America*, 115:1934, 2004. 4.1.1.5, 4.3.2, 7.1.1

[292] James F Kelly and Robert J McGough. A time-space decomposition method for calculating the nearfield pressure generated by a pulsed circular piston. *Ultrasonics, Ferroelectrics and Frequency Control, IEEE Transactions on*, 53(6):1150–1159, 2006.

[293] Duo Chen, James F Kelly, and Robert J McGough. A fast near-field method for calculations of time-harmonic and transient pressures produced by triangular pistons. *The Journal of the Acoustical Society of America*, 120:2450, 2006. 4.1.1.5

[294] James F Kelly and Robert J McGough. An annular superposition integral for axisymmetric radiators. *The Journal of the Acoustical Society of America*, 121:759, 2007.

[295] Duo Chen and Robert J McGough. A 2D fast near-field method for calculating near-field pressures generated by apodized rectangular pistons. *The Journal of the Acoustical Society of America*, 124:1526, 2008. 4.1.1.5, 4.3.2

[296] J.W. Goodman. *Introduction to Fourier optics*. Roberts & Company Publishers, 2nd edition, 2005. 4.1.2, 4.1.2.1, 4.1.2.1, 4.1.2.1, 4.1.2.2

[297] ME Schafer, PA Lewin, and JM Reid. Propagation through inhomogeneous media using the angular spectrum method. In *IEEE 1987 Ultrasonics Symposium*, pages 943–946, 1987. 4.1.2.1, 4.1.2.2, 4.1.2.3, 4.1.2.3, 4.1.2.3, 4.1.2.3

[298] C. Vecchio and P.A. Lewin. Finite amplitude acoustic propagation modeling using the extended angular spectrum method. In *Engineering in Medicine and Biology Society, 1992. Vol.14. Proceedings of the Annual International Conference of the IEEE*, volume 1, pages 362–363, Oct-1 Nov 1992. 4.1.2.3

[299] DP Orofino and PC Pedersen. Efficient angular spectrum decomposition of acoustic sources. I. Theory. *IEEE Transactions on Ultrasonics, Ferroelectrics and Frequency Control*, 40(3):238–249, 1993. 4.1.2.2

[300] D. Belgroune, JF de Belleval, and H. Djelouah. Modelling of the ultrasonic field by the angular spectrum method in presence of interface. *Ultrasonics*, 40(1-8): 297–302, 2002. 4.1.2.1, 4.1.2.3

[301] C. Vecchio and P.A. Lewin. Analysis of vibrating structures in nonlinear media using the extended angular spectrum method. In *Biomedical Engineering Days, 1992., Proceedings of the 1992 International*, pages 112–116, Aug 1992. doi: 10.1109/IBED.1992.247076.

[302] CJ Vecchio, ME Schafer, and PA Lewin. Prediction of ultrasonic field propagation through layered media using the extended angular spectrum method. *Ultrasound in medicine & biology*, 20(7):611, 1994. 4.1.2.2, 4.1.2.3

[303] M.E. Schafer and P.A. Lewin. Transducer characterization using the angular spectrum method. *The Journal of the Acoustical Society of America*, 85:2202, 1989. 4.1.2.3, 4.1.2.3, 4.1.2.3, 4.1.2.3

[304] Roger J Zemp, Jahangir Tavakkoli, and Richard SC Cobbold. Modeling nonlinear ultrasound propagation in tissue from array transducers and application to tissue harmonic imaging. In *Ultrasonics Symposium, 2002. Proceedings. 2002 IEEE*, volume 2, pages 1741–1744. IEEE, 2002. 4.1.2.3

[305] Roger J Zemp, Jahangir Tavakkoli, and Richard SC Cobbold. Modeling of nonlinear ultrasound propagation in tissue from array transducers. *The Journal of the Acoustical Society of America*, 113:139, 2003. 4.1.2.3

[306] Waiter Kessinger. Extended split-step fourier migration. In *1992 SEG Annual Meeting*, 1992. 4.1.2.4

[307] Lian-Jie Huang and Michael C Fehler. Accuracy analysis of the split-step fourier propagator: Implications for seismic modeling and migration. *Bulletin of the Seismological Society of America*, 88(1):18–29, 1998.

[308] PL Stoffa, Jacob T Fokkema, RM de Luna Freire, and WP Kessinger. Split-step fourier migration. *Geophysics*, 55(4):410–421, 1990. 4.1.2.4

[309] T.D. Mast, L.M. Hinkelman, L.A. Metlay, M.J. Orr, and R.C. Waag. Simulation of ultrasonic pulse propagation, distortion, and attenuation in the human chest wall. *The Journal of the Acoustical Society of America*, 106:3665, 1999. 4.2.1.2, 4.2.1.4

[310] S. Ginter. Numerical simulation of ultrasound-thermotherapy combining nonlinear wave propagation with broadband soft-tissue absorption. *Ultrasonics*, 37(10):693–696, 2000.

[311] Y. Ukai, S. Ishida, N. Hata, T. Azuma, S. Umemura, and T. Dohi. A 3-D simulation of focused ultrasound propagation for extracorporeal shock wave osteotomy. In *International Congress Series*, volume 1256, pages 658–663. Elsevier, 2003.

[312] S. Ginter, M. Liebler, E. Steiger, T. Dreyer, and R.E. Riedlinger. Full-wave modeling of therapeutic ultrasound: Nonlinear ultrasound propagation in ideal fluids. *The Journal of the Acoustical Society of America*, 111:2049, 2002. 4.2.2, 4.2.2.1, 4.2.2.2

[313] J.F. Aubry, M. Tanter, M. Pernot, J.L. Thomas, and M. Fink. Experimental demonstration of noninvasive transskull adaptive focusing based on prior computed tomography scans. *The Journal of the Acoustical Society of America*, 113:84, 2003. 4.3.7, 8.1.1.2

[314] B. Guo and J. Li. Waveform diversity based ultrasound system for hyperthermia treatment of breast cancer. *IEEE Transactions on Biomedical Engineering*, 55(2 Part 2):822–826, 2008. 4.2.1.2

[315] A Taflove and SC Hagness. *Computational Electrodynamics: The Finite-Difference Time-Domain Method*. Artech House, 3rd edition edition, 2005. 4.2.1.2, 5.1, 5.1.3, 5.1.3, 5.3, 5.3.1, 5.3.1.1, 5.3.2, 5.3.2.1

[316] Olgierd Cecil Zienkiewicz and Robert Leroy Taylor. *The finite element method*, volume 3. McGraw-hill London, 1977. 4.2.1.2

[317] F. Fahy. *Foundations of engineering acoustics*. Academic Pr, 2001. ISBN 0122476654. 4.2.1.3

[318] M.C.M. Wright. *Lecture notes on the mathematics of acoustics*. Imperial College Pr, 2005. 4.2.1.3

[319] N. Raghuvanshi, R. Narain, and M.C. Lin. Efficient and accurate sound propagation using adaptive rectangular decomposition. *IEEE Transactions on Visualization and Computer Graphics*, pages 789–801, 2009. 4.2.1.3

[320] MJ Lighthill. On sound generated aerodynamically. I. General theory. *Proceedings of the Royal Society of London. Series A, Mathematical and Physical Sciences*, 211 (1107):564–587, 1952. 4.2.1.3

[321] Olgun Adem Kaya, Ali Sahin, and Devkan Kaleci. Pressure field of rectangular transducers at finite amplitude in three dimensions. *Ultrasound in Medicine & Biology*, 32(2):271 – 280, 2006. 4.2.2, 4.2.2.1, 4.2.2.2

[322] Bengt O. Enflo and Claes M. Hedberg. *Theory of Nonlinear Acoustics in Fluids*, volume 67 of *Fluid Mechanics and its Applications*. Kluwer Academic Publishers, 2004. 4.2.2.1

[323] James A. TenCate. An experimental investigation of the nonlinear pressure field produced by a plane circular piston. *The Journal of the Acoustical Society of America*, 94(2):1084–1089, 1993. 4.2.2.1, 4.2.2.2, 4.3.1

[324] Y.-S. Lee and M. F. Hamilton. Time-domain modeling of pulsed finite-amplitude sound beams. *Acoustical Society of America Journal*, 97:906–917, February 1995. 4.2.2.1

[325] J. Hoffelner, H. Landes, and R. Lerch. Numerical simulation of nonlinear effects in high power ultrasound applications. In *Ultrasonics Symposium, 2001 IEEE*, volume 1, pages 645–648 vol.1, 2001.

[326] T. Kamakura. Two model equations for describing nonlinear sound beams. *Japanese Journal of Applied Physics*, 43(no. 5 b):2808–2812, 2004. 4.2.2.1, 4.2.2.2, 4.2.3.1, 4.2.3.1

[327] Yang-Sub Lee. *Numerical Solution of the KZK Equation for Pulsed Finite Amplitude Sound Beams in Thermoviscous Fluids*. PhD thesis, University of Texas, Austin, 1993. 4.2.2.2

[328] Xing Cai and Asmund Adegard. Parallel simulation of 3D nonlinear acoustic fields on a linux-cluster. *Cluster Computing, IEEE International Conference on*, 0:185, 2000. 4.2.2.2

[329] I. Kostin and G. Panasenko. Khokhlov–Zabolotskaya–Kuznetsov type equation: Nonlinear acoustics in heterogeneous media. *Comptes rendus-Mécanique*, 334(4): 220–224, 2006.

[330] G.F. Pinton and G.E. Trahey. A comparison of time-domain solutions for the full-wave equation and the parabolic wave equation for a diagnostic ultrasound transducer. *Ultrasonics, Ferroelectrics and Frequency Control, IEEE Transactions on*, 55(3):730–733, March 2008. ISSN 0885-3010. doi: 10.1109/TUFFC.2008.698. 4.2.3.1, 4.2.3.2

[331] Gianmarco Pinton, Jeremy Dahl, Stephen Rosenzweig, and Gregg Trahey. A heterogeneous nonlinear attenuating full-wave model of ultrasound. *Ultrasonics, Ferroelectrics and Frequency Control, IEEE Transactions on*, 56(3):474–488, 2009. 4.2.2.2, 4.2.3.1, 4.2.3.1, 4.2.3.2, 4.3.1, 5.2.1.4, 5.2.2.1

[332] P.J. Westervelt. Parametric acoustic array. *The Journal of the Acoustical Society of America*, 35:535, 1963. 4.2.3

[333] Jonathan S. Thierman. *Sources of difference frequency sound in a dual-frequency imaging system with implications for monitoring thermal surgery*. PhD thesis, Harvard University–MIT Division of Health Sciences and Technology., 2004. URL http://dspace.mit.edu/handle/1721.1/28762. 4.2.3.1

[334] I.M. Hallaj and R.O. Cleveland. FDTD simulation of finite-amplitude pressure and temperature fields for biomedical ultrasound. *JOURNAL-ACOUSTICAL SOCIETY OF AMERICA*, 105:7–12, 1999. 4.2.3.1

[335] I.M. Hallaj, R.O. Cleveland, and K. Hynynen. Simulations of the thermo-acoustic lens effect during focused ultrasound surgery. *The Journal of the Acoustical Society of America*, 109:2245, 2001.

[336] M. Cizek and J. Rozman. Acoustic wave equation simulation using FDTD. In *Radioelektronika, 2007. 17th International Conference*, pages 1–4, 2007. 4.2.3.1, 4.2.3.2, 5.2.1.4, 5.2.2.1

[337] J. Huang, R.G. Holt, R.O. Cleveland, and R.A. Roy. Experimental validation of a tractable numerical model for focused ultrasound heating in flow-through tissue phantoms. *The Journal of the Acoustical Society of America*, 116:2451, 2004. 4.2.3.2

[338] R.W. Graves. Simulating seismic wave propagation in 3D elastic media using staggered-grid finite differences. *Bulletin of the Seismological Society of America*, 86(4):1091, 1996. 4.2.4, 4.2.4.1, 4.2.4.1, 4.2.4.1, 4.3.3

[339] Y. Nagatani, H. Imaizumi, T. Fukuda, M. Matsukawa, Y. Watanabe, and T. Otani. Applicability of finite-difference time-domain method to simulation of wave propagation in cancellous bone. *Japanese Journal of Applied Physics*, 45(9A):7186–7190, 2006. 4.2.4.2

[340] Y. Nagatani, K. Mizuno, T. Saeki, M. Matsukawa, T. Sakaguchi, and H. Hosoi. Numerical and experimental study on the wave attenuation in bone–FDTD simulation of ultrasound propagation in cancellous bone. *Ultrasonics*, 48(6-7):607–612, 2008.

[341] M. Matsukawa, K. Mizuno, and Y. Nagatani. The fast wave propagation in bovine cancellous bone-experiments and simulation. *Journal of the Acoustical Society of America*, 123(5):3512, 2008.

[342] A. Hosokawa. Simulation of ultrasound propagation through bovine cancellous bone using elastic and Biot's finite-difference time-domain methods. *The Journal of the Acoustical Society of America*, 118:1782, 2005.

[343] G. Luo, J.J. Kaufman, A. Chiabrera, B. Bianco, J.H. Kinney, D. Haupt, J.T. Ryaby, and R.S. Siffert. Computational methods for ultrasonic bone assessment. *Ultrasound Med. Biol*, 25(5):823–830, 1999. 4.3.8

[344] T. Koizumi, K. Yamamoto, Y. Nagatani, H. Soumiya, T. Saeki, Y. Yaoi, and M. Matsukawa. Propagation of ultrasonic longitudinal wave in the cancellous bone covered by the subchondral bone of bovine femur. pages 146–149, Nov. 2008. doi: 10.1109/ULTSYM.2008.0035.

[345] RS Schechter, HH Chaskelis, RB Mignogna, and PP Delsanto. Real-time parallel computation and visualization of ultrasonic pulses in solids. *Science*, 265(5176): 1188, 1994.

[346] E. Bossy, M. Talmant, and P. Laugier. Three-dimensional simulations of ultrasonic axial transmission velocity measurement on cortical bone models. *The Journal of the Acoustical Society of America*, 115:2314, 2004. 4.3.3

[347] F. Padilla, E. Bossy, G. Haiat, F. Jenson, and P. Laugier. Numerical simulation of wave propagation in cancellous bone. *Ultrasonics*, 44:239–243, 2006. 4.3.3

[348] Y. Tanikaga, T. Sakaguchi, and Y. Watanabe. A Study on analysis of intracranial acoustic wave propagation by the finite difference time domain method. In *Proceedings of Forum Acusticum, Sevilla*, 2002. 4.2.4.1, 4.2.4.2

[349] Wilhelm Schaberle and B. Herwig. *Ultrasonography in Vascular Diagnosis: A Therapy-Oriented Textbook and Atlas*. Springer, 2005. 4.2.4.2

[350] C Payan, V Garnier, J Moysan, and PA Johnson. Applying nonlinear resonant ultrasound spectroscopy to improving thermal damage assessment in concrete. *The Journal of the Acoustical Society of America*, 121(4):EL125–EL130, 2007. 4.2.4.2

[351] LK Zarembo and VA Krasil'Nikov. Nonlinear phenomena in the propagation of elastic waves in solids. *Physics-Uspekhi*, 13(6):778–797, 1971.

[352] Koen EA Van Den Abeele, Alexander Sutin, Jan Carmeliet, and Paul A Johnson. Micro-damage diagnostics using nonlinear elastic wave spectroscopy (news). *Ndt & E International*, 34(4):239–248, 2001.

[353] KE-A Van Den Abeele, Paul A Johnson, and Alexander Sutin. Nonlinear elastic wave spectroscopy (news) techniques to discern material damage, part i: nonlinear wave modulation spectroscopy (nwms). *Research in nondestructive evaluation*, 12 (1):17–30, 2000.

[354] Marie Muller, Alexander Sutin, Robert Guyer, Maryline Talmant, Pascal Laugier, and Paul A Johnson. Nonlinear resonant ultrasound spectroscopy (nrus) applied to damage assessment in bone. *The Journal of the Acoustical Society of America*, 118:3946, 2005. 4.2.4.2

[355] Ferroelectrics IEEE Ultrasonics and Frequency Control Society. Ultrasound Software, 2013. URL http://www.ieee-uffc.org/ultrasonics/software.asp. 4.3

[356] Jørgen Arendt Jensen. Field: A program for simulating ultrasound systems. In *10TH NORDICBALTIC CONFERENCE ON BIOMEDICAL IMAGING, VOL. 4, SUPPLEMENT 1, PART 1: 351–353*. Citeseer, 1996. 4.3.1

[357] J. Jenne. FIeld II Simulation Program, 2013. URL http://field-ii.dk/. 4.3.1

[358] Jørgen Arendt Jensen, Darshan Gandhi, and William D O'Brien Jr. Ultrasound fields in an attenuating medium. In *Ultrasonics Symposium, 1993. Proceedings., IEEE 1993*, pages 943–946. IEEE, 1993. 4.3.1

[359] Jørgen Arendt Jensen. Ultrasound fields from triangular apertures. *The Journal of the Acoustical Society of America*, 100:2049, 1996.

[360] Jørgen Arendt Jensen. Simulating arbitrary-geometry ultrasound transducers using triangles. In *Ultrasonics Symposium, 1996. Proceedings., 1996 IEEE*, volume 2, pages 885–888. IEEE, 1996.

[361] Jørgen Arendt Jensen. A new approach to calculating spatial impulse responses. In *Ultrasonics Symposium, 1997. Proceedings., 1997 IEEE*, volume 2, pages 1755–1759. IEEE, 1997.

[362] Jørgen Arendt Jensen and Peter Munk. Computer phantoms for simulating ultrasound b-mode and cfm images. In *Acoustical Imaging*, pages 75–80. Springer, 1997.

[363] Jørgen Arendt Jensen. A new calculation procedure for spatial impulse responses in ultrasound. *The Journal of the Acoustical Society of America*, 105:3266, 1999.

[364] Jørgen Arendt Jensen. Linear description of ultrasound imaging systems. *Notes for the International Summer School on Advanced Ultrasound Imaging, Technical University of Denmark July*, 5, 1999.

[365] Jørgen Arendt Jensen and I Nikolov. Fast simulation of ultrasound images. In *Ultrasonics Symposium, 2000 IEEE*, volume 2, pages 1721–1724. IEEE, 2000.

[366] Jørgen Arendt Jensen. Speed-accuracy trade-offs in computing spatial impulse responses for simulating medical ultrasound imaging. *Journal of Computational Acoustics*, 9(03):731–744, 2001.

[367] Malene Schlaikjer, Søren Torp-Pedersen, and Jørgen Arendt Jensen. Simulation of rf data with tissue motion for optimizing stationary echo canceling filters. *Ultrasonics*, 41(6):415–419, 2003. 4.3.1

[368] John Gamelin, Anastasios Maurudis, Andres Aguirre, Fei Huang, Puyun Guo, Lihong V Wang, and Quing Zhu. A real-time photoacoustic tomography system for small animals. *Optics express*, 17(13):10489, 2009. 4.3.1

[369] Stephen A McAleavey, Manoj Menon, and Jarrod Orszulak. Shear-modulus estimation by application of spatially-modulated impulsive acoustic radiation force. *Ultrasonic imaging*, 29(2):87–104, 2007.

[370] Jesper Udesen, Michael Bachmann Nielsen, Kristina Rue Nielsen, and Jorgen Arendt Jensen. Examples of¡ i¿ in vivo¡/i¿ blood vector velocity estimation. *Ultrasound in medicine & biology*, 33(4):541–548, 2007.

[371] Torbjørn Hergum, Stian Langeland, Espen W Remme, and Hans Torp. Fast ultrasound imaging simulation in k-space. *Ultrasonics, Ferroelectrics and Frequency Control, IEEE Transactions on*, 56(6):1159–1167, 2009.

[372] Oliver Kutter, Ramtin Shams, and Nassir Navab. Visualization and GPU-accelerated simulation of medical ultrasound from CT images. *Computer methods and programs in biomedicine*, 94(3):250–266, 2009.

[373] Thanassis X Misaridis, Kim Gammelmark, Christian H Jørgensen, Niklas Lindberg, Anders H Thomsen, Morten H Pedersen, and Jørgen A Jensen. Potential of coded excitation in medical ultrasound imaging. *Ultrasonics*, 38(1):183–189, 2000.

[374] Hang Gao, Hon Fai Choi, Piet Claus, Steven Boonen, Siegfried Jaecques, G Harry van Lenthe, Georges Van der Perre, Walter Lauriks, and Jan D'hooge. A fast convolution-based methodology to simulate 2D/3D cardiac ultrasound images. *Ultrasonics, Ferroelectrics and Frequency Control, IEEE Transactions on*, 56(2): 404–409, 2009.

[375] Ramtin Shams, Richard Hartley, and Nassir Navab. Real-time simulation of medical ultrasound from ct images. In *Medical Image Computing and Computer-Assisted Intervention–MICCAI 2008*, pages 734–741. Springer, 2008.

[376] María J Ledesma-Carbayo, Jan Kybic, Manuel Desco, Andrés Santos, M Suhling, Patrick Hunziker, and Michael Unser. Spatio-temporal nonrigid registration for ultrasound cardiac motion estimation. *Medical Imaging, IEEE Transactions on*, 24 (9):1113–1126, 2005. 4.3.1

[377] Xiaozheng Zeng and Robert J McGough. Optimal simulations of ultrasonic fields produced by large thermal therapy arrays using the angular spectrum approach. *The Journal of the Acoustical Society of America*, 125:2967, 2009. 4.3.2

[378] Matthew R Jennings and Robert J McGough. Using FOCUS to determine the radiation impedance for square transducers. In *AIP Conference Proceedings*, volume 1481, page 149, 2012.

[379] Yi Zhu, Thomas L Szabo, and Robert J McGough. A comparison of ultrasound image simulations with focus and field ii. In *Ultrasonics Symposium (IUS), 2012 IEEE International*, pages 1694–1697. IEEE, 2012. 4.3.2, 7.1.1

[380] Robert J McGough. FOCUS: Fast Object-oriented C++ Ultrasound Simulator, 2013. URL http://www.egr.msu.edu/~fultras-web/. 4.3.2

[381] Xiaozheng Zeng and Robert J McGough. Evaluation of the angular spectrum approach for simulations of near-field pressures. *The Journal of the Acoustical Society of America*, 123:68, 2008. 4.3.2, 8.1.2.2

[382] James F Kelly and Robert J McGough. Transient fields generated by spherical shells in viscous media. In *AIP Conference Proceedings*, volume 1113, page 210, 2009.

[383] Mario Hlawitschka, Robert J McGough, Katherine W Ferrara, and Dustin E Kruse. Fast ultrasound beam prediction for linear and regular two-dimensional arrays. *Ultrasonics, Ferroelectrics and Frequency Control, IEEE Transactions on*, 58(9): 2001–2012, 2011. 4.3.2, 7.1.1

[384] Emmanuel Bossy, Frédéric Padilla, Françoise Peyrin, and Pascal Laugier. Three-dimensional simulation of ultrasound propagation through trabecular bone structures measured by synchrotron microtomography. *Physics in medicine and biology*, 50(23):5545, 2005. 4.3.3

[385] E. Bossy. SimSonic: FDTD simulation of ultrasound propagation, 2013. URL http://www.loa.espci.fr/_michael/fr/acel/aceltest.htm. 4.3.3

[386] Jean Virieux. P-sv wave propagation in heterogeneous media: Velocity-stress finite-difference method. *Geophysics*, 51(4):889–901, 1986. 4.3.3

[387] Emmanuel Bossy, Maryline Talmant, and Pascal Laugier. Effect of bone cortical thickness on velocity measurements using ultrasonic axial transmission: A 2D simulation study. *The Journal of the Acoustical Society of America*, 112:297, 2002. 4.3.3

[388] Frederic Padilla, Emmanuel Bossy, and Pascal Laugier. Simulation of ultrasound propagation through three-dimensional trabecular bone structures: comparison with experimental data. *Japanese journal of applied physics*, 45:6496, 2006.

[389] Emmanuel Bossy, Pascal Laugier, Françoise Peyrin, and Frédéric Padilla. Attenuation in trabecular bone: A comparison between numerical simulation and experimental results in human femur. *The Journal of the Acoustical Society of America*, 122:2469, 2007.

[390] Christiano Bittencourt Machado, Wagner Coelho de Albuquerque Pereira, Maryline Talmant, Frédéric Padilla, and Pascal Laugier. Computational evaluation of the compositional factors in fracture healing affecting ultrasound axial transmission measurements. *Ultrasound in medicine & biology*, 36(8):1314–1326, 2010.

[391] Christiano Bittencourt Machado, Wagner Coelho de A Pereira, Mathilde Granke, Maryline Talmant, Frédéric Padilla, and Pascal Laugier. Experimental and simulation results on the effect of cortical bone mineralization in ultrasound axial transmission measurements: A model for fracture healing ultrasound monitoring. *Bone*, 48(5):1202–1209, 2011.

[392] Didier Cassereau, Pierre Nauleau, Quentin Grimal, Jean-Gabriel Minonzio, Aniss Bendjoudi, Emmanuel Bossy, and Pascal Laugier. Coupling of finite difference elastodynamic and semi-analytic rayleigh integral codes for the modeling of ultrasound propagation at the hip. *The Journal of the Acoustical Society of America*, 133(5):3498–3498, 2013.

[393] Didier Cassereau, Pierre Nauleau, Aniss Bendjoudi, Jean-Gabriel Minonzio, Pascal Laugier, Emmanuel Bossy, and Quentin Grimal. A hybrid FDTD-Rayleigh integral computational method for the simulation of the ultrasound measurement of proximal femur. *Ultrasonics*, 2013. 4.3.3

[394] S. Holm. Ultrasim: interactive ultrasound field simulation, 2013. URL http://www.mn.uio.no/ifi/english/research/groups/dsb/resources/software/ultrasim/index.html. 4.3.4

[395] K. Epasinghe and S. Holm. Simulation of 3D acoustic fields on a concurrent computer. In *Proceedings from the Nordic symposium on Physical Acoustics*, 1996. 4.3.4

[396] Trond Varslot and Gunnar Taraldsen. Computer simulation of forward wave propagation in soft tissue. *Ultrasonics, Ferroelectrics and Frequency Control, IEEE Transactions on*, 52(9):1473–1482, 2005. 4.3.5

[397] Trond Varslot and Svein-Erik Masoy. Forward propagation of acoustic pressure pulses in 3d soft biological tissue. *Modeling, Identification and Control*, 27(3): 181–200, 2006. 4.3.5

[398] T. Varslot. Abersim: ultrasound simulation software, 2013. URL http://www.ntnu.no/isb/abersim. 4.3.5

[399] Trond Varslot, S-E Masoy, Tonni F Johansen, and Bjørn Angelsen. Aberration in nonlinear acoustic wave propagation. *Ultrasonics, Ferroelectrics and Frequency Control, IEEE Transactions on*, 54(3):470–479, 2007. 4.3.5

[400] Martijn Egbert Frijlink, Halvard Kaupang, Trond Varslot, and S-E Masoy. Abersim: a simulation program for 3D nonlinear acoustic wave propagation for arbitrary pulses and arbitrary transducer geometries. In *Ultrasonics Symposium, 2008. IUS 2008. IEEE*, pages 1282–1285. IEEE, 2008.

[401] T Varslot, G Taraldsen, TF Johansen, and BAJ Angelsen. Computer simulation of forward wave propagation in non-linear, heterogeneous, absorbing tissue. In *Ultrasonics Symposium, 2001 IEEE*, volume 2, pages 1193–1196. IEEE, 2001.

[402] Safiye Dursun, Trond Varslot, Tonni Johansen, Bjørn Angelsen, and Hans Torp. Fast 3D simulation of 2nd harmonic ultrasound field from arbitrary transducer geometries. *Measurements*, 20:0, 2005.

[403] Svein-Erik Måsøy, Trond Varslot, and Bjørn Angelsen. Iteration of transmit-beam aberration correction in medical ultrasound imaging. *The Journal of the Acoustical Society of America*, 117:450, 2005.

[404] Svein-Erik Måsøy, Bjørn Angelsen, and Trond Varslot. Variance analysis of arrival time and amplitude estimates from random speckle signal. *The Journal of the Acoustical Society of America*, 121:286, 2007. 4.3.5

[405] Bradley E Treeby and Benjamin T Cox. k-wave: Matlab toolbox for the simulation and reconstruction of photoacoustic wave fields. *Journal of biomedical optics*, 15 (2):021314–021314, 2010. 4.3.6

[406] Bradley E Treeby and BT Cox. Modeling power law absorption and dispersion for acoustic propagation using the fractional laplacian. *The Journal of the Acoustical Society of America*, 127:2741, 2010.

[407] Bradley E Treeby, Jiri Jaros, Alistair P Rendell, and BT Cox. Modeling nonlinear ultrasound propagation in heterogeneous media with power law absorption using a k-space pseudospectral method. *The Journal of the Acoustical Society of America*, 131:4324, 2012. 4.3.6

[408] B. Treeby. k-Wave: A MATLAB toolbox for the time-domain simulation of acoustic waves, 2013. URL http://www.k-wave.org/. 4.3.6

[409] Makoto Tabei, T Douglas Mast, and Robert C Waag. A k-space method for coupled first-order acoustic propagation equations. *The Journal of the Acoustical Society of America*, 111:53, 2002. 4.3.6, 5.1.4

[410] T Douglas Mast, Laurent P Souriau, D-LD Liu, Makoto Tabei, Adrian I Nachman, and Robert C Waag. A k-space method for large-scale models of wave propagation in tissue. *Ultrasonics, Ferroelectrics and Frequency Control, IEEE Transactions on*, 48(2):341–354, 2001. 4.3.6, 5.1.4

[411] QH Liu. The pstd algorithm: A time-domain method requiring only two cells per wavelength. *Microwave and Optical Technology Letters*, 15(3):158–165, 1997. 4.3.6

[412] Bradley E Treeby, Edward Z Zhang, and BT Cox. Photoacoustic tomography in absorbing acoustic media using time reversal. *Inverse Problems*, 26(11):115003, 2010. 4.3.6

[413] Bradley E Treeby and BT Cox. A k-space green's function solution for acoustic initial value problems in homogeneous media with power law absorption. *The Journal of the Acoustical Society of America*, 129:3652, 2011.

[414] Benjamin T Cox and Bradley E Treeby. Artifact trapping during time reversal photoacoustic imaging for acoustically heterogeneous media. *Medical Imaging, IEEE Transactions on*, 29(2):387–396, 2010.

[415] BT Cox and PC Beard. Fast calculation of pulsed photoacoustic fields in fluids using k-space methods. *The Journal of the Acoustical Society of America*, 117:3616, 2005.

[416] BT Cox, S Kara, SR Arridge, and PC Beard. k-space propagation models for acoustically heterogeneous media: Application to biomedical photoacoustics. *The Journal of the Acoustical Society of America*, 121:3453, 2007. 4.3.6

[417] Mathieu Pernot, Jean-Francois Aubry, Mickael Tanter, Jean-Louis Thomas, and Mathias Fink. Experimental validation of 3d finite differences simulations of ultrasonic wave propagation through the skull. In *Ultrasonics Symposium, 2001 IEEE*, volume 2, pages 1547–1550. IEEE, 2001. 4.3.7

[418] Mathieu Pernot, Jean-François Aubry, Mickael Tanter, and Mathias Fink. Predicting and preventing skull overheating in non invasive brain hifu treatment protocols. In *AIP Conference Proceedings*, volume 754, page 147, 2005.

[419] Thu-Mai Nguyen, J-L Gennisson, Mathieu Couade, David Touboul, Philippe Humbert, Jeremy Bercoff, Mathias Fink, and Mickaël Tanter. Shear wave propagation in complex sub wavelength tissue geometries: Theoretical and experimental implications in the framework of cornea and skin shear wave imaging. In *Ultrasonics Symposium (IUS), 2010 IEEE*, pages 1145–1148. IEEE, 2010. 4.3.7

[420] M Tanter. Finite differences simulation of the ACoustic and ELastic Waves (ACEL) equations, 2013. URL http://www.loa.espci.fr/_michael/fr/acel/aceltest.htm. 4.3.7

[421] JJ Choi, M Pernot, TR Brown, SA Small, and EE Konofagou. Spatio-temporal analysis of molecular delivery through the blood–brain barrier using focused ultrasound. *Physics in medicine and biology*, 52(18):5509, 2007. 4.3.7

[422] F Marquet, M Pernot, JF Aubry, G Montaldo, L Marsac, M Tanter, and M Fink. Non-invasive transcranial ultrasound therapy based on a 3d ct scan: protocol validation and in vitro results. *Physics in medicine and biology*, 54(9):2597, 2009. 8.1.1.3

[423] Javier Brum, J-L Gennisson, Thu-Mai Nguyen, Nicolas Benech, Mathias Fink, Mickael Tanter, and Carlos Negreira. Application of 1D transient elastography for the shear modulus assessment of thin-layered soft tissue: comparison with supersonic shear imaging technique. *Ultrasonics, Ferroelectrics and Frequency Control, IEEE Transactions on*, 59(4):703–714, 2012.

[424] Bastien Arnal, Mathieu Pernot, and Mickael Tanter. Experimental reverse time migration for imaging of elasticity changes. In *Ultrasonics Symposium (IUS), 2010 IEEE*, pages 1039–1042. IEEE, 2010.

[425] Mickaël Tanter, David Touboul, J-L Gennisson, Jeremy Bercoff, and Mathias Fink. High-resolution quantitative imaging of cornea elasticity using supersonic shear imaging. *Medical Imaging, IEEE Transactions on*, 28(12):1881–1893, 2009.

[426] Youliana Younan, Thomas Deffieux, Benoit Larrat, Mathias Fink, Mickael Tanter, and Jean-Francois Aubry. Influence of the pressure field distribution in transcranial ultrasonic neurostimulation. *Medical physics*, 40:082902, 2013.

[427] N Dominguez and V Gibiat. Non-destructive imaging using the time domain topological energy method. *Ultrasonics*, 50(3):367–372, 2010.

[428] ARNAUD DERODE, MICKAËL TANTER, ARNAUD TOURIN, LAURENT SANDRIN, and MATHIAS FINK. Numerical and experimental time-reversal of acoustic waves in random media. *Journal of Computational acoustics*, 9(03):993–1003, 2001.

[429] M Pernot, J Porquet, C Saint Olive, F Vignon, D Cassereau, JF Aubry, M Tanter, and M Fink. 3d finite difference simulation of coupled acoustic wave and bio-heat equations: skull heating prediction for non invasive brain hifu therapy". *Proc WCU Paris*, 2003.

[430] Nicolas Dominguez, V Gibiat, and JL Arnaud. Flaw imaging with ultrasound: the time domain topological gradient method. In *AIP Conference Proceedings*, volume 760, page 859, 2005.

[431] M Pernot, J-F Aubry, M Tanter, F Andre, and M Fink. Prediction of the skull overheating during high intensity focused ultrasound transcranial brain therapy. In *Ultrasonics Symposium, 2004 IEEE*, volume 2, pages 1005–1008. IEEE, 2004. 4.3.7

[432] Jonathan J Kaufman, Gangming Luo, and Robert S Siffert. Ultrasound simulation in bone. *Ultrasonics, Ferroelectrics and Frequency Control, IEEE Transactions on*, 55(6):1205–1218, 2008. 4.3.8

[433] CyberLogic Inc. Wave: Software for computational ultrasonics, 2013. URL http://www.cyberlogic.org/software.html. 4.3.8

[434] Hengchang Jing. Improved array SAFT imaging algorithm. In *Instrumentation & Measurement, Sensor Network and Automation (IMSNA), 2012 International Symposium on*, volume 1, pages 147–150. IEEE, 2012. 4.3.8

[435] Al-Hassan Aly, Howard J Ginsberg, and Richard SC Cobbold. On ultrasound imaging for guided screw insertion in spinal fusion surgery. *Ultrasound in medicine & biology*, 37(4):651–664, 2011.

[436] MF Souzanchi, PE Palacio-Mancheno, L Cardoso, and SC Cowin. The fabric anisotropy effect on elastic and yield behavior of the human calcaneus trabecular bone.

[437] QIUFENG LI, XUEJUAN YANG, PAN HUANG, and YIN LIAO. Ultrasonic array imaging method for concrete materials. *Journal of Theoretical and Applied Information Technology*, 47(2), 2013.

[438] Vincent Le Floch, Donald J McMahon, Gangming Luo, Adi Cohen, Jonathan J Kaufman, Elizabeth Shane, and Robert S Siffert. Ultrasound simulation in the distal radius using clinical high-resolution peripheral-ct images. *Ultrasound in medicine & biology*, 34(8):1317–1326, 2008.

[439] Arthur H Chan, Victor Y Fujimoto, Donald E Moore, Roy W Martin, and Shahram Vaezy. An image-guided high intensity focused ultrasound device for uterine fibroids treatment. *Medical physics*, 29:2611, 2002.

[440] R Barkmann, S Lüsse, B Stampa, S Sakata, M Heller, and C-C Glüer. Assessment of the geometry of human finger phalanges using quantitative ultrasound in vivo. *Osteoporosis international*, 11(9):745–755, 2000.

[441] Jonathan J Kaufman, Gangming Luo, Bruno Bianco, Alessandro Chiabrera, and Robert S Siffert. Computational methods for NDT. In *Nondestructive Evaluation Techniques for Aging Infrastructures & Manufacturing*, pages 173–181. International Society for Optics and Photonics, 1999.

[442] AS Aula, J Töyräs, MA Hakulinen, and JS Jurvelin. Effect of bone marrow on acoustic properties of trabecular bone-3D finite difference modeling study. *Ultrasound in medicine & biology*, 35(2):308–318, 2009.

[443] SHamid R Hosseini, Xinliang Zheng, and Shahram Vaezy. Effects of gas pockets on high-intensity focused ultrasound field. *Ultrasonics, Ferroelectrics and Frequency Control, IEEE Transactions on*, 58(6):1203–1210, 2011.

[444] J Garcia-Alvarez, Y Yañez, JL Prego, A Turo, JA Chavez, MJ Garcia, and J Salazar. Noise level analysis in buffer rod geometries for ultrasonic sensors. *Ultrasonics*, 44:e1093–e1100, 2006.

[445] Jonathan J Kaufman, Gangming Luo, and Robert S Siffert. On the relative contributions of absorption and scattering to ultrasound attenuation in trabecular bone: A simulation study. In *Ultrasonics, 2003 IEEE Symposium on*, volume 2, pages 1519–1523. IEEE, 2003.

[446] SHR Hosseini, Xinliang Zheng, and Shahram Vaezy. P1B-8 experimental investigation of the effects of gas pockets on HIFU field. In *Ultrasonics Symposium, 2007. IEEE*, pages 1309–1312. IEEE, 2007.

[447] Javier García-Álvarez, Miguel J García-Hernández, Daniel F Novoa-Díaz, Antoni Turó Peroy, Juan Antonio Chávez Domínguez, and Jordi Salazar Soler. Resizing buffer rods for ultrasound testing of food products with acoustic noise considerations. *Ultrasonics*, 2012.

[448] R Barkman, W Timm, S Sakata, M Heller, and C-C Gluer. Simulation of ultrasound interaction with bone structure based on 3D high-resolution-magnetic-resonance- and micro-CT-images. In *Engineering in Medicine and Biology Society, 2000. Proceedings of the 22nd Annual International Conference of the IEEE*, volume 4, pages 2666–2669. IEEE, 2000.

[449] M Torres and FR Montero de Espinosa. Ultrasonic band gaps and negative refraction. *Ultrasonics*, 42(1):787–790, 2004.

[450] ZQ Chen, JC Hermanson, MA Shear, and PC Pedersen. Ultrasonic monitoring of interfacial motion of condensing and non-condensing liquid films. *Flow Measurement and Instrumentation*, 16(6):353–364, 2005.

[451] Jonathan J Kaufman, Gangming Luo, and Robert S Siffert. Ultrasound simulation for 3D-axisymmetric models. In *Ultrasonics, 2003 IEEE Symposium on*, volume 2, pages 2065–2068. IEEE, 2003. 4.3.8

[452] Gregory L Wojcik, DK Vaughan, N Abboud, and J Mould Jr. Electromechanical modeling using explicit time-domain finite elements. In *Ultrasonics Symposium, 1993. Proceedings., IEEE 1993*, pages 1107–1112. IEEE, 1993. 4.3.9

[453] G Wojcik, J Mould Jr, N Abboud, M Ostromogilsky, and D Vaughan. Nonlinear modeling of therapeutic ultrasound. In *Ultrasonics Symposium, 1995. Proceedings., 1995 IEEE*, volume 2, pages 1617–1622. IEEE, 1995.

[454] Najib N Abboud, Gregory L Wojcik, David K Vaughan, John Mould Jr, David J Powell, and Lisa Nikodym. Finite element modeling for ultrasonic transducers. In *Medical Imaging'98*, pages 19–42. International Society for Optics and Photonics, 1998.

[455] John C Mould, Gregory L Wojcik, Laura M Carcione, Makoto Tabei, T Douglas Mast, and Robert C Waag. Validation of fft-based algorithms for large-scale modeling of wave propagation in tissue. In *Ultrasonics Symposium, 1999. Proceedings. 1999 IEEE*, volume 2, pages 1551–1556. IEEE, 1999.

[456] Gerald Harvey and Anthony Gachagan. Simulation and measurement of nonlinear behavior in a high-power test cell. *Ultrasonics, Ferroelectrics and Frequency Control, IEEE Transactions on*, 58(4):808–819, 2011. 4.3.9

[457] Weidlinger Associates. PZFlex, 2013. URL http://www.pzflex.com/. 4.3.9

[458] Bogdan Piwakowski and Khalid Sbai. A new approach to calculate the field radiated from arbitrarily structured transducer arrays. *Ultrasonics, Ferroelectrics and Frequency Control, IEEE Transactions on*, 46(2):422–440, 1999. 4.3.10

[459] Axel Guiroy, Dominique Certon, Philippe Boy, Marc Lethiecq, and Franck Levassort. 2D numerical modeling for transducers with combined pseudospectral and finite difference methods: application to high frequency linear arrays. In *Acoustical Imaging*, pages 351–361. Springer, 2012.

[460] Johan E Carlson, Jesper Martinsson, F Hagglund, and Amin Saremi. Calibration of simulation models for ultrasonic transducers based on implicit calibration. In *Ultrasonics Symposium, 2008. IUS 2008. IEEE*, pages 1528–1531. IEEE, 2008. 4.3.10

[461] B. Piwakowski. DREAM: Discrete REpresentation Array Modelling, 2013. URL http://www.signal.uu.se/Toolbox/dream/index.shtml. 4.3.10

[462] Fredrik Lingvall and Tomas Olofsson. On time-domain model-based ultrasonic array imaging. *Ultrasonics, Ferroelectrics and Frequency Control, IEEE Transactions on*, 54(8):1623–1633, 2007. 4.3.10

[463] L Satyanarayan, Ajith Muralidharan, Chittivenkata Krishnamurthy, and Krishnan Balasubramaniam. Application of a matched filter approach for finite aperture transducers for the synthetic aperture imaging of defects. *Ultrasonics, Ferroelectrics and Frequency Control, IEEE Transactions on*, 57(6):1368–1382, 2010.

[464] E Wennerstrom, Tadeusz Stepinski, and Tomas Olofsson. An iterative synthetic aperture imaging algorithm with correction of diffraction effects. *Ultrasonics, Ferroelectrics and Frequency Control, IEEE Transactions on*, 53(5):1008–1017, 2006.

[465] Shuhui Bu, Zhenbao Liu, Tsuyoshi Shiina, and Kazuhiko Fukutani. Matrix compression and compressed sensing reconstruction for photoacoustic tomography. *Electronics and Electrical Engineering*, 18(9):101–104, 2012.

[466] Adrien Marion and Didier Vray. Toward a real-time simulation of ultrasound image sequences based on a 3-d set of moving scatterers. *Ultrasonics, Ferroelectrics and Frequency Control, IEEE Transactions on*, 56(10):2167–2179, 2009.

[467] Meng-Lin Li, Yi-Chieh Tseng, and Chung-Chih Cheng. Model-based correction of finite aperture effect in photoacoustic tomography. *Optics Express*, 18(25):26285–26292, 2010.

[468] B Piwakowski and B Delannoy. Method for computing spatial pulse response: Time-domain approach. *The Journal of the Acoustical Society of America*, 86:2422, 1989. 4.3.10

[469] Kane Yee. Numerical solution of initial boundary value problems involving maxwell's equations in isotropic media. *Antennas and Propagation, IEEE Transactions on*, 14(3):302–307, 1966. 5.1

[470] David B Davidson. *Computational electromagnetics for RF and microwave engineering*. Cambridge University Press, 2005. 5.1.2, 5.1.4

[471] Thomas Rylander, Anders Bondeson, and Pär Ingelström. *Computational electromagnetics*, volume 51. Springer, 2012. 5.1.4

[472] Dennis M Sullivan. *Electromagnetic simulation using the FDTD method*. Wiley-IEEE Press, 2013. 5.1.2

[473] Richard Courant, Kurt Friedrichs, and Hans Lewy. On the partial difference equations of mathematical physics. *IBM journal of Research and Development*, 11(2):215–234, 1967. 5.1.3

[474] Ercılia Sousa. The controversial stability analysis. *Applied Mathematics and Computation*, 145(2):777–794, 2003. 5.1.3

[475] Steven G Johnson. Notes on perfectly matched layers (PMLs). *Lecture notes, Massachusetts Institute of Technology, Massachusetts*, 2008. 5.3, 5.3.2, 5.3.2.1

[476] Gerrit Mur. Absorbing boundary conditions for the finite-difference approximation of the time-domain electromagnetic-field equations. *Electromagnetic Compatibility, IEEE Transactions on*, (4):377–382, 1981. 5.3.1, 5.3.1.1

[477] Björn Engquist and Andrew Majda. Absorbing boundary conditions for numerical simulation of waves. *Proceedings of the National Academy of Sciences*, 74(5):1765–1766, 1977. 5.3.1

[478] D Zhou, WP Huang, CL Xu, DG Fang, and B Chen. The perfectly matched layer boundary condition for scalar finite-difference time-domain method. *Photonics Technology Letters, IEEE*, 13(5):454–456, 2001. 5.3.2, 5.3.2.1, 5.3.2.1, 5.3.2.1, 5.3.2.1

[479] Theodoros K Katsibas and Christos S Antonopoulos. An efficient PML absorbing medium in FDTD simulations of acoustic scattering in lossy media. In *Ultrasonics Symposium, 2002. Proceedings. 2002 IEEE*, volume 1, pages 551–554. IEEE, 2002. 5.3.2, 5.3.2.1

[480] J.P. Berenger. A perfectly matched layer for the absorption of electromagnetic waves. *Journal of computational physics*, 114(2):185–200, 1994. 5.3.2

[481] Gianmarco F Pinton. *Numerical methods for nonlinear wave propagation in ultrasound*. PhD thesis, 2007. 5.3.2, 5.3.2.1, 5.3.2.1

[482] Weng Cho Chew and William H Weedon. A 3D perfectly matched medium from modified maxwell's equations with stretched coordinates. *Microwave and optical technology letters*, 7(13):599–604, 1994. 5.3.2.1

[483] Jason Sanders and Edward Kandrot. *CUDA by example: an introduction to general-purpose GPU programming*. Addison-Wesley Professional, 2010. 6.2.1, 6.2.2, 6.2.2.1

[484] Rohit Chandra, Ramesh Menon, Leo Dagum, David Kohr, Dror Maydan, and Jeff McDonald. *Parallel programming in OpenMP*. Morgan Kaufmann, 2000. 6.2.1.1

[485] Barbara Chapman, Gabriele Jost, and Ruud Van Der Pas. *Using OpenMP: portable shared memory parallel programming*, volume 10. MIT press, 2008. 6.2.1, 6.2.1.1

[486] Paulius Micikevicius. 3d finite difference computation on gpus using cuda. In *Proceedings of 2nd Workshop on General Purpose Processing on Graphics Processing Units*, pages 79–84. ACM, 2009. 6.2.2.1, 6.2.2.2

[487] J Cohen and M Jeroen Molemaker. A fast double precision CFD code using CUDA. *Parallel Computational Fluid Dynamics: Recent Advances and Future Directions*, pages 414–429, 2009. 6.2.2.1

[488] Rob Farber. *CUDA application design and development*. Morgan Kaufmann, 2011. 6.2.2.1

[489] David B Kirk and W Hwu Wen-mei. *Programming massively parallel processors: a hands-on approach*. Morgan Kaufmann, 2010. 6.2.2.1

[490] Rached Abdelkhalek, Henri Calandra, Olivier Coulaud, Jean Roman, and Guillaume Latu. Fast seismic modeling and reverse time migration on a GPU cluster. In *High Performance Computing & Simulation, 2009. HPCS'09. International Conference on*, pages 36–43. IEEE, 2009. 6.2.2.1

[491] Vaclav Simek, Radim Dvorak, Frantisek Zboril, and Jiri Kunovsky. Towards accelerated computation of atmospheric equations using cuda. In *Computer Modelling*

*and Simulation, 2009. UKSIM'09. 11th International Conference on*, pages 449–454. IEEE, 2009.

[492] Julien C Thibault and Inanc Senocak. Cuda implementation of a navier-stokes solver on multi-gpu desktop platforms for incompressible flows. In *Proceedings of the 47th AIAA Aerospace Sciences Meeting*, pages 2009–758, 2009.

[493] Davy Pissoort, Chen Wang, Hany Fahmy, and Amolak Badesha. Using cuda enabled fdtd simulations to solve multi-gigahertz emi challenges. In *Electromagnetic Compatibility (APEMC), 2010 Asia-Pacific Symposium on*, pages 912–915. IEEE, 2010.

[494] Min Li. Parallel fdtd simulation using cuda. In *Computer, Mechatronics, Control and Electronic Engineering (CMCE), 2010 International Conference on*, volume 1, pages 196–199. IEEE, 2010.

[495] Shane Ryoo, Christopher I Rodrigues, Sara S Baghsorkhi, Sam S Stone, David B Kirk, and Wen-mei W Hwu. Optimization principles and application performance evaluation of a multithreaded gpu using cuda. In *Proceedings of the 13th ACM SIGPLAN Symposium on Principles and practice of parallel programming*, pages 73–82. ACM, 2008. 6.2.2.1

[496] Harry H Pennes. Analysis of tissue and arterial blood temperatures in the resting human forearm. *Journal of applied physiology*, 1(2):93–122, 1948. 6.3.2

[497] ANTJ Kotte, GMJ Van Leeuwen, and JJW Lagendijk. Modelling the thermal impact of a discrete vessel tree. *Physics in Medicine and Biology*, 44(1):57, 1999. 6.3.2

[498] Wei Jie Song, Sheldon Weinbaum, and Latif M Jiji. A theoretical model for peripheral tissue heat transfer using the bioheat equation of weinbaum and jiji. *Journal of biomechanical engineering*, 109(1):72–78, 1987. 6.3.2

[499] Stephen A Sapareto and William C Dewey. Thermal dose determination in cancer therapy. *International Journal of Radiation Oncology\* Biology\* Physics*, 10(6): 787–800, 1984. 6.3.2, 9.2.3, 10.2.3

[500] Esra Neufeld. *High resolution hyperthermia treatment planning*. Hartung-Gorre Verlag, 2008. 6.3.2, 6.3.3, 8.3.3

[501] Esra Neufeld, Sven Kühn, Gabor Szekely, and Niels Kuster. Measurement, simulation and uncertainty assessment of implant heating during mri. *Physics in medicine and biology*, 54(13):4151, 2009. 6.3.2, 7.2.4

[502] American Institute of Ultrasound in Medicine. *Methods for specifying acoustic properties of tissue mimicking phantoms and objects*. AIUM Technical Standards Committee, 1995. Bibliography: p. 12-13. 7.2.1.3

[503] Ernest L Madsen, Fang Dong, Gray R Frank, Brian S Garra, Keith A Wear, Thaddeus Wilson, James A Zagzebski, Heather L Miller, K Kirk Shung, SH Wang, et al. Interlaboratory comparison of ultrasonic backscatter, attenuation, and speed measurements. *Journal of ultrasound in medicine*, 18(9):615–631, 1999. 7.2.1.3

[504] Lanxess. Preventol-d7 product information, November 2008. URL http://www.lidorr.com/_Uploads/dbsAttachedFiles/D7(1).pdf. 7.2.2.1

[505] JE Carlson, J Van Deventer, A Scolan, and C Carlander. Frequency and temperature dependence of acoustic properties of polymers used in pulse-echo systems. In *Ultrasonics, 2003 IEEE Symposium on*, volume 1, pages 885–888. IEEE, 2003. 7.2.3, 7.2.4.2

[506] IEC BIPM, ILAC IFCC, IUPAP IUPAC, and OIML ISO. Evaluation of measurement data—guide for the expression of uncertainty in measurement. jcgm 100: 2008, 2008. 7.2.4

[507] Barry N Taylor. *Guidelines for Evaluating and Expressing the Uncertainty of NIST Measurement Results (rev*. DIANE Publishing, 2009. 7.2.4

[508] Daniel A Low, William B Harms, Sasa Mutic, and James A Purdy. A technique for the quantitative evaluation of dose distributions. *Medical physics*, 25(5):656–661, 1998. 7.2.5.2

[509] Daniel A Low and James F Dempsey. Evaluation of the gamma dose distribution comparison method. *Medical physics*, 30(9):2455–2464, 2003. 7.2.5.2

[510] Nzhde Agazaryan, Wolfgang Ullrich, Steve P Lee, and Timothy D Solberg. A methodology for verification of radiotherapy dose calculation. *Special Supplements*, 101:356–361, 2004. 7.2.5.2

[511] Ann Van Esch, Tom Depuydt, and Dominique Pierre Huyskens. The use of an asi-based epid for routine absolute dosimetric pre-treatment verification of dynamic imrt fields. *Radiotherapy and oncology*, 71(2):223–234, 2004.

[512] Mathilda van Zijtveld, Maarten LP Dirkx, Hans CJ de Boer, and Ben JM Heijmen. Dosimetric pre-treatment verification of imrt using an epid; clinical experience. *Radiotherapy and oncology*, 81(2):168–175, 2006.

[513] EM Franken, JCJ De Boer, and BJM Heijmen. A novel approach to accurate portal dosimetry using ccd-camera based epids. *Medical physics*, 33(4):888–903, 2006. 7.2.5.2

[514] Maarten de Bruijne, Theodoros Samaras, Nicolas Chavannes, and Gerard C van Rhoon. Quantitative validation of the 3d sar profile of hyperthermia applicators

using the gamma method. *Physics in medicine and biology*, 52(11):3075, 2007. 7.2.5.2

[515] John Mandel. *The statistical analysis of experimental data*. Courier Dover Publications, 2012. 7.2.5.2

[516] DJ Phillips, SW Smith, O Von Ramm, and F Thurstone. Sampled aperture techniques applied to b-mode echoencephalography. *Acoustical Holography*, 6:103–120, 1975. 8.1.1

[517] SW Flax and Matthew O'Donnell. Phase-aberration correction using signals from point reflectors and diffuse scatterers: Basic principles. *Ultrasonics, Ferroelectrics and Frequency Control, IEEE Transactions on*, 35(6):758–767, 1988. 8.1.1

[518] Mathias Fink. Time reversal of ultrasonic fields I: Basic principles. *Ultrasonics, Ferroelectrics and Frequency Control, IEEE Transactions on*, 39(5):555–566, 1992. 8.1.1

[519] J-L Thomas and Mathias A Fink. Ultrasonic beam focusing through tissue inhomogeneities with a time reversal mirror: application to transskull therapy. *Ultrasonics, Ferroelectrics and Frequency Control, IEEE Transactions on*, 43(6):1122–1129, 1996. 8.1.1

[520] Mathias Fink, Gabriel Montaldo, and Mickael Tanter. Time-reversal acoustics in biomedical engineering. *Annual review of biomedical engineering*, 5(1):465–497, 2003. 8.1.1

[521] Mickaël Tanter, Jean-Louis Thomas, and Mathias Fink. Focusing and steering through absorbing and aberrating layers: Application to ultrasonic propagation through the skull. *The Journal of the Acoustical Society of America*, 103:2403, 1998. 8.1.1

[522] F Vignon, JF Aubry, M Tanter, A Margoum, and M Fink. Adaptive focusing for transcranial ultrasound imaging using dual arrays. *The Journal of the Acoustical Society of America*, 120:2737, 2006. 8.1.1

[523] Kullervo Hynynen and Ferenc A Jolesz. Demonstration of potential noninvasive ultrasound brain therapy through an intact skull. *Ultrasound in medicine & biology*, 24(2):275–283, 1998. 8.1.1.1

[524] Greg T Clement and Kullervo Hynynen. Micro-receiver guided transcranial beam steering. *Ultrasonics, Ferroelectrics and Frequency Control, IEEE Transactions on*, 49(4):447–453, 2002. 8.1.1.1, 8.1.1.1, 8.1.4

[525] Ralf Seip, Philip VanBaren, and Emad S Ebbini. Dynamic focusing in ultrasound hyperthermia treatments using implantable hydrophone arrays. *Ultrasonics, Ferroelectrics and Frequency Control, IEEE Transactions on*, 41(5):706–713, 1994. 8.1.1.1

[526] Kullervo Hynynen, Gregory T Clement, Nathan McDannold, Natalia Vykhodtseva, Randy King, P Jason White, Shuki Vitek, and Ferenc A Jolesz. 500-element ultrasound phased array system for noninvasive focal surgery of the brain: A preliminary rabbit study with ex vivo human skulls. *Magnetic resonance in medicine*, 52(1):100–107, 2004. 8.1.1.1, 8.1.2.2

[527] Mathieu Pernot, Jean-Francois Aubry, Mickael Tanter, Anne-Laure Boch, Fabrice Marquet, Michele Kujas, Danielle Seilhean, and Mathias Fink. In vivo transcranial brain surgery with an ultrasonic time reversal mirror. *Journal of neurosurgery*, 106 (6):1061–1066, 2007. 8.1.1.1

[528] Mathieu Pernot, Gabriel Montaldo, Mickael Tanter, and Mathias Fink. "ultrasonic stars" for time-reversal focusing using induced cavitation bubbles. *Applied physics letters*, 88(3):034102–034102, 2006. 8.1.1.2

[529] Jérôme Gâteau, Laurent Marsac, Mathieu Pernot, J-F Aubry, Mickaël Tanter, and Mathias Fink. Transcranial ultrasonic therapy based on time reversal of acoustically induced cavitation bubble signature. *Biomedical Engineering, IEEE Transactions on*, 57(1):134–144, 2010. 8.1.1.2

[530] Kevin J Haworth, J Brian Fowlkes, Paul L Carson, and Oliver D Kripfgans. Towards aberration correction of transcranial ultrasound using acoustic droplet vaporization. *Ultrasound in medicine & biology*, 34(3):435–445, 2008. 8.1.1.2

[531] G. Pinton, J. F. Aubry, M. Fink, and M. Tanter. Numerical prediction of frequency dependent 3D maps of mechanical index thresholds in ultrasonic brain therapy. *Med Phys*, 39(1):455–467, Jan 2012. 8.1.1.3

[532] Gianmarco Pinton, Jean-Francois Aubry, Mathias Fink, and Mickael Tanter. Effects of nonlinear ultrasound propagation on high intensity brain therapy. *Medical Physics*, 38:1207, 2011. 8.1.1.3

[533] Gianmarco F Pinton, J-F Aubry, and Mickael Tanter. Direct phase projection and transcranial focusing of ultrasound for brain therapy. *Ultrasonics, Ferroelectrics and Frequency Control, IEEE Transactions on*, 59(6):1149–1159, 2012. 8.1.1.3

[534] Yun Jing, F Can Meral, and Greg T Clement. Time-reversal transcranial ultrasound beam focusing using a k-space method. *Physics in medicine and biology*, 57(4): 901, 2012. 8.1.1.3

[535] Nicolas Leduc, Kohei Okita, Kazuyasu Sugiyama, Shu Takagi, and Yoichiro Matsumoto. Focus control in hifu therapy assisted by time-reversal simulation with an iterative procedure for hot spot elimination. *Journal of Biomechanical Science and Engineering*, 7(1):43–56, 2012. 8.1.1.3

[536] GT Clement and Kullervo Hynynen. Correlation of ultrasound phase with physical skull properties. *Ultrasound in medicine & biology*, 28(5):617–624, 2002. 8.1.2.1, 8.1.3

[537] GT Clement and K Hynynen. A non-invasive method for focusing ultrasound through the human skull. *Physics in medicine and biology*, 47(8):1219, 2002. 8.1.2.2

[538] GT Clement, PJ White, and K Hynynen. Enhanced ultrasound transmission through the human skull using shear mode conversion. *The Journal of the Acoustical Society of America*, 115:1356, 2004. 8.1.2.2

[539] Laurent Marsac, Dorian Chauvet, Benoît Larrat, Mathieu Pernot, B Robert, Mathias Fink, Anne-Laure Boch, Jean-François Aubry, and Mickaël Tanter. Mr-guided adaptive focusing of therapeutic ultrasound beams in the human head. *Medical Physics*, 39:1141, 2012. 8.1.3

[540] Y Hertzberg, A Volovick, Y Zur, Y Medan, S Vitek, and G Navon. Ultrasound focusing using magnetic resonance acoustic radiation force imaging: application to ultrasound transcranial therapy. *Medical physics*, 37:2934, 2010. 8.1.3

[541] William A Grissom, Elena Kaye, Kim Butts Pauly, Yuval Zur, Desmond Yeo, Yoav Medan, and Cynthia Davis. Rapid HIFU autofocusing using the entire MR-ARFI image. In *AIP Conference Proceedings*, volume 1503, page 162, 2012. 8.1.3

[542] Urvi Vyas, Elena Kaye, and Kim Butts Pauly. Transcranial phase aberration correction using beam simulations and mr-arfi. In *AIP Conference Proceedings*, volume 1503, page 185, 2012. 8.1.3

[543] MC Gosselin, E Neufeld, H Moser, F Di Gennaro, E Huber, S Farcito, I Hilber, L Gerber, W Kainz, and N Kuster. Development of the next generation of high-resolution anatomical models: The virtual population 3.0. In *International Workshop on Computational Phantoms for Radiation Protection, Imaging and Radiotherapy Proceedings*, 2013. 8.3.1.2, 9.2.1.2

[544] Xiaoming He and John C Bischof. Quantification of temperature and injury response in thermal therapy and cryosurgery. *Critical Reviews in Biomedical Engineering*, 31(5&6), 2003. 8.3.3.1

[545] PR Stauffer and SN Goldberg. Introduction: Thermal ablation therapy. *International Journal of Hyperthermia*, 20(7):671–677, 2004. 8.3.3.1

[546] Ashley F Emery and K Michael Sekins. The use of heat transfer principles in designing optimal diathermy and cancer treatment modalities. *International Journal of Heat and Mass Transfer*, 25(6):823–834, 1982. 8.3.3.1

[547] Ilkka Laakso and Akimasa Hirata. Dominant factors affecting temperature rise in simulations of human thermoregulation during rf exposure. *Physics in medicine and biology*, 56(23):7449, 2011.

[548] Manuel Murbach, Esra Neufeld, Myles Capstick, Wolfgang Kainz, David O Brunner, Theodoros Samaras, Klaas P Pruessmann, and Niels Kuster. Thermal tissue damage model analyzed for different whole-body sar and scan durations for standard mr body coils. *Magnetic Resonance in Medicine*, 2013. 8.3.3.1

[549] JW Hand, A Shaw, N Sadhoo, S Rajagopal, RJ Dickinson, and LR Gavrilov. A random phased array device for delivery of high intensity focused ultrasound. *Physics in medicine and biology*, 54(19):5675, 2009. 9.2.1.1

[550] Stephen A Goss, Leon A Frizzell, Jeffrey T Kouzmanoff, Joseph M Barich, and Jeffrey M Yang. Sparse random ultrasound phased array for focal surgery. *Ultrasonics, Ferroelectrics and Frequency Control, IEEE Transactions on*, 43(6):1111–1121, 1996. 9.2.1.1

[551] Paolo Togni, Jan Vrba, and Luca Vannucci. Water bolus influence on temperature distribution of applicator for small melanoma tumors. In *Microwave Conference, 2009. EuMC 2009. European*, pages 874–877. IEEE, 2009. 9.2.3, 10.2.3

[552] Seyed Ali Aghayan, Dariush Sardari, Seyed Rabii Mahdi Mahdavi, and Mohammad Hasan Zahmatkesh. Estimation of overall heat transfer coefficient of cooling system in rf capacitive hyperthermia. 2013.

[553] ML Van der Gaag, M De Bruijne, T Samaras, J Van der Zee, and GC Van Rhoon. Development of a guideline for the water bolus temperature in superficial hyperthermia. *International journal of hyperthermia*, 22(8):637–656, 2006. 9.2.3, 10.2.3

[554] C Damianou and K Hynynen. The effect of various physical parameters on the size and shape of necrosed tissue volume during ultrasound surgery. *The Journal of the Acoustical Society of America*, 95:1641, 1994. 9.2.3, 10.2.3

[555] Isaac A Chang. Considerations for thermal injury analysis for rf ablation devices. *The open biomedical engineering journal*, 4:3, 2010. 9.2.3, 10.2.3

[556] Duo Chen, Rongmin Xia, Xin Chen, Gal Shafirstein, Peter M Corry, Robert J Griffin, Jose A Penagaricano, Ozlem E Tulunay-Ugur, and Eduardo G Moros. Sonoknife: Feasibility of a line-focused ultrasound device for thermal ablation therapy. *Medical Physics*, 38:4372, 2011. 10.1, 10.2.1.1, 10.2.2.1, 10.3

[557] J-L Lefebvre. Current clinical outcomes demand new treatment options for SC-CHN. *Annals of oncology*, 16(suppl 6):vi7–vi12, 2005. 10.1

[558] David Chin, Glen M Boyle, Sandro Porceddu, David R Theile, Peter G Parsons, and William B Coman. Head and neck cancer: past, present and future. 2006. 10.1

[559] Rongmin Xia, Duo Chen, Gal Shafirstein, Xin Chen, Peter Corry, Robert Griffin, and Eduardo G Moros. Experimental characterization of a sonoknife applicator. In *SPIE BiOS*, pages 79010Q–79010Q. International Society for Optics and Photonics, 2011. 10.1

[560] Xin Chen, Duo Chen, Rongmin Xia, Gal Shafirstein, Peter Corry, and Eduardo G Moros. Thermal treatment planning for sonoknife focused-ultrasound thermal treatment of head and neck cancers. In *Proceedings of SPIE*, volume 7901, page 790109, 2011. 10.2.1.2

[561] Duo Chen, Rongmin Xia, Peter M Corry, Eduardo G Moros, and Gal Shafirstein. Sonoknife for ablation of neck tissue: In vivo verification of a computer layered medium model. *International Journal of Hyperthermia*, 28(7):698–705, 2012. 10.1, 10.2.1.1, 10.2.3

# Curriculum Vitae

**Personal Data**

| | |
|---|---|
| Name | Adamos Kyriakou |
| Date of birth | $13^{th}$ January 1987 |
| Place of birth | Xanthi, Thrace, Greece |
| Citizenship | Greek |

**Education**

| | |
|---|---|
| 2009 – 2014 | *ETH Zurich, Computer Vision Laboratory, Switzerland* <br> Doctoral studies |
| 2004 – 2009 | *Democritus University of Thrace, Greece* <br> Undergraduate studies in Electrical and Computer Engineering <br> Graduation with the degree Dipl.-Ing. |
| 1998 – 2004 | *3rd General High School of Xanthi, Greece* <br> Secondary Education Degree, Exact Sciences |

**Work Experience**

| | |
|---|---|
| 2009 – 2014 | *IT'IS Foundation, Zurich, Switzerland* <br> Research Associate |
| 2009 – 2014 | *Schmid & Partner Engineering AG, Zurich, Switzerland* <br> Application Engineer (Ad-hoc position) |